MICROCOPY RESOLUTION TEST CHART

NATIONAL BUREAU OF STANDARDS-1963-A

LEVEL

AGARD-CP-238-VOL. I

AGARD

ADVISORY GROUP FOR AEROSPACE RESEARCH & DEVELOPMENT

7 RUE ANCELLE 92200 NEUILLY SUR SEINE FRANCE
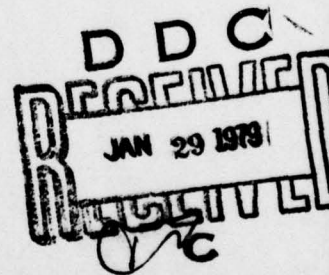
AGARD CONFERENCE PROCEEDINGS No. 238

Operational Modelling of the Aerospace Propagation Environment

Edited by

H. Soicher

Volume I

D D C
RECEIVED
JAN 29 1979
C

NORTH ATLANTIC TREATY ORGANIZATION

DISTRIBUTION AND AVAILABILITY
ON BACK COVER

NORTH ATLANTIC TREATY ORGANIZATION

ADVISORY GROUP FOR AEROSPACE RESEARCH AND DEVELOPMENT

(ORGANISATION DU TRAITE DE L'ATLANTIQUE NORD)

Conference proceedings,

AGARD Conference Proceedings No.238

OPERATIONAL MODELLING OF THE
AEROSPACE PROPAGATION ENVIRONMENT. Volume I.

(IN TWO VOLUMES)

Edited by

H.Soicher
DRDCO-COM-RF
US Army CORADCOM
Fort Monmouth, NJ 07703
USA

Nov 78

VOLUME 1

Haim / Soicher

420p.

Papers presented at a Meeting of the Electromagnetic Wave Propagation Panel
held in Ottawa, Canada, 24–28 April 1978.

JOB

400 043   79 01 26 084

THE MISSION OF AGARD

The mission of AGARD is to bring together the leading personalities of the NATO nations in the fields of science and technology relating to aerospace for the following purposes:

— Exchanging of scientific and technical information;

— Continuously stimulating advances in the aerospace sciences relevant to strengthening the common defence posture;

— Improving the co-operation among member nations in aerospace research and development;

— Providing scientific and technical advice and assistance to the North Atlantic Military Committee in the field of aerospace research and development;

— Rendering scientific and technical assistance, as requested, to other NATO bodies and to member nations in connection with research and development problems in the aerospace field;

— Providing assistance to member nations for the purpose of increasing their scientific and technical potential;

— Recommending effective ways for the member nations to use their research and development capabilities for the common benefit of the NATO community.

The highest authority within AGARD is the National Delegates Board consisting of officially appointed senior representatives from each member nation. The mission of AGARD is carried out through the Panels which are composed of experts appointed by the National Delegates, the Consultant and Exchange Programme and the Aerospace Applications Studies Programme. The results of AGARD work are reported to the member nations and the NATO Authorities through the AGARD series of publications of which this is one.

Participation in AGARD activities is by invitation only and is normally limited to citizens of the NATO nations.

Ŧ¢p

THEME

High-performance current and planned military and civilian systems operating in the aerospace environment require propagation media characterization to meet reliability and accuracy goals. The atmosphere, ionosphere, and the space environment constitute the media within which waves propagate. The users of communication, navigation and surveillance systems must have continuous background information regarding the state of these media as well as their variability and their response to natural disturbances.

Ideally, such information is available through sophisticated forecasting techniques based on media models and supported by periodic (or real-time) updating of data at specified locations. Modelling, and consequently forecasting, can and must be improved significantly through a better understanding of the governing processes of all the interrelated parts of the space environment.

The purpose of this symposium is to stimulate discussion of techniques to improve media characterization models, and to bring together scientists and engineers who are developing modelling techniques, and those who need and use them, so that they might understand each others problems.

iii

PROGRAM AND MEETING OFFICIALS

PROGRAM CHAIRMAN: Dr Haim Soicher
DRDCO-COM-RF
US Army CORADCOM
Fort Monmouth, N.J. 07703
USA

MEMBERS

Dr Kenneth Davies
NOAA/ERL
Boulder, Colorado 80302
USA

Dr Dieter H.Hohn
FPO-FGAN
Konigstrasse 2
D-5307 Wachtberg-Werthoven
F.R.G.

Dr Tudor B.Jones
Physics Dept.
University of Leicester
Leicester LE1 7RH
UK

Dr G. Lange-Hesse
Max-Planck-Institut für
Ionosphärenphysik
3411, Lindau/Harz
F.R.G.

Mr M.Petit
CNET/CRPE
38-40, rue du Général Leclerc
92131 Issy-les-Moulineaux
France

Dr C.M.Rush
AFGL/XOP
Hanscom AFB, Mass. 01731
USA

ELECTROMAGNETIC WAVE PROPAGATION PANEL

CHAIRMAN: Dr H.J.Albrecht
FGAN
Königstrasse 2
D-5307 Wachtberg-Werthhoven
Germany

DEPUTY CHAIRMAN: Dr J.Aarons
Senior Scientist
Air Force Geophysics Laboratory
L.G. Hanscom Field
Bedford, Mass. 01730, USA

HOST COORDINATOR

Dr J.S.Belrose
Communications Research Centre
Department of Communications
P.O. Box 11490, Station H
Ottawa
Canada

PANEL EXECUTIVE

Cdr D.G.Carruthers
AGARD

iv

EDITOR'S COMMENTS

It is hoped that these proceedings will constitute the state-of-the-art document on aerospace electromagnetic wave propagation models based on media characterization. These proceedings represent the totality of the AGARD/EPP symposium on "Operational Modelling of the Aerospace Propagation Environment" held in Ottawa, Canada, 24–28 April 1978.

The papers appearing in the proceedings of this symposium have been printed from copies furnished directly by the authors. For the most part, the question-and-answer comments which followed individual presentations, were written by the discussors for inclusion in these proceedings. This procedure gave the discussors the opportunity to rephrase and possibly re-think their comments. Wherever a written record of these comments was not available, the editor interpreted the comments from the taped transcription of the discussion periods. The session summaries, which highlight the subject matter presented and discussed during the session, were mostly prepared by the session chairmen. The editor wishes to thank them for their efforts here and for ably directing the presentation and discussion periods during the symposium. The general discussion portions of these proceedings were summarized by the editor from taped transcriptions. Quite often the coherency of thought is lost in the transcription, and the editor used considerable freedom in the interpretation of the comments. The editor apologizes for any changes in meaning or style that may have been made in preparing a printable version of the discussions.

The success of the symposium was assured by the collective support afforded by members of the program committee whose names are given elsewhere in these proceedings.

The editor wishes to thank the EPP Chairman and Deputy Chairman for their interest and support in the preparation and execution of the symposium. Further, he wishes to acknowledge the support of the EPP Executive and his staff in the preparation of these proceedings.

HAIM SOICHER

SESSION CHAIRMEN

SESSION I   REVIEW/IONOSPHERIC ENVIRONMENT I

Dr H.Soicher   DRDCO-COM-RF
US Army CORADCOM
Fort Monmouth, NJ 07703
USA

SESSION II   REVIEW/IONOSPHERIC ENVIRONMENT II

Dr C.M.Rush   NTIA/OT
Boulder, CO 80302
USA

SESSION III   HF (LONG TERM EMPHASIS)

Dr T.B.Jones   University of Leicester
Leicester, UK

SESSION IV   HF (SHORT TERM EMPHASIS)

Dr K.Davies   NOAA/ERL
Boulder, CO 80302
USA

SESSION V   TRANSIONOSPHERIC PROPAGATION

Dr J.Aarons   AFGL/PHP
Hanscom AFB, MA 01731
USA

SESSION VI   SOLAR-TERRESTRIAL EFFECTS

Dr G.Lange-Hesse   Max Planck Inst. für Aeronomie
Katlenberg-Lindau, FRG

SESSION VII   OPTICAL/IR ENVIRONMENT

Dr H.J.Albrecht   FGAN
Wachtberg-Werthhoven, FRG

SESSION VIII   OPTICAL SYSTEMS/PROJECTS

Dr L.F.Drummeter, Jr   NLR
Washington

SESSION IX   TROPOSPHERIC TURBULENCE

Dr J.Belrose   CRC
Ottawa, Canada

SESSION X   EHF PROPAGATION

Dr B. Van Dijl   Technology University
Eindhoven, Netherlands

CONTENTS

VOLUME 1

Page

SUMMARY OF SESSION I

REVIEW/IONOSPHERIC ENVIRONMENT

by

Dr H.Soicher
Session Chairman

This introductory session focused on four main topics: Ionospheric predictions, user propagation requirements, real time dissemination of propagation environment data to a specific system user, and geophysical disturbance conditions which may be detrimental to EM propagation.

Davies surveyed the state of the art in ionospheric predictions across the RF spectrum. While current Ionospheric prediction techniques are adequate for the long term propagation planning of communication, navigation and surveillance systems, short term predictions (forecasts) for system operation are far from adequate. The state-of-the-art in ionospheric predictions has been achieved not through a better understanding of the physical processes of the ionospheric medium, but through global data acquisition, processing and dissemination. Future improvements, however, will have to come from a better understanding of ionospheric Physics.

Thompson described the scope of capabilities and types of support offered by the Air Weather Service to users of military systems which operate in, through, or use the upper atmosphere and nearby space. The requirements include predictions with lead times from hours to months, real-time notification of solar and geophysical events within minutes, forecasts tailored to specific user requirement, and detailed post-event analysis.

Rothmuller outlined the PROPHET real-time environmental assessment terminal, which uses models to translate data from satellite and ground-based sources into performance predictions for specific systems in the frequency range of ELF to UHF. Current propagation conditions are given to an operator. When solar activity (as manifested by solar X-Ray flux) rises to levels which might affect propagation, PROPHET warns the operator of impending effects and advises him of alternatives. The normal tendency to blame "faulty" equipment for propagation outages is thus averted.

Thrane discussed the different types of disturbances in the upper atmosphere which cause anomalous propagation effects at the various bands of the RF spectrum. These include sudden Ionospheric disturbances, solar cap absorption, magnetic storms, auroral absorption, relativistic electron precipitation, travelling Ionospheric disturbances, winter anomaly, stratospheric warming, and man-made effects. The emerging understanding of the main physical mechanisms triggered by the disturbance sources, should result in usable prediction schemes for propagation effects in the future.

IONOSPHERIC PREDICTION AND EXTRAPOLATION

Kenneth Davies
Space Environment Laboratory
NOAA Environmental Research Laboratories
Boulder, Colorado 80302

I. INTRODUCTION

The ionosphere is defined as "that part of the Earth's atmosphere, above about 50 km, which contains sufficient ionization to affect the propagation of radio waves." The importance of the ionosphere to NATO follows directly from this definition because radio is a primary means of communications especially when one or both terminals is mobile (e.g. airplane, ship, land vehicle). The ionosphere affects radio signals in two ways: (a) advantageously by enabling communication (e.g., reflection) and (b) adversely by scattering, absorbing, producing multipath, etc., that interfere with optimum traffic requirements.

The radio frequency spectrum is a very valuable natural resource. It is available to be used and abused. Its efficient use is of vital importance to both military and civilian communities and it is here that modeling of the aerospace environment is important in effective planning for future utilization of the radio spectrum. Models of the radio environment are essential for prediction of radio conditions (both in the ionized and nonionized parts of the atmosphere) to enable effective circuit planning. Such models include climatological maps of: ionospheric penetration frequencies and heights, radio signal strengths, atmospheric radio noise, etc. These maps are of great value in circuit design such as frequency allocation, antenna design, transmitter power requirements, etc., all of which will be discussed, to some extent, at this meeting.

In addition to the communications uses of the ionosphere there are several other important aspects of human involvement with the ionosphere as, for example: (a) its role in producing disturbances in the geomagnetic field, (b) auroral excitation, and (c) scientific studies, etc. A list of some typical civilian and military users is given in Table 1. Geomagnetic disturbances induce large voltages in long electrical conductors such as: electrical power distribution systems (Slothower and Albertson, 1967; Albertson and Van Baelon, 1969), the 1,100 km Alaska pipeline (EOS, 1977), and also they affect geophysical prospecting and the prediction of volcanic activity based on magnetic detection (Decker, 1978).

There are, in general, two types of ionospheric predictions: (1) long term (years in advance) predictions required for the design of radio circuits, e.g. selection of radio frequencies, power requirements and antenna design, and (2) short term (days to weeks in advance) forecasts intended for use of station operators. The present ionospheric prediction systems are essentially adequate for the long term planning of frequency allocation on an international basis, and for the design of many long-distance communications circuits on high frequencies. They are also adequate for broad planning of navigation systems on very low frequencies and for the design of broadcasting services on medium frequencies.

On the other hand, short term predictions (usually called forecasts) are far from adequate. Both civilian and military communicators require improved forecast services that would enable them (a) to provide for alternative means of communication, (b) to initiate or delay rescue operations, and (c) to inform users of the cause of their transmission problems. At the present time, prospects for improvement must be considered moderate. Indeed financial cutbacks in recent years have resulted in a deterioration in forecasting services. The biggest improvements in recent years, in both long-term predictions and short-term forecasts have resulted largely from technological advances in data acquisition, processing and distribution.

2. SOCIETAL CONCERNS

Society in general, and the NATO community in particular, is vitally concerned with the ionosphere because of its role in radio communications, navigation and surveillance as well as the various other aspects given in Table 1: By far, the major societal concern with the ionosphere is the effective management and efficient utilization of radio for these purposes. Radio is important for: (1) mobile communications with high frequency waves reflected from the ionosphere, (2) communications in sparsely populated areas where alternative methods are uneconomical, and (3) communications in high latitudes where the ionosphere is frequently disturbed and which may include (1) and (2). Ionospheric communications are particularly important in Alaska, for example, where the Federal Communications Commission has assigned a special frequency of 4383.8 kiloHertz for statewide emergency use only.

Society is concerned with a number of aspects of communications, among which are the following three: (1) safety, (2) commercial, and (3) personal. In the case of safety, the value of an accurate communications forecast in saving lives can be of great importance. On the other hand, commercial usage is basically a matter of economics, and personal communications are, in general, a matter of convenience or recreation in which forecasting is of less value.

In the utilization of the radio spectrum, we must be concerned with the following characteristics (see Radio Spectrum Utilization, 1964):

(1) This resource is used--not consumed; it is wasted when not in use,
(2) It has the dimensions of space, time and frequency that can be shared,
(3) It is an international resource--available to all,
(4) The resource is wasted when assigned to tasks that can be done better in other ways,
(5) The resource is wasted when its characteristics are not correctly applied (e.g., AM broadcast band),
(6) It is subject to pollution and, therefore, needs policing.

Perhaps the greatest social pressure is that resulting from the increasing mobility of the world's population, in both business and recreation. There are more people on the move at higher speeds and radio is about the only means of communication. Communications insures more efficient business, public and private safety and national security. Thus any medium that affects radio propagation, both advantageously and adversely, is of vital concern to society.

The efficient use of the spectrum is a primary concern of radio circuit planners and operators and of national and international regulatory agencies both civilian and military. An enormous investment exists in radio equipment and this has, in several cases, been based on inadequate performance predictions, particularly when new parts of the spectrum have been newly opened. For example, the discovery of the ionosphere arose because of a wrong prediction. In 1901 Marconi successfully established radio communication between England and Newfoundland in the face of theoretical predictions that radio waves could not possibly bend around the Earth. About World War I, the prevailing prediction, based on the Austin-Cohen formula, was that for long distance transmission, long waves were superior to short waves. This prediction was upset in 1923 when the American Radio Relay League (amateurs) showed that the higher the frequency (shorter the wavelength) the higher the signal strength (see Davies, 1969, Chapter 1). In the 1950's it was incorrectly predicted that high frequency communications, which tend to be unreliable in high latitudes, would shortly be superseded by other ionospheric mechanisms that would not be affected. For example, it was predicted that the JANET system operating on radio echoes from meteor trails was free of these disturbances. The system was blacked out in its first week of trials by a polar cap absorption (see Folkestad, 1968, pages 173 and 440). With the advent of satellites it was predicted that, since the radio waves were transmitted through, rather than reflected from, the ionosphere, ionospheric effects would diminish as the square of the frequency and, therefore, be negligible on frequencies near 136 MHz. The occurrence of scintillation on these, and much higher, frequencies again showed our inability to predict correctly the characteristics of the ionosphere. Thus over and over again the feeling has been that we know enough about the ionosphere to adequately predict (or extrapolate) the behavior of an unexplored part of the spectrum only to find that we were wrong.

The state of the propagation environment is one of a number of geophysical quantities that require predictions for planning and utilization. The improvement of these predictions is of considerable importance to those involved, and efforts are underway to improve the predictions by data collection and increased understanding of the Earth's atmosphere. In assessing the effort that should go into such improvements society has to keep its relative priorities in perspective. Consider the field of geophysical predictions which include, for example: earthquakes, volcanoes, landslides, hurricanes, tornadoes, floods, tsunamis, etc.; it is important to balance improvement in one area against the demands of others and "cost effective" analyses are required. For illustration, ionospheric storms have resulted in relatively small loss of human lives whereas the July 28, 1976 earthquake took some 600,000 lives in Tangshan, the May 8, 1902 eruption of Mount Pelee, Martinique killed around 30,000 and some 200,000 persons were drowned in Bengal floods (Landsberg, 1978).

In assessing the value of a prediction, we need to know how accurate the prediction needs to be. There is no advantage in refining a prediction beyond the stage at which a user can take advantage of it.

3. THE PHYSICAL PROBLEM

3.1 The Data Base

The normal ionosphere, produced by solar extreme ultraviolet (EUV) and X-radiations, is multilayered and depicted in Figure 1. The layers are labeled alphabetically (due to Sir Edward Appleton) starting with the C layer and going up to the F layer which sometimes splits into the F1 and F2 layers. About two thirds of the total ionization in the ionosphere lies above the peak of the F2 layer, so that the topside is important in the propagation of radio signals between high orbit satellites and ground. The E region is sometimes characterized by the presence of intense partially reflecting ionization called Sporadic-E that can reflect radio waves on very high frequencies. The F region sometimes contains small scale intense irregularities (called spread F from its appearance on radio reflections) that are responsible for rapid fluctuations of radio signals.

Important ionospheric parameters for radio communications are the maximum electron density, which is related to the maximum radio frequency reflected from the overhead ionosphere, and the height of each layer. When the electron density is low a radio signal may be transmitted through the layer, if the density is sufficiently high, the signal is reflected. Alternatively, the radio power may be absorbed in the D region

because of friction between electrons and neutral molecules. These three radio effects are illustrated in Figure 2 for some sample radio frequencies.

The structure of the ionosphere and its spatial and temporal variations have been explored since 1926 using the radio pulse or ionosonde technique. The number of sounding stations have steadily increased and the distribution during the International Geophysical Year (1957-58) is shown in Figure 3. These soundings have shown that the layer densities and heights vary markedly with time of day, season, epoch of the sunspot cycle and with disturbances on the Sun.

The network of sounding stations revealed that the morphology of the ionosphere was a much more complicated function of time, geographical location, etc., than had been previously predicted. World maps of many monthly median parameters of the ionosphere were constructed from the data. One such map of the F2 layer is given in Figure 4 and shows the marked geomagnetic control of the ionosphere. These (monthly median) climatological maps have been constructed for maximum densities, layer heights, D region absorption, probabilities of sporadic E, regions of spread F, etc., and they have served an invaluable role in predicting the general state of the ionosphere. One of the problems with global ionospheric prediction is evident in Figure 3, namely the uneven distribution of sounding stations. Whereas there is a surfeit of stations in Western Europe there is a paucity in the ocean areas. Since 1962 these ground-based data sources have been supplemented by satellite-borne instruments such as the Canadian Alouette topside sounder. Radio beacons on board satellites observed on the ground enable the measurement of the total number of electrons along the raypath called the total electron content. There are also a small number of incoherent scatter radars (see Farley, 1970).

3.2 Spatial Variations

The ionosphere can be conveniently described in terms of four sets of geographical zones: the equatorial zone, two middle latitude zones, north and south auroral zones and the two polar caps.

Under normal (quiet) conditions the ionosphere in middle latitudes is relatively well behaved and some parameters, e.g. the maximum frequencies of the E and F1 layers, are simple functions of the sunspot number and the solar zenith angle (see Davies, 1965). As seen in Figure 4, in the equatorial zone the F2 layer is dominated by the geomagnetic anomaly, i.e. two maxima on either side of the magnetic equator. In the evening hours, especially near the equinoxes, the intense small scale (10 to 1000 meters) irregularities, or spread F, develop in the equatorial zone that disrupt radio communications.

The most pronounced disturbances to radio communications occur in the auroral zones which are two, approximately circular, annulii about 3° wide located near $+68^{\circ}$ of magnetic latitude in which visible aurorae are most frequently observed overhead. The aurorae result from excitation of the atmosphere by energetic electrons and protons precipitating from the magnetosphere by a triggering action of the solar wind (see White, 1977), i.e. the ionized gas flowing out from the Sun. The auroral ionosphere is characterized by: (a) high D region absorption of radio waves, (b) enhanced sporadic E and (c) spread F.

The polar caps are the circular areas lying within the two (northern and southern) auroral zones. Generally, in the polar caps the ionosphere is less disturbed than in the auroral annuli except during polar cap absorption (PCA) events. These result from intense D region ionization by energetic protons that are guided to the polar caps by the geomagnetic field and cause "polar blackout" of radio signals. PCAs are essentially daylight phenomena and last up to 2 to 3 days.

3.3 Long Term Variations

As mentioned above, the ionosphere is created by solar radiations and the most salient variations are those associated with the Sun's position (diurnal and seasonal variations), the eleven year sunspot cycle, and the prevailing state of solar flare activity. The diurnal, seasonal and sunspot variations have been mapped in the manner illustrated in Figure 4. The sunspot cycle control of the F2 and E layers for a middle latitude location can be seen in Figure 5. For sunspot numbers between 0 and about 120 there is an approximately linear relationship and above 120 the F2 penetration or critical frequencies are essentially independent of sunspot number.

Thus long term predictions of the ionosphere depend on prediction of the sunspot cycle. The magnitudes and periods of the cycles over the past 250 years, shown in Figure 6, have been so irregular that there is no reliable method of predicting a future cycle before it starts. When a new cycle is established, the predictor can extrapolate the rate of increase.

Another periodicity of the Sun, that is reflected in the ionosphere, is the approximately 27 day east-to-west rotation of the Sun. Enhanced solar radiations come from localized regions on the disc and can last for several solar rotations consequently there is an approximately 27 day variation of geomagnetic and ionospheric phenomena. This recurrence is particularly evident in the declining parts and minima of the sunspot cycles when the recurrence is not obscured by the random occurrence of new active regions (e.g., flares). This periodicity provides a welcome tool for prediction purposes.

3.4 Short Term Variations

The major short term variations, i.e. up to a few days, are associated directly or indirectly with solar flares that are large explosions on the surface (see White, 1977). The optical flare is normally observed in red H-alpha (Hα) light. Generally, the larger a flare the longer the duration which may last from 3 or 4 min. to 2 or 3 hr, the average lifetime being about one-half hour. In addition to the optical enhancement, flares emit enhanced electromagnetic radiation (X-rays and EUV), particles (electrons, protons, etc.) and radio noise. Solar flares are assigned an optical "importance" based on area S, 1, 2, 3, where S denotes a subflare, and brightness (faint F, normal N, bright B). The soft X radiation in the 1 to 8A wavelength range is also used to classify flares as C, M and X according to their peak emission. This flare classification gives a much better indication of the ionospheric importance of a flare than does the optical classification.

Solar flares are responsible for a variety of ionospheric effects, both immediate and delayed, some of which are given in Figure 7 and Table 2. The immediate effects of solar flares are grouped under the term sudden ionospheric disturbance (SID). Although they can be quite severe, fortunately they are of relatively short duration. Class X flares usually result in complete loss of an HF signal, class M flares cause minor enhancement in HF radio absorption whereas class C and smaller flares produce negligible effects on ionospheric radio waves.

Two delayed effects, viz. the polar cap absorption and the ionospheric storm, that produce the most disruptive effects on radio communications are also given in Figure 7. Flares which result in polar cap absorption are often called "proton" flares. The phases and amplitudes of very low frequency waves are particularly sensitive to PCA events. Polar cap absorptions start within a few hours of the responsible flares and decay over a few days. They are essentially daylight phenomena.

Ionospheric storms are the most disruptive of flare effects. They originate in the auroral zones, from one to three days after a large flare, and spread to other latitudes, although not all large flares are followed by storms and some storms cannot be identified with specific flares. In general, there are two stages to an F2-layer storm: (i) an enhancement of the F2 maximum density on the afternoon of the first day of the storm followed by a depression on the next few days during which recovery phase the layer returns to normal. There is also an increase in D-region ionization.

A common phenomenon in the midlatitude ionosphere is the passage of wavelike disturbances with periods ranging from about one minute to several hours. These are thought to be manifestations of acoustic-gravity waves in the neutral atmosphere and often consist of a few, one, two or three, crests and troughs. They have wavelengths of the order of a few hundred (200-400) km and speeds of the order of 100 to 600 m sec^{-1}. Ionospheric disturbances originating in earthquakes (Yuen et al., 1969) and severe thunderstorms (Davies and Jones, 1972) have also been identified. The ionospheric waves from severe thunderstorms over the central USA have periods near 4 min and travel with speeds near 1 km sec^{-1}. It is sometimes possible to predict their presence in the ionosphere from the surface radar weather charts.

Another class of short term ionospheric phenomena is that of man-made or artificial modification. This was first noticed in 1933 when it was found that the programs of one broadcasting station were sometimes impressed on a second. This is the result of the heating and cooling of the D region by the radio signals from the first station (Bailey and Martyn, 1934). Modification of the F region with powerful radio waves (Utlaut, 1975) have shown that the radio absorption in the F region increases rather than decreases as had been predicted. Another example of artificial modification includes atomic explosions (Georges, 1968) that black-out radio communications for a short time and affect the ionosphere for several days. The reaction products of rocket launches (Mendillo et al., 1975) produce holes in the F region and there are possible ionospheric effects produced by power line radiation (Helliwell et al., 1975) and very low frequency transmitters (Helliwell and Katsufrakis, 1974).

4.   IONOSPHERIC PREDICTIONS

4.1 The Radio Spectrum

The relevant radio spectrum is given in Table 3. While frequencies lower than 3 kiloHertz are affected by the ionosphere, they do not have a major societal impact. The frequencies of importance to society that are affected by the ionosphere, range from around 3 KHz to about 10,000 MHz. For an understanding of the importance of the ionosphere in radio transmission, it is necessary to review briefly the properties of the radio spectrum. We shall do this in terms of increasing radio frequency.

The lower frequency bands (VLF) have the disadvantage of limited bandwidth, high cost of installations and high ambient noise levels. The phases and amplitudes of these waves tend to be stable (under quiet conditions) and are, therefore, suitable for navigation, e.g. OMEGA navigation system. Higher frequencies have more bandwidth but are increasingly subject to phase and amplitude fluctuations, particularly those that depend on the position of the Sun (diurnal) and solar activity, e.g. sudden phase anomalies, polar cap absorptions, storms, etc.

One of the more used parts of the entire radio spectrum is the medium frequency range because of the presence of the amplitude modulated broadcast band. The operation of the broadcast band depends mainly on the reception of a dominant ground wave and this state of affairs obtains during the day when the ionosphere absorbs the sky wave. At night, when the absorption practically disappears, the sky wave is enhanced and the result is interference between stations operating on the same channel. This is an example where lack of information on the ionosphere in the early days led to a poor use of the spectrum but the enormous financial investment has prevented correction of the mistake.

The advantages of the high frequency band are: (a) the world-wide coverage and (b) the relatively low installation costs. For many years HF was the main means of long distance communication but nowadays this role is being eroded by geostationary communications satellites. The propagation of HF signals is limited on the high frequency side by the maximum electron density and on the low frequency side by radio absorption that varies inversely as the square of the radio frequency. The usable frequency range lies between the lowest usable frequency (LUF) and the maximum usable frequency (MUF). To obtain maximum signal, one should use a frequency as close as possible to the MUF. The median MUF would allow communication only 50 per cent of the time, and the radio predictors recommend an optimum working frequency (FOT from the French) of 0.85 MUF which allows communication about 90 per cent of the time at a particular hour. The MUFs and, hence, the FOTs are obtained for a given path midpoint and hour from maps such as that of Figure 4. The prediction of the optimum working frequency, while logical in principle, has turned out to be less than optimum in practice. This arises because the world's population distribution tends to be localized and the predicted MUFs and, hence, FOT are essentially the same for a large number of users. The result is spectrum congestion and radio operators often find that frequencies near the LUF give better performance; for, although the received signal is weaker, the interference is lower. The diurnal, seasonal and sunspot variations of MUF and LUF require the allocation of a set of radio frequencies for a given radio circuit. This is where ionospheric prediction is important in the planning of a major communications network. A minimum of two frequencies is necessary for 24 hour communications as illustrated in Figure 8.

The principal effect of the ionosphere on ground-to-ground communication in the lower part of the VHF band is one of providing occasional skywave interference to existing communications by one of several propagation modes via F2 and sporadic E. Sporadic E propagation is occasionally observed as high as 150 MHz. It is a common occurrence during summer mornings and evenings on the low-band TV channels (channels 2-6: 54-88 MHz) where the viewer may find a local station suddenly replaced by one in a city 150 km away.

Propagation between a ground station and an orbiting or geostationary satellite can be affected by the ionosphere up to frequencies as high as 6 GHz. This came as quite a shock as the predicted ionospheric effects fell off as inverse frequency squared and should be negligible on 100 MHz or slightly higher. That ionospheric scintillations could occasionally produce significant effects at SHF (see Table 3) was discovered in the late sixties and is found to be particularly prevalent during equinoctial evenings for propagation paths transiting the ionosphere within $\pm 20^{\circ}$ of the geomagnetic equator. In high latitudes scintillations are observed on SHF, while in middle latitudes ionospheric scintillation is less troublesome. Needless to say, considerable research is needed in this area.

A different concern in transionospheric telecommunications comes about in connection with precision navigational satellites where the group delay of ground-to-satellite signals needs to be known to a high order of accuracy. The frequency variation of the delay leads to signal distortion. Thus a knowledge of the total electron content along the radio raypath is vital to prediction of ionospheric effects.

4.2 Long Term Predictions

Long term predictions of D-region radio absorption, E, F1 and F2 penetration frequencies and layer heights are needed for the design of radio circuits. From the data base of ionospheric soundings, the world-wide and temporal variations of the ionospheric parameters have been expressed in analytical terms and stored in computers--see, for example, Haydon et al. (1976), (CCIR, 1967). For a given input, e.g. path terminals, date, time, the computer determines the maximum usable frequencies and, hence, the optimum frequencies for the various layers, angles of elevations, strength of signal, natural noise level and several other parameters of interest to the radio communicator. This type of numerical model is used extensively for applications ranging from broadcast coverage to time sharing on geographically spaced circuits. Other models for predicting vertical electron density profiles have been developed (e.g., Nisbet, 1971; Jones and Stewart, 1970).

Systems for predicting radio propagation, e.g. signal strength, have been adopted by the Consultative Committee on International Radio of the International Telecommunications Union. These include predictions for very low frequencies, low frequencies (CCIR, SG-6, 1975, p. 123) and medium frequencies (CCIR, SG-6, 1975, p. 186). The latter encompass the AM broadcast band which is the most heavily used part of the radio spectrum. The field strengths depend on time of day, magnetic latitude of the path midpoint, path length, frequency and so on. Because of the congestion of the radio spectrum in this range, accurate measurements of signal strength are difficult to make and universal agreement is difficult to achieve. Indeed, we have the peculiar situation in

which our knowledge of ionospheric propagation is least on frequencies which are used most. Much of the data for the MF prediction methods was gathered in Europe and in the U.S.A. When these predictions were applied to the magnetic equatorial zone they were found to be erroneous. One reason for this is that, for efficient radiation, vertical antennas are used for AM broadcasting, these excite the ordinary wave in middle and high latitudes, whereas, near the equator the extraordinary wave is excited which at these frequencies is heavily absorbed in the D region.

Above the high frequency band lies the very high frequency band (30-300 MHz) over which the ground wave dominates. Not infrequently, however, intense sporadic E can result in long distance propagation of VHF signals that can produce unwanted co-channel interference. A prediction method for estimating the field strength on VHF due to sporadic E reflections is given in the Annex to Report 259-3 (CCIR, SG-6, 1975, p. 223). It pertains to temperate latitudes and offers a means of estimating signal strength from world-wide levels of sporadic E. Frequencies above about 100 MHz are rarely reflected from the ionosphere, but ionospheric irregularities can produce undesirable effects on signals transmitted through the ionosphere as in ground to satellite communication. The quantities of interest here are: (a) total electron content, (b) polar cap absorption-- see CCIR, SG-6, 1975, p. 223; CCIR, SG-6, 1976, p. 86--and (c) areas of scintillations (Fremouw and Rino, 1973).

As signal-to-noise ratio is the primary parameter of interest in telecommunications, prediction of atmospheric and man-made noise are also needed. Atmospheric noise is treated in the CCIR (1964). Noise charts at VLF may be found in Watt (1967). Man-made noise is treated in Report 258-2, 3 (CCIR, SG-6, p. 68; CCIR, SG-6, 1976, p. 133).

The question often arises "How accurate are these predictions?" There is no simple answer to this question since the accuracy depends on the parameter involved, e.g. maximum F2 frequency. It also depends on the accuracy of the prediction of sunspot number which is not an ionospheric parameter, the geographical location, season, etc. The E and F1 layers are relatively well behaved and, for an accurate sunspot number, their predicted monthly median maximum electron densities are accurate to a few (≈ 5) per cent. The predictions of more variable parameters such as the maximum F2 density, sporadic E, D-region absorption are less accurate. However even at Churchill, Canada, in the highly variable auroral zone, the predicted monthly median F2 maximum frequency were only 8 per cent higher than the observed median values for June 1960 (Folkestad, 1968, 257). Probably of greater practical importance than the accuracy of the medians is the variability. The normal variations of F2 maximum frequencies in middle latitudes can easily reach $\pm$ 20% of the monthly median. The largest departures occur during magnetic disturbances. Median predicted critical frequencies of sporadic E are within 0.7 MHz of the observations. With a median value of around 3 MHz the lower decile runs around 2 MHz and the upper decile is about 6 MHz. As will be discussed later, the value of a prediction depends more on the usage than on statistics.

Some improvement in predictions can be achieved in real time by using data from selected sounding stations to update the numerical (monthly median) maps. This approach has had only limited success because the structure of the ionosphere on any one day bears only sight resemblance to the median maps. For example, a mid-latitude trough may always have a sharp latitudinal gradient of electron density, but because of its day to day movement, the gradient is smoothed out in the median maps.

4.3 Ionospheric Forecasting

Predictions for periods equal to and less than one (27 day) solar rotation are called forecasts, especially those ionospheric phenomena associated with solar flares and magnetic disturbances. Another important and useful service is ionospheric disturbance warning which is a notification that a disturbance is in progress. Forecasting and warning essentially require the same solar observation program, the main difference being in the customer requirements and the rapid communications facilities required for notification.

The first attempts at systematic forecasting of high frequency (HF) disturbances in the U.S.A. were undertaken in 1941 by the National Bureau of Standards (Agy, 1970, Chap. 2) in collaboration with the Department of Terrestrial Magnetism of the Carnegie Institution, in the form of a weekly "Advance Forecast of Radio Propagation Conditions." These forecasts were initially designed for the North Atlantic area. In 1951, this work was expanded by the Central Radio Propagation Laboratory to include the North Pacific and these forecasts were continued under the new Environmental Science Services Administration and then the Institute for Telecommunications Sciences where they were finally terminated on September 30, 1976 because of insufficient funding.

There are two preliminary data gathering stages in the preparation of these forecasts viz: solar and geophysical. The solar data include optical observations of the structure, evolution, and locations of solar active regions (plages, filaments, etc.), radio bursts, X-rays, extreme ultraviolet and where possible, particle fluxes measured by deep space probes. Essentially all solar X-ray flares observable by satellites from near the Earth are being detected. Because of the high time resolution ($\approx$ 3 sec) and intensity resolution the early rise in emission can usually be detected minutes before the flare intensity is high enough to produce significant terrestrial effects.

From information of this nature the forecaster prepares a largely subjective evaluation of the future course of solar flare activity. Practice has shown that sufficiently experienced forecasters have been able to predict the solar activity with a surprising accuracy (between 80% and 90%) and have been able to announce in advance a number (between 50% and 70%) of the more outstanding events (Agy, 1970, Chap. 5). In the present state of the forecasting art it appears that while forecasters can predict that a moderate or large flare will occur in the next several days, they cannot accurately predict when the flare will erupt nor its duration. Predictors have demonstrated skill in predicting the size of flares, i.e. large and medium. Some large flares rise and fall impulsively in Xrays while others rise and fall gradually; we are unable to predict which.

Geophysical monitoring include observations of the geomagnetic field, ionospheric radio soundings, measurements of signals from radio stars and monitoring of radio circuits over a wide frequency range. For many applications a knowledge that a disturbance is imminent or in progress is all that a user needs. When quantitative estimates are required the estimated radiation enhancement, e.g. X-rays and/or energetic particles, is used to calculate the enhanced D-region ionization and, hence, the increase in radio absorption (e.g. Morfitt, 1971; Bleiweiss, 1972).

PCAs are the results of proton flares. Because they are delayed effects (20 min to 20 hours) the forecaster has the advantage of being able to examine optical and radio data from a flare and assessing whether it will produce a PCA. Good forecasting appears to be achieved by combination of X-ray observations and the occurrence of radio noise bursts (see Agy, 1970, Chap. 11). Real-time data on energetic proton fluxes, measured by satellite instrumentation, and radio star signal strengths provide a good warning method.

By far the most important of the short term disturbances is the ionospheric storm. Since the onset of an ionospheric storm is later than that of the associated flare by between 24 hours and 72 hours, a forecaster has a relatively good opportunity to forecast it from the flare characteristics. Ionospheric storms are fairly closely related to geomagnetic storms which may last from a few hours to several days. They are also associated with auroral activity and the D-region effects associated with storms are often referred to as auroral absorption events because they are most intense near the auroral zone.

From a climatological viewpoint storm occurrence follows the sunspot cycle, with some phase lag, and exhibits a marked 27-day recurrence. This recurrence provides a successful prediction technique especially at sunspot minima. The most probable time of occurrence is in the morning and the least probable occurrence in the evening. The intense absorption leads to radio blackout on HF. The total time of occurrence of radio blackout in the northern hemisphere shows two peaks, one near Alaska, the other near Scandinavia, with about 8 per cent blackout (Davies, 1965, Chap. 6). The blackout pattern and the region of depressed F2 critical frequency tends to move around with the sun and, once recognized, the progress of the storm can be forecast. On the afternoon following a magnetic sudden commencement the F2 critical frequency, over North America, may rise to exceptionally high values (positive phase) and this is often followed on the next day by severely depressed critical frequencies and, hence, a constricted usable frequency spectrum.

Although the climatological (average) picture of ionospheric storms has been established with reasonable confidence it is of little value in forecasting the detailed history of an individual storm. It is now clear that at a given geographical location no two storms are exactly alike and a given storm, at two different locations, rarely produces identical responses.

Turning to forecasting procedures, the primary solar forecasting centers in the U.S.A. are the U.S. Air Force operation located at Global Weather Central in Omaha, Nebraska, and the NOAA Space Environment Forecast Center in Boulder, Colorado. The solar part of the Air Force forecasting is carried out jointly with NOAA, with Air Force personnel stationed in Boulder. As of 1971, Simon and McIntosh (see McIntosh and Dryer, 1972, p. 343) report that there were about 14 centers issuing short term forecasts of solar activity and/or ionospheric parameters. Of the fourteen, twelve are grouped into the International Ursigram and World Days Service (IUWDS) for the exchange of data and cooperation in solar geophysical observations. The IUWDS provides a means of exchange of data information within 48 hours of its collection for the preparation of short-term forecasts. Once a day the regional centers exchange summaries on solar-geophysical data.

Disturbance warning and/or forecasting is achieved via four stages: (1) observations and data transmission, (2) data processing and display, (3) evaluation and forecast, and (4) dissemination (see Williams, 1976). This involves the use of satellites: (a) to acquire data and (b) to transmit in real time data from ground-based sensors to a central data base. Additional data are taken in pictorial form and transmitted on facsimile systems similar to those used for satellite weather pictures. A sample solar-geophysical forecast is given in Figure 9. Normal data dissemination procedures include direct computer-to-computer links with real-time systems, user terminals, telephones, teletype reports and forecasts, a weekly summary of solar-terrestrial activity issued by the Space Environment Services Center (SESC), and special requests. The solar and geomagnetic data are converted by the Global Weather Central of the U. S. Air Force

into a plain language HF Radio Propagation Report, an example of which is shown in Figure 10.

Several studies have been made to establish the quantitative verification of solar flare forecasts (e.g. McIntosh and Dryer, 1972, p. 343, p. 429) and the statistics show that, given the active solar centers, the one day forecasts are about 80% successful (Agy, 1970, Chap. 5). These success scores do not necessarily imply their usefulness because of the wide variety of user needs. Most users are more concerned with the catastrophic events than in minor disturbances so that the statistics may be misleading. Thus a forecaster may err in 98 small events but if he correctly forecasts the two major storms, his statistical performance will be poor but his reputation good. This argument may apply to the unconventional method of flare prediction based on planetary conjunctions (e.g. Gassmann, 1963, p. 293, and Agy, 1970, Chap. 7).

Various systems have been devised to ascertain the usefulness and reliability of short term ionospheric disturbance forecasts (see CCIR, 1963). Tests made in the United Kingdom lead to the following: (1) The 27 recurrence cycle is good enough to use in radio traffic handling decisions. (2) For nonrecurrent storms the forecasts are essentially that which would be expected by chance. (3) The short term (1 to 6 hour) forecasts are accurate enough to justify their use.

5. CONCLUDING REMARKS

It has been seen that major errors have been made in predicting the role of the ionosphere in radio telecommunications several of which have resulted in major economic consequences. With the advent of submarine cables, tropospheric microwave links and satellite transmissions, predictions that "HF communications will soon be dead" have been common. Such predictions have not been realized because world conditions have changed and especially the demands of new nations for places in the short-wave band, with its relative economy, have led to unprecedented congestion of the HF band.

In spite of many shortcomings the various methods of predicting maximum usable frequencies have proven invaluable over the past 30 or 40 years in optimum circuit design and efficient frequency utilization of the high frequency radio spectrum. It is often argued that more accurate ionospheric data are needed for this type of prediction but this is only partly true. There is little point in predicting parameters to an accuracy that the user is incapable of applying, e.g. predicting sunspot numbers above 120 for the determination of critical frequencies. The radio frequency allocation system tends to be inflexible and, once an operator has received his (her) frequency allocation his ability to use accurate ionospheric predictions is severely circumscribed. Ionospheric predictions are of value, however, in alerting the operator so that transmitter frequency changes can be made with the minimum of disruption to circuit operation. The present frequency prediction systems are, therefore, sufficient for many user purposes and future progress is likely to come not by increased accuracy but by more intelligent application.

Turning now to the value of short term forecasts, these are of considerable value to certain users especially those in isolated high-latitude locations at which ionospheric communication is the only contact with the outside world. Some ways in which the forecasts have been of value are: (a) the priority material can be passed before the radio channel closes, (b) the operator can switch to an alternative more expensive link such as cable, satellite, low latitude relay if any of these are available, and (c) the operator is warned his equipment is not malfunctioning and it is not necessary to call a service man. It goes without saying that educated operators are essential for effective utilization of ionospheric predictions and forecasts.

ACKNOWLEDGMENTS

REFERENCES

Agy, V., ed. (1970). *Ionospheric Forecasting*. AGARD Conference Proceedings No. 49, Technical Editing and Reproductions Ltd., London.

Albertson, V. D. and J. A. Van Baelon (1969). Electric and magnetic fields at the earth's surface due to auroral currents. IEEE Trans., v. PAS-89, pp. 578-584.

Bailey, V. A. and D. F. Martyn (1934). The influence of electric waves on the ionosphere. Phil. Mag, v. 18, p. 369.

Bleiweiss, M. P. (1972). Solar X-ray spectrum definition and the prediction of ionospheric radio wave propagation. Technical Report No. NELC/TR 1840, Naval Electronics Laboratory Center, San Diego, California.

CCIR (1963). Documents of the Xth Plenary Assembly. Vol. II. International Telecommunication Union, Geneva, pp. 252-254.

CCIR (1964). World Distributions and Characteristics of Atmospheric Noise. Report 322. International Telecommunication Union, Geneva.

CCIR (1967), CCIR Atlas of Ionospheric Characteristics, Report 340, International Tele-communication Union, Geneva.

CCIR SG-6 (1975). Ionospheric Propagation (SG-6), CCIR XIIIth Plenary Assembly; Geneva, 1974; Volume VI. International Telecommunication Union, Geneva.

CCIR SG-6 (1976). Conclusions of the Interim Meeting of Study Group 6 (Ionospheric Propagation), Geneva, 16 Feb. - 3 March 1976. DOC 6/177-E International Telecom-munication Union, Geneva.

Davies, K. (1965). Ionospheric Radio Propagation. NBS Monograph 80, U.S. Govt. Print-ing Office, Washington, DC 20402; also Dover Publications Inc., New York (1966); also (In Japanese) Corona Press Ltd., Tokyo (1966).

Davies, K. (1969). Ionospheric Radio Waves. Ginn-Blaisdell, Waltham, Mass.

Davies, K. and J. E. Jones (1972). Ionospheric Disturbances Produced by Severe Thunder-storms. NOAA Professional Paper No. 6, U.S. Govt. Printing Office, Washington, DC 20402.

Decker, R. W. (1978). State-of-the-art in volcano forecasting. In Geophysical Pre-dictions, editor H. Landsberg, National Research Council, U.S.A.

EOS (1977), Trans. Am. Geophys. Union, 58, (9), 846.

Farley, D. T. (1970), Incoherent scattering at radio frequencies, J. Atmos. Terr. Phys., v. 32, (4), 693-704.

Folkestad, K., ed. (1968). Ionospheric Radio Communications. Plenum Press, New York.

Fremouw, E. J. and C. L. Rino (1973). An empirical model for average F-layer scintil-lation at VHF/UHF. Radio Sci., v. 8, pp. 213-222.

Gassmann, G. J., ed. (1963). The Effect of Disturbances of Solar Origin on Communica-tions. AGARDograph 59, Pergamon Press, Oxford.

Georges, T. M., ed. (1968). Acoustic-Gravity Waves in the Ionosphere. U.S. Government Printing Office, Washington, D. C. 20402.

Haydon, G. W., M. Leftin and R. Rosich (1976). Predicting the Performance of High Frequency Sky-wave Telecommunication Systems (the use of the HFMUFES 4 Program). OT Report 76-102, Institute for Telecommunication Sciences, Office of Telecommuni-cations, U.S. Department of Commerce, Boulder, CO 80302. U.S. Government Printing Office, Washington, DC 20402.

Helliwell, R. A. and J. P. Katsufrakis (1974). VLF wave injection into the magneto-sphere from Siple Station, Antarctica. J. Geophys. Res., v. 79, pp. 2511-2518.

Helliwell, R. A., J. P. Katsufrakis, T. F. Bell and R. Raghuram (1975). VLF line radi-ation in the earth's magnetosphere and its association with power system radiation. J. Geophys. Res., v. 80, pp. 4249-4258.

Joint Technical Advisory Committee (1964). Radio Spectrum Utilization. Institute of Electrical and Electronic Engineers and Electronic Industrial Association, New York.

Jones, W. B. and F. G. Stewart (1970). A numerical method for global mapping of plasma frequency. Radio Sci., v. 5, pp. 773-784.

Landsberg, H. (1978), Geophysical Predictions, National Research Council, Washington, D. C., U.S.A.

McIntosh, P. S. and M. Dryer, eds. (1972). Solar Activity and Predictions. Progress in Astronautics and Aeronautics, v. 30, MIT Press, Cambridge, Mass.

Mendillo, M., G. S. Hawkins and J. A. Klobuchar (1975). A sudden vanishing of the ionospheric F region due to the launch of Skylab. J. Geophys. Res., v. 80, pp. 2217-2228.

Morfitt, D. G. (1971). Analysis of a Multimode Propagation Concept for Predicting VLF Signal Strengths at Night. Technical Report No. NELC/TR 1798, Naval Electronics Laboratory Center, San Diego, California.

Nisbet, J. S. (1971). On the construction and use of a simple ionospheric model. Radio Sci., v. 6, pp. 437-464.

Slothower, J. C. and V. D. Albertson (1967). The effects of solar magnetic activity on electric power systems. J. Minn. Acad. Sci., v. 34, pp. 94-100.

Utlaut, W. F. (1975). Ionospheric modification induced by high-power HF transmitters--a potential for extended range VHF-UHF communications and plasma physics research. Proc. IEEE, v. 63, pp. 1022-1043.

Watt, A. D. (1967). VLF Radio Engineering. Pergamon Press, New York.

White, O. R. (1977). The Solar Output and its Variability, Colorado Associated University Press, Boulder, Colorado 80302.

Williams, D. J. (1976). SELDADS: An Operational Real-Time Solar-Terrestrial Environment Monitoring System. NOAA Tech. Report ERL 357-SEL 37, U.S. Govt. Printing Office, Washington, DC 20402.

Yuen, P. C., P. F. Weaver, R. K. Suzuki, and A. S. Furumoto (1969). Continuous, traveling coupling between seismic waves and the ionosphere evident in May 1968 Japan earthquake. J. Geophys. Res., Space Phys., v. 74, pp. 2256-2264.

TABLE 1

Typical Users of the Ionosphere

Primary customer application areas and times when their systems are most affected by environmental anomalies, primarily local.

customer	day or night effects*	type of activity producing effect
Civilian satellite communication	night	Magnetic storms
Commercial aviation—mid-latitude communication (VHF)	day	Solar radio emissions
Commercial aviation—polar cap communication (HF)	day & night	PCA, magnetic storms
Commercial aviation navigation (VLF)	day & night	PCA, magnetic storms
Electric power companies	day & night	Magnetic storms
Long line telephone communication	day & night	Magnetic storms
High altitude polar flights, radiation hazards	day & night	Solar proton events
Civilian HF communication Coast Guard, GSA, commerical companies, VOA	day & night	X-ray emission, U.V. emission, magnetic storms
Geophysical exploration	day	Magnetic storms
Satellite orbital variation military and civilian	day & night	U.V. emission, magnetic storms
DOD SATCOM communication	night	Magnetic storms
DOD HF communication	day & night	X-ray emission, U.V. emission, PCA, magnetic storms
DOD reconnaissance	day & night	PCA, magnetic storms
DOD navigation	day & night	X-ray emission, U.V. emission
ERDA communication prospective customers	day & night	X-ray emission, U.V. emission, magnetic storms
International community	day & night	All
Scientific satellite studies IMS, Solar Maximum mission, Shuttle, solar constant measurements, stratospheric ozone variation, interplanetary missions	day & night	Optical solar flares, magnetic storms, X-ray emission, U.V. emission, solar proton events, solar features
Scientific rocket studies IMS, magnetosphere, ionosphere, upper atmosphere, sun	day & night	Optical solar flares, solar features, magnetic storms, solar proton emission, X-ray emission
Scientific ground studies IMS, sun, interplanetary, magnetosphere, ionosphere, upper atmosphere, stratosphere, troposphere, seismological/geomagnetic	day & night	Optical solar flare, magnetic storms, solar proton emission, X-ray emission, U.V. emission, solar features

*at or near solar maximum.

TABLE 2

Sudden Ionospheric Disturbances

PHENOMENON	FREQUENCY BANDS INVOLVED
Sudden Frequency Deviation (SFD)	HF
Short-Wave Fadeout (SWF)	HF and Lower VHF
Sudden Phase Anomaly (SPA)	VLF
Sudden Enhancement of Atmospherics (SEA)	LF
Sudden Enhancement of Signal (SES)	VLF
Sudden Cosmic Noise Absorption (SCNA)	HF and Lower VHF

TABLE 3

The Radio Spectrum

Name	Frequency Range	Primary Propagation Modes	Primary Uses
Very Low Frequency (VLF)	3 - 30 kHz	Waveguide (between Ground and Lower Ionosphere) and Ground Wave	Navigation, Communications Standard Frequency and Time
Low Frequency (LF)	30 - 300 kH⁻	Waveguide and Ground Wave	Maritime, Loran C, Broadcasting
Medium Frequency (MF)	300 - 3000 kHz	E Region Reflection (Night) and Ground Wave	Maritime, Aeronautical, International Distress AM Broadcasting, Maritime and Land Mobile
High Frequency (HF)	3 - 30 MHz	Reflection from E and F Regions	Maritime and Aeronautical Fixed Services, Broadcasting, Amateurs, Citizens
Very High Frequency (VHF)	30 - 300 MHz	Line of Sight, Scatter from Ionospheric Irregularities, E_s	Television, FM Broadcasting Public Safety, Mobile, Aeronautical
Ultra High Frequency (UHF)	300 - 3000 MHz	Line of Sight, Affected by Ionospheric Irregularities	Space Communications, Television, Radar, Broadcasting, Navigation Fixed, Mobile
Super High Frequency (SHF)	3000 - 30,000 MHz	Line of Sight, Tropospheric, Affected by Ionospheric Irregularities	Space Communications, Television, Radar, Broadcasting, Navigation Fixed, Mobile
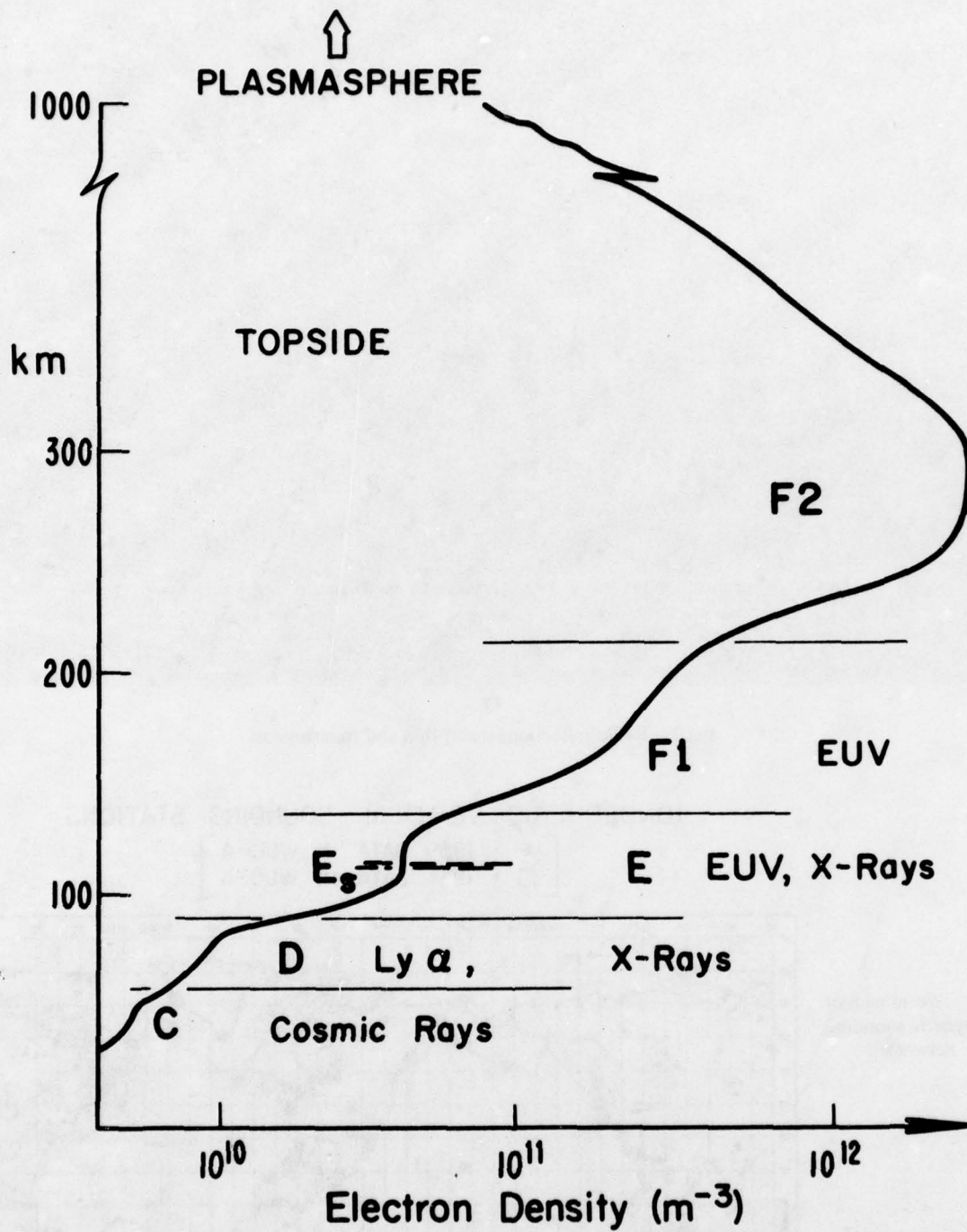
Fig. 1 Vertical profile of ionosphere

HIGH FREQUENCY (SHORT WAVE) TRANSMISSION PATHS THROUGH THE IONOSPHERE

AS THE FREQUENCY OF THE RADIO WAVE INCREASES, THE WAVES PENETRATE DEEPER INTO THE IONOSPHERE, UNTIL A MAXIMUM FREQUENCY IS REACHED ABOVE WHICH REFLECTION IS IMPOSSIBLE BECAUSE THE ELECTRON DENSITY IS INSUFFICIENT.

AS THE FREQUENCY IS DECREASED, THE WAVE SUFFERS GREATER ABSORPTION IN THE "D" REGION, WHERE THE WAVE ENERGY IS CONVERTED INTO HEAT. THERE IS A LOWER FREQUENCY LIMIT BELOW WHICH THE REFLECTED WAVE IS TOO WEAK TO BE OF USE.

Fig.2   Radio reflection, absorption and transmission

IONOSPHERIC VERTICAL SOUNDING STATIONS

● = 1959 DATA IN WDC-A
□ = 1961 DATA IN WDC-A

Fig.3   World map of ionospheric sounding network
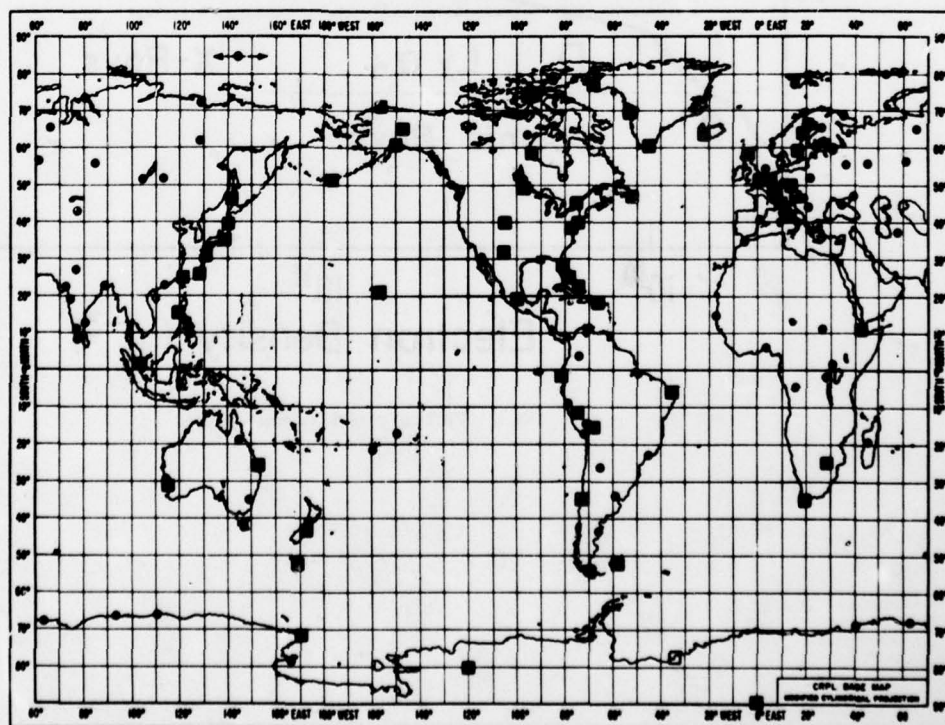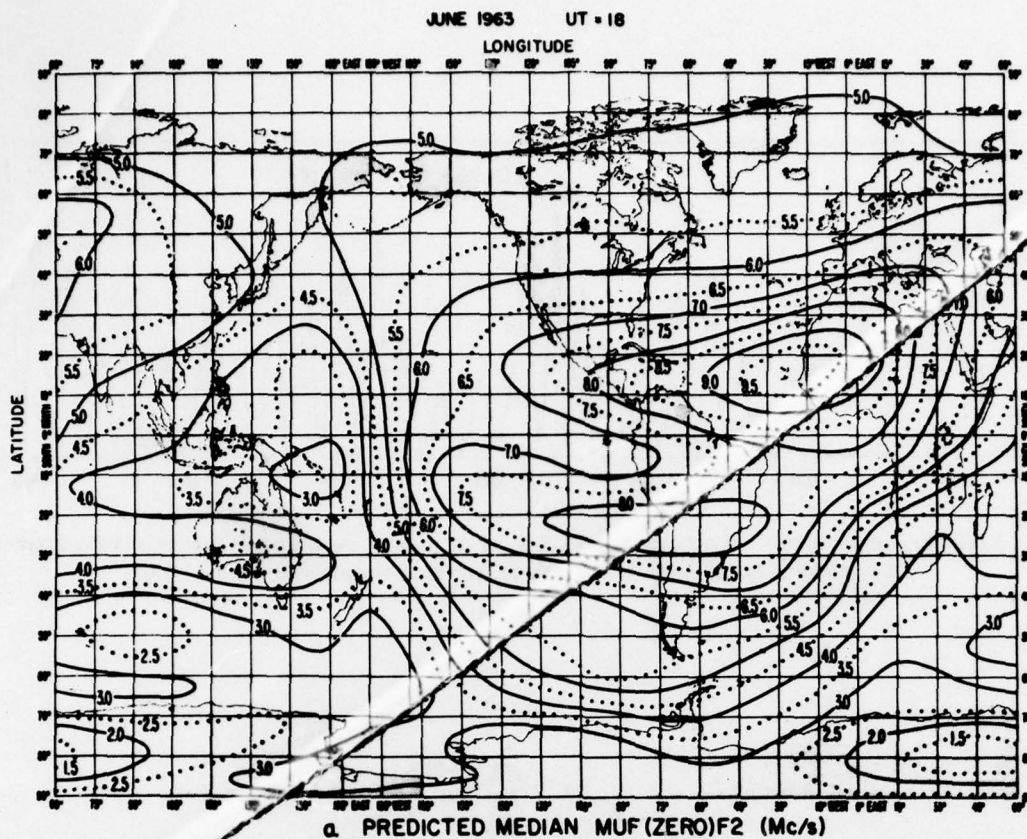
Fig.4 World map of maximum frequency reflected from F2 with vertical propagation
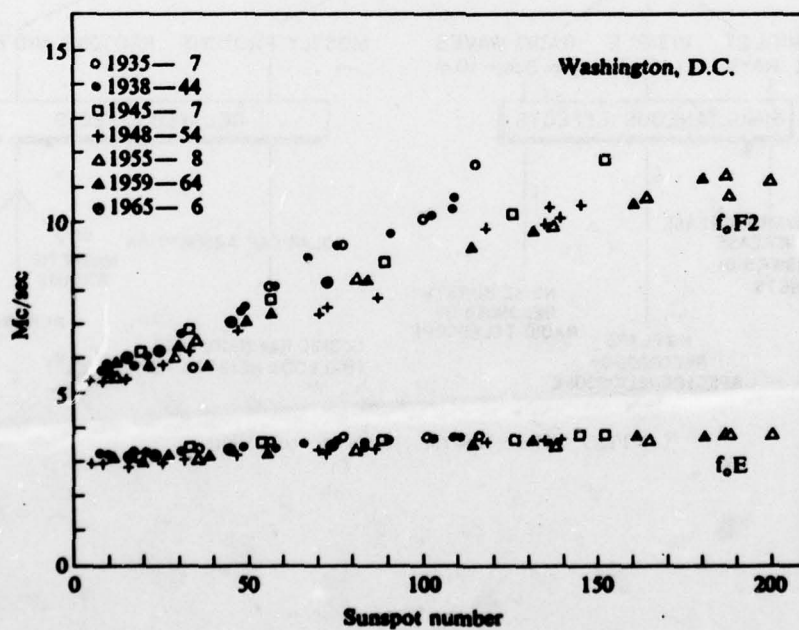
Fig.5 Variation of critical frequencies with sunspot number
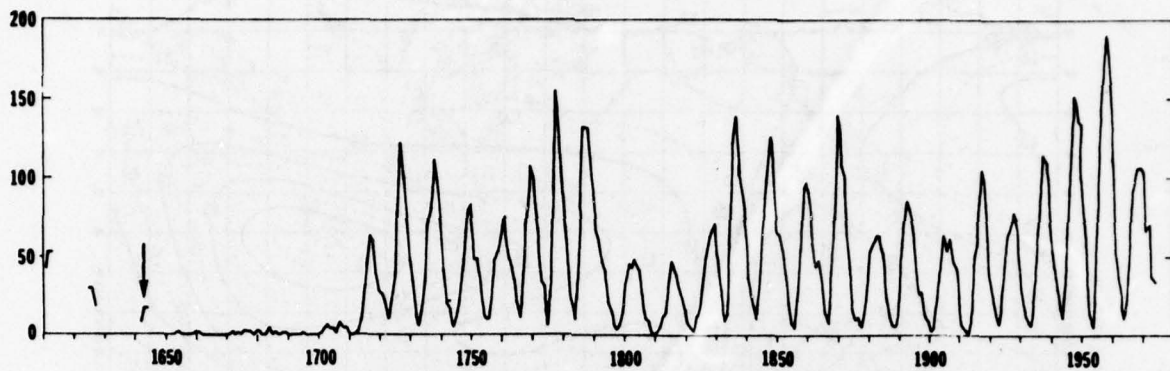
Fig.6   Sunspot numbers 1610-1970 A.D. (Akasofu, S.-I., 1976, Solar cycle review, in *Physics of Solar-Planetary Environments, Vol.1*, editor D.J.Williams, American Geophysical Union, 1-33)
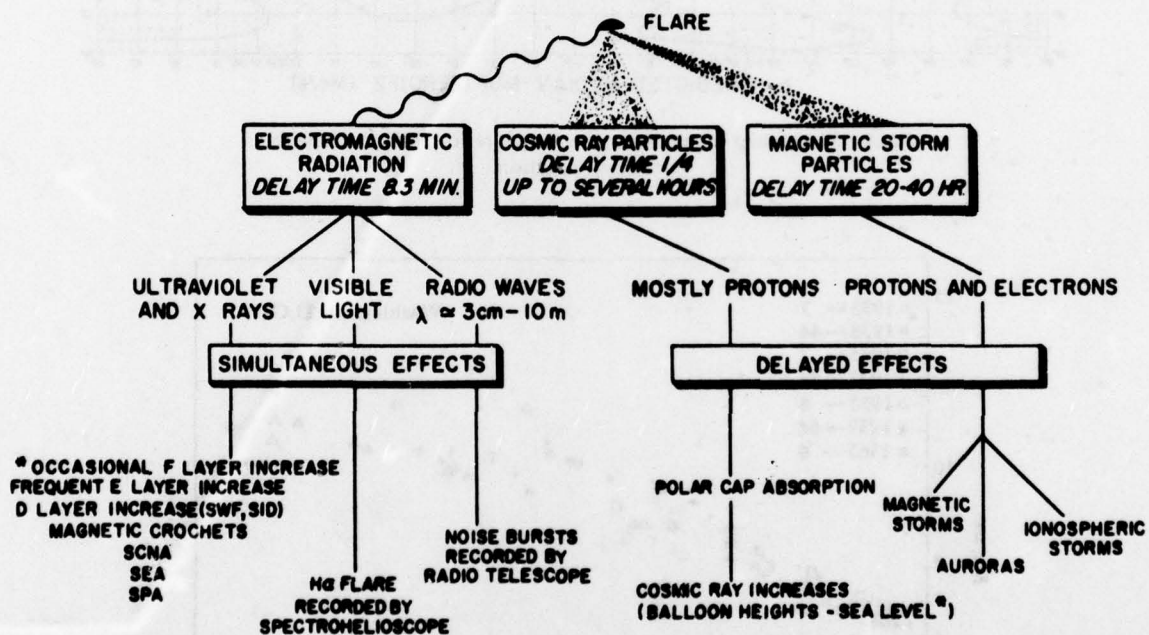
Fig.7   The terrestrial effects of a solar flare
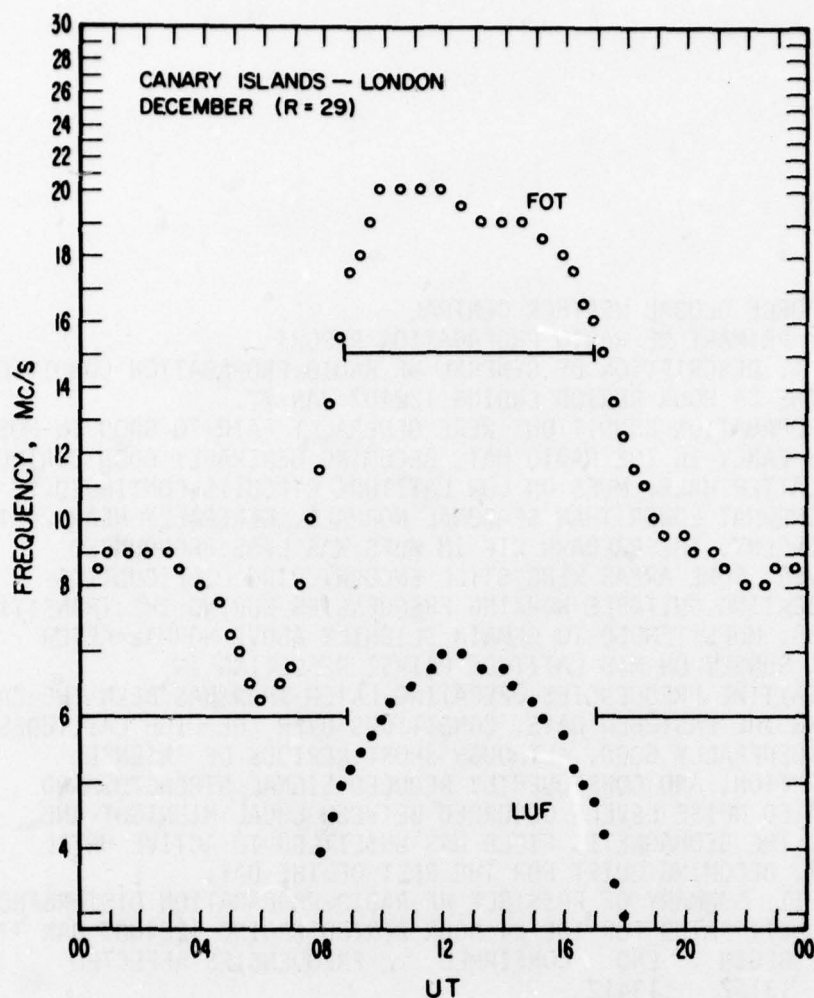
Fig.8 Diurnal variations of optimum working frequency and lowest usable frequency

FROM SPACE ENVIRONMENT SERVICES CENTER BOULDER COLO
SDF NUMBER 200
JOINT AFGWC/SESC PRIMARY REPORT OF SOLAR AND GEOPHYSICAL ACTIVITY ISSUED
2200Z 19 JULY 1974
IA. SOLAR ACTIVITY HAS BEEN VERY LOW WITH THREE NON-ENERGETIC SUBFLARES
REPORTED DURING THE PAST 24 HOURS. REGIONS 438 (S08W72) AND 443 (S12E06)
HAVE BEEN STABLE. MINOR INTENSITY FLUCTUATIONS HAVE OCCURRED IN REGIONS
442 (S10W34) AND 445 (S04W37). AN ACTIVE PROMINENCE (S13E90) PARTIALLY
ERUPTED, AND THEN TOTALLY DISSIPATED, BETWEEN 0715-0840Z. NO OTHER ACTI-
VITY HAS BEEN REPORTED TO SUBSTANTIATE AN ACTIVE RETURN OF OLD REGION 435.
IB. SOLAR ACTIVITY IS EXPECTED TO REMAIN LOW.
II. THE GEOMAGNETIC FIELD HAS BEEN QUIET. IT IS EXPECTED TO BE QUIET TO
UNSETTLED.
III. EVENT PROBABILITIES 20 - 22 JULY
CLASS M 03/03/03
CLASS X 01/01/01
PROTON 01/01/01
PCAF GREEN
IV. OTTAWA 10.7 CM FLUX
OBSERVED 19 JULY 84
PREDICTED 20 - 22 JULY 83/85/85
90-DAY MEAN 19 JULY 90
V. GEOMAGNETIC A INDICES
OBSERVED FREDERICKSBURG 18 JULY 06
ESTIMATED AFR/AP 19 JULY 04/06
PREDICTED AFR/AP 20 - 22 JULY 07/08 - 09/10 - 11/12

Fig.9 Sample report of solar and geophysical activity.

AIR FORCE GLOBAL WEATHER CENTRAL
DAILY PRIMARY HF RADIO PROPAGATION REPORT
PART I. DESCRIPTION OF GENERAL HF RADIO PROPAGATION CONDITIONS
FOR THE 24 HOUR PERIOD ENDING 1224OZ JAN 77.
HF PROPAGATION CONDITIONS WERE GENERALLY FAIR TO GOOD IN MOST
AREAS EARLY IN THE RADIO DAY, BECOMING GENERALLY GOOD DURING
THE LATTER HALF. MUFS ON LOW LATITUDE CIRCUITS CONTINUED TO
BE SOMEWHAT LOWER THAN SEASONAL NORMALS, GENERALLY NEAR 20 TO
30 PERCENT. THE PREDAWN DIP IN MUFS WAS LESS PRONOUNCED
HOWEVER, SOME AREAS WERE STILL ENCOUNTERING DIFFICULTIES
IN LOCATING SUITABLE WORKING FREQUENCIES DURING THE TRANSITION
PERIOD. MUFS TENDED TO REMAIN SLIGHTLY ABOVE NORMAL AFTER
LOCAL SUNSET ON MID LATITUDE PATHS, RESULTING IN
THE DAYTIME FREQUENCIES OPERATING LATER THAN HAS BEEN THE CASE
DURING THE PAST FEW DAYS. CONDITIONS OVER THE HIGH LATITUDES
WERE GENERALLY GOOD, ALTHOUGH SHORT PERIODS OF INTENSE
ABSORPTION, AND CONSEQUENTLY REDUCED SIGNAL STRENGTHS AND
ELEVATED NOISE LEVELS OCCURRED BETWEEN LOCAL MIDNIGHT AND
DAWN. THE GEOMAGNETIC FIELD WAS UNSETTLED TO ACTIVE UNTIL
1500Z, BECOMING QUIET FOR THE REST OF THE DAY.
PART II. SUMMARY OF POSSIBLE HF RADIO PROPAGATION DISTURBANCES
ON SUNLIT PATHS FOR THE 24 HOUR PERIOD ENDING 1224OZ JAN 77.

BEGIN	END	CONFIRMED	FREQUENCIES AFFECTED
1315Z	1341Z		
1746Z	1825Z		
1924Z	1944Z		
2144Z	2220Z	YES	UP TO 11 MHZ

PART III. OUTLOOK FOR GENERAL HF RADIO PROPAGATION CONDITIONS
FOR THE 24 HOUR PERIOD BEGINNING 1304OOZ JAN 77.
HF PROPAGATION CONDITIONS WILL CONTINUE TO SHOW IMPROVEMENT
OVER MOST AREAS. MUFS WILL REMAIN GENERALLY BELOW SEASONAL
NORMALS OVER THE LOWER LATITUDES, BUT WILL BE NEAR NORMALS
ELSEWHERE. THE GEOMAGNETIC FIELD SHOULD BE GENERALLY
QUIET, ALTHOUGH SOME SLIGHTLY UNSETTLED PERIODS ARE LIKELY
FOR BRIEF PERIODS DURING THE NIGHTTIME HOURS. THE CHANCE OF
A SOLAR FLARE INDUCED SHORT WAVE IS MODERATE.

Fig.10   Sample HF radio propagation report

DISCUSSION

H.Soicher, US

Would you describe the Bottomside Sounder Program at NOAA? What is the current number and geographic spread of Ionosondes used?

Author's Reply

NOAA is developing new computer-controlled sounders, which may be programmed to do different types of soundings. Data analysis is facilitated by digital techniques. The number of Ionosondes in the world network has stayed fairly constant, although the Ionosondes are getting older and are increasingly difficult to operate.

E.R.Schmerling, US

With 50 years of background Ionospheric data:

(1) Under quiet solar conditions, do we have sufficient information so that we can make one spot calibration measurement (either radiation from the sun, or Ionosonde Profile), get the map that approximately corresponds to those conditions and have a pretty fair picture of what the Ionosphere looks like?

(2) Under sporadic conditions (flares, substorms) can we again search for a background map that approximates the average Ionosphere occurring under those conditions, and superimpose on that theory based on measuring solar activity within the past few days?

Author's Reply

Maps are fine for long-term purposes (monthly medians etc.). If one makes a spot measurement at, say, Ottawa and discovers the MUF to be 1 MHz above the average, one cannot say that the MUF at, say, Boulder will be similarly 1 MHz above the average, there.

The thing that has changed the Ionospheric prediction picture is not what we have learned about the physics of the Ionosphere, but rather Technology: Data acquisition, processing and dissemination.

L.W.Barclay, UK

Dr Davies has indicated that long-term Ionospheric predictions are possible now while short-term predictions need to be improved and depend on the subjective interpretation of the man who is doing the forecast. How can the forecaster be trained to be objective in his predictions?

USER REQUIREMENTS OF AEROSPACE
PROPAGATION-ENVIRONMENT
MODELING AND FORECASTING

RICHARD L. THOMPSON, Major, USAF
HQ AFGWC
Offutt AFB, Nebraska

ABSTRACT

The Air Weather Service provides both broadscale and mission tailored support to military electromagnetic communications, surveillance, and warning systems which operate in, through, or use the upper atmosphere and nearby space. The Space Environmental Support System, a component of the Air Weather Service, provides environmental forecasting and specification services in these major technical areas: (1) forecasting and specification of ionospheric variability, (2) forecasting and specification of solar flare and solar particle events, and (3) providing geomagnetic and solar indices to users for determining density variability. Customer requirements for support include forecasts with lead times ranging from hours to months, real-time notification of solar and geophysical events within minutes, forecasts tailored to specific user requirements, and detailed post-analysis studies. Specification and prediction models currently in operational use, the worldwide solar and geophysical observing network, and the data handling and processing system are described. The development and present status of operational forecasting and skills in the areas of High Frequency propagation, vertical electron density profiles, total electron content, solar and geophysical indices, and solar radiation are discussed. Future military applications and use of space environment support are also discussed along with selected technologically deficient areas.

1.   INTRODUCTION

    The United States Air Force has been active in space environment forecasting activities for the past fourteen years. The Space Environmental Support System (SESS) of the Air Weather Service (AWS) was chartered to provide environmental support to military space and communication systems whose operation was affected by either the sun or the near earth environment. Fulfillment of this mission requires a variety of data, techniques, models, specially trained personnel, and large computer resources. This paper will trace the development of SESS, present the present capabilities and models, and look toward future research requirements.

2.   HISTORY

    Although earlier pioneers in space forecasting were active shortly after World War II, the only Air Force interest in the sun was manifested by the construction of the Sacramento Peak Observatory in New Mexico. After launch of the Soviet Sputnik in 1957, the Air Force asked the Air Weather Service to form an organization to provide support to space operations, much as lower atmospheric meteorological support is provided to aircraft by meteorologists. The system began to take shape in the early sixties and by October 1962, the USAF issued its first solar forecast from Scott Air Force Base, Illinois. The operation expanded rapidly and moved to Ent Air Force Base, Colorado, where it began continuous operation in September 1965. Shortly thereafter, the operation moved into the newly constructed Cheyenne Mountain Complex where it stayed for the next eight years. During this time, a worldwide solar optical observing network was established along with two radio observing sites (Sagamore Hill, Massachusetts and Manila, Republic of the Philippines). Solar x-radiation and proton data were observed by the VELA satellite system. The center operated during the solar maximum conditions of solar cycle 20, and provided support to North American Air Defense Command (NORAD) radar surveillance systems, Strategic Air Command (SAC) high frequency (HF) radio circuits, and a variety of the space systems.

    In 1973, the production center of SESS was moved from Cheyenne Mountain to the Air Force Global Weather Central (AFGWC), Offutt AFB, Nebraska. This allowed the SESS to grow by significantly increasing the use of computers to assist the forecasters. One of the first undertakings was to convert the manual processing of VELA data at Sunnyvale, California, to computer processing and detection of solar events at AFGWC. This task was accomplished by utilizing a great deal of assistance from the Air Force Geophysical Laboratory (AFGL) (formerly Air Force Cambridge Research Laboratory). VELA data are still processed but are now severely limited due to spacecraft age. The Space Environmental Support Branch at AFGWC continues the trend toward automation and now automatically processes data from a variety of sources to support its DoD commitments.

    As in any other endeavor, SESS is no better than its people. Generally, one of the forecasters on duty at AFGWC has an advanced academic degree in an area of the space sciences. The other two members of the production team are trained to use and handle the diverse data flowing into AFGWC. These data, gathered from ground based optical and radio telescopes, vertical incident ionosondes, polarimeters, neutron monitors, riometers, magnetometers, plus space data on solar x-rays, high and low energy protons, visual aurora, precipitating electrons, electron density, and a passive ionospheric monitor make up what can truly be called a complex data set. Many of these data are computer processed and sorted, but many analyses and nearly all forecast decisions are still the responsibility of the personnel who make this system function.

3.   DATA SOURCES

3.1 Background

    As has been reported in earlier papers to AGARD (Damon, 1970; Packnett and Doeker, 1970), the conference on theoretical Ionospheric Models (Thompson, 1972), the Sixth Conference on Aerospace and Aeronautical Meterology (Snyder, 1974), and the Ionospheric Effects Symposiums (Flattery and Ramsay, 1975; von Flotow, 1978), the Air Weather Service has been an active user of scientific community research efforts in the space sciences. AWS has also been an active contributor of data to the scientific community.

3.2 Solar Data

The data received at AFGWC are constantly changing. We presently are replacing our Razdow telescopes with a new generation telescope, the Solar Observing Optical Network (SOON). These new computerized tele- scope systems are currently in operation in Hawaii, New Mexico, and Puerto Rico. During 1979, Australian and Middle East sites will complete the worldwide network. Each of these sites will be connected to AFGWC by high-speed data links. The solar radio observing network is also upgrading to computerized equipment and the first site in Hawaii is operational. Additional radio sites will be in Australia and the Middle East. We also receive solar x-ray data from the Geostationary Operational Environmental Satellites (GOES) through the NOAA computers at Boulder.

3.3 Ionospheric Data

The Northern Hemisphere ionosphere data set consists of approximately 45 ionosondes and 11 polarimeters. Just recently, data became available from special sensors flown on the Defense Meteorological Satellite Program (DMSP) satellites. These satellites are polar orbiting sun-synchronous at an altitude of 840 km. We have been monitoring and analyzing auroral information for years from these satellites. A special sensor for measuring the plasma density, temperature, and mean ion mass is currently being flown on the DMSP spacecraft. Unfortunately, the sensor on the latest launch prior to the writing of this paper, is only providing limited data so information from this sensor has not been incorporated into operational use. However, this Air Force Geophysics Laboratory developed sensor is scheduled to fly on additional DMSP spacecraft during the next 5-8 years. Another important sensor is a passive ionospheric monitor. This sensor is a high frequency reciever which passively monitors the ionospheric noise breakthrough frequencies. These are some of the major steps being taken by the Air Force to improve the space environment data set. The data received from these sensors are available to the scientific community through the World Data Center-A in Boulder, Colorado.

4.   NOTIFICATION AND ALERT FORECASTING SERVICES

4.1 Event Notification

Since the state-of-the art in accurately forecasting solar and geophysical events is poor, we have concentrated on providing rapid notification to system operators of conditions which could degrade the performance of their systems. Rapid event notification is provided for decision assistance to all levels within the military chain of command.

Typical types of notification include; (1) solar events which cause disruptions to high frequency communications on sunlit paths, (2) solar radio bursts which may cause disruptions to communication systems and/or interference to radar systems, (3) solar proton events which can produce radiation hazards to both men in space and spacecraft, (4) ionospheric disturbances which can cause degradation to HF and satellite communication systems, and (5) magnetospheric disturbances which affect the orbital parameters of low altitude satellites. AFGWC notifications of solar events are usually provided within five minutes, and are specifically tailored for each system operator.

Rapid event notification requires a responsive data acquisition and communication system. Worldwide high speed data links speed data to AFGWC from the solar and radio observatories within minutes of event detection. These data are analyzed by the duty forecaster along with space data obtained from satellites to identify which DoD systems could be affected. Notification is provided either by telephone or a direct computer link to the user.

4.2 Forecasting Ionospheric Variability

AFGWC is probably the only full time 24-hour per day ionospheric forecasting unit providing a broad spectrum of ionospheric forecasts. An ionospheric forecaster is on duty at all times to monitor the state of the ionosphere in conjunction with the sun and magnetosphere to provide a variety of ionospheric dependent systems notifications and forecasts of irregularities that would affect system performance. A more detailed description was presented by von Flotow (1978). These services consist of real-time and quasi long range forecasts.

(a) HF service can be provided in real-time, along with specification and forecasting of electron density profiles and total electron content. Large scale fields of parameters such as foF2 are also avail- able. The present capability for specification and forecasting is shown in Table 1. AFGWC provides real- time specification and forecast of HF propagation conditions every six hours. An example of our HF propaga- tion message is found in Figure 1, less detailed messages are transmitted at 0000Z, 1200Z and 1800Z.

(b) The primary long-range forecasting requirements are for HF propagation. AFGWC uses the latest ITS-78 (Barghausen, et al, 1969) program on our computers. It has been modified for direct interface to the AUTODIN (Automatic Digital Network) both for receiving requests and for transmitting its output to our worldwide military users. Approximately 300 requests are processed each month.

4.3 Forecasting Magnetospheric and Neutral Density Parameters.

AFGWC monitors variation of the magnetosphere through use of ground based magnetometers. Currently, AWS has access to magnetometers in Alaska, Canada, England, and the United States. Information from these sensors are processed at AFGWC to develop a pseudo A sub p, which is transmitted to users for real-time use in their density models. Recently, AFGWC has expanded its magnetospheric monitoring by using real- time low energy particle data from operational DoD geostationary spacecraft. Preliminary results are extremely encouraging in using data observed in the mid night sector to identify magnetospheric disturbances. This information will be used as a supplement to the ground based magnetometers, and has great potential to improve our ability to specify and forecast parameters which affect orbital characteristics of low altitude satellites and can cause charging to spacecraft flying near geostationary altitudes.

AFGWC also provides short and long term forecasts of A sub p and F10 (the 10.7 cm solar radio flux). The daily forecast (See Figure 2) consists of a three day forecast of each of these parameters. In addition seven and 27 day forecasts are provided to several military users.

5.   MODELS

5.1 Solar Flare Forecasting

The Air Force SOON was specifically designed to provide consistent, rapid flare observations and data for reliable short term solar flare forecasting. Currently the actual work on exploitation of the SOON data by applying advanced modeling techniques is being accomplished by the Air Force Geophysics Laboratory and the Space Environmental Laboratory (SEL) located at Boulder, Colorado. The Air Force has three people assigned at the SEL in Boulder. This exploitation of the SOON will continue to receive great emphasis during the foreseeable future.

5.2 Solar Proton Prediction Models

AFGWC presently uses the latest published versions of the Proton Prediction Study (Smart and Shea, 1977 and 1977a) on our computers. The model was developed by AFGL from empirical data, and incorporates all available technology. The forecaster can activate the program through a real-time computer device in the SESS work center using, as initial inputs, any radio and x-ray data available. The program output includes a time envelope for particles greater than 50 MeV and approximately 10 MeV, expected riometer absorption at high latitudes, and proton fluxes for approximately 15 channels monitored on the GOES and Defense Support Program (DSP) satellite systems. When accurate radio data are available, this model is relatively accurate. For example, it performed well during the September 1977 solar proton events.

5.3 HF Propagation Models

The ITS-78 (Barghausen, et al., 1968) is the primary HF propagation model used at AFGWC. This model has been modified over the years by the Institute of Telecommunications Service (ITS) and the AFGWC version incorporates all known changes. The maximum usable frequencies from the ITS-78 program are modified by field units using information in the AFGWC HF Propagation Reports to provide assistance in real-time frequency management.

5.4 Ionospheric Specification

The model used by AFGWC to process ionospheric data was reported earlier by Flattery and Ramsay (1975). This method involves using spectral techniques to modify the ITS coefficient fields with observed data to give a more representative description of the ionosphere. One attribute of this method is complete compatibility with all programs that use the ITS coefficients. This feature makes the technique extremely versatile and incorporates "quasi-real-time" ionospheric features into the ITS programs.

The Flattery-Ramsay model has some serious deficiencies which include 1) non-orthogonal functions; 2) the inability to handle strong gradients such as those encountered near sunrise and the auroral oval, 3) it is only continuous in three dimensions (latitude, longitude and time); and 4) it is unable to easily integrate a variety of ionospheric data.

The vertical electron density profile (EDP) model used by AFGWC is a modified version of the Damon and Hartranft model (1970). This model incorporates three Chapman layers for E, F_1, and F_2 and uses a variable scale height for the topside of the ionosphere. This model, combined with ITS or updated ITS coefficients, makes up one of the current AFGWC capabilities for ionospheric specification.

During operational use of the Flattery - Ramsay model, it was noted that as the observed data varied from monthly ITS median values when updated over the land areas the ocean areas remained at the ITS median value. This caused artificial gradients to be developed along the coastal areas of the northern hemisphere. A solution was developed to account for the variation due to solar ionizing flux by deriving the input sunspot number used by ITS from world-wide ionospheric observations. The first-guess field now has intelligence from observed data applied worldwide, so when the spectral fit of observed data is made, no systematic coastal gradients appear. This model has been in production at AFGWC for approximately two years and has verified well.

5.5 Four-Dimensional Ionospheric Model

The Four-Dimensional (4D) model was developed to correct some of the deficiences of the earlier spectral analysis model. The ITS coefficients are generated in spherical harmonics which is mathematically efficient. This representation of the ionosphere can adequately handle much sharper gradients in latitude, longitude and time. The fourth dimension, the vertical, is represented by four eigenvectors which can be modified to incorporate electron density data from polar orbiting Defense Meteorological Satellite Program (DMSP) satellites. Data observed at 840 km have the necessary information to calculate scale height. This provides a more representative value when it is integrated for total electron content (TEC) than the previously used Chapman layers of the Damon-Hartranft model. The 4-D ionospheric model description was presented at the 1977 summer URSI meeting by Flattery and Davenport (1977).

The 4-D ionospheric model is presently used at AFGWC for certain functions. We feel the model will be able to accommodate an advanced polar model and has possibilities of more efficient ray-tracing, especially in reducing computer time. Three dimensional ground to satellite ray-tracing is a promising area if the computer costs are as low as expected. This portion of the model is several man-years from completion.

6.   FUTURE

6.1 Solar

The proliferation of space systems and advanced state of electronic systems since the last solar cycle have resulted in increasingly stringent requirements for predictive capabilities of solar events which affect these systems. The USAF Scientific Advisory Board (1977) recommended methods which could decrease the degradation to these systems. Considerable research is in progress to exploit the data from the new SOON and radio systems to improve space environmental support to our DoD customers. It is important to note that AFGWC has a full appreciation for the importance of vigorous solar research and actively supports the efforts of the Air Force Geophysics Laboratory and the Space Environmental Laboratory in Boulder. Several SEL developments are currently used as a basis for direct support to many DoD systems.

6.2 Ionosphere

AFGWC supports many DoD systems dependent on, or affected by, the ionosphere. We expend considerable in-house technique development to improve support. Many areas of ionospheric specification and prediction have serious deficiencies. The global dimension of our mission currently requires extensive data sets and models. The immediate need is to understand and specify the large-scale irregularities of the ionosphere during storm time, with a follow-on natural extension to a forecast capability. Longer term goals include global capability for specification of much smaller irregularities which affect coherent wave fronts, e.g., phase and amplitude scintillations. This will include the development and expansion of methods to observe parameters which can be applied to advanced operational models.

REFERENCES

1. BARGHAUSEN, A.F., et. al., 1969, "Prediction Long-Term Operational Parameters of High Frequency Sky-Wave Telecommunications Systems. Institute for Telecommunications Sciences, Boulder, CO., (ESSA TRERL 110-ITS-78).

2. DAMON, T.D., 1970, "USAF Solar Forecast Facility Ionospheric Services", Proceeding of the AGARD Symposium on Ionospheric Forecasting.

3. DAMON, T.D. & HARTRANFT, F.R., 1970, Ionospheric Electron Density Profile Model, Aerospace Environmental Support Center Technical Memorandum 70-3.

4. PACKNETT, D.S. and DOEKER, R.B., 1970, "U.S. Activities in Operational Solar-Geophysical Forecasting", Proceeding of the AGARD Symposium in Ionospheric Forecasting.

5. FLATTERY, T.W. & DAVENPORT, G.R., 1977, "Four Dimensional Ionosphere Model", Presented at URSI meeting, Stanford University, 22-24 June, 1977.

6. FLATTERY, T.W. & RAMSAY, A.C., 1975, "Derivation of Total Electron Content for Real-Time Global Applications", Effects of the Ionosphere on Space Systems and Communications, Edited by Goodman, J.M.

7. "Report of the USAF Scientific Advisory Board ad hoc Committee on Aeronomy", 1977, Scientific Advisory Board, United States Air Force.

8. SMART, D.F. & SHEA M.A., 1977, "Proceedings of the 15th International Cosmic Ray Conference", Vol 5, pg 131.

9. SMART, D.F. & SHEA, M.A., 1977a, Space Research 18 (in press).

10. SNYDER, A.L. Jr., 1974, "Real-Time Magnetospheric and Ionospheric Monitoring", Paper presented at Sixth Conference on Aerospace and Aeronautical Meteorology, El Paso, TX, 12-14 Nov 1974.

11. THOMPSON, R.L., 1972, "Synopsis of the Ionospheric Forecast and Analysis Function at the USAF Aerospace Environmental Support Center", Proceedings of the Conference on Theoretical Ionospheric Models held June 14-16, 1971 at University Park, Pennsylvania, (PSU-IRL-SCl 401, Edited by John S. Nisbet).

12. VON FLOTOW, C.S., 1978, "Ionospheric Forecasting at Air Force Global Weather Central", Ionospheric Effects Symposium, Arlington VA, (in press) Jan 1978.

CURRENT AFGWC IONOSPHERIC SPECIFICATION

Fof2 Northern Hemisphere	$\pm$ .5 MHz
MUF/FOT Northern Hemisphere	$\pm$ 3.0 MHz
TEC Northern Hemisphere	$\pm$ 25%
Electron Density Profile (EDP)	25% RMS Error

FUTURE AFGWC IONOSPHERIC SPECIFICATION*

*Assumes a morning and noon DMSP satellite with Ionospheric sensors:

Fof2 Northern Hemisphere	$\pm$ .5 MHz
MUF/FOT Northern Hemisphere	$\pm$ 3.0 MHz
TEC Northern Hemisphere	$\pm$ 15%
EDP	15% RMS

TABLE 1

UNCLAS
DEFSMAC SIZ PASS TO SHOE
SUBJ: HF RADIO PROPAGATION REPORT
SPACE ENVIRONMENTAL SUPPORT BRANCH
AIR FORCE GLOBAL WEATHER CENTRAL
PRIMARY HF RADIO PROPAGATION REPORT ISSUED AT 070600Z FEB 78.
PART I.   SUMMARY 070000Z TO 070600Z FEB 78/
          FORECAST 070600Z TO 071200Z FEB 78.

		QUADRANT			
		I	II	III	IV
		0 TO 90W	90W TO 180	180 TO 90E	90E TO 0
REGION	POLAR	N6	U5	N5	N6/+30
	AURORAL	U5	U4	N6	N6/+30
	MIDDLE	N6	N7	N7	N7
	LOW	N7/+30	N7	N7	N7
	EQUATORIAL	N7	N7	N7	N7

PART II.   GENERAL DESCRIPTION OF HF RADIO PROPAGATION CONDITIONS
OBSERVED DURING THE 24 HOUR PERIOD ENDING 05/2400Z FEB 78 AND
FORECAST CONDITIONS FOR THE NEXT 24 HOURS.
THE GEOMAGNETIC FIELD WAS QUIET TO UNSETTLED, WITH BRIEF ACTIVE
PERIODS. THE FIELD SHOULD REMAIN QUIET TO UNSETTLED.
EQUATORIAL THROUGH MID LATITUDES. . . . HF PROPAGATION WAS GENER-
ALLY GOOD. REPORTED SUNRISE TRANSITIONS WERE MILD. MUFS WERE
ENHANCED 25 PCT AT MID LATITUDES FROM SUNRISE TO NOON. OTHER
MUFS WERE NEAR SEASONAL NORMALS.
AURORAL AND POLAR LATITUDES. . . . PROPAGATION WAS GENERALLY GOOD
DURING LOCAL DAYTIME HOURS AND GOOD TO FAIR DURING NIGHT HOURS.
MUFS WERE ENHANCED 30 PCT DURING MIDDAY HOURS. OTHER MUFS WERE
GENERALLY NORMAL. SHORT PERIODS OF FAIR OCCASIONALLY POOR PROP-
AGATION WERE REPORTED AT NIGHT DUE TO FADING, SPORADIC E, AND
ENHANCED NOISE. SPREAD F WAS ALSO PREVALENT AT ALL HOURS IN
SOLAR LATITUDES AND GAVE SOME FAIR TO POOR PROPATAION.
PART III.   SUMMARY OF SOLAR FLARE INDUCED IONOSPHERIC DISTURBANCES
WHICH MAY HAVE PRODUCED SHORT WAVE FADES IN THE SUNLIT HEMISPHERE
DURING THE 24 HOUR PERIOD ENDING 06/2400Z . . . NONE.
PROBABILITY FOR THE NEXT 24 HOURS....STRONG.
PART IV.   OBSERVED/FORECAST F10 AND K/AP.
THE OBSERVED 10.7 CM FLUX FOR 06 FEB 78 WAS 161. THE PREDICTED
10.7 CM FLUX FOR 07, 08, 09 FEB 78 ARE 163, 162, AND 160.
THE OBSERVED K/AP VALUES FOR 06 FEB 78 ARE 02/09. THE FORECAST
K/AP VALUES FOR 07, 08, 09 FEB 78 ARE 03/12, 03/10, AND 02/08.

FIGURE 1

UNCLAS
DEFSMAC SIZ PASS TO SHOE
JOINT AFGWC/SESC PRIMARY REPORT OF SOLAR AND GEOPHYSICAL ACTIVITY
ISSUED 2200Z 08 FEBRUARY 1978
IA.   SOLAR ACTIVITY HAS BEEN MODERATE. REGIONS 998 {N27W11} AND
1001 {N17E30} HAVE BEEN HIGHLY FLARE PRODUCTIVE. SIGNIFICANT
FLARES INCLUDE, FROM REGION 998. A 1-B{M-1} AT 08/0716Z, AND,
FROM REGION 1001, A 2-B{M-2} AT 08/0359Z. THESE SAME FLARES WERE
CLASSED AS SUB-NORMALS BY CULGOORA. BOTH REGIONS CONTAIN WEAK
DELTA'S AND ARE MORE COMPLEX THAN YESTERDAY AND 1001 CONTINUTES
TO GROW IN WHITE LIGHT. NEW REGION 1004 {S22E73} IS THE RETURN
OF OLD 981 AND IS AN H-TYPE SPOT WITH WEAK PLAGE. OTHER REGIONS
ARE GENERALLY QUIET.
IB.   SOLAR ACTIVITY SHOULD REMAIN MODERATE. FURTHER ENERGETIC
ACTIVITY CAN BE EXPECTED FROM REGIONS 998 AND 1001.
II.   THE GEOMAGNETIC FIELD HAS BEEN QUIET TO SLIGHTLY UNSETTLED.
THE FIELD IS EXPECTED TO BE GENERALLY UNSETTLED THRU THE PERIOD.
III.   EVENT PROBABILITIES 09 FEBRUARY - 11 FEBRUARY
CLASS M   90/90/90
CALSS X   40/40/40
PROTON   40/40/40
PCAF   YELLOW
IV.   OTTAWA 10.7 CM FLUX
OBSERVED   08 FEBRUARY 166
PREDICTED   09-11 FEBRUARY 165/165/165
90-DAY MEAN   08 FEBRUARY 109
V.   GEOMAGNETIC A INDICES
OBSERVED FREDERICKSBURG   07 FEBRUARY 05
ESTIMATED AFR/AP   08 FEBRUARY 10/10
PREDICTED AFR/AP   09-11 FEBRUARY 10/10 - 10/10 - 10/10

FIGURE 2

DISCUSSION

N.G.Gerson, US

If the system described is implemented, what effect would it have on HF communications practice? Would the information supplied to the communication station be of sufficient help and reliability to be used by the operators? Would implementation be worth the cost?

Author's Reply

The system described was specification of TEC and electron density profiles (EDP) to 15 percent RMS error. Agreed that HF forecasting (or specification) is probably not needed within 10%, but for certain applications TEC and EDP within 15% is required. So, it is felt that it is worth the effort and costs.

H.Soicher, US

How are the measurements (at 840 km) of particles and temperatures (scale heights) applied to the aims of AFGWC modelling? How do the data outputs compare with results obtained by other methods?

Author's Reply

One of the requirements of AFGWC is the specification and forecasting of total electron content (TEC). We had no method to observe the ionospheric topside in quasi-real-time. AFGL proposed a sensor to be flown on Defense Meteorological Satellite Program at 840 km to measure electron density and temperature. AFGWC has devised modelling methods to incorporate the data. Until continuous data are received, the last question cannot be answered. AFGL feels it will compare very well.

REAL-TIME PROPAGATION ASSESSMENT

Ilan J. Rothmuller
EM Propagation Division
Naval Ocean Systems Center
San Diego, CA 92152

SUMMARY

The performance of a wide variety of Naval electromagnetic systems depends on ionospheric conditions. For example, solar disturbances of the ionosphere can interrupt communications, render surveillance systems useless and cause navigation system inaccuracies. Real-time propagation assessment is a technique to optimize system performance by allowing knowledge of current ionospheric conditions to be used to minimize detrimental effects of an unknown or disturbed propagation environment. An environmental prediction and assessment system (EPAS), comprised of a variety of real-time sources of solar/geophysical data and a center which collects, processes and selectivity disseminates these data to regional propagation assessment terminals, can provide real-time knowledge of propagation conditions. The US Naval Ocean Systems Center is developing a terminal called PROPHET (for propagation forecasting), a key element of the EPAS that uses real-time solar/geophysical data to make regional assessments which are tailored to specific system useage. PROPHET uses models to translate data from satellite and ground based sources into performance predictions for specific systems. PROPHET is presently being evaluated at a Naval Communication Station and has proved to be useful to operational personnel.

1.   INTRODUCTION

To obtain high performance from a wide variety of Navy electromagnetic systems, the effects of the propagation channel - the aerospace environment or ionosphere - must be accounted for. An environmental prediction and assessment system (EPAS) provides this capability. An EPAS is an integration of three elements: (1) a variety of real-time solar/geophysical data sources; (2) a center collecting, processing and selectively disseminating these data to; (3) propagation assessment terminals where real-time regionalized and tailored products are issued.

The US Naval Ocean Systems Center is developing a real-time assessment terminal called PROPHET, a key element of the EPAS. PROPHET "products" are designed to be used to optimize specific system performance. Optimization may be achieved, for example, by real-time corrections to navigation systems affected by variations in ionospheric parameters, or frequency selection advice, or other user oriented information.

This paper describes development of operational environmental models used in PROPHET, PROPHET products, and results of testing the terminal and the EPAS concept in an operational environment.

2.   MODELING SOLAR EFFECTS ON SYSTEMS

The chief influence on the near-earth space environment is the sun. Variations in solar emissions cause variations in this environment which, in turn, cause variations in performance of many electromagnetic systems. Large solar disturbances such as flares can affect ionospheric conditions so that communication links may be interrupted, surveillance systems rendered useless and navigation systems made inaccurate. Examples of solar disturbance related outages are: short wave fade (SWF) in the HF band due to flare x-rays, phase errors and deep fades in VLF signals due to solar proton impact on the polar ionosphere, deep fades in VHF/UHF satellite communication systems due to ionospheric scintillations.

An important aspect of models developed at NOSC is that they are _tailored_ to a specific system application and that the output is in easily used terms (e.g. navigation correction in miles, lowest useable frequency, etc.). The NOSC model development approach is illustrated by the following chart.

Cause	Environment	System Effects
Solar Effluence	Ionospheric Reaction	HF: Comm. Outage - SWF VLF: Nav. Error - PCA, SPA VHF: Comm. Outage - Scintillation
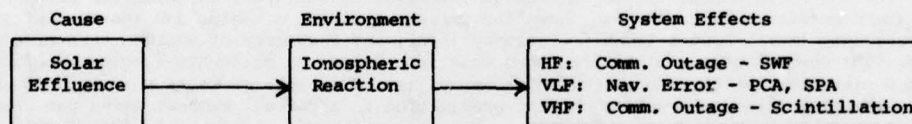
Three approaches can be taken to develop models assessing the propagation environment: phenomenological, statistical, and semi-empirical. The phenomenological is based on an understanding of the physical processes relating cause and effect. The statistical approach is based on synoptic studies and assumes that predictions can be made based on historic data. The semi-empirical method (presently used most often by the NOSC modeling group) combines knowledge of the basic physical causes with observational data to generate simplified models which obviate modeling the complicated processes between the basic driving cause and final effect.

An illustration of a semi-empirical model is the effect of high energy solar proton emission on the Omega VLF navigation system. The physics of the process is that the polar D-region of the ionosphere (50-90 km) is anomalously ionized by high energy (E >10 MeV) protons. This anomalous ionization causes more than normal phase advance of signals crossing the affected regions and thus, if unaccounted for, cause navigation errors. This also causes high absorption in the HF (and VHF) band which has given rise to the term polar cap absorption or PCA.

The Omega correction model developed by NOSC (Argo, 1975) translates solar proton flux measured at satellite altitudes into phase error corrections. These corrections are in form similar to those now routinely used to account for time of day, season, etc. The model has as parameters integrated proton flux (E > 10 MeV), time of day and path length through the "polar cap" (defined to be greater than 63° geomagnetic latitude). Figure 1 shows both corrected and uncorrected positional information for a PCA event.

The model is thus seen to correct back to the nominal 2 km accuracy of Omega. An important point to note is that a PCA event, unlike some other flare related events, can last two to three days.

Another model developed by NOSC is the effect of an x-ray flare on HF communications. This model has two "components". One models the time history of the flare. The other models the effect of the 1-8Å x-ray flux on the HF spectrum. The flare duration model predicts the duration once the flare has reached its peak. The prediction technique uses the discovery by NOSC that flares decay with one of a small set of definite decay rates. The risetime and peak amplitude are used to estimate the decay rate (Argo, et al., 1978). The model adjusts itself in case of multiple flares and can update the decay estimate. Figure 2 illustrates these and other aspects of the prediction model's capabilities. The figure shows data taken by SOLRAD-9 and how the model's predictions follow recurring flares and changes in decay slope. The vertical lines in the figure indicate times of updating. This figure also illustrates how, when operationally implementing such a model, care must be taken to strike a balance between number of updates and accuracy of predictions. It also shows the difference between a theoretical model and its application as a real-time aid using real-time data which can have gaps and other difficulties. During periods of continuous, smooth data the model does extremely well. However, when data gaps appear, the fit is not as good.

The flux thus predicted is converted to lowest observable frequency (LOF) in the HF band with a model deduced from the relationship between x-ray flux and LOF illustrated in Figure 3 (Rose, et al., 1974). This displays the propagation characteristics of the HF spectrum over a 24 hour period containing two bursts of solar x-rays during the daytime portion. Frequency is plotted versus time with vertical deflections indicating signal strength. The 1-8Å solar x-ray flux peaks at 1840 and 2100 GMT making the entire HF spectrum unuseable by causing two SWFs.

The NOSC model thus can continually in real-time calculate the LOF and, once a flare has reached its peak, also predict the duration of the outage.

This semi-empirical approach has yielded several other models relating space-environmental data to systems effects. Argo and Hill (1976) have developed a model relating absorption of transpolar HF and polar region VHF/UHF satellite communications during a PCA event.

To perform predictions of HF propagation characteristics on a daily basis, a model developed by the Air Force (1973) is used. This is an hourly update to a statistically based model - the updating done by refitting to data obtained from an HF ionospheric sounder network. To make longer range predictions, NOSC has developed a model also based on a statistical model.

Another statistical model adapted for Navy use, is the scintillation depth of fading model (LaBahn, 1974). This is an adaptation of the model developed by Fremouw and Rino (1973) and modified by Pope (1974).

Present work is aimed at modeling the effects of geomagnetic storms on a variety of systems and a phenomenological basis for a scintillation model.

3.   A REAL-TIME ASSESSMENT TERMINAL: PROPHET

To implement the models discussed earlier, NOSC has developed a real-time propagation assessment terminal called PROPHET. The object of the NOSC effort was to develop a terminal to be used by operational personnel. PROPHET products were designed to be understood and applied easily. This requirement motivated the earlier described modeling of system effects rather than modeling only environmental effects.

The PROPHET terminal consists of a stand alone minicomputer with an interactive graphic display and hard copy unit. An example of a PROPHET product is shown in Figure 4 illustrating the concept of regionalized tailored assessments. The graphic display shows the area of concern for the communications controller. For the Naval communication Station (NAVCOMMSTA) at Stockton, CA (near San Francisco, CA) this is the eastern Pacific Ocean. The map shows the current position of ships and (on the left) the maximum useable frequency (MUF), lowest useable frequency (LUF), and frequency of optimum transmission (FOT) for each ship. The communications controller uses this information to guide his frequency selection. The current and past hour satellite measured solar x-ray flux, a measure of solar activity, is also displayed. When the x-ray flux rises to levels such that propagation is affected, PROPHET warns the circuit control officer and produces updated frequency advice. Such a warning not only alerts communication personnel that it is an environmental disturbance causing an outage rather than equipment failure, but also allows some flexibility to alleviate problems.

A very important PROPHET capability is the ability to produce ray traces which depict the path of the electromagnetic wave fronts. Figure 5 is an example of a 3000 km path. A number of important propagation features are evident from this presentation. No communication is possible for ranges out to approximately 1200 km. This so-called skip zone may be of advantage if an unwanted receiver is located within this range. Focusing, i.e. several rays concentrating in a small area, occurs between 1230-1330 km and, because of different wave travel times along the rays, signal degradation through interference may be expected. A similar interference must be expected at larger ranges (2500-2700 km) where rays reflected once from the ionosphere and rays reflected twice (after being reflected from the ocean's surface) are superimposed. Another application of the ray trace picture is the selection of specific antennas having launch angles favoring desired rays and suppressing undesired rays for a particular optimum coverage situation. The model ionosphere used here is a statistically derived one.

Implementation and PROPHET presentation of the fade model described earlier is illustrated in Figures 6 and 7. Subsequent to a solar flare, PROPHET issues a warning and displays a list of all active circuits with predicted recovery times (under columns headed "RCVR MIN") (Figure 6). This prediction can be examined on a circuit by circuit basis as shown in Figure 7. In this example, the MUF is 15 MHz where the predicted fade is only 10 minutes. This kind of display shows not only how to shorten the effect of a

SWF but also allows the recognition that the SWF was caused by a solar flare rather than an equipment malfunction.

4.   REAL-TIME PROPAGATION ASSESSMENT: A TEST

NOSC conducted a field test of the PROPHET assessment terminal at the Naval Communication Station, Stockton, CA. The general test objectives were to test the utility (and reliability) of real-time, tailored and regionalized propagation assessments in an operational environment and to specify the needs and uses of various components of an environmental prediction and assessment system (EPAS).

As noted earlier, a real-time environmental prediction and assessment system is an integration of three elements. These are: (1) a variety of solar/geophysical data sources; (2) a facility which collects, processes and selectively disseminates these data to; (3) a propagation assessment terminal where real-time, regionalized and tailored "products" are issued.

Figure 8 illustrates the conceptual information flow in an EPAS. Figure 9 shows the information flow for the NOSC field test. A variety of solar/geophysical data flow into La Posta Astrogeophysical Observatory (LPAO) where the data were sorted and combined with local data. Selected data were sent on to the PROPHET terminal. Data sources included SOLRAD 11B, GOES-1, SMS-1, GOES-2, NOAA-5, as well as other data from SELDADS (Williams, 1976) and the Air Force Global Weather Central (AFGWC, 1973).

The field test was evaluated by analyzing the log tapes (which contain useage information as well as commentary by COMMSTA personnel) and questionnaires filled out by the users. Thus both qualitative and quantitative results were obtained.

Analysis to date has shown that: (1) COMMSTA personnel made frequent use of PROPHET - terminal access averaged once per nine minutes (during each 24 hour period); (2) using PROPHET predictions, QSYs (number of frequency shifts) and outages due to propagation were reduced by 15% with duration of outages reduced by 15%-20%; (3) COMMSTA personnel gave a qualitative general "usefulness" rating to PROPHET of eight on a scale of ten.

The ray tracing capability provided some unexpected returns. It not only was useful as an educational tool providing insight to the operational personnel into the process of HF propagation, but was found to give personnel an added (and previously unused) flexibility to perform antenna selection. For example, a 6 MHz transmission from Stockton was not heard by a ship despite the fact that this frequency was within the MUF/LUF envelope. A PROPHET ray trace was called and showed the ship to be in the skip zone for the antenna in use. The ray trace was redone using an antenna with a different take off angle so that rays would reach the ship. The transmitting antenna was shifted and the frequency/antenna combination provided six hours of solid communications.

5.   CONCLUSIONS

The initial field test in an operational environment of a propagation assessment terminal has shown that such information can be useful and will be used if it is tailored to the users needs. This points out the need to continue model development beyond only a description of the environment. A knowledge (or awareness) of environmental dependencies of systems is thus useful in development of operational models.

Another important test result is the realization that a terminal such as PROPHET provides a useful vehicle for modelers of the propagation environment. Present modeling capabilities are limited by lack of phenomenological pictures of some ionospheric processes. Future work must be aimed at removal of these limitations.

6.   REFERENCES

Air Force Global Weather Central, 1973, AFGWC Manual 105-1.

Argo, P. E., 1975, "Modeling Omega PCA Phase Advances," Naval Electronics Laboratory Center Technical Report 1950.

Argo, P. E. and J. R. Hill, 1976, "High Frequency Polar Cap Absorption Model: SOLRAD Application," Naval Electronics Laboratory Center Technical Note 3249.

Argo, P. E., J. R. Hill, and W. Loomis, 1978, "X-Ray Flare and Short Wave Fade Duration Model," Naval Ocean Systems Center Technical Report, in preparation.

Fremouw, E. J. and C. L. Rino, 1973, "Modeling of Transionospheric Radio Propagation," Radio Sci., 8, 213.

LaBahn, R. W., 1974, "Development of a Scintillation Grid," Naval Electronics Laboratory Center Technical Note 2814.

Pope, J. H., 1974, "High Latitude Ionospheric Irregularity Model," Radio Sci., 9, 675.

Rose, R. B., J. R. Hill and M. P. Bleiweiss, 1974, "Sudden Ionospheric Disturbance Grid," Naval Electronics Laboratory Center Technical Report 1938.

Williams, D. J., 1976, "SELDADS: An Operational Real-Time Solar-Terrestrial Environment Monitoring System," NOAA Technical Report ERL-357-SEL37.
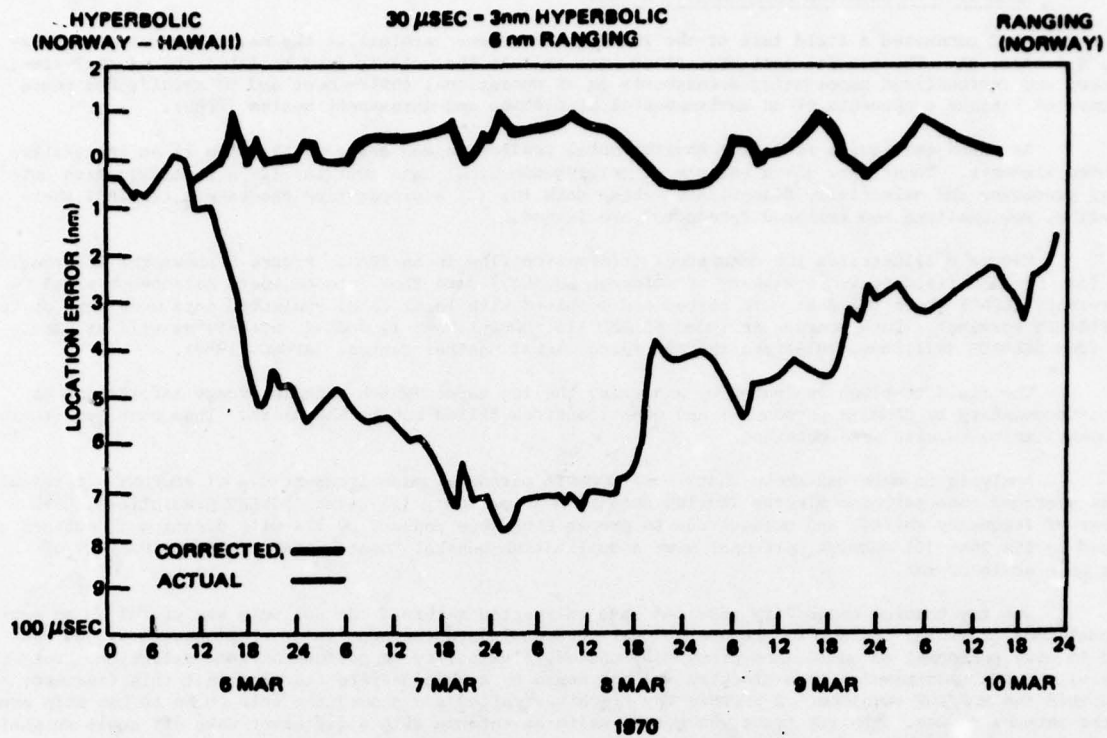
Figure 1. Corrected and uncorrected Omega positioning errors.
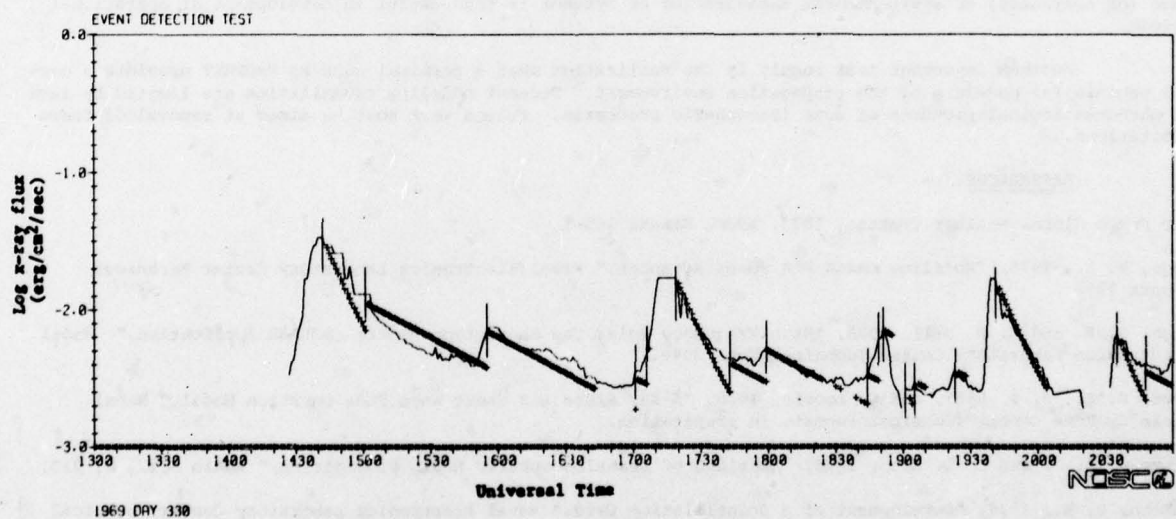
Figure 2. Solar flare 1-8Å x-ray flux (solid curve) and flare forecasting results (x's)
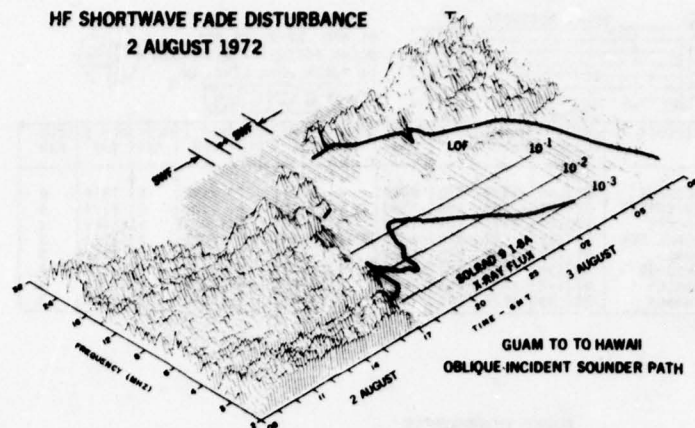
Figure 3. Propagation channel characteristics for the HF band during two solar flares.
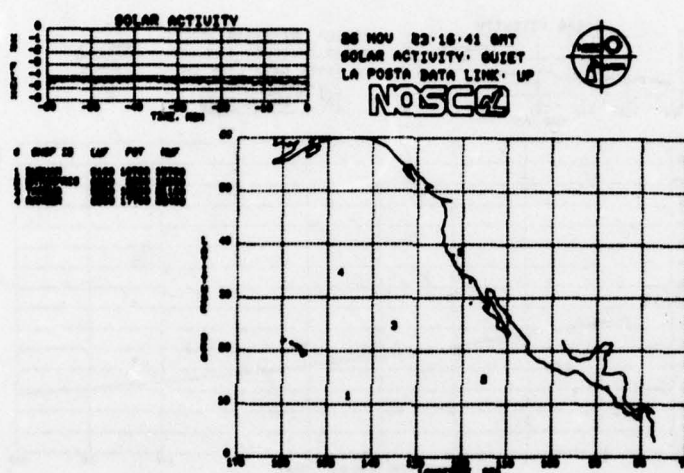
Figure 4. PROPHET display showing propagation characteristics between the Naval Communication Station (asterisk at 121°W, 38°N) and the ships Durham, Enterprise, Tarawa and Ranger.

Figure 5. PROPHET raytrace display.

SOLAR ACTIVITY

01 APR 20:21:29 GMT
SOLAR ACTIVITY: DISTURBED
LA POSTA DATA LINK UP
NOSC

CIRCUIT ID	LAT DEG	LON DEG	RANGE NM	BRNG DEG	SEND1 KHZ	RCVR MIN	SEND2 KHZ	RCVR MIN	REC 1 KHZ	RCVR MIN	RCV 2 KHZ	RCVR MIN
DUBUQUE	25	100	1373	118	9800	4	9900	4	8500	6	7680	0
ENTERPRIS	32	128	459	220	4720	6	5800	4	5100	5	5174	5
CONNIE	17	112	1371	154	15010	1	15150	1	14915	1	14980	1
CORAL SEA	53	153	1560	315	10250	3	10400	3	10865	3	10950	3
HONO	21	157	2069	250	6340	3	6480	3	6800	3	6856	3
CHICAGO	46	139	888	308	12350	0	12050	2	16200	0	14200	3
RANGER	31	142	1063	252	15000	8	13500	2	12500	3	10000	5
TARAWA	28	90	1720	100	17500	0	19000	0	16200	8	14080	3

EVENT IN PROGRESS

Figure 6. PROPHET display subsequent to a solar flare showing affected circuits.

SOLAR ACTIVITY

22 SEP 21:03:18 GMT
SOLAR ACTIVITY DISTURBED
LA POSTA DATA LINK UP
NOSC

Figure 7. PROPHET display predicting time to recovery from a solar flare for the ship Durham.

Figure 8. Environmental Prediction and Assessment System (EPAS) concept.
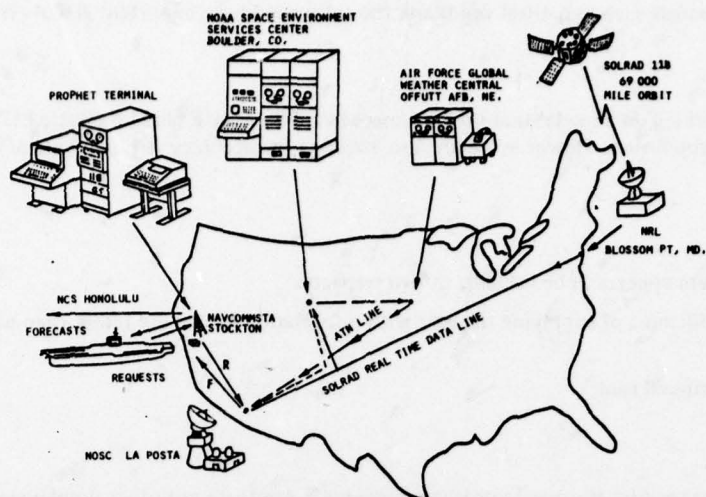
Figure 9. NOSC PROPHET field test information flow.

DISCUSSION

J.Aarons, US

While advances have been made in forecasting, the effect of soft X-rays and solar protons in the 1–20 MeV range, what has been done about dealing with the great variability in foF2 in middle latitudes during magnetically quiet periods? Perhaps, factors such as neutral winds and the solar wind have important global effects that we still do not understand.

Author's Reply

We are presently working on a model that predicts/assesses foF2 or MUF based on Solar EUV and other factors such as neutral winds as you noted. However, we are also assessing the accuracy requirements of the operational HF systems.

K.Davies, US

The PROPHET system appears to be valuable in two respects:

(1) Resolving the dilemma of supplying the user with information he can use rather than what the predictor thinks the user needs.

(2) Valuable educational tool.

N.G.Gerson, US

Would this system be used by the operators if implemented? Are there not other simpler systems available? What communications are required to support the system? The present practice, I believe, in Navy circles is to radiate the same information at a number of frequencies simultaneously or periodically; the ship copies at the frequency providing the best ratio of signal/noise. This latter method, although wasteful of frequency space, provides a reasonable low-cost operational answer to the outage problem. Will it be replaced?

Author's Reply

The PROPHET terminal is designed to provide personnel with environmental advice for a variety of Navy systems from ELF to UHF. This will consist of real-time as well as predictive advice. Our present experience is that Navy personnel will use the products issued by PROPHET. An advantage of PROPHET is, by the way, that it provides the reason for a short wave fade, thus saving efforts trying to re-establish communications by repairing "faulty" equipment.

J.S.Nisbet, US

This is a very exciting system in that it allows very sophisticated models to be used simply by unskilled operators. In the use of models, it is desirable to get feedback on how well they predict so that they can be improved. What arrangements do you make for this feedback?

Author's Reply

The accuracy of predictions is actually difficult for us to check precisely. We do check with the personnel on a regular schedule for comments on accuracy, timeliness and appropriateness of the predictions.

J.S.Belrose, Canada

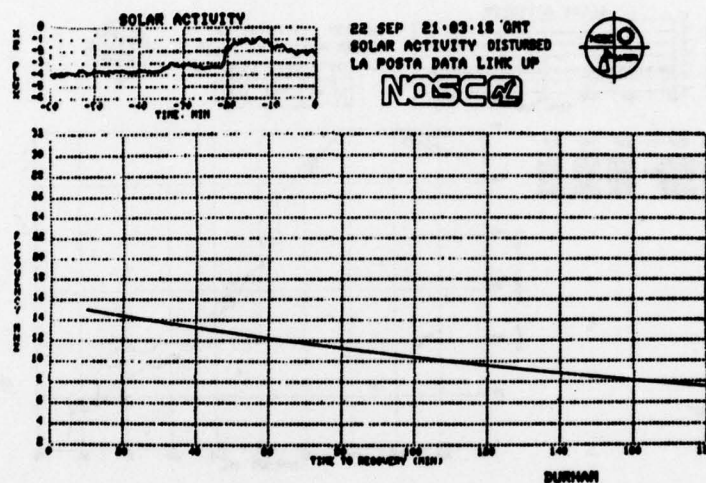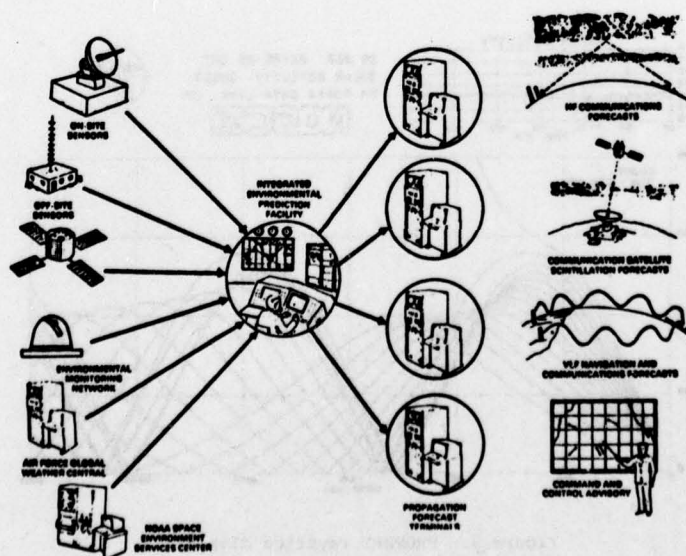I must say I am somewhat overwhelmed by the shear magnitude of the undertaking, viz. to provide real-time propagation assessment for a variety of users employing sensors widely-located. I am somewhat pessimistic, however, about the real value of such a centralized system for HF propagation assessment particularly at high latitudes, because of the rapid time variation of the propagation media and the limited correlation distance for such disturbances. In Canada we have recognized this as a problem many years ago, and we opted for a system that we have called CHEC, which is a code name for channel evaluation and calling. This system can be as simple or as complex as the user desires, and it does provide real-time assessment over the particular path of concern to each operator. The system does not predict, it provides evaluation right up to the present, and background knowledge because today's assessment can be compared with yesterday's. A special sounding transmitter is not required; channel sounding can be accomplished by using the communications transmitters, which in the case of fleet broadcast are all being keyed in any case. An alternative for correcting VLF navigation errors is "differential Omega", in which a mobile is corrected using data recorded by a nearby fixed monitor. Your evaluation of PROPHET has to be judged against these, and other alternatives which your paper did not address.

Author's Reply

The PROPHET idea is to provide real-time advice as well as long-term forecasting advice using whatever methods are available for the region and system to be helped. Sounding the path to be used at HF (either actively or passively) certainly can work and could be used in high latitudes where propagation is so highly variable. However a sounding

system by itself will not help during a flare where prediction of outage duration and recovery profile is presently available. Thus, at high latitudes a "data source" to PROPHET should be a sounder as well as satellite x-ray and particle data.

GEOPHYSICAL DISTURBANCE EFFECTS AND THEIR PREDICTABILITY

E V Thrane
Norwegian Defence Research Establishment
P O Box 25 - N-2007 Kjeller, Norway

ABSTRACT

Different types of disturbances in the upper atmosphere can change its properties as a propagation medium for electromagnetic waves. The paper reviews the most important of these disturbances, and discusses the possibility of predicting, not their actual occurrence, but rather their effect on the atmosphere once they have occurred. The review is based upon current knowledge of ionospheric and upper atmosphere physics, and concentrates on effects of importance to radio wave propagation. Both natural phenomena, such as magnetic storms, and man-made disturbances are discussed.

1.   INTRODUCTION AND OUTLINE

Different types of geophysical disturbances influence the state of the upper atmosphere and change its properties as a propagation medium for electromagnetic waves. This paper discusses the problem of predicting these changes. The prediction of the actual occurrence of a certain disturbance will not be dealt with here. I shall start by assuming that the occurrence of a disturbance with certain characteristics has been (correctly) predicted, and then discuss the possibilities we have at present for estimating the atmospheric changes, relevant to wave propagation, that will result.

A definition of a geophysical disturbance in the context of this paper is not straightforward, and will of necessity be somewhat arbitrary. The upper atmosphere has certain regular variations that repeat from day to day and from year to year. Superimposed on this regular pattern are changes that do not repeat themselves in a systematic manner. These irregular changes are, to the extent that they influence wave propagation, the disturbances that are of interest in this discussion. When the irregular changes are frequent and pronounced it may not be easy to establish a regular background pattern. Such is the case at high latitudes, particularly in the auroral zones, where strongly irregular behaviour of the medium is the rule, rather than an exception. Although it is difficult to give an exact definition of what we mean by a disturbance, certain types of major disturbances may usually be identified, and these are discussed in the following sections. Section 2 briefly describes the important types of disturbances and their effect on radio wave propagation. The remaining sections deal with these types of disturbance one by one, discussing their causes and the possibility of predicting their effects on propagation.

2.   THE MOST IMPORTANT TYPES OF DISTURBANCE

There are many ways of classifying upper atmospheric, or ionospheric disturbances, none of them very satisfactory. Most, but not all disturbances of importance for radio wave propagation are part of the sequence of very complicated phenomena called a magnetic storm. Time does not permit a discussion of all aspects of magnetic storms, and I choose to list and discuss a few selected important types of disturbance, without any attempt at systematic classification according to cause. Table 1 gives this list.

TABLE 1   IONOSPHERIC DISTURBANCES (Rishbeth and Garriott, 1969)

Disturbance	Propagation effects	Time and duration	Possible cause
Sudden Ionospheric Disturbance (SID)	In sunlit hemisphere, strong absorption, anomalous VLF-reflection, F-region effects	All effects start approx simultaneously. Duration ~½ hour	Enhanced solar x-ray and EUV flux from solar flare
Polar Cap Absorption (PCA)	Intense radiowave absorption in magnetic polar regions. Anomalous VLF-reflection	Starts a few hours after flare. Duration one to several days	Solar protons 1-100 MeV
Magnetic Storm	F-region effects; increase of foF2 during first day, then depressed foF2, with corresponding changes in MUF E-region effects, storm Es D-region effects, enhanced absorption, VLF-anomalies	May last for days with strong daily variations	Interaction of solar low energy plasma with earth's magnetic field, causing energetic electron precipitation
Auroral Absorption (AA)	Enhanced absorption along auroral oval in areas hundred to thousand kilometers in extent. Sporadic E may give enhanced MUF	Complicated phenomena lasting from hours to days	Precipitation of electrons with energies a few tens of keV
Relativistic Electron Precipitation (REP)	Enhanced absorption VLF-anomalies at sub-auroral latitudes	Duration 1-2 hours	Precipitation of electrons with energies of a few hundred keV
Travelling Ionospheric Disturbances (TID)	Changes of foF2 with corresponding changes of MUF sometimes periodic	Typically a few hours	Atmospheric waves
Winter Anomaly (WA)	Enhanced absorption at midlatitudes	One to several days	Probably many causes, such as changes in concentration of minor species, temperature changes, particle precipitation
Stratospheric Warming	Changes in absorption, VLF-anomalies	Days or weeks, in late winter	Changes in global circulation pattern

We are interested in the propagation effects of the disturbances. Propagation is determined mainly by the spatial and temporal variations of the electron density in the ionosphere. For extremely low frequencies ions may also be important. Our primary concern is therefore to predict the changes in plasma density resulting from a disturbance. Once these changes are known, the propagation effects can normally be estimated with reasonable certainty.

3. SUDDEN IONOSPHERIC DISTURBANCES (SID's)

It is well established that SID's are associated with solar flares and are caused by enhanced X-ray and EUV emissions. Whereas the X-ray intensity may increase by orders of magnitude during such a flare, the EUV flux normally only increases by a few tens of per cents. The main propagation effects are produced in the lower ionosphere by radiation with wavelengths in the range 0.05 - 102.7 nm, and extend over the sunlit hemisphere. They are: HF-absorption, sudden frequency deviations (SFD) of HF-signals, sudden phase anomalies (SPA) of VLF-signals (See Figure 1). The capability of a flare to produce an SID depends upon the flux level as well as on spectral composition. Bain and Hammon (1975) find that SPA's are the most sensitive indicators of an SID, and report on the observed percentage of optical (Hα) flares of various classes associated with SPA's. The percentage increases from 12% for subflares to 100% for class 3 flares. Fluxes greater than $6 \cdot 10^{-7}$ $Jm^{-2}s^{-1}$ in the 0.05 - 0.3 nm band will always give an SPA. Detailed studies of SID effects by for example Rowe et al. (1970), Montbriand and Belrose (1972) and Desphande and Mitra (1972) have shown that the X-rays not only cause enhanced ion production, but that they also influence the ion chemistry and produce changes in the ionization loss rate. Figure 2 shows electron density profiles $N_e(h)$ measured during a flare of moderate strength (Montbriand and Belrose, 1972). From satellite measurements of X-ray and EUV flux, the ion production profiles q(h) may be determined, provided that the height variations of the density of the major neutral atmospheric constituents are known. Using a simple form of the continuity equation

$$\frac{dN_e}{dt} = q(h) - \psi(h)N_e^2(h) \tag{1}$$

the effective recombination rate $\psi(h)$ may be determined.

There are several problems involved in estimating the ionospheric effects of a flare. First, very accurate knowledge of the spectral composition is required to compute an accurate ion production profile. The usual satellite instrumentation, such as the Vela satellites, did not provide sufficient spectral resolution, particularly at the shortest wavelengths, and model spectra have had to be fitted to the observed X-ray intensities. New satellites have brought the evaluation of SID's to a turning point, however. The EUV and X-ray fluxes over the full wavelength region are now available with high time resolution and in near real time (Donnely, 1976).

Secondly, the ion production profile will be quite sensitive to the state of the neutral atmosphere, and accurate information on atmospheric density and composition is necessary.

Thirdly, accurate knowledge of the ion chemistry in the lower ionosphere is required to predict the changes in effective ionization loss rate during an SID. Figure 3 shows experimental evidence that the loss rate decreases during a flare, and that the decrease depends upon the strength of the flare. Thus the changes in loss rate will enhance the effects of an increase in ion production. Studies of the lower ionosphere by means of mass spectrometers have given us very detailed knowledge of the positive ion chemistry. In terms of this chemistry a decrease in loss rate between 70 and 85 km may be explained by a decrease in the concentration of hydrated cluster ions with large recombination rates, relative to the concentration of the molecular ions O_2^+ and NO^+ which recombine rapidly. The reaction chains leading to cluster ion formation are not completely mapped, however, and modelling is still bound to be uncertain. This is even more true for modelling of the negative ion formation, that is important below about 75 km. The effective loss rate derived during a moderately strong flare by Montbriand and Belrose (1972) shows a very large decrease relative to normal conditions near 70 km and below. This indicates that the negative ion population may have been depleted during the flare, but no models of the negative ion chemistry have as yet been developed to explain such observations. We must conclude that the effects of an X-ray flare can only be predicted in gross terms at the lowest heights in the ionosphere.

4. POLAR CAP ABSORPTION EVENTS (PCA)

The energetic particle bombardement of the polar cap ionospheres during a PCA cause long-lasting and large changes of plasma density, particularly in the lower ionosphere. Severe disruptions of HF-communication as well as large errors in positioning by means of VLF-navigation systems result. The frequency of occurrence of PCA events varies from a few events per year during sunspot minimum conditions to one or more per month in sunspot maximum years. A PCA covers the entire polar caps down to about $60°$ magnetic latitude and lasts for a few to several days per event. The intense ionization in the lower ionosphere is caused mainly by solar protons. Figure 4 (Reagan, 1977) shows the ion production profile for the August 1972 event, one of the strongest ever recorded. In the region below 80 km the ion production is enhanced by a factor of $10^3 - 10^4$ relative to quiet daytime conditions. From a knowledge of the proton energy spectrum the ion production profile may be computed, but such events are also believed to have profound influence on the chemistry of the region, and therefore on the electron loss rate. Figure 5 (Reagan, 1977) shows results of a neutral and ion chemistry analysis during the August 1972 event based on incoherent scatter measurements of ionization densities. Note the large decrease in electron loss rate near 80 km relative to quiet conditions and the increase near 60 km.

The effects on propagation of a PCA event of this magnitude are dramatic. Large absorption may completely wipe out ordinary HF communication, although the decrease in signal strength over a communication link is partly compensated for by a decrease in noise level. Absorption at riometer frequencies (~30 MHz) may be 10-20 dB above normal, corresponding to 100-200 dB at 10 MHz. An empirical relationship between proton flux and riometer 30 MHz absorption is quoted by Reid (1972)

$$J(>20 \text{ MeV}) = 60 \text{ A}^2 \tag{2}$$

when J is the 2π omnidirectional flux in $cm^{-2}s^{-1}$ and A the absorption in desibels. Although it is derived for a particular event (February, 1965), (2) is nevertheless a useful approximate guide.

In the lower frequency bands VLF (30-30 kHz) and LF (30-300 kHz) both phase and amplitude changes are observed on transpolar paths during PCA's.(Westerlund et al., 1969). Amplitude changes, particularly for paths crossing the Greenland ice cap, seem to be erratic and difficult to predict, but the major effect on all paths is a phase advance, corresponding to a lowering of the reflection height. Theory predicts an approximately linear relationship between phase shift and the loglog of the proton flux. Figure 6 shows that this assumption is reasonably accurate (Westerlund et al., 1969). The phase shifts during PCA events are important for navigation systems such as Omega, and tests with a partially deployed Omega system show that errors in position fixes by as much as 10 km may occur (Swanson, 1971). It should be noted that, due to the configuration of the earth's magnetic field, there is a marked longitudinal variation in the particle precipitation, the fluxes being greatest in the American sector.

5. MAGNETIC STORM EFFECTS IN THE F-REGION

Magnetic storms have a profound influence on the F-region, particularly at high latitudes. The critical frequency in the F2-layer may decrease significantly and the F-layer becomes thicker. The total electron content normally decreases. Figure 7 shows typical behaviour of N_mF_2 for strong and weak storms, for various latitudes (Matsushita, 1959). F-region storm effects present many problems and are probably due to several different causes, such as heating causing thermal expansion of the atmosphere, storm induced composition changes, acceleration of the neutral atmosphere due to ion drag. Considerable progress has been made in recent years in understanding how energy is deposited in the ionosphere during a magnetic storm, and in particular how electric fields can influence composition, density and movement, both of ions and neutral atmospheric gases.

Models have been developed (Mayr and Hedin, 1977; Roble, 1977) to predict the effects on thermospheric circulation and composition of storm induced heating, and these show reasonable agreement with observations. Near the daytime F2-layer peak, observations during a storm show (Hedin et al., 1977; Prölss and von Zahn, 1974; Chandra and Spencer, 1976) that there is a close correlation between the electron density N_e and the ratio $[O]/[N_2]$. Examples are shown in Figures 8 and 9. The results fit with theoretical predictions that the ionosphere at these heights (≈ 200 km) is in photochemical equilibrium, the ion production from atomic oxygen being balanced by charge transfer to molecular constituents. It is also clear from Hedin et al. (1977) that, at the same invariant latitude, the storm effects are different at different longitudes.

During storms it is well established that electric fields are a common feature of the high latitude ionosphere. Generally the magnitude of these fields are of the order 25-150 mV m^{-1}, but fields larger than 200 mV m^{-1} have been observed. It has been pointed out (Banks, 1974) that such fields can significantly influence the ion composition and thereby the electron density in the E- and F-regions. Recently, Schunk et al. (1977) have estimated the effect of electric fields on the daytime high latitude ionosphere. Figure 10 shows that substantial decreases of F-region electron densities may occur. The effect is mainly due to the reactions $O^+ + N_2 \rightarrow NO^+ + N$ and $O_2^+ + O_2 \rightarrow O_2^+ + O$, the rates of which depend strongly on ion energy. The electric fields will increase these reaction rates through Joule heating and through the dependence of the reactions upon the relative speeds of ion and neutral gases. The ratio of atomic ion density to molecular ion density will decrease and electron loss rates increase as a consequence.

Much work remains to be done before an understanding of F-region storm effects satisfactory from a prediction point of view is reached. However, recent advances in theory and in observational evidence have uncovered several important mechanisms that seem to govern the state of the upper ionosphere during storms.

6. STORM EFFECTS IN THE LOWER IONOSPHERE

The magnetic storm effects in the lower ionosphere are caused by complex global patterns of energetic particle precipitation that cause enhanced ionization, as well as changes in loss rate and ion and neutral composition. Both increased radio wave absorption in the D-region and improved reflection properties from sporadic E-layers may result. We have already discussed PCA events caused by solar protons, arriving within hours of certain types of solar flares, and in this section we shall discuss the effects of electron precipitation. These depend strongly upon geomagnetic latitude, and also longitude, and may somewhat arbitrarily be divided into three classes; a) auroral absorption and E_S, b) mid-latitude afterstorm effects, and c) relativistic electron precipitation events.

6.1 Auroral Absorption

Auroral phenomena are often associated with radio blackouts. While the aurora itself is caused by soft electrons (1-10 keV), the enhanced absorption is caused by electrons with energies in excess of 10 keV penetrating into the D- and lower E-region. Although the general morphology of the auroral zone is well mapped on a statistical bases, the auroral structure is exceedingly complex, and anyone who has witnessed an auroral break-up will appreciate the difficulty in predicting its detailed behaviour. The auroral particle precipitation occurs in two zones as shown in the now classical Figure 11 by Hartz and Brice (1967), a diffuse zone with drizzle type precipitation and a zone with discrete, splash type precipitation. Figure 12 shows the occurrence pattern of auroral absorption (Hartz et al., 1963) expressed as the percentage of time the absorption exceeded 1 dB at 30 MHz. As will be seen the absorption has maximum occurrence rate along the auroral oval and shows a strong dependence on local geomagnetic time with greatest values in the morning hours, corresponding to the behaviour of the diffuse zone. In general auroral absorption at any one location will have time scales of hours and spatial extent of a few hundred kilometers. A great number of ionization density profiles have been measured during auroral events by rocket techniques. Figure 13 shows some examples with labels indicating the associated riometer absorption (Jespersen et al., 1968). The great variability in the profiles reflects the variability in time and space of the spectrum of precipitating particles. As discussed earlier (section 3) large ionization rates may also influence the ion chemistry in the lower ionosphere and change the ionization loss rates. These pro-

cesses are not fully understood, which makes the prediction of the effect of a disturbance on radio wave propagation all the more difficult.

Radio communication may also be favoured in auroral conditions by formation of strongly reflecting E_s layers produced by soft particles not penetrating below 100 km. Figure 14 shows the percentage occurrence rates of E_s and illustrates that the time variation corresponds to the behaviour of the discrete auroral zone. This type of E_s ($fE_s > 7$ MHz) is thus most frequent at a time of day when absorption is least probable.

6.2   The mid-latitude storm after effect

It is well established that radio wave absorption at mid-latitudes may be enhanced a few days after the onset of a magnetic storm (Belrose and Thomas, 1968). This storm after effect has recently been studied in detail by Larsen et al. (1976) who used simultaneous observations of particle spectra in satellites and ground based observations of electron density to study the response of the lower ionosphere to the storm particles. Figure 15 shows the latitudinal variation of electron flux (>130 keV) before and after the storm, illustrating the enhanced precipitation down to lower latitudes after the storm. Figure 16 shows the corresponding values of electron loss rates at Ottawa. There is a strong variability in the height range 75-90 km, and no simple relation between the intensity of ion production and electron loss rate is evident from this study. One must conclude that even when a detailed particle spectrum is available and hence the ion production is known, the electron density profile and the radio propagation effects cannot yet be predicted with reasonable accuracy in the lower ionosphere. We obviously lack sufficient knowledge of the photochemistry of this region.

6.3   Relativistic electron precipitation events

Bailey and Pomerantz (1967) first noted a type of ionospheric disturbance affecting the very lowest part of the D-region causing radio wave absorption, enhanced VHF forward scatter and large phase changes of VLF waves. The disturbances are closely correlated with substorms and are usually restricted to subauroral latitudes. It is clear that the effects are caused by precipitation of relativistic electrons (Matthews and Simons, 1973) with energies $\gtrsim$500 keV. Rosenberg et al. (1972) and Thorne and Larsen (1976) have studies such events. They conclude that substorm activity is a necessary condition for REP events, but that not all substorms lead to the intense precipitation causing REP's. Apparently the absolute intensity of the substorm is not a good indicator of whether or not a REP event will occur. An interesting feature is the absence of REP events in the early morning hours (local time) as observed in Alaska. Daytime events are often delayed by several hours relative to the onset of a substorm, whereas nighttime events are directly correlated with substorm activity. Thorne and Kennel (1971) Thorne (1974) suggest that REP events are triggered by ion cyclotron waves in the magnetosphere causing parasitic electron scattering. A definite test of this theory is still lacking, and the prediction of REP events and their effect on propagation can only be made on a statistical basis. Large absorption (>10 dB at 30 MHz) and large phase advances at VLF (for short paths 50-100 µs) are common features of REP events. As discussed in earlier sections, strongly enhanced ion production in the lower D-region will change the ion and neutral composition and thereby influence the ionization loss rate.

7.   THE WINTER ANOMALY IN IONOSPHERIC ABSORPTION

At middle latitudes, 35-60°, ionospheric radio wave absorption in winter does not follow the simple solar zenith angle dependence to be expected from averaged summer observations. The general background of winter absorption is enhanced relative to summer values at the same zenith angles, and in addition days or groups of days occur in winter when HF-absorption is greatly enhanced and seriously affects radio communication. The frequency of occurrence of such events increases with increasing latitude. No doubt this is partly due to the influence of particle precipitation, such as the storm after effects discussed earlier. However, it now seems clear that at least at the lower latitudes, the main winter anomaly effect is due to interactions of the ionosphere with the neutral atmosphere at and below ionospheric heights. This "meteorological type" of winter anomaly was recently studied during the "Western Europe Winter Anomaly Campaign" conducted from Southern Spain during the winter 1975-76 (Offermann, 1977). The enhanced absorption was due to increased electron densities in the height region 75-95 km. These enhanced electron densities were, however, not caused by increased ionizing radiation, in the form of solar electromagnetic radiation or energetic particles, but appeared to be due to at least three different factors (Thrane et al., 1978):

a)   Enhanced density of mesospheric nitric oxide NO causing increased ionization by solar H-Lyman-α radiation.

b)   Decreased electron loss rate in the range, 75-85 km. This decrease coincided with a depletion of heavy positive water cluster ions with large recombination rates.

c)   Enhanced density of mesospheric excited molecular oxygen O_2 ($^1\Delta_g$) causing increased ionization by solar UV radiation.

The period of enhanced absorption in January 1976 was associated with wavelike structures giving marked deviation of the atmosphere from the reference atmosphere (CIRA 1972). Figure 17 shows the noon A3 absorption and Figure 18 shows rocket measurements of atmospheric temperature clearly demonstrating a temperature wave distorting the normal stratospheric- and mesospheric temperature profile (Offermann, 1977, Becker et al., 1978). The disturbance could be traced all the way to the ground. The new results promise better understanding of ionosphere-atmosphere coupling and show the way towards possible prediction of such events. A further indication of the possible role of transport processes was given by Geller et al. (1976 who showed a connection between D-region electron densities at Urbana, Illinois and meteor radar drift observations. Drifts from the north was correlated with enhancements of electron density. Such observations could be explained by southward transport of nitric oxide produced by particle precipitation in the auroral zone.

8.   STRATOSPHERIC WARMINGS

The coupling between the ionosphere and stratosphere was first clearly demonstrated in studies of the correlation between ionospheric absorption and stratospheric warmings (Shapley and Beynon, 1965) who showed that ionospheric absorption increased a few days after a temperature increase in the stratosphere. Stratospheric-mesospheric midwinter warmings are synoptic scale events associated with a reversal or "breakdown" of the polar circulation at altitudes at least as low as 30 km (Labitzke, 1977). A major warming may result in temperature increases in the upper stratosphere and lower thermosphere of more that 50 K. The events occur in late winter and last for days or weeks. They are apparently forced from the troposphere, but no complete explanation has been given.

In view of the recent results from studies of the winter anomaly it seems clear that changes in the state of the neutral atmosphere, such as changes in composition and temperature, can influence ionospheric parameters. A better understanding of the coupling mechanisms may lead to reliable synoptic prediction of the lower ionosphere based partly on the meteorological situation at lower levels.

9.   TRAVELLING IONOSPHERIC DISTURBANCES (TID)

Radio communications are sometimes disrupted by moving ionospheric irregularities that may alter the characteristics of the wave (phase, amplitude, polarization, direction of propagation) on time scales ranging from seconds to hours. Extensive studies have been made to identify the sources and map the behaviour of such travelling disturbances. A review of the results has been given by Georges (1967). He identifies three distinct types of travelling disturbances:

a) Very large disturbances retaining a wavelike structure over large distances. An example is shown in Figure 19. Such disturbances are closely correlated with magnetic storms, an almost one-to-one correspondence is observed between this kind of disturbance and storms with Kp indices greater than 5. The source is believed to be Joule heating by the auroral electrojet. Typical speeds are >300 m/s and typical periods 30 minutes to more than one hour.

b) A second type of TID is the "medium scale" events which travel at speeds less than the speed of sound and have periods from 10 to 40 minutes. These TID's do not retain their shapes over a more than 100 km and are not well correlated with known geophysical phenomena. They have the characteristics of internal atmospheric waves and may originate in the lower atmosphere.

c) A third type of disturbance seems to be directly associated with severe weather systems such as large thunderstorms, and show oscillations of the order of 3 minutes.

Prediction for communication purposes of TID's would seem difficult until their behaviour is better understood. A possible exception are the very large disturbances that are clearly correlated with severe magnetic activity.

10.   MAN-INDUCED IONOSPHERIC DISTURBANCES

Man may, inadvertently or on purpose, alter the state of the upper atmosphere and produce disturbances of importance for radio propagation. Such disturbances fall into three different categories.

a) Changes induced by heating the ionosphere from the ground by powerful radio waves.

b) Release of chemically active substances in the atmosphere that alter the composition and photochemical properties of the medium.

c) Nuclear detonations releasing ionizing radiation and producing shock waves that significantly change the state of the upper atmosphere.

Effects of all three kinds of disturbance have been observed and are now reasonably well understood. The first category includes the classical cross modulation, or Luxembourg effect, and the creation of irregularities or spread F conditions. Since appreciable power is needed for the "heating" transmitter, the affected areas have limited geographical extent, of the order of 100 km in the F-region (Bailey and Martyn, 1937; Utlaut and Cohen, 1971).

Releases of chemically active substances also have transient and limited effects unless very large amounts of material are released. For example an ionospheric effect was observed after the release of water into the ionosphere during the launch of Skylab (Mendillo et al., 1975). There is, however, the possibility that man's activity over longer periods may change the state of the upper atmosphere through releases of long lived species that are transported from the lower atmosphere to greater heights.

Undoubtedly nuclear explosions in the upper atmosphere have produced the strongest and most extensive changes in the propagation medium. Radiation from a nuclear charge has produced ionospheric effects such as black-outs, phase deviations and TID's over areas many thousands of kilometers in extent. With present day knowledge of the atmospheric response to radiation, effects of a known type of nuclear weapon discharged at a known height should be predictable with reasonable accuracy.

11.   CONCLUSIONS

Geophysical disturbance effects in the upper atmosphere present a very complex and sometimes bewildering picture to the scientist as well as the user. Predictions of conditions relevant to radio communications have been greatly improved in recent years as far as short time forecasts of certain kinds of disturbances are concerned. However, our knowledge of the propagation medium is far from complete, and predictions of the response of the medium to an imposed stimuli such as particle precipitation, increased temperature etc are as yet bound to be uncertain and qualitative in nature. A picture is nevertheless

emerging of the main physical mechanisms triggered by the disturbance sources, and the extensive efforts made in the field should result in usable prediction schemes in the future.

REFERENCES

Bailey, V.A. and D.F. Martyn (1934). Phil. Mag. 18, pp. 369.

Bailey, D.K. and M.A. Pomerantz (1965). Relativistic electron precipitation into the mesosphere at subauroral latitudes. J. Geophys. Res. 70, pp. 5823.

Bain, W.C. and E. Hammond (1975). Ionospheric solar flare effect observations. J. Atm. Terr. Phys. 37, pp. 573-574.

Banks, P.M., R.W. Schunk and W.J. Raitt (1974). NO^+ and O^+ in the high latitude F-region. Geophys. Res. Lett. 1, pp. 239-242.

Becker, M., J. Bäte, V.H. Friedrich, A. Loidl, D. Offermann, D.G. Papanikas, H.Schwentek and E.V. Thrane. Density and temperature profiles measured in the mesosphere and lower thermosphere during winter anomaly conditions. J. Atmos. Terr. Phys, to be published.

Belrose, J.S. and L. Thomas (1968). Ionization changes in the middle latitude D-region associated with geomagnetic storms. J. Atmos. Terr. Phys. 30, pp. 1397-1413.

Chandra, S. and N.W. Spencer (1976). Thermosphere storms and related ionospheric effects. J. Geophys. Res. 81, pp. 5018-5026.

Deshpande, S.D. and A.P. Mitra (1972). Ionospheric effects of solar flares-III. The quantitative relationship of flare X-rays to SID's. J. Atmos. Terr. Phys. 34, pp. 243-253.

Donnelly, R.F. (1976). Solar flare X-ray and EUV emission; A terrestrial viewpoint. In: Physics of solar planetary environments. Proceedings of the International Symposium on Solar-Terrestrial Physics. Ed. D.J. Williams. American Geophysical Union, pp. 178-192.

Geller, M.A., G.C. Hess and D. Wratt (1976). Simultaneous partial reflection and meteor radar wind observations at Urbana, Illinois, during the winter of 1974-1975. J. Atm. Terr. Phys. 38, pp. 287-290.

Georges, T.M. (1967). Ionospheric effects of atmospheric waves. ESSA Technical Report IER 57-ITSA 54, Boulder, Colorado.

Hartz, T.R. (1968). The general pattern of auroral particle precipitation and its implications for high latitude communication systems. In: Ionospheric radio communications. Ed. K. Folkestad. Plenum Press, New York, pp. 9-32.

Hartz, T.R. and N.M. Brice (1967). Planet. Space Sci. 15, pp. 301.

Hartz, T.R., L.E. Montbriand and E.L. Vogan (1963). Canad. J. Phys. 41, pp. 581.

Hedin, A.E., P. Bauer, H.G. Mayr, G.R. Carignan, L.H. Brace, H.C. Brinton, A.D. Parks and D.T. Pelz (1977). Observations of neutral composition and related ionospheric variations during a magnetic storm in February 1974. J. Geophys. Res. 82, pp.3183-3189.

Jespersen, M. and B. Landmark (1968). Electron density observations during auroral absorption related to radio wave communication problems. In: Ionospheric Radio Communications. Ed. K. Folkestad, Plenum Press, New York, pp. 73-80.

Labtizke, K. (1977). Stratospheric-mesospheric mid-winter warmings. In: Dynamical and Chemical Coupling of Neutral and Ionized Atmosphere. Ed. B. Grandal and J.A. Holtet. Reidel Publ. Co., Dordrecht/Holland, pp. 17-34.

Larsen, T.R., J.B. Reagan, W.L. Imhof, L.E. Montbriand and J.S. Belrose (1976). A coordinated study of electron concentrations over Ottawa during disturbed conditions. J. Geophys. Res. 81, pp. 2200-2213.

Mathews, D.L. and D.J. Simons (1973). Observations of relativistic electron precipitation at L = 6. J. Geophys. Res. 78, pp. 7539-7542.

Matsushita, S. (1959). A study of the morphology of ionospheric storms. J. Geophys. Res. 64, pp. 305-321.

Mayr, H.G. and A.E. Hedin (1977). Significance of large-scale circulation in magnetic storm characteristics with application to AE-C neutral composition data. J. Geophys. Res. 82, pp. 1227-1234.

Mendillo, M., G.S. Hawkins and J.A. Klobuchar (1975). A sudden vanishing of the ionospheric F-region due to the launch of Skylab. J. Geophys. Res. 80, pp. 2217-2228.

Montbriand, L.C. and J.S. Belrose (1972). Effective electron loss rates in the lower D-region during the decay of solar X-ray flare events. Radio Sci. 7, pp. 133-142.

Offermann, D (1977). Some results from the European Winter Anomaly Campaign 1975-76. In: Dynamical and Chemical Coupling of Neutral and Ionized Atmosphere. Ed. B. Grandal and J.A. Holtet. Reidel Publ. Co., Dordrecht/Holland, pp. 235-252.

Prölss, G.W. and U. von Zahn (1974). ESRO 4 gas analyser results, 2. Direct measurements of changes in neutral composition during an ionospheric storm. J. Geophys. Res. 79, pp. 2535-2539.

Reagan, J.B. (1977). Ionization processes. In: Dynamical and Chemical Coupling of Neutral and Ionized Atmosphere. Ed. B. Grandal and J.A. Holtet. Reidel Publ. Co., Dordrecht/Holland, pp. 145-160.

Reid, G.C. (1972). A review of ionospheric radio propagation effects associated with solar proton events. In: Proceedings of COSPAR Symposium on Solar Particle Event of November 1969. Ed. James C. Ulwick. AFCRL-72-0474, pp. 201.

Risbeth, H. and O.K. Garriott (1969). Introduction to ionospheric physics. International Geophysics Series Volume 14, Academic Press.

Roble, R.G. (1977). Variations of the mean meridional circulation in the thermosphere. In: Dynamical and Chemical Coupling of Neutral and Ionized Atmosphere. Ed. B. Grandal and J.A. Holtet. Reidel Publ. Co., Dordrecht/Holland, pp.217-234.

Rosenberg, T.J., L.J. Lanzerotti, D.K. Bailey and J.D. Pierson (1972). Energy spectra in relativistic electron precipitation events. J. Atmos. Terr. Phys. 34, pp. 1977.

Rowe, J.N., A.J. Ferraro, H.S. Lee, R.W. Kreplin and A.P. Mitra (1970). Observations of electron density during a solar flare. J. Atmos. Terr. Phys. 32, pp. 1609-1614.

Schunk, R.W., W.J. Ratts and P.M. Banks (1975). Effect of electric fields on the daytime high-latitude E and F-regions. J. Geophys. Res. 80, pp.3121-3130.

Shapley, A.H. and W.J.G. Beynon (1965). Winter anomaly in ionospheric absorption and stratospheric warmings. Nature 206, pp. 1242.

Swanson, E. (1971). J. Inst. Navigation 18, pp. 168-175.

Thorne, R.M. (1974). A possible cause for dayside relativistic electron precipitation events. J. Atmos. Terr. Phys. 36, pp. 635.

Thorne, R.M. and C.F. Kennel (1971). Relativistic electron precipitation during magnetic storm main phase. J Geophys. Res. 76, pp. 4446.

Thorne, R.M. and T.R. Larsen (1976). An investigation of relativistic electron precipitation events and their association with magnetospheric substorm activity. J. Geophys. Res. 81, pp. 5501-5506.

Thrane, E.V., W. Bangert, D. Beran, M, Friedrich, B. Grandal, O. Hagen, A. Loidl, K. Spenner, H. Schwentek, K.M. Torkar and F. Ugletveit. Ion production and effective loss rate in the mesosphere and lower thermosphere during the Western Europe Winter Anomaly Campaign 1975-76. J. Atmos. Terr. Phys, to be published.

Utlaut, W.F. and R. Cohen (1971). Modifying the ionosphere with intense radio waves. Science 174, pp. 245-254.

Westerlund, S., F.H. Reder and C. Abom (1969). Effects of polar cap absorption events on VLF transmissions. Planet. Space Sci. 17, pp.1329.
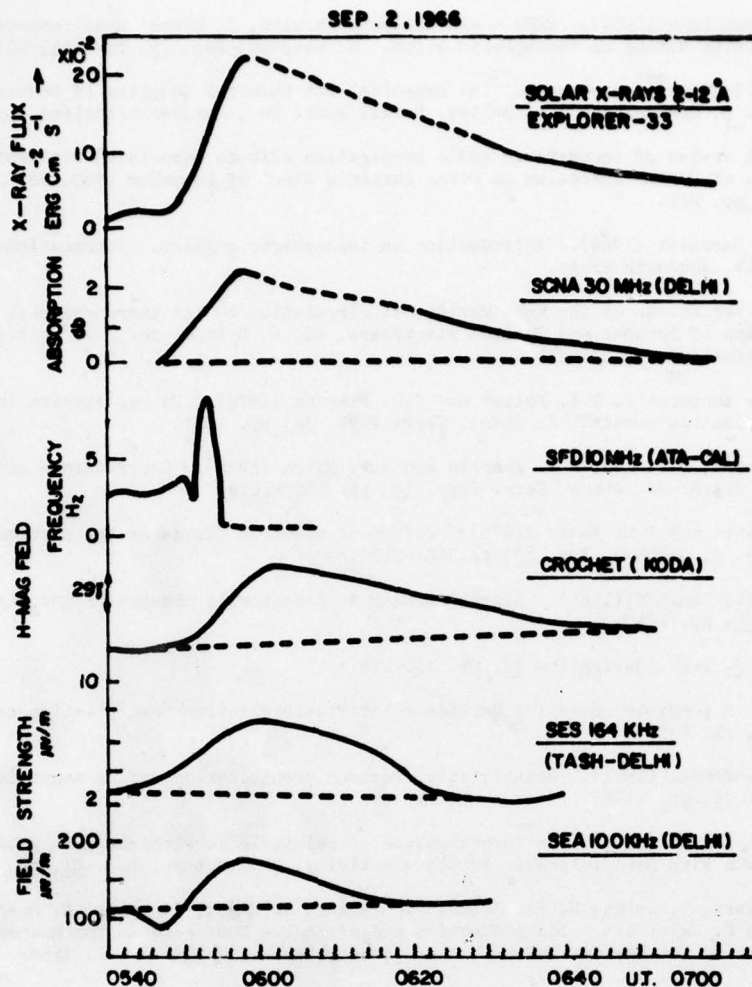
Figure 1   Time variation of X-ray flux and various SID's for a flare on
            Sept 2 1960 (Desphande and Mitra, 1972)
            SCNA   Sudden cosmic noise anomaly
            SFD   Sudden frequency deviation
            Crochet   Magnetic disturbance
            SES and SEA Field strength changes of LF waves
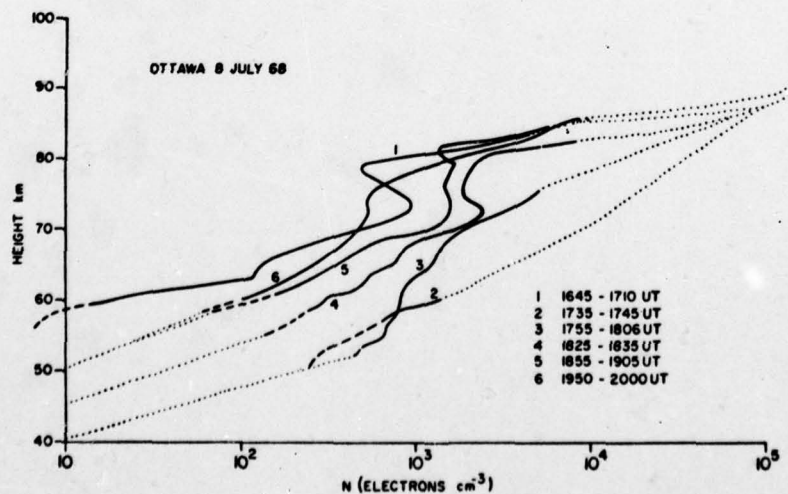
Figure 2   Electron density versus height profiles for a large flare
            on July 8 1969 (Montbriand and Belrose, 1972).
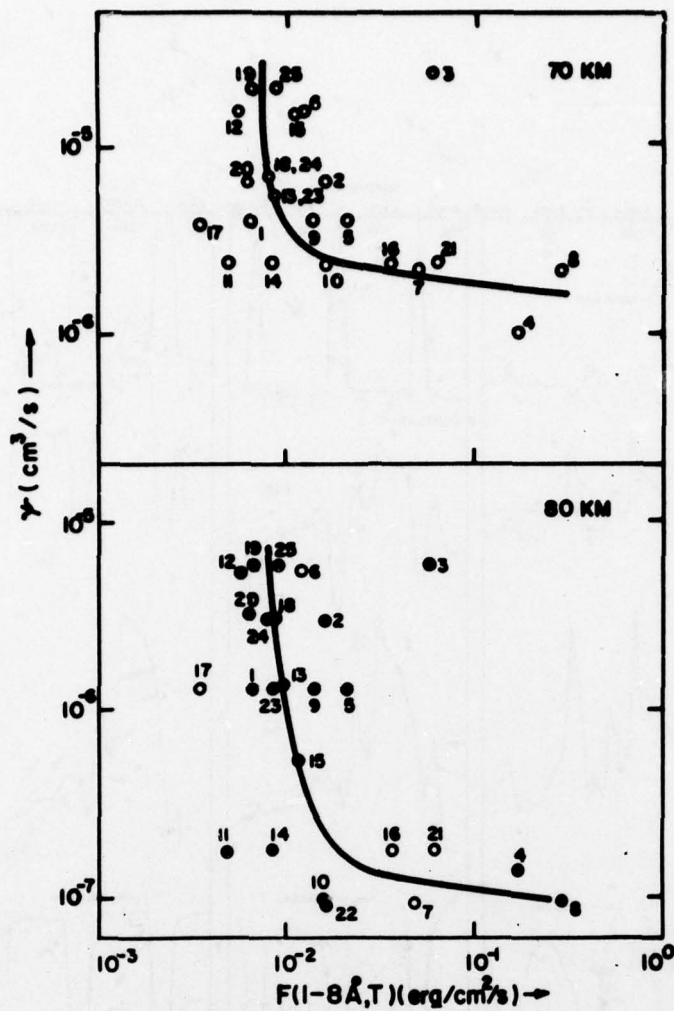
Figure 3 Effective recombination coefficient versus real flux in 0-8 A band for flare - SCNA events for 80 and 70 km heights (Desphande and Mitra, 1972).
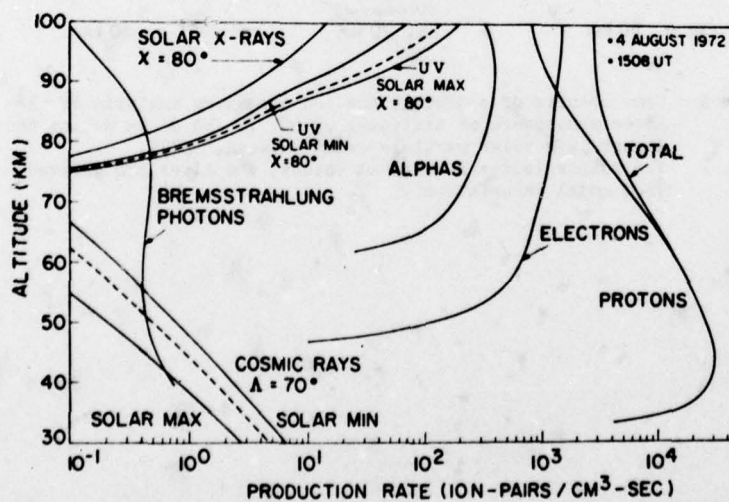
Figure 4 The contribution of the various solar particle, solar radiations, bremsstrahlung and cosmic rays to the total ion-par production in the August 1972 solar particle event (Reagan, 1977).
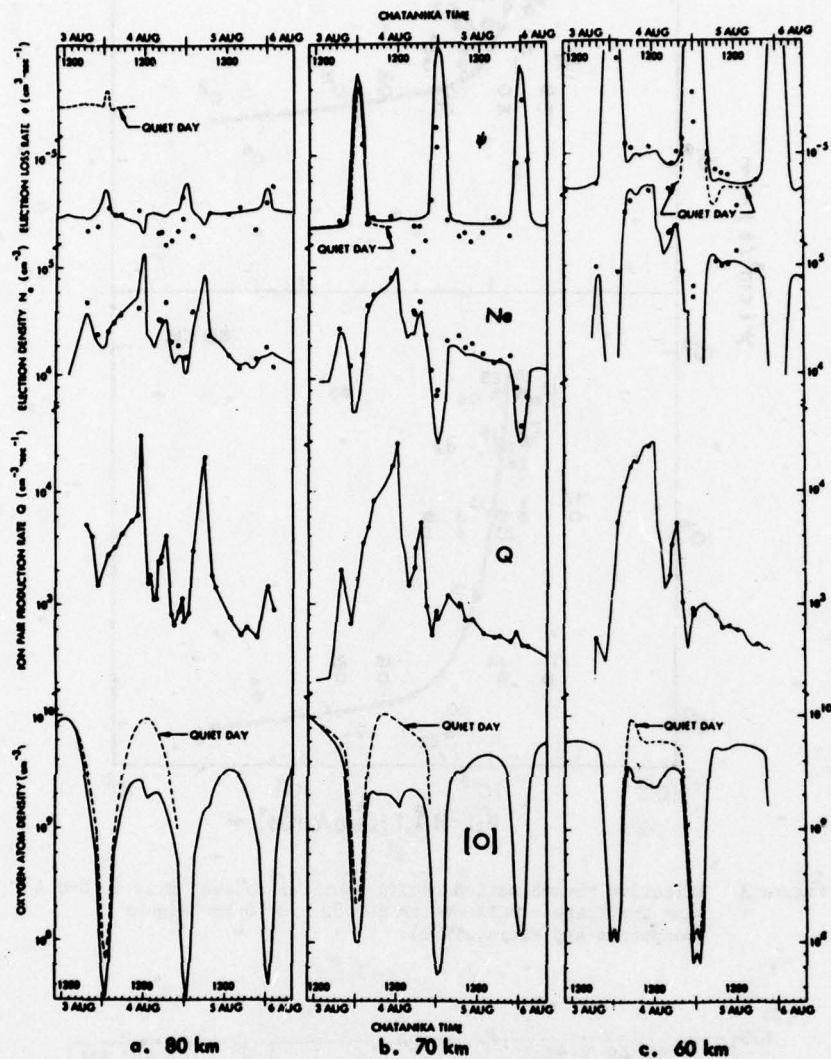
Figure 5   Some results of a neutral and ion chemistry analysis of the
lower atmosphere at altitudes of 80, 70 and 60 km during the
August 1972 solar particle event (Reagan, 1977).
The points indicate observed values, the lines are derived
from model calculations.
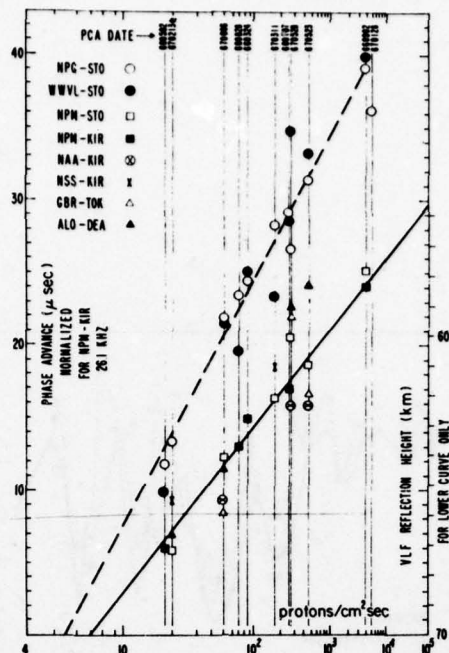
Figure 6   Daytime phase advance on high-latitude VLF circuits as a func-
tion of the flux of protons with energy greater than 25 MeV.
Phase advances have been normalized to a frequency of 26.1 kHz
and to a PCA-affected path portion of 5300 km. From Westerlund
et al. (1969).
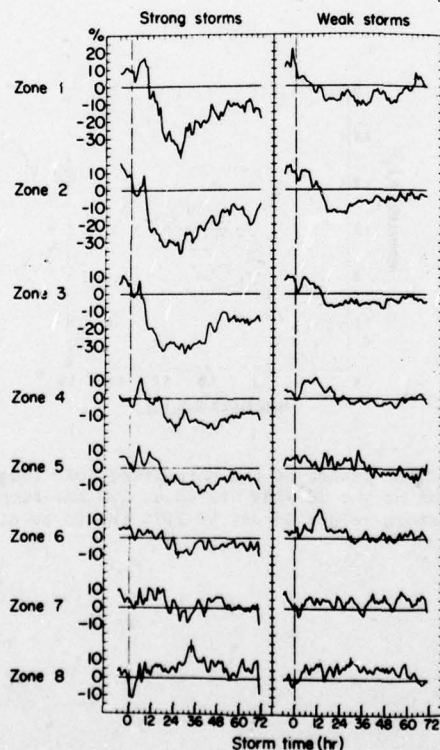
Figure 7   Dst variations of N_mF2 in each of eight latitude zones for
strong and weak magnetic storms with sudden commencements.
The ordinate is the approximate percentage deviation from the
quiet day behavior versus storm time (in hours). The zone num-
ber is shown in parenthesis between the applicable geomagnetic
latitudes: 60° (1) 55° (2) 50°(3) 45° (4) 40° (5) 30° (6)
20° (7) 10° (8) - 10° (Matsushita, 1959).
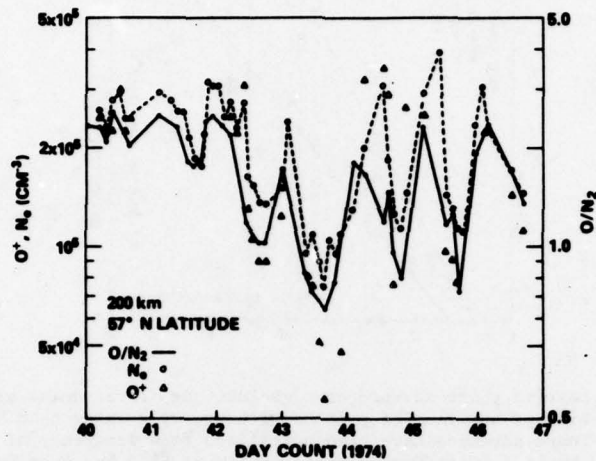
Figure 8   Temporal variation of the [O]/[N$_2$] ratio, [O$^+$], and N$_e$ at
           200 km (57°) (Hedin et al., 1977).
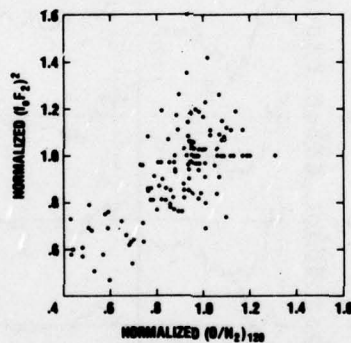
Figure 9   Plot of the square of the normalized foF2 frequency as a
           function of the [O]/[N$_2$] ratio at 120 km. Both are normalized
           by prestorm values on day 40 1974 (Hedin et al., 1977).
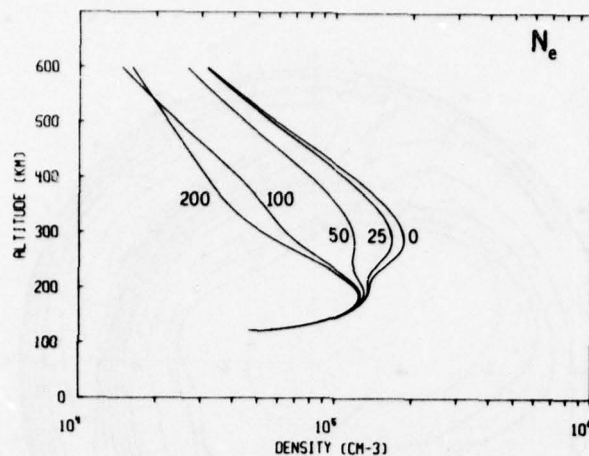
Figure 10 Altitude profiles of electron density for several effective
electric field strengths (mV m^{-1}) (Schunk et al., 1975).
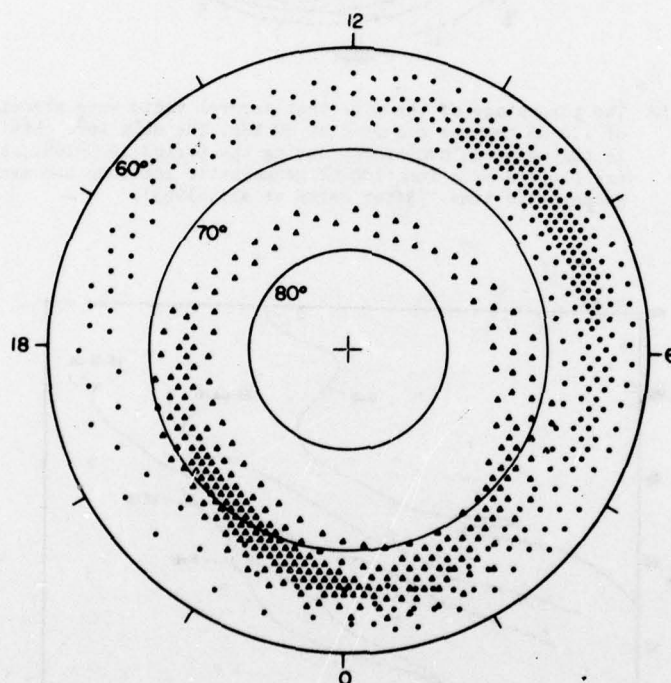
Figure 11 An idealized representation of the two main zones of auroral
particle precipitation in the northern hemisphere, where the
average intensity of the influx is indicated very approximate-
ly by the density of symbols and the coordinates are geomag-
netic latitude and geomagnetic time. The "discrete" events
are represented by triangles (which closely correspond to the
undisturbed "auroral oval") and the "diffuse" events are indi-
cated by the dots (Hartz and Brice, 1967). (Geomagnetic time
is local solar time measured with respect to geomagnetic
longitude.)
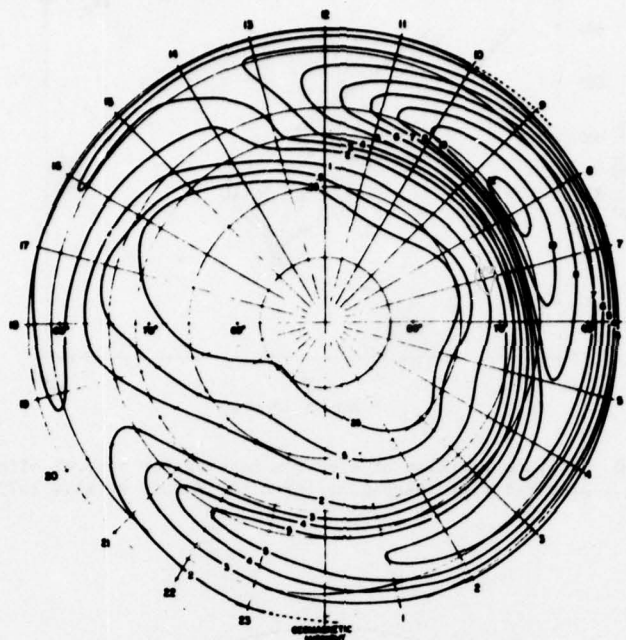
Figure 12   The percentage of the time that auroral radio wave absorption
of 1.0 dB or more occurred at 30 MHz. The data were obtained
in the northern hemisphere during the period 1959-1961, and
are plotted as a function of geomagnetic latitude and mean
geomagnetic time. (After Hartz et al., 1963).
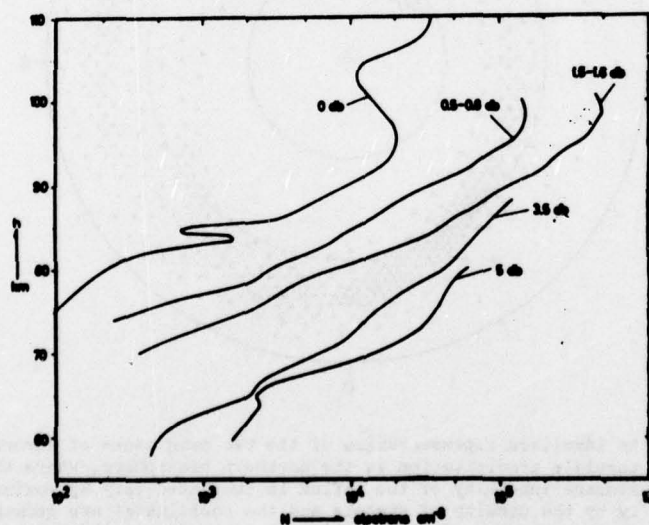
Figure 13   Average electron density profiles for different amounts of
auroral absorption (Jespersen and Landmark, 1968).
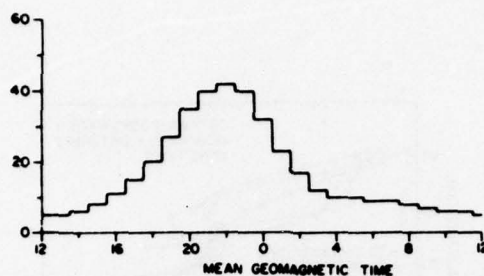
Figure 14 The diurnal variation in the percentage occurrence of spora-
dic E echoes that extend beyond 7 MHz on ionograms from auro-
ral-zone stations: the data are the average of 5 years' data
at Point Barrow (68.4°N), Churchill (68.7°N) and Ft-Chimo
(69.6°N) (Hartz, 1968).
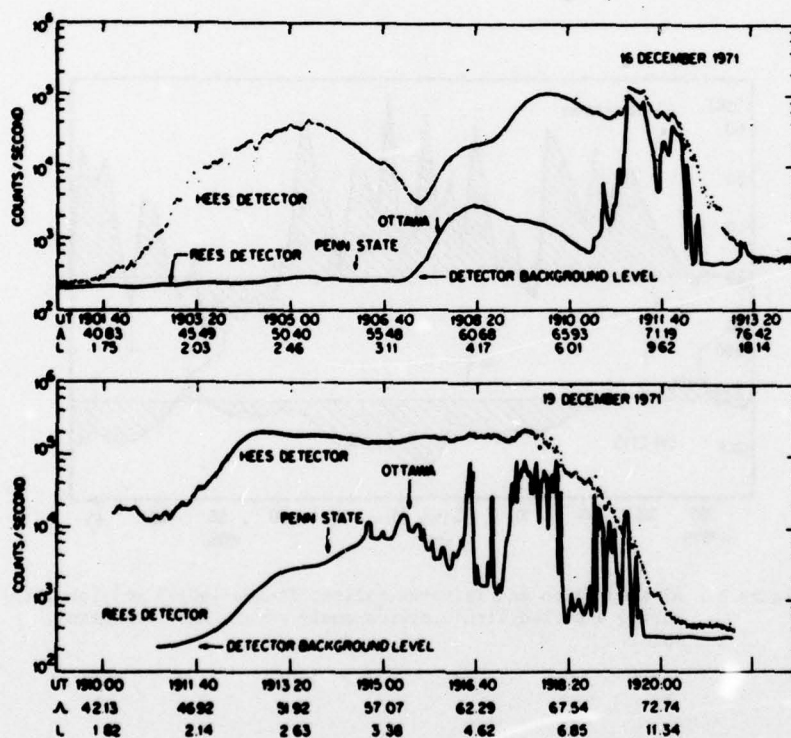
Figure 15 Latitudinal flux profiles of the locally-trapped (HEES) and
locally-precipitating (REES) electrons > 130 keV before (upper
panel) and after (lower panel) the magnetic storm of Decem-
ber 17 1971 (Larsen et al., 1976).
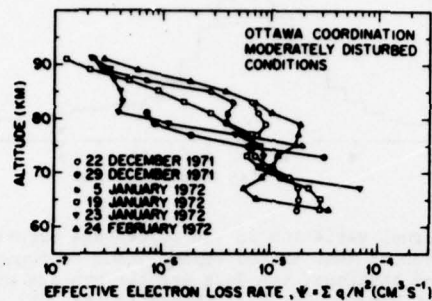
Figure 16 Effective electron loss rates, $\psi = \Sigma \, {}^q/N_e^2$ as a function of
height for moderately disturbed conditions (Larsen et al.,
1976).
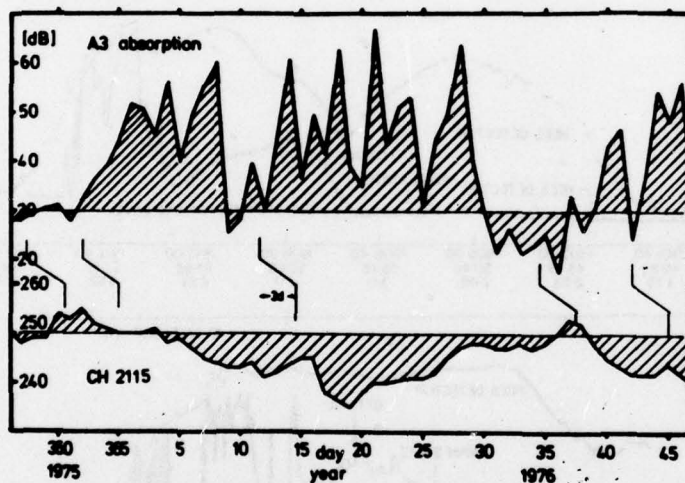
Figure 17 A3 absorption and infrared radiant fluxes (40-45 km) (ch 2115)
during a period with winter anomaly conditions (Offermann,
1977).
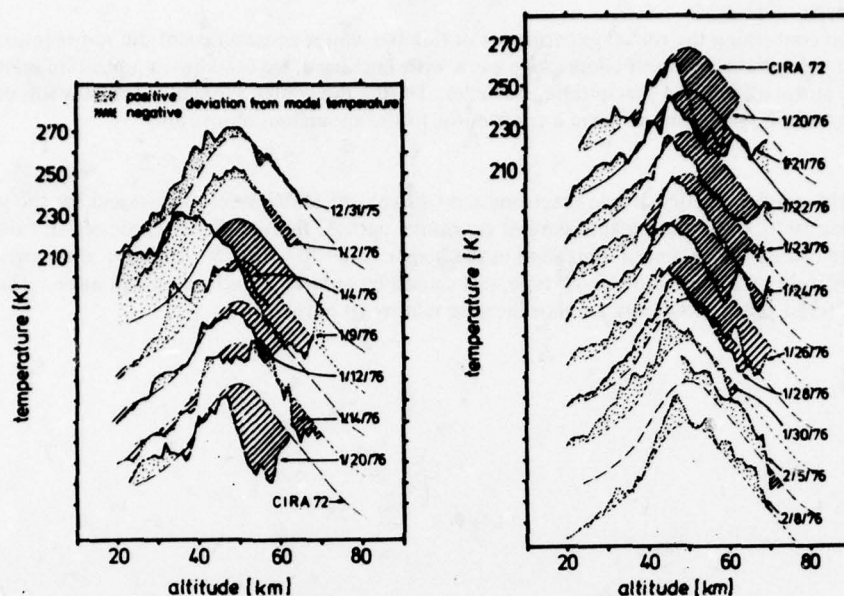
Figure 18 Rocket temperature measurements compared to CIRA 72 model profiles. Rocket flights are labelled by their dates (Offermann, 1977).
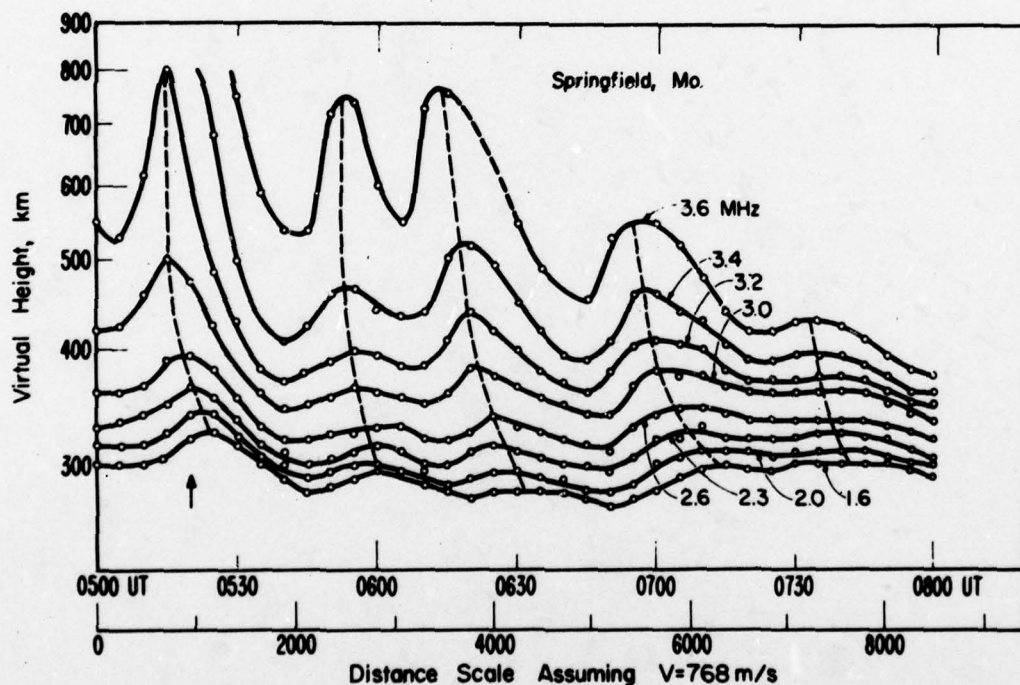
Figure 19 Virtual height variations observed during a large scale travelling ionospheric disturbance (Georges, 1967).

DISCUSSION

E.Montbriand, Canada

The Discussion concerning the rocket experiments during the winter anomaly event did not mention if any energetic particles were precipitating. In our cooperative work with Lockheed, we established a position relationship between past magnetic storm effects and precipitating particles. During the winter anomaly event studied, could precipitating particles be positively ruled out as being a contributor to the anomalous absorption?

Author's Reply

The rockets did carry energetic particle spectrometers (40 keV – 1 MeV, for electrons) and for the winter anomaly day, 21 January 1976, these instruments showed very small particle fluxes. The ion production from these fluxes could not have caused the enhanced ionization in the height range 70 – 100 km. It seems, therefore, that the absorption event was truly of a "meteorological" type, not caused by enhanced particle precipitation. The solar X-ray flux was also monitored and showed only a minor increase relative to normal.
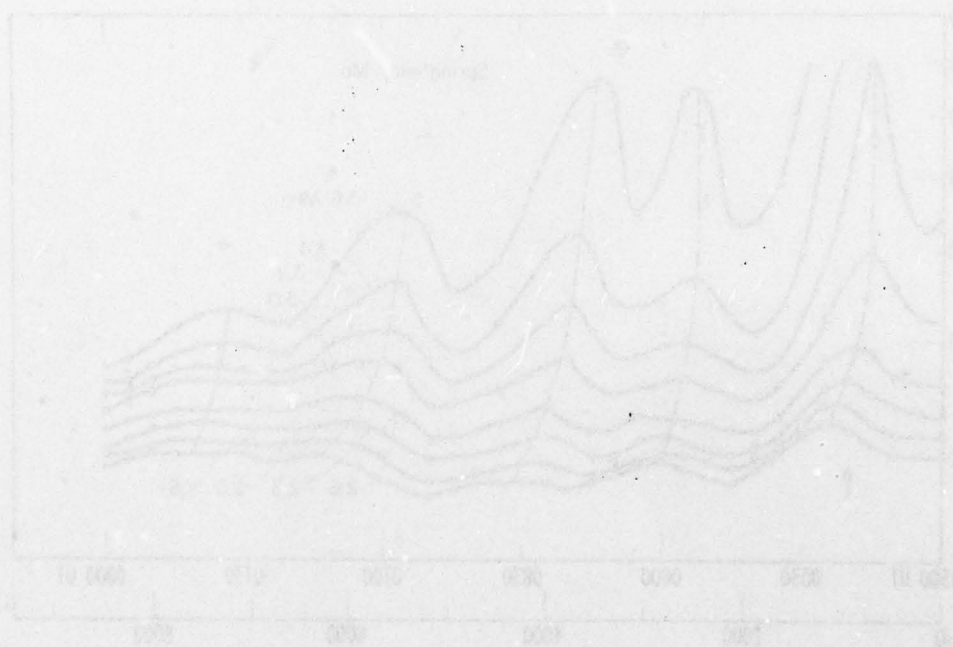
SUMMARY OF SESSION II

REVIEW/IONOSPHERIC ENVIRONMENT

by

Dr C.M.Rush
Session Chairman

The session opened with an invited talk by **Professor Nisbet** of the Pennsylvania State University entitled "*Operational Physical Models of the Ionosphere*". The talk focused on the current state of knowledge of the physical and chemical mechanisms responsible for the formation, as well as the changes in the structure, of the ionosphere. The importance of the dynamics of the neutral atmosphere in the determination of the ionospheric structure was stressed. Professor Nisbet pointed out the various types of approaches to ionospheric modeling and the strengths and weaknesses of each. The state-of-the-art of ionospheric modeling is such that the average ionospheric structure can be well modeled but the day-to-day variability can not.

The intentions and the approach to developing the International Reference Ionosphere (IRI) was next described in a paper by **Rawer** et al. Professor Rawer was unable to attend the meeting and the paper was read by Dr Albrecht. The IRI is a joint URSI and COSPAR effort. The IRI is a computer-based ionospheric model that yields the following parameters: electron density, electron and ion temperature, and relative ion composition. The model relies quite heavily on measured data and the areas where the model is lacking in accuracy because of a scarcity of observations were described in full. The utilization of satellite data to supplement ground-based observations has proved to be viable means for obtaining a realistic ionospheric model, particularly over ocean areas.

The propagation of VLF signals from one hemisphere to another along lines of force of the geomagnetic field was described by **Bernhardt** and **Park**. Using a model of the ionosphere and magnetosphere charged particle populations, they were able to model the ducting of VLF waves in the natural environment. The modeled results were consistent with direction finding measurements of VLF waves observed in the plasmasphere.

Following this paper, a general discussion period was undertaken. The comments resulting from this discussion period are given elsewhere.

The last two papers of the session were devoted to correcting for ionospheric induced errors in satellite systems. **Tomljanovich** and **Long** described a method to update in real-time the range correction for a space surveillance radar. The method relies on the adaptation of measurements of total electron content (TEC) made using the TRANSIT satellites to provide a correction to the TEC estimate over the entire radar coverage area. Methods to extrapolate the observations were developed and described in full. The results of on-site measurements at Clear, Alaska, were presented to illustrate the improvement in radar accuracy.

Dr Rodney Bent presented the last paper dealing with ionospheric correction in satellite-to-satellite tracking. It was pointed out that the tracking of satellites were subjected to errors such as: satellite height, localized ionospheric perturbations and electron density changes. The use of a sophisticated model to reduce these errors was described. This model of electron density provides for a global representation of the electron density as is particularly appropriate for representing the electron density in the ionosphere above the F-layer peak.

Operational Physical Models of the Ionosphere

John S. Nisbet

Ionosphere Research Laboratory
The Pennsylvania State University
University Park, Pennsylvania 16802

ABSTRACT

Recent series of measurements most notably by the OGO, Aeros and Atmospheric Explorer series of satellites have completely revised the global models of the neutral constituents relevant to ion density models and improved our knowledge of the ion chemistry. New information has been provided on the pressure gradients that control the wind system and much has been learned about the electric field systems due to balloon, satellite and incoherent scatter measurements. The implication of these results to the development of global ionospheric models is discussed. While such models can reproduce the average electron densities in the ionosphere the large day to day variations are much more difficult to model. The current state of knowledge of the factors controlling these fluctuations and possible approaches for operational models are reviewed.

1.   INTRODUCTION

(Nisbet, J.S., 1975) discussed the status of models of the ionosphere. The purpose of this review is to discuss the progress that has been made since then and to expand on the needs and requirements of such models for the development and operation of engineering systems.

Three main types of models of the ionosphere may be considered. The first is the mean morphological model similar to the Penn State Mark I, (Nisbet, J.S., 1971), the (Ching, B.K., Chiu, Y.T., 1973), and (Chiu, Y.T., 1975) models. These models of the electron density, like their atmospheric counterparts the CIRA 1965 and 1972 models and the more recent MSIS model (Hedin, A.E. et al., 1977a, b), attempt to provide a global description of the average behavior for a given day, solar and magnetic conditions. It is this type of model that has received the greatest attention. Its uses for the development of operational systems consist in allowing series of calculations of the effects of the ionosphere to be made for varying conditions and in allowing extrapolations to be made of the implication of measurements made at one season or set of solar conditions to those at other solar conditions. The long period of the solar cycle compared with the development time for a typical operational system and the wide range of activity at solar maxima make such calculations necessary in very many cases.

Mean morphological models have the major disadvantage for many applications that they do not model those very ionospheric parameters that may be of importance to the operation of a system. Many systems are quite tolerant of ionospheric effects that do not have large horizontal gradients or in which there are no fluctuations in density on scale sizes comparable to a wavelength, and these are not normally considered part of a mean morphological model. What is needed here, it would seem, is a class of dynamic models that can be used in system development. One can envisage models of ionosphere under quiet, medium or highly disturbed conditions in which an attempt has been made to build in to the densities horizontal and vertical gradients values typical of those developing during a period of time due to gravity waves or other neutral atmospheric induced variations and due to ionospheric instabilities. The aim would be to not necessarily reproduce ionospheric conditions at any given location at any given time but to build the equivalent of an automobile "test track" which could be used to test the relative immunities of various systems to ionospheric influences.

The third class of ionospheric model has its analog in weather forecasting and will be called the forecast model. In its crudest form its aim is to allow frequencies to be chosen that will be optimum for given ionospheric paths. More sophisticated applications have been envisaged in which it is desired to correct in real time for ionospheric effects such as refractive errors that cannot be directly measured. This model is much more complicated in its ultimate development than the first two classes because of the complexity of the processes causing the ionospheric "weather" and the extreme difficulty of measuring them in real time and the lack of understanding of the causes of many of the variations in space and time that are seen.

1.1   Mean Morphological Models of the Ionosphere

Neutral atmospheric models for morphological models of the ionosphere have improved enormously in recent years due to the OGO 6, ESRO 4, Aeros A and B and the Atmospheric Explorer satellites. CIRA (1972) provided excellent models of the average behavior of total density as a function of altitude, latitude and local time but failed to model many of those aspects of the ionosphere related to the diurnal, latitudinal and seasonal variation. The reasons for this are that the F region, in particular, is very dependent on the ratio of atomic oxygen which controls the predominant production process to molecular nitrogen and oxygen which control the predominant chain of electron loss processes. CIRA (1972) used a "one family" set of models in which exospheric temperature was uniquely related to a temperature and set of density profiles. The effects of vertical transport on the atomic oxygen densities is very important and because atomic oxygen is the major constituent in the region of the atmosphere responsible for the orbital decay of most of the satellites used to derive CIRA (1972) the temperature and molecular densities were seriously in error.

A new model of the thermosphere, the MSIS model, (Hedin, A.E., et al., 1977a, b) is based on satellite Mass Spectrometer and Incoherent Scatter data and does not suffer from these disadvantages. It models accurately the mean latitudinal behavior of the major constituents of important for F region models so that such effects as the seasonal anomaly can be modeled theoreticaly. Also of importance are the pressure gradients because these control the horizontal wind system that is important in controlling the F layer altitudes and densities and hence the latitudinal and longitudinal variations. (Roble, R.G., et al., 1977) have used the MSIS 1977 model to calculate the zonal mean circulation in the thermosphere with encouraging

results. Considerable progress has also been made in the variations of minor, but important, constituents such as atomic nitrogen (Mauesberger, K., et al., 1976, and Engebretson, M.J., et al., 1977). Molecular oxygen measurements have also been considerably improved with the use of the open source mass spectrometers in the fly through mode on the atmospheric explorer satellites (Potter, W.E., et al., 1977).

High latitude theoretical ionospheric models have been much less realistic than those at low latitudes. Not only is the neutral atmosphere more complicated and the ionizing energetic particles are very variable but convection is so important that the transport times of the ions are short compared with their lifetimes in the F region. (Knudsen, W.C., et al., 1977) have presented a numerical model of the convecting F_2 layer. In this model time-dependent behavior of tubes of F layer plasma is computed for tubes carried around several flow paths in the polar region. It was found that their proposed convection pattern produced a tongue of F layer plasma over the polar cap with electron concentrations consistent with the measured concentrations. Had the F layer been assumed to be nonconvecting over the polar cap, the computed concentrations would have been a factor of 10 too small. Rapid convection of plasma across the cleft prevented significant increase in N_mF_2 at that region. A midlatitude trough was found to be formed by the proposed convection pattern with only normal F layer recombination processes operating.

In the equatorial region the effects of the transport normal to the field lines by the electric fields and along the field lines by the winds are of great importance. These effects have been modeled by (Anderson, D.N, 1973) and shown to produce large declination and hence longitude effects. It has now been shown by (Rishbeth, H., et al., 1977) that the vertical motions produce large ion temperature changes which must also be included in realistic models.

Important improvements have been made in the knowledge of the EUV and particle fluxes that control the production and of the electric fields that control the transport.

For the mean morphological model then there have been major improvements in recent years on the physical understanding on which the models are based and many fewer ad hoc assumptions are now necessary in relating theory to observations.

1.2   Dynamic Models of the Ionosphere

In this section the factors affecting the development of models of the ionosphere having realistic gradients will be discussed. Before examining the approaches to modelling that may be applicable let us first examine the causes for these variations as they are now understood.

Best understood of the large scale variations are those associated with magnetic storms. During a magnetic storm the particle inputs to the auroral zone increase causing increased ionization, increased heating, due mainly to the energy deposited by currents flowing in the ionosphere, and enhanced circulation caused by the ion motions due to the increased electric fields. Additional effects are caused by waves induced by the dynamic heating in the auroral electrojet (Testud, J., 1970, Reber, C.A., et al., 1975; Mayr, H.G., and Volland, H., 1976; and Eun, H. and Gross, S.H., 1976). Major effects are produced by the heating which raises the thermospheric pressure causing winds to flow to lower latitudes (Richmond, A.D. and Matsushita, S., 1975; Davies, K. and Ruster, R., 1976; Ruster, R. and King, J.W., 1976; and Mayr, H.G. and Hedin, A.E., 1977). Atomic oxygen is the major constituent and has a larger scale height than molecular nitrogen and molecular oxygen and the pressure gradient equalizes quite rapidly at altitudes around 400 km. The upward diffusion of atomic oxygen through the molecular constituents reduces the ratio of atomic oxygen to the molecular constituents in the lower thermosphere (Nisbet, J.S. and Glenar, D.A., 1977) particularly in the post midnight sector. The winds flowing equatorward blow the ionization up field lines reducing recombination rates while the reduced O/N_2 and O/O_2 ratios at F region heights at high latitudes cause the densities there to be reduced, particularly during the day. The changes in the thermosphere during magnetic storms have been analyzed extensively using satellites (Trinks, H.S, et al., 1975; Prölss, G.W., et al., 1975; Jacchia, L.G., et al., 1976; Chandra, S. and Spencer, N.W., 1976; and Hedin, A.E., et al., 1977). The effects of magnetic storms thus include effects ranging from gigahertz scintillations due to the large density gradients in auroral forms, strong absorption at lower frequencies due to enhanced particle ionization in regions where the collision frequencies are large, areas of global extent where F layer critical frequencies are enhanced, and depleted, and travelling disturbances due to gravity waves.

While these effects are dramatic and the energy inputs and transport are beginning to be understood the ions are a minor constituent and effects due to the "meteorology" of the neutral atmosphere are large and not well related to causitive mechanisms. There are variations in the F region of +50 percent in the total electron content and +4 hours in the time of the maximum even on quiet days and at mid-latitudes (Kane, R.P., 1975) and these variations have scale lengths as small as 3000 km. The F region densities have, however, been shown to be closely related to the O/N_2 ratio at the peak of the layer (Prölss, G.W., and von Zahn, 1976; Trinks, H., et al., 1976). The D region the winter absorption anomaly appears to have a meteorological cause and to be associated with the planetary wave structure and probably the redistribution of a minor constituent such as nitric oxide.

While magnetic storm effects have a relatively clear association between "input" energy and "output" response instability mechanisms can cause large local perturbations starting from conditions that are much less dramatic. Most important of this type of irregularity are the "plasma bubbles" in the nighttime equatorial ionosphere which produce irregular reductions in ion density of up to three orders of magnitude on scales of 10 to 200 km.

To develop operational models of such effects it is necessary to know both the morphological structure of the variation and the probability of occurrence. Two approaches seem possible. In the first statistical parameters of the structure can be presented. Shape parameters of the spatial and temporal autocorrelation function as a function of the geophysical parameters that control them are needed. It is obvious that the amount of information contained in any such model is much larger than in a mean ionospheric model and that both the data available and the theoretical understanding on which such a model could be based are much less extensive. In the second approach secondary parameters such as scintillation indices or the probability of seeing spread F (Singleton, D.G., 1975) are modeled. This approach has the advantage that the modeled

parameters are closely related to the observations. The problem with this approach is that there is no guarantee that the parameters modeled are related in any simple way to the parameters that are of importance to another system. If theoretical understanding is missing on the relationship of the parameters to the geophysical variables it may well be that there is no logical way of interpreting the relevance of the data to the new system or extrapolating the observed data to other conditions.

A second problem arises with dynamic effects, such as those discussed above, due to their time evolution. It may become possible eventually to develop fully dynamic theoretical models which would be able to reproduce the ionospheric behavior based on given initial conditions. It would be much easier to develop "case study" models of the ionosphere with typical gradients under quiet, disturbed and very disturbed conditions. It would then be necessary to determine from long term studies the probability distribution for occurrence of the disturbances and thus establish statistical parameters for the percentage of time a given range of conditions is likely to be encountered. This last approach seems most promising providing the statistical basis is adequate.

1.3   Forecasting Models

Forecasting models of the ionosphere were extensively developed during World War II for use in predicting high frequency propagation conditions and in particular maximum usable frequencies. Such models reproduced the variation with latitude season and sunspot number and were a valuable aid in frequency allocation. They generally belonged to the class of mean morphological models and did not attempt to reproduce the large gradients frequently found in practice.

Many applications now exist such as navigational satellites and radars in which it would be desirable to be able to correct for such gross ionospheric parameters as refraction on a real time basis. In practice most of such systems require a knowledge of the total electron content along the ray path. (Johanson, J.M., et al., 1978) have examined the standard deviations from mean monthly values of total electron content for six stations between 11° and 71° geomagnetic north latitude for three seasons and years of high sunspot activity represented by 1969 and low activity represented by 1974. Their results show values in the day-time which are typically between 20 and 30 percent rising to values of about 60 percent during hours of darkness at the higher latitudes. Apart from isolated periods of storm activity they show that the histograms were well fitted to a gaussian distribution. These variations are quite large compared with the accuracy with which the mean monthly total electron content can be predicted and give a good measure of the improvement in ionospheric error reduction that can be obtained with a mean monthly model. It seems unlikely that a reduction in the maximum errors by a factor of as much as five can be obtained consistently in this way.

This has led investigators such as (Donatelli, D.E., and Allen, R.S., 1978),(Millman, G.H., 1978), and (Somayajulu, U.V. and Ghosh, A.B., 1978) to consider updating model calculations by the use of current data such as satellite electron content measurements, ionosonde critical frequencies or transponder responses. The correlation distance for irregularities in the ionosphere is comparable with the distance to the F region on an oblique path and large perturbations take place at even mid and low latitudes in time scales of the order of an hour (Doupnik, J.R. and Nisbet, J.S., 1968). Such schemes thus work best when both the time of measurement and propagation path are identical for the correcting signal and that to be corrected. Under such circumstances there seems little need for model measurements and to my mind the future of ionospheric forecasting models is not promising in the near future.

2.   SUMMARY AND CONCLUSIONS

Global ionospheric models that reproduce the mean monthly ionospheric behavior can now be developed which have departures from the mean that are smaller than the standard deviation about that mean. Case study models can be developed that will reproduce developing ionospheric conditions over periods of time which can be used to study the immunity of systems to ionospheric dynamic effects.

The development of these models requires theory coupled with examination of the available data base and new measurements. It is a complex task and one that would lead to new theoretical concepts and understanding. It would be useful because the time scale for system development is short compared with the solar cycle. It is, however, difficult to justify. The costs are large and the development times long compared with the needs of any one system or even of any one agency. As a result small efforts, with small data bases, which do not advance the state of the art measurably, continue. Meanwhile systems are designed on the basis of inadequate data, obtained with difficulty from data bases of short duration or which were obtained for other purposes.

To break out of this cycle requires a coordinated effort and a long term program. The needs continue as do the small scale modeling efforts. We will assuredly pay for good ionospheric models whether we develop them or not.

3.   ACKNOWLEDGEMENT

4.   REFERENCES

Anderson, D.N., 1973, "A Theoretical Study of the Ionospheric F Region Equatorial Anomaly--II. Results in the American and Asian Sectors", Planetary Space Science, 21, 421-442.

Chandra, S. and N.W. Spencer, 1976, "Thermospheric Storms and Related Ionospheric Effects", Journal of Geophysical Research, 81, 28, 5018-5026.

Ching, B.K. and Y.T. Chiu, 1973, "A Phenomenological Model of Global Ionospheric Electron Density in the E, F_1 and F_2 Regions", Journal of Atmospheric and Terrestrial Physics, 35, 1615-1630.

Chiu, Y.T., 1975, "An Improved Phenomenological Model of Ionospheric Density", Journal of Atmospheric and Terrestrial Physics, 37, 1563-1570.

Davies, K. and R. Ruster, 1976, "Theoretical Studies of Storm Effects in Ionospheric Total Electron Content, Planetary Space Science, 24, 862-872.

Donatelli, D.E. and R.S. Allen, 1978, "Temporal Variability of Ionosphere Refraction Correction", Proc., 1978 Symposium, Naval Research Laboratory, Washington, D. C., January 24-26, paper 6-5.

Doupnik, J.R. and J.S. Nisbet, 1968, "Fluctuations of Electron Density in the Daytime F-region", Journal of Atmospheric and Terrestrial Physics, 30, 931-961.

Engebretson, M.J., K. Mauersberger, D.C. Kayser, W.E. Potter, and A.O. Nier, 1977, "Empirical Model of Atomic Nitrogen in the Upper Thermosphere", Journal of Geophysical Research, 82, 4, 461-471.

Eun, H. and S.H. Gross, 1976, "Ionospheric Disturbances and Gravity Waves", Journal of Geophysical Research, 81, 19, 3261-3270.

Hedin, A.E., P. Bauer, H.G. Mayr, G.R. Carignan, L.H. Brace, H.C. Brinton, A.D. Parks and D.T. Pelz, 1977, "Observations of Neutral Composition and Related Ionospheric Variations During a Magnetic Storm in February 1974", Journal of Geophysical Research, 82, 22, 3183-3190.

Hedin, A.E., C.A. Reber, G.P. Newton, N.W. Spencer, H.C. Brinton, F.G. Mayr and W.E. Potter, 1977, "Global Thermospheric Model Based on Mass Spectrometer and Incoherent Scatter Data MSIS 2. Composition", Journal of Geophysical Research, 82, 16, 2148-2156.

Hedin, A.E., J.E. Salah, J.V. Evans, C.A. Reber, G.P. Newton, N.W. Spencer, D.C. Kayser, D. Alcayde, P. Bauer, L. Cogger and J.P. McClure, 1977, "A Global Thermospheric Model Based on Mass Spectrometer and Incoherent Scatter Data MSIS 1. N_2 Density and Temperature", Journal of Geophysical Research, 82, 16, 2139-2147.

Jacchia, L.G., J.W. Slowfy and U. von Zahn, 1976, "Latitudinal Changes of Composition in the Disturbed Thermosphere from Esro 4 Measurements", Journal of Geophysical Research, 81, 1, 36-42.

Johanson, J.M., M.J. Buonsanto and J.A. Klobuchar, 1978, "The Variability of Ionospheric Time Delay", Proc., 1978 Symposium, Naval Research Laboratory, Washington, D. C., January 24-26, paper 6-3.

Kane, R.P., 1975, "Day-to-Day Variability of Ionospheric Electron Content at Mid-Latitudes", Journal of Geophysical Research, 80, 22, 3091-3099.

Knudsen, W.C., P.M. Banks, J.D. Winningham and D.M. Klumpar, 1977, "Numerical Model of the Convecting F_2 Ionosphere at High Latitudes", Journal of Geophysical Research, 82, 29, 4784-4792.

Mauersberger, K., M.J. Engebretson, D.C. Kayser and W.E. Potter, 1976, "Diurnal Variation of Atomic Nitrogen", Journal of Geophysical Research, 81, 13, 2413-2448.

Mauersberger, K., D.C. Kayser, W.E. Potter and A.O. Nier, 1976, "Seasonal Variation of Neutral Thermospheric Constituents in the Northern Hemisphere", Journal of Geophysical Research, 81, 1, 7-11.

Mayr, H.G. and A.E. Hedin, 1977, "Significance of Large-Scale Circulation in Magnetic Storm Characteristics With Application to AE-C Neutral Composition Data", Journal of Geophysical Research, 82, 7, 1227-1234.

Mayr, H.G. and H. Volland, 1976, "Composition Waves in the Thermosphere", Journal of Geophysical Research, 81, 4, 671-676.

Millman, G.H., 1978, "Ionospheric Propagation Effects on HF Backscatter Radar Measurements", Proc., 1978 Symposium, Naval Research Laboratory, Washington, D. C., January 24-26, paper 3-7.

Nisbet, J.S., 1975, Atmospheres of Earth and the Planets. "Models of the Ionosphere", Dordrecht-Holland, D. Reidel Publishing Company, 245-258.

Nisbet, J.S., 1971, "On the Construction and Use of a Simple Ionospheric Model", Radio Science, 6, 4, 437-464.

Nisbet, J.S. and D.A. Glenar, 1977, "Thermospheric Meridional Winds and Atomic Oxygen Depletion at High Latitudes", Journal of Geophysical Research, 82, 29, 4685-4693.

Potter, W.E., D.C. Kayser, H.C. Brinton, L.H. Brace and M. Oppenheimer, 1977, "Comparison of Measured and Calculated Thermospheric Molecular Oxygen Densities", Journal of Geophysical Research, 82, 32, 5243-5248.

Prölss, G.W. and U. von Zahn, 1976, "Large and Small Scale Changes in the Disturbed Upper Atmosphere", Journal of Atmospheric and Terrestrial Physics, 38, 655-659.

Prölss, G.W., U. von Zahn and W.J. Raitt, 1975, "Neutral Atmospheric Composition, Plasma Density, and Electron Temperature at F Region Heights", Journal of Geophysical Research, 80, 25, 3715-3718.

Reber, C.A., A.E. Hedin, D.T. Pelz, W.E. Potter and L.H. Brace, 1975, "Phase and Amplitude Relationships of Wave Structure Observed in the Lower Thermosphere", Journal of Geophysical Research, 80, 34, 4576-4580.

Richmond, A.D. and S. Matsushita, 1975, "Thermospheric Response to a Magnetic Substorm", Journal of Geophysical Research, 80, 19, 2839-2850.

Rishbeth, H., T.E. Van Zandt and W.B. Hanson, 1977, "Ion Temperature Troughs in the Equatorial Topside Ionosphere", Planetary Space Science, 25, 629-642.

Roble, R.G., R.E. Dickinson and E.C. Ridley, 1977, "Seasonal and Solar Cycle Variations of the Zonal Mean Circulation in the Thermosphere", Journal of Geophysical Research, 82, 35, 5493-5504.

Ruster, R. and J.W. King, 1976, "Negative Ionospheric Storms Caused by Thermospheric Winds", Journal of Atmospheric and Terrestrial Physics, 38, 593-598.

Singleton, D.G., 1975, "An Empirical Model of Global Spread-F Occurrence", Journal of Atmospheric and Terrestrial Physics, 37, 1535-1544.

Somayajulu, U.V. and A.B. Ghosh, 1978, "Modelling for Low Latitude Ionosphere", Proc., 1978 Symposium, Naval Research Laboratory, Washington, D. C., January 24-26, paper 2-9.

Testud, J., 1970, "Gravity Waves Generated During Magnetic Substorms", Journal of Atmospheric and Terrestrial Physics, 32, 1793-1805.

Trinks, H., S. Chandra, N.W. Spencer and U. von Zahn, 1976, "A Two-Satellite Study of the Neutral Atmosphere Response to a Major Geomagnetic Storm", Journal of Geophysical Research, 81, 28, 5013-5017.

Trinks, H., K.H. Fricke, U. Laux, G.W. Prölss and U. von Zahn, 1975, "Esro 4 Gas Analvzer Results 3. Spatial and Temporal Structure of the Mid-Latitude Atmosphere During a Geomagnetic Storm", Journal of Geophysical Research, 80, 34, 4571-4575.

DISCUSSION

E.R.Schmerling, US

I agree that the broad-scale understanding of the ionosphere is important. Now the sunspot number variation in the F region is in conflict with a simple-minded explanation of the seasonal anomaly. Did I hear the speaker state that the seasonal effect is now understood?

Author's Reply

I believe that if you use the new MSIS (Mass Spectrometer and Incoherent Scatter) neutral atmosphere model with the winds that are derived from it and the electric fields as they are now understood you can explain, very well, both the seasonal variations in the height of the peak and the peak density during the day at mid and low latitudes.

J.Aarons, US

I would like to defend the trade of construction of mean morphological models. Even with a full understanding of the physics of the depletion regions in the equatorial ionosphere, one would need a mean morphological model to give to systems users information on the extent, occurrence, statistics, etc., of the occurrence of these irregularitity regions. The answer is to attack the problem, by understanding the physics as well as by detailing the statistics of a phenomenon.

Author's Reply

I agree entirely. I do feel, however, that for a lot of system design problems engineers need models with typical gradients as well as typical values.

E.J.Fremouw, US

You mentioned a relation between gravity waves and electron-density depletion or "bubble" near the equator. Ossakow et al. have had some success in numerically simulating the depletions as due to the collisional Rayleigh Taylor instability. Are you suggesting gravity waves as a triggering mechanism for the instability?

Author's Reply

The work I was referring to explains the initiation of the bubbles by a resonant condition which occurs when the gravity wave velocity and plasma drift velocity are the same.

INTENTIONS AND BUILD-UP OF THE INTERNATIONAL REFERENCE IONOSPHERE

K. RAWER, D. BILITZA, S. RAMAKRISHNAN, N. SHEIKH[+]
Institut für physikalische Weltraumforschung der Fraunhofer-Gesellschaft, Heidenhofstrasse 8,
D-7800 Freiburg, F.R.G.

Abstract

The International Reference Ionosphere (IRI) is a joint activity of the international scientific organis-
ations URSI and COSPAR. The project should be seen in relation with the COSPAR International Reference
Atmosphere (CIRA). However, since the ionospheric parameters are considerably more variable than those
of the neutral atmosphere, a different approach had to be chosen. This approach is adapted to computer
use, thus not in tabular form but in a computer program. Similar to CIRA, vertical profiles for different
conditions are the main content of the model. This could be used for general information, for the estim-
ation of environmental effects and for comparison with theoretical results. Therefore, IRI is to be based
upon observed results rather than aeronomic theory.
The parameters described in the present model are electron density, electron and ion temperature and
relative ion composition. Since IRI should rely upon reliably measured data the scarcity of relevant
observations is still a serious limitation - except for electron density. In fact, international co-
operative work in the project has proved lack of reliable data to an extent which was not expected. The
geographic distribution of ground observations being rather inhomogeneous, satellite observations play an
important role. It is, however, still difficult to produce from such observations reliable local profiles.
Some of the relevant problems will be discussed in the paper.
Discussion amongst international specialists was incited by the project and quite a few scientific results
came out from this cooperation.

1. Introduction

As early as 1960 COSPAR decided to establish the "COSPAR International Reference Atmosphere", abbrev-
iated CIRA, which was originally thought to be one simple set of profile tables for the main parameters
characterizing the neutral atmosphere. With the information available at that time, the first edition
was given out in 1961 (CIRA 1961, see Kallmann-Bijl, 1961) with just one average profile for each para-
meter, accompanied by a lower and an upper limit curve. It was soon found out that this was too much
simplified because the upper atmosphere was found to be more variable than it had appeared at the
beginning of space operations: the day-to-night change was found to be much greater than expected;
also, large variations could be shown to depend on the activity of the Sun. A second edition appeared
in 1965. For the thermosphere, it applied a completely different approach in so far as a theoretical
model was used, based upon work of Harris and Priester (1963). At that time many workers in the field
felt that so many data were at hand and theory was so well advanced that it could describe the facts in
a satisfying manner. Some time later it was found out that the heat source admitted in this model was
unrealistic. The energy balance of the atmosphere was found to be more involved than assumed in this
model. Thus, the next edition went back to a more empirical basis for the tables describing the ther-
mosphere by 16 sets of profiles which are ordered after the exospheric temperature.

Now, for the ionosphere it is known since many decades that its variability is much greater than that
of the neutral atmosphere. Thus, when in 1969 URSI and COSPAR established a Steering Committee for
promoting the new project "International Reference Ionosphere" (abbreviated IRI) its promoters were
well aware that three facts which make the tasks much more difficult than that of CIRA:

(1) First there is a large variability not only with time, season and solar cycle, but also with the
geographic location. Since the upper ionosphere is under geomagnetic control the dependences are rather
complex. Unfortunately, the variations of the different parameters were not so well known that a full,
world-wide description could reasonably be intended at that time. It was therefore decided to edit a
set of profile-tables for two or three typical latitudes only, for noon and midnight, and for typical
seasons and classes of solar activity.

(2) Ionospheric parameters show much larger dispersion than do neutral atmospheric data. For example,
the peak electron density of the ionosphere for a given month and for a given hour shows a day-to-day
variation in a range of at least ±30 %. (Apart from this, much larger fluctuations occur when a per-
turbation event occurs during which conditions can be very different from normal.) It is clear that IRI
cannot intend to describe this fluctuation in detail but should give representative median values for a
period of about one month. However, the user of IRI should of course know that this fluctuation is to
be expected so that he must envisage to find large deviations from the data given in IRI. This is par-
ticular important for predictions f.e. of the environmental conditions during a planned space experiment.

(3) Profile tables of the main parameters characterizing the ionospheric plasma was asked for, namely:
electron density, electron and ion temperature and (positive) ion composition. It was evident that the
quality of the data basis for these parameters was not homogeneous at all. There exists a large thes-
aurus of data on electron density, while measurements of electron and ion temperature and even more of
ion composition were very few at the time when it was decided to establish a Reference Ionosphere.
Therefore, it was quite clear that description of the ionosphere given by IRI could not be equally
reliable for all four parameters.

[+] on leave from: Dept. Electr. Engineering, University of Engineering & Technology, Lahore/Pakistan.

2. Intentions of IRI

It is understood that IRI should be a <u>descriptive, empirical model</u> of the ionosphere. Meanwhile, there exist a few theoretical models· which under certain assumptions, are derived from aeronomic computations. The relative merits of such models are discussed in another contribution. COSPAR and URSI felt that a theoretical model should have one or a few individuals for authors and be considered as their personal work. An international organization being unable to decide on one or another theory should, however, establish a descriptive model trying to compile information from different sources, decide in cases of ambiguity and, finally, indicate supplementary measurements needed to improve the data basis. For example, the Steering Committee has stimulated investigations of ion composition through the whole ionosphere, and also measurements in the lower ionosphere.

2.1 Thus, it is the intention of IRI to summarize existing information about the ionosphere in a condensed and significant manner, and so allow users to obtain estimates of expected conditions from these profile tables. As a common project of COSPAR and URSI the environmental aspect of IRI is more pronounced than it was the case with earlier efforts on the radio scientific side aiming to describe just the electron density distribution. Of course, these earlier efforts had to be taken into account, in particular the description of the (F2-layer) electron density peak as established by CCIR from the data of many ionosonde stations. It will be shown in the following (Sect. 3) that this is still the most important and readily accessible source of data summarizing the results from the world-wide ionosonde network. On the other hand, the goal of IRI is profiles and not mapping of specific values. In order to remain in line with earlier CCIR and URSI work it was decided that the CCIR <u>description of the peak</u> should provisionally be incorporated into IRI, but that it should be possible to introduce peak values from other sources where appropriate. For this end and other good reasons the profile description is given in <u>relative electron densities</u> to be multiplied by a peak value in order to obtain absolute values.

The earliest request for ionospheric data was for radio wave propagation on h.f. waves which are reflected in the ionosphere. In order to make predictions, the most important parameters are plasma density and height at the electron density peak. This is no more true for propagation through the ionosphere which has become very important in connection with satellites, in particular for navigational purposes. In these applications, the propagation effect depends mainly on the electron content of the ionosphere. Therefore, apart from the peak itself, a kind of effective thickness of the whole ionosphere is needed here. However, if we consider the interests of aeronomists, of scientist interested in environmental problems and, in particular, of space research workers, we arrive at larger requirements. In these cases one really needs profiles through the whole ionosphere and also a full description of the ionospheric plasma, not only electron density. IRI 1978 is to describe <u>four plasma parameters</u>, namely: electron (plasma) density, electron and ion temperature, and ion composition.

2.2 The <u>temperature</u> indications, in addition to the neutral temperature given in CIRA are essential because the ionospheric plasma is not in thermal equilibrium, the electrons being usually much hotter than ions and neutrals. Thus, electron and ion temperatures must be indicated. It was one of the conditions of COSPAR that the temperature profiles of IRI should fit with the neutral CIRA model. This was taken account of by matching the IRI ion temperatures to CIRA profiles, in particular by adopting at 120 km the average value of the neutral CIRA temperature, which is 335 K.

Different temperature of the three constituents of the ionospheric plasma means of course different average kinetic energy. Apart from this, satellite probe measurements have shown another deviation from the normal Maxwellian behaviour usually supposed in simple kinetic theory: For the electrons in daytime conditions, but at higher altitudes also at night, there exists a small population of hotter electrons which is mainly produced by the photoelectrons originating in primary ionization processes. At present, information of this component is rather scarce (Spenner and Wolf, 1976). Therefore, in spite of its importance, it was not felt this particular feature could at present time be numerically described in IRI.

2.3 The <u>chemistry</u> of the ionospheric plasma has become more and more important with the advance of space research and, as a consequence, of atmospheric sciences. It is one of the major aims of aeronomy to understand the chemical composition and behaviour of the upper atmosphere. Therefore, for an aeronomist, the ion composition is a very important feature of the ionosphere. Above 100 km only positive ions are important and their total number density equals that of the electrons. It was therefore decided to produce ion composition data as far as feasible with the existing information. It must, however, be stated that the state of the art in this field is much less advanced than for example in the determination of electron density profiles and also that the number of relevant measurements is still quite small.

2.4 There is another problem which refers to the <u>geographic variations</u>. While at the very beginning of the project profiles was asked for at a few locations only it became recently evident that nowadays the task of IRI would reasonably be generalized so that profiles could be obtained for any location and time for all four ionospheric parameters. Unfortunately, this is not yet feasible because not enough reliable data are now at hand. Therefore, the IRI 1978 edition admits geographic variations only for the electron density indications. As for the other parameters, it should be considered as a first attempt which needs later correction, improvement and generalisation.

2.5 In fact, the Steering Committee sees the IRI 1978 edition as a first step towards its goal. In a second step the profiles which were established with a limited basic material should be <u>checked</u> with data from all available sources. This is, in particular, the case with the electron density profiles, because there is a rather large amount of propagation information and also of systematic groundbased observations which were not taken as basic input data for IRI. (This was decided with good arguments at the 1973 Symposium at Konstanz, see Rawer, 1974.) The Steering Committee is now asking for critical remarks and suggestions from all interested colleagues and shall then try to make improvements wherever possible.

3. Existing electron density compilations

While IRI is the first effort to obtain an empirical model for all four parameters which were specified above, there exist a few earlier compilations which are concerned with the electron density profile only. The most important one is a descriptive model, officialized by CCIR (the Comité Consultatif International des Radiocommunications at Geneva) which on a basis of a large number of bottomside ionosonde observations established a computer program representing two characteristing parameters which can easily be deduced from ionograms.

3.1 One may say that this computer program which we call in the following CCIR-program (1967) summarizes the measurements of about a hundred stations all over the world during quite a long period of observations. This program uses monthly median values of these two parameters for basic input, namely: the so-called "critical frequency" of the F2-layer, the square of which is proportional to the peak electron density. The second parameter is a quantity called M3000. Originally this parameter was only used for propagation computations, and is still used for these.

3.2 On the other hand M3000 is narrowly connected with the altitude of the electron (plasma) density peak. A first relation for deducing the peak altitude was indicated by Shimazaki (1955). Since his pioneer work there have been a few more efforts to find a relation between M3000 and the peak altitude which could be used at all latitudes. Improvements were made by Bradley and Dudeney (1973), then by Eyfrig (1974), Bilitza (1978) and quite recently in a joint study by Bilitza and Eyfrig (1978). The result is that the simple inverse relationship originally found by Shimazaki is now replaced by a more involved one. Since M3000 is obtained from the ionogram which is a virtual height versus frequency trace, it is in fact, influenced by the underlying ionization of the E-region. The more recent relations take account of this influence which must be corrected for when trying to deduce the peak altitude of the F2-layer.

3.3 The CCIR program is mainly based upon work done in the USA by Jones and Gallet (1960, 1962a, b) who first described the diurnal, monthly median variation of each of the two parameters by a seven order Fourier decomposition. In the following analysis they dealt with each Fourier component separately by applying a Legendre development in geographic coordinates on a world-wide scale. By this analysis the original information which is given by station is finally hidden in the set of Legendre coefficients which is build up for the Fourier amplitudes.

This description encountered two difficulties: One was due to the irregular distribution of sounding stations over the world. While there are more stations in highly industrialised regions of the world, i.e. at midlatitudes in the northern hemisphere, there are almost no stations at all in the big ocean, and the number of stations in the southern hemisphere is also very poor. Therefore, when the first attempts were made to go straight-forward through such analysis, negative electron densities came out in the middle of the Pacific Ocean. This, of course, could not be accepted, and therefore a rather ingenious though somewhat arbitrary method of improvement was introduced: In order to obtain some information in the not desserved oceanic areas fictive stations were artificially introduced into such areas. At these so-called "screening points" the data of suitably chosen stations in a neighbouring continent were fed in once again. This procedure allowed finally to avoid unreasonable values but, of course, the procedure remains rather arbitrary. A second difficulty stems from the fact that the description by a Legendre development is in fact an interpolation procedure. Now, since the number of stations is rather small as compared with the latitudinal and longitudinal variations a development after geographic coordinates cannot easily take account of the magnetic control of the F2-region which, however, is well known to exist. Therefore, when CCIR checked the Gallet-Jones method, it was found that a development after a coordinate —which is adapted to this influence— could better take account of the observed data. After extensive comparative computations it was finally found out that a particular kind of coordinate, first introduced by Rawer (1963), was more suitable than any of the other considered coordinates. This is the so-called "modified dip" (Modip). This coordinate is almost exclusively determined by the magnetic dip in the equatorial region, but at high latitude it is nearer to geographic coordinates. The definition formula is (C.C.I.R., 1967):

$$\tan (\text{Modip}) = \psi \, / \, (\cos \phi)^{1/2}$$

where ϕ is geographic latitude and ψ the magnetic dip.

3.4
The program of CCIR was widely used during the last decade. Nowadays most radio propagation predictions are established on this empirical basis. Nevertheless, it must be realized that there is some bias in favour of those regions in the world from which many basic data were obtained. This influence may have a greater influence than usually expected. Comparison with satellite measurements of peak electron density is only rarely possible. In spite of the enormeous effort in the topside sounding project, the majority of the topside ionograms do not allow the peak electron density to be determined accurately. Extrapolation over 50 ... 100 km is needed, and this, of course, is difficult. However, King and collaborator (1973a, b) showed that the CCIR description is not equally good at all places. Recently, we compared with measurements of the AEROS satellites and found out that the longitude effects are considerably more pronounced than shown in the CCIR program (see Fig. 1).
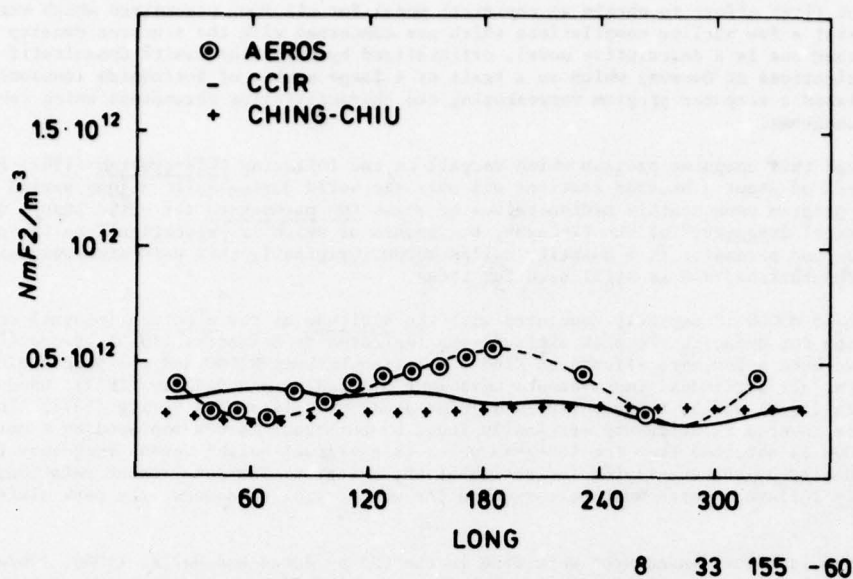
Fig. 1. Longitudinal variation of peak electron density at Modip 60°S, August 1974.
        Satellite data from AEROS at greater height were reduced to the peak value by Bent's profile.

It is understandable that the method with the "screenig points" tends, of course, to smooth out longitud-inal effects. The same must be true with latitudinal effects in region where the latitudinal density of stations used in the CCIR program is insufficient. This is in particular the case of the southern hemis-phere (Fig. 2).
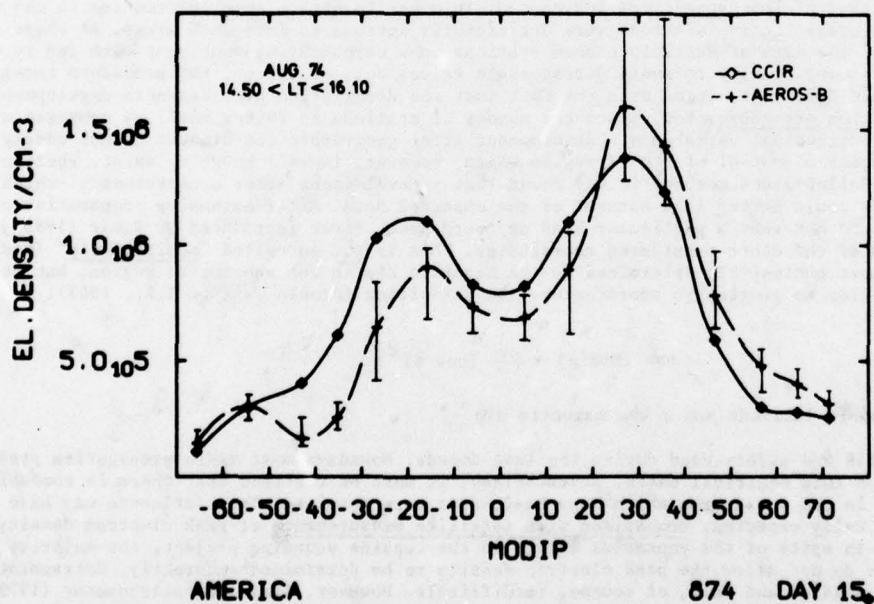
Fig. 2. Comparison of variation with Modip of peak electron density: AEROS observations in August 1974
        (reduced to peak altitude) and CCIR prediction for August 1974. (a) America (b) Pacific.
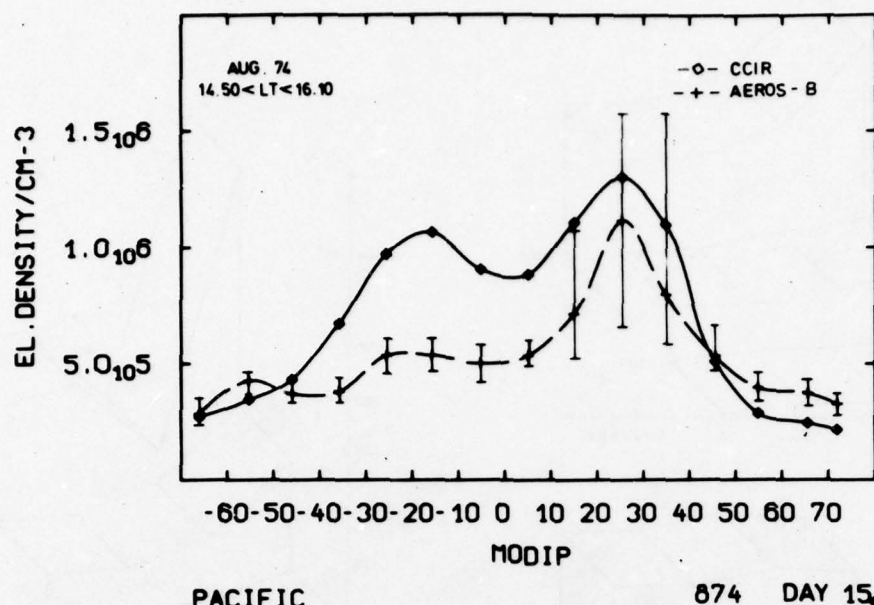
Fig. 2b

There may appear another effect which might even be more serious: Since the majority of stations used in the Legendre development is situated on the northern hemisphere, it is quite certain that the description of the southern hemisphere is to a certain extent influenced by the measurements on the northern hemisphere. This might be the reason for the large difference in Fig. 2b.

3.5 Apart from the CCIR program, there appeared recently another compilation (Ching and Chiu, 1973) trying to build up the profile as a sum of three Elias-Chapman functions and describe the world-wide behaviour by a rather simple system of descriptive expressions, some of which are taken over from Yonezawa (1971). When comparing the AEROS data with the CCIR program and with this model, we found out that the Ching and Chiu model applies by far too much smoothing so that the real variations with the geographic locations are smoothed away (see for example, Fig. 1). Thus, we feel that the CCIR program is still the best compilation available at this time, but that it urgently needs improvement by the introduction of in situ satellite measurements. Unfortunately, it is not so easy to feed satellite data obtained with a quickly variable location into a computing system which was built up with fixed stations. It is hoped that some progress may be made in the near future. At present, we take the CCIR program as it stands as one major input for IRI.

3.6 A large mass of measured data is now available from soundings from the topside, namely the ALOUETTE and ISIS satellites. As stated earlier, the topside electron density profiles do usually not reach the peak of the profile. Therefore, with the usual presentation of topside data, it is quite difficult to obtain reliable information on the profile shape. Fortunately, Bent and Llewellyn (1970) using a large number of topside profiles obtained over both Americas established a descriptive model for the electron density profile in which the ALOUETTE data are incorporated. Beginning at the peak altitude, these authors describe the topside ionosphere by a first parabolic part and at greater altitudes, by three consecutive layers with exponential decrease. The coefficients in the exponent were determined from the topside profiles and are reproduced in a summary matrix depending on the peak electron density (four values) and on the latitude (three values). This means that the shape of the topside decrease of electron density is supposed to depend on the peak value. Since this is the most easy accessable resume of the ALOUETTE measurements, we felt that we should take these values into IRI. However, when trying to give a continuous description of the coefficient in the exponent describing the height variation, we found considerable difficulties. In fact, the variation in the three height ranges chosen by Bent and with frequency is not so smooth as it should be expected. Therefore, when trying to describe the profile by a suitable approximating function, the parameters of this function had not the smooth variation with frequency, height and latitude as should be expected.
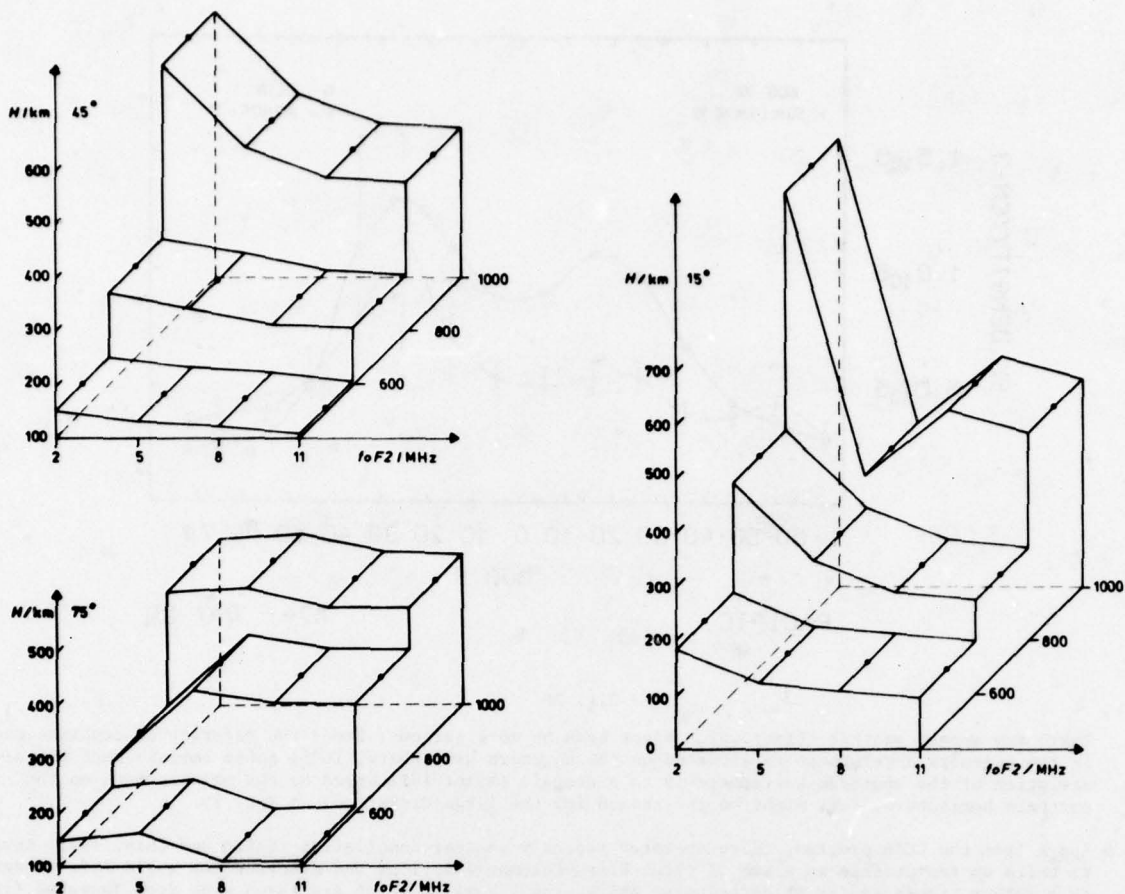
Fig. 3. Bent and Llewellyn's array of coefficients described as a 'scale height' depending on peak density (characterized by the critical frequency of the F2-layer) and height range.
(a) for 75°N (b) for 45°N (c) for 15°N , America. Low solar activity (Covington index 70).

Therefore, we take now a continuous description of the 'scale height' which is not too far from Bent's but avoids the irregularity of the original arrays. At this procedure data from the AEROS mission were very helpful because comparative profiles (Fig. 4) could be deduced from these (Sheikh, 1977).
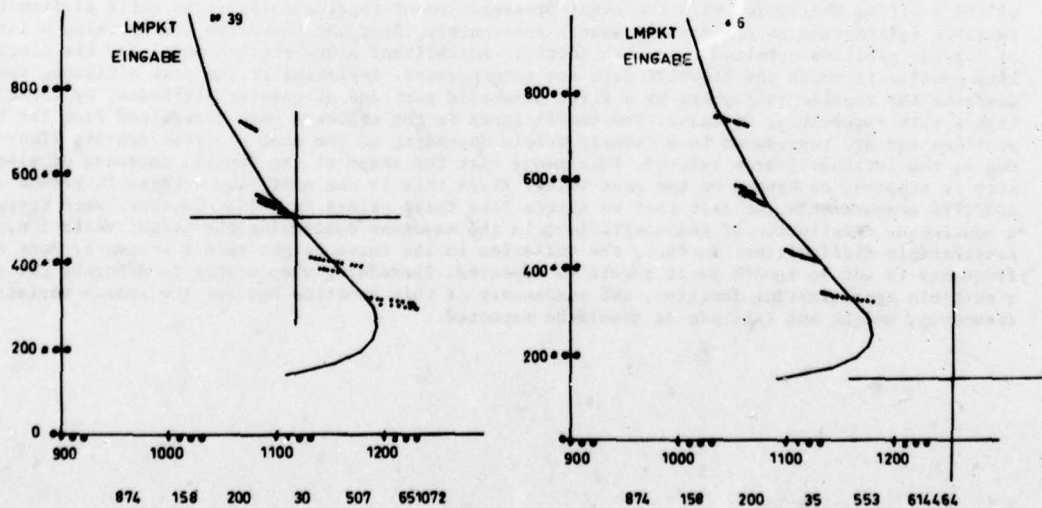
Fig. 4. Bent's topside profile (*NmF2* and *M3000* taken from CCIR model) compared with electron densities measured at passes of the AEROS satellite. (a) and (b) two different locations.

3.7 We shall not describe in detail here the rules applied for describing the *bottomside ionosphere*. Since some IRI users are interested in the layered structure it was clear that Bent's oversimplified model for the bottomside is not acceptable, though it may be quite satisfying for its original intention, namely the computation of refraction effects with penetrating v.h.f. waves. Well established empirical equations are used to describe the variations of *foE* and *foF1*. As for the 'valley' some information was available from incoherent scatter sounding.

4. Temperatures

Electron and ion temperature is obtained at incoherent scatter stations which, unfortunately, are only very few all over the world. Apart from this ground based technique, which is essentially a Doppler measurement, there are now also measurements aboard satellites with probes. The technique of temperature probing has only been fully developed during the last year only the more recent measurements are really helpful. Knudsen (1966) has shown how to obtain ion temperatures by a retarding potential analyzer with positive potential. This method was taken up by Hanson et al. (1970). For IRI 1978 we mainly had data of the AEROS satellites (Dumbs et al, 1977) so as to have interpolation in latitude between the few incoherent scatter stations.

4.1 Since, except for very high altitude, the heat contact between ions and neutrals is rather good, the ion and neutral temperatures are almost identical below about 350 km. Only above that altitude the ion temperature tends to be higher than the neutral one. This is a good criterion for measured ion temperatures – which was in fact used when analyzing the AEROS data (Dumbs et al., 1977).

4.2 The situation is more involved for electron temperature. Here again the incoherent scatter measurements are considered to be reliable. Most probe measurements published in the literature give higher electron temperature than those found from the incoherent scatter stations. This is not astonishing because a detailed discussion of the different probe methods for determining in situ electron temperatures has shown that all errors apparently give a higher temperature. Temperature determination is essentially based upon the distribution function of this kinetic energy. The temperature is for example derived from the steepest point in a semi-logarithmic plot of electron current versus retarding potential. If on board a ground reduction system fails to find this point a higher temperature is deduced. Also if the assumptions, which are made in the theory of the instrument are not completely fulfilled, normally a higher temperature is deduced than the right one. This is for example the case of a planar analyzer when electrons are entering under larger angles. It can now be stated that the best instruments (Brace, 1970, Spenner et al., 1974) determine reliable electron temperatures. Of course, the first publications (Brace, 1970) gave no world-wide model. The first descriptive models of satellite measurements were only established last year and are not yet fully published. One example from the AEROS model is shown in Fig. 5.
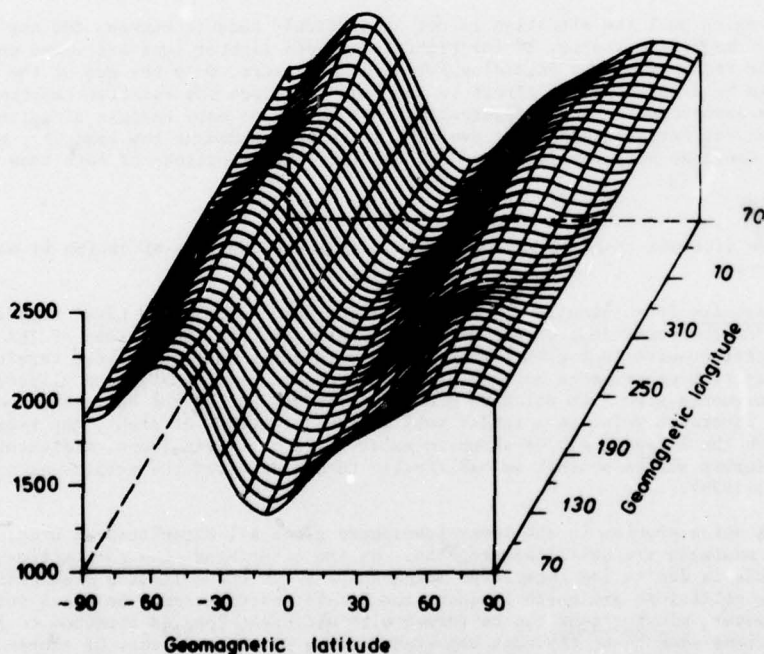
Fig. 5. Electron daytime (15 ... 16 h LT) temperature at 300 km average obtained by a Legendre development of the AEROS-B measurements in the first quarter of 1973 (Plugge and Spenner, 1978).

Therefore the latitudinal interpolation between the data obtained from the few incoherent scatter facilities is still less certain than was hoped. It should also not be forgotten that the statistical weight of the incoherent scatter (i.sc.) measurements available until now is much smaller than that of the routine measurements at classical sounding stations. In the past, all i.sc. stations were only working for a few days every month so that the fluctuation inside a month is not necessarily avoided as

it is for continuous measurements. For our electron temperature model we used observations of Millstone
Hill (Massachusetts), Arecibo (Puerto Rico) and Jicamarca (Peru). (This is the order of decreasing
number of available data.)

5. Ion composition

The positive ion composition is a very important parameter for aeronomic studies. Since ionization
cross sections are now well known, composition can rather easily be deduced from a model of the neutral
atmosphere if the solar spectral irradiation is known. However, it is not easy at all to determine
theoretically the final ion composition because a large number of chemical processes are going on, in
particular where ions of rather high ionization potential are formed. The importance of such secondary
reactions decreases of course with increasing height, since the probability of collisions decreases.
In the E-region the secondary ion composition is quite different from the primary one: Almost all
primary $N2^+$ ions are finally transformed into NO^+ which has much smaller ionization potential.   The
second main ion is O_2^+.

5.1 For aeronomic computations it would be very important to have a good knowledge of minor ionic constitu-
ents too. In fact, the loss of ionization goes through dissociative recombination, which is only possible
when starting from a molecular ion. Some evidence from mass-spectrometric measurements on minor ion
populations exists. But it would not be reasonable at present time to present numerical indications.
Therefore, IRI 1978 is restricted to major ion populations with a relative importance of at least 1 %.

5.2 Satellite data are missing at altitudes below about 200 km. There, our input is limited to rocket
observations which are rather scarce. Results concerning the composition of major ions in this height
range have been compiled by Danilov and his cooperators (1978), but it must be noted that in spite of
the effort made by this team there are still important gaps in the basic data. Even at northern middle
latitudes true night measurements are rare. Data from other latitudes are almost missing including the
equatorial region and the southern hemisphere. It is therefore not feasible to describe at present in
a significant way the latitudinal variation of ion composition profiles.

5.3 The situation is somewhat better at higher altitudes where satellite data are available. Reliable data
were only obtained during the last few years and are still not in a shape that they could easily be in-
corporated. IRI needs relative composition data while most experimenters indicate absolute ion densi-
ties. For a user, these absolute values are not very helpful, because the plasma density is more vari-
able than the relative importance of a given ion. Also, for most aeronomic problems relative values
are required. The main input used for IRI 1978 stems from the AEROS Retarding Potential Analyzer measure-
ments. The method of producing ion composition data with this instrument was indicated early by Knudsen
(1966). It was then adapted to the working conditions on a spinning satellite by Spenner and his co-
workers; a systematic collection of data from the AEROS-B mission is available since very short time
(Dumbs et al., 1977).

Around the F-region peak the situation is not so difficult because between 200 and 400 km the ion O^+ is
the only one of major importance. As for higher altitudes lighter ions are found more and more, but
these cannot be resolved by the Retarding Potential Analyzers. Only the sum of the light ions, namely
H^+ and He^+, can be determined. An effort is now made to deduce the relative importance of thes two
ions from mass spectrometric data. Apparently, this is not so easy because of calibration difficulties.
It may be taken for certain that H^+ is everywhere the more abundant ion than He^+, but for aeronomic
reasonings it would be very important to know the relative importance of both ions at high altitudes.

6. Lower ionosphere

Considering the altitude range below 100 km, we must state that the situation is much worse than for
the higher levels.

6.1 The electron density is not routinely observed from ground because the usual sounding methods are not
applicable under the conditions of the D-region. Therefore, the indications of IRI are almost entirely
based upon rocket observations with probes but only in cases were these were carefully checked by
valuable propagation experiments between ground and the rocket (Mechtly and Bilitza, 1974). Again, al-
most all measurements stem from northern middle latitudes. During the day, they seem to show a typical
shape with an inversion point at a rather well defined altitude. At night, the ionization is very small,
only a layer in the E-region can be shown to exist regularly. Even there, different compilations re-
sulted in different shapes so that we had finally to decide after the results of propagation experiments
(Rawer et al., 1978).

6.2 Temperature is not a problem in the lower ionosphere since all three temperatures, that of ions,
electrons and neutrals are quite near together. On the other hand, ion composition is a very difficult
case. Again this is due to ion chemistry. Below about 90 km the collision frequencies are high enough
so that triple collisions are quite frequent and triple reactions must be taken into account. With such
reactions, however, cluster ions can be formed with different species attached to a simple positive
ion. Hydrated ions seem to be the most important series of cluster ions. Of course, it would be impossible
to take up all the different types of cluster ions which were observed into a descriptive model like
IRI. For most applications, the total percentage of cluster ions is of first importance, and there are
now a few data available with which some indication can be worked out. It must, however, be clearly
stated that only a few rocket flights have produced valuable composition data in the D-region. Thus,
our indications concerning the ion composition in the D-region are extremely provisional.

This is also and even more true for negative ions. Such ions occur by attachment processes in which an
electron is connected to a neutral molecule. As compared with the ionization energy (which is needed
to form a positive ion) the attachment energy is quite small. Therefore, the electrons can easily be
detached, for example by visible light. Thus, negative ions are very sensitive to external influences.
Negative cluster ions also formed at lower altitudes in the D-region. Until now, there is one group
only which has made reliable negative ion determinations (Arnold and Krankowsky, 1977).
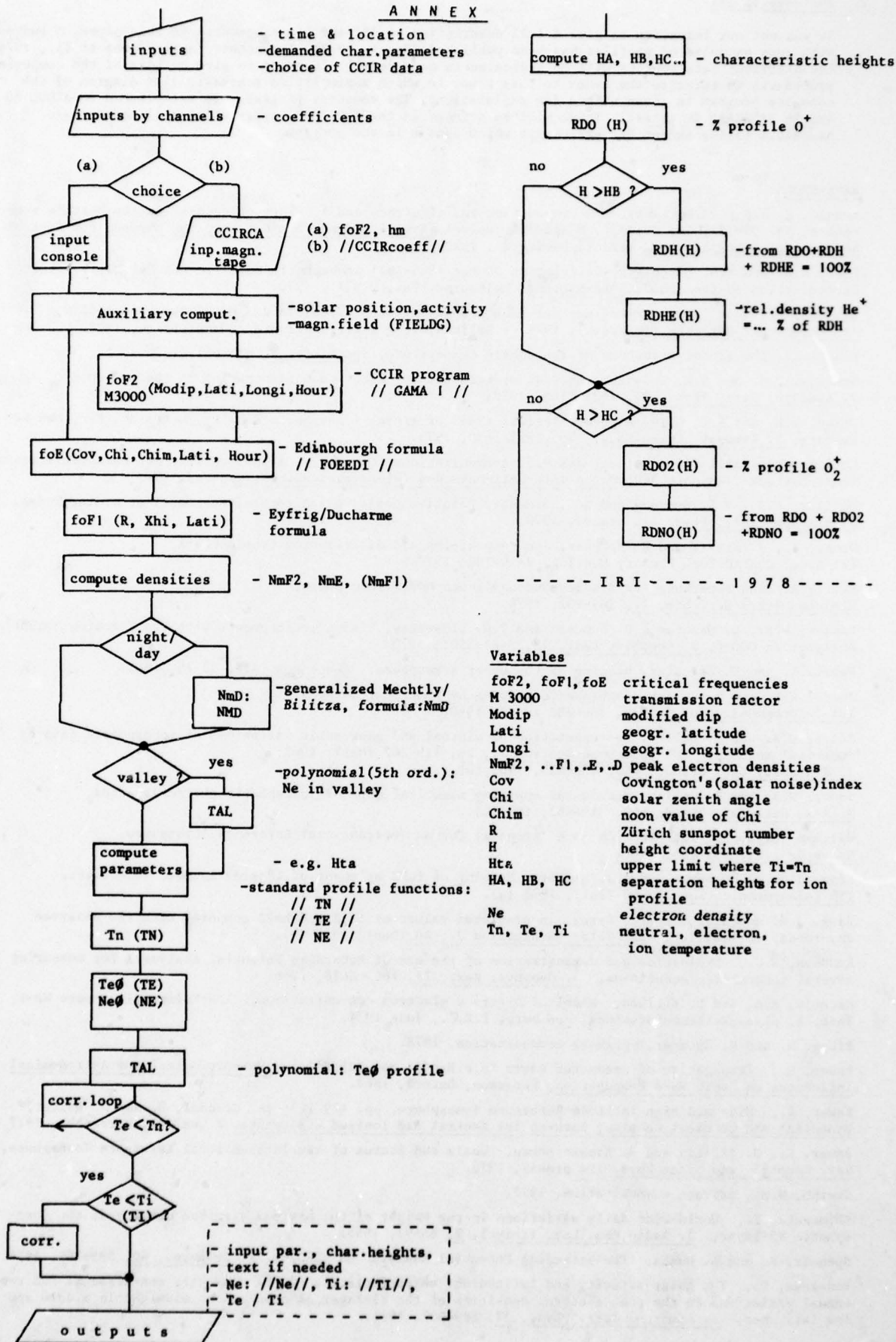
7. Build-up of IRI

It was not our intention to give a full description of IRI and its procedures in this paper. A survey with some examples of profiles has been published (Rawer, 1977). In another paper (Rawer et al., 1978) the different data sources will be indicated in more detail. In order to give an idea of the computing procedures we refer to the Annex to this paper in which a simplified schematic flux diagram of the computer program is given with a few explanations. The computer programs are established in ALGOL 60 and in FRONTRAN IV as well. These will be printed in the IRI 1978 report which will not contain numerical tables except for parameters which appear in the program.

REFERENCES:

Arnold, F. and D. Krankowsky, Ion composition and electron- and ion-loss processes in the Earth's atmosphere, pp. 93-127, in: Grandal, B and J.A. Holtet, Dynamical and Chemical Coupling between the Neutral and Ionized Atmosphere, D. Reidel, Dordrecht, 1977.

Bent, R.B. and S.K. Llewellyn, Description of the 1965-1971 Ionospheric Model in the Definitive Orbit Determination System (DODS), DBA-Systems, Melbourne, Fa., U.S.A., 1970.

Bilitza, D., Modell zur Darstellung der Höhe des F2-Maximums mit Hilfe des M3000-Wertes des CCIR, Kleinheubacher Berichte (in press), 1978. - Bilitza,D., R.Eyfrig, private communication, 1978.

Brace, L., The global structure of ionosphere temperature, Space Res. X, 633-651, 1970.

Bradley, P.A. and J.R. Dudeney, Vertical distribution of electron concentration in the ionosphere, J. Atmosph. Terr. Phys., 35, 2131-2146, 1973.

Ching, B.K. and Y.T. Chiu, A phenomological model of global ionospheric density in the E-, F1-, and F2-regions, J. Atmosph. Terr. Phys., 35, 1615-1630, 1973.

Comité Consultatif International des Radiocommunications (C.C.I.R.), Atlas C.C.I.R. des caractéristiques ionosphériques, Rapport 340, Union Internationale des Télécommunications, Genève, 1967.

Danilov, A.D., V.K. Semenov and A.G. Simonov, Relative positive ion composition model at midlatitudes, J. Atmosph. Terr. Phys. (in press), 1978.

Dumbs, A., J. Slavik and K. Spenner, Ion composition and distribution from AEROS-A, Tel-Aviv, COSPAR 20th Plenary Meeting, 7-18 June 1977.

Eyfrig,R., Eine Bemerkung zur Bradley-Dudeney'schen Modellionosphäre, Kleinheubacher Berichte, 17, 199-202, 1974.

Hanson, W.B., S. Sanatani, D. Zuccaro and T.W. Flowerday, Plasma measurements with the Rearding Potential Analyzer on OGO-6, J. Geophys. Res., 75, 5483-5501, 1970.

Harris I. and W. Priester, Heating of the upper atmosphere, Space Res. III, 53-75, 1963.

Jones, W.B. and R. Gallet, Ionospheric mapping by numerical methods. IUT Telecommunication J., 27, 280-282 (Dec), 1960.

Jones, W.B. and R. Gallet, Representation of diurnal and geographic variations of ionospheric data by numerical methods, IUT Telecommunication J., 29, 129-147 (May), 1962; J. Res. Nat. Bur. Stand., 66D, 419-438, 1962 (a).

Jones, W.B. and R. Gallet, Methods of applying numerical maps of ionospheric characteristics, J. Res. Nat. Bur. Stand., 66D, 649-662, 162 (b).

Kallmann-Bijl, H., Introduction to a proposal for an International Reference Atmosphere, Space Res. II, 889-895, 1961.

King, J.W., J.D. Burge and A.J. Slater, Mapping of foF2 by means of topside sounder satellites, ITU Telecommunication J., 40 (Jul), 1973 (a).

King, J.W. and A.J. Slater, Errors in predicted values of foF2 and hmF2 compared with the observed day-to-day variability, ITU Telecommunication J., 40 (Dec), 1973 (b).

Knudsen, W.C., Evaluation and demonstration of the use of Retarding Potential Analyzers for measuring several ionospheric quantities, J. Geophys. Res., 71, 4669-4678, 1966.

Mechtly, E.A. and D. Bilitza, Model of D-region electron concentrations, IPW-Scientific Report WB-i, Inst. f. phys. Weltraumforschung, Freiburg, F.R.G., June 1974.

Plugge R. and K. Spenner, private communication, 1978.

Rawer, K., Propagation of decameter waves (H.F.Band), pp. 221-250 in: Meteorological and Astronomical Influences on Radio Wave Propagation, Pergamon, Oxford, 1963.

Rawer, K., Mid- and high latitude Reference Ionosphere, pp. 129-143, in: Grandal, B. and J. Holtet, Dynamical and Chemical Coupling between the Neutral and Ionized Atmosphere, R. Reidel, Dordrecht, 1977.

Rawer, K., D. Bilitza and S. Ramakrishnan, Goals and Status of the International Reference Ionosphere, Rev. Geophys. and Space Phys. (in press), 1978.

Sheikh, N.M., private communication, 1977.

Shimazaki, T., World-wide daily variations in the height of the maximum electron density in the ionospheric F2-layer, J. Radio Res. Lab. (Tokyo), 2, 85-97, 1955.

Spenner, K. and A. Dumbs, The Retarding Potential Analyzer on AEROS-B, J. Geophys., 40, 585-592, 1974.

Yonezawa, T., The solar-activity and latitudinal characteristics of the seasonal, non-seasonal and semi-annual variations in the peak electron densities of the F2-layer at noon and at midnight in middle and low latitudes, J. Atmosph. Terr. Phys., 33, 889-907, 1971.

A N N E X

inputs
- time & location
- demanded char.parameters
- choice of CCIR data

inputs by channels — coefficients

(a)   (b)
choice

input console   CCIRCA inp.magn. tape
(a) foF2, hm
(b) //CCIRcoeff//

Auxiliary comput.
- solar position, activity
- magn.field (FIELDG)

foF2
M3000 (Modip, Lati, Longi, Hour)
- CCIR program
// GAMA 1 //

foE (Cov, Chi, Chim, Lati, Hour)
- Edinbourgh formula
// FOEEDI //

foF1 (R, Xhi, Lati)
- Eyfrig/Ducharme formula

compute densities — NmF2, NmE, (NmF1)

night/day

NmD: NMD
- generalized Mechtly/ Bilitza, formula: NmD

valley ?   yes
- polynomial(5th ord.): Ne in valley

TAL

compute parameters
- e.g. Hta

- standard profile functions:
// TN //
// TE //
// NE //

Tn (TN)

Teø (TE)
Neø (NE)

TAL — polynomial: Teø profile

corr.loop
Te < Tn?

yes

Te < Ti (TI) ?

corr.

- input par., char.heights,
- text if needed
- Ne: //Ne//, Ti: //TI//,
- Te / Ti

outputs

compute HA, HB, HC... — characteristic heights

RDO (H) — % profile O+

no   yes
H > HB ?

RDH(H)
- from RDO+RDH + RDHE = 100%

RDHE(H)
- rel.density He+
= ... % of RDH

no   yes
H > HC ?

RDO2(H) — % profile O2+

RDNO(H)
- from RDO + RDO2 + RDNO = 100%

- - - - - I R I - - - - - 1 9 7 8 - - - - -

Variables

foF2, foF1, foE	critical frequencies
M 3000	transmission factor
Modip	modified dip
Lati	geogr. latitude
longi	geogr. longitude
NmF2, ..F1, .E, .D	peak electron densities
Cov	Covington's (solar noise) index
Chi	solar zenith angle
Chim	noon value of Chi
R	Zürich sunspot number
H	height coordinate
Hta	upper limit where Ti=Tn
HA, HB, HC	separation heights for ion profile
Ne	electron density
Tn, Te, Ti	neutral, electron, ion temperature

MODELING OF VLF DUCTS IN THE PLASMASPHERE

P. A. Bernhardt and C. G. Park
Radioscience Laboratory
Stanford University
Stanford, California 94305

SUMMARY

Numerical simulations of the ionosphere and protonsphere have been used to investigate diurnal and seasonal variations in magnetospheric plasma density enhancements capable of ducting VLF (whistler-mode) radio waves. During winter and equinoxes, VLF ducts may extend down to 300 km altitude at night, but usually terminate above 1800 km during the day. In summer, ducts terminate above 1000 km altitude at all local times. The duct termination height affects the angle-of-arrival, and the signal strength of whistler-mode waves received on the ground.

I. INTRODUCTION

Very low frequency (VLF) wave propagation in the magnetosphere is strongly influenced by the presence of field-aligned electron density irregularities or ducts. Figure 1 illustrates schematically a ray path from a source in one hemisphere to a receiver in the conjugate hemisphere. The ray follows a snake-like path inside a duct which extends through most of the magnetosphere. Electron density gradients associated with the duct keep the ray direction and wave normal angle confined within a small cone about the field line. Rays may leave the duct and propagate in an untrapped mode to the bottom of the ionosphere. If the wave normals are nearly perpendicular to the ionosphere, signals will couple into the earth-ionosphere waveguide. By contrast, ray paths of unducted waves generally deviate outward from the starting field line and their wave normal angle with respect to the geomagnetic field becomes so large that penetration of the conjugate ionosphere is not possible (e.g., Helliwell, R. A., 1965). Instead, these unducted waves are magnetospherically reflected where the local lower hybrid resonance (LHR) frequency is equal to the wave frequency (Edgar, B. C., 1972 and 1976). Thus all ground based observations of VLF waves that originate in or propagate through the magnetosphere rely on the presence of ducts.

J. J. Angerami (1970) made a detailed ray tracing analysis of whistlers received on OGO 3 satellite to distinguish ducted whistlers from unducted ones based on their dispersion characteristics. He deduced that the ducts were ~500 km diameter at the equator and had density enhancements of ~10-20% above the background. Edgar (1972) showed that the irregular frequency-time behavior of magnetospherically reflected whistlers received on OGO 3 could be accurately reproduced by ray tracing calculations in a magnetosphere that contains field-aligned irregularities. U. S. Inan and T. F. Bell (1977) have suggested that the plasmapause may be used as a one-sided duct. We consider only the behavior of two-sided ducts in this paper.

Although there is strong theoretical and experimental evidence for the existence of ducts, little is known about their origin or physical properties. The coupling of wave energy into and out of a duct may depend on how low the duct extends downward in altitude and on electron density gradients near its endpoints (e.g., Walker, A. D. M., 1972, 1976; Alexander, P. H., 1971; and James, H. G., 1972). It is difficult to directly measure these duct parameters for comparisons with wave observations. It is likely that progress in this area will depend largely on the interpretation of wave observations in terms of model ducts based on accepted theories of the ionosphere and protonosphere. The aim of the present work is to predict certain aspects of duct behavior using a coupled ionosphere-protonosphere model.

Two fundamentally different mechanisms have been suggested for the formation of VLF ducts. In the first mechanism, localized electric field mixes tubes of plasma through $\vec{E} \times \vec{B}$ drift. Such mixing, or tube interchange motion, results in field-aligned density irregularities unless the plasma content per tube with a unit magnetic flux is uniform in space. C. G. Park and R. A. Helliwell (1971) showed that an electric field of only 0.1 mV/m in the equatorial plasma could form a whistler duct at L = 4 in about an hour. Such localized electric fields could originate in giant thunderclouds (Park, C. G., and Helliwell, R. A., 1971; Park, C. G., and Dejnakarintra, M., 1973) or in polarization charges in the ionosphere arising from unsymmetrical wind or conductivity patterns at the ends of the geomagnetic field lines (Cole, K. D., 1971). The second mechanism involves localized enhancements in ionospheric plasma pressure which tend to increase upward plasma flux into the magnetosphere, or alternatively, decrease the magnitude of downward flux. Localized ionospheric pressure enhancements could be the result of small-scale variations in neutral atmosphere parameters or localized energetic particle precipitation from the magnetosphere. This second mechanism has not yet been studied quantitatively, but the results of the present work suggest that it is unlikely to be important except during long winter nights. The physical reason for this will become clear in a later section. However, we do not attempt in this paper to deal with the formation of ducts. Instead, we take assumed density enhancements in the protonosphere as a starting point and then examine their spatial and temporal behavior as a function of local time and season.

The next section describes the ionosphere-protonosphere model we have adopted for duct simulation, followed by a discussion of the behavior of the ionosphere-protonosphere interface. The last two sections describe the results of duct simulation and the implications of these results for VLF wave propagation in the magnetosphere.

II. THE IONOSPHERE-PROTONOSPHERE MODEL

The numerical ionosphere-protonosphere model adopted for the present study is illustrated with a block diagram in Figure 2. Magnetic flux tubes extending from 100 km altitude to the equator are divided into sections, and self-consistent plasma densities and temperatures are calculated for each

In the lowest section, between 100 and 500 km, the ionic species considered include NO_2^+, O_2^+, and N_2^+ as well as O^+. (The molecular ions are included for the sake of completeness, but make little difference in the results of this study.) O^+ densities are described by time-dependent continuity equations that include the effects of production, loss, ambipolar diffusion, and drift imposed by neutral air winds. In the case of molecular ions, the transport terms in the continuity equations are neglected. Electron and ion temperatures are described by a heat balance equation, including heating of the ambient electron gas by photoelectrons, heat transfer among the electron, ion and neutral gases, and conduction along geomagnetic field lines. The neutral atmosphere model by J. C. G. Walker (1965) is combined with the exospheric temperatures and neutral wind velocities based on the work of R. G. Roble and R. D. Dickinson, (1974), and R. G. Roble et al. (1977). Further details of the model of the 100-500 km section can be found in Antoniadis, D. A. (1977).

The middle section, extending from 500 to 3000 km altitude, is assumed to be populated by a mixture of O^+, H^+, and electrons. O^+ ions are assumed to be in diffusive equilibrium, while the H^+ density profile is described by a time-dependent continuity equation that includes the effects of charge exchange reaction, $O + H^+ \rightleftarrows O^+ + H$, as well as field-aligned diffusion through the ambient O^+ ions. Electron temperatures in this section are calculated from a heat equation assuming constant heat flow throughout the entire altitude range. O^+ and H^+ temperatures are assumed to be equal and are calculated from electron and neutral temperatures using expressions developed previously (e.g., Banks, P. M., and Kockarts, G., 1973; Chapter 23). A detailed description of the model between 500 and 3000 km can be found in Park, C. G., and Banks, P. M. (1974, 1975).

The region between 3000 km altitude and the geomagnetic equator is treated like a finite reservoir of H^+ and electrons. The plasma is assumed to be in diffusive equilibrium at all times so that the density at any point along the flux tube is simply proportional to the tube plasma content. The temperature profiles for this uppermost section are not calculated. Instead, this section is treated like a heat reservoir of infinite capacity, capable of supplying whatever heat flux is consistent with the calculated temperature profiles at lower altitudes.

Calculations of plasma densities and temperatures below 3000 km require numerical solutions of the above mentioned equations subject to the following boundary conditions. At the 3000 km boundary, we assume an initial plasma density as well as the plasma content in the reservoir above that altitude. As time progresses, calculated fluxes into and out of the reservoir give time variations of the plasma content and therefore of the density at 3000 km. At 100 km we assume a state of chemical equilibrium, and at the 500 km boundary we require that plasma densities and temperatures be continuous. A detailed description of the coupled ionosphere-protonosphere model can be found in Bernhardt, P. A. (1976).

III.   BEHAVIOR OF THE IONOSPHERE-PROTONOSPHERE INTERFACE

In this section we examine some aspects of the coupled ionosphere-protonosphere system that are relevant to the study of ducts. Sample calculations were made for 60° invariant latitude (L = 4) and 49° geographic latitude at the foot of the field line, a combination appropriate for eastern North America. No electric field was assumed to exist so that the plasma would simply corotate with the earth. Time-dependent solutions were obtained for complete diurnal cycles during equinox, summer and winter so that diurnal and seasonal variations in coupling fluxes and the O^+-H^+ transition height can be examined.

The contour maps of Figure 3 show calculated heavy (O^+, O_2^+, N_2^+, and NO^+) and light (H^+) ion concentrations and electron temperatures at equinox. The calculations were initiated with steady state solutions at 12 LT. After the steady state solutions are formed, the plasma and thermal continuities equations are solved with the inclusion of the time-varying terms. The transition from steady state solutions to time dependent solutions occurs in less than 30 min. The solution is carried out over a 24-hour period. A relatively empty protonosphere was assumed with an initial density of 1000 cm^{-3} at 3000 km and an initial tube content of 3×10^{13} electrons between 3000 km and the magnetic equator (see Park, C. G., 1974). The flux tube has 1 cm^2 cross-sectional area at 500 km altitude. In Figure 3a, molecular ions are important only during sunlight hours (06-20 LT) and below 200 km. The general behavior of the ionosphere is in good agreement with observations (Titheridge, J. E., 1976) as well as the results of previous theoretical calculations (Roble, R. G., 1975; Murphy, J. A., et al., 1976).

Figure 4 shows two fundamentally different ion density profiles for a "full" protonosphere with an initial concentration of 3000 cm^{-3} at 3000 km altitude. Figure 4a illustrates a nighttime situation where the O^+ layer is maintained by the charge exchange reaction of H^+ ions ($H^+ + O \rightarrow O^+ + H$) that diffuse downward from the protonosphere. Both O^+ and H^+ profiles are close to diffusive equilibrium distributions. By contrast Figure 4b shows dynamic daytime profiles that depart sharply from diffusive equilibrium. Large upward fluxes of H^+ significantly deplete the H^+ density and raise the O^+-H^+ transition height. Such effects have been discussed by a number of authors including C. G. Park and P. M. Banks (1975) and J. A. Murphy et al. (1976). An important point to be noted here is that they can occur even when the protonosphere has relatively high densities that are typical of the plasmasphere. Figure 5 shows diurnal variations of O^+ density, H^+ density, and H^+ flux at 1400 km altitude. Dramatic composition changes and flux reversals occur near sunrise and sunset.

If the same calculations described above are repeated with lower initial protonospheric densities, the results remain essentially unchanged except for the fact that the daytime depletion of H^+ in the topside ionosphere and consequent raising of the transition height are more pronounced. For example, a reduction in the 3000 km density from 3000 cm^{-3} to 1000 cm^{-3} causes the daytime transition height to increase from 1200 km to 2000 km. The daytime O^+ layer, produced by photoionization, is not significantly affected by density changes in the overlying protonosphere (also see Park, C. G., and Banks, P. M., 1975). At night, both O^+ and H^+ densities are reduced by a factor of approximately 3, and no significant change in the transition height results.

Returning to Figure 3a, we note that ionospheric densities decrease rapidly after sunset, but become stabilized around 22 LT and remain essentially unchanged until sunrise near 05 LT. The stable nighttime

ionosphere is maintained by downward flux from the overlying protonosphere. This nighttime behavior changes with season as sunlight conditions and neutral air wind patterns change. In the winter, the stable nighttime ionosphere persists for longer periods, but its qualitative behavior is similar to that near equinoxes. However, the summer night ionosphere is significantly different, as shown in Figure 6. The format of Figure 6 is identical to that of Figure 3. The summer ionosphere decays much more slowly after sunset both due to slower rates of change in the solar zenith angle and to earlier reversal in the neutral wind from poleward to equatorward direction (e.g., Antoniadis, D. A., 1976). This equatorward shift in wind direction lifts the ionosphere to higher altitudes where the loss rates are smaller. Thus the summer night ionosphere does not reach low density levels where it can be strongly influenced by downward fluxes from the protonosphere. Figure 7 shows diurnal variations of O^+ density, H^+ density, and H^+ flux at 1400 km in the same format as Figure 5.

IV.   MODELING OF ENHANCEMENT DUCTS

In this section we examine the spatial and temporal behavior of ducts. We consider a meridional plane with a horizontal plasma density variation specified at 3000 km altitude as an initial boundary condition. An enhancement duct is described by

$$n_e \Big|_{3000 \text{ km}} = 3 \times 10^3 [1 + \phi \exp(-x^2/2\sigma^2)] \text{ cm}^{-3} ,$$

where

   n_e = electron concentration,

   x = horizontal distance, measured in km, from the center of the duct at 3000 km altitude,

   ϕ = the enhance factor = 15%, and

   σ = the duct radius = 20 km.

The duct is centered on an L = 4 field line, which intersects the earth's surface at 49° geographic latitude (appropriate for eastern North America).

The ionosphere-protonosphere model described earlier was used to study how the duct extends down to lower altitudes and how its behavior depends on local time and season. Time-dependent calculations were performed for a number of neighboring field lines in order to see the evolution of the duct shape in two dimensions. Figure 8 shows the results of the duct simulation for equinox with a sequence of meridional plane contour maps at four different local times. The calculations were initiated at 11 LT, but the results are presented only after 12 LT after complete transition from a steady state to a time-varying simulation. The dashed lines represent the magnetic field line passing through the center of the duct. It is apparent that the duct termination altitude (arbitrarily defined as the altitude where the enhancement factor is reduced to one tenth of the value at 3000 km) is a strong function of local time and ranges from ~300 km at midnight to ~1800 km at noon.

Figure 9 shows the enhancement factor at the center of the duct as a function of altitude at noon and midnight. The enhancement factor decreases sharply below 2500 km at noon, but at midnight it remains constant down to ~1200 km, then increases to a slight maximum near 400 km before dropping to zero at ~200 km.

The diurnal variation of the duct termination height can be understood in terms of the ionization source for the ionosphere discussed in the previous section. During daylight hours, photoionization produces a dense ionosphere sending large fluxes of plasma into the overlying protonosphere. The ionospheric O^+ densities are not affected by small changes in protonospheric densities, and a duct would effectively terminate at the O^+-H^+ transition height. At night, when the ionosphere is maintained by a downward flux from the protonosphere, the flux is directly proportional to the protonospheric density so that small density variations in the protonosphere are reflected all the way down through the ionosphere. This is clearly illustrated in Figure 10 where the duct termination height is plotted as a function of local time. Also plotted in the figure is the O^+-H^+ transition height. When the ionosphere is under solar control, the duct terminates at the transition height, but extends to lower altitudes as the nighttime protonosphere becomes an important source of ionization.

When the ionosphere is sunlit, upward plasma flow is insensitive to the plasma density in the overlying protonosphere (also pointed out by Murphy, J. A., et al., 1976). For example, if the protonospheric density is increased by 15%, the upward flux is decreased by only 2%. Thus the filling flux is nearly uniform and tends to smear out any spatial density gradients in the protonosphere. The result is to shorten the duct lifetime. By contrast, downward plasma flux at night is proportional to the protonospheric density so that the duct enhancement factor remains unaffected. Figure 11 shows a plot of the duct enhancement factor at 3000 km altitude as a function of time. The initial condition was 15% enhancement at 11 LT, but the plot begins at 12 LT to allow for a short transition from steady-state to time-dependent solutions (see Figure 3). It can be seen in Figure 11 that the duct enhancement factor decreases during daylight hours, but remains approximately constant at night. The half-life of the duct due to this process is estimated to be 2.5 days.

The foregoing discussion applies to equinox conditions. The behavior of the duct depends on the season as the nature of protonosphere-ionosphere coupling changes with season. Figures 12 and 13 show the duct behavior in winter and summer, respectively, in the same format as Figure 9. The winter duct terminates at the O^+-H^+ transition height during the day, but extends close to the bottom of the ionosphere at night. The winter behavior is similar to the equinox behavior discussed above, except that the night

is longer in winter. In the summer, however, the duct endpoint remains high at all local times. This can be understood in terms of the behavior of the summer night ionosphere, discussed in the previous section. In the summer the ionosphere decays very slowly after sunset, and the night is not long enough to allow the densities to reach levels where the protonospheric flux plays an important role for their maintenance. Thus the protonosphere never exerts much influence over the underlying ionosphere throughout the night. Figure 14 shows a plot of the duct termination altitude as a function of local time in the summer. The duct never extends below 1000 km even at night, in sharp contrast to the winter and equinox behavior.

V.   DISCUSSION AND CONCLUDING REMARKS

We have used an ionosphere-protonosphere model to study certain properties of VLF ducts. In particular, we have found that the height of the duct endpoint depends strongly on local time and season. This is important for magnetospheric VLF studies for several reasons. If a duct terminates at a high altitude, much of the propagation path may lie in an unducted region resulting in spreading of waves in the topside ionosphere. When these waves are reflected (or refracted) upward, they may couple into neighboring ducts and return to the conjugate hemisphere thus giving rise to mixed-path propagation (Helliwell, R. A., 1965). The waves that leave the duct at high altitudes may deviate significantly from the duct field line before emerging into the earth-ionosphere waveguide. If ground-based direction finders are used to locate the duct, corrections must be made to the apparent duct exit point. By contrast, a duct that extends down to the bottom of the ionosphere may keep the waves trapped on a fixed field line. A VLF ray tracing program has been used to determine the latitude where a ray emerges from an L = 4 duct. Figure 15 illustrates the variation in the latitude with duct endpoint height for a duct intersecting the ground at 49° geographic latitude.

The efficiency of signal coupling between the earth-ionosphere waveguide and magnetospheric ducts is of importance to studies of VLF amplification in the magnetosphere. Measurements indicate as much as 30 dB amplification by wave-particle interaction in the magnetosphere (Helliwell, R. A., and Katsufrakis, J. P., 1974). The overall efficiency of the "magnetospheric amplifier" is a function of the coupling into and out of the ducts. These problems have been investigated by using a combination of the duct simulation program discussed here and a VLF ray tracing program. Figure 16 illustrates the width of the region in the duct which captures VLF waves at 6 kHz as a function of the duct endpoint height. This "electromagnetic" cross section varies from 6 to 60 km as the duct endpoint is varied. The ducts used in these calculations have a Gaussian cross section with a standard deviation (σ) of 20 km.

In this paper, we ignored the effects of electric fields on ducts. As mentioned earlier, it is likely that small-scale electric fields are responsible for the formation of most ducts. If these fields persist after the ducts are formed, the resulting flux tube interchange motion would continuously change the duct shape and size (Park, C. G., and Helliwell, R. A., 1971). Enhanced wave activity inside a duct could conceivably modify the electric field by modulating the E-region conductivity through particle precipitation.

Another effect not considered in this paper is the precipitation of low-energy particles that are deposited in the F region. These particles may provide a significant source of ionization for the nighttime F layer, but their effects on ducts depend on the spatial distribution as well as the magnitude of precipitation flux. In the case of uniform precipitation, ducts are not expected to extend as low as the results of the previous section indicated. This is because corpuscular ionization makes the ionosphere less dependent on thermal plasma flow from the protonosphere, and therefore makes the nighttime ionosphere behave more like a daytime ionosphere. On the other hand, if enhanced wave activity inside a duct produced a local enhancement in precipitation flux through wave-particle interactions, the resulting effects on ducts would be quite different. First, the duct enhancement factor would be increased at ionospheric heights due to corpuscular ionization, and second, the resulting increase in ionospheric pressure would reduce the nighttime downward flux thus increasing duct enhancement factor in the protonosphere. The latter may be an important positive feedback mechanism by which ducts can grow at night. Particle precipitation is not expected to be important during daytime when photoionization is the dominant plasma production mechanism.

ACKNOWLEDGMENTS

REFERENCES

ALEXANDER, P. H., 1971, "Computation of Ray Paths for Very Low Frequency Radio Waves Propagating through the Magnetospheric Plasma," Ph.D. thesis, University of Southampton, England.

ANGERAMI, J. J., 1970, "Whistler Duct Properties Deduced from VLF Observations with the OGO-3 Satellite Near the Magnetic Equator," J. Geophys. Res., 75, 6115.

ANTONIADIS, D. A., 1976, "Thermospheric Winds and Exospheric Temperatures from Incoherent Scatter Radar Measurements in Four Seasons," J. Atmos. Terr. Phys., 38, 187.

ANTONIADIS, D. A., 1977, "Determination of Thermospheric Quantities from Simple Ionospheric Observations Using Computer Simulation," J. Atmos. Terr. Phys., in press.

BANKS, P. M. and G. Kockarts, 1973, _Aeronomy_, _Vols. A and B_, Academic Press, New York.

BERNHARDT, P. A., 1976, "The Response of the Ionosphere to the Injection of Chemically Reactive Vapors," Tech. Rept. No. 17, SU-SEL-76-009, Stanford University, Stanford, California.

COLE, K. D., 1971, "Formation of Field Aligned Irregularities in the Magnetosphere," _J. Atmos. Terr. Phys._, _33_, 741.

EDGAR, B. C., 1972, "The Structure of the Magnetosphere as Deduced from Magnetospherically Reflected Whistlers," Ph.D. thesis, Stanford Electronics Labs., Stanford University, Stanford, California.

EDGAR, B. C., 1976, "The Upper and Lower Frequency Cutoffs of Magnetospherically Reflected Whistlers," _J. Geophys. Res._, _81_, 205.

JAMES, H. G., 1972, "Refraction of Whistler Mode Waves by Large Scale Gradients in the Middle Latitude Ionosphere," _Ann. Geophys._, _28_, 301.

HELLIWELL, R. A., 1965, _Whistlers and Related Ionospheric Phenomena_, Stanford University Press, Stanford California.

HELLIWELL, R. A., and J. P. Katsufrakis, 1974, "VLF Wave Injection into the Magnetosphere from Siple Station, Antarctica," _J. Geophys. Res._, _79_, 2511.

INAN, U. S., and T. F. Bell, 1977, "The Plasmapause as a VLF Waveguide," _J. Geophys. Res._, in press.

MURPHY, J. A., G. J. Bailey, and R. J. Moffett, 1976, "Calculated Daily Variations of O^+ and H^+ at Mid-latitudes, I. Protonospheric Replenishment and F-region Behavior at Sunspot Minimum," _J. Atmos. Terr. Phys._, _38_, 351.

PARK, C. G., 1974, "Some Features of Plasma Distribution in the Plasmasphere Deduced from Antarctic Whistlers," _J. Geophys. Res._, _79_, 169.

PARK, C. G., and P. M. Banks, 1974, "Influence of the Thermal Plasma Flow on the Mid-latitude F2 Layer: Effects of Electric Fields and Neutral Winds in the Plasmasphere," _J. Geophys. Res._, _79_, 4661.

PARK, C. G., and P. M. Banks, 1975, "Influence of Thermal Plasma Flow on the Daytime F2 Layer," _J. Geophys. Res._, _80_, 2819.

PARK, C. G., and M. Dejnakarintra, 1973, "Penetration of Thundercloud Electric Fields into the Ionosphere and the Magnetosphere, 1. Middle and Subauroral Latitudes," _J. Geophys. Res._, _78_, 6623.

PARK, C. G., and R. A. Helliwell, 1971, "The Formation by Electric Fields of Field-Aligned Irregularities in the Magnetosphere," _Radio Science_, _6_, 299.

ROBLE, R. G., 1975, "The Calculated and Observed Diurnal Variation of the Ionosphere over Millstone Hill on March 23-24, 1970," _Planet. Space Sci._, _23_, 1017.

ROBLE, R. G., and R. D. Dickinson, 1974, "The Effect of Displaced Geomagnetic and Geographic Roles on the Thermospheric Neutral Winds," _Planet. Space Sci._, _22_, 623.

ROBLE, R. G., and J. E. Salah, and B. A. Emery, 1977, "The Seasonal Variation of the Diurnal Thermospheric Winds over Millstone Hill during Solar Maximum," _J. Atmos. Terr. Phys._, in press.

TITHERIDGE, J. E., 1976, "Plasmapause effects in the Topside Ionosphere," _J. Geophys. Res._, _81_, 3227.

WALKER, A. D. M., 1972, "The Propagation of Very Low Frequency Waves in Ducts in the Magnetosphere," _Proc. Roy. Soc., London_, _Ser. A_, 329.

WALKER, A. D. M., 1976, "The Theory of Whistler Propagation," _Rev. of Geophys. and Space Physics_, _14_, 629.

WALKER, J. C. G., 1965, "Analytic Representation of Upper Atmosphere Densities Based on Jacchia's Static Diffusion Models," _J. Atmos. Sci._, _22_, 462.
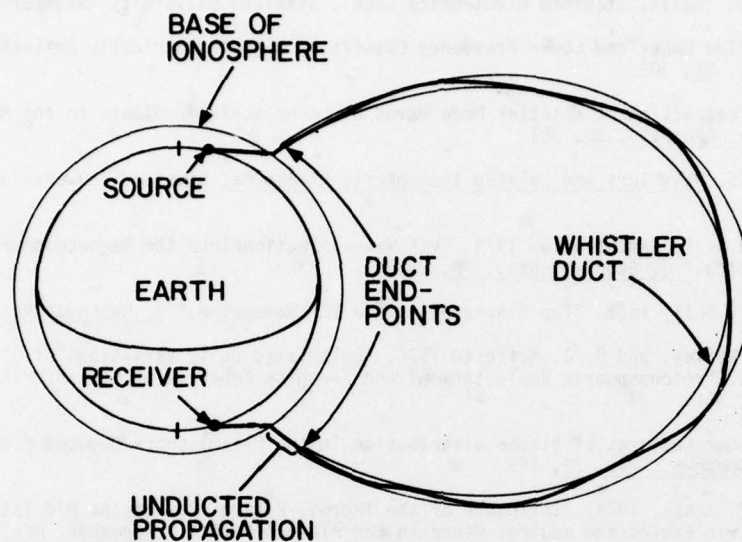
Figure 1. Schematic of the magnetospheric propagation circuit for VLF waves. Changes in the altitude of the duct endpoints may affect the coupling between the earth-ionosphere waveguide and the magnetospheric duct.
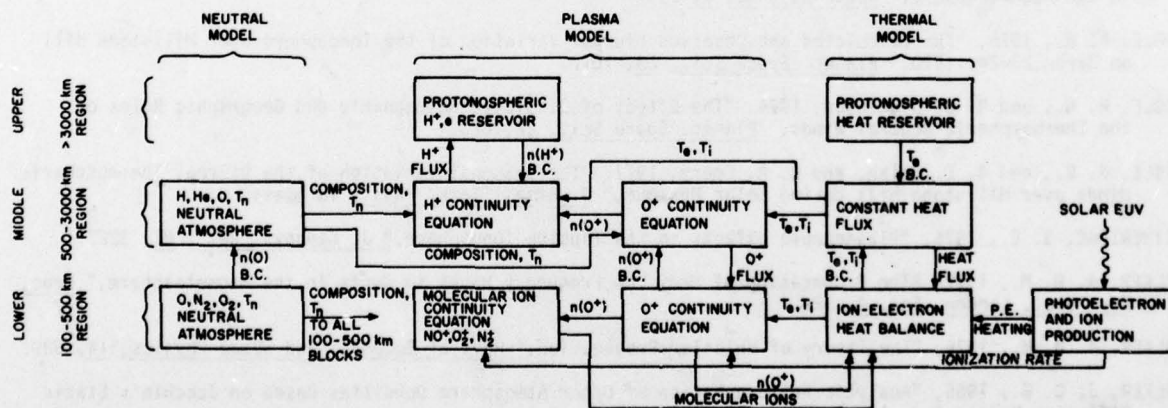
Figure 2. Block diagram of the protonospheric-ionospheric model.
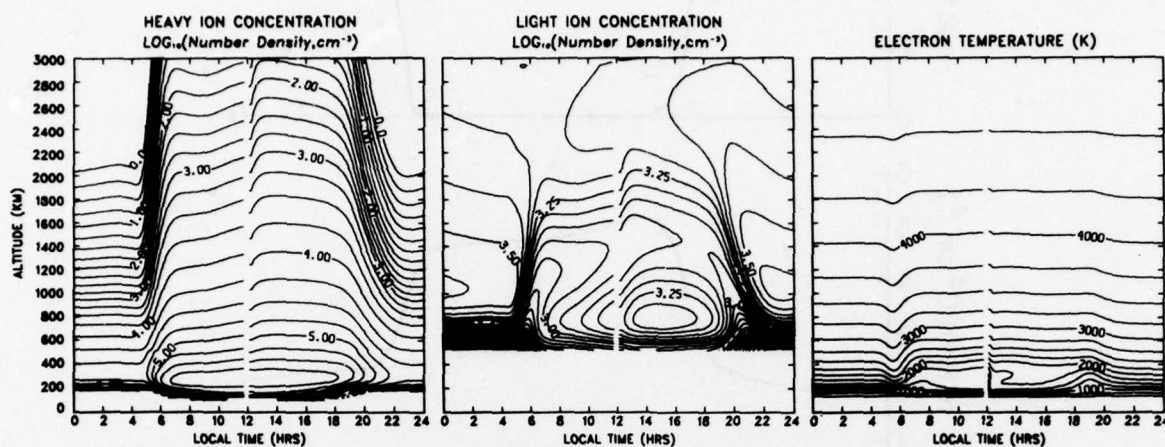
Figure 3. Diurnal behavior of the (a) O^+ and molecular ion concentrations, (b) H^+ concentration, and (c) the electron temperature during equinox with an initial protonospheric concentration of 1000 cm^{-3} at 3000 km altitude.
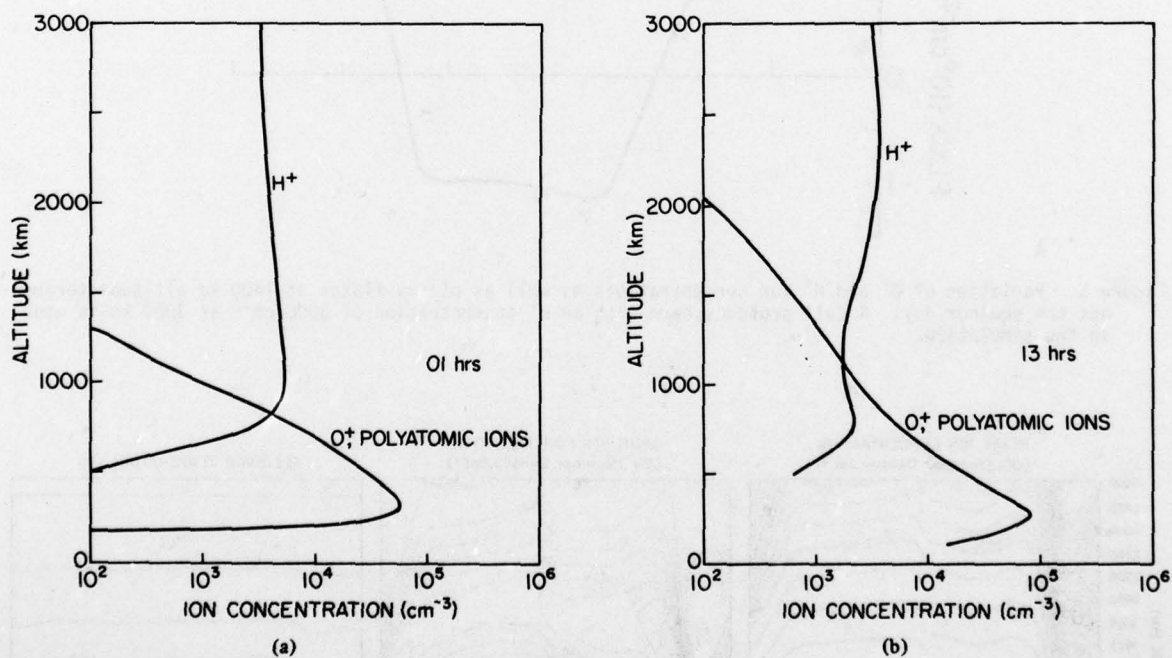
Figure 4. Profiles of the O^+-molecular ions and H^+ ion layers during equinox at (a) nighttime, and (b) daytime.
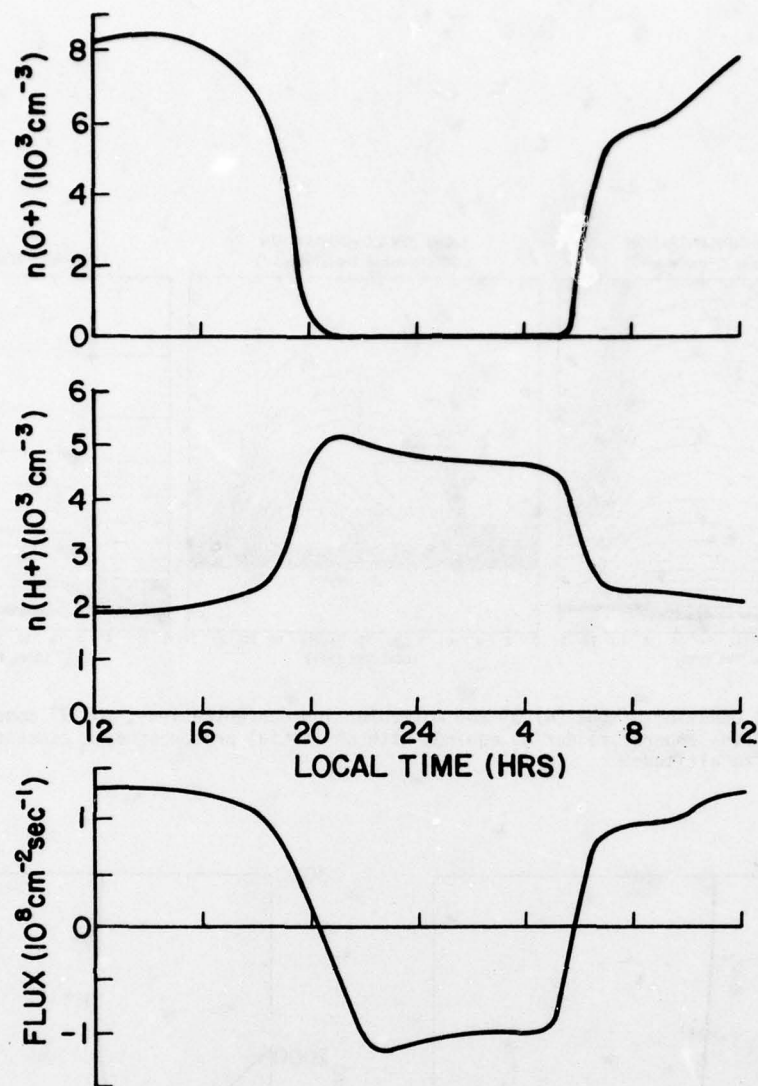
Figure 5. Variation of O^+ and H^+ ion concentrations as well as plasma fluxes at 1400 km altitude throughout the equinox day. A full protonosphere with an H^+ concentration of 3000 cm^{-3} at 3000 km is used in the simulation.
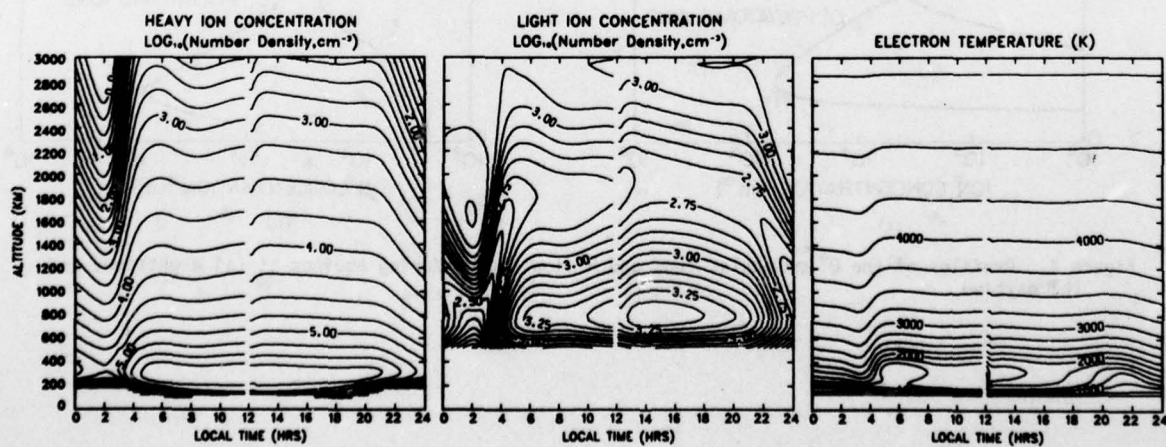
Figure 6. Diurnal behavior of the (a) O^+ plus molecular ion concentration, (b) H^+ ion concentration, and (c) the electron temperature during summer with an initial progonospheric concentration of 1000 cm^{-3} at 3000 km altitude.

Figure 7. Variation of O⁺ and H⁺ ion concentrations as well as plasma fluxes at 1400 km altitude through-out the summer day. A full protonosphere with an H⁺ concentration of 3000 cm⁻³ at 3000 km is used in the simulation.

ELECTRON CONCENTRATION
LOG_{10} (Number Density, cm⁻³)
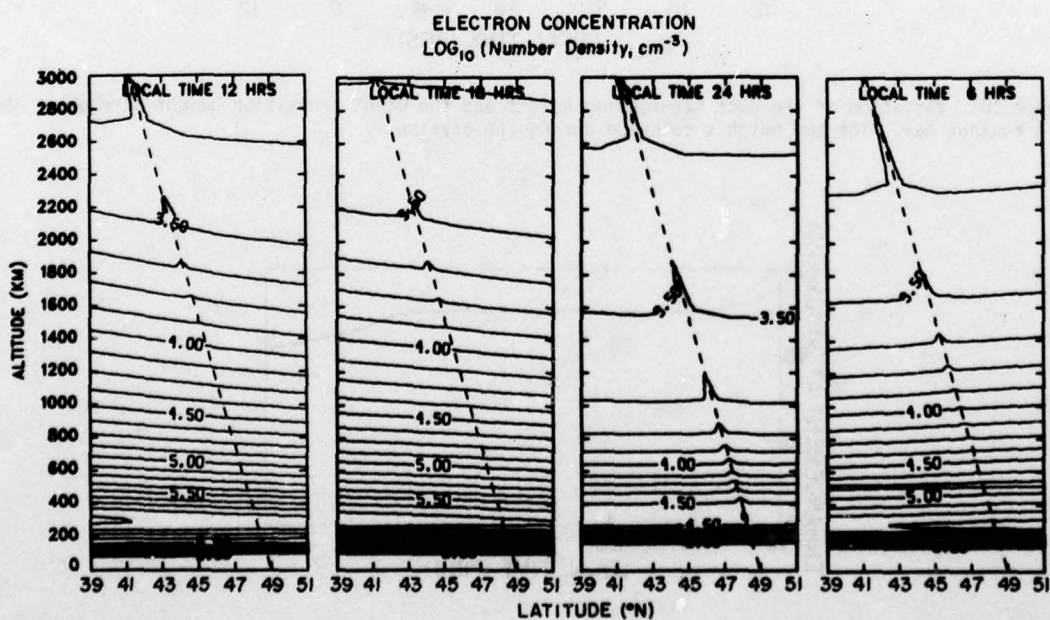
Figure 8. Variations in the equinox plasmasphere containing a 15% enhancement duct at L = 4. The field line is indicated by the dashed line. Perturbations in the contour lines indicate the presence of an enhanced tube of plasma.
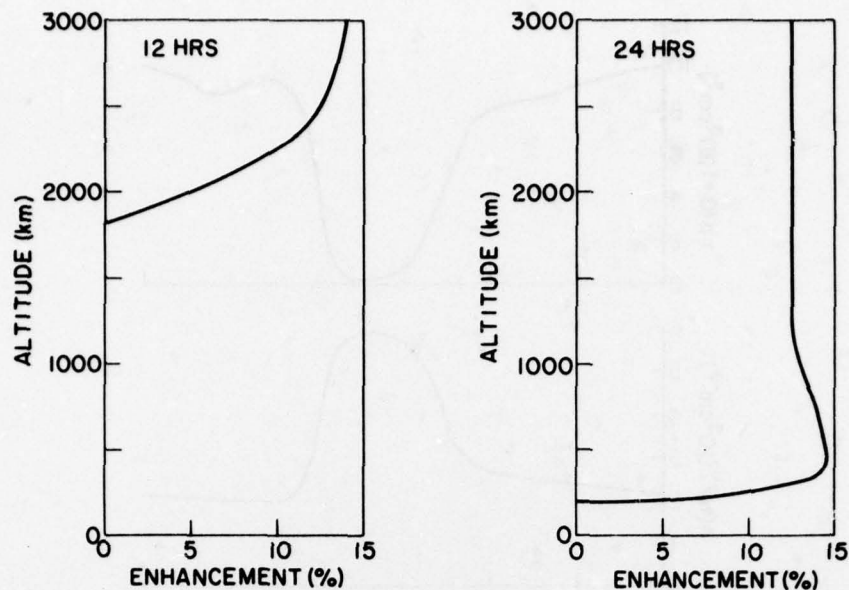
Figure 9. Profiles of equinox duct endpoints at (a) noon, and (b) midnight.
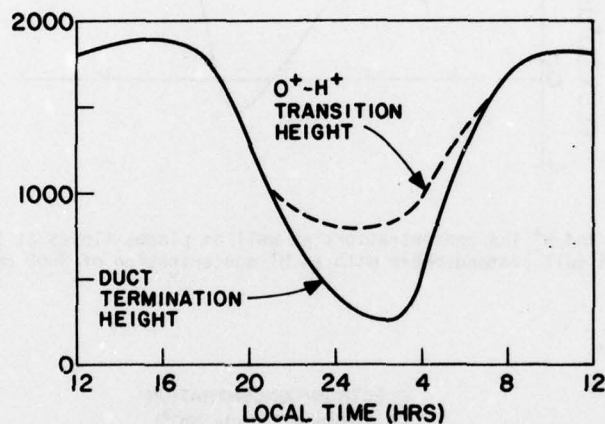
Figure 10. Variation of the duct termination height and the O^+-H^+ transition height throughout the equinox day. The two heights coincide during the daytime.
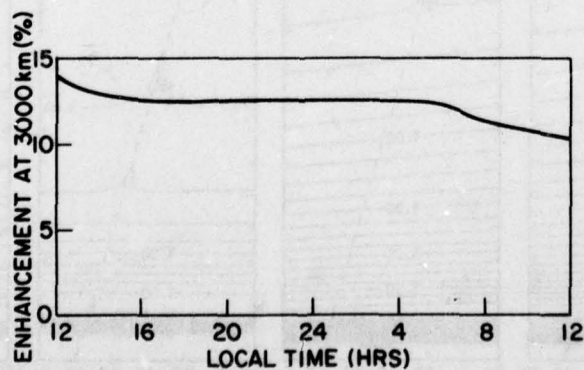
Figure 11. Decay of the enhancement level at 3000 km during equinox. The enhancement level drops steadily during the daytime. The half-life of the duct is 2.3 days.

ELECTRON CONCENTRATION
LOG_{10} (Number Density, cm^{-3})
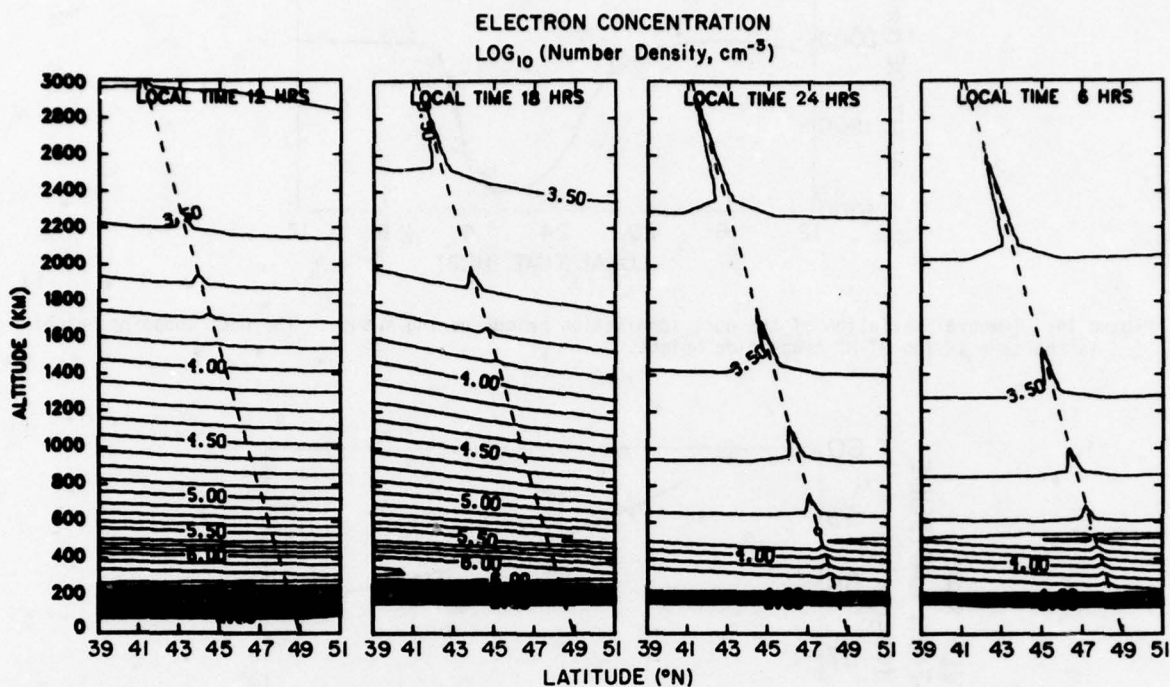
Figure 12. Variations in the winter plasmasphere containing a 15% enhancement duct at L = 4.

ELECTRON CONCENTRATION
LOG_{10} (Number Density, cm^{-3})
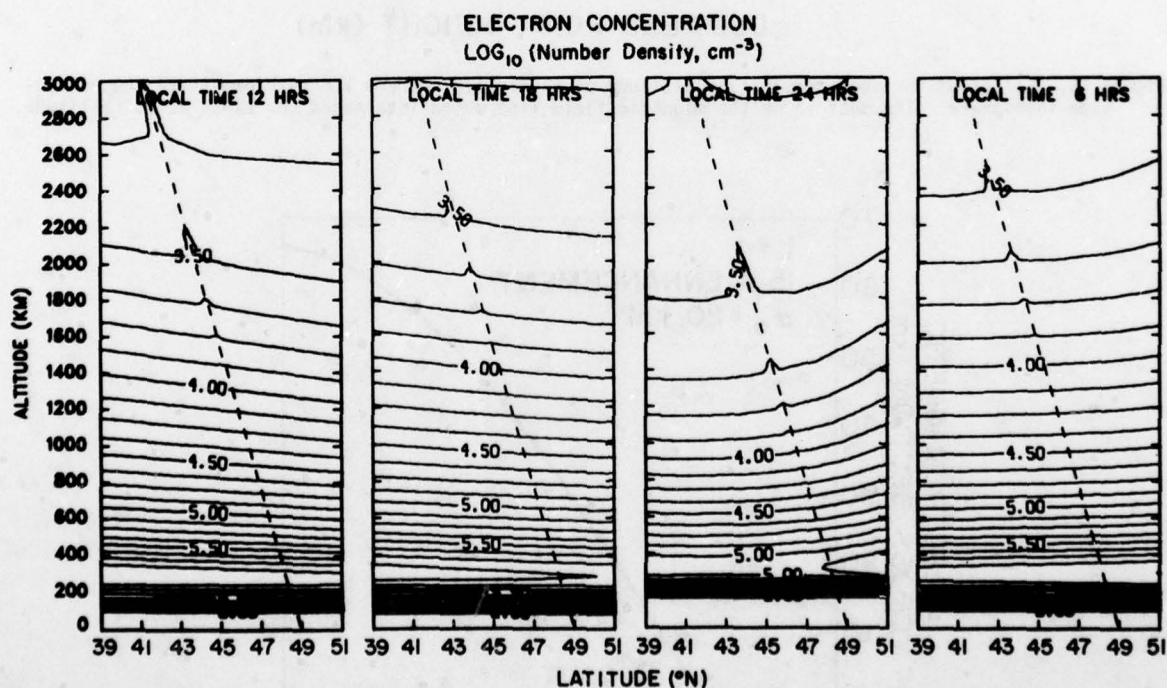
Figure 13. Variations in the summer plasmasphere containing a 15% enhancement duct at L = 4.
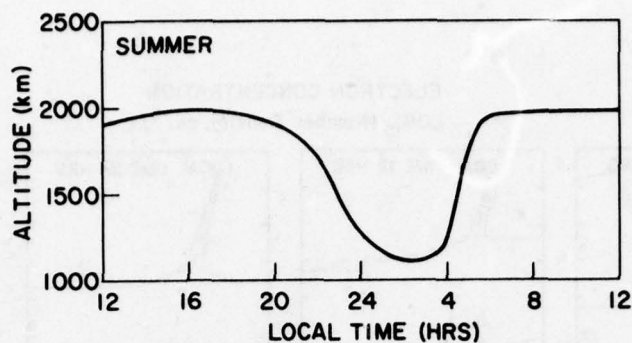
Figure 14. Temporal variation of the duct termination height during summer. The duct endpoint height is the same as the O^+-H^+ transition height.
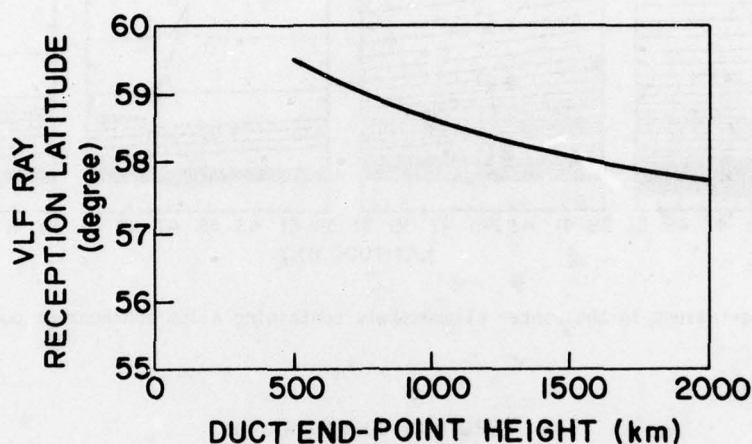
Figure 15. Effect of the duct termination altitude on the latitude where VLF rays penetrate the bottom-side ionosphere. The duct is on the magnetic field line which intersects the earth at 60° latitude.
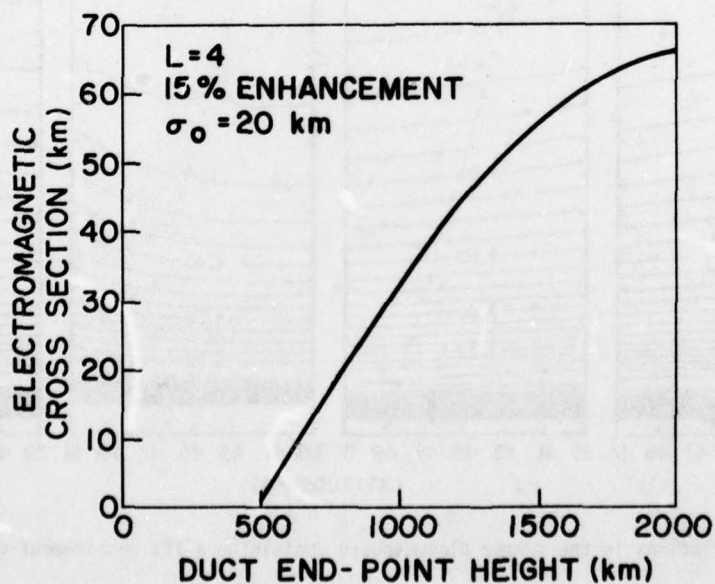
Figure 16. Effective capture cross section of a VLF duct as a function of the endpoint height. The electromagnetic cross section becomes equal to the physical cross section for ducts terminating at high altitudes.

DISCUSSION

J.Röttger, FRG

You mentioned that waves transmitted near the ground (e.g., by thunderstorms) propagate via a duct up to the magnetosphere where they trigger particle precipitation into the lower atmosphere thus causing, for example, aurora. My comment is (1) is there evidence for a significant correlation of thunderstorm lightning strokes with precipitating particles or (2) is the mechanism the other way around: precipitating particles trigger thunderstorm lightning or cause auroral? The VLF waves, generated by these aurora or lighning strokes, propagate through the magnetosphere and consequently can be recorded by ground-based methods.

Author's Reply

There is overwhelming evidence that lightning (or other VLF sources) can produce precipitation. Pertubations of the earth-ionosphere waveguide have been observed in conjunction with whistlers. Similarly, air-glow emissions have been attributed to precipitation triggered by VLF waves in the magnetosphere. Temporal analysis of these observations indicate that lightning is the cause and precipitation is the effect.

We have no evidence of precipitation causing lightning. We, however, have not made an extensive study in this area.

H.James, Canada

In your analysis of VLF signals that tend to go from a discrete signature in the frequency-time records to a diffuse shape, you postulated path mixing. Can this mixing occur in a smooth ionosphere? What is your model for this mixing?

Author's Reply

The coupling of VLF signals into enhancement ducts occurs most efficiently for high-altitude endpoints. Rays leaving the end of a duct will travel down to the bottom-side ionosphere and may be reflected upward. After reflection, the rays can couple into adjacent ducts. This path mixing may occur in both smooth and irregular ionospheres.

The coupling between ducts with low altitude endpoints is inefficient because reflection occurs inside the duct. Observations of multipath propagation may provide information about the duct endpoints.

R.W.Jenkins, Canada

We have recently been making cooperative measurements and have evidence of high-energy electron deposition in the D-Region by VLF emissions.

SATELLITE-REFERENCED IONOSPHERIC PROPAGATION CORRECTION
FOR USAF SPACETRACK RADARS*

Nicholas M. Tomljanovich/Richard J. Long**
The MITRE Corporation
Bedford, Massachusetts, U.S.A.

SUMMARY

The tracking accuracy of space surveillance radars is limited by ionospheric propagation effects. Available correction procedures based on predictions from the monthly behavior of the ionosphere are inadequate to account for its short-term variability.

A technique using Navy Navigation Satellite System (NNSS or TRANSIT) signals in near-real time to determine the actual short-term behavior of the ionosphere has been developed to support U. S. SPACETRACK radars. Since the existing constellation of 5 TRANSIT satellites provides worldwide coverage, ionosphere propagation errors for any UHF radar can easily be compensated with the correction technique using an off-the-shelf NNSS receiver and a minicomputer.

A discussion of the concepts and implementation of the TRANSIT-referenced correction technique are presented, followed by test results from Bedford, Massachusetts, which show potential for a factor of 4 improvement over monthly average predictions.

Results of tests conducted with an operational radar at a high-latitude site during the summer of 1977 are also presented.

1. INTRODUCTION

At the transmission frequencies utilized by most USAF SPACETRACK radars, variations in ionospheric propagation effects impose an important limitation to the tracking accuracy that can be realized in operational usage. Ionospheric propagation errors can only be partially corrected by currently available compensation techniques that rely on propagation predictions based on the monthly median behavior of the ionosphere.

Correction procedures based on predictions from the monthly median behavior of the ionosphere are incapable to account for the short-term variability of the ionosphere which can be large (Kane 1975). As an example, Figure 1 illustrates the expected day-to-day behavior of the ionospheric range error that a typical UHF radar would experience at Clear, Alaska, for a target at 5^0 elevation, during solar maximum and worst season conditions (Klobuchar 1976). Even with the mean curve properly predicted, short-term errors are experienced of magnitude indicated by the "max" and "min" curves. The spread about the mean and the rms error (20 - 30% of the monthly average) indicates the uncertainty remaining after corrections due to short-term variations. Disturbed ionospheric conditions and local features, such as the high-latitude trough or travelling ionospheric disturbances (TIDs), are examples of phenomena which are too volatile to be incorporated in monthly average predictions.

Additional errors of 5% - 15% arise because the mean cannot be predicted perfectly (Mulken 1976). Predictions are usually employed to provide a worldwide time-dependent model of the major ionospheric parameters from a finite data base collected at a limited number of locations and errors result due to the extensive interpolation and model fitting procedures that are necessary (Lee 1975).

Although it is generally accepted that the use of local ionospheric measurements can lead to improved propagation correction techniques, two distinct approaches for incorporating the on-site measurements are possible. On-site measurements can be used as normalization factors to scale up or down the climatological prediction map available to each site, or the on-site measurements can be used to directly account for the short-term behavior of the ionosphere and its spatial variations and generate the proper corrections for ionospheric propagation behavior. The next section will show how TRANSIT-satellite signals can be conveniently used to accomplish the more ambitious and more accurate direct compensation, as well as the scaling operation.

2. SATELLITE-REFERENCED PROPAGATION CORRECTION CONCEPT

Range and elevation errors are the dominant degradation effects experienced by transionospherically propagated signals. At VHF frequencies and higher, both errors can easily be corrected once the integrated electron density along the propagation path is known.

The TRANSIT satellites transmit two harmonically related VHF and UHF frequencies which receivers at ground locations utilize to remove first-order ionospheric effects by measuring the "differential Doppler", f_{DD}, where

$$f_{DD} = f_D^{UHF} - \frac{8}{3} f_D^{VHF}$$

For propagation correction, the differential Doppler, combined with the satellite ephemeris, can be processed in near-real time to determine the actual total electron content (TEC) along each pass.

---

* This work was sponsored by the Electronic Systems Division of the U. S. Air Force Systems Command.

** Now at Lincoln Laboratory, Lexington, Massachusetts.
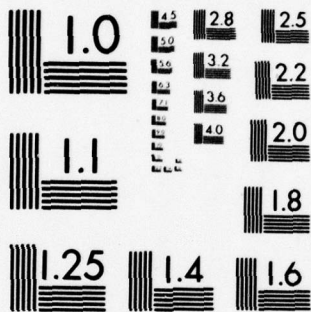
MICROCOPY RESOLUTION TEST CHART
NATIONAL BUREAU OF STANDARDS-1963-A

Since only the time rate-of-change of the phase path is available in the differential Doppler, a direct integration recovers TEC apart from an unknown constant of integration ΔP_0:

$$2\pi \int_0^t f_{DD} \ dt = 2\pi \ C \ TEC \ sec \ \psi - \Delta P_0$$

$$where \quad C = -\frac{55}{24} \ \frac{40.3}{c \ f_{VHF}}$$

and where TEC is the "equivalent vertical" electron content expressed in electrons/m^2, "sec ψ" is the obliquity factor accounting for the slant path geometry, f is expressed in MHz, and c is the speed of light. The above equation shows that if TEC is known at any point along the TRANSIT pass, the integration constant ΔP_0 can be computed and thus TEC can be evaluated at all other points along the pass.

However, although different techniques are available to measure TEC (Yeh 1961), the difficulty of obtaining a simultaneous independent measurement of TEC at a point along the TRANSIT pass necessitates the use of the differential Doppler data to directly deduce the integration constant.

A new algorithm to determine both the constant of integration and TEC along a TRANSIT pass has been developed that offers important improvements over algorithms that have been previously studied (Garriot 1963). The analytical form of the algorithm is shown in Table I (Tomljanovich 1978).

The major feature of the improved TEC algorithm is the optimization of processing parameters to reduce errors resulting from the inherent assumptions required to obtain the integration constant. An approximate 6 minute processing window, symmetric in angle about the closest approach point is utilized and the ionosphere is modelled as a spherically symmetric layer with a linear variation of TEC within the processing window. A simulation study revealed the algorithm's immunity to both TEC tilts and representative types of travelling ionospheric disturbances (TIDs).

A potential implementation of the differential Doppler technique for providing ionospheric propagation correction for U. S. SPACETRACK radars is schematically illustrated in Figure 2. The unique operational advantage of this technique is its ability to measure TEC at all points along the North-South TRANSIT passes that are in the vicinity of the radar.

In contrast, other techniques, such as the use of Faraday rotation data from geostationary satellites, only can furnish TEC measurements at few points in the northern hemisphere.

3.   TESTS OF TEC MEASUREMENTS AT MID-LATITUDE

The utility of the differential Doppler technique depends on the accuracy with which TEC is determined by the process.

Tests of the accuracy of differential Doppler measurements of TEC were conducted using mid-latitude data. Two years of differential Doppler data from TRANSIT passes collected by J. Evans at the Lincoln Laboratory Millstone Hill facility during the 1971-1973 period (Evans 1973) were used as inputs and processed by our differential Doppler algorithm to determine the vertical TEC along each pass. Independent measurements of TEC that had been made during the same period by the Air Force Geophysical Laboratory at Hamilton, Mass., using Faraday rotation measurements of ATS-3 signals, were provided by J. Klobuchar and compared with TEC measurements determined by the algorithm. To insure a valid comparison, computer sorting was used to select only those TRANSIT passes which were within $\pm$ 1.0 degrees of longitude of the subionospheric point of the ATS-3 measurements made from Hamilton, Mass.

Results of the analysis for all daytime passes in shown in Figure 3. The histogram of the relative percentage errors in TEC for the differential Doppler technique, compared to Faraday data, shows a factor of 4 improvement over present climatological predictions. Furthermore, since the TEC residuals also contain errors due to inaccuracies in the Faraday reference, the accuracy attributed here to the differential Doppler technique is probably pessimistic.

For nighttime passes, our analysis shows a poorer percentage compensation for the differential Doppler technique, (RMS spread: 20%) but less absolute TEC error than for the daytime passes. While the Faraday rotation reference is also more inaccurate at night, the greater irregularities in the nighttime ionosphere are believed to be the primary cause of the reduced percentage compensation. Nonetheless, since typical nighttime values of TEC and hence ionospheric range errors are about a third of the daytime values, absolute residual range errors after correction by the differential Doppler technique are lower for the nighttime cases than for the daytime cases.

4.   EXTRAPOLATION OF TEC MEASUREMENTS

TEC measurements from TRANSIT passes provide unique data for correcting ionospheric propagation effects over the full radar coverage. For any radar target located in the proximity of a nearly simultaneous TRANSIT pass, the TEC measurements can be directly utilized to determine the propagation effects on the radar measurements.

Compensation of propagation effects over the entire radar coverage requires the combination of successive TRANSIT observations to extend the collected TEC information to other regimes of time and space. A TEC extrapolation algorithm has been developed for this purpose which uses monthly TEC predictions from the Air Force Global Weather Center (AFGWC) to aid in extrapolating, over the radar coverage, the TEC measurements from consecutive TRANSIT passes. The extrapolated TEC acquires the value of the measured TEC in the vicinity of the TRANSIT passes, and tapers in both space (longitude) and time to the AFGWC climatologically predicted TEC values for distances and times which are large

compared to the typical correlation length ($L_0 \simeq 4000$ km) and correlation time ($T_0 \simeq 2$ hrs.) of the ionosphere (Klobuchar 1977).

Figure 4 summarizes the fundamental principles governing the extrapolation algorithm.

The extrapolated value of TEC at any space - time location is generated by a linear estimator which uses all the preceeding TRANSIT passes that are still valid. An optimum linear predictive filter, constructed to minimize the variance of the estimator, leads to a determination of the optimum tapering weights in terms of the previously determined autocorrelation function of the TEC differences between the TRANSIT observations and the monthly averages.

5.   TESTS OF TEC MEASUREMENT AT HIGH LATITUDE

Further testing on the TEC measurement accuracy was conducted at Clear, Alaska, in the summer of 1977 to determine the effectiveness of the TRANSIT-referenced technique in providing a near-real time propagation correction for typical SPACETRACK radars at high-latitude locations. In addition, the TRANSIT satellites were also used in an overall TRANSIT-referenced calibration procedure as on-line calibration references to determine the radar biases, and further reduce radar measurement errors.

The operational configuration of these tests is illustrated in Figure 5. While complete reduction and analysis of the data is in progress, representative results are next presented to illustrate the outputs from the differential Doppler technique, the outputs from the extrapolation algorithm and the comparisons being performed in the analysis to establish the capabilities of the developed propagation correction technique.

Figure 6 shows the ground tracks of five TRANSIT passes (Passes 30, 31, 32, 34 and 40) observed at Clear on July 7 and 8.

In Figures 7-11, actual measurements of TEC (DD), converted to corresponding range error in meters at 425 MHz for a target at a fixed 5° elevation, are presented as function of subionospheric latitude for each pass.

The AFGWC monthly average predictions (CLIMATOLOGY) of the ionospheric range errors for signal propagation through the entire ionosphere are plotted in these figures for comparison. Furthermore, simultaneous measurements of Faraday rotation from ATS-1 are used as a check on the accuracy of DD technique. Note that, although two reference points are given for the ATS-1 measurements, only the lower value should be used for the TRANSIT data to account for the 1100 km height of the TRANSIT orbit.

The measurements from all TRANSIT passes on July 7 show a decrease in the ionospheric content with higher latitudes. This behavior agrees in trend but not in value with climatology predictions. On pass 40 (Figure 11) on July 8, however, a southward depression is present which is absent from climatological predictions both in trend and value. The observed nighttime trough, further confirmed by the ATS-1 measurements, illustrates one of many commonly occurring differences between actual and predicted ionospheric behavior which can be compensated by this propagation correction technique.

Utilization of TRANSIT pass measurements over the entire radar coverage is illustrated in Passes 31, 32 and 34 (Figures 8 through 10). Ionospheric measurements for Pass 30 are extrapolated to the positions and time of Pass 31 and compared to both on-site measurements and climatology (Figure 8). Measurements for Passes 30 and 31 are then used to obtain an extrapolated curve for Pass 32 and so on. Although several correlation lengths are being tested within the extrapolation algorithm, the presented results use the two extreme values: 2000 km and 6000 km.

The "correlation length" is here defined as that longitudinal distance away from a TRANSIT observation at which the TEC uncertainty with monthly average predictions reduces by 10% using the TRANSIT TEC measurements.

The extrapolated curves show a close agreement with the TRANSIT measurements and a substantial improvement over AFGWC climatology. Furthermore, analysis of other daytime results have shown that the largest correlation length ($L_0 \simeq 6000$ km) gives the best agreement with measurements. This is somewhat larger than a recently reported calculation for the longitudinal correlation distance of the mean daytime TEC computed using mid-latitude data (Klobuchar 1977). The difference between the reported value of 2,900 km, which translates by our different definition of correlation length to 4,000 km, and our observed value may indicate a latitudinal dependence for the correlation length.

Radar tracks on TRANSIT passes have also been collected at Clear, Alaska, to establish the actual improvements in radar tracking accuracy with the improved propagation correction procedure. A plot of representative data is shown in Figure 12 which gives the percent reduction in the residual range errors after corrections.

The residual range errors are computed by taking the difference between the radar-measured range to a TRANSIT satellite and its "true" range as deduced from the TRANSIT broadcast ephemeris. The percent reduction of the residual range errors is plotted at 10 second intervals for two different types of ionospheric corrections: the monthly average climatological corrections and the satellite-referenced differential Doppler (DD) corrections. For the pass of Figure 12, Figure 13 presents the difference between the measured ionospheric range error curve from TRANSIT data, and the monthly average range error curve from AFGWC climatology.

6.   CONCLUSIONS

A satellite-referenced propagation correction technique using TRANSIT data has been developed to support U. S. SPACETRACK radars.

Preliminary results from the Clear, Alaska, tests show that significant improvement in radar accuracy can be achieved using the near-real time propagation correction procedure.

The data analyzed indicates that the technique provides an important capability for near-real time monitoring of short-term ionospheric behavior and propagation effects over an entire radar coverage.

7. REFERENCES

1. Evans, J. V., 1973, "Millstone Hill Radar Propagation Study", ESD-TR-73-259.

2. Garriot, O. K. and F. DeMendonca, 1963, "A Comparison of Methods Used for Obtaining Electron Content from Satellite Observations", Journal Geophysical Research, Vol. 68, p. 4917-4927.

3. Kane, R. P., 1975, "Day-to-Day Variability of Ionospheric Electron Content at Mid-Latitudes", Journal Geophysical Research, Vol. 80, No. 22, p. 3091-3099.

4. Klobuchar, J. A. and R. S. Allen, 1976, "Maximum Ionospheric Range Errors for Air Defense Command Radars", AFGL-TR-76-0042.

5. Klobuchar, J. A. and J. M. Johanson, 1977, "Correlation Distance of Mean Daytime Electron Content", AFGL-TR-77-0185.

6. Lee, M. K. and J. S. Nisbet, 1975, "Propagation Predictions and Studies Using a Ray Tracing Program Combined with a Theoretical Ionospheric Model", IEEE Transactions on Antennas & Propagation, Vol. AP-23, p. 132-136.

7. Mulken, F. A., 1976, "Comparison of Predicted Monthly Medians of TEC with Field Observations", AFGL-TR-76-0158.

8. Tomljanovich, N. M., 1978, "Determination of Ionospheric Electron Content Using TRANSIT Satellite Signals", MITRE Technical Report MTR-3481.

9. Yeh, K. C. and G. W. Swenson, 1961, "Ionospheric Electron Content and its Variations Deduced from Satellite Observations", Journal Goephysical Research, Vol. 66, p. 1061-1067.

TABLE I: TEC ESTIMATION ALGORITHM

- IONOSPHERIC TEC MODEL : LINEARLY VARYING IN LATITUDE

- ESTIMATION CRITERION: $\int (\Delta P - \Delta P_E) \, d\lambda = 0$

- SOLUTION FOR ΔP_0:

$$\Delta P_0 = - \frac{\overline{\Delta P_i} - \overline{\sec \psi} \ \overline{\Delta P_i \cos \psi}}{[1 - \overline{\sec \psi} \ \overline{\cos \psi}]}$$

$$\Delta P_i = \int_{t=0}^{t} \dot{\Delta P} \, dt$$

- INSENSITIVE TO TEC TILTS FOR A SYMMETRIC ANGLE WINDOW
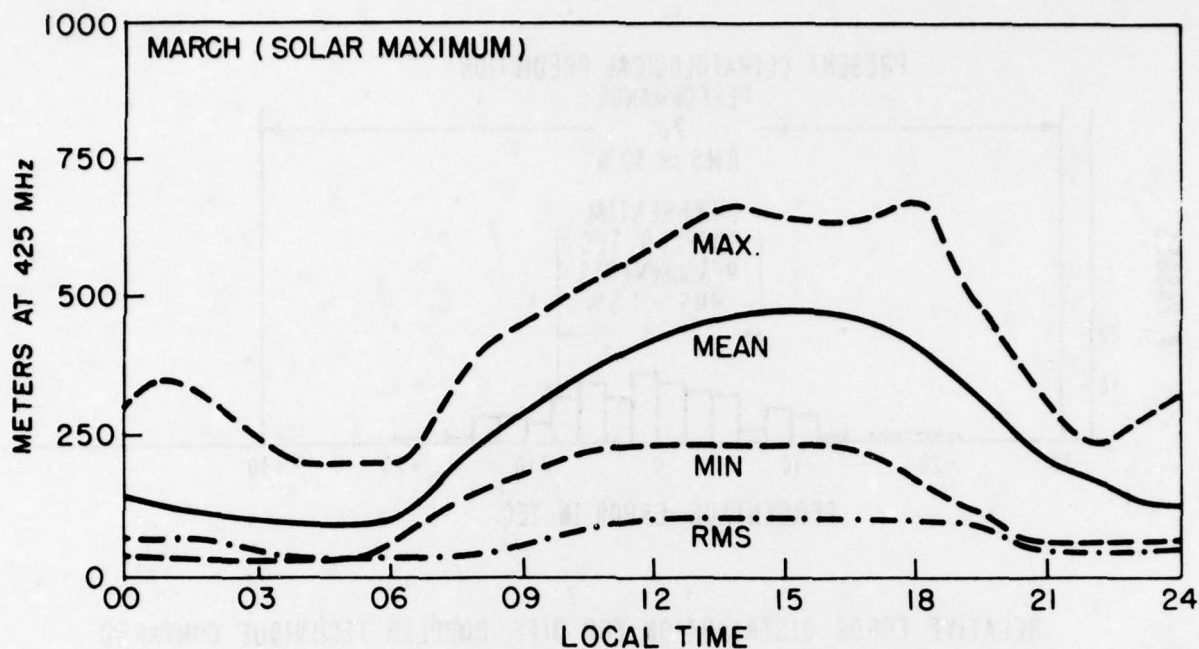
FIGURE 1:   IONOSPHERIC RANGE ERROR AT CLEAR, ALASKA
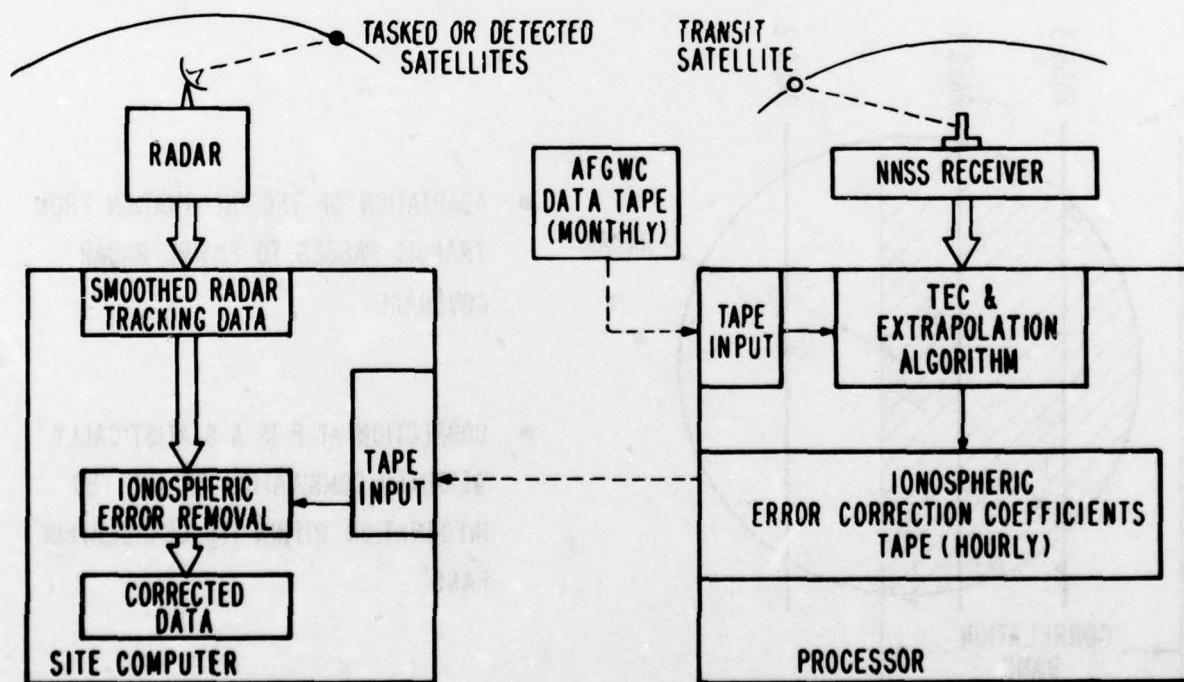
FIGURE 2:   POTENTIAL APPLICATION OF IONOSPHERIC PROPAGATION CORRECTION

PRESENT CLIMATOLOGICAL PREDICTION
PERFORMANCE:
2σ
RMS ≃ 30%

DIFFERENTIAL
DOPPLER TEC
MEASUREMENTS
RMS ≃ 7 5%
2σ

\# PASSES

PERCENTAGE ERROR IN TEC
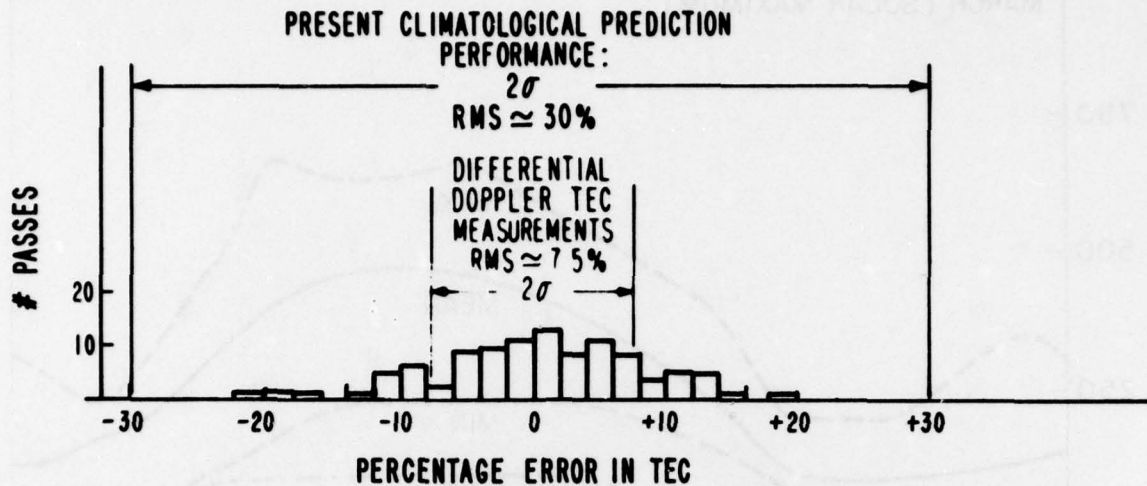
RELATIVE ERROR DISTRIBUTION FOR DIFF. DOPPLER TECHNIQUE COMPARED
TO FARADAY DATA ON 87 NNSS DAYTIME PASSES.

1971 - 73 DATA

FIGURE 3:   ACCURACY OF TEC MEASUREMENT ALGORITHM

PASS 3   PASS I   PASS 2

RADAR

CORRELATION
BAND

• ADAPTATION OF TEC INFORMATION FROM
TRANSIT PASSES TO ENTIRE RADAR
COVERAGE

• CORRECTION AT P IS A STATISTICALLY
WEIGHTED COMBINATION OF ALL TEC
INFORMATION WITHIN ITS CORRELATION
BAND
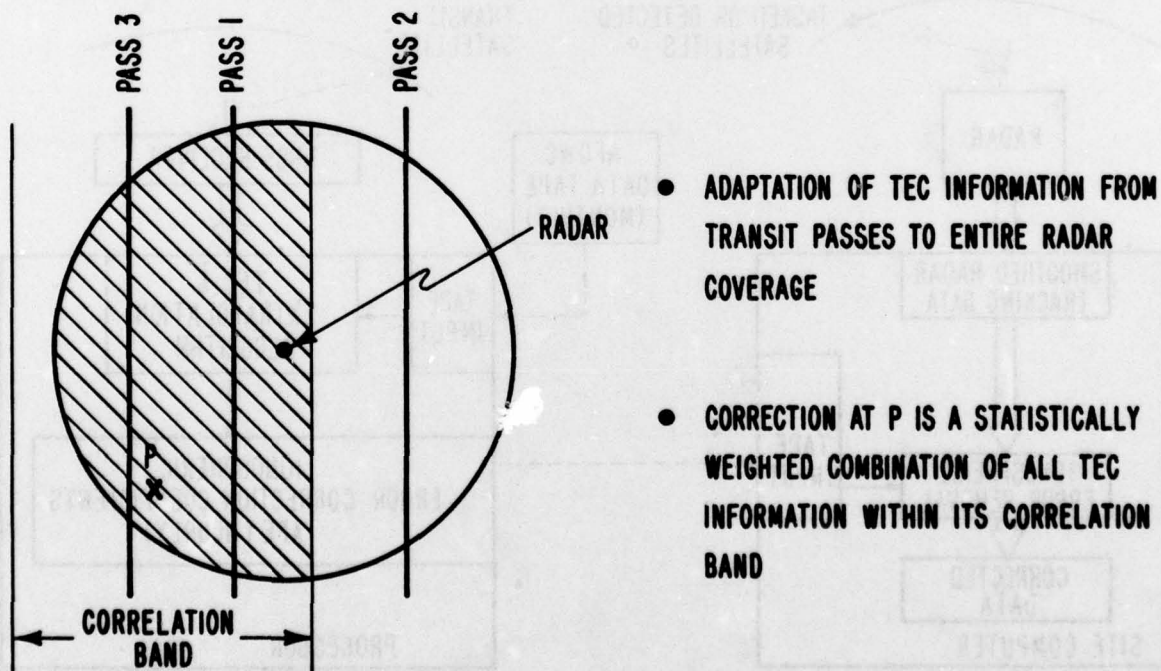
FIGURE 4:   TEC EXTRAPOLATION CONCEPT
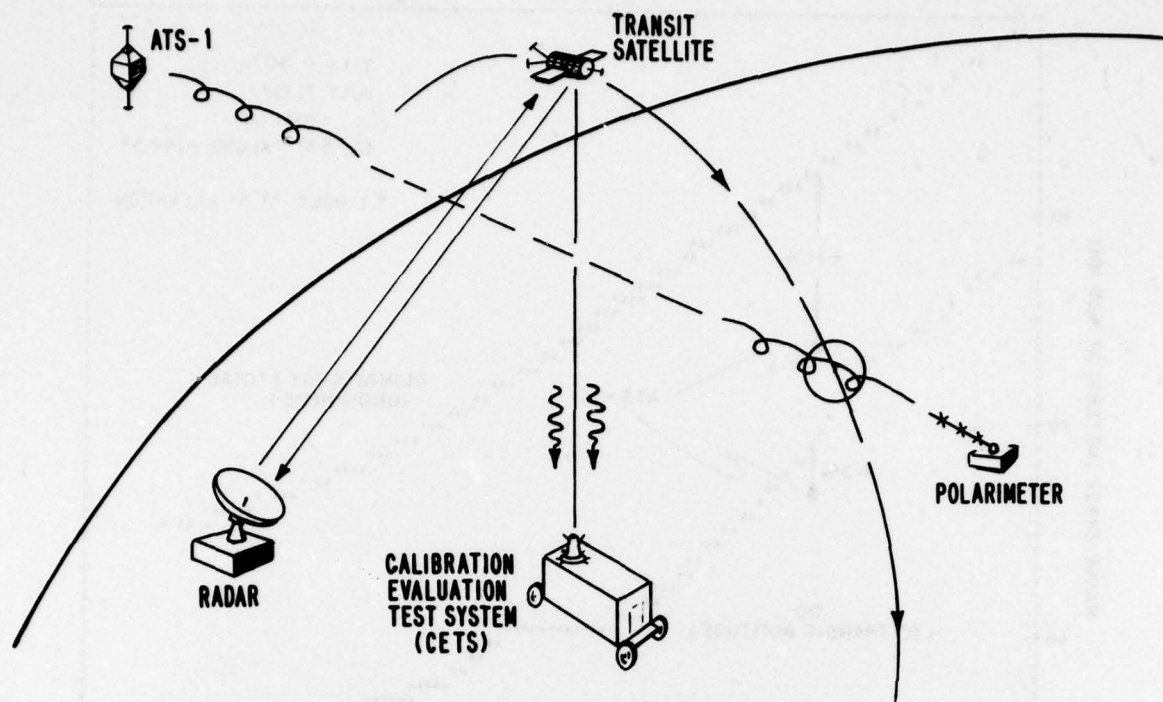
FIGURE 5: HIGH LATITUDE TEST CONFIGURATION
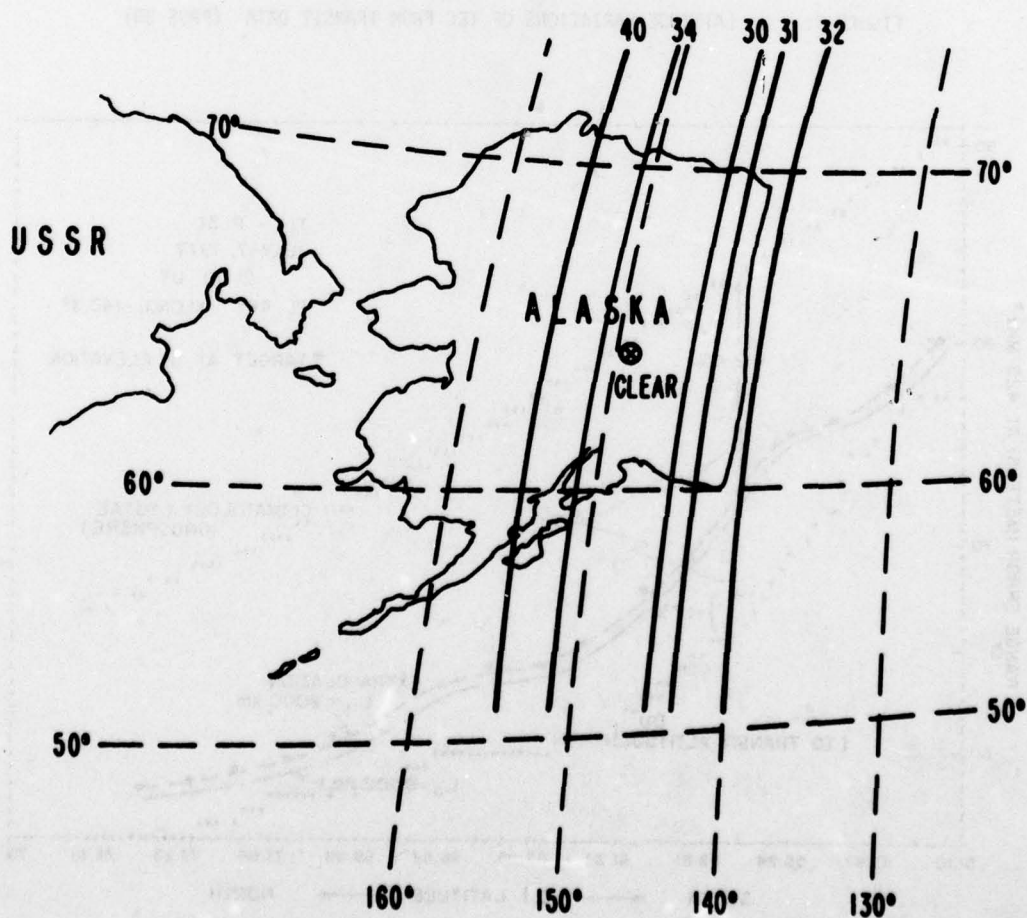
FIGURE 6: TRANSIT PASS GEOMETRY
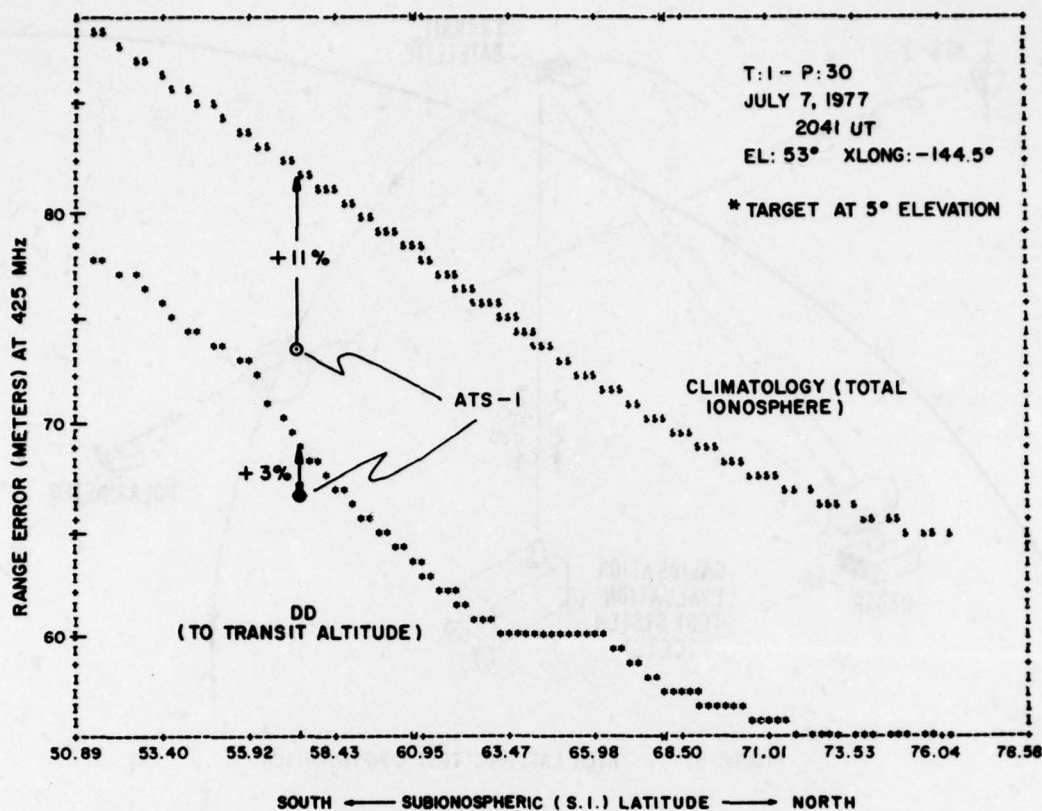
FIGURE 7:   LATITUDE VARIATIONS OF TEC FROM TRANSIT DATA   (PASS 30)
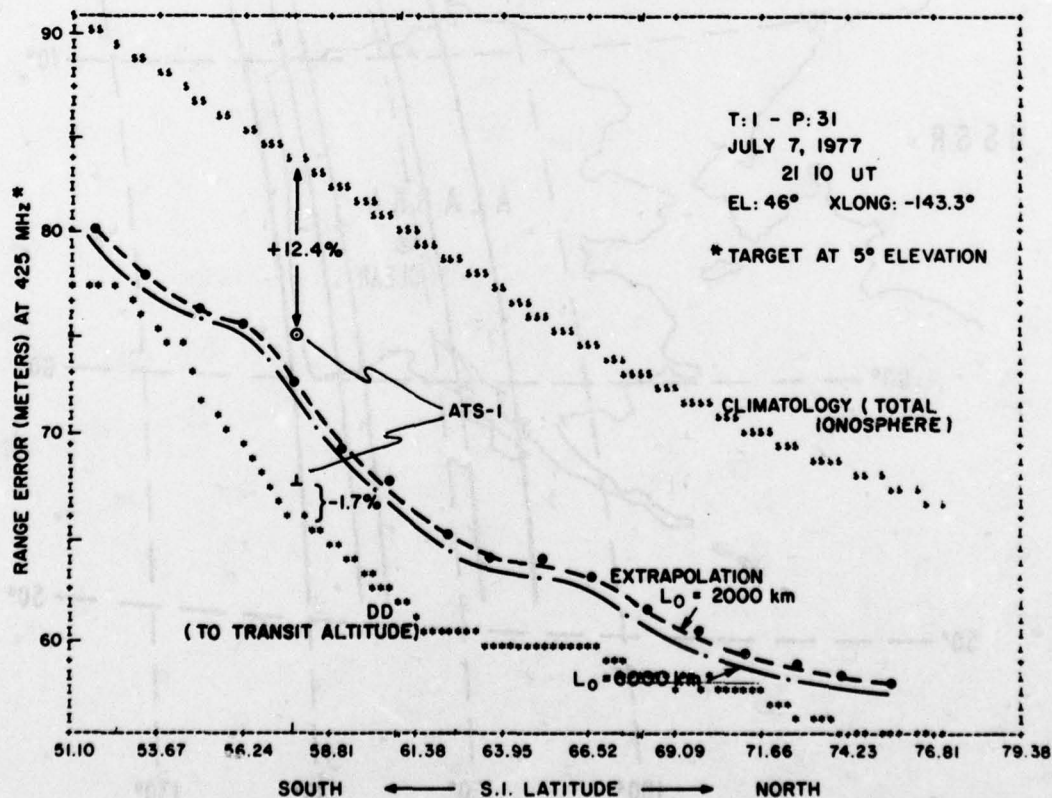
FIGURE 8:   LATITUDE VARIATIONS OF TEC FROM TRANSIT DATA   (PASS 31)
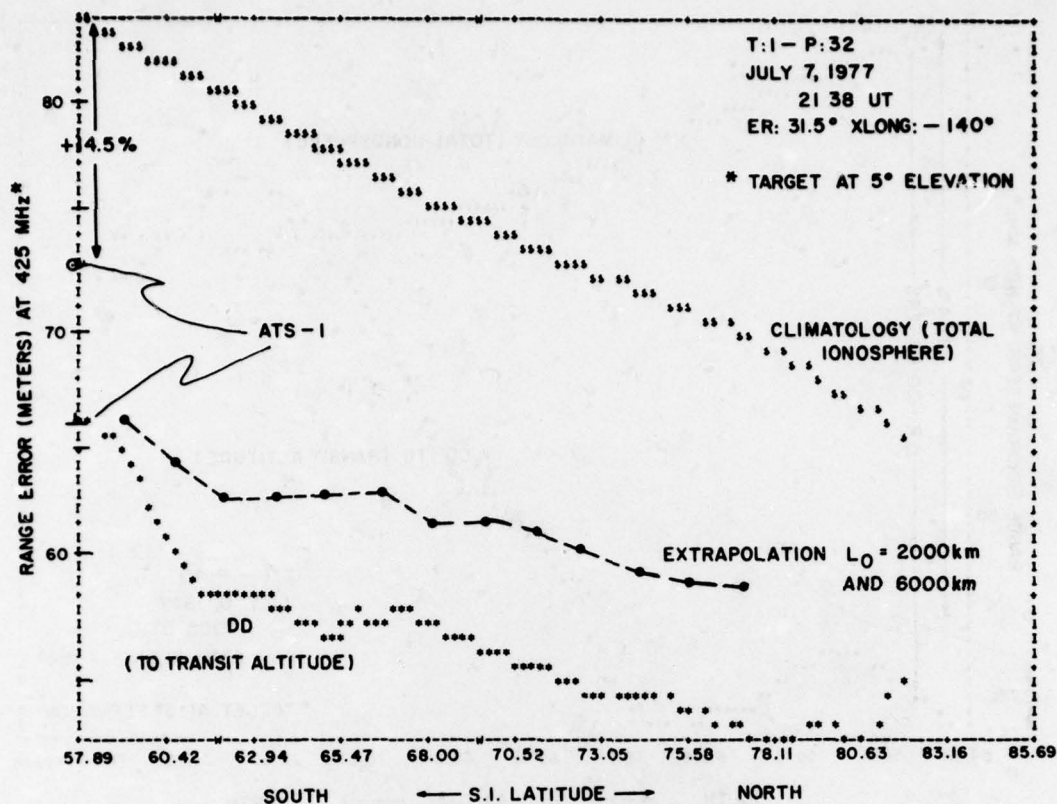
FIGURE 9: LATITUDE VARIATIONS OF TEC FROM TRANSIT DATA (PASS 32)
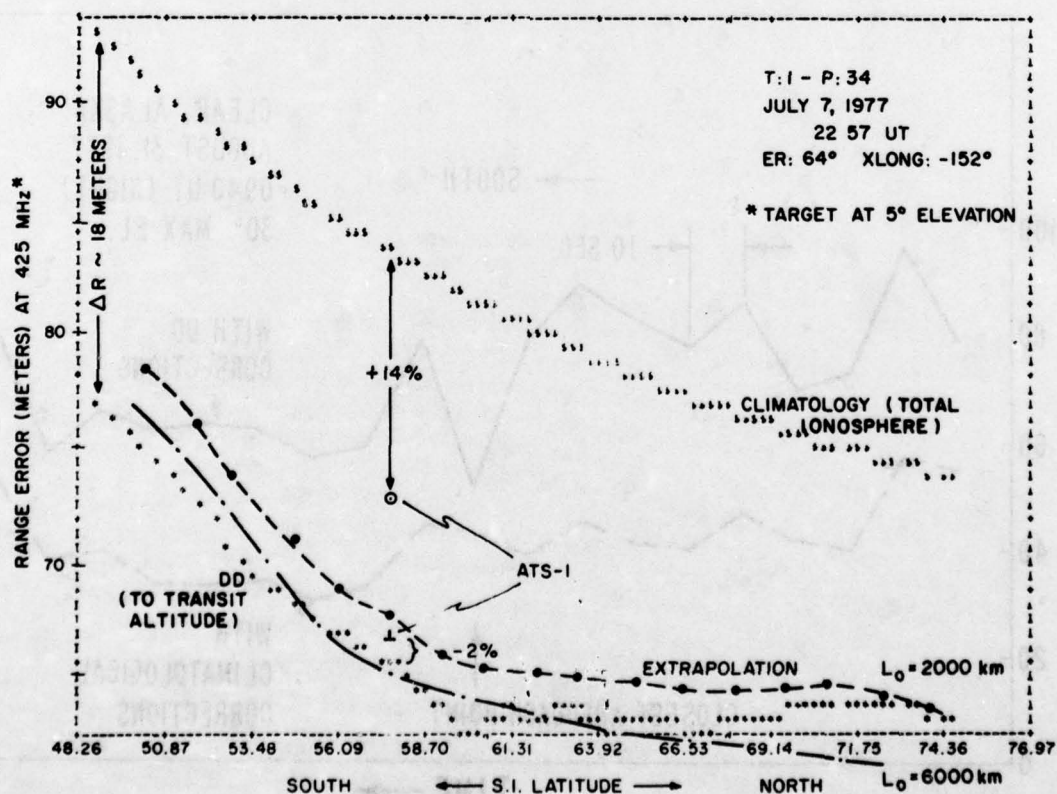
FIGURE 10: LATITUDE VARIATIONS OF TEC FROM TRANSIT DATA (PASS 34)
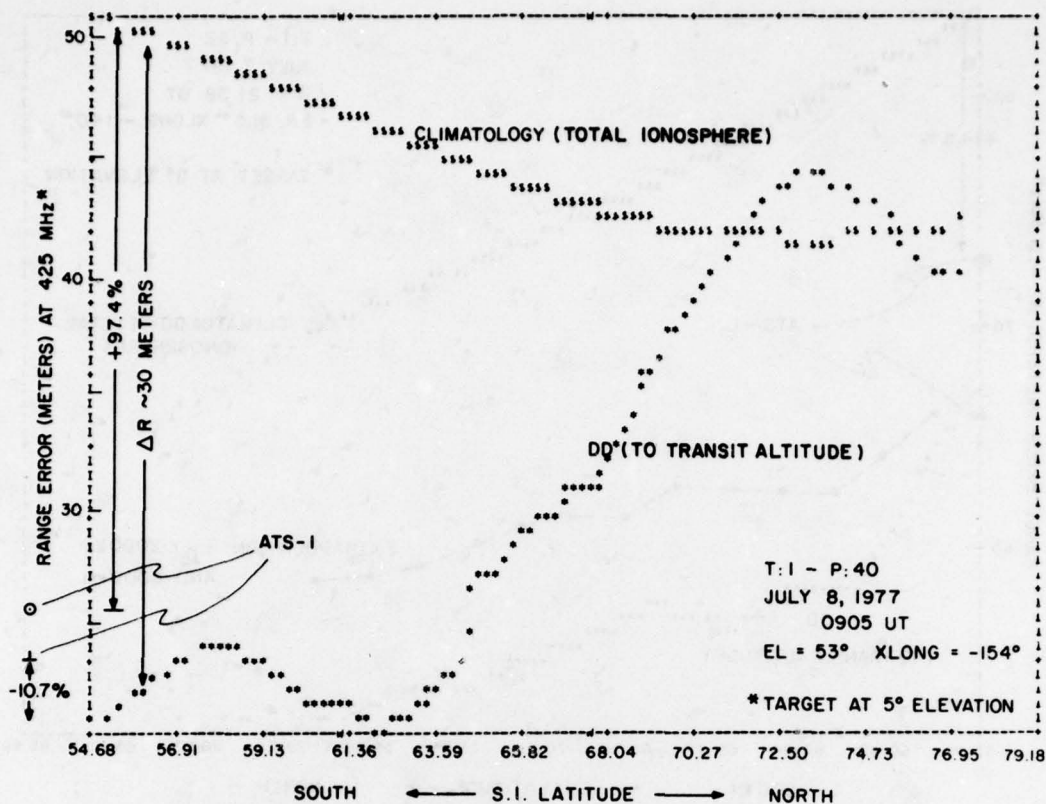
FIGURE 11:   LATITUDE VARIATIONS OF TEC FROM TRANSIT DATA   (PASS 40)
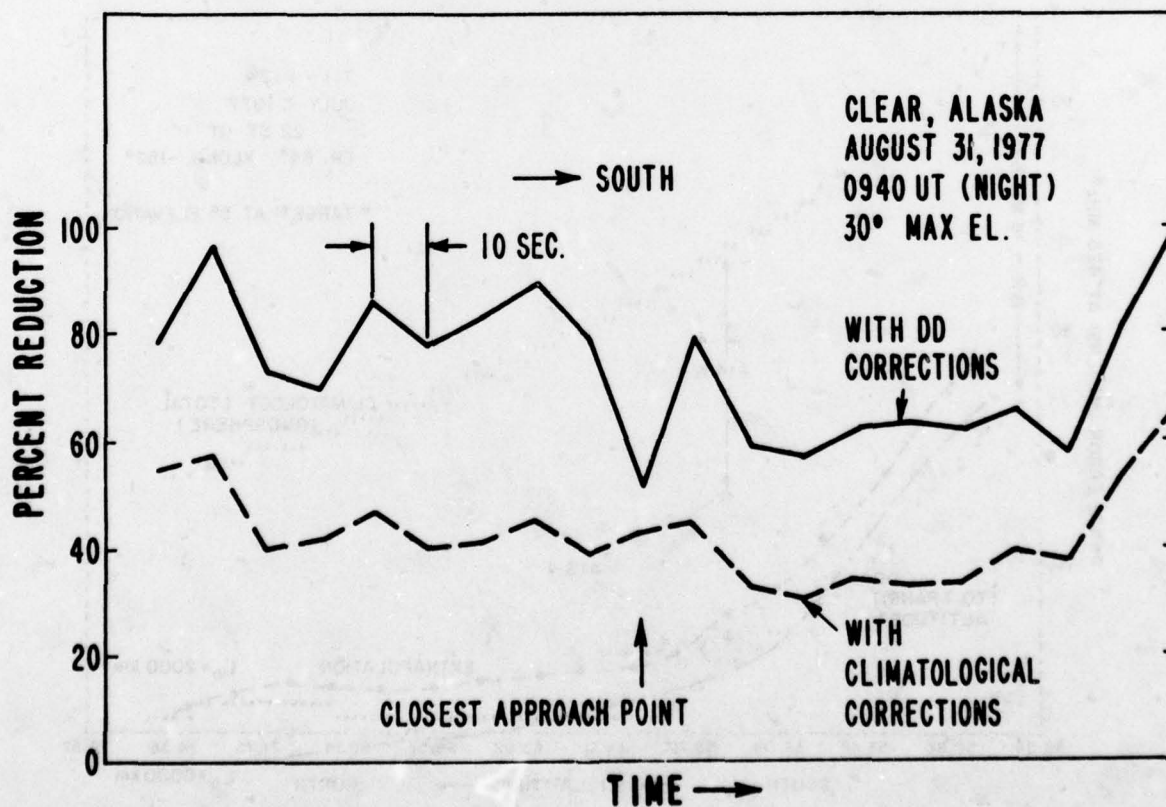
FIGURE 12:   REDUCTION IN RADAR RANGE RESIDUALS
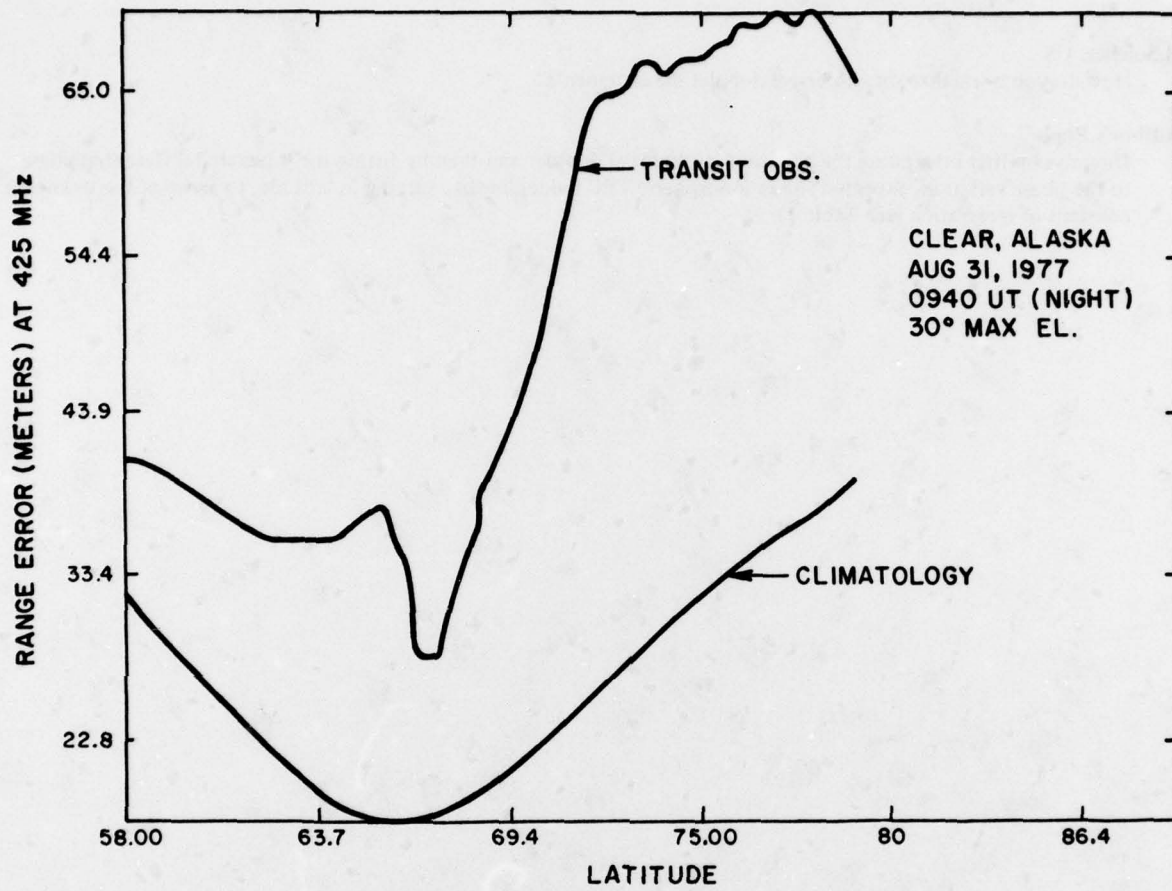
FIGURE 13:   IONOSPHERIC RANGE CORRECTIONS ALONG A TRANSIT PASS

DISCUSSION

E.J.Fremouw, US

What do you mean by climatology? I would expect any climatological model to have the main trough in it.

Author's Reply

The AFGWC monthly average predictions, which we refer to as climatology, were obtained from the ITS-78 program and do not model the nighttime high-latitude trough.

H.Soicher, US

How do you normalize the dispersive doppler measurements?

Author's Reply

Directly, by first integrating the measured differential doppler and then by fitting the integrated differential phase to the phase variation, expected for an ionospheric TEC model linearly varying in latitude, to arrive at the unknown constant of integration (see Table 1).

IONOSPHERIC RANGE-RATE EFFECTS
IN
SATELLITE-TO-SATELLITE TRACKING

Rodney B. Bent, Judy R. Lipofsky, Sigrid K. Llewellyn

Atlantic Science Corp
P.O. Box 3201
Indialantic, Florida 32903

and

Paul E. Schmid-NASA/Goddard Space Flight Center

SUMMARY

Investigations of ionospheric range and range-rate corrections in satellite-to-satellite tracking have pointed out major problems and defined the magnitude of errors that have to be considered for communications between satellites and related experiments.

The two major causes of the sudden and sometimes large variations apparent in the ionospheric range and range-rate corrections along the satellite arc are the geometric effects of the raypath and the curved ionosphere, and the localized perturbations in electron density along the satellite-to-satellite line of sight. The raypath may follow along the region of maximum electron density for a considerable distance, it may pierce the ionosphere at two separated locations, pass through it once, or only partially, or remain above it, allowing for a great range in the magnitude of the effect. Significant gradients in the electron density, as occur in the equatorial anomaly, result in very large perturbations.

Ionospheric tracking errors are greatly effected by the following parameters, whose influence was thoroughly investigated: satellite height, height of maximum electron density, localized ionospheric perturbations and gradients, and electron density variations with diurnal, day-to-day, seasonal and solar cycle patterns. Changes in these parameters can produce large variations in the magnitude of errors as well as time shifts of the peak errors along the satellite arc.

The results point to the need of using a sophisticated modeling approach incorporating daily solar data, and where possible actual ionospheric measurements as update information, as a simple median model cannot possibly account for the complex interaction of the many variables. The findings provide a basis from which the residual errors can be estimated after ionospheric modeling has been incorporated in the reduction.

Simulations were performed for satellites at various heights: Apollo, Geos, and Nimbus tracked by ATS-6; and in two different geometric configurations: coplanar and perpendicular orbits.

1. INTRODUCTION

The need for this study was indicated by the results of a NASA/GSFC experiment[1] to detect gravity anomalies using the Apollo-Soyuz/ATS-6 satellite configuration. This experiment was intended to improve the knowledge of the earth's gravitational field in localized areas by measuring local gravity variations by detecting small velocity changes of the low orbiting spacecraft. Two of the gravity anomalies "detected" in this experiment are shown in Figure 1b. The corresponding Apollo-Soyuz orbits are shown in Figure 1a. The Indian Ocean anomaly as well as an anomalous region in the Himalayas are indicated by the relatively large variations in range-rate residuals.

Earlier analysis [2] of satellite-to-satellite ionospheric range-rate corrections for the ATS-6 to Apollo-Soyuz geometrical configuration indicated values that were of significant magnitude compared to the gravitational effects. Such results are illustrated in Figures 1b and c and imply that most of the suggested gravitational anomaly may, in fact, be due to ionospheric effects. The geometric configurations of the high (ATS-6) and the low (Apollo-Soyuz) satellite are shown in Figure 1d. The low satellite is shown at three different positions in its orbit which, in this case, is below the height of maximum electron density. In Figure 1e it can be seen that ionospheric range corrections (ΔR) reach a peak at point B and are greater at C than at A. This is because the line of sight between the high and low satellite passes through a greater portion of the ionosphere at B than at A or C. Range-rate corrections ($\Delta \dot{R}$) will pan through zero at B.

Ionospheric effects, therefore, lead to errors in the gravitational data unless they can be adequately removed by modeling. The purpose of this study is to investigate these effects and understand their origin and characteristics so that a better approach to gravitational experiments can be organized. In order to understand the basic ionospheric range-rate errors, a simple uniform ionospheric model was investigated with certain orbits; the simple model was then varied in height, and perturbations were added in discreet places. Seasonal and solar cycle variations were examined as well as actual orbits of varying inclination and height.

2.   EFFECTS OF A SIMPLE UNIFORM IONOSPHERE
ON COPLANAR SATELLITE ORBITS

In satellite-to-satellite tracking the effects of ionospheric refraction are difficult to predict because of complex orbit configurations with changing ionospheric conditions. Evaluating the effects of a simple uniform ionosphere on coplanar satellite orbits at various altitudes clarified the size and duration of refraction errors incurred purely by the geometry of the slanted raypath through the curved ionosphere. Modification of the ionospheric characteristics of the maximum electron density and the corresponding height illustrated the variations that refraction errors will undergo for changing conditions. The height of the ionosphere often changes by $\pm$ 50 km per day, and differences of 5 to 10 MHz in critical frequency can easily be caused by localized perturbations, diurnal variations, day-to-day changes, by seasonal effects and solar cycle patterns. To further investigate the effects of local perturbations, steep ionospheric gradients were injected into the otherwise uniform ionosphere, as they are observed in the equatorial anomaly region, and sunrise region and during irregular occurring ionospheric disturbances.

In the following analysis, the high satellite was considered stationary at a height of about 36,000 km, the low satellite height is varied, and the orbits are coplanar. A tracking frequency of 1 GHz is used and one-way corrections are computed. Each arc was started where the high and low satellites were aligned with the earth's center, and terminated when the low satellite disappeared from the view of the high satellite. The simple model used was based on the Bent Ionospheric Model[3]. This is an emperical world-wide model capable of accurately estimating the electron density profile and the associated delay and directional changes of a wave due to refraction. The model computes an electron density versus height profile with five exponential topside layers, a bi-parabolic bottomside layer, and an interconnecting parabola. The simplified model used in this study does not include any horizontal gradients as it was held constant world-wide and in time. Different conditions were simulated by varying the critical frequency, f_0F2, and the height of maximum electron density, h_m.

2.1 Effects of Satellite Height

The ionospheric range-rate corrections due to a geometric effect along the satellite arc are illustrated in Figure 2 for different altitude satellites. The low satellite passes over the horizon and becomes invisible to the high satellite. The very large range-rate corrections immediately before the invisible region are caused by the changing geometric conditions of the satellite raypath through the curved ionosphere as it disappears (see Figure 1). The higher the low satellite orbit is, the larger are the range-rate corrections caused by this effect. The reason for this is that for a low satellite at a relatively high altitude the tracking raypath remains above most of the ionosphere over large segments of its orbit and penetrates significant electron density layers only when the satellite is near the point of disappearance. The higher the satellite is, the faster it passes from the region where the satellite raypath pierces the ionosphere to the point of invisibility. This faster rate of change produces larger amplitudes in the range-rate corrections. The lower the satellite orbit is, the shorter is its period of visibility from the high tracking satellite, and the longer is the time period over which ionospheric corrections are orders of magnitude larger than in ground-to-satellite tracking. Considering coplanar orbits, for Apollo-Soyuz at 200 km the last 13 minutes of its arc show such large corrections, for Geos at 850 km the last 7.5 minutes, and for Nimbus at 1100 km the last 5.5 minutes. However, if low and high satellites are moving at right angles to each other and are close to the point of disappearance, then such large effects can be observed for extended periods of time.

Range-rate correction curves as a function of time along the arc have steeper slopes and larger positive and negative peaks the higher the satellite altitude is. At h_m = 250 km, f_0F2 = 15 MHz and a tracking frequency of 1.0 GHz the maximum corrections are 1.5 m/sec, 3.5 m/sec, 4.3 m/sec for Apollo, Geos and Nimbus respectively.

2.2 Effects of Ionospheric Height

Changes in the height of the ionosphere which are typically $\pm$ 25 km, produce very significant effects on the range-rate corrections, as shown in Figure 3. Time shifts of the peak values along the arc are experienced; for a 50 km shift in h_m they are of the order of 0.9 minutes for Apollo and 0.35 minutes for Geos and Nimbus. Such time changes are significant when attempting to derive localized gravitational effects. In addition, for the Apollo spacecraft which always remains below h_m, large changes in the maximum correction values are apparent. Increases of about 0.3 m/sec in the peak value occur for each 25 km drop in h_m at f_0F2 = 15 MHz. Such changes in peak values are, however, not apparent from the higher satellite data from Geos and Nimbus.

2.3 Effects of Electron Density

Changes in electron density effect the amplitude of the range-rate corrections such that the peak correction values for each satellite are approximately in the same ratios as the squares of the f_0F2's. Time shifts of the peak corrections along the satellite arc are not associated with changes in f_0F2. See Figure 4.

2.4 Effects of Ionospheric Perturbations

Ionospheric perturbations with associated steep gradients in electron density can greatly modify the smooth range-rate correction curves as predictable from geometric effects in satellite-to-satellite

tracking. The peak values may experience drastic increases or decreases in amplitude as well as shifts in time, and additional maxima and minima can occur along the arc. Such effects were simulated by injecting into the previously uniform ionosphere variations in electron density, which have maximum effect at the perturbation center and gradually decrease with increasing distance from the center. An exponential weighting function was used, $w = e - (d/D)^2$, with $D = 400$ NM; d is the distance from the center of perturbation. As shown in Figure 5, the effects of the perturbations on the Geos corrections are of larger amplitude, but the effects on the Apollo arc are of greater relative severity persisting over a longer period of time.

For different size disturbances under otherwise fixed conditions the range-rate corrections show similar patterns. However, the greater the amplitude of the electron density perturbation and the steeper the slopes of the gradients, the more severe are the deviations from the smooth unperturbed correction curve. See Figure 6.

Shifting the location of the perturbation center to different latitudes close to the Apollo-Soyuz arc manifested itself mainly in a large time shift, of the order of minutes, of the additional single or double peak extremum. The earlier the perturbation center appears along the arc, the earlier does the extra peak occur.

3. SPACIAL AND TEMPORAL EFFECTS

In this section the effects of actual variations and gradients in the ionosphere on satellite-to-satellite range-rate corrections are investigated. These gradients occur along the arc of a low satellite being tracked by a high satellite. For this purpose the 3-dimensional world-wide Bent ionospheric prediction model was used to show the effects of steep spacial gradients as well as of short and long term temporal gradients, such as diurnal variations, day-to-day deviations from the monthly mean, seasonal and solar cycle variations.

3.1 Simulated Orbits

To capture the ionospheric variations, the orbit configuration was chosen quite different from the coplanar orbits used for the simple model investigations. The satellite orbits were simulated perpendicular to each other, the stationary high satellite in an equatorial orbit, and the low satellites at various heights in polar orbits both prograde and retrograde. The angular separation between the satellites was chosen in the proximity of the disappearance points, and under such circumstances significant range-rate corrections exist along most of the orbit. Tracking frequencies of 1GHz were used in the simulations. The range-rate corrections are presented as the one-way values.

In Figure 7 one of the orbit configurations is shown. The low satellite in a prograde orbit disappears from sight of the high satellite for a portion of its orbit and becomes visible again as it crosses the equator. Three such cases were considered for low altitude satellites at 200, 300 and 850 km and the high tracking satellite at about 36,000 km. Figure 7 shows the 300 km orbit superimposed on a world map of the ionospheric characteristic of $f_x F2$. Where the $f_x F2$ equal value lines are concentrated, large ionospheric gradients exist, and it is indicated where the ionospheric pierce point curve crosses these gradients. The intersection of the satellite-to-satellite line of sight with the region of maximum electron density establishes the ionospheric pierce point. When the low satellite is at an altitude above the height of maximum density, as is the case for Geos and Nimbus, two distinct pierce points may occur.

3.2 Spacial Gradients

To examine the effect of the low satellite altitude on the range-rate corrections along the arc, the geometric conditions were fixed, such as the high satellite position and the ionospheric pierce point location at the equator crossing and with that also the satellite line of sight, and only the height of the orbit was varied. The range-rate corrections for the orbit depicted in Figure 7 and for four additional orbits are correlated in Figure 8. The low satellite is in a polar orbit and crosses the equator at 6 UT, April 1, 1968. The orbits corresponding to Figure 8a are prograde, in 8b they are retrograde.

In Figure 8a there is an invisible portion for all satellite orbits, but at 6 UT they become visible again as they cross the equator. The 200, 300 and 850 km satellites all lie along the same line of sight from the high satellite. The very large deviations to both sides of the invisible region are caused by the changing geometric conditions of the satellite raypath through the curved ionosphere as it disappears, which is illustrated in Figure 1.

Superimposed on these geometric effects in Figure 8a are the ionospheric gradient effects, because the ionospheric density and height along the line of sight changes as the low satellite travels along its orbit.

The geometric effects are minimized in Figure 8b by decreasing the high to low satellite separation angle by about 3 degrees at the equator crossing and maintaining visibility throughout the half-orbits. The difference between the range-rate corrections along the 300 and 850 km orbits are now mainly due to the gradients in ionospheric density and height. Again the higher altitude orbit displays the larger amplitude refractive effects, but they are only about half as large as those caused by the geometric conditions in Figure 8a.

To better understand how the variations in the refraction corrections along the satellite path are caused by the ionospheric conditions, two low satellite orbits, the ionospheric densities depicted in the f_xF2 world map, the ionospheric heights and the satellite angular separation shown in Figure 9 were examined in detail and were correlated to the range-rate corrections also shown in Figure 9.

In the orbit corresponding to Figure 9a the low satellite, at 300 km, passes east of the high satellite and remains visible throughout the simulated half-orbit. A retrograde orbit was used to provide better geometric conditions, keeping the satellite distance fairly constant over the equatorial anomaly region, assisted by the slight longitude shift due to the earth rotation.

Figure 9b corresponds to another retrograde orbit, this time crossing the equatorial anomaly west of the high satellite over some very dense regions.

From the curve giving the angular separation between the satellites it is apparent that while this separation varies somewhat at the beginning and end of the arc, it is fairly constant over the central region of the equatorial anomaly where most of the large range-rate deviations occur. Hence, in the region of interest the corrections are mostly due to ionospheric gradients, because the geometric configuration remains nearly fixed.

The marked zero crossings of the range-rate corrections (Figure 9) correspond very clearly to the maxima or minima of f_xF2 shown on the world map (Figure 7). This is to be expected since extrema in f_xF2 cause extrema in electron density and range corrections, hence zero crossings in range-rate correction. The range-rate corrections give a very clear picture of the gradients encountered as the satellite connecting beam sweeps the equatorial anomaly.

Not just the electron density, but also height at the maximum undergoes steep gradients in the anomaly region. In Figure 9 it is shown that the height of the pierce point has a definite maximum at the magnetic equator around which the equatorial anomaly is centered, and its values vary between 314 and 456 km over the arc. The smaller variations in the range-rate corrections toward the ends of the arc in Figure 9b might be influenced by the ionospheric height changes.

It should be noted that different vertical scales are employed in Figure 9. Maximum absolute amplitudes in b) are about seven times as large as in a). The major reason for this lies in the satellite configurations. The satellite with range-rate results in a) remains barely above the horizon when crossing the equator, 97° away from the high satellite, and the line of sight pierces the ionosphere at a slanted angle. The satellite with results in b), however, is closer to the high satellite separated by 81° at the equator. The 300 km satellite used in both these examples is below the height of maximum density which varies in b) between 350 and 456 km in the equatorial region, and the line of sight between the satellites pierces the ionosphere at extremely slanted angles, remaining in the vicinity of the maximum electron density over very long distances, hence the very large refraction effects. In addition, slightly steeper gradients exist in ionospheric height and density for b) than exist for a) which also contributes to the larger range-rate corrections in b). The maximum pierce point of f_oF2 in b) was 14.2 MHz, in a) 12.9 MHz.

In using the April 1968 data, the spacial gradient investigations were performed for average solar maximum conditions; the smoothed sunspot number was 107. It should be recognized, however, that during a more severe solar cycle the range-rate corrections could be significantly larger than the 0.8 m/sec in Figure 9. During the maximum cycle recorded in 1958, the smoothed sunspot number went as high as 201 in March.

3.3 Temporal Gradients

The effects of short and long term ionospheric temporal gradients on satellite-to-satellite range-rate corrections was investigated by comparing the corrections along the orbits, which were obtained for ionospheric situations where all conditions, except the one tested parameter, were held constant.

3.3.1 Diurnal Effect

The diurnal effect on range-rate corrections was examined by computing corrections for satellites crossing the equator at 6 hours and at 14 hours universal time to provide information with high and low gradients, and the results show large differences in amplitude. In Figure 10a, the ionospheric pierce point occurs at longtitude 222° or 21 hours local time. At this time very rapid changes in electron density are encountered as the satellite connecting ray sweeps across the equatorial anomaly while following the low satellite orbit. The steep gradients are apparent along the pierce point curve in Figure 7, and the resulting range-rate corrections are large. In Figure 10b, the satellite crosses the equator at 14 hours UT. Here the ionospheric pierce point occurs at 5 hours local time, when the ionospheric gradients along the pierce point curve and hence, the corresponding range-rate corrections are about as small as they can get for such an orbit configuration.

3.3.2 Seasonal Effects

Range-rate corrections were compared for April 1968 and July 1968 to examine the effect of seasonal variations on range-rate corrections. The solar activity did not influence the result significantly, because the smoothed sunspot numbers were very similar, 107.2 in April and 105.2 in July. Polar orbits at 300 km

and 850 km altitude were examined, both having the equator crossing fixed at 6 hours UT. Range-rate corrections corresponding to the 300 km orbit are presented in Figure 11. In each case, maximum ionospheric effects occur in April and minimum effects in July. For other months the effects would be expected to be of intermediate amplitude. Significant changes in peak amplitudes are apparent, as well as time shifts of the peak correction values.

3.3.3 Solar Cycle Effects

The effect of the solar cycle on range-rate corrections was also considered. Three years were chosen to represent the extremes of solar activity, and in all cases the month of April was selected to eliminate seasonal effects.

Year	Smoothed Sunspot Number
1958	196.8
1968	107.2
1975	18.6

The 1958 solar cycle was the all-time maximum recorded. During 1968 and 1975, the maximum and minimum activity occurred for the last solar cycle. Figure 12 shows the results for a 300 km orbit. The 1958 corrections are in all cases significantly larger than the 1968 results by factors of 1.5 to 2.5. The 1968 results in turn exceed the 1975 results by similar amounts. Shifts in the time of the peak range-rate correction occur for several peaks but without a simple pattern.

3.3.4 Temporal Gradient Tests with Apollo-Soyuz Orbits

The effect of day-to-day variations in the ionospheric density and height on the range-rate corrections along the satellite link were investigated using an orbit of the Apollo-Soyuz data. Revolution 8 on 16 July 1975, with the tracking frequency of 2.16 GHz was used, and the ionospheric conditions of interest were simulated.

To examine the influence of the deviations in f_oF2 from the monthly mean due to daily variations of solar flux, the month of February 1968 was chosen for the simulations; 1968 was the year of average maximum solar activity. The monthly mean of the solar flux was 173, and corrections were computed for February 1st when solar flux was at a monthly maximum 262, and for February 18th when the flux was at the minimum of 138. As shown in Figure 13, the increased solar flux causes a sharp increase in peak ionospheric range-rate corrections by a factor of 1.1 to 1.8, while the same pattern is maintained for the variations along the arc. This points to the necessity to adjust the monthly mean ionospheric correction model for daily variations as is done in the Bent model.

The height of maximum electron density was computed using the ionospheric model, and then it was raised and lowered by 50 km during the simulations. Such variations represent the possible day-to-day changes in the ionospheric height, and result in changes in the amplitude of the range-rate corrections as well as in a time shift of the peaks, see Figure 14. Lowering the ionosphere by 50 km causes an increase in the amplitude by a factor of 1.4 and a shift of the peak in increasing time along the arc. Raising the ionosphere by 50 km causes a decrease in amplitude and a 40 second shift of the peak in decreasing time along the arc.

Acknowledgements

References

1. Bent, R. B., Llewellyn, S. K., Lipofsky, J. R., 1976, " Apollo-Soyuz/ATS-6 Ionospheric Refraction Corrections", unpublished, NASA contract NAS5-20744, Mod 4.

2. Llewellyn, S. K., Bent, R. B., 1973, "Documentation and Description of the Bent Ionospheric Model" prepared for Space and Missile Systems Organization, Department of the Air Force.

3. Vonbun, F. O., Kahn, W. D., Bryan, J. W., Schmid, P. E., Wells, W. T., Conrad, T. D., 1975, "Gravity Anomaly Detection-Apollo-Soyuz", NASA/GSFC document X-920-75-308.
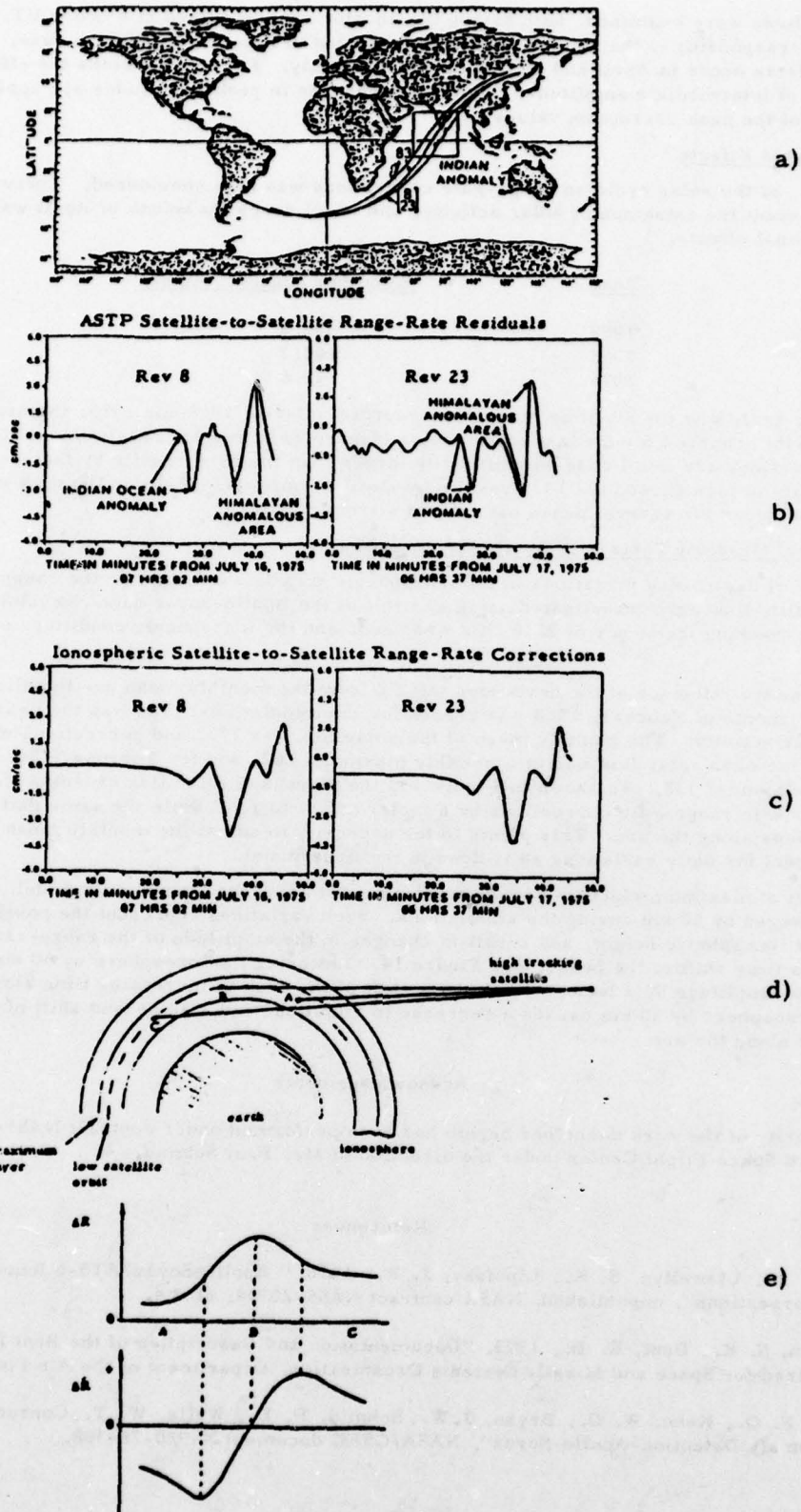
Fig. 1 Comparison of gravitational effects and ionospheric
effects on Apollo-Soyuz orbits
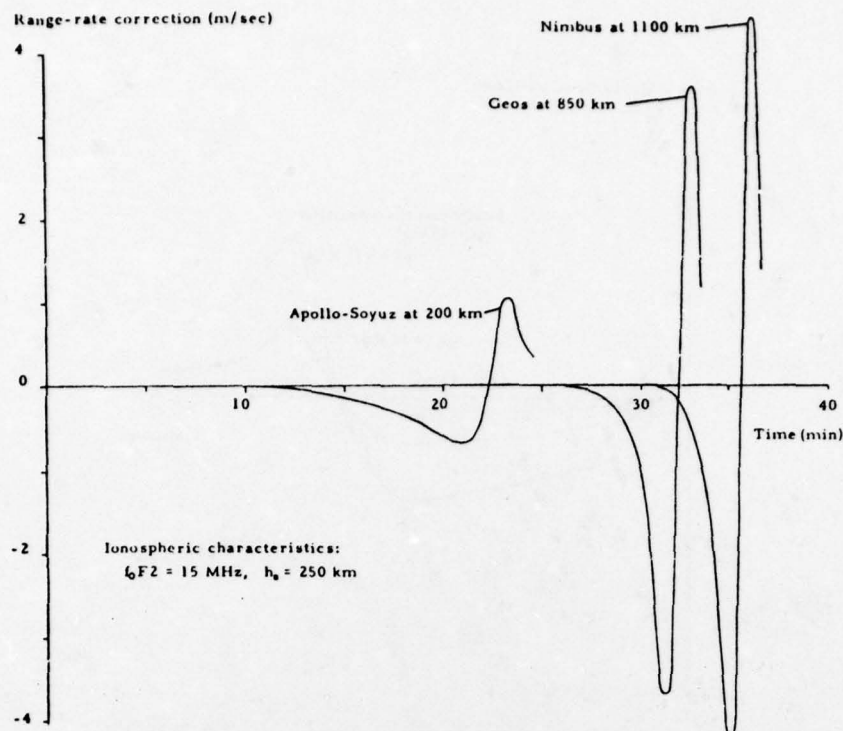
Fig.2   Ionospheric range-rate corrections for three different satellite arcs
from orbit points underneath the high satellite to the points of
disappearance computed at one minute intervals
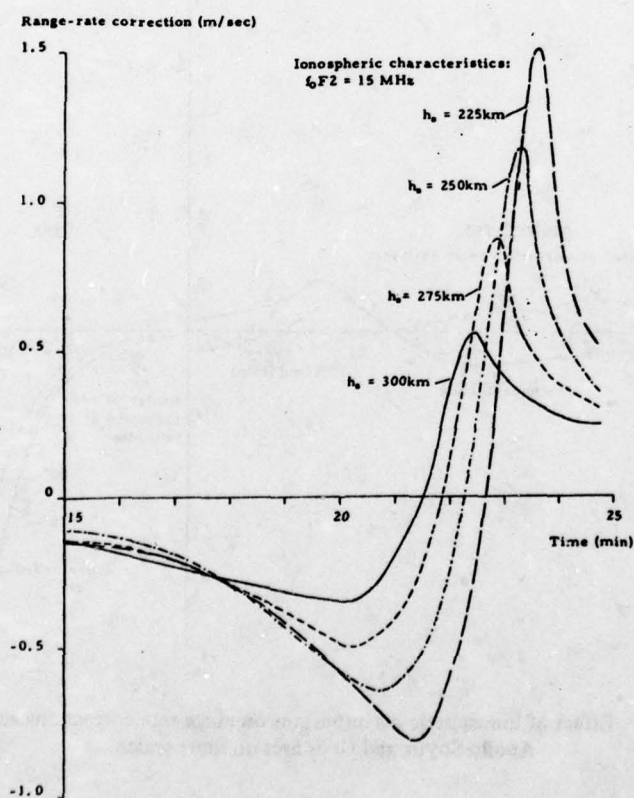
Fig.3   Range-rate corrections during last ten minutes of Apollo-Soyuz arc
using uniform ionosphere at several different heights
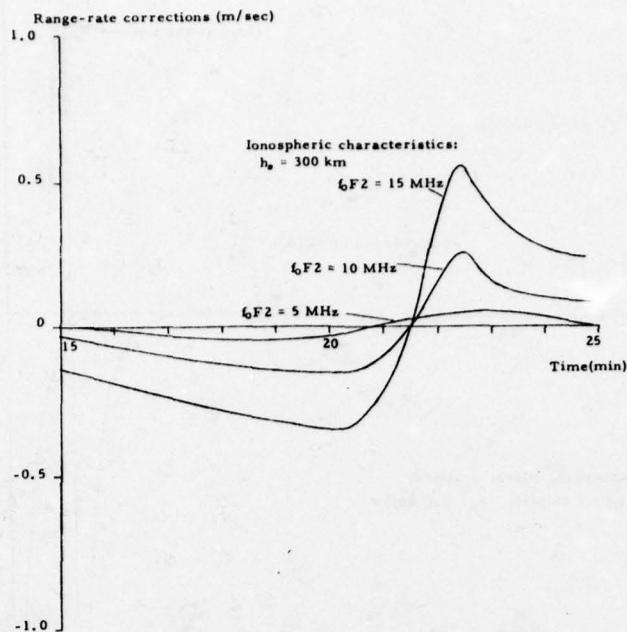
Fig.4   Effect of different ionospheric densities on range-rate corrections
during last ten minutes of Apollo-Soyuz arc
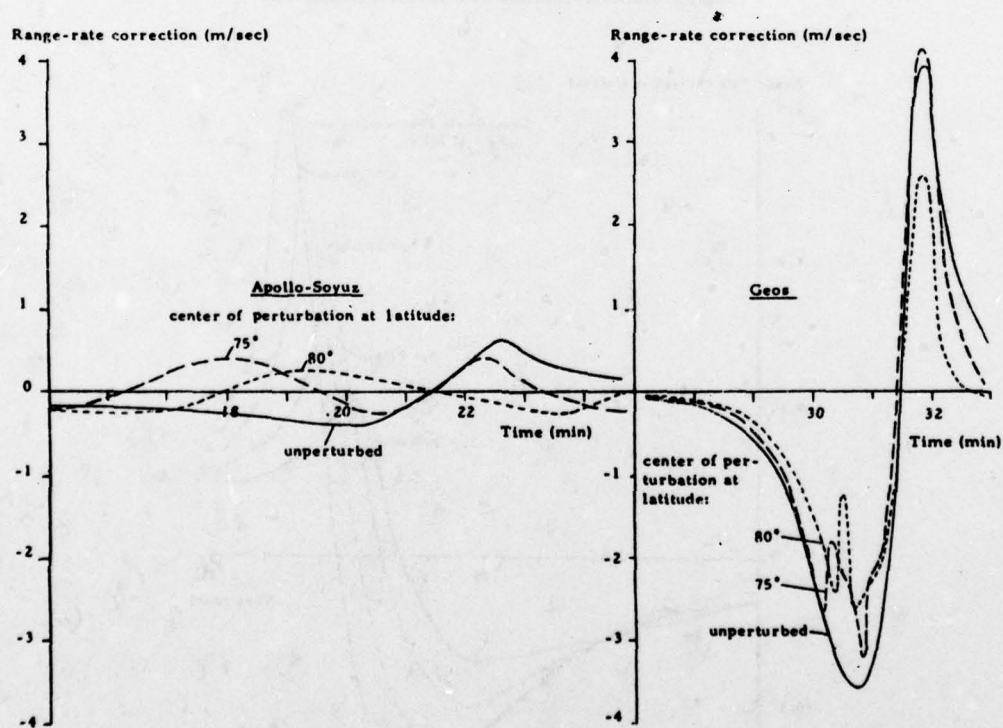
Fig.5   Effect of ionospheric perturbations on range-rate corrections along
Apollo-Soyuz and Geos arcs on same scales
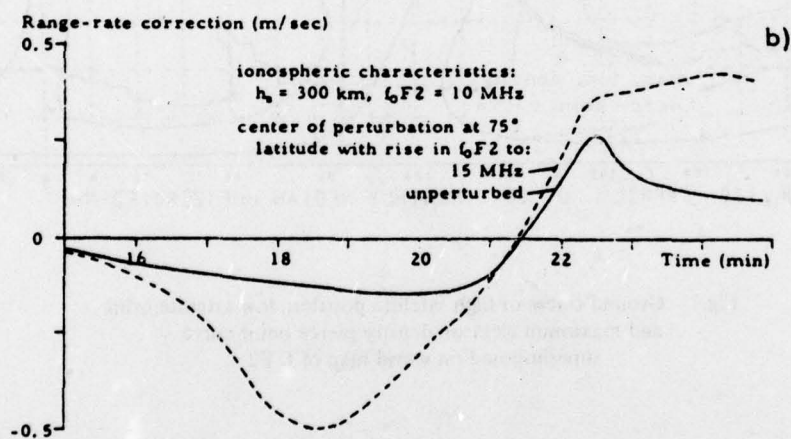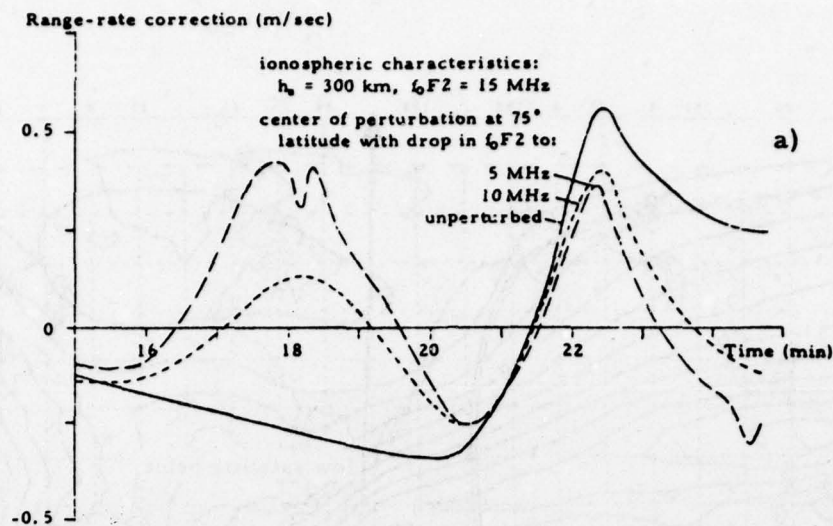
Fig.6 Effect of ionospheric perturbations of different magnitude on range-rate corrections along the Apollo-Soyuz arc
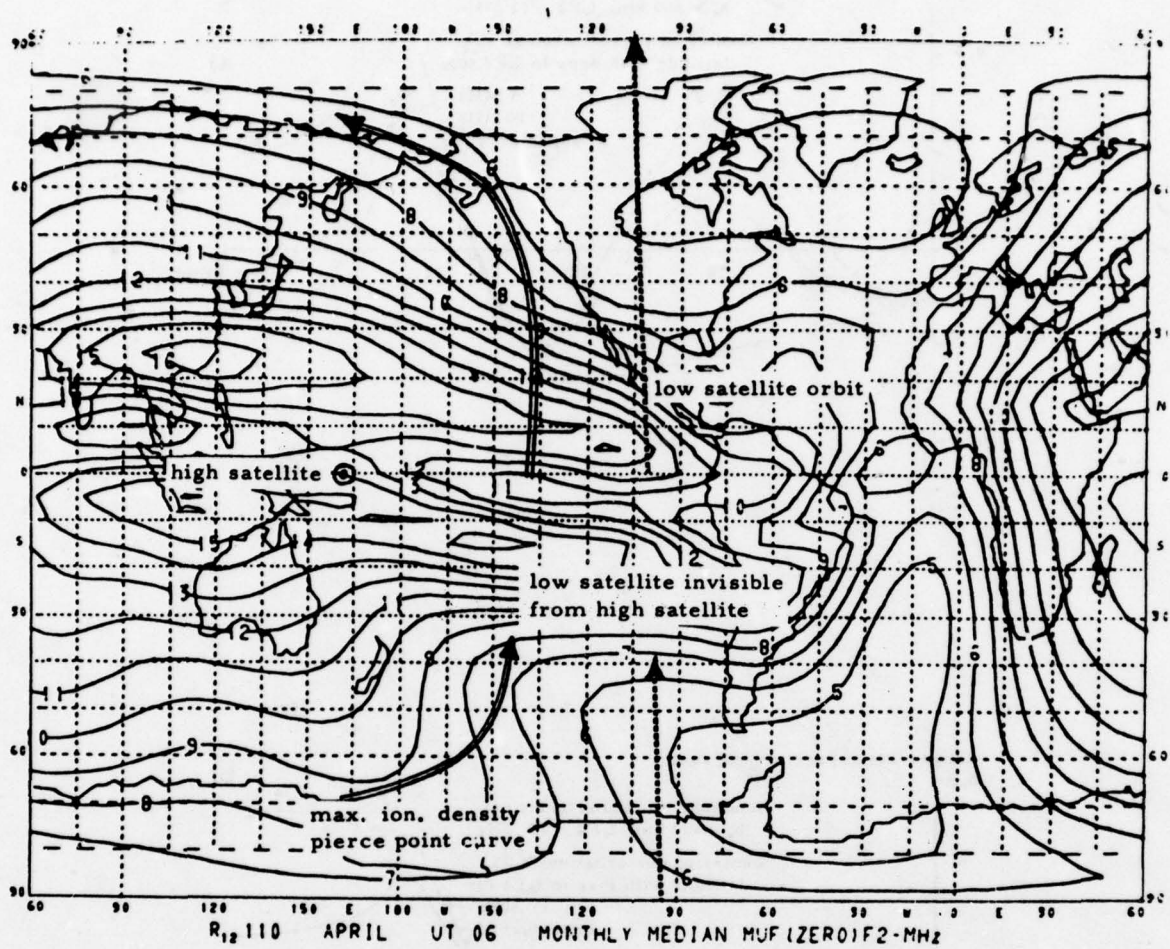
Fig.7 Ground traces of high satellite position, low satellite orbit
and maximum electron density pierce point curve
superimposed on world map of $f_x F2$
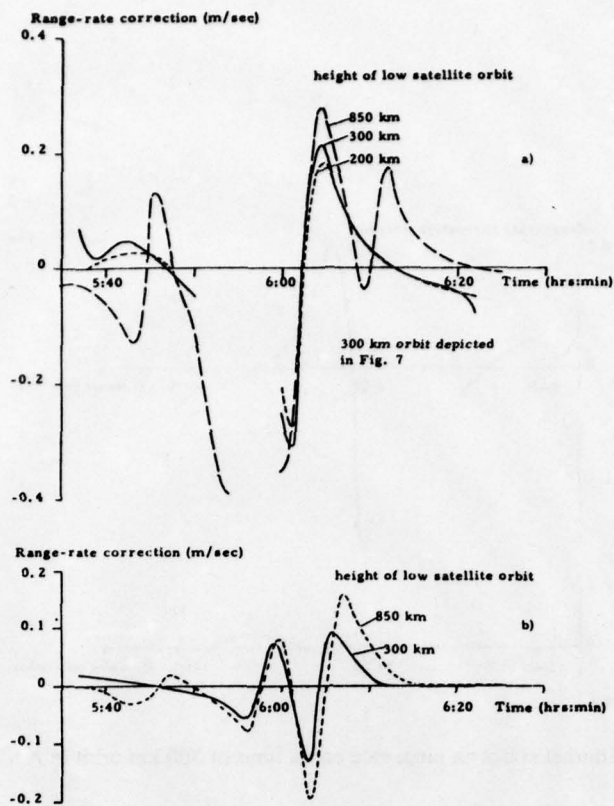
Fig.8   Effect of satellite height on range-rate corrections in April 1968.
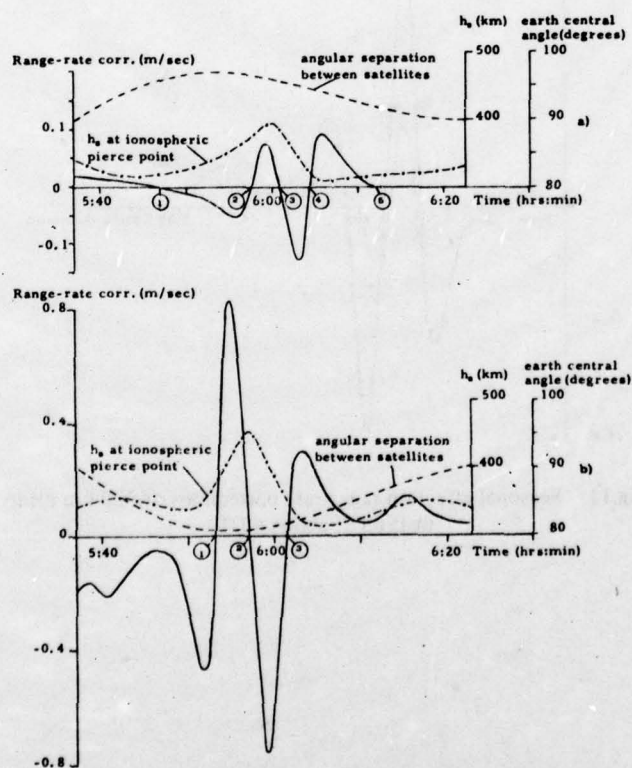
Fig.9   Variations in ionospheric range-rate corrections along 300 km
low satellite arcs in April 1968 around 6 UT
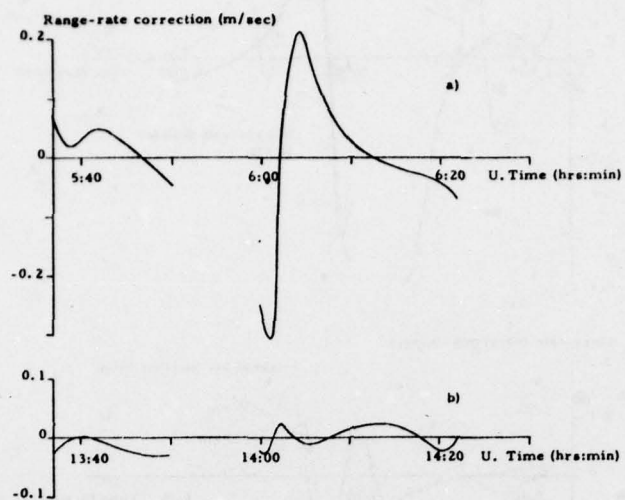
Fig.10   Diurnal effect on range-rate corrections of 300 km orbit in April 1968
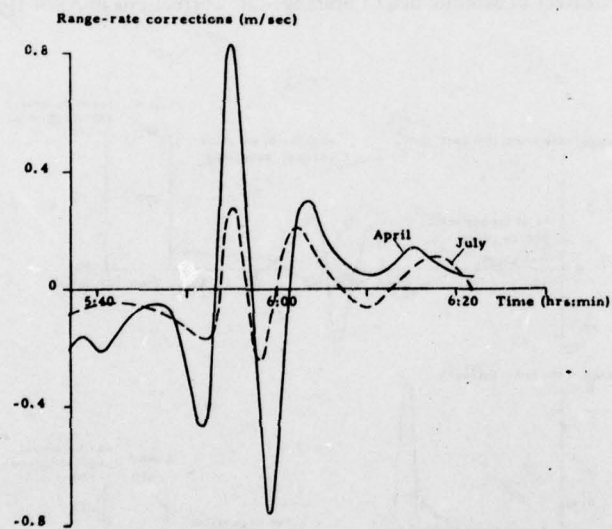
Fig.11   Seasonal effect on range-rate corrections of 300 km orbits
in 1968 at about 6 UT

Range-rate correction (m/sec)
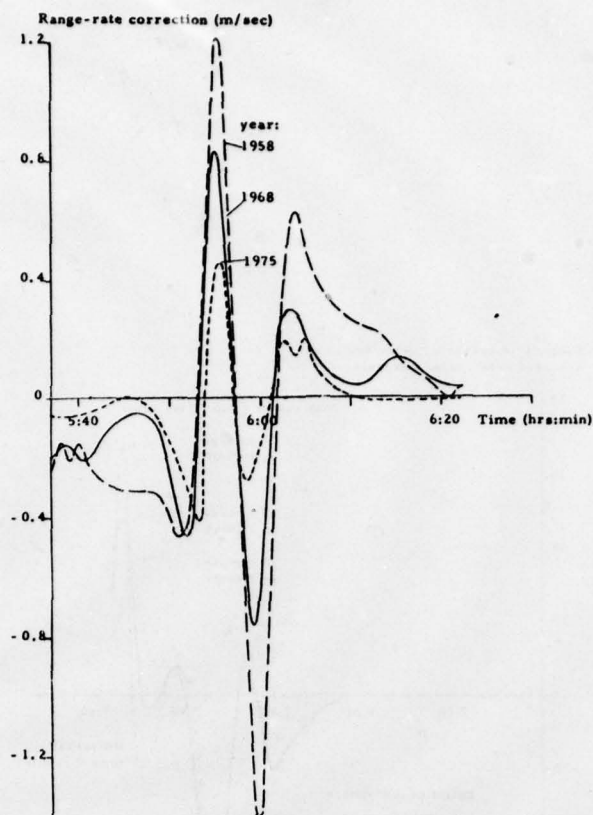
Fig.12   Solar cycle effect on range-rate corrections of 300 km orbits
during April at about 6 UT

Range-rate correction (mm/sec)
averaged over 1 min. intervals

62, 57

1 Feb 68, Flux = 262
18 Feb 68, Flux = 138

Universal time
(hrs:min)

-96, -67
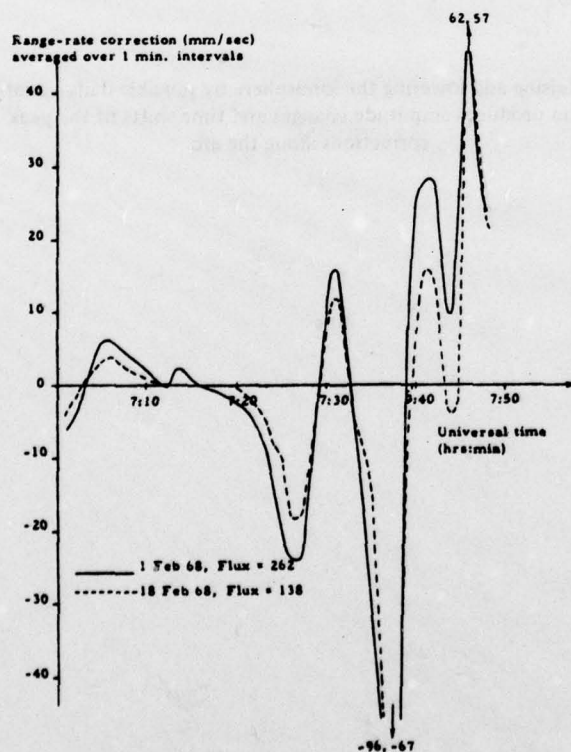
Fig.13   Deviations from monthly mean due to daily variations of solar flux
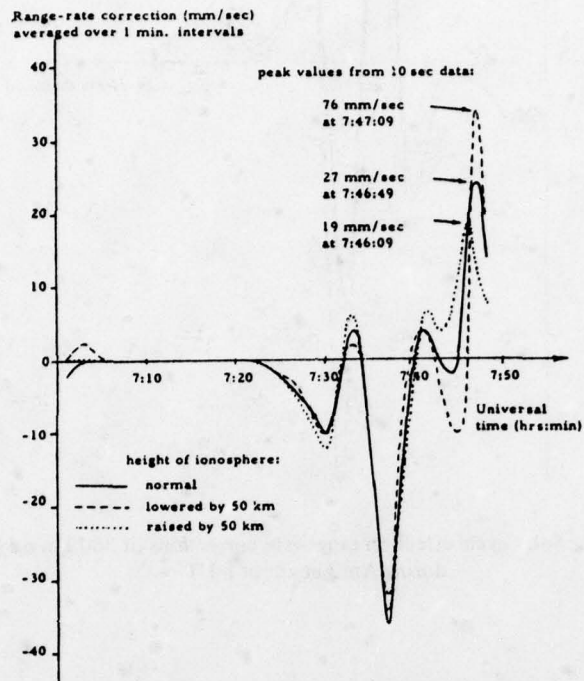
Fig.14   Raising and lowering the ionosphere by possible daily variations of
50 km produces amplitude changes and time shifts of the peak
corrections along the arc

DISCUSSION

J.S.Nisbet, US

Can you use a two-frequency responder for these corrections?

Author's Reply

There are plans to use GPS Satellite with a low-orbit satellite. However, this requires another frequency on the satellite which is quite costly. Another possibility is to try to get the gravitation anomaly when the elevation between the two satellites is very high, thus effectuating a very simple experiment which reduces the error enormously.

SUMMARY OF SESSION III

HF (LONG TERM EMPHASIS)

by

Dr T.B.Jones
Session Chairman

It is important in the planning and operation of H.F. radio systems that the working frequency is selected so as to optimise system performance. This session was concerned with techniques for predicting the characteristics of the ionosphere on a long term basis in order to achieve this objective.

The ionosphere imposes both an upper limit (MUF) and a lower limit (LUF) on the usable frequency band for a given propagation path. The session commenced with a review (**Bradley**) of techniques for predicting these frequency limits. This review also included a detailed discussion of the new C.C.I.R. prediction method. Even when accurate predictions are available, the problem of their statistical significance must be examined because of the day to day variability of the ionosphere. The problem of statistically modelling an H.F. link was considered (**Barclay**) and methods of assessing system performance were outlined.

Since the ionosphere is a time dependent medium, any direct sensing of its parameters is of value in predicting propagation conditions. The use of H.F. backscatter radar for this purpose was described (**Goutelard** and **Caratori**). A range of model ionospheres derived from this technique were presented.

Further consideration of direct sensing was presented by (**Lauche**) who described the use of the oxygen green line emission for detecting the onset of days of high absorption in winter, known as the "winter anomaly". Changes in absorption can also be produced by artificially modifying the lower ionosphere. This in turn, affects the lowest usable frequency (LUF). The use of non-contaminant in situ, experiments for D-region modification were described by **Widdel**.

The final contribution by **Gourvez** and **Hanbaba** considered the influence of steep gradients in the electron density distribution on the propagation of H.F. waves. A three dimensional ray tracing analysis was used for the investigation which demonstrated that marked propagation anomalies can occur in the presence of these steep gradients.

The session proved to be extremely valuable both to the ionospheric scientists and the communications engineers present. This interest was demonstrated by the many questions and lively discussion which followed the presentation of the formal papers.

Main points concerning the discussion period following Session III (Long Term Predictions)

The session provoked many questions during the discussion period. Both the radio scientists and the communication engineers present expressed strong views on the needs and merits of long term predictions. Some of the major topics covered in the discussion were:

(1) The importance of statistics in assessing system performance. How do we interpret them and how are they related to predictions?

(2) Strong views were expressed by the Users (Netherlands military and others) that we should do more to present scientific results in a more usable form. A user orientated prediction programme might be considered.

(3) There was much discussion of Bradley's new model and of the new C.C.I.R. prediction method.

(4) The effect of tilts, although well known, are often neglected. How can they be included in assessing system performance?

(5) What are the usefulness of certain precursors e.g. the green line emission of O_2 observed before the onset of the Winter Anomaly? Do we understand the physical mechanisms involved.

(6) How do you assess and quantify the performance of data transmission systems?

DEVELOPMENTS IN TECHNIQUES FOR PREDICTING HF SKY-WAVE FIELD STRENGTHS

P. A. Bradley

S.R.C., APPLETON LABORATORY

Ditton Park, Slough SL3 9JX

United Kingdom

SUMMARY

The roles of predictions in system planning, frequency management and frequency assignment are discussed. The need for a compromise between prediction complexity and accuracy is stressed, with regard to available resources and uncertainties in current knowledge of the behaviour of the ionosphere. It is concluded that no single prediction procedure can be optimum for all purposes. The philosophy is considered of alternative means of approach based on either an empirical fit to past measured field-strength data or to allowances which take account of the separate physical factors known to be of importance. Difficulties of estimating the accuracy of prediction methods are examined.

Some features of the latest prediction method adopted at the Interim Meeting of Study Group 6 of the CCIR are discussed and those areas where further studies are needed or improvements seem possible in the foreseeable future are examined. In particular, consideration is given to models of the height distributions of electron concentration and methods of determining raypaths - the importance of iono-spheric tilts and off-great-circle propagation. Developments in the prediction of auroral absorption and of sporadic-E obscuration and reflection losses are described. The difficulties which are encountered for predictions at frequencies close to the maximum usable frequency are highlighted and the need for an 'above the MUF' loss allowance is reviewed. Means of extending predictions to combine data for different propagation modes and to give assessments of the likelihood of multipath are also considered.

1. INTRODUCTION: THE NEED FOR PREDICTIONS

Since the earliest days of radio transmissions, the requirements for propagation and system-performance predictions have been recognised. Many groups in different countries have, over the years, been pursuing the perfection of prediction techniques. Their efforts stand as testimony to the diffi-culties of the tasks and the disparity of views as to how these should be accomplished.

Predictions are needed for system planning. They can yield estimates of the frequency coverage required and of the transmitter power needed to provide a specified grade of service; also they indicate the types and size of the most suitable antennas. Undoubtedly at the present time there is an upsurge in the use of the HF part of the radio-frequency spectrum both for civilian and military applications, particularly in the newly-developing countries. Much of this activity relates to transmissions involving sky waves. Many systems are being installed in new operational theatres where there is no background of past practical performance experience on which to draw. Systems are tending to be more complex and the user is becoming critical in expecting high quality. Ideally it is often required to make these a part of, or to integrate them with, other systems, without any marked degradation in standard of performance. The vagaries of the ionosphere make this usually a forlorn hope, but the demand for optimisation is considerable. It is nowadays a common requirement for commercial organisations who tender for the supply of radio systems to have to demonstrate to their prospective customers on the basis of the best available predictions that the proposed equipment is the minimum necessary to fulfil the intended function.

There is no doubt that predictions are also of value for frequency management: to determine firstly what frequency assignment complement is needed and secondly what frequency from this complement is likely to be most suitable on a given occasion. Unfortunately, however, in this second role existing predictions are of only limited use because the requirement is for a so-called short-term prediction based on the state of the ionosphere for the particular day. Undoubtedly because of this, much effort has been devoted to trials with sounder systems and to studies of channel-evaluation techniques in order to derive viable alternative procedures. These must add to system complexity and the extent to which they can be justified depends on the importance of the system to the user. It is a personal belief of the author that ultimately channel-evaluation techniques involving the sequential sampling of all available assigned frequencies to determine the best to use will form the accepted basis of optimum frequency determination procedures, but that for the present the pursuit of possible short-term prediction methods is still appropriate. However, this paper is not concerned with these.

A further requirement for predictions is associated with transmitter licensing and is concerned with the assessment of the possible interference caused by any new system. The International Frequency Registration Board (IFRB) of the International Telecommunication Union (ITU) is charged with this task. Use is made of Technical Standards to give estimates of the intensities of proposed new transmissions at the receiving sites of all existing co-channel systems which may possibly be affected.

Both for the IFRB studies and also when submitting tender documentation in support of international contracts the requirements are for internationally accepted prediction methods. Hence, the International Radio Consultative Committee (CCIR) - the technical radio advisory body of the ITU - has a Study Programme in being to develop such agreed procedures. This specific task was assigned to Interim Working Party 6/1 (IWP 6/1) in 1956 and deliberations have been proceeding since then. An interim prediction method was

developed in 1970 (CCIR, 1970) and a second method was produced in 1976 (CCIR, 1976a). The computer program for this second method is still in course of preparation. At the same time various participating organisations are attempting to formulate further improvements in prediction techniques.

This paper reviews the current position. Section 2 examines the requirements to be fulfilled by prediction methods and the criteria that must be taken into account when developing and assessing them. Section 3 looks at the determination of prediction accuracy. Section 4 considers the philosophy of approach and notes the factors to be included in a prediction procedure. Selected features of the latest CCIR method and aspects needing further development are discussed briefly in Section 5.

2. PREDICTION METHOD REQUIREMENTS

It is evident that the requirements are for the simplest prediction method giving the desired accuracy, but not so obvious what this accuracy should be. Clearly this is the first point to establish, since some trade-off between complexity and accuracy is to be expected. A review of the applications for predictions reveals that a case can be made for a family of different prediction methods ranging from the most sophisticated needing the use of high-speed computers with considerable storage to simple manual methods requiring only modest aids.

Greatest accuracy is probably needed for purposes of system design. Some engineers would argue that an accuracy of $\pm$ 1 dB in received signal intensity is then wanted - after all, 3 dB corresponds to doubling the transmitter power, with system costs increased appreciably more. Others would say that since the decile range of day-to-day variations in signal intensity is typically 20 dB, corresponding to a standard deviation of about 8 dB, this is the order of accuracy to seek to achieve in predicting median values. An alternative approach is to assume that the required accuracy should be comparable to that with which measurements can be made. According to the CCIR, field strengths at HF can be measured to an accuracy of $\pm$ 2 dB; it is probably reasonable to suppose that transmitter powers can be given with this same precision, leading to a requirement for a prediction accuracy of 4 dB. Now in practice, the choice of transmitter power of any proposed system must be based on a statistical analysis involving subjective estimates of the required grade of service: the signal/noise ratio to be equalled or exceeded for a specified fraction of the time. Uncertainties exist in both the required signal/noise ratios and in the values of noise intensity likely to be encountered; also estimates must involve assumptions concerning the dominant type of noise. The more important the system to the user, the greater is the required fraction of time with adequate signal/ noise ratio. This means that calculations tend to involve the 'tails' of the day-to-day amplitude distributions so that errors are large and greater tolerances in median estimates become acceptable. From all standpoints a prediction accuracy of 6 dB appears a reasonable objective to seek to attain. Any method giving this accuracy for 90% of occasions would almost certainly represent a significant improvement over existing methods.

Whilst undoubtedly it would be desirable for the prediction method to be adopted for use by the IFRB to have this same accuracy, the need to make several thousand sets of calculations each week means that some loss in accuracy may have to be tolerated in order to bring the amount of calculation, even using modern computing aids, to manageable proportions. Certainly the IFRB could not hope to employ a manual prediction method for all routine calculations; also it is most unlikely that any quick manual method could be devised having the accuracy needed for system-planning purposes as noted above. Yet, whereas computing time and costs are not likely to be of prime importance in system planning by comparison with overall costs, acceptable resources to the IFRB preclude lengthy amounts of computation. Hence, within the constraints of available computers, the IFRB needs a method relying more on data storage and less on calculation. The system planner is not restricted in this way. For 'once off' tasks, he can arrange for computations to be made at a centre possessing appropriate computing facilities.

In addition to the above needs, IWP 6/1 recently identified three other separate requirements for so-called 'manual' predictions where more limited aids than a large computer are available and where reduced accuracy is acceptable -

(i) When rapid results are needed by trained engineers within minutes, perhaps in support of technical discussions. Resources may well be restricted to a pocket calculator, or a set of charts and nomograms.

(ii) As an adjunct to mobile radio-system operation by non-specialised personnel. Look-up books of tables are most appropriate.

(iii) When a main computer is temporarily unavailable, results are required urgently, and a desk-top minicomputer is at hand.

The policy which is being followed by the CCIR, with the object of producing ultimately a hierarchy of prediction methods meeting the above needs, is to concentrate at present on the development of the most accurate method possible, without overdue regard for its complexity. It is argued that controlled simplifications can then be introduced when their likely effects have been examined and quantified. That is not to say the task of agreeing internationally what simplifications are acceptable will be easy, but rather that this exercise must be accomplished later. It is recognised that where one worker fits a linear regression line through a scattered data set and quotes gradient and intercept to three significant figures, there are others who represent the same results by a cubic with five significant figures. In principle it should be possible to check the differences that arise from such separate representations, but comparisons are complicated by step effects. Whereas one representation gives a particular propagation mode as present another does not, so that in extreme circumstances signal-strength differences of say 20 dB could arise in the two cases. This could happen under some conditions however close the representations. Also, errors in factors in the prediction process are cumulative, and it is not easy to assess their combined magnitudes.

3.   DETERMINATION OF PREDICTION ACCURACY

A major difficulty to assessing prediction accuracy is that despite the widespread use of HF sky-waves there are very few reliable measured signal-intensity data from calibrated transmitters with which predictions can be compared. The CCIR has maintained a Data Bank of measurements since 1962 and in the last two years this has been critically reviewed, revised and extended. Nevertheless, useful though they are, present data cover only a restricted range of conditions which are not truly representative, and have other limitations. Many relate to long paths whereas the typical sky-wave path length is only about 1500 km. Many measurements are made for commercial circuits involving the use of high-gain transmitting and receiving antennas with a performance which cannot be reliably assessed. Special links employing simple low-gain antennas such as dipoles, short vertical monopoles or loops are preferable because the practical performance of these more closely matches theory, even though signals may then be too weak to measure some of the time.

Measurements relate to receiver voltages and involve calibration factors based on receiving-system losses in order to give available receiver powers. The conversion to corresponding sky-wave field strengths requires not only a knowledge of receiving-antenna gain but also of signal-arrival directions. These latter are rarely measured and must usually be inferred. It is common to quote field strengths on the basis of typical arrival directions but in general these will differ from figures given by and used in the predictions. This means that an inconsistency exists when comparing predicted and so-called measured field strengths; comparisons are best made on the basis of available receiver powers.

Results of studies carried out in three countries between a sample of measured field-strength data from the Data Bank and values given by the first CCIR prediction method (CCIR, 1970) were presented to the 1978 Final Meeting of Study Group 6 (CCIR, 1978a). Monthly median figures from the measurements were compared with the corresponding monthly median predicted field strengths of the strongest mode, restricting attention to those occasions for which this mode was predicted as present for at least half the days. Combining such results for the different hours, months and circuits gave a median discrepancy corresponding to a predicted field strength 3 dB greater than measured. 90% of the discrepancies were less than 20 dB. Further comparisons are planned in terms of available receiver powers.

Procedures for standardising the collection, tabulation and analysis of future measured data have been agreed (CCIR, 1978b). Groups are encouraged to make further measurements in the manner indicated and to submit their results for inclusion in the Data Bank. More studies are required of additional ways of comparing the measurements and predictions, particularly to assess the predicted day-to-day scatter in signal intensity and the predicted mode availabilities - the probabilities of there being a sky-wave path to support mode occurrence. Problems occur when measured data do not exist for all days of the month and it is important to know whether absent values arise from there being no attempt at measurement, raypath failure, or large transmission loss. New scaling procedures have been defined to assist in this respect but there remain a number of difficulties to resolve such as when the threshold of signal detection is a variable from day to day because of interference and when different modes are strongest on the separate days.

4.   PREDICTION PROCEDURES

Two different approaches to sky-wave signal-intensity prediction are possible. One is to fit empirical equations to measured data for different paths, times and frequencies. The other is to estimate intensity in terms of a number of separate factors known to influence the signals. These factors may be given by expressions which have been deduced either from theory or measurement. Unfortunately both approaches have limitations. The former is likely to be simpler but unless a large data base exists, trends must be inferred and are liable to error. The latter approach is conceptually more elegant and enables variations to be specified in a physically meaningful manner. However, there remains the possibility of error due to failure to allow for a significant term or to an inexact allowance. There is also a likelihood of devising a method which is over-complex and for which the accuracy achieved does not merit some of the complications that have been introduced.

The CCIR has recommended for provisional use a prediction method at LF/MF (150-1600 kHz) involving empirical equations fitted to past signal-intensity data (CCIR, 1974). This policy is considered justified when it is appreciated that these frequencies are allocated to the sound-broadcasting service and many years of reliable synoptic measured data, collected under standardised conditions, have been used in developing the method. Also, since at MF signal strengths are markedly influenced by ionospheric absorption for which adequate ways of deriving estimates have yet to be developed, any alternative method based on the separate-factor approach is liable to be less accurate. By contrast, at HF and particularly for the lower frequencies, there are still problems in determining ionospheric absorption but these are less serious. In view of the shortage of measured signal data discussed in Section 3 above, it is generally agreed that prediction methods should rely on allowances for the separate factors. Existing methods differ in regard to what factors to include and what allowances to use for these.

Prediction methods for the applications discussed above usually yield monthly medians of hourly smoothed field strengths and their statistical day-to-day variations about these values. The separate-factor approach involves specifying models of the height distributions of electron concentration in terms of global representations of the standard vertical-incidence ionospheric characteristics (Piggott and Rawer, 1972) given from the world network of ionosondes. The raypaths of all propagation modes that can exist between the transmitter and receiver are determined using some form of ray tracing. The probabilities of mode occurrence (availabilities) are evaluated from estimates of the mode MUF's and their day-to-day variability. Signal strengths are given by computing the separate terms contributing to the transmission loss of each mode, with due allowance for the raypath angles involved. The terms included vary for the different methods, but all methods allow for the most important factors which are generally agreed as transmitter power, transmitting and receiving antenna gains, spatial attenuation and ionospheric absorption. Data based on relative signal-intensity measurements (Barghausen et al., 1969), for which there are many more available than absolute measurements, give the likely day-to-day scatter in signal intensity about the predicted monthly-median values.

5.   SOME FEATURES OF THE LATEST CCIR METHOD

It is not the purpose of this paper to describe fully the second CCIR prediction method, but rather to highlight and expand a selection of topics requiring further development, as mentioned in a proposed new CCIR Report (CCIR, 1978c).

5.1   Global Representations of Ionospheric Characteristics

Use is made of representations of foF2 and M(3000)F2 by Jones et al. (1969), of h'F,F2 (Leftin et al., 1967) and foEs (Leftin et al., 1968), all based on spherical harmonic fits to past data. These representations are the results of major mapping exercises and are unrivalled in their usefulness and accuracy. Nonetheless, it is accepted that they merit revision by incorporation of more recent observational ionosonde data now available; also they need supplementation with other types of data to provide improved interpolated values in regions not served by ionosondes, particularly over the oceans. In some cases results for 1958 have been mapped as representative of high solar-activity conditions, yet it is known that year was abnormal with occurrence of saturation effects.

Satellite topside-sounder and probe data offer possibilities for inclusion in any new representations, but although these give good spatial coverage there are problems due to day-to-day ionospheric variations in relation to the typical satellite orbits. Some recent studies with thermospheric wind theory appear promising. One proposal is to derive scaling factors to match calculated height distributions of electron concentration of the F-region to measured ionosonde data and then to use these factors with other calculations to give values of the ionospheric characteristics at intermediate locations. It follows that secular changes in the Earth's magnetic field, particularly in the mid-Atlantic region close to the magnetic equator, in the auroral regions and at certain temperate latitude locations where there are large variations in declination, will lead to changes in ionisation over a much larger time scale than a solar cycle. These need to be taken into account. There are two separate stages to improvements in mapping: firstly it is necessary to demonstrate the feasibility of making the improvements, and then to find the necessary effort or cost justification to carry them through. It is to be hoped that some increased activity along the directions indicated will soon be possible.

An empirical representation of foE developed by Muggleton (1975) is used. This has recently been revised (CCIR, 1978d) to improve its accuracy at twilight and at high latitudes in the winter when the sun never rises. It is clear that the method still gives large errors in the auroral regions since it does not allow for particle-induced ionisation. Work is in progress to try to include this. Both for E- and F-region ionospheric characteristics, the possibility of taking account of the varying position and size of the auroral oval for different levels of magnetic activity appears to merit consideration.

5.2   Model of the Vertical Height Distributions of Electron Concentration

The present model (Bradley and Dudeney, 1973) consists of E- and F2-layer segments in which the electron concentration varies parabolically with height, together with an intermediate region in which it has a linear variation. This is an idealisation with certain limitations. In particular, there is a gradient discontinuity at the height of intersection of the F2-parabolic and linear segments giving a spurious cusp on the resulting ionogram. On the other hand, this model was selected for its ease of generation and because the corresponding raypath equations are relatively simple to evaluate. Studies are needed to determine the heights requiring the most accurate representation. Since improved accuracy tends to be associated with greater model complexity, it is not obvious what is optimum. Figure 1 shows a sample true-height profile determined from a measured ionogram by the technique developed by Jackson (1971) and the corresponding model given by a new method of Dudeney (1978). This model consists of four segments represented by parabolic and trigonometric expressions and has no gradient discontinuities. It provides a better overall match than the model currently being used, but suffers from the limitation that expressions cannot be formulated in terms of readily available functions to give the corresponding vertical-incidence ionogram needed for oblique raypath determinations. Figure 2 shows the ground ranges attained at a number of frequencies as a function of launch elevation angle, deduced by ray tracing in the absence of the Earth's magnetic field. There is good agreement between results for the new model with those from the true-height profile, except in regions of defocusing close to the skip distance and for the high-angle rays. These are conditions which are not of great practical importance. Principal differences in raypaths from those for the present model occur for F1-modes; the low-angle E and F2 mode-results are very similar.

5.3   Semithickness of the F2-Layer

The height of maximum electron concentration of the F2-layer is given quite accurately from an empirical equation in terms of M(3000)F2 after Shimazaki (1955), but with inclusion of a correction for retardation due to underlying ionisation. The other important model height parameter for the F2-region is the semithickness. This is currently derived from equations based on the ionospheric characteristic h'F, F2. Whilst the procedure is fundamentally valid, errors arise because of limitations in the ionogram scaling and global numerical representation of this characteristic. It is desirable therefore to consider other possible approaches. With the height of maximum electron concentration assumed given, these include the use of empirical representations of the ratio of height of maximum electron concentration to semithickness presented by Lucas and Haydon (1966) - see Figure 3 - and expressions formulated by Rush and Elkins (1975) in terms of neutral-density scale heights. Limited comparisons with a selection of measured true-height data suggest that the procedure of Lucas and Haydon may be the most accurate for median prediction purposes, even though this does not include any longitude or seasonal dependence. Further comparison tests are required.

5.4   Propagation Modes and Raypaths

Rays are traced through successive ionospheric reflections taking some suitable launch direction and using model ionospheres generated for the reflection positions. Homing procedures are employed both to find these reflection positions and to determine the launch direction giving propagation to the desired receiving location. The technique requires advance selection of the possible propagation modes; if this

selection is too large, calculations become unnecessarily cumbersome and slow. More work is needed to establish the important modes under different propagation conditions.

There is particular lack of information on the extent to which it is necessary to take account of mixed modes involving reflection from different layers on different hops. Procedures have been developed to allow for longitudinal ionospheric tilts which give rise to different elevation angles at the transmitting and receiving terminals, and can also produce long hops without intermediate ground reflection. Not unexpectedly, these lead to the requirement for increased numbers of homing iterations. It is not clear, however, whether predicted tilts resulting from gradients in the numerical representations of ionospheric characteristics are meaningful. Their magnitudes are determined by the particular harmonic orders selected to match the measured ionospheric data and may correspond to smoothing over a different spatial scale from that appropriate to ray-reflection conditions. Raypaths are assumed to follow the great-circle path and for frequencies below the MUF this appears a reasonable assumption. The need for tilt allowances is linked to the question of how many positions along the great-circle path require generation of a different ionospheric model.

An alternative to the homing procedure is to use the rayset approach in which rays are traced for a series of all possible launch directions (say every 2° of elevation angle) and a table prepared of corresponding ground ranges. Interpolation within the table for the distance of interest gives all possible modes without these having to be specified in advance. However, different tables are needed for each ionospheric model, many of the entries are for inappropriate distances leading to unnecessary computations and there is a need to interpolate tabulated values, leading to some error. On the other hand, since modes are usually represented by triangular raypaths with apogees given as virtual heights for equivalent frequencies at vertical incidence, there is economy with rayset data when results for a series of oblique-wave frequencies are required. The approach deserves further study.

5.5 Maximum Usable Frequencies

MUF's need to be determined in order to estimate both mode availabilities and the extra losses that occur at higher frequencies (see Section 5.9 below). Although empirical equations exist giving MUF in terms of vertical-incidence critical frequency, M-factor and distance, values are not identical to those derived from ray tracing via model ionospheres. The use of a varying ionospheric model over the path tends to preclude any analytic solution. One possibility is to make raypath calculations at a series of closely spaced frequencies, but this is an inefficient procedure. It is probable that a raypath approach to MUF determination could be formulated, perhaps associated with the rayset technique mentioned in Section 5.4, with skip distance given as a function of wave frequency and interpolation to the distance of interest. At present, fractional day-to-day variations of MUF about the median value are taken as independent of distance, but this should be confirmed from measured data.

5.6 Antenna Gain

Existing equations for antenna radiation resistance (Barghausen et al., 1969) apply to antennas sited over perfect ground; extension is needed to the case of a ground of finite conductivity and finite dielectric constant. Most antennas are designed to radiate or receive horizontally or vertically polarised waves along the great-circle path between the transmitter and receiver, but in other general directions such as those involved in interference calculations the response is to waves of elliptical polarisation. In order to calculate polarisation-coupling loss the need is for antenna expressions which indicate this polarisation as well as the power gain.

5.7 Ionospheric Absorption

An allowance for auroral absorption is included in the current prediction method based on riometer measurements. These have been standardised in terms of absorption values derived from a limited amount of simultaneous rocket and incoherent-scatter measurements of electron concentration. A spatial and temporal representation of the absorption has been defined which is consistent with the model of Hartz and Brice (1967) for precipitating energetic electrons (Figure 4). The absorption is taken as the sum of two terms corresponding to the splash and drizzle precipitation, each showing a Gaussian variation with latitude and time. Longitude, season and solar-cycle changes are also represented. There is considerable scepticism in several quarters as to the validity of riometer measurements; unfortunately the few other data with which comparisons can be made have their own limitations. In view of the importance of auroral absorption to the operational theatres served by NATO forces, further efforts should be carried out to confirm the degree of validity of the formulation. Improvements should be introduced as necessary.

The prediction procedure needs extending to cover the frequency range 1.5 - 2 MHz. The modifications involved are concerned principally with the allowances for non-deviative absorption. Techniques based on the determination of mean effective collision frequencies for the D-region seem most appropriate and should be pursued.

5.8 Sporadic-E Reflection and Transmission Losses

Sporadic-E reflection losses are determined from the curves of Figure 5 produced by Interim Working Party 6/8 of the CCIR (CCIR, 1976b) and based mainly on measured VHF oblique-path signal data. These give reflection loss in terms of the ratio of wave frequency to foEs and involve the assumption of a statistical correlation between the exceeded percentile values of the day-to-day distributions of foEs and the corresponding percentile values of loss exceeded. Hence for a known distribution of foEs the amplitude distribution of Es-mode signals is given. At present, median amplitudes only are considered and Es-modes are taken into account only when modes involving reflection from regular layers have an availability of less than 50%. An alternative procedure would be to always allow for Es-modes and to compare their day-to-day amplitude variations with those of regular modes when assessing the probability of exceeding a desired signal/noise ratio. Further studies of the optimum approach are required.

Developments are proceeding in knowledge of the spatial structure and temporal occurrence of sporadic-E irregularities, leading to a better understanding of the mechanisms responsible for wave

reflection and scattering. Other equations for sporadic-E reflection losses derived from oblique-path HF signal measurements have been formulated by Sinno et al. (1976). These are given in terms of the ratio of wave frequency to foEs multiplied by the secant of the angle of incidence. Assuming that the power transmitted through an Es-layer is the difference between the incident and reflected power, transmission losses are consistent with the observed difference between foEs and fbEs (see Figure 6). For vertical-incidence propagation the empirical equations give 20 dB of reflection loss but very little transmission loss at foEs. On the other hand for fbEs = 0.55 foEs, a typical value, the reflection loss is small and there is 7 dB of transmission loss. There are some suggestions that losses may vary for the different classes of sporadic-E irregularity, and so be latitude dependent. The possibility of empirical equations based on the simultaneous use of the characteristics foEs and fbEs, which are available in mapped form, seems worth pursuing.

5.9 Propagation at Frequencies above the MUF

If signal-intensity measurements were made at a series of frequencies on all days, results similar to those shown in the idealised Figure 7 would be obtained. Median amplitudes would increase with frequency to some maximum value, as would also the sample count. The predicted MUF for reflection from regular ionospheric layers would be likely to differ from the frequency at which signals were received for half the days. Propagation above the MUF is possible via side-scatter from ground irregularities, as well as from sporadic-E modes. Such paths are often significantly longer than the great-circle path, and so have appreciably greater MUF. Even for reflection from the regular F-layer it has been suggested (Wheeler, 1966) that it is legitimate to regard this layer as composed of a number of separate patches of ionisation, each with its own MUF. Hence the number of patches supporting wave reflection falls with increase of frequency and there is no single frequency giving an abrupt signal cut-off.

The frequency with greatest median signal intensity is usually lower than the MUF, but this feature is not yet taken into account. At frequencies above the predicted MUF propagation modes are assumed to exist with an additional 'above-the-MUF' loss given by an empirical equation in terms of the ratio of wave frequency to predicted MUF. There is experimental evidence (Dieminger and Rose, 1961) that the rate of decrease of field strength above the MUF depends on path length and on whether the ionosphere is disturbed. More detailed investigations of the effect are in progress (Damboldt, 1976).

5.10 Long-Distance Paths

There is no doubt that errors in mode determination arising from uncertainties in the state of the ionosphere increase with mode order and path length. Also, for long paths with low elevation angles total ionospheric absorption tends to be independent of the number of hops. These features therefore suggest that propagation predictions can best be achieved for long paths by an approach which does not involve the identification of specific propagation modes as at present. One suggestion is to allow for transmitting and receiving antenna gains in the directions where the antenna gain minus the ionospheric absorption is a maximum and then to include a loss factor proportional to path length. The calculations need not necessarily be restricted to great-circle paths.

5.11 Multipath and Contributions from Different Modes

Multipath is judged to exist when two or more modes have a signal intensity differing by less than some predetermined amount and also a difference in propagation time greater than a specified figure. Hence the probability of multipath is concerned both with the simultaneous existence of different modes and with their relative variations in intensity. Existing predictions use representations of median ionospheric conditions to indicate the modes present and their median intensities. Tables give values of parameters of the expected day-to-day statistical distributions of MUF and signal strength for different paths and times. Appropriate theory needs to be developed for ways of combining signal contributions from different modes. For instance, if modes A and B have availabilities of 80% and 50% respectively, what is the probability of at least one mode? Does it exceed 80%? The answer must involve a study of the spatial correlation of day-to-day changes in E- and F-region ionisation, since it depends on how many of the days with B present are also days when A exists. Theory for uncorrelated modes is easy to formulate, but is probably inappropriate in many instances. Day-to-day amplitude variations for the different modes result mainly from changes in ionospheric absorption and so studies should also take account of spatial correlations in the D-region.

6. CONCLUSIONS

There is a need for a family of internationally agreed signal-strength prediction procedures, ranging from the most accurate and complex involving the use of large high-speed computers to simple manual methods relying only on desk or pocket aids. Objectives should be to develop a prediction method accurate to within 6 dB for a large proportion of occasions, approaching 90%. Other shorter methods with reduced accuracy may be derived from this by means of controlled simplifications.

The most important topics requiring further study in relation to existing methods are the global representations of ionospheric characteristics, procedures for determining active modes and MUF's, allowances for ionospheric absorption at frequencies below about 3 MHz, ways of comparing propagation via regular layer modes and sporadic-E signals at frequencies above the median MUF, and techniques for combining signal contributions from separate propagation modes having different probabilities of occurrence. Attention should also be paid to an appropriate procedure for long-distance paths for which conventional mode analyses tend to be inaccurate.

7. ACKNOWLEDGMENTS

8.   REFERENCES

BARGHAUSEN, A. F., FINNEY, J. W., PROCTOR, L. L. and SCHULTZ, L. D. 1969,
    'Predicting long-term operational parameters of high-frequency sky-wave telecommunication systems',
    ESSA Tech. Rept. ERL 110 - ITS 78, U.S. Government Printing Office, Washington.

BRADLEY, P. A. and DUDENEY, J. R., 1973, 'A simple model of the vertical distribution of electron concen-
    tration in the ionosphere', J. Atmosph. Terr. Phys., 35, 2131-2146.

CCIR, 1970, 'CCIR interim method for estimating sky-wave field strength and transmission loss at
    frequencies between the approximate limits of 2 and 30 MHz', Report 252-2, Documents of XIIth
    Plenary Assembly, International Telecommunication Union, Geneva.

CCIR, 1974, 'Prediction of sky-wave field strength between 150 and 1600 kHz', Recommendation 435-2,
    Documents of XIIIth Plenary Assembly, International Telecommunication Union, Geneva.

CCIR, 1976a, 'Second CCIR computer-based interim method for estimating sky-wave field strength and trans-
    mission loss at frequencies between 2 and 30 MHz', Report 252-2 (Rev. 76), Documents of Interim
    Meeting of Study Group 6, International Telecommunication Union, Geneva.

CCIR, 1976b, 'VHF propagation by regular layers, sporadic-E or other anomalous ionization', Report 259-3
    (Rev. 76), Documents of Interim Meeting of Study Group 6, International Telecommunication Union,
    Geneva.

CCIR, 1978a, 'Comparisons between observed and predicted sky-wave field strength and transmission loss at
    frequencies between 2 and 30 MHz', Report 571 (Rev. 78), Documents of Final Meeting of Study Group 6,
    International Telecommunication Union, Geneva.

CCIR, 1978b, 'Measurement of sky-wave signal intensities at frequencies above 1.6 MHz', Report 253-2 (Rev.
    78), Documents of Final Meeting of Study Group 6, International Telecommunication Union, Geneva.

CCIR, 1978c, 'Developments in the estimation of sky-wave field strength and transmission loss at frequen-
    cies above 1.6 MHz', Draft New Report, Documents of Final Meeting of Study Group 6, International
    Telecommunication Union, Geneva.

CCIR, 1978d, 'CCIR atlas of ionospheric characteristics', Report 340-2 (Rev. 78), Documents of Final
    Meeting of Study Group 6, International Telecommunication Union, Geneva.

DAMBOLDT, T., 1976, 'A comparison between the Deutsche Bundespost ionospheric HF radio propagation
    predictions and measured field strengths' in 'Radio systems and the ionosphere', edited by W. T.
    Blackband., AGARD Conf. Proc. 173, paper 12.

DIEMINGER, W. and ROSE, G., 1961, 'Zum Feldstärkenverlauf and Rande der toten Zone (On the variation of
    field strength near the border of the skip zone)', NTZ, 14, 492-495.

DUDENEY, J. R., 1978, 'An improved model of the variation of electron concentration with height in the
    ionosphere', J. Atmosph. Terr. Phys., 40, 195-203.

HARTZ, T. R. and BRICE, N. M., 1967, 'The general pattern of auroral particle precipitation', Planet.
    Space Sci., 15, 301-329.

JACKSON, J. E., 1971, 'The P'(f) to N(h) inversion problem in ionospheric soundings', Goddard Space Flight
    Center Rept. X-625-71-186, Greenbelt, Maryland.

JONES, W. B., GRAHAM, R. P. and LEFTIN, M., 1969, 'Advances in ionospheric mapping by numerical methods',
    ESSA Tech. Rept. ERL 107 - ITS 75, U.S. Government Printing Office, Washington.

LEFTIN, M., OSTROW, S. M. and PRESTON, C., 1967, 'Numerical maps of monthly median h'F,F2 for solar-cycle
    minimum and maximum', Institutes for Environmental Research Tech. Mem. 69, Boulder, Colorado.

LEFTIN M., OSTROW, S. M. and PRESTON, C., 1968, 'Numerical maps of foEs for solar cycle minimum and
    maximum', ESSA Tech. Rept. ERL 73 - ITS 63, U.S. Government Printing Office, Washington.

LUCAS, D. L. and HAYDON, G. W., 1966, 'Predicting statistical performance indexes for high frequency
    ionospheric telecommunications systems', ESSA Tech. Rept. IER 1 - ITSA 1, U.S. Government Printing
    Office, Washington.

MUGGLETON, L. M., 1975, 'A method of predicting foE at any time and place', Telecommunication Journal,
    42, 413-418.

PIGGOTT, W. R. and RAWER, K., 1972, 'URSI handbook of ionogram interpretation and reduction', Rept. UAG-23,
    World Data Center for solar-terrestrial physics, NOAA, Boulder, Colorado.

RUSH, C. M. and ELKINS, T. J., 1975, 'An assessment of the magnitude of the F-region absorption on HF
    radio waves using realistic electron density and collision frequency models', Telecommunication
    Journal, 42, 476-488.

SHIMAZAKI, T., 1955, 'World-wide daily variations in the height of the maximum electron density of the
    ionospheric F2 layer', J. Radio Res. Labs. Japan, 2, 85-97.

SINNO, K., KAN, M. and HIRUKAWA, Y., 1976, 'On the reflection and transmission losses for ionospheric radio wave propagation via sporadic E', J. Radio Res. Labs. Japan, 23, 65-84.

WHEELER, J. L., 1966, 'Transmission loss for ionospheric propagation above the standard MUF', Radio Science, 1, 1303-1308.
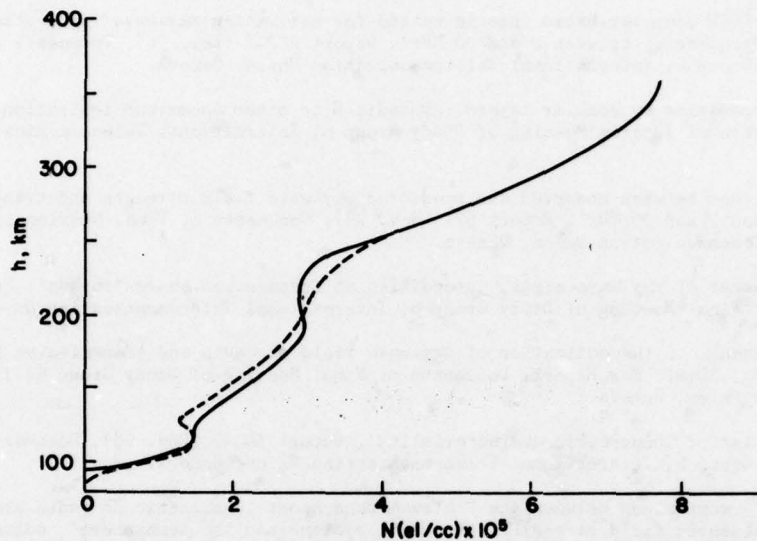
FIGURE 1: Sample comparison between electron concentrations given from true-height analysis and by the model of Dudeney (1978)

Data for Argentine Islands, 31 December 1967, 1330LT

- - - - true-height analysis
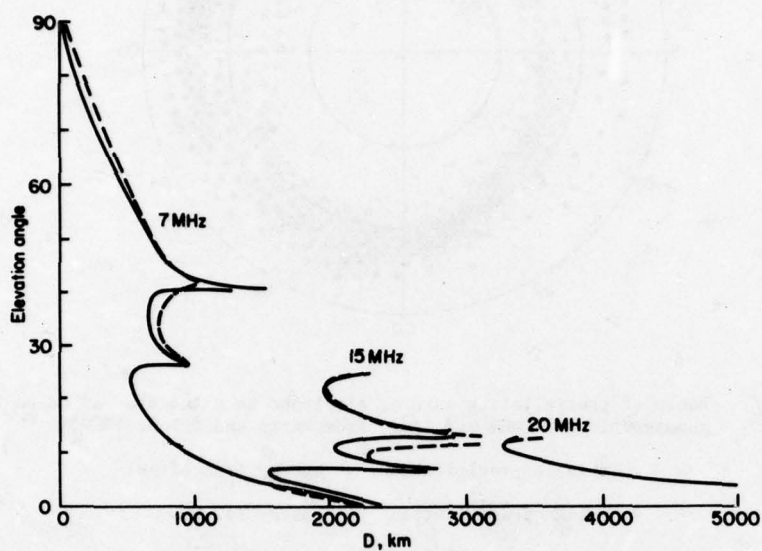
———— model

FIGURE 2:   Ground range as a function of elevation angle for rays launched at selected frequencies via the ionospheres of figure 1

- - - - true-height analysis

———— model
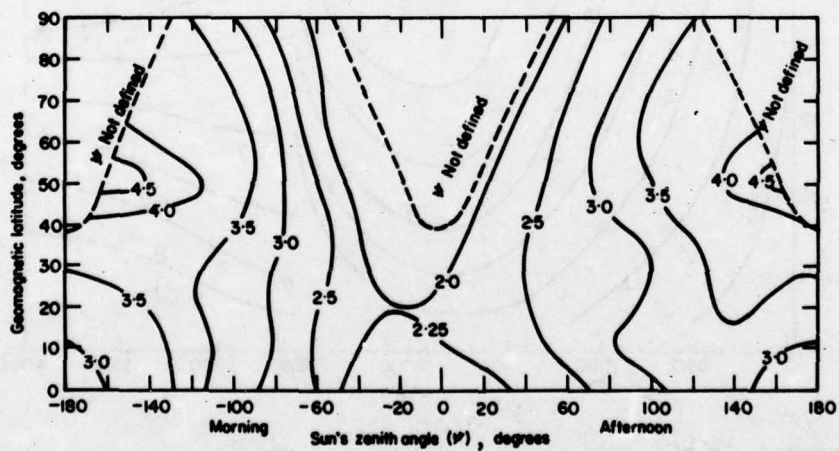
FIGURE 3:   Ratio of F2-layer height of maximum electron concentration to semi-thickness for high solar activity conditions (from Lucas and Haydon, 1966).
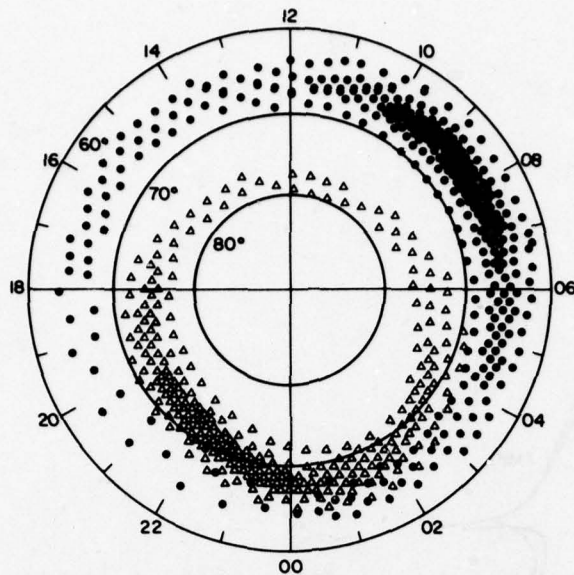
FIGURE 4: Zones of precipitating auroral electrons as a function of corrected geomagnetic latitude and time (from Hartz and Brice, 1967)

. drizzle precipitation — energy tens of keV

△ splash precipitation — energy few keV
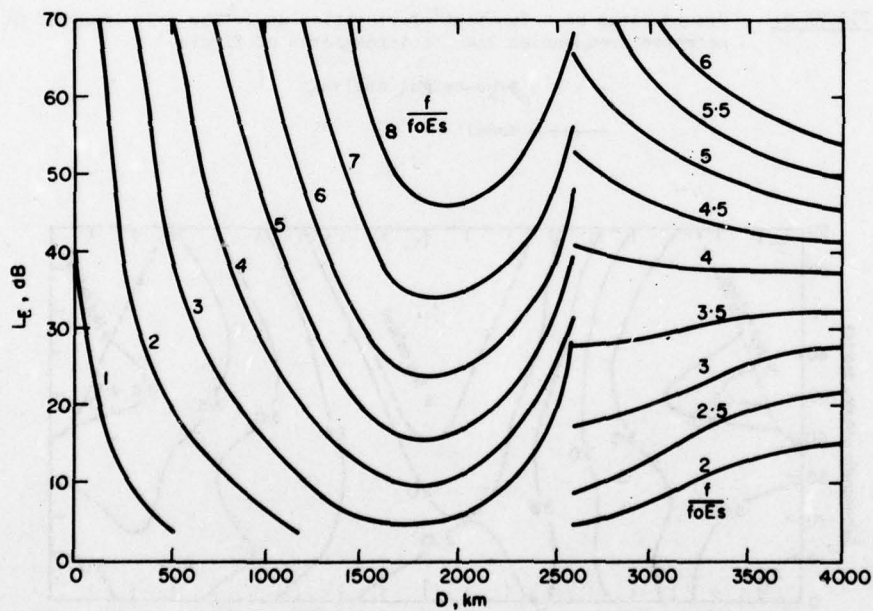
FIGURE 5: Sporadic-E reflection loss L_E (from CCIR Report 259-3 (Rev. 76))

Curves relate to a single hop for D < 2500 km and to two hops for greater distances.
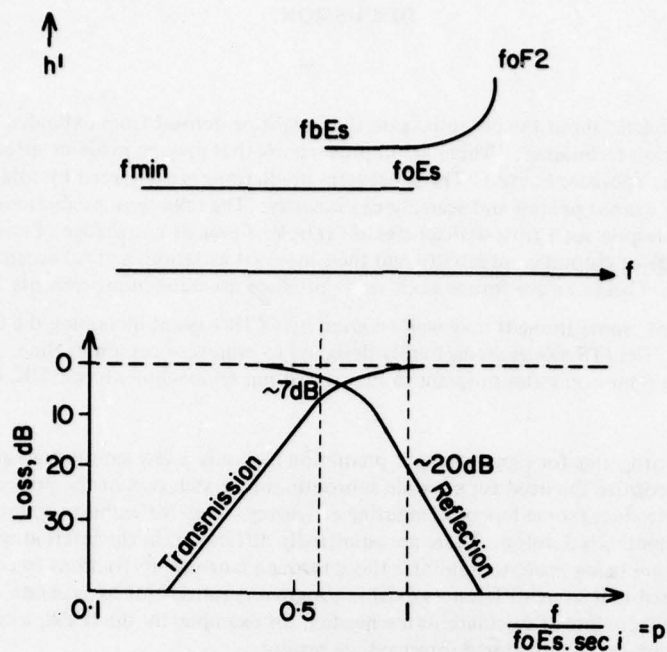
FIGURE 6: Relationship between sporadic-E reflection and transmission loss at vertical and oblique incidence (from Sinno et al. 1976)

Upper section shows an idealised ionogram for vertical incidence and lower section gives the corresponding transmission and reflection losses indicated by an empirical equation fitted to measured oblique-path data.
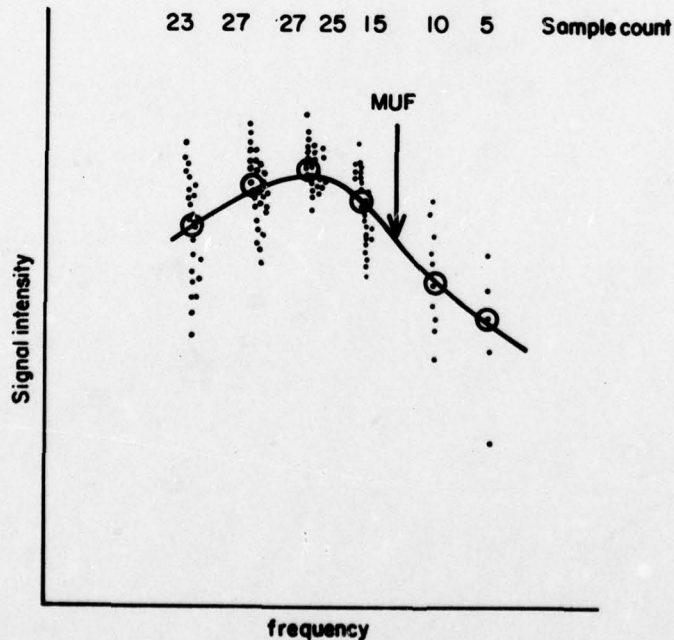
FIGURE 7: Idealised diagram illustrating daily variations of HF signal intensity

. measured values

⊖ median of measured values

arrow shows median MUF

DISCUSSION

N.G.Gerson, US

I feel somewhat pessimistic about the potential gain that might be derived from extended or large-scale efforts to improve MUF prediction techniques. (There are improvements that may be made in specialized topics; e.g., absorption over polar regions, sporadic E, etc.). The short-term predictions are triggered by solar and even atmospheric effects which we now cannot predict and scarcely can identify. The long-term predictions seem fairly adequate for planning purposes — despite such gross deficiencies as (a) lack of precise knowledge of antenna patterns, (b) lack of adequate knowledge of ground conductivity and their seasonal variation, and (c) acceptance of the deficiency CCIR noise maps, etc. Can intensive future work really produce dramatic improvements in HF predictions?

As a separate comment; some thought may well be given by CCIR toward increasing the efficiency of existing MUF prediction programs. The ITS model seems hardly designed to minimize computer time. Further, a problem exists in reprogramming the same computer program so that it will run on machines in the UK, Germany, Canada, etc.

Author's Reply

Some past computer programs for signal-strength prediction had only a few subroutines and many of these were very lengthy. Now, we recognize the need for separate subroutines to match cost of the principal propagation factors so that, although this introduces some loss of computing efficiency, there is flexibility to incorporate changes relatively readily as prediction methods develop. There are admittedly difficulties in the international exchange of computer programs but efforts are being made to minimize these through language restrictions to compatible elements. Nevertheless, it is emphasized that some differences exist in program requirements by separate users, even for a single prediction method. Where lots of calculations are needed, for example, by the IFRB, a case can be made for a large-storage requirements program with stored intermediate results.

I agree that the prediction-accuracy goals discussed in the paper may turn out to be unattainable. However, this does not mean we are completely failing in our task. Provided a prediction procedure can be agreed internationally as the best available at a particular point in time, it is value to use this for system-design tendering and for frequency-assignment purposes.

STATISTICAL MODELLING OF HF LINKS

L W Barclay
Home Office
Directorate of Radio Technology
Waterloo Bridge House
LONDON SE1 8UA

SUMMARY

Computer programs which predict the monthly median received signal/external noise ratio as a function of frequency and of the system characteristics have been available for some years. Other programs are available for the prediction of the probability that a particular service grade will be achieved.

Such a prediction may include 3 separate probability statements: the probability that a message will be acceptably error free, the proportion of messages (or of time) during which this performance may be expected, and the confidence level of the estimate.

It is not always easy for the user to appreciate the implications of such multi-level statements. The most appropriate presentation depends upon the users' requirements and some of the alternatives are discussed.

The time-dispersion/amplitude characteristics of the signal are also important for high speed telegraphy. Each contributing signal mode will fade independently and will have a different probability of ionospheric support. The problems associated with performance prediction in such circumstances are discussed.

1.   INTRODUCTION

Ionospheric models have been developed over many years and are used for predicting the performance of hf radio systems. In order to make a full assessment of the expected performance information is required on:

(1)   the ionospheric propagation data for the specified path,

(2)   the radio noise data for the receiver location,

(3)   the specification of the relevant radio equipment parameters including the antenna radiation pattern and efficiency, transmitter power, modulation method, etc.,

(4)   the criteria which define the minimum acceptable service quality.

Computer programs which predict the monthly median ratio of the received signal to external noise as a function of frequency and of the system characteristics have been available for some years (1). The predicted median ratio may then be compared with the recommended ratios for various 'grades of service' listed in CCIR Recommendation 339-3(2). The recommendation includes a fading margin and makes allowance for the day-to-day variability in the signal and noise levels. The comparison of the prediction and the Recommendation will indicate whether or not the specified 'grade of service' will be obtained. However, if the predicted ratio is poorer than that recommended there is no indication of the quality that may be expected. In addition, such a method does not make use of all the statistical data which are available (for example, only typical values are used for the inter-decile range of the noise and signal levels). More complex prediction models may be considered when warranted by the importance of the circuit being evaluated.

However, the meaning of more precise statistical statements are not always readily understood and it is necessary to consider in detail the specification of the user's requirement.

Some definitions, given by Barghausen et al (3), are in use and any other statistical definitions should be consistent with these. It is thus appropriate to start by reviewing the existing definitions.

2.   THE UPPER FREQUENCY LIMIT

Predictions of ionospheric support - of whether the selected frequency can propagate to the desired range - are based on median values of ionospheric characteristics. Predictions of the median standard maximum usable frequency (MUF_{50}) must be modified to give the standard MUF for other percentages of days of the month. The 'optimum working frequency' (OWF or FOT) is defined as the frequency which will be available on 90% of the month (or sometimes, less precisely, on "all undisturbed days"), and the highest probable frequency (HPF) as the frequency available on 10% of the days of the month. For many years the OWF for the F2 layer was taken to be $0.85 \times MUF_{50}$ but Davis and Groome (4) have established the OWF and HPF ratios in more detail. In general F_u (HPF/MUF_{50}) and F_ℓ (OWF/MUF_{50}) are not reciprocal and the ionospheric-support distribution is skewed. However the halves of two normal distributions, with standard deviations of $F_u/1.28$ and $F_\ell/1.28$ provide a good fit to the ionospheric data. Indeed, Bradley and Bedford (5) have still further simplified the form of the distribution to a simple analytic expression.

Sporadic-E support is more difficult to deal with. Numerical maps are available for the values of foEs with occurrences of 10, 50 and 90%. In this case, the distributions are highly skewed and it has not yet been determined whether it is sufficient to assume a pair of normal half-distributions or whether the more complex χ^2 distribution described by Zacharisen and Crow (6) is necessary.

From such distributions the fraction of days on which a circuit will have ionospheric support, q_f, can be predicted. Some prediction methods may modify the above procedure to include propagation modes above the classical MUF in the determination of q_f.

3. SIGNAL TO NOISE RATIO

Field strength or signal power predictions are usually given for monthly median conditions during a specified hour. CCIR Reports 322-1 and 258-2 gives seasonal median noise levels for specified time blocks. The predicted monthly median signal to noise ratios (R_{50}) may then be compared with the recommended ratios for the various "grades of service" listed in CCIR Recommendation 339-3. The 14 dB allowance for day to day variability of the within-the-hour signal to noise ratio should be included to determine whether the performance will be satisfactory at the stated grade of service on 90% of days. This is a simple procedure and it is convenient when predicting the lowest usable frequency (LUF) for the operation of established circuits. However this method is of limited use for circuit planning, since it only gives the go/no-go indication commented on earlier.

4. CIRCUIT RELIABILITY

A refinement of the above technique is to examine in more detail the day to day variations in the hourly values of both signal and noise. In both cases the variations are assumed to have normal half-distributions. Values for the upper and lower standard deviations of the signal (S_u and S_ℓ) are listed by Barghausen et al (2) and the deciles of the noise variations (1.28 of the standard deviations N_u and N_ℓ) are given in CCIR Report 322-1.

The signal to noise ratio (R_{90}) required to ensure that communication will be of the specified quality in 90% of days at that hour is given by:

$$R_{90} = R_{50} + 1.28 \ (N_u^2 + S_\ell^2)^{1/2} \ \dots\dots\dots\dots\dots\dots\dots\dots\dots\dots\dots\dots\dots(1)$$

where R_{50} is the datum "grade of service" requirement, given for example in the Table of Recommendation 339-3, and the second term is a replacement for the 14 dB allowance.

Similarly the ratio to ensure the required service for 10% of hours is:

$$R_{10} = R_{50} - 1.28 \ (N_\ell^2 + S_u^2)^{1/2} \ \dots\dots\dots\dots\dots\dots\dots\dots\dots\dots\dots\dots\dots(2)$$

A distribution fitted to R_{10}, R_{50} and R_{90} may be compared with the median signal to noise ratio predicted for the circuit to give the probability, $q_{S/N}$, that the predicted ratio exceeds the requirement. This is illustrated in Fig. 1.

The overall circuit reliability, taking account of ionospheric support, is then given by:

$$REL = q_f \ x \ q_{S/N} \ \dots\dots\dots\dots\dots\dots\dots\dots\dots\dots\dots\dots\dots\dots\dots\dots\dots(3)$$

Although circuit reliability is apparently a simple and easily understood concept it is based on a number of assumptions. In particularly the values of R_{50} for the median hourly requirement of a fading signal include models for the fading distribution and, in some cases, for the amplitude probability distribution of the noise and are also for various 'grades of service' which may not be appropriate for the communications requirement. In addition the reliability is that for an "average" circuit (i.e the confidence level that the results will apply to a specific circuit is 50%) since no account is taken of uncertainties in the prediction data or in the actual requirements.

5. TIME AVAILABILITY

The circuit reliability gives, in effect, the number of days during which the required performance may be expected, as a function of the frequency. As an alternative the above procedure may be reversed; the time availability may be specified as a part of the communications requirement and the predicted signal to noise ratio which will be required to meet this may be determined. This is illustrated in Fig. 2.

6. SERVICE PROBABILITY

All of the parameters used in the circuit performance prediction are somewhat uncertain, and a standard error may be ascribed to each one. The terms involved include the uncertainty in the predictions of the median noise and signal levels, and of the standard deviations of the noise and signal variations, together with the uncertainty in predicting the short term fading range of the signal and the noise a.p.d, and in specifying the signal to noise ratio requirement.

The total uncertainty variance, σ_T^2, is found by adding as many of the individual uncertainty variances as are appropriate. The uncertainty distribution may then be used to find the service probability, q_T as shown diagrammatically in Fig. 3. q_T is the confidence level with which the results may be expected to apply to a specific circuit. Note that the total service probability should also include the probability of ionospheric support: i.e the total service probability $= q_T \times q_f$.

The service probability gives the proportion of circuits which will have a specified error rate (grade of service) for a specified percentage of days (time availability). This kind of multi-level statement can be confusing and even though the propagation engineer is trying to be precise in his estimate of the circuit performance it is all too easy for the user to assume that the statistics are being used to disguise vagueness.

One way to make an apparent simplification is to predefine the grade of service (e.g by selecting one of the Rec. 339-3 values) and the time availability (e.g q_T = 90%) at an early stage of a study and then to indicate only the service probability percentage as a simple statement of the likelihood of a specified circuit being satisfactory.

7.   THE LONG TERM PROBABILITY

As an alternative the above procedure may be inverted. The confidence level may be pre-defined (e.g q_T = 90%) and the margin to combat long term fluctuations may be deduced as shown in Fig. 4. This seems to be the most useful way of indicating the likely performance of a circuit. For telephony, and for telegraphy with a specified average error rate, the long term probability is simply a generalized variant of the circuit reliability.

Slator (private communication) originally introduced long term probability for a more complex case. Instead of assuming an average error rate, his requirement was that a uniform stream of messages of similar length should each have not more than a specified number of errors. This technique, which involves integrating the probability of an error-free message with respect to the signal to noise ratio, leads to the long term probability that a message will be satisfactory.

8.   DISCUSSION

One of the above definitions will probably satisfy the user operating or planning a high grade circuit. For example the circuit reliability, $q_{s/n}$, gives the percentage of days in the month during which the signal to noise ratio will be adequate, taking account of the fluctuation of both signal and noise. Similarly the ionospheric support probability, q_f, gives the percentage of days during which the service will be adequate taking account of variations in ionospheric density. If both $q_{s/n}$ and q_f are high percentages, the total availability, $q_{s/n} \times q_f$, will also be high and will give satisfactory guidance to the user. On the other hand the two cases of a powerful transmitter (high $q_{s/n}$) operated on too high a frequency (low q_f), and of a weak transmitter (low $q_{s/n}$) operated on a lower frequency (high q_f), might both have similar overall reliabilities but would appear to the user to have quite different operational characteristics. The product, $q_{s/n} \times q_f$, will indicate the amount of traffic he may expect to transmit successfully during a given hour within the month but it does not offer him the information which is available about the reasons for failure.

Frequency management procedures, which may take account of daily short-term forecasts, may make substantial changes to the ionospheric support probability, q_f.

Circuit reliability or, long term probability etc., is much more a function of the system design and the equipment provision.

Perhaps the best way of system planning is to predict the frequency for a given value of q_f (say 90%) and then to predict the value of $q_{s/n}$, etc. at that frequency. Adjustments to the system design would be made using the predicted values of $q_{s/n}$. Once operational it would be up to the frequency manager to optimize the overall product $q_{s/n} \times q_f$ on a day-to-day basis.

9.   MULTI-MODE PROPAGATION

The paper so far has discussed the signal level and the ionospheric support as if only one propagation mode were active at one time. In many cases this is an adequate approximation. When several modes are predicted it is usual to add the powers of each contributing signal mode to give the total power. Where the mode with the highest value of q_f also has dominant power the association of the total signal power with the q_f for one mode will not lead to significant errors. For telephony it may be assumed that the interference fading between the active signal modes has been included in the fading model used to specify the grade of service, so that $q_{s/n}$ may be predicted using the total signal power.

For high-speed telegraphy, however, it is not sufficient to consider only the signal power since the time dispersion of the active modes is also important. Instead, the median signal level of each mode (and indeed of each magneto-ionic component of each mode) may be predicted, together with the time dispersion from a ray-tracing path-length procedure. Fig. 5 shows an example of the median signal to noise ratio for 3 modes (e.g 1E, 1F2 and 2F2) each with 2 magneto-ionic components. Each component mode will fade independently and may have a log-normal fading distribution. It may be sufficient to combine the 2 components of each mode, say by predicting only the ordinary wave and assuming that its fading distribution is approximately Rayleigh. However, where a polarization prediction is included in the model it would be appropriate to predict each component.

The multi-path limitation on the system performance will be governed by the differing ionospheric support for each mode as well as by the fading characteristics. It is not at all clear that any simple statement may be made about the performance.

One important aspect is likely to be a detailed consideration of the demodulator design. Can an envelope be defined in the signal to noise ratio/time dispersion plane which will describe the tolerance of the modem. Fig. 6, for example, is such an envelope for a hypothetical system. In some cases this might not be an adequate representation as a weak signal mode followed by a stronger one may affect the system synchronization.

Once the modem limitations have been defined, however, the fading and variations of the signals which are predicted may be modelled to determine the probability that they remain within the acceptable envelope. So far as the author knows this has not yet been done. The detailed prediction of signal modes and the fading/multi-path assessment would have to be repeated for each hour and each frequency of interest and may be prohibitive in computer time.

10.   CONCLUSIONS

Probability predictions of circuit performance are of value provided that they are understood by the user. Multi-level probability statements can be confusing; if some of the variables, e.g grade of service, confidence level, can be predefined, the prediction of long-term probability may be the most useful choice. However, in some cases the older techniques of LUF prediction continue to be quite adequate. There is a danger in combining the probability of ionospheric support with other assessments of performance since the effects on the communications circuit are different. The performance of high speed telegraphy circuits depends on the time dispersion of the signal modes as well as on the signal level; techniques for such performance prediction have not yet been developed but are likely to be complicated.

11.   ACKNOWLEDGEMENT

12.   REFERENCES

(1)   Barclay, L W, "HF predictions and ionospheric forecasting". Point-to-Point Communication, Vol. 17, pp 25-33.

(2)   CCIR Recommendation 339-3, "Bandwidths, signal-to-noise ratios and fading allowances in complete systems" CCIR XIIIth Plenary Assembly, Vol. III, Geneva 1974.

(3)   Barghausen, A F, Finney, J W, Proctor, L L, and Schultz, L D, "Operational Parameters of high Frequency Sky-Wave Telecommunication Systems" ESSA Tech. Rpt. ERL 110-ITS 78, Institute for Telecommunication Sciences, Boulder, Colo, 1969.

(4)   Davis, R M, and Groome, N L, "Variations of the 3000 km MUF in time and space", NBS Report 8498, 1964.

(5)   Bradley, P A, and Bedford, C, "Prediction of HF Circuit Availability", Electronics Letters, Vol. 12, No. 1 1976.

(6)   Zacharisen, D H, and Crow, E L, "The use of the chi-square distribution to represent skewed data distributions", Radio Science, Vol. 5, 1970.

$$\text{OVERALL REL.} = q_f \times q_{S/N}$$

Fig 1   Circuit Reliability, $q_{S/N}$

V is the standard normal variate corresponding to the required time availability
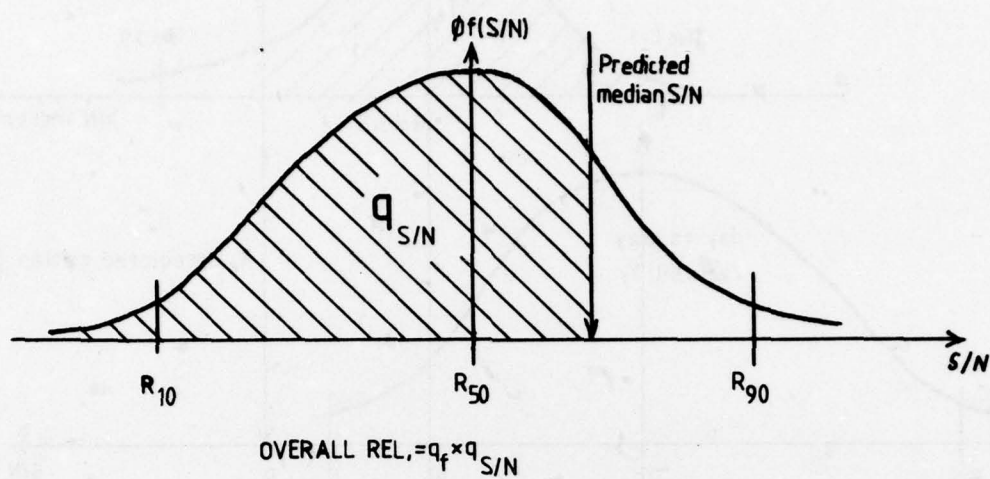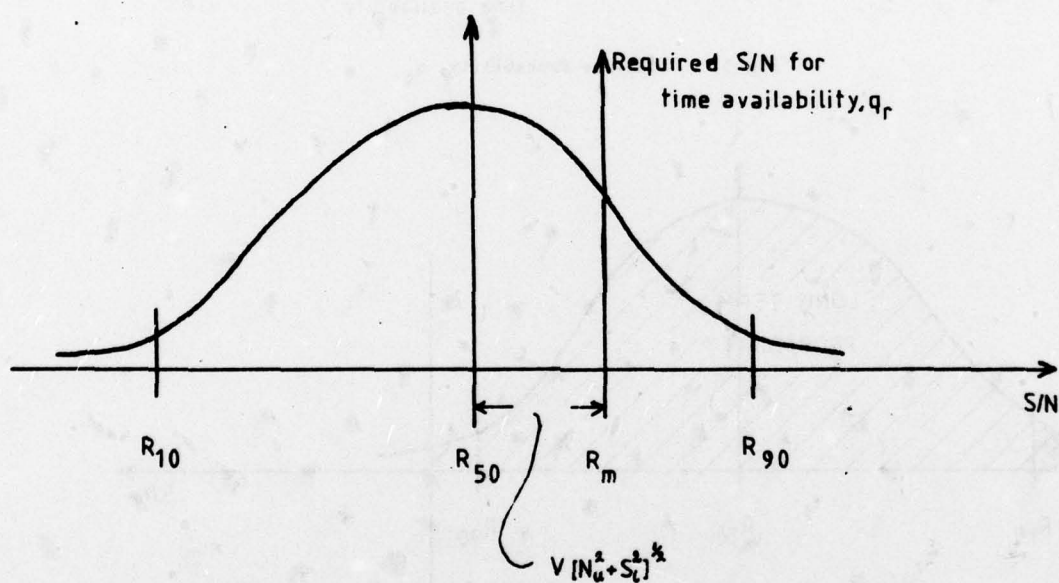
Fig 2   Time Availability, q_r
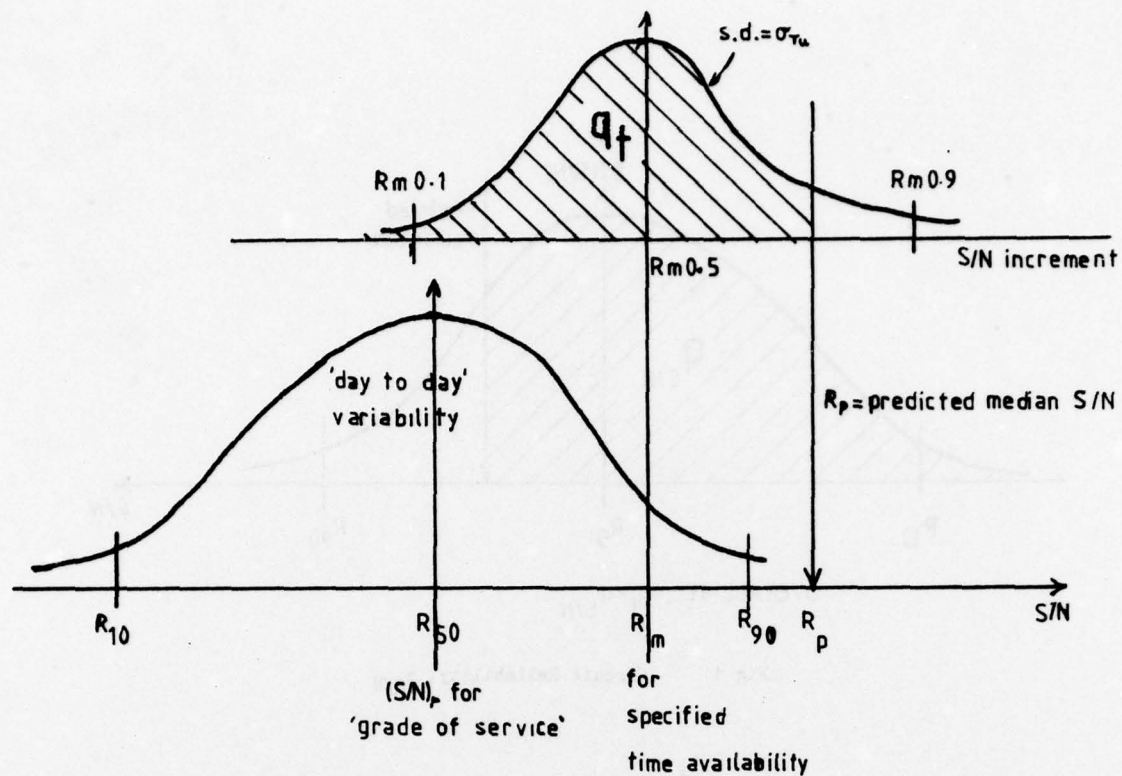
Fig 3   Service Probability, q_t
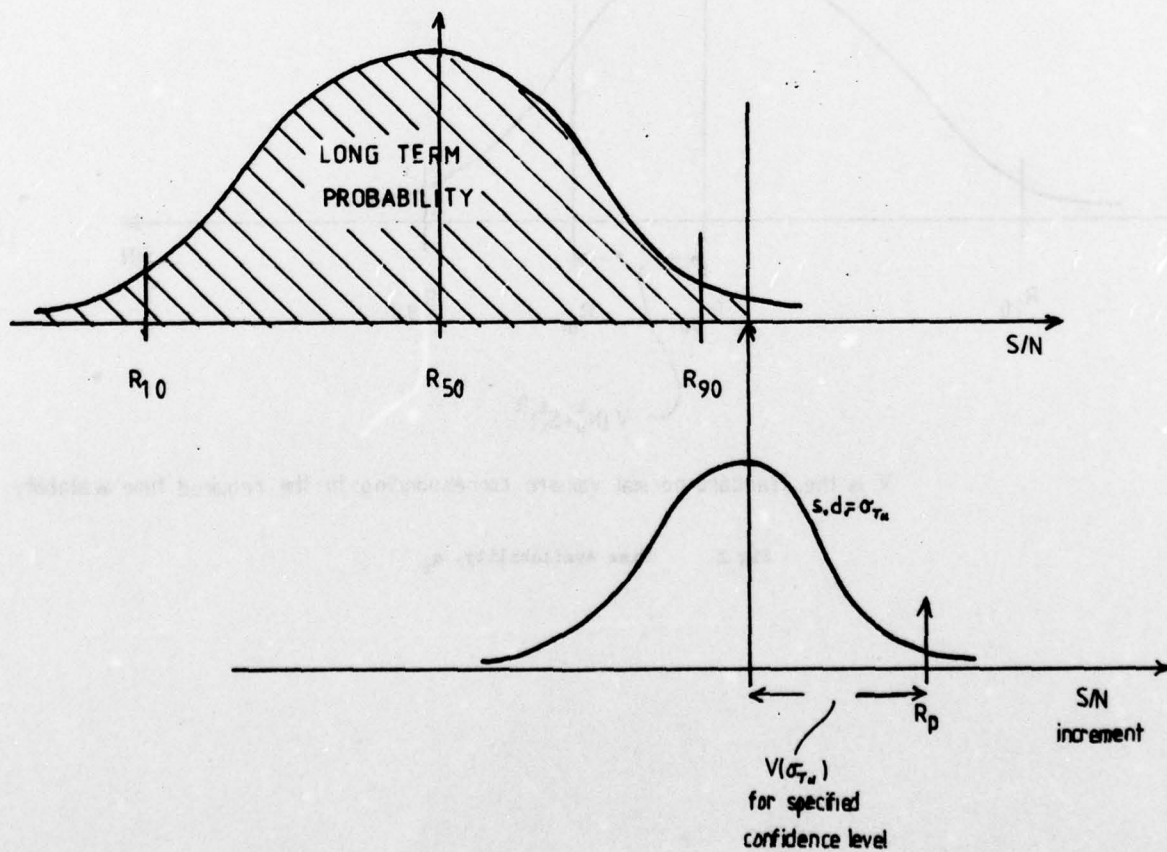
Fig 4   Long Term Probability
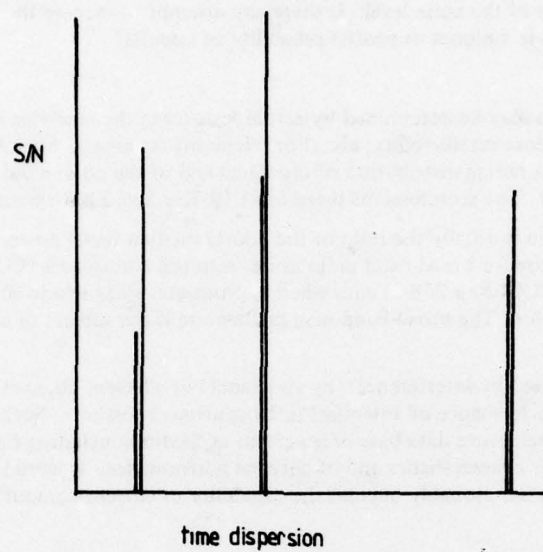
Fig 5   Multi-path Modes
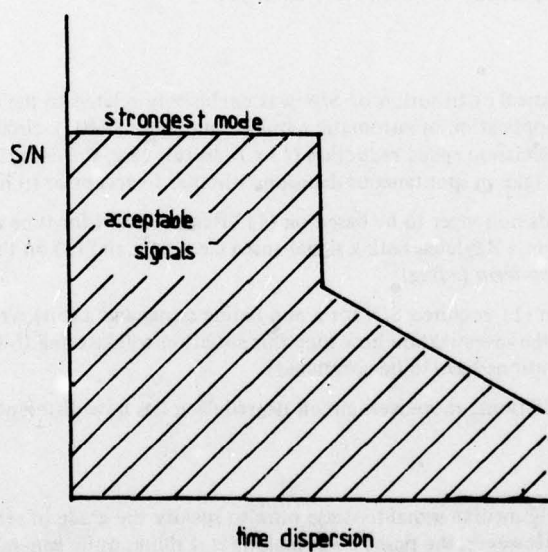
Fig 6   Modem Specification

DISCUSSION

J.Röttger, FRG

How is the signal-to-noise ratio defined? I see there are some attempts to improve the reliability of forecasting the signal strength and also the prediction of the broad-band noise level. However, man-made narrow-band noise should also be included in the definition of the noise level. Is there any attempt to include the latter type of noise (i.e. man-made interference) into the techniques to predict reliability of circuits?

Author's Reply

The required signal-to-noise ratio may be determined by actual tests using the receiving equipment (for example, by determining the percentage sentence intelligibility, etc. For telephony schemes). Such tests would have to include simulation of the within-the-hour fading distribution of the signal and of the noise a.p.d. Alternatively the system may be modeled mathematically. The requirements listed in CCIR Rec.339-3 have been determined in such ways.

The predicted signal-to-noise ratio is usually the ratio of the hourly median signal power to the hourly median noise power. These noise predictions are for broad-band radio noise from the atmosphere (CCIR Rep.322-1), from un-intentional man-made sources (CCIR Rep.258-2) and, when appropriate, also include contributions from the Galaxy and due to the receiver noise factor. The broad-band man-made noise is the subject of a new program of study by a CCIR interim working party.

Man-made noise may also be caused by interference: by co-channel or adjacent channel transmissions (which may be dependent on the side-lobe performance of antennas) or by spurious emissions. Such interference is not included. To do so would require a comprehensive data-base of spectrum utilization, including time occupancy, together with details of transmitter and receiver characteristics and of antenna performance. It would be of great interest to make such predictions but I think they are probably beyond the capability of current computational methods, except for special cases.

T.B.Jones, UK

This paper brings to mind the problem of the scientist trying to tell the propagation expert who, in turn, is trying to tell the user what is going on. The problem of communication among these participants, has been addressed in previous meetings, but has apparently not been resolved as yet.

B. Van Dijl, Netherlands

In the presentation, the statistical distribution of S/N was exclusively related to the character error rate (c.e.r.) in case of telegraph. With the application of automatic request equipment (ARQ), circuit performance would have to be specified in terms of transmission speed reduction (t.s.r.). In this case, the design of the circuit can be based on the fact that the channel can take in spontaneous decisions whether to accept or to reject the received signal.

The design of the circuit needs no longer to be based on (1) "Required S/N for time availability" which is, when correctly understood, based on a Rayleigh fading signal and a c.e.t. of x and (2) on the investigation how long this situation is present *due to long-term fading*.

With ARQ, it can be based on (1) required S/N for a non-fading signal and a (bit) error rate of y (leading now to speed reduction) and (2) on the investigation how long this situation will last due to the combined effect of short and long-term fading (distributions have to be correlated).

I think this, also, affects predictions; moreover, circuit degradation has now different character: the circuit speed slows down and finally stops.

Author's Reply

I quite agree. I used the hourly median signal-to-noise ratio to specify the grade of service as, probably, the most widely applicable example. However, the point I was making is, I think, quite general; it is important to establish the way the user wishes to specify the grade of service and then to allow for the statistical distributions of the important characteristics.

In the case of an ARQ system, a suitable requirement might indeed be the average data rate during an hour. We would model the system using Slator's technique for determining the long-term probability. First, we would assume a steady signal level and the expected noise a.p.d., and we would determine the ratio of the signal to the hourly median voice levels which would give the required data rate (circuit speed). We would then, as you suggest, combine the within-the-hour fading distribution (which may be approximately Rayleigh) and the day-to-day distribution of the hourly levels of signal and noise (which may be approximately log normal). The combination of these two distri-butions would then be used to find the long-term probability that they previously specified a signal-to-noise ratio would be exceeded.

C.Goutelard, France

An interesting answer to the problems of multiple trajectories would be the determination of the relative amplitudes

of the various trajectories. In fact, in many models, the probabilities of error are directly related to these relative amplitudes, which are themselve predictable "a priori".

However, in accordance with what you said, I do not think it is possible to predict the real noise level, mainly because of intererences and local noise.

Author's Reply

It seems to me that the problem is that we must determine not only the median relative amplitudes (which are predictable) but also the instantaneous relative amplitudes which result from the independent fading characteristics of each mode. It is because the bit-by-bit performance of a particular type of data modem depends on these instantaneous relative amplitudes, that we must understand and specify the modem characteristics.

Editorial note: Reply to the comments made on narrowband, man-made interference is identical to that offered to Dr Röttger's question above.

MODELISATION DE L'IONOSPHERE DANS LES PROBLEMES DE GESTION DE RESEAUX DE TRANSMISSION H F

par

C.Goutelard et J.Caratori
Laboratoire d'Etude des Transmissions Ionospheriques
Universite Paris Sud
9, avenue de la Division Leclerc
94230 – Cachan

RESUME : *Les transmissions effectuées par réflexion des ondes HF sur l'ionosphère sont caractérisées par la fréquence d'émission, les pertes de transmission, l'effet doppler, le fading et les trajectoires multiples. Ces paramètres sont liés à l'état de l'ionosphère : gradients verticaux et horizontaux de l'ionisation et leurs variations temporelles, champ magnétique terrestre......*
Une méthode de mesures, à partir d'une station centralisée a été développée. Elle permet la détermination des paramètres de transmission pour des liaisons entre deux points quelconques d'une zone de plusieurs milliers de kilomètres centrée sur la station.
La méthode est essentiellement basée sur la recherche de modèles d'ionosphère tenant compte, notamment, des gradients d'ionisation horizontaux.
Dans la première partie de l'étude, le choix du modèle est discuté et comparé aux autres modèles utilisés par d'autres auteurs. Il est alors montré de quelle façon, pour le modèle choisi, il est possible de mesurer ses paramètres de façon systématique à partir d'une station centralisée.
Dans la seconde partie, on fait apparaitre l'interêt qu'il y a à retenir deux classes de mesures :
- la mesure des paramètres dits statiques qui permettent la détermination des paramètres du modèle ionosphérique.
- la mesure des paramètres dynamiques qui rendent compte de leur vitesse de variation instantanée. L'ensemble de ces mesures conduit à un système d'équations d'état du modèle ionosphérique.

Ce système d'équations permet de dresser une cartographie des conditions de propagation à l'intérieur de la zone et d'établir des prévisions.
Les résultats expérimentaux obtenus sont présentés.
La méthode est ensuite comparée aux méthodes proposées par d'autres auteurs . Ses limites sont précisées et son champ d'application est défini.

1 - INTRODUCTION

La connaissance des paramètres ionosphériques sur une zone étendue est nécessaire pour l'établissement des plans de fréquences des liaisons à effectuer à l'intérieur de cette zone.

L'établissement de prévisions de transmission à trés court terme impose la mesure directe de ces paramètres. Ce principe est appliqué dans les systèmes de sondages obliques bistatiques (1) (2) où les fréquences à utiliser sont fournies avec une probabilité de bon établissement de 99 %, mais la variabilité des conditions de propagation rend le système moins efficace dès que la liaison à réaliser s'écarte de plus de 5 à IO° de la liaison testée. L'utilisation d'une station de sondage par rétrodiffusion, équipée d'une antenne rotative résoud, théoriquement, l'ensemble de ces problèmes. Cependant une difficulté apparait dans l'exploitation des résultats de mesure. En effet, l'ionogramme de rétrodiffusion ne donne pas directement la distance de bond en fonction de la fréquence mais le temps de propagation, ce qui interdit, même pour des liaisons radiales de lire directement la MUF .

L'étude présentée ici vise à rechercher une méthode de gestion de réseau de transmission simple utilisant une station centralisée équipée d'un sondeur à rétrodiffusion et, éventuellement d'un sondeur zénithal. La méthode proposée repose sur la détermination du profil moyen de l'ionosphère à partir de l'ionogramme de rétrodiffusion.

L'étude du cas général est compliquée par le fait qu'il n'existe pas de relation analytique entre le profil vertical des couches et l'ionogramme de rétrodiffusion. Pour trouver une solution simple à l'inversion de l'ionogramme, on a choisi un modèle parabolique du profil d'ionisation et un procédé de calcul basé sur la recherche de courbes de régression polynomiales des lois reliant les paramètres de l'ionogramme à ceux des couches. Le modèle parabolique, souvent adopté dans ces cas doit être complété par la prise en compte des gradients d'ionisation horizontaux et par l'existence, de jour, de la couche E. On a dû faire intervenir pour obtenir une représentation correcte deux types de gradients horizontaux pouvant exister simultanément. La couche E dont l'influence a été étudiée peut être prise en compte à partir des cartes de prévisions compte tenu de la bonne connaissance de ses variations.

.../...

II - CAS D'UN MODELE IONOSPHERIQUE SANS GRADIENTS D'IONISATION HORIZONTAUX

2.1. Cas d'une couche unique - Définition du modèle.

En absence de gradients horizontaux d'ionisation, l'ionosphère a été définie par une couche parabolique caractérisée par :

- Sa fréquence critique Fc
- L'altitude du maximum d'ionisation Hm
- La demi épaisseur Ym

Compte tenu des fréquences utilisées en rétrodiffusion, l'influence des chocs est négligeable dans la détermination des rayons et il est possible de tenir compte, de façon simple, de l'influence du champ magnétique (3)

Le calcul des rayons peut alors être fait à partir du modèle de la figure 1 qui permet de calculer la trace frontale de l'ionogramme de rétrodiffusion (figure 2) dont la mesure est faite directement à partir des enregistrements (figure 3).

La recherche de paramètres caractérisant la trace frontale a été faite de plusieurs manières par la recherche de polynomes caractéristiques, de fonctions puissances et de fonctions exponentielles. Ce dernier modèle a paru donner les meilleurs résultats. En effet, l'ionogramme tracé en échelle semi logarithmique log T_F = f (F/ Fc) (figure 4) présente un point d'inflexion, donc une partie quasi rectiligne caractéristique qui peut dans l' exploitation pratique, s'ajuster par la méthode des moindres carrés, et donner une relation de la forme

$$\log T_F = Ao\, X + Bo = A\, F + B\, o \quad \text{où } X = F/Fc$$

La généralité de ce modèle a été vérifiée sur 44 couples de valeurs (Hm, Ym) couvrant , pour toutes les fréquences critiques F c possibles, tous les cas usuels (figure 5).

Les paramètres Ao et Bo dépendent de Hm et Ym. Les figures 6 et 7 montrent les variations de Ao et Bo. Une succession d'ajustements par la méthode des moindres carrés permet de donner à Ao et Bo des expressions analytiques. :

$$Ao = A\, Fc = 1.1\ IO^{-5}\ Ym + 1.892\ IO^{-2}\ Hm^{0.46} \tag{1}$$

$$Bo = O.5I9\ \log_{IO} Hm - O.6223 \left(\frac{Ym}{Hm}\right)^2 + O.3558 \left(\frac{Ym}{Hm}\right) - O.8544 \tag{2}$$

Les courbes de régression reportées sur les figures 6 et 7 montrent la bonne concordance avec les courbes réelles. Une étude plus complète a montré que l'erreur commise sur Ao était de l'ordre de O.7% et celle commise sur Bo de l'ordre I.2%.

2.2. Inversion de l'ionogramme

L'ionogramme de rétrodiffusion fournit deux paramètres A et Bo qui ne permettent donc pas de déterminer les trois paramètres Fc, Hm, Ym de la couche. Il est donc nécessaire d'ajouter une relation supplémentaire. Nous avons finalement choisi d'adopter pour les ionosphères nocturnes la relation de Schimazaki (4) et pour les ionosphères diurnes la relation de Bradley-Dudeney (5) . Associées à l'hypothèse du modèle parabolique de l'ionosphère elles fournissent une troisième relation. La formule de Schimazaki conduit à la relation :

$$Ym = O.I7O9\ IO^{-6}\ HM^3 + 1.227\ IO^{-3}\ Hm^2 + O.435I\ Hm \tag{3}$$

L'inversion des ionogrammes de rétrodiffusion peut alors être effectuée à l'aide des relations (1), (2), (3). Les résultats sont résumés par les courbes des figures 8 et 9 qui montrent que Hm et Ym se déduisent directement de Bo tandis que Fc se déduit de A et Bo

.../...

Par une méthode de régression semblable à celles utilisées auparavant, il est possible de donner les expressions analytiques de ces courbesmais une précision de 1% implique des polynomes de neuvième degré (6). Une vérification de l'inversion de l'ionogramme faite sur l'ensemble des 44 couples définis sur la figure 5 a montré qu'une bonne précision était, en général, obtenue, la plus grande erreur intervenant sur Ym. le tableau ci-dessous montre un échantillonnage de ces résultats.

Paramètres de la couche			A et Bo déduits de l'ionogramme simulé		Paramètres de la couche déduite A et Bo					
Fc MHz	Hm km	Ym km	A	Bo	Fc MHz	Hm km	Ym km	Fc	Hm	Ym
5	300	200	0.057	0.397	5	307	198	0%	2.3%	-1%
5	400	275	0.0654	0.451	4.94	391	256	-1.2%	-2.2%	-6.9%
5	500	325	0.0722	0.520	5.05	497	310	1%	-0.6%	-4.6%

Une vérification expérimentale (6) réalisée en comparant les résultats obtenus avec des sondeurs zénithaux à ceux obtenus par cette méthode a montré qu'une bonne corrélation était obtenue dans le cas où il n'existe pas de gradients d'ionisation horizontaux.

2.3 Extension au cas d'une ionosphère à deux couches . Influence de la couche E

Le modèle parabolique étudié jusqu'ici est valable pour les ionosphères nocturnes. De jour, la présence de la couche E, et l'été de la couche F 1 conduisent à compliquer le modèle. Une étude semblable à la précédente a donc été faite dans le cas d'un modèle représenté par deux couches paraboliques définies par leurs paramètres Fc1, Hm 1, Ym 1 et Fc 2, Hm 2, Ym 2 et reliées par un profil de transition. L'ensemble de ces paramètres permet de simuler une grande variété de profils, mais nous nous sommes attachés dans cette étude à une simulation des couches E et F 2. Pour ce cas, le modèle de BRADLEY s'impose pour les avantages qu'il offre.

L'étude effectuée sur 63 cas représentatifs des cas réels, a montré que la trace frontale de la seconde couche est caractérisée par la même valeur du paramètre A mais que le paramètre BO est modifié d'une quantité R qui dépend de Fc 2 et des paramètres de la couche inférieure. Ce résultat est illustré par les exemples de la figure IO.

III - INVERSION DE L'IONOGRAMME EN PRESENCE DE GRADIENTS HORIZONTAUX

3.1 Modèles adoptés

Dans le paragraphe II nous avons supposé l'ionosphère uniforme dans toute la zone traversée par les rayons issus du sondeur. En pratique, cependant, il existe toujours, même en période calme, des gradients d'ionisation horizontaux liés, plus ou moins directement, aux variations géographiques du flux solaire. Ces gradients horizontaux modifient sensiblement les trajectoires des rayons, et peuvent donner lieu à des propagations anormales, notamment au lever et au coucher du soleil. Il s'avère donc nécessaire, de modifier le modèle simple précédemment utilisé pour la simulation des ionogrammes de rétrodiffusion, afin d'y inclure l'influence des gradients horizontaux.

Nous avons conservé l'hypothèse d'une ionosphère à couche unique dont le profil vertical d'ionisation est parabolique, et nous avons admis comme hypothèse supplémentaire que le rapport Ym/ Hm de la couche reste constant dans toute la zone explorée. Cette hypothèse, imposée par la nécessité de réduire le nombre de paramètres, se justifie par l'influence mineure de Ym sur la forme de l'ionogramme simulé (voir paragraphe II).

.../...
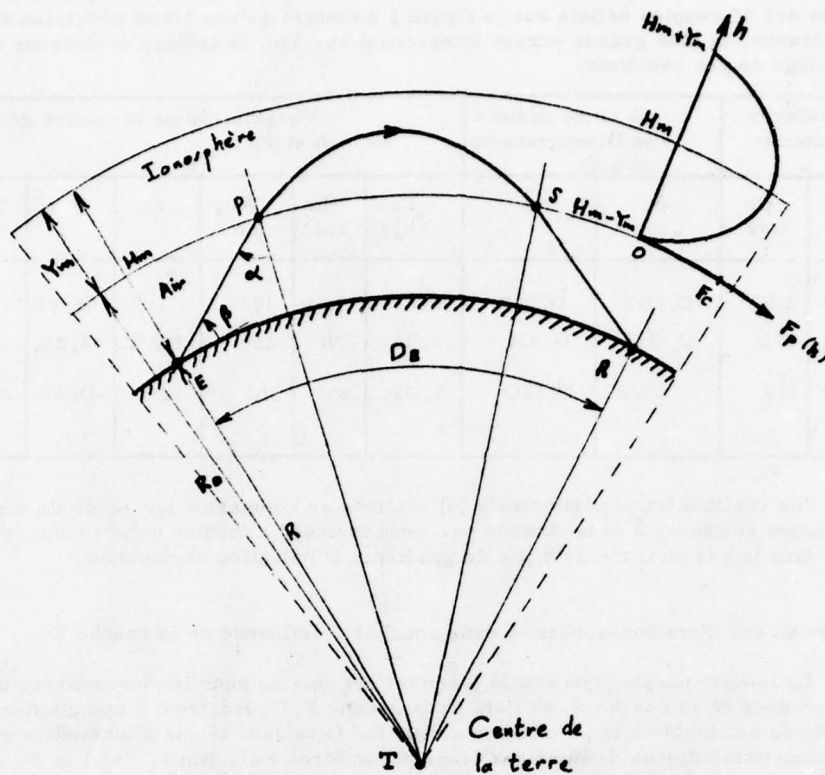
Figure 1
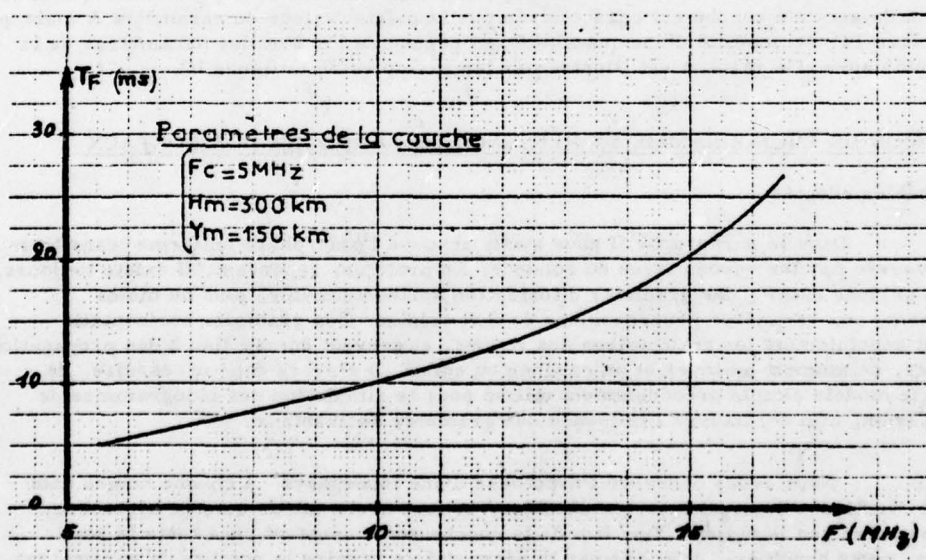
Figure 2

BRUZ   le 18/09/75

à   15h55mn

Azimut 180°

Figure 3

Paramètres de la couche

Hm = 300 km
Ym = 150 km
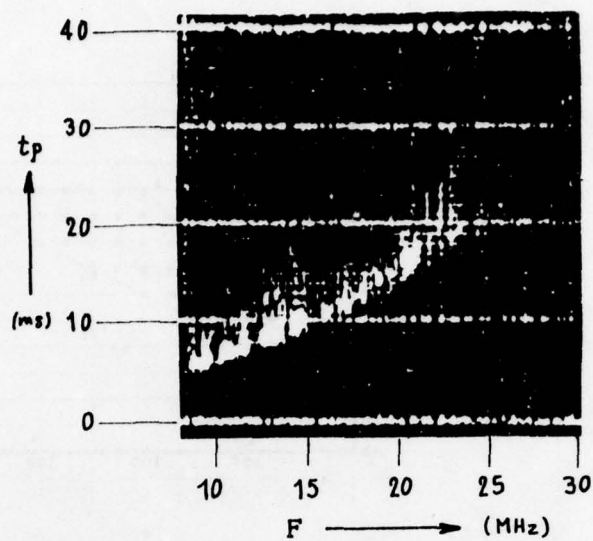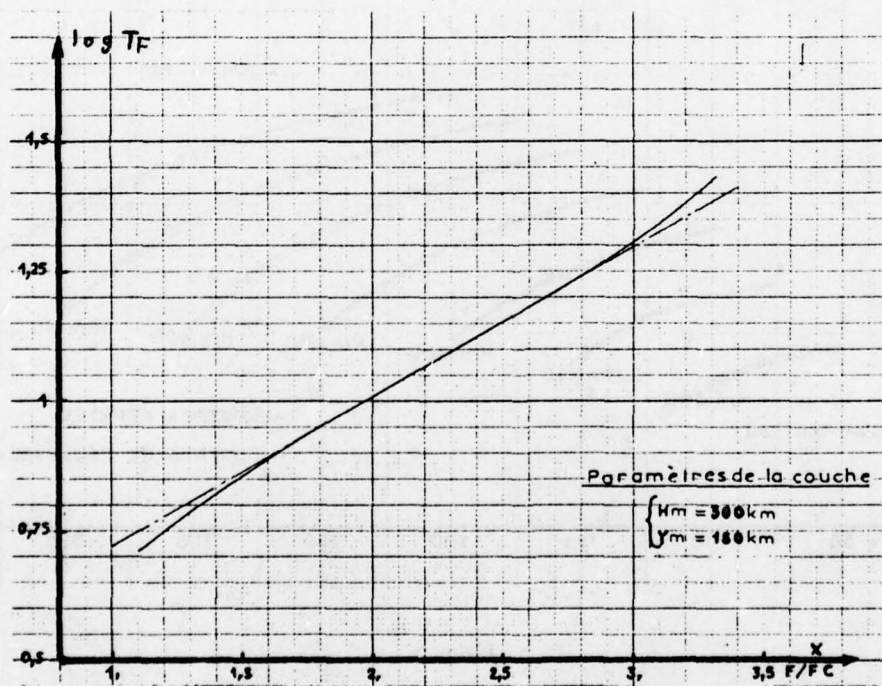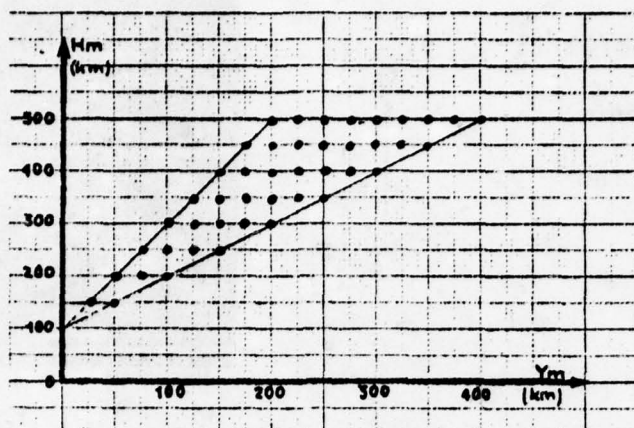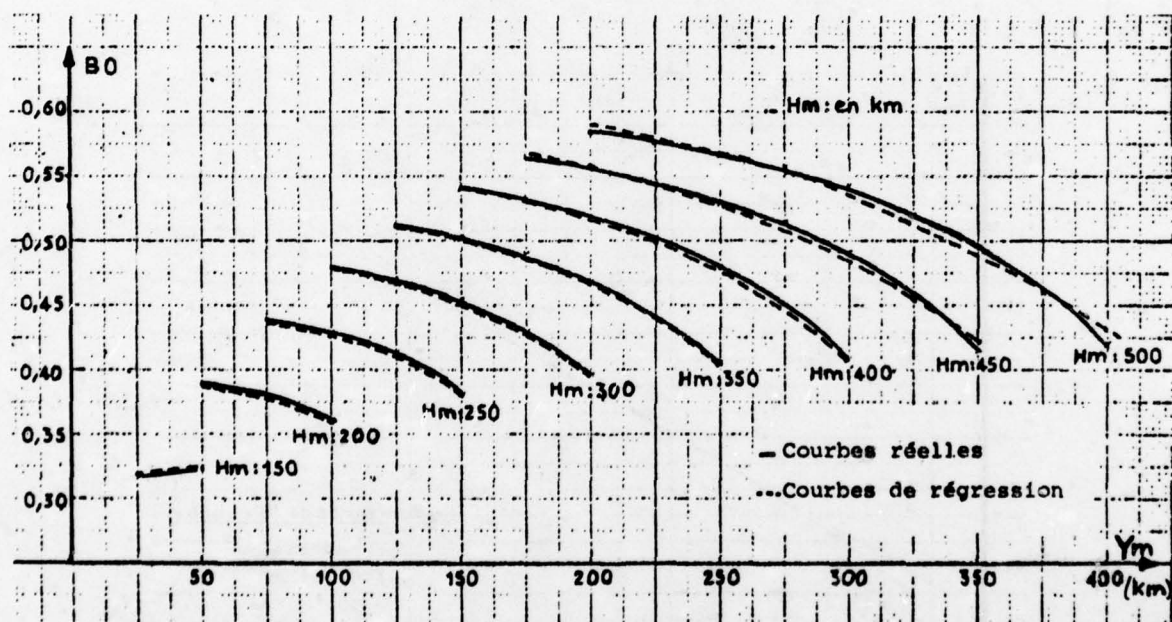
Figure 4

Figure 5

Figure 6

Figure 7

Figure 8

METHODE GRAPHIQUE
données A et BO
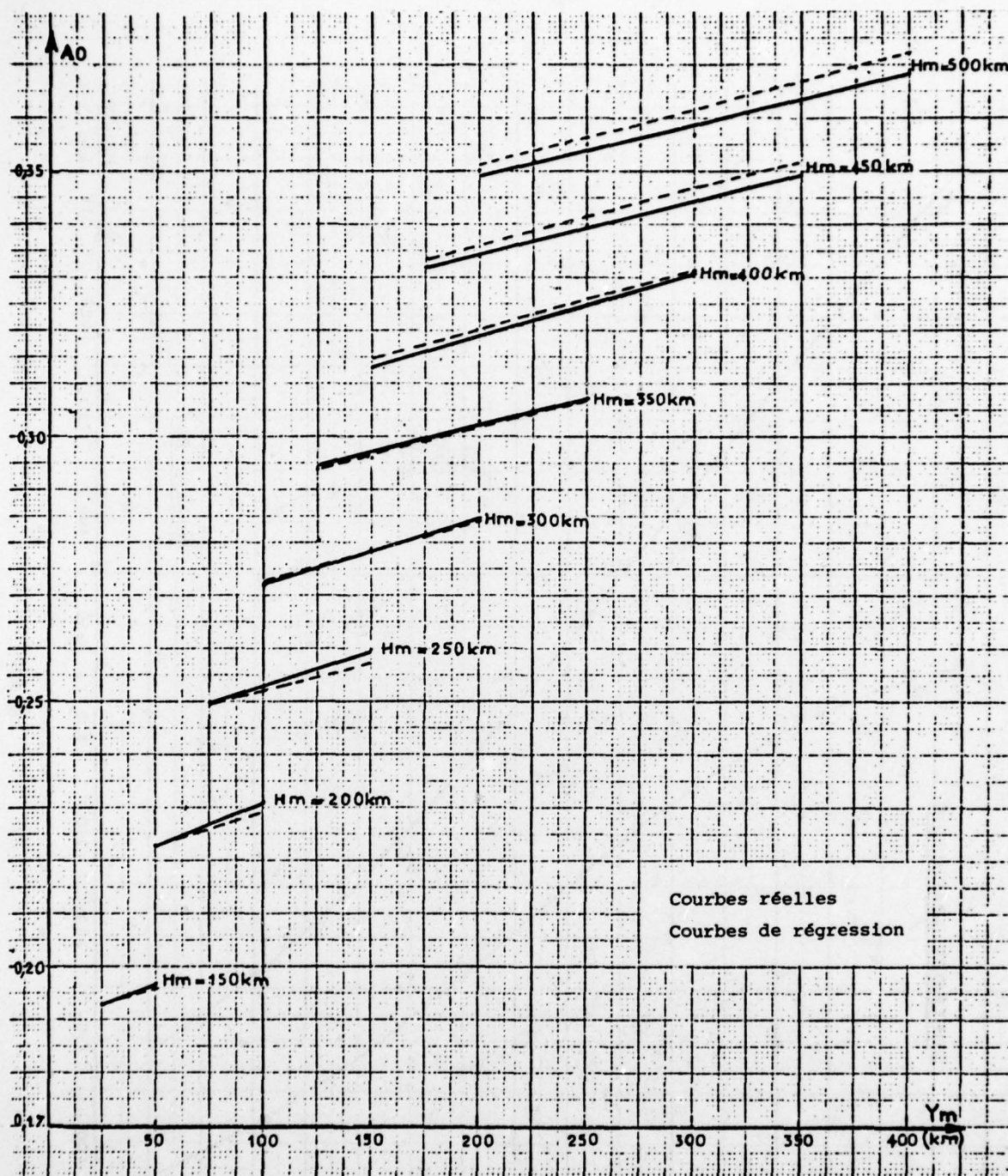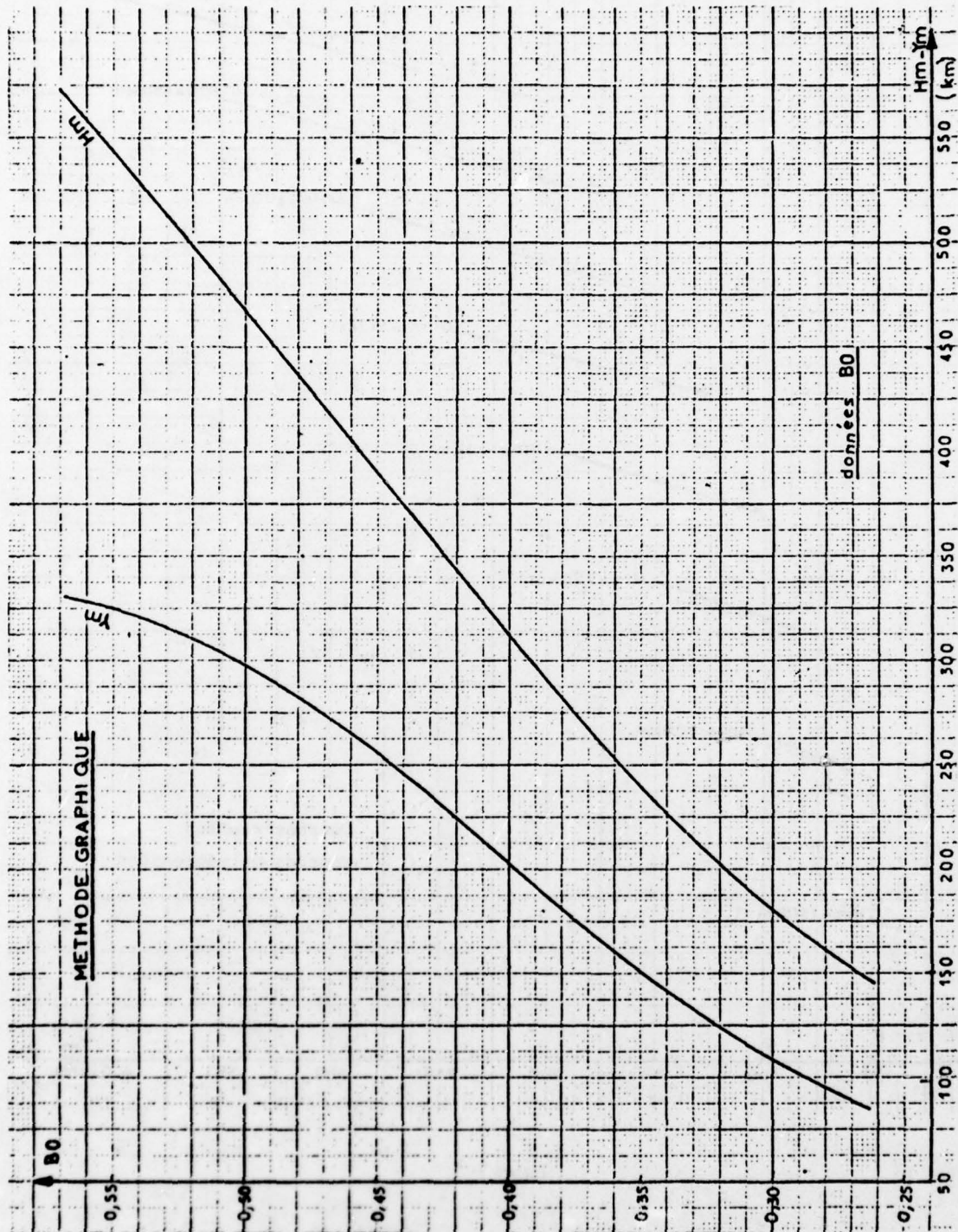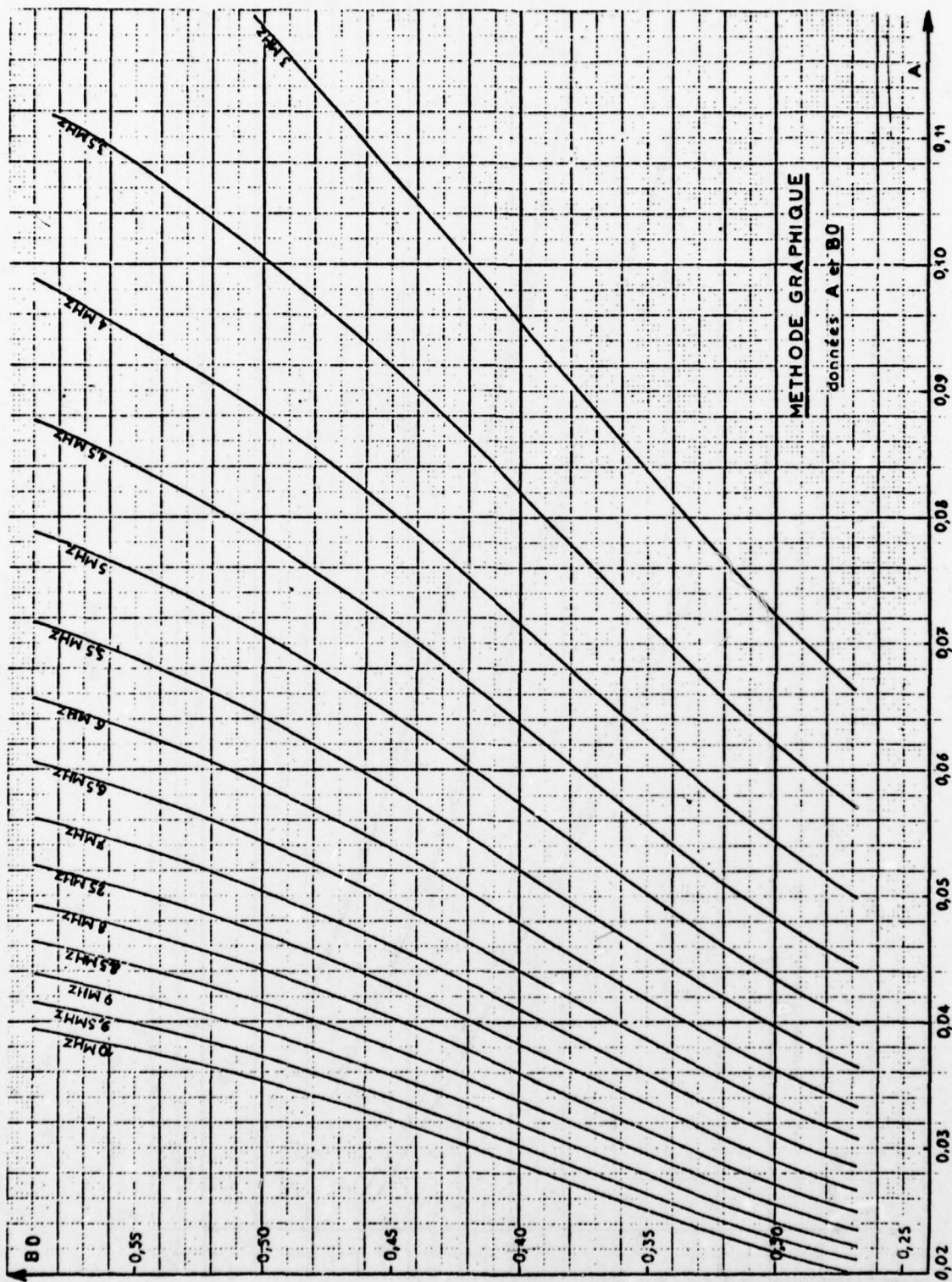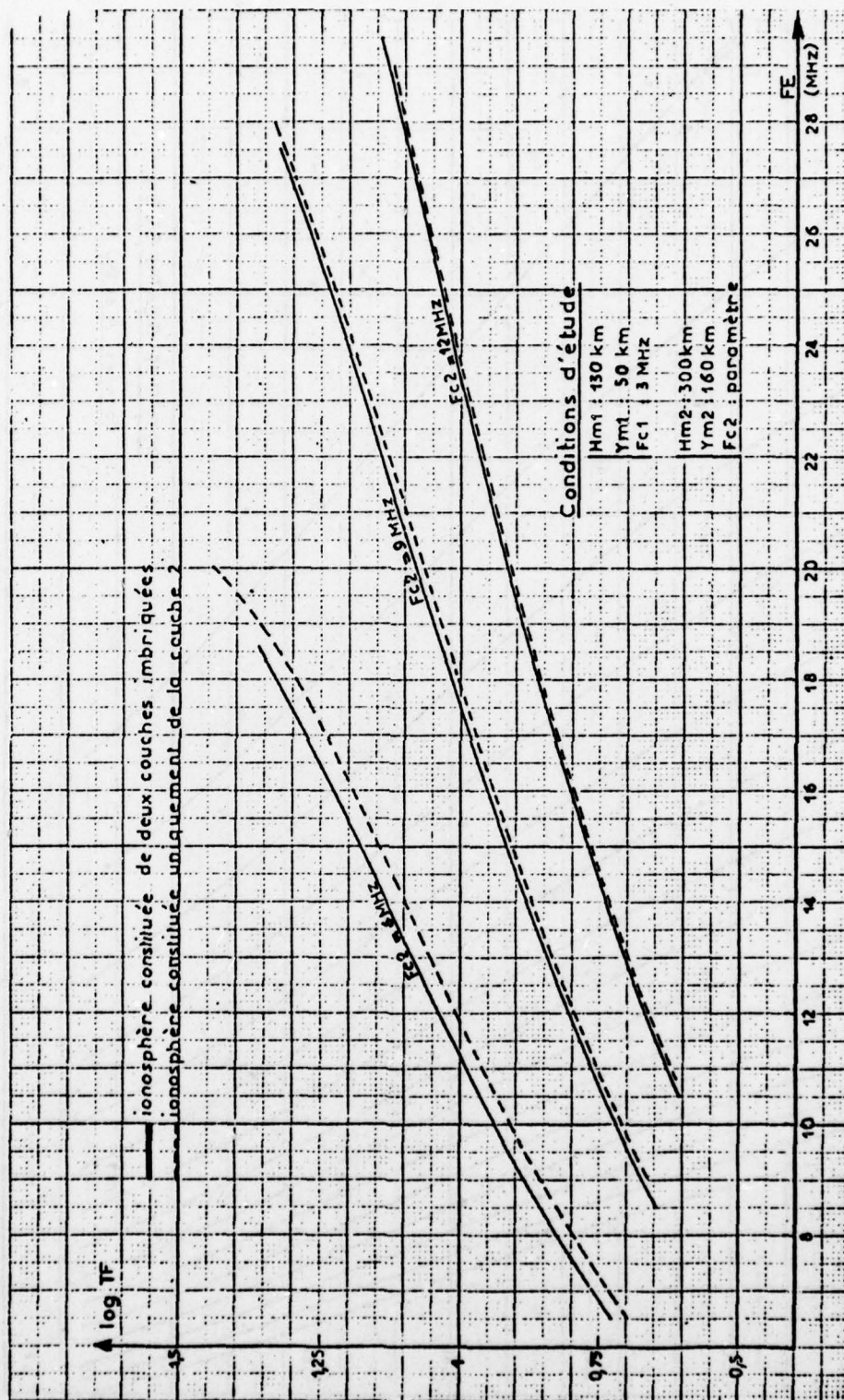
Figure 9

Figure 10

L'étude a comporté plusieurs étapes, qui nous ont conduit à étudier d'abord l' effet d'un gradient horizontal de hauteur, puis celui d'un gradient horizontal d'ionisation, et enfin une combinaison des deux appelée gradient mixte. Les gradients que nous avons cherché à représenter sont ceux dus aux variations géographiques régulières de la densité d'ionisation et non dus à des perturbations ionosphériques.

3.1.1. Modèle incluant un gradient horizontal de hauteur

Certains gradients d'ionisation horizontaux peuvent être interprétés en supposant une inclinaison globale des couches (7) (8). Nous avons adopté un modèle simplifié dans lequel la terre et l'ionosphère sont sphériques mais excentrées (figure 11). Ce modèle, caractérisé par l'inclinaison ε_o des couches à la verticale de la station, présente l' avantage de permettre un calcul extrémement simple des caractéristiques de la propagation.
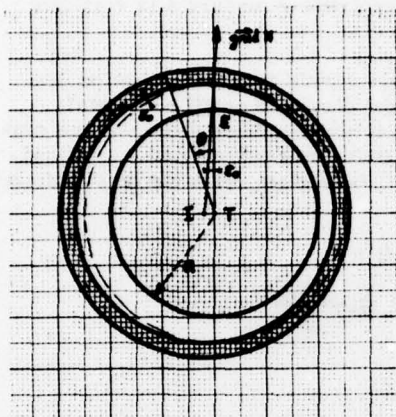
T : Centre de la terre

I : Centre de courbure de l'ionosphère

ε_o : Inclinaison des couches à la verticale du sondeur

E : Emplacement de l'émetteur

Figure 11

L'inclinaison des couches ε_o est liée à l'intensité du gradient de hauteur par la relation :

$$\text{tg } \varepsilon_o = \frac{d \, Hm}{d \, (R \, \Theta)}$$

où $R \Theta$ est la distance par rapport à l'émetteur. Comme ε_o est généralement inférieur à 5°, on peut confondre la tangente et son argument pour écrire :

$$\varepsilon_o = \frac{d \, Hm}{d \, (R \, \Theta)}$$

Dans le but de simplifier l'interprétation des résultats, nous avons limité l' étude au cas où le plan d'émission est confondu avec le plan T I E, car alors les trajectoires sont des courbes planes toutes entières contenues dans ce plan.

3.I.2. Modèle incluant un gradient horizontal d'ionisation dû à Fc

Le modèle adopté est une couche unique concentrique à la terre et dont le profil d'ionisation est parabolique selon la verticale et linéaire selon l'horizontale. Les rayons sont supposés émis dans le plan vertical contenant le vecteur gradient, d'où il résulte que la trajectoire est une courbe plane inscrite dans le plan d'émission. Par conséquent, la densité d'ionisation peut être exprimée en fonction de deux variables seulement. Nous avons choisi une distribution de la forme

$$N (r, \theta) = \text{Nmo} \left(1 - \left(\frac{r - \text{Rm}}{\text{Ym}}\right)^2 \right) (1 + \lambda \, R \theta)$$

avec - r, θ : coordonnées géocentriques polaires dans le plan de la trajectoire

- Rm = R + Hm : rayon du maximum d'ionisation

- Nmo : densité d'ionisation maximum à la verticale de l'émetteur (θ = O)

- λ : paramètre caractérisant l'intensité du gradient horizontal

Le paramètre λ est lié à l'intensité du gradient d'ionisation horizontal par la relation :

$$\lambda = \left[\frac{2}{\text{Fc}} \cdot \frac{d\,\text{Fc}}{d\,(R \theta)} \right]_{\theta = 0}$$

Il représente le double de l'accroissement relatif de fréquence critique mesuré à la verticale de l'émetteur.

L'avantage de la loi de distribution retenue réside dans la séparation des variables r et θ , qui entraine la séparation du profil vertical d'avec le profil horizontal. Cependant, l'indice d'ionisation dépend ici de deux variables et non pas d'une seule comme dans le cas précédent. Le calcul des caractéristiques de la propagation en est fortement compliqué, car il nécessite la résolution des équations d'Euler Lagrange, lesquelles résultent de l'application du principe de Fermat au rayon (9)

Le système d'équations à résoudre s'écrit :

$$\frac{d}{ds} \left(n \, \frac{dr}{ds} \right) - n\,r \left(\frac{d\theta}{ds} \right)^2 = \frac{\partial n}{\partial r}$$

$$\frac{d}{ds} \left(n\,r^2 \, \frac{d\theta}{ds} \right) = \frac{\partial n}{\partial \theta}$$

avec : - $n (r, \theta)$: indice de réfraction de l'ionosphère fonction de $N (r, \theta)$

- S : abscisse curviligne d'un point de la trajectoire

Par un changement de variables adéquat, ces équations se ramènent à un système de 4 équations différentielles du premier ordre qui fournit directement la distance de bond. Afin d'obtenir le chemin de groupe Pg, qui est la caractéristique essentielle en rétrodiffusion, il est nécessaire d'adjoindre à ce système une cinquième équation :

$$\frac{d\,\text{Pg}}{ds} = \frac{1}{n}$$

Le système obtenu ne possède pas de solution analytique, aussi faut-il recourir à une intégration numérique approchée (10). Nous avons adopté la méthode de Runge Kutta d'ordre 4 qui conduit à un bon compromis rapidité-précision.

3.1.3. Modèle incluant un gradient horizontal mixte

Ce modèle résulte de la combinaison des deux précédents. L'ionosphère est excentrée et affectée d'un gradient linéaire d'ionisation. Nous avons admis que les deux gradients sont alignés et contenus dans le plan d'émission, d'où il résulte que les trajectoires sont planes et inscrites dans ce plan.

3.2 Méthodes d'inversion

Deux méthodes principales sont envisageables pour inverser l'ionogramme de rétrodiffusion : une méthode itérative et une méthode analytique fournissant directement les paramètres du profil en fonction de ceux déduits de l'ionogramme.

3.2.1 Méthode itérative

Considérons à titre d'exemple le cas où il existe un gradient de hauteur. L'ionogramme de rétrodiffusion nous fournit 2 paramètres A et Bo, tous deux fonction des caractéristiques du modèle : Fc, Hm, Ym et ξ_θ, ce que nous pouvons écrire :

.../...

$$A = f(Hm, Ryh, \mathcal{E}_o) \cdot Fc = Ao \cdot Fc$$
$$Bo = g(Hm, Ryh, \mathcal{E}_o) \tag{4}$$

où $Ryh = Ym/Hm$

Le problème qui se pose est celui de la résolution d'un système de 2 équations à 4 inconnues. Nous savons que dans un tel cas la solution est indéterminée. Pour lever l' l'indétermination, il est nécessaire de fixer deux des paramètres du profil. Plusieurs solutions sont alors envisageables :

- on peut utiliser les prévisions permanentes pour fixer les deux paramètres les moins influents à leurs valeurs les plus probables

- on peut utiliser un sondage zénithal pour fixer deux paramètres

Si nous adoptons cette dernière hypothèse, qui est certainement celle qui conduit à la plus faible incertitude, nous pouvons fixer les paramètres, Fc et Hm, car ils sont faciles à déduire d'un ionogramme zénithal. Le système à résoudre prend alors forme :

$$Ao = F(Ryh, \mathcal{E}_o)$$
$$Bo = G(Ryh, \mathcal{E}_o) \tag{5}$$

Ces équations définissent une transformation qui est biunivoque si son Jacobien est non nul dans tout le domaine de variation des variables Ryh et $\mathcal{E}_o$. Dans cette éventualité, il est possible d'obtenir une solution approchée du système en utilisant une méthode de calcul numérique classique telle que la méthode d'itération. Dans la mesure où le processus converge, il fournit Ryh et $\mathcal{E}_o$ avec une précision quelconque fixée à l'avance.

3.2.2. Méthode analytique directe

Cette méthode vise à éviter le calcul par itération en résolvant directement, et une fois pour toutes, le système d'équations (1) en fonction de Ryh et $\mathcal{E}_o$ ce qui donne :

$$Ryh = h(Ao, Bo, Hm)$$
$$\mathcal{E}_o = k(Ao, Bo, Hm) \tag{6}$$

Dans ces relations Hm est obtenu par un sondage zénithal, Ao et Bo sont déduits de l'ionogramme de rétrodiffusion et de Fc qui est mesurée en zénithal.

3.2.3. Comparaison des méthodes d'inversion

La méthode d'itération ne nécessite pas une analyse trés poussée des relations qui lient Ao et Bo aux paramètres, mais son utilisation pratique met en oeuvre un processus dont la convergence n'est pas forcément très rapide, ce qui peut être un handicap dans le cas où le traitement est effectué par un microprocesseur.

Au contraire, la méthode analytique directe nécessite une analyse numérique approfondie des relations entre les paramètres de l'ionogramme et ceux du modèle, mais son exploitation est ensuite extrêmement simple. C'est ce critère d'exploitation simple et rapide qui nous a conduit à retenir cette méthode plutôt que la méthode itérative.

3.3. Inversion de l'ionogramme de rétrodiffusion.

3.3.1 Cas du gradient de hauteur

Le modèle que nous avons décrit au paragraphe 3.1.1. nous a permis de simuler la trace frontale de l'ionogramme de rétrodiffusion pour les 616 combinaisons suivantes des paramètres :

7 valeurs de Hm, de 200 à 500 km par pas de 50 km

8 valeurs de Ryh de 0,2 à 0,8 par pas de 0,1 plus la valeur de Ryh déduite de la relation de Schimazaki

11 valeurs de $\mathcal{E}_o$ de -5° à +5° par pas de 1°

.../...

Le tracé des ionogrammes dans un plan aux échelles semi-logarithmiques montre (figure 12) que l'allure rectiligne est conservée même en présence d'un gradient de hauteur. En conséquence, l'ionogramme modifié peut encore être caractérisé par la pente Ao et l'ordonnée à l'origine Bo de sa tangente au point d'inflexion. L'ensemble des paramètres Ao, et Bo, calculés pour tous les triplets (Hm, Ryh $\mathcal{E}_o$) a servi à l'analyse des relations entre profil et ionogramme.

Nous avons montré au paragraphe 3.2.1. qu'il est nécessaire de fixer 2 paramètres du modèle : Fc et Hm. Ceux-ci sont déduits d'un ionogramme zénithal relevé par la station centralisée qui est située au milieu de zone explorée. Ce choix suppose que les paramètres restent constants dans tout le domaine d'investigation du sondeur, ce qui est conforme aux hypothèses formulées pour le modèle, à savoir qu'il vise à représenter uniquement les gradients réguliers ou gradients à grande échelle.

Les paramètres Fc et Hm étant fixés, les coefficients Ao et Bo ne sont plus fonction que de Ryh et de $\mathcal{E}_o$ (formule 5). La figure 13 illustre la relation qui existe entre ces grandeurs et montre clairement que, dans le cas général, à un couple (Ao, Bo) correspond plusieurs couples (Ryh, $\mathcal{E}_o$). Les équations 5 ne définissent pas une transformation biunivoque. Il en résulte qu'il est impossible de déterminer simultanément Ryh et $\mathcal{E}_o$ à partir des coefficients Ao et Bo de l'ionogramme lorsque Hm et Fc sont fixés.

Cette constatation nous a conduit à fixer aussi le paramètre Ryh. En fait, nous avons déjà signalé que Ryh a une influence mineure sur la forme de l'ionogramme. La figure 14 montre que cela est encore vrai en présence d'un gradient de hauteur. D'autre part, ce paramètre peut être estimé grâce au sondage zénithal. La méthode d'inversion ne permet donc d'obtenir que l'inclinaison des couches $\mathcal{E}_o$ et apparait alors comme une méthode de "correction" des paramètres mesurés en zénithal.

Lorsque Ryh est fixé, les équations (2) s'écrivent :

$$Ao = F_2 (\mathcal{E}_o)$$
$$Bo = g_2 (\mathcal{E}_o)$$

Chacune de ces relations permet, à priori, le calcul $\mathcal{E}_o$. En fait, la figure 13 montre que seule la première d'entre elles est biunivoque, aussi avons nous cherché à exprimer $\mathcal{E}_o$ sous la forme :

$$\mathcal{E}_o = k (Ao, Hm, Ryh)$$

où Hm et Ryh sont des paramètres et Ao la variable.

La figure 15 montre que les courbes $\mathcal{E}_o = k (Ao)$ à Ryh constant avec Hm en paramètre sont pratiquement parallèles. Il suffit alors d'ajuster l'une d'entre elles, appelée courbe de base par la méthode des moindres carrés, les autres s'en déduisant grâce au changement de variable :

$$a = Ao - g (Hm, Ryh)$$

où g (Hm, Ryh) représente l'écart entre la courbe courante et la courbe de base.
Pour réduire le degré du polynôme d'ajustement, nous avons scindé l'intervalle d'étude en 2 parties : il apparait en effet que pour $\mathcal{E}_o \geqslant 0$ la relation $\mathcal{E}_o = k (Ao)$ est linéaire, par contre pour $\mathcal{E}_o < 0$ la précision requise de 1% nécessite l'emploi d'un polynôme du 5ème degré. La fonction g (Hm, Ryh) peut être ajustée par un polynôme du second degré en Hm et du premier degré en Ryh.

Dans la pratique la procédure d'inversion est la suivante (les formules sont données pour Ryh = 0.4)

- on mesure Fc, Hm et Ryh à l'aide d'un sondage zénithal

- on mesure Ao à partir d'un sondage par rétrodiffusion, et on en déduit A = Ao. Fc

- on calcule g (Hm) = - 3,151697.IO^{-2} Hm^2 + 6,202370.IO^{-4} Hm - O,178II77

où Hm est exprimé en Km, puis on forme la différence a = Ao - g (Hm)

- si a $\geqslant$ O,2902 on calcule $\mathcal{E}_o = 34,360. a - 9,8917$ où $\mathcal{E}_o$ est exprimé en degrés

.../...

si a $<$ 0,2902 on applique la relation :

$$\mathcal{E}_o = 48373.\,a^5 - 16520.\,a^4 - 4856,5.\,a^3 + 1410,4.\,a^2 + 358,04.\,a - 86,333$$

Afin de contrôler la précision de ces équations, nous sommes partis des quadruplets (Ao, Hm, Ryh, $\mathcal{E}_o$) dont nous avons extrait les triplets (Ao, Hm, Ryh) que nous avons reportés dans les formules d'inversion. Les histogrammes de la figure 16 et le tableau ci-dessous résument les résultats de cette étude.

Ryh	0,2	0,4	0,6	0,8	Schimazaki
$\sigma(\mathcal{E}_o)(°)$	0,109	0,142	0,192	0,398	0,183

Il apparaît que, dans tous les cas usuels, l'erreur quadratique moyenne est toujours très faible $(\sigma(\mathcal{E}_o) < 0,2°)$ et qu'elle atteint 0,4° dans le cas rare dans la pratique, où Ryh = 0,8

3.3.2 Cas du gradient d'ionisation dû a Fc

L'étude peut être calquée point par point sur la précédente. En particulier les courbes Bo = f (Ao) tracées à λ ou Ryh constant (figure 17) montrent qu'il est nécessaire de fixer Ryh pour déterminer λ . La précision des formules d'inversion est alors comparable à celle obtenue dans le cas du gradient de hauteur.

3.3.3. Cas du gradient mixte

Dans ce cas nous avons admis dès le départ que Fc, Hm et Ryh sont connus grâce à un sondage zénithal. Les coefficients Ao et Bo déduits de l'ionogramme de rétrodiffusion peuvent alors s'exprimer en fonction de λ et de $\mathcal{E}_o$, ce qui peut s'écrire :

$$Ao = f (\lambda, \mathcal{E}_o)$$
$$Bo = g (\lambda, \mathcal{E}_o)$$

Ce sont les équations de deux surfaces que l'on peut représenter de différentes manières. Ainsi il est possible de dessiner la surface Bo = g $(\lambda, \mathcal{E}_o)$ et de tracer sur celle-ci les courbes à Ao constant (figure 18). Les intersections de cette surface avec les plans $\mathcal{E}_o = 0°$ et $\lambda = 0$ km^{-1} se déduisent aisèment des graphes des figures 13 et 17 correspondants à la valeur de Ryh mesurée en zénithal. L' allure générale de ces courbes d'intersection est conservée lorsque l'on découpe la surface Bo par des plans à λ ou $\mathcal{E}_o$ constants et non nuls.

Dans ces conditions, la mesure de Ao fixe une courbe sur la surface Bo donc une relation entre λ et $\mathcal{E}_o$. L'intersection de cette courbe avec le plan de côte Bo est un point M (figure 18) dont la projection m a pour coordonnées λ et $\mathcal{E}_o$.
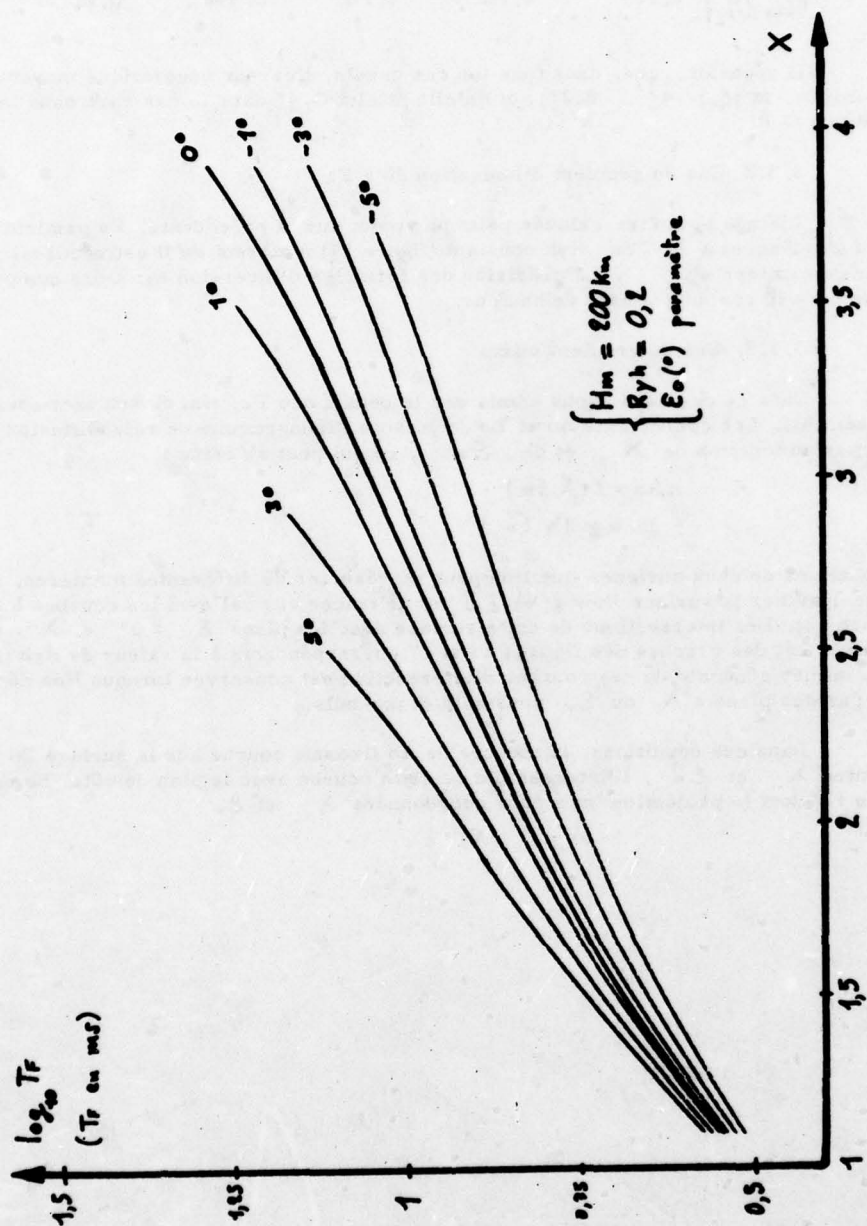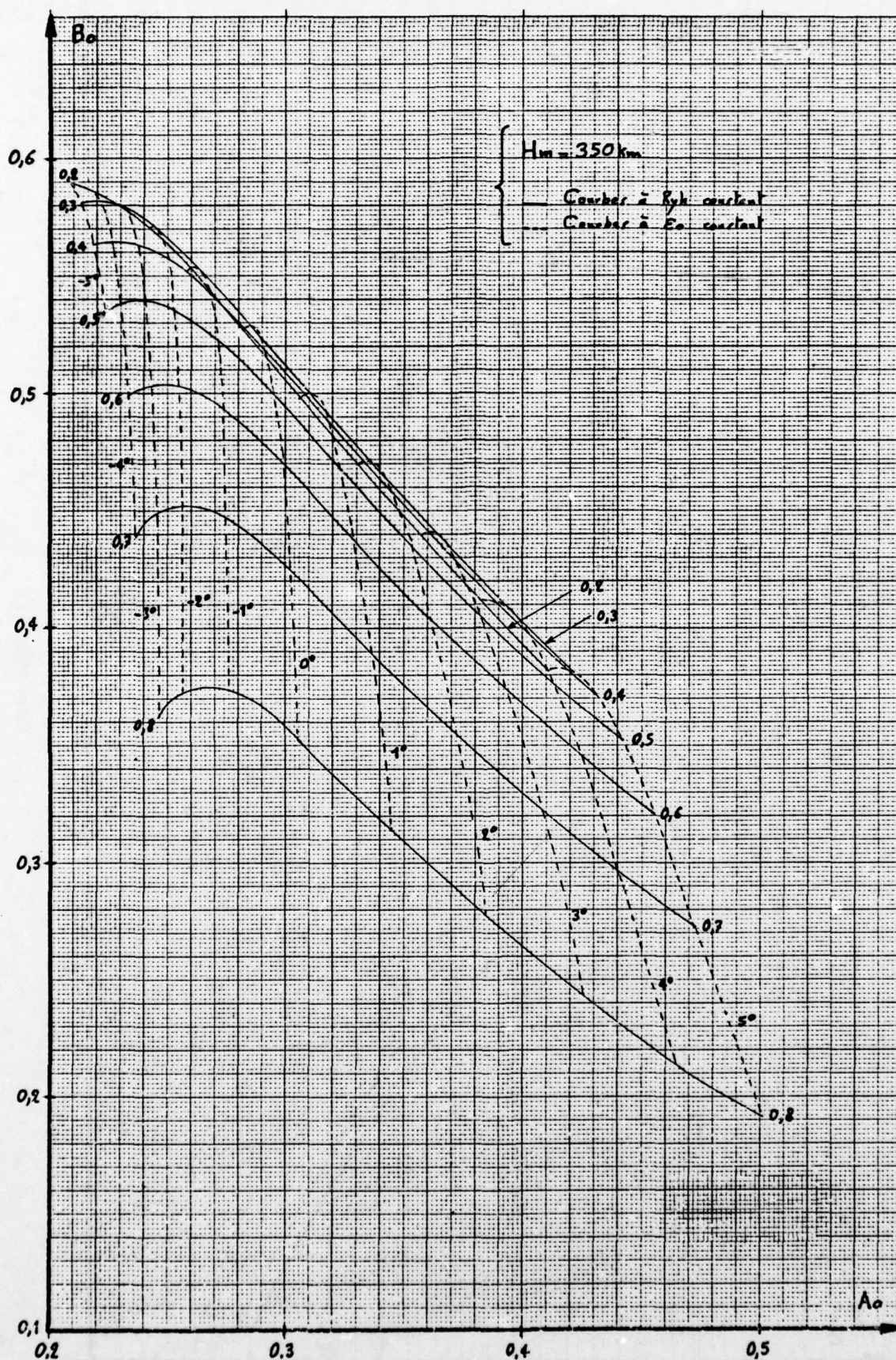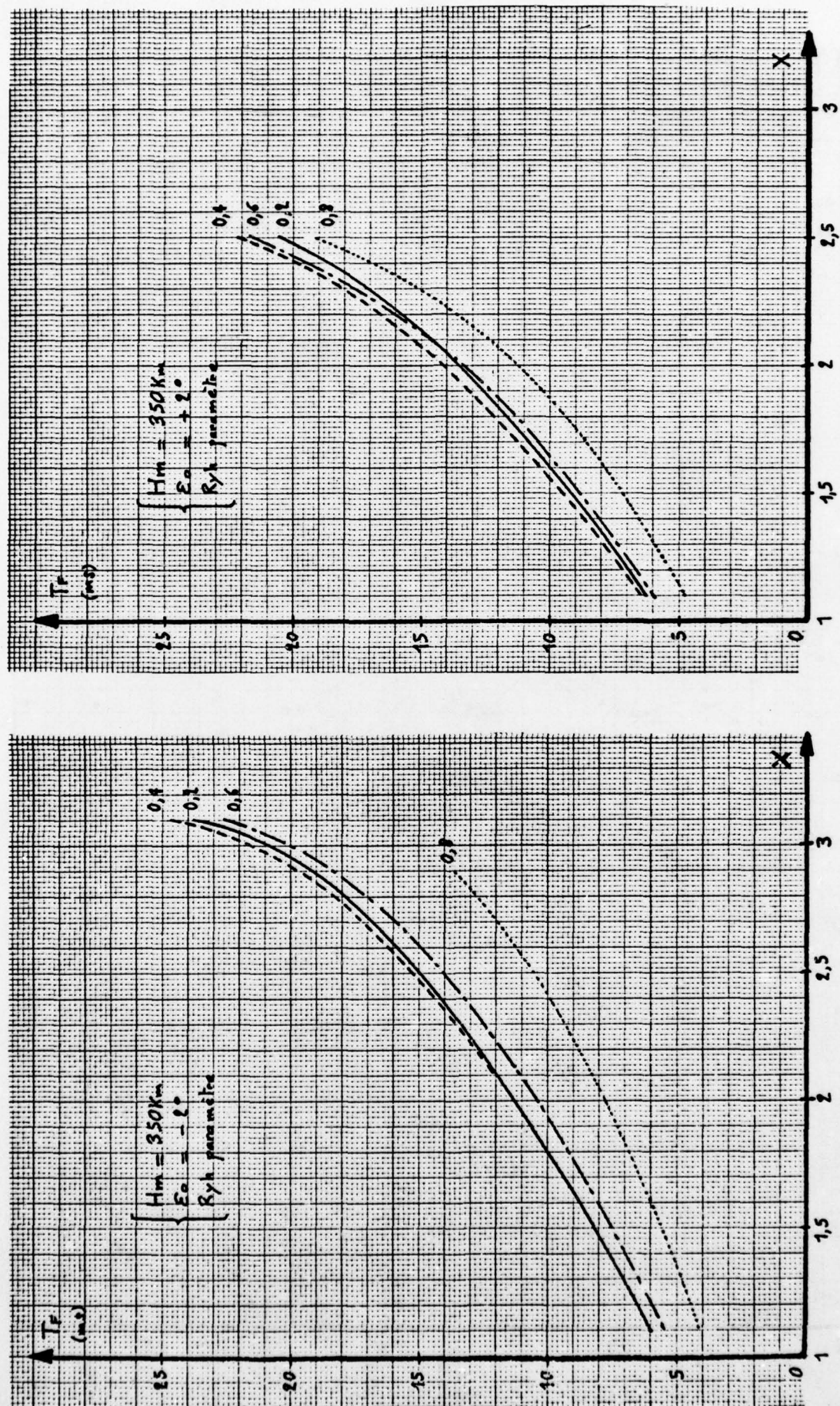
Figure 12

Figure 13

Figure 14
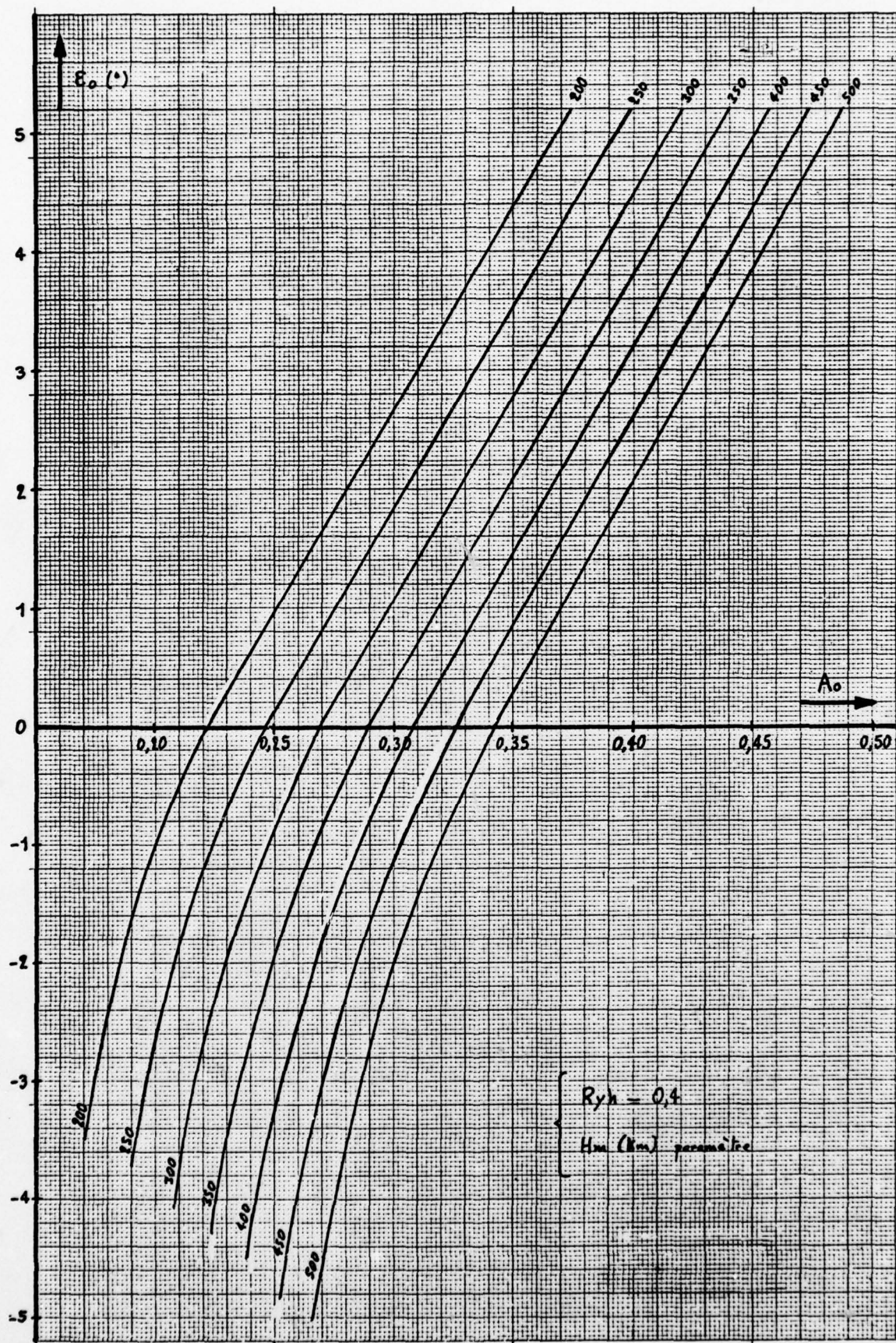
Figure 15
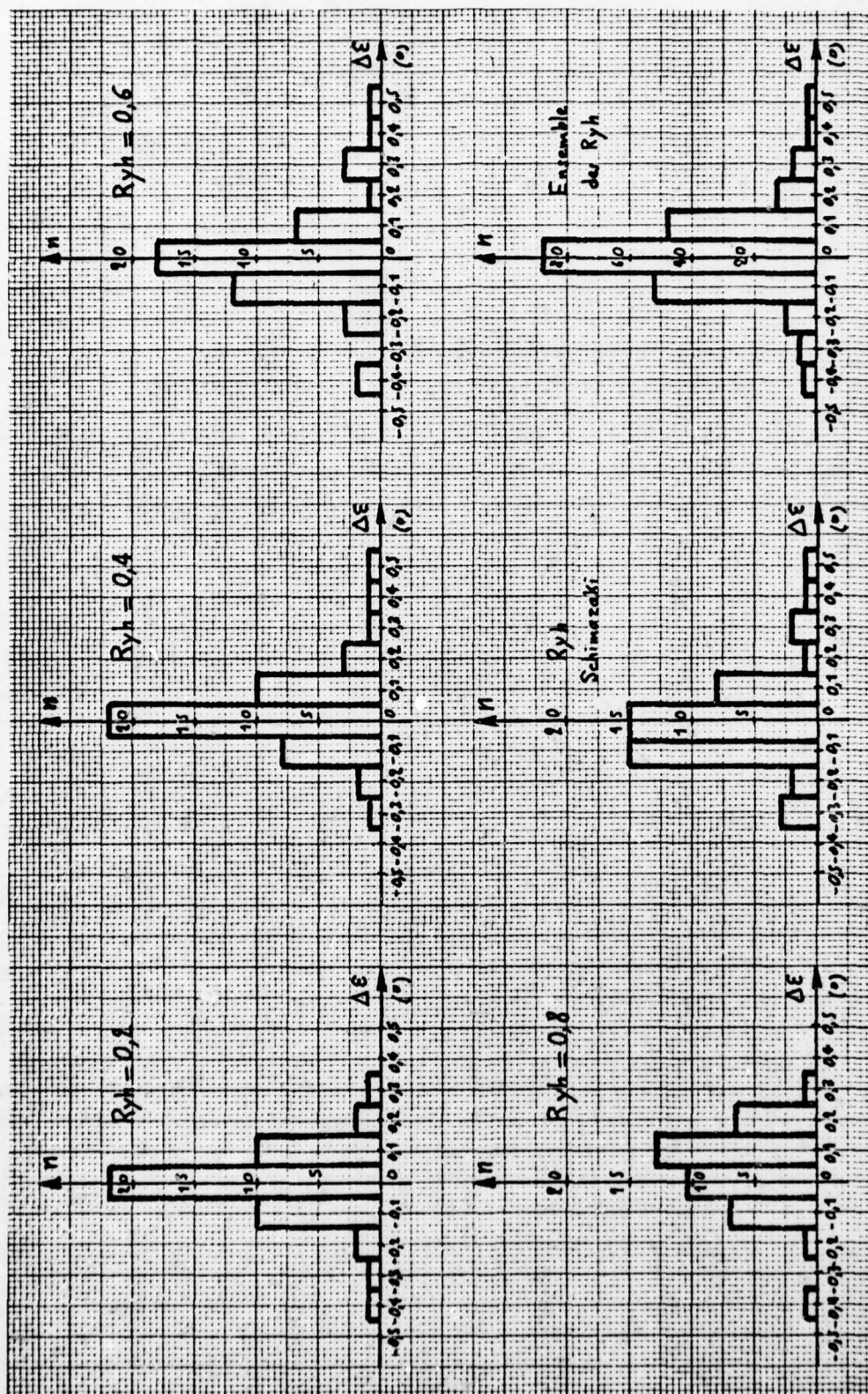
Figure 16
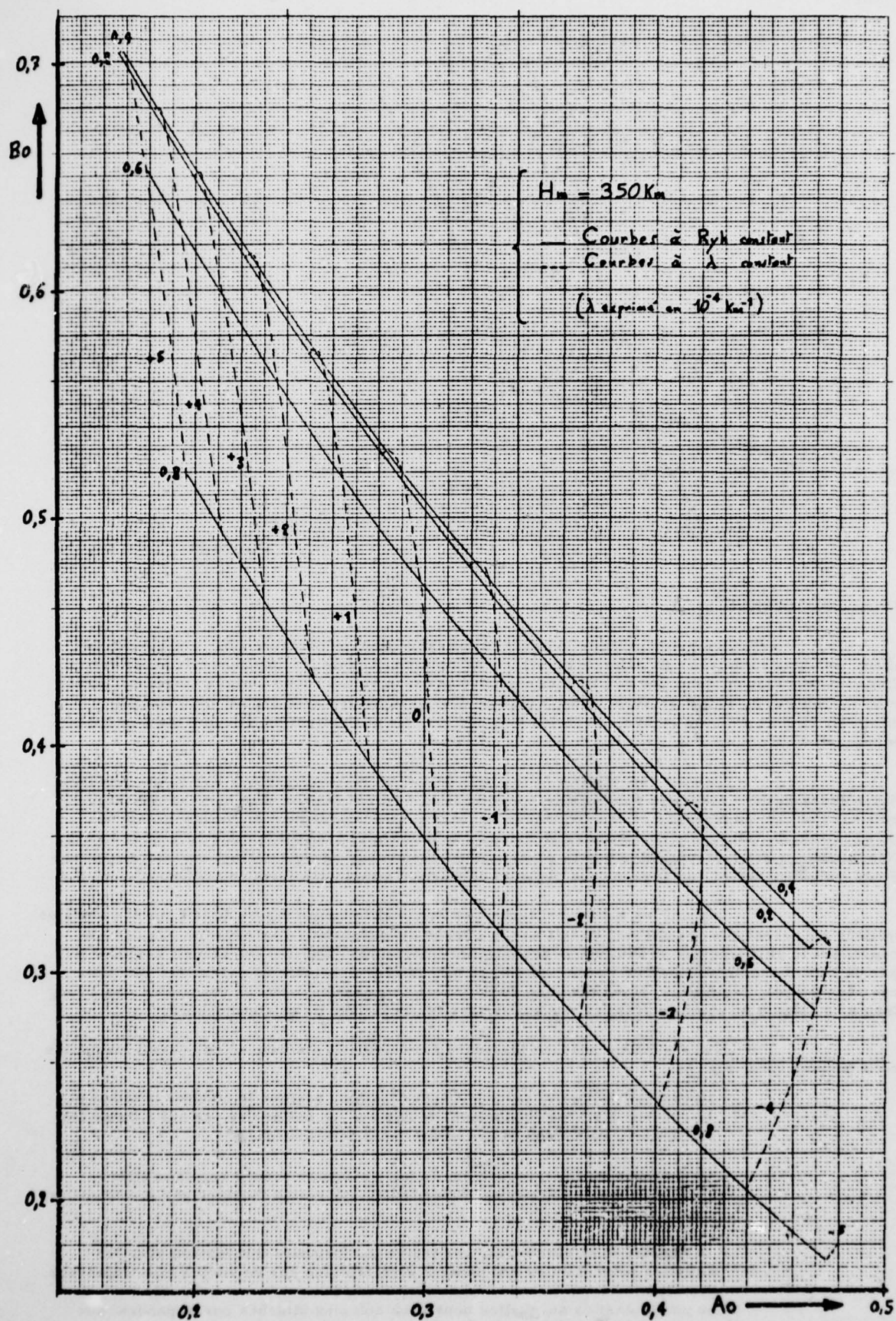
Figure 17
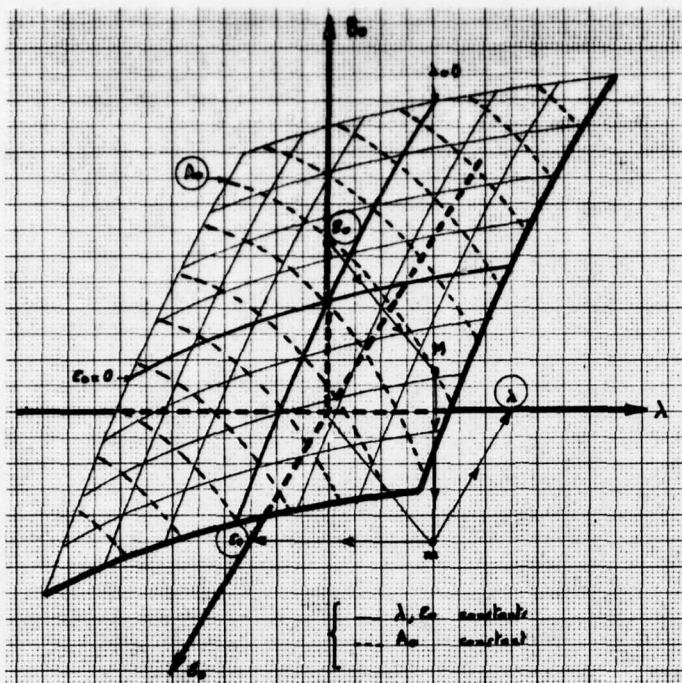
Figure 18

IV - CONCLUSION

Le principe de la méthode d'inversion peut se résumer ainsi : le modèle est défini par 5 paramètres : Fc, Hm, Ryh λ et $\mathcal{E}_o$ qui constituent les inconnues du problème. Les mesures doivent donc fournir au minimum 5 données, comme l'ionogramme de rétrodiffusion n'en fournit que 2, il faut en rechercher 3 autres. Ces paramètres sont déduits d'un sondage zénithal, ce sont Fc, Hm et Ryh. Associés à A et à Bo, ils permettent de calculer les 2 grandeurs manquantes λ et $\mathcal{E}_o$ avec une précision convenable.

On peut reprocher à la méthode le fait qu'elle suppose que Ryh et les gradients horizontaux restent constants dans tout le domaine situé entre la station et la zone de réflexion, soit sur 1500 km en moyenne. Cette hypothèse se justifie raisonnablement en milieu de journée ou en milieu de nuit, mais devient invalide pendant la période de transition entre le jour et la nuit. Néanmoins, il est vraisemblable que la régularité du phénomène devrait permettre, moyennant une étude complémentaire, de dégager une règle de correction simple des formules donnant λ et $\mathcal{E}_o$

Parmi les autres critiques que l'on peut formuler figure le fait que les modèles utilisés supposent que la réflexion se fait sur la couche supérieure de l'ionosphère. Ce cas est cependant le plus fréquent et l'influence des couches inférieures (E et F 1) se traduit simplement par un retard supplémentaire de l'onde, ou encore par un accroissement du paramètre Bo. Comme ces couches sont régulières, il est possible de déduire leurs caractéristiques des prévisions à long terme, ou bien d'un sondage zénithal, et de corriger le coefficient Bo en conséquence.

Notre méthode possède plusieurs particularités intéressantes, parmi lesquelles nous pouvons citer :

- la centralisation des moyens d'investigation, puisque le sondeur zénithal et le sondeur à rétrodiffusion sont réunis sur un même site, ce qui élimine les problèmes de liaison et de transfert des informations.

- l'autonomie qu'elle procure par le fait qu'aucune donnée supplémentaire (cartes d'ionisation par exemple), autre que celles fournies par les sondeurs, n'est exigée.

- la rapidité et la simplicité, car toutes les formules d'inversion sont des formules polynomiales qui peuvent être traitées par un simple micropresseur.

Ces particularités auxquelles nous nous sommes attachés correspondent aux caractéristiques d'un système de gestion simple d'un réseau de transmission.

BIBLIOGRAPHIE
========================

(1)   J. W.   AMES, R. D. EGAN - Digital recording and short-term prediction of
        oblique ionospheric propagation. IEEE Antennas and propagation.vol AP
        I5 n° 3 MAY 1967

(2) The use of ionospheric sounders to improve H. F communication.
        Grange associates technical bulletin n°3 March 66

(3) C. GOUTELARD - Analyse de la structure fine des échos de sol obtenus par
        rétrodiffusion des ondes décamétriques sur le sol.
        Thèse d'Etat 1968

(4) T. SCHIMAZAKI - Worl - wide daily variations in the heigt of the maximum electron
        density in the ionospheric F 2 layer. J. Radio Research Laboraty -Japan -
        2 (1) -85-97   1955

(5) P. A BRADLEY and J. R. DUDENEY. A simple model of the vertical distribution
        of electron concentration in the ionosphere. Journal of Atmospheric and
        terrestrial physics - 1973 -Vol 35 p. 2131 à 2146

(6) GOUTELARD. C. - CARATORI. J. - COATANHAY J. L. - ROLLAND R. - Application
        de la technique backscatter aux prévisions de transmission ionosphèrique
        à trés court terme. 23ème Symposium AGARD ou Electromagnetic Wave
        Propagation - Cambridge - U. S. A. - Octobre I977

(7) RAO N. N. - Synthesis of three - dimensionnal ionograms - Radio Science - Vol. 8
        n°5 - May 1973 - pages 449 -45I

(8) FOLKESTAD K. - Exact ray computations in a tilted ionosphere with no magnetic field
        Radio Science Vol. 3 New series - n°1 -

(9) BORN M. and WOLF E. - Principles of optics - Pengamon Press - 1965

(10) INSTON H. H. and CURTIS A. R. - Ray tracing and its application to the computation
        of frequency deviations in a high - frequency signal - Radio Science - Vol 3
        New series n° 1 - January 1968

DISCUSSION

P.A.Bradley, UK

Have you made any comparisons between the ionization gradients found from your measurements with those given from predictions?

Author's Reply

We have compared the horizontal ionization gradients which we have included in our model with those which we have derived from the ionization charts. This comparison leads us to three remarks:

— The model is utilizable in the areas of mid latitudes, which limits its application to these areas, as I pointed out.

— The model is not applicable to the equatorial and polar regions, in view of the excessively reduced extent of the constant gradients.

— The application of the model to mid latitudes is based on the assumption that the gradients can be regarded as constant throughout the portion of the ionosphere crossed by the rays of the backscatter sounder. However, an approximation can be admitted, since the influence on transmission parameters generally remains small. However, the introduction of a corrective term for day to night transitions, when errors are at their maximum, has been considered.

T.B.Jones, UK

This is the first mention at this meeting of the use of measurement of the parameters of the model by direct experimental methods to update prediction programs. This is an interesting and fruitful way to proceed.

WINTER ANOMALY OF RADIO WAVE ABSORPTION
AND D-REGION MODIFICATION

Hans-Ulrich Widdel
Max-Planck-Institut für Aeronomie
D-3411 Katlenburg-Lindau 3, FRG

1.   THE PHENOMENOLOGY OF WINTER-ANOMALOUS RADIO WAVE ABSORPTION

Winter-anomalous radio wave absorption is a phenomenon which is observed in every winter over places located above about 35° latitude independent of solar activity. This is illustrated in Fig. 1 which shows the results of short wave radio wave absorption measurements obtained in southern Spain (38° northern latitude).

For a quantitative description of winter-anomalous radio wave absorption one has the choice between a number of different parameters, each having its advantages and disadvantages. We decided to use the average noon absorption L_M (1100-1400 local time) which is presented on the left of Fig. 1, and the parameter $L_D = L(\cos X(t)\ d\ (\cos X(t)$ (L is the absorption value measured at sun's zenith angle X) shown on the right of Fig. 1. This latter parameter L_D has the advantage that the seasonal variation of the sun's zenith angle is eliminated and is by this very suitable for quantitative comparisons of results obtained over locations in different latitudes and longitudes (ROSE et al., 1974). Further, this parameter was found to yield the best correlation when the results obtained on two locations were compared. To data obtained in southern Spain is referred here because they represent a time series of measurements on a latitude which corresponds to that of Wallops Island and which is not too different from that of White Sands. A fairly large number of in-situ measurements were performed over White Sands and Wallops Island in the past with sounding rockets and we have reasons to assume that the morphology of winter-anomaly over these locations is similar to that what we have observed in southern Europe. The results shown in Fig. 1 show clearly that the winter-anomalous absorption occurs over this latitude in groups of days ("waves") which are separated by shorter or longer periods of very low absorption. The same peculiarity was found in observations which were made in similar or even lower latitudes over Japan (e.g. WAKAI et al., 1970). It would be of interest to know if this peculiarity is also common to comparable latitudes in the North American continent.

The amount of winter-anomaly and its beginning (phase) was found to vary from year to year. This can be demonstrated in two ways: If one applies Fourier analysis to the data sets of one complete year and synthesizes the trend by taking into account only the first five Fourier coefficients, and determines then the maximum, one sees that the phase of the maximum is modulated by a period of roughly four years (Fig. 2). This period is also obtained if one averages the absorption for the winter months September to December, as is shown in Fig. 3. The general slope of the curve shown in Fig. 3 might represent the influence of the suns' activity while the peaks represent the phase modulation. If one averages the data of the second half of the winter (January to May), negative peaks appear (Fig. 4). This results suggests that the phase modulation of the onset of the winter-anomalous absorption derived from the data was real. The variation of the average sunspot number over the years of absorption is shown in Fig. 5. It is of interest to note that winter anomaly was quite strong in winter 1974/75 despite decreasing sunspot activity and its beginning was earlier than in the two years before. Unfortunately the series of continuous observation was not long enough to establish the significance of the quasi-four-years period which the data might suggest.

In more northern latitudes, the group structure of the winter anomaly is often masked by a background anomaly which starts and ends at about solstices (e.g. SCHWENTEK, 1971). Winter anomalous absorption seems to occur there more symmetrical to midwinter than it seems to be the case in low latitudes.

2.   SUGGESTION OF THE CAUSE OF WINTER-ANOMALOUS RADIO WAVE ABSORPTION

Comprehensive reviews about winter-anomaly and its causes have been given by SECHRIST (1972), THOMAS (1974) and SECHRIST (1975). They cover both the different theories and discuss the observations made in North America. Following MANSON (1971), GREGORY and MANSON (1969, 1970, 1975), ZIMMERMANN and NARCISI (1970) and THOMAS (1975), winter-anomaly, especially its group structure, is a manifestation of meteorological phenomena in the atmosphere of the ionospheric D-region, while MAEHLUM (1967) suggests that winter anomaly is caused by drizzling particles. Both suggestions have in common the supposition that an increased number density of nitric oxide is the primary source for the enhanced electron density in the D-region under winter-anomalous conditions.

3.   EXPERIMENTAL CHECKS

The meteorologic interpretation for the cause of winter-anomalous absorption gets quite some support if satellite radiance maps are compared which show the movement of large structures over the hemispheres. We could assign qualitatively the movement of certain structures seen in the radiance maps with the onset or disappearance of groups of days with winter-anomalous high absorption but a quantitative analysis did not yield a significant result because the satellite data lacked spatial resolution. (We had only data from the Oxford-Heriot radiometer to compare with which was flown on Nimbus IV).

3.1.   Correlation between local wind and radio wave absorption.

If there is a connection between meteorological phenomena and winter-anomalous absorption, one should expect a relation between winds in the D-region atmosphere and winter-anomalous absorption. To prove that such a relation exists, is, however, somewhat difficult because one cannot expect a 1:1 correlation between winds measured in different heights and the absorption which is measured from the ground as an integral value. A fairly large set of data pairs of wind and absorption measurements is required which has to cover both winter-anomalous and non-winter-anomalous conditions. This is hard to meet during one winter only. The most promising conditions for a successful attempt for this kind of correlation are found in locations where the winter-anomaly effect occurs in groups of days which are
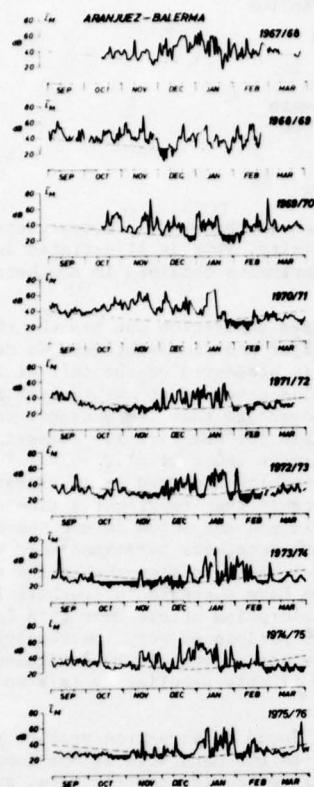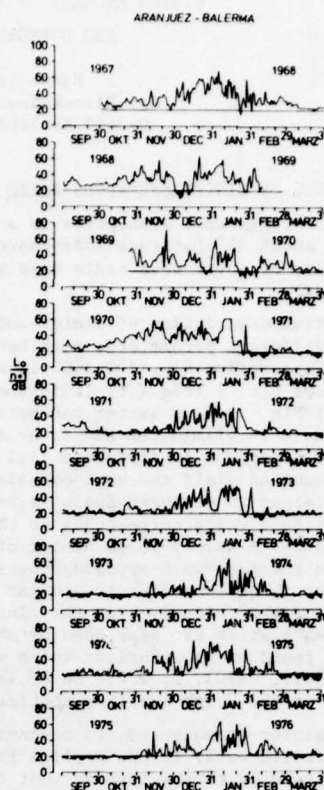
Fig. 1a   Fig. 1b

Fig. 1   Results of short wave radio wave absorption obtained in Spain (38°N, A3 Method). Left: noon averages, right: parameter $L_D = L_o/n+1$. This parameter does not contain anymore the seasonal variation of the sun's zenith angle. Shaded areas: periods of very low absorption. (Reference level: Summer-time average of L_D.)
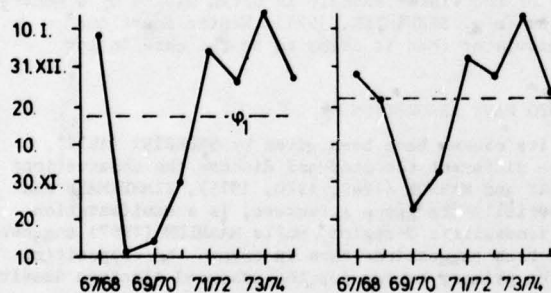
Fig. 2   Phase modulation of maximum of winter-anomalous absorption left: subsolar absorption L_o, right: parameter $L_o/n+1$.

Fig. 3   Phase modulation of occurrence of winter-anomalous absorption. Means 1 September to 31 December of each winter. Indication of a quasi-four years period. Symbols "+" and "-" indicate sign of significant correlation coefficients between (tropospheric) vorticity area index and short wave radio wave absorption.

MEANS OF ABSORPTION PARAMETER L_D
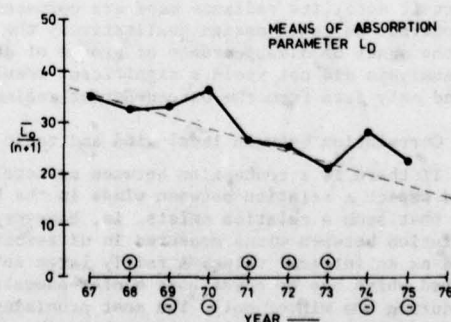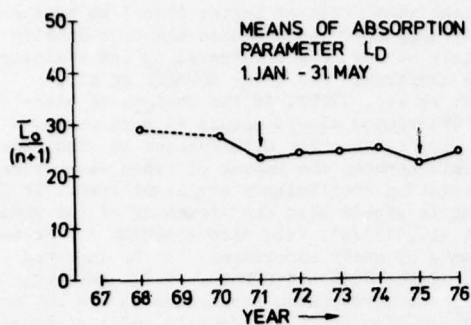
Fig. 4   Same as Fig. 3, but means of absorption
          1 January to 31 May of relevant year.
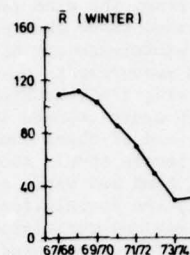
Fig. 5   Corresponding average sunspot numbers
          (for winter months) of observation
          period.
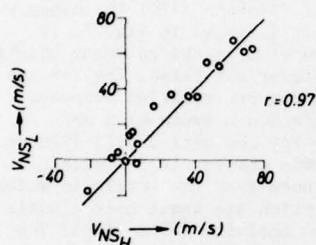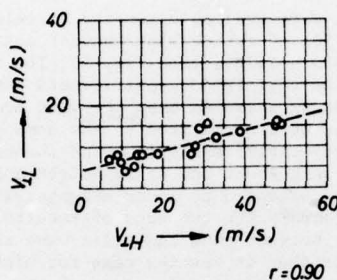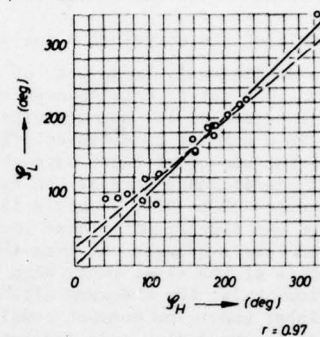
Fig. 6a   Fig. 6b   Fig. 6c

Fig. 6   Results of an experiment in which two foil clouds were released simultaneously in the same
          height. The elements of the foil clouds had the same size (9 mm wide, 50 mm long) but differed
          in weight by a factor 5 (cloud 1: (index H, heavy) foil thickness 10 μm; cloud 2: (index L,
          light) foil thickness 2.5 μm. The latter elements were used in all other experiments referred
          to here.) v_{NS}: meridional component, $v_\perp$: descend velocity, φ: azimuth.
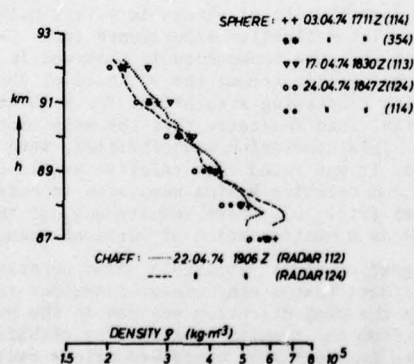
Fig. 7   Comparison between air densities
          derived from falling spheres and
          from foil clouds. Each experiment
          (with one excemption) was tracked
          by two independent precision radars.

well separated by periods of very low absorption. This is the case over comparatively low latitudes remote from the auroral zone. The wind measurement should have a height resolution of better than 1 km because the results of ground-based absorption measurements suggest already that the enhanced electron density which causes the winter-anomaly effect occurs mainly in a fairly narrow height interval in the vicinity of 85 km. In-situ measurements performed over Wallops Islands confirmed this (e.g. BOWHILL et al., 1967; MECHTLY et al., 1967; MECHTLY and SHIRKE, 1968; SECHRIST et al., 1969). If the changes of electron density which cause changes in the amount of radio wave absorption always occurs in more or less the same heights, and if these changes are connected in some way or the other with changes in wind, the sensitive height levels should show up in a correlation analysis between the amount of radio wave absorption measured on the ground and winds as regions in which the correlation coefficients are significant. It is possible to modify the correlation analysis in such a way that it yields also the direction of the wind which causes the maximum correlation with absorption (ROSE et al., 1972a). (See also Appendix 1.) We used foil clouds ("chaff") for our wind measurements. The performance of chaff experiments can be improved when the cloud is generated in a special manner (ROSE et al., 1972b, ROSE and WIDDEL, 1977). Further, when the elements of the chaff cloud are properly matched in their aerodynamic properties to the environs where they are supposed to yield useful measurements, some information about air density and its changes can also be obtained. However, the sensitivity of chaff clouds against strong wind shears and turbulent air motions which impair the quality of the data cannot be completely removed.

What can be achieved is shown in Fig. 6 and Fig. 7: Fig. 6 shows the result of an experiment in which two foil clouds were released in the same height and were independently tracked by two radars. The reflector elements differed by weight and width. Fig. 7 shows the results of a comparison between air densities derived from falling spheres and from foil clouds which were flown over the same location in the same period. Each experiment was tracked with two independently operating precision radars.

3.1.1.Result of the correlation analysis between wind and absorption

Two sufficiently large sets of data were available for the correlation analysis between wind and absorption. One set of data covered a period of rather high sunspot activity (1968 to 1970) the other was obtained a period of low sun activity (1973 - 1976). (See Fig. 5). The result is shown in Fig. 8. It displays in a compass card presentation the correlation coefficients between wind in the relevant height level and the amount of radio wave absorption measured when the wind measurement was taken. The circles represent significance levels. The figures were normalized to the same size for presentation purposes. For the period 1968-1970, we could identify three levels in which the correlation between wind and absorption was significant. These levels were about one scale height apart. For the period 1973-1976 we found four levels because the measurements extended to lower heights. This was the result of certain improvements of the experiment. When we compare the two sets of results we note that the levels in which correlations exist for the same direction between wind and radio wave absorption are about half a scale height higher under low sunspot conditions than it was the case for high sun activity (1968-1970). The fall rates of the foil clouds indicate a corresponding increase of the air pressure parallel to the decrease of the sun's activity at least in the height region around 88 to 80 km. Below that height the accuracy of the measurement is impaired by turbulent air motions which produce quite some scatter of the data. It was therefore difficult to relate observed changes in the descend velocity to density variations there. The variation of EUV radiations with solar activity (SCHMIDTKE, 1977) may have caused the observed differences in air density and height levels for which a correlation between wind and absorption was found. It may also explain the more pronounced correlation between absorption and wind in the 90-93 km level for the period 1968-1970 when the activity of the sun was high.

It is however difficult to assess if these levels of correlation between absorption and wind mean advection of minor consistuents or if they mirror convection processes, but there are indeed some indications in favour of convection:

When the height distribution of strong windshears (Fig. 9) is related to the levels in which significant correlations were found between wind and absorption, one finds that these levels are located within the windshear bands. This indicates that turbulence and by this, convection processes play an important role for changes of absorption. The height distribution of shears is very similar to that found for the height distribution of preferred echoes in partial reflection experiments (e.g. GREGORY, 1961, TITHERIDGE, 1962). This similarity suggests to assume that the same phenomenon is observed in both cases. It could be shown (WIDDEL, 1978) that a vertical subsidence motion around the 90 km level which was indicated by an increase of airglow intensity does correlate with increasing absorption. For high winter-anomalous absorption however this correlation ceases to exist. This indicates that the main contribution to absorption is then delivered from levels far below 90 km. This conclusion was confirmed, when the height distribution of absorption contribution was considered. It was found that relative maxima of absorption contribution were located in levels of wind shears and relative minima were seen in heights were such strong wind shears were absent for most of the time (Fig. 10). These results suggest that the correlations between wind and absorption can be interpreted as a manifestation of vertical transport and mixing phenomena.

Advection in the sense of transport of easily-ionisable minor constituents is more difficult to prove. The local wind measurements indicate that strong winter-anomalous radio wave absorption is linked to westerlies and ceases to exist when the wind direction changes in the D-region. This observation confirms a conclusion which can be drawn from the results published by SECHRIST et al. (1969) which were obtained over Wallops Island. Therefore it seems that winter-anomalous radio wave absorption is entrapped in a large low-pressure system. When the results of ground-based short wave radio wave absorption obtained over different sites separated by at least 800-1500 km are analyzed, one can derive a "pattern drift" from west-north-west to east-south east with a speed in the order of a few meters per second (ROSE and WIDDEL, 1977). This kind of analysis, however, is rather difficult and ambiguous and yields only rough figures.

3.2 Electron density profiles:
Time history of the development of the winter-anomalous state of the D-region

Electron density profiles representing the so-called "normal" and the "winter-anomalous" state of the D-region have been measured with in-situ-techniques over several places in the world, in the US (e.g. SECHRIST et al., 1969), in the U.K. (e.g. BEYNON and WILLIAMS, 1970, 1976; DICKINSON et al., 1977), in Norway (e.g. FOLKESTAD, 1970), and southwest Europe (e.g. DIEMINGER et al., 1974) on several occasions.
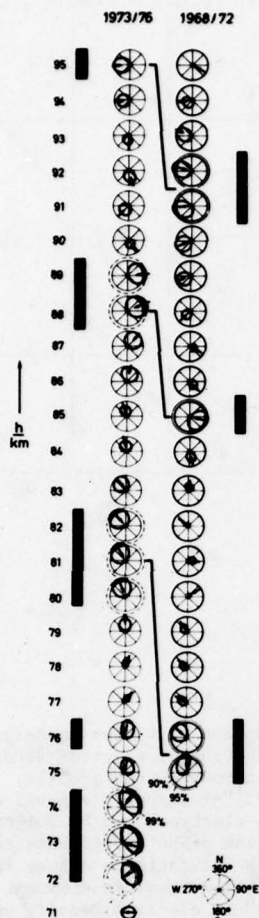
Fig. 8 Results of a correlation analysis between local wind and radio wave absorption measured simultaneously during flight. Left: period of very low solar activity. Right: period of high solar activity. The better height coverage for the period 1973-1976 was the result of certain improvements of the payload in respect to foil cloud generation.
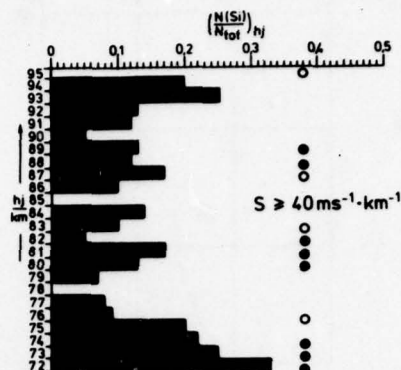
Fig. 9 Relation between wind shears and levels of significant correlations between absorption and wind. Levels of significant correlations between wind and absorption are located in height regions in which strong wind shears are present. This may be taken as an indication that vertical mixing processes play an important role for the formation of winter-anomalously high absorption.
Open circle: 90 % significance, shaded circles: ≥ 95 % significance.
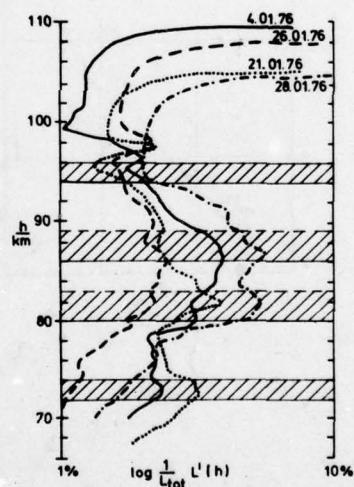
Fig. 10 Wind shear bands and absorption contribution ($L'(h) \sim N_e(h) \cdot v(h)$. (This parameter links directly the height distribution of electron density with the short wave radio wave absorption measured from the ground during the rocket's flight.) Relative maxima of absorption contribution are found predominantly in regions where strong wind shears are present. This suggests to assume that the height levels of prevailing echoes observed with partial reflections are identical with those in which strong wind shears are predominantly observed.
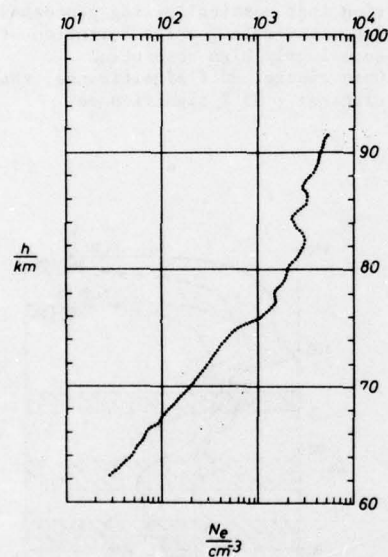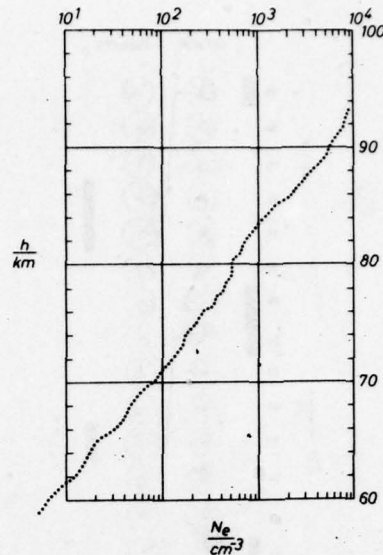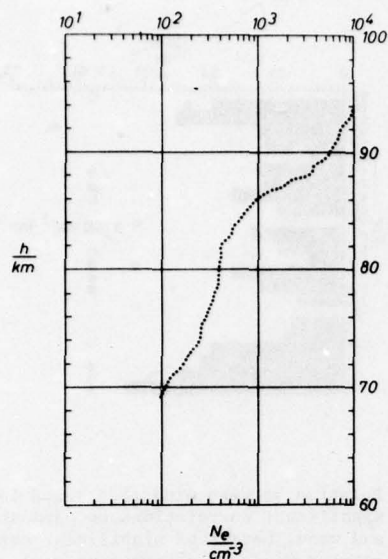
Fig. 11   Development of winter anomalous
(above   distribution of electron density.
and   Left: summer/autumn profile,
left)   middle: "precursor" (removal of the
           ledge, electrons can be followed with
           guardring probe experiments to lower
           heights indicating a change in the
           λ- ratio), right: development of a
           "bulge" in electron density under
           winter-anomalous conditions in about
           the same height level where the
           summer time ledge in electron density
           (depletion) is observed.

Fig. 12   Absorption contribution of an electron
(right)   density profile for different frequencies
           of an A3-absorption experiment.
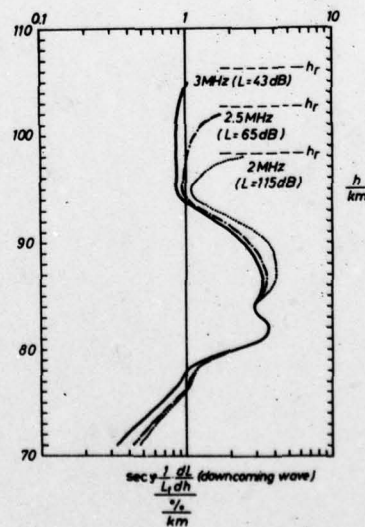
A common feature of all so-called normal profiles is that they display a more or less pronounced depletion of electron concentration in certain heights, the "ledge", which either disappears completely or is found to be shifted to lower heights when winter-anomalously high absorption is present (e.g. MECHTLY and SHIRKE, 1968; DICKINSON et al., 1977). We used for our own measurements a guardring probe (ROSE et al., 1972). The guardring of the probe provides certain advantages over the Standard configuration in respect to charge-up of insulator surfaces which shifts the potential and can be by this very annoying. In general, such probes have to be calibrated to yield absolute electron densities. This has been done with a wave propagation experiment flown on the same rocket (MECHTLY, 1974, THRANE, 1974). Certain constraints however prevented us from doing so and we replaced the in-situ-wave propagation experiment by ground-based experiments performed on the range. The procedure which we used for the conversion of the measured probe currents into ambient electron densities was described by (ROSE and WIDDEL, 1977). The probe was an isolated cone at the tip of the rocket to which a time-linear driving voltage swept from plus 3 Volt to minus 3 Volt and vice versa was applied. This allowed us to distinguish between currents caused by ions and electrons and to measure the probe-current voltage characteristics in the different height regions. Experience has shown that the zero shift in these current-voltage characteristics was very small on most of the flights.

Using meteorological rockets originally intended for measurements up to about 70-75 km which were modified to reach an apogee between 92-98 km, we could collect quite a few profiles of electron density which covered different states of the D-region. The largest number of these profiles were measured around noon time. This time was chosen because the D-region ionisation is then in most cases fully developed and does not change very much with time. From this collection of height profiles of electron density we could draw the following conclusions:

We found that the winter-anomalous state begins with a removal of the summer-like ledge in the electron profile (it stretches out to become nearly exponential with height). When the absorption increases and becomes highly winter-anomalous, a bulge of electron concentration develops in about the same height region where the "ledge" is found when conditions are "normal". Fig. 11 shows a selection of profiles which demonstrates this development which was observed in every year.

3.2.1. Winter anomaly precursors

This, however, is not the only peculiarity: When we inspect the profile in the middle of Fig. 11 more closely which is obviously a transitional or "precursor" profile for winter anomalous absorption, we note that we could distinguish electrons from ions in the current/voltage characteristics of our probe at much lower heights than was normally the case. This increase of density of free electrons in lower heights is obviously caused by a change of the ratio λ = number density of negative ions to the number density of free electrons. This change of electron density in lower heights is hard to detect by ground-based absorption measurements because their contribution to total absorption is very small. This is shown in Fig. 12 in which the absorption contribution for a given electron density profile is presented. The increase of electron density (or the change of λ) in heights below about 70 km before winter-anomalously high absorption commences was a regular feature. This can be seen in the time sequence of electron density profiles shown in Fig. 13. These electron density profiles were measured in the afternoon. At this time the electron density is reduced already by recombination or by the formation of negative ions. The corresponding absorption which was measured by ground-based means during that period is shown in Fig. 14. The absorption which was measured under precursor conditions was in most cases of medium amount. Medium absorption however corresponds at latitudes over which we made our measurements either to a height distribution of electron density which is very close to that observed under summer conditions or to a pre-phase of winter-anomalous absorption. This raises the question to what kind of profile a winter-anomalous height distribution of electron density should be referred to in order to derive electron density enhancement factors which allow a comparison of results obtained over different sites in different latitudes. This problem was discussed in part by BEYNON and WILLIAMS (1970). We observed that precursor profiles have another peculiarity which is by no means detectable by ground-based methods. This peculiarity is shown in Fig. 15. We had means to convert not only the probe currents caused by electrons into ambient electron densities but also for the currents caused by ions in the height levels below the D-region because we have flown a number of parachuted Gerdien experiments short before the guardring probes were launched. These Gerdien experiments yielded absolute data for ion density and mobility which allowed us to determine the calibration factor of the guardring probes. We found that the ion density was by a factor of 14-20 higher in the 40 km level when precursor conditions were present. In one case we found also that free electrons were present in appreciable numbers down to a height of about 38 km. This profile, though shown in the raw data of Fig. 15 was not converted into ambient ion densities because we were not sure if we could apply in this case the calibration factor derived for positive and negative ions. In-situ-measurements obtained on a separate flight which was launched shortly after the guardring probe experiment was terminated showed that this increase of ion density was not related to neutral air temperature. Further, we could not find an indication for a marked change in cosmic radiation assumed to be the dominant source for ionization in this height region. The simplest explanation for this observation is to assume a marked change of the loss rate of ionization. We shall refer to this later.

3.2.2. Consideration of the parameter: "Normalized absorption contribution"

When differences in the height distribution of electron density are to be related to the changes observed in the results of the ground-based absorption measurements, the importance of changes of electron density found in different heights is not immediately seen because the electron collision frequency as the second important parameter of relevance to short-wave radio wave absorption is not taken into account. For such references, the height distribution of absorption contribution Ne(h) v(h) is more suitable. A further advantage is obtained when the absorption contribution is normalized to the total absorption which is measured during the rocket's flight as an integral value. By doing this, profiles obtained under widely different absorption conditions can be compared directly and this allows to assess the importance of certain height regions of the D-region ionosphere in respect to absorption observed on the ground-based absorption monitor propagation path. This is shown in the sequence of profiles presented in Fig. 16. It presents absorption contribution profiles derived from noon measurements performed between 1973 and 1975 and a result which was obtained during the Aeronomy program in
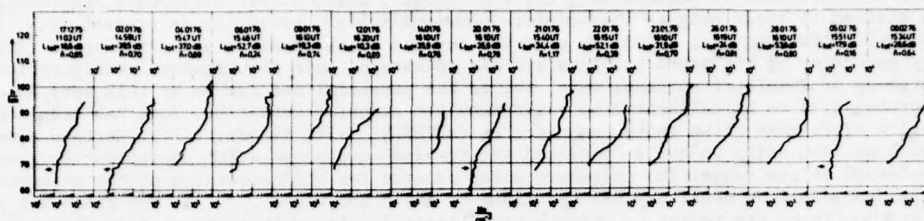
Fig. 13   Time sequence of electron density profiles measured in the afternoon during
           winter 1975/76 over El Arenosillo (Spain, 37°N)
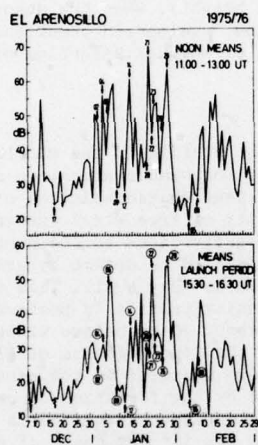
Fig. 14   Results of ground-based
           absorption measurements in
           the same period of time.
           Above: noon averages,
           below: means around launch
           time.
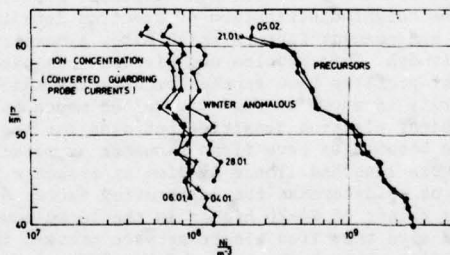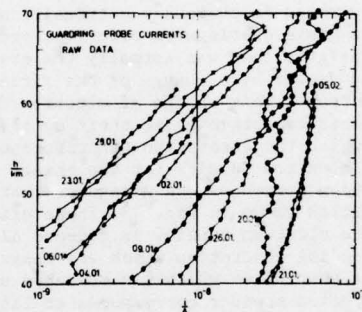
Fig. 15   Ion density changes below 60 km measured
           during winter 1975/76. Above: raw data
           (probe currents) below: converted into
           ambient ion densities using mobility
           data derived from Gerdien condenser
           experiments flown almost simultaneously.

winter 1976. The profiles were sorted into groups of about equal amount of absorption. The contributions from height levels above about 92-95 km are delivered mainly by deviative absorption. It was found that this contribution was fairly constant under all conditions. Because this deviative contribution is of no particular interest here it was omitted in this presentation. The profiles within the different groups show differences which are related to the shape of the diurnal variation of absorption. This diurnal variation of absorption is described by the $\cos^n$ X-law: $L(t) = L_o \cdot \cos^n X(t)$. L_o (Subsolar absorption) and exponent "n" are determined from the measured data by least-square fit methods. Despite the accuracy which can be obtained for "n" is not very high and this kind of work is in general considered to be not too much rewarding, we noted however that a noon profile which displays a higher contribution (relative maximum) below about 78 km was related to a higher $\cos^n$ X-index n than that which had a larger contribution from height levels above about 80-82 km or at the 88-90 km level. This was true also for summer-time profiles. When the absorption was winter-anomalously high, the $\cos^n$ X-index n is in most cases very low and we find that the contribution to absorption from levels below about 78 km becomes less important. The main contribution is then delivered from height levels between about 78 and 86 km. HAUG and LADMARK (1970) developed a two-ion model to explain the diurnal variation of absorption which was applied and eludicated by several authors, e.g. FOLKESTAD and ARMSTRONG (1970), FOLKESTAD et al., 1972; ARMSTRONG et al., 1970). This model comprised two electron loss processes, and SECHRIST (1972) has suggested to use three different electron loss rate constants to be applied in different height intervals. RAWER generalized in 1943 early work of BEST and RATCLIFFE (1938) and derived different cos X-exponents "n" by considering the relative scale height of minor constituents assumed to be the source of ionisation in respect to the scale height of the atmosphere. He assumed the reflector for the wave to be at a fixed height (an assumption which is quite well met when the A3-method for absorption measurement is used and the operational frequency of the circuits is properly chosen) and neglected the influence of deviative absorption. He obtained for "small" scale heights a cos X-exponent n = o.5 when the electron loss process L is proportional to N_e^2, for a loss process $L \propto N_e$ (attachment-like) n was = 1, and for a scale height of the trace constituent equal to the scale height of the atmosphere he obtained $n = 1.5$ ($L \propto N_e^2$) and $2(L \propto N_e)$. Taking into account that the deviative absorption tends to lower the $\cos^n$ X-exponent n and that the height regime below about 80 km is ruled by water clusters (which means that an appreciable amount of water must be present there), while the height regime above about 88 km is governed by a loss process proportional N_e^2 (recombination in its different forms) and that water clusters seem to be confined to heights below that level we are tempted to interprete the observed $\cos^n$ X-indices as being caused by contributions from fairly well-defined height levels governed by different electron loss processes. One level is located below about 80 km (the electron loss process is there $\propto N_e$, equivalent to attachment) and the other above about 80-82 km in which the electron loss process is $\propto N^2$. The low cos X-index "n" often found suggests that recombination is then the dominant loss process, and, to put the argument further, that a substantial depletion of the water content in this region occurs under such conditions. This seems to be indeed the case as shall be outlined later. But we have to check first if the interpretation that two quite well-defined height levels (fairly well separated by the mesopause and ruled by different electron loss processes) determine the diurnal variation of absorption by supplying varying amounts of contribution to absorption can be supported by more arguments. One support is given by the fact that up to now we did not find any noon-time absorption contribution profile which had a dominant maximum contribution to absorption from height levels above 82 km when the diurnal variation of absorption was described by a large (n $>$ 1) $\cos^n$ X-index, or a noon profile which indicated a dominant contribution from height levels below 78-80 km when the $\cos^n$ X-index n was small. Further, one would expect a relatively large contribution from height levels below about 78-80 km on a winter-anomalous day when the absorption is described by a large (n $>$ 1) cos X-exponent. This was indeed observed as is shown in the examples presented in Fig. 17. Another support is given by the observation that on days on which the noon absorption was about the same and their diurnal variation of absorption was described by about the same $\cos^n$ X-index, the relevant absorption contribution profiles had a very similar height distribution. Within certain limits set by principle, the $\cos^n$ X-index n and the absorption contribution profile supplies therefore some information about D-region processes.

4. ABSORPTION CONTRIBUTION AND THE DEVELOPMENT OF THE WINTER-ANOMALOUS STATE OF THE D-REGION

A series of electron density profiles obtained by conversion of guardring probe measurements was presented in Fig. 13. These measurements were performed in the afternoon hours on a number of days during winter 1975/76. At this time, the faster electron loss processes have removed already a certain number of electrons in the lower part of the D-region. The results of our guardring probe measurements indicated that the formation of negative ions was then the dominant loss process there.

Fig. 18 shows the change of the normalized absorption contribution profile during the development of two "winter anomaly waves" which started on 2. and 20 January. The "winter-anomaly wave" which started on 20 January developed about two times faster than that which began on 2 January. The profiles shown in Fig. 18 represent therefore more or less the same phases of winter anomaly development. These profiles show that the maximum of absorption contribution profile travels upwards and that a ledge in absorption contribution travels upwards too and then downwards or disappears when high winter-anomalous absorption is present. This winter-anomalous state is ended by a removal of the bulge and a re-formation of a ledge which could not be defined with confidence for the profile determined for the 9 January because the number density of negative ions was then too high but it was clearly seen on 23 January 1976 (Fig. 18, right). Variations in the height of the ledge have been observed frequently for winter-time electron density profiles (e.g. DICKINSON et al., 1976) and were sometimes interpreted as the result of downward transport. Mass spectrometer measurements were performed on 4 and 21 January about one hour before the guardring probe was launched (ARNOLD and KRANKOWSKY, 1978). As Fig. 19 shows (ARNOLD and KRANKOWSKY) the ledge which was observed on those two days was found to start in the same height level where the number density of water cluster ions started to become reduced. This observation agrees with earlier results which showed that a seasonal variation of the height up to which cluster ions can be observed does exist (e.g. KRANKOWSKY et al., 1972). It is higher in summer and lower in winter.

Fig. 16a

Date	UT	L(dB)	n	X(°)	
07.12.73	1132	27.3	0.62	61.9	—
12.12.73	1108	28.4	0.95	64.0	---

Fig. 16b

Date	UT	L(dB)	n	X(°)	
05.12.73	1146	33.5	0.72	61.2	---
19.01.74	1133	33.3	0.96	59.8	—

Fig. 16c

Date	UT	L(dB)	n	X(°)	
25.01.73	1147	39.5	0.87	58.5	---
16.12.73	1129	43.5	1.22	62.9	—

Fig. 16d

Date	UT	L(dB)	n	X(°)	
06.01.76	1546	52.7	0.31	76.9	---
22.01.76	1616	52.1	0.31	78.1	—·—
28.01.76	1610	53.8	0.36	76.1	—
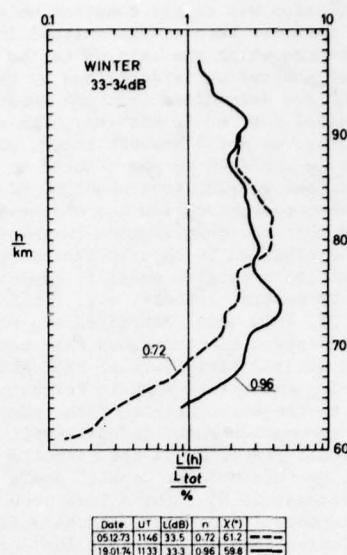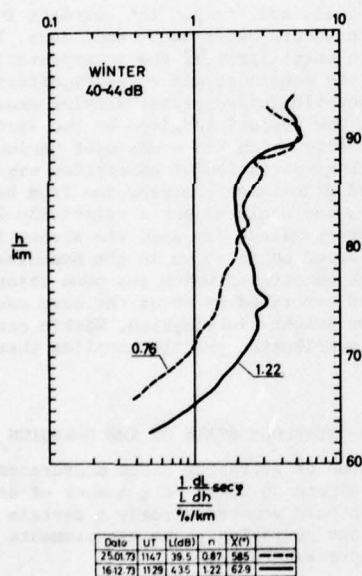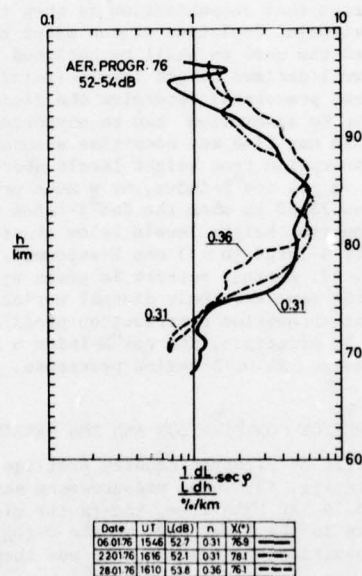
Fig. 16   Normalized absorption contribution profiles for different states of absorption which
show the relation between the height distribution of absorption and the form of
diurnal variation of absorption: When the diurnal variation of absorption is described
by a large "n" in the $\cos^n$ X-approximation, the relative contribution to absorption
is higher below about 80 km compared to the case when the same amount of absorption
is measured but the diurnal variation of absorption is described by a low "n" in the
$\cos^n$ X-law. Absorption contribution along the ray path (angle of incidence φ).
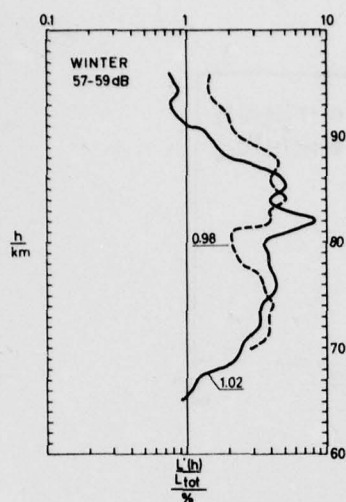
Fig. 17 Height distribution of normalized absorption contribution for winter-anomalously high absorption when the diurnal variation is described by a large "n" (n ≥ 1) in the cos^n X-law.
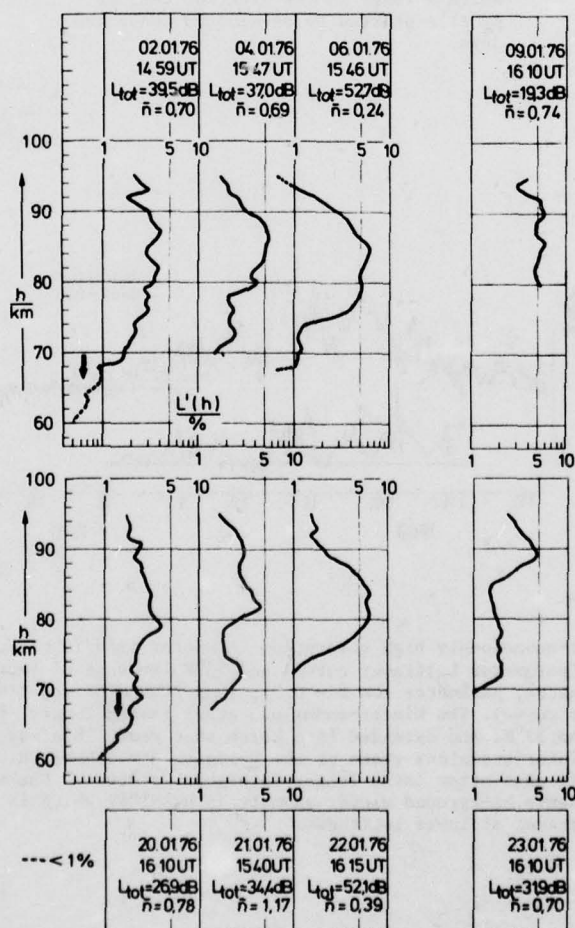
Fig. 18 The change of normalized absorption contribution during the development of "winter-anomaly waves" (in the sense of group of days with nomalously high absorption). Winter-anomalous high absorption starts with a reduction of the λ-ratio in heights below about 65 km.
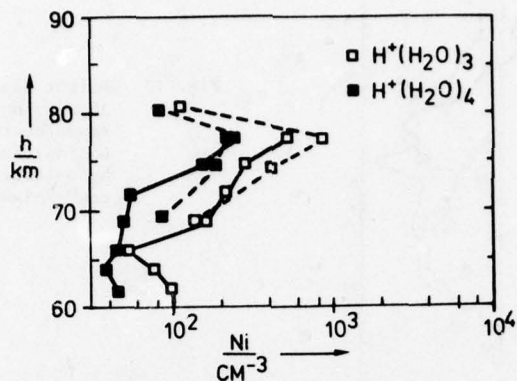
Fig. 19 Results of mass spectrometer measurements
of water cluster ions performed by ARNOLD
and KRANKOWSKY on 4 and 21 January 1976.
The height in which the water cluster ions
disappear coincided with the height in
which a ledge in the electron density
profile started to develop on these two
days.
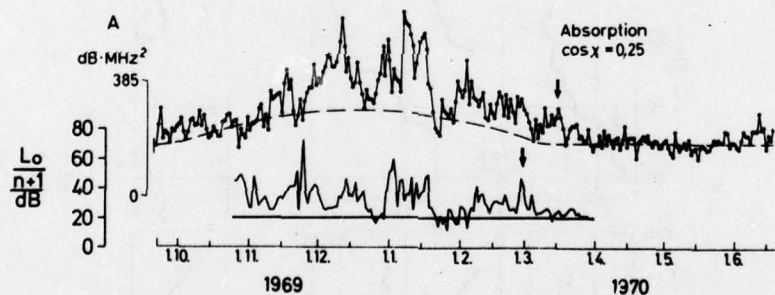
Fig. 20 Winter-anomalously high absorption in winter 1969/70 measured at
37°N (parameter L_D)(lower curve) and 53°N (average of three propaga-
tion paths, parameter cos X = 0.25, from SCHWENTEK and TIMPE, 1972)
(upper curve). The winter-anomalous state lasted longer over 53°N
than on 37°N, and extended into March that year. This suggests that
the winter-anomalous state of the D-region atmosphere which causes
WA high absorption lasts longer in higher latitudes. Dashed line
represents background winter anomaly (SCHWENTEK) which is apparently
not present at lower latitudes.

CONCLUSIONS

The results suggest that the enhanced electron density in the middle part of the D-region which manifests itself in winter-anomalously high absorption may be caused by the absence of a powerful scavenging agent which removes electrons through a fast electron loss process. This loss process includes the formation of negative ions, at least in lower heights. Negative ions have been measured by NARCISI (1972) and by ARNOLD et al. (1971) in March 1970 but the authors got different results. ARNOLD et al. found heavy clusters up to 80 (85) km only. NARCISI, however, who made his measurements in the same month saw a layer of rather large clusters in the height region between about 85 and 90 km which is the height range in which the ledge of electron density is found during summer time. The results seem to be conflicting at a first sight but this is not the case when the actual season and not the Julian date is considered. NARCISI made his measurements over White Sands which is located at about the same latitude as southern Spain. Over Southern Spain (as many seen from Fig. 1) the winter-anomalous state has ended in most cases in March, but sometimes post-cursors of winter-anomaly occur. This was the case at the end of February which lasted until about 10 of March. Going to more northern latitudes (Lindau, 53°N) we see that the state of the D-region was still winter-anomalous in March 1970. This state ended there approximately at the end of March (Fig. 20) (SCHWENTEK and TIMPE, 1972). For even higher latitudes, 63°N (Andoya) where ARNOLD et al. made their measurements, the winter-anomalous state of the D-region atmosphere must have been still present there at this time because it has been shown (ROSE, 1965) that the winter-anomalous state begins earlier and ends later in such high latitudes. Therefore we can suppose that NARCISI et al.'s measurements were made under summer conditions while the data of ARNOLD et al. represent still the winter state of the D-region. In order to check if negative ions are present in the height region above 86-90 km during summer at times when no eclipse occurs, we launched guardring probes under conditions more or less equivalent those under which NARCISI made his measurements. The result is shown in Fig. 21. The first launch was put a little too early. We could not distinguish electrons from negative ions until apogee. A partial reflection experiment which was operated simultaneously showed that electrons were present shortly above the apogee of the rocket at that time, rapidly developing downwards to lower heights with the increase of the sun's zenith angle. The next launch was made also at sunrise but at a little higher sun elevation. The results are shown in the middle of Fig. 21. We would distinguish electrons from ions above about 62 km up to about 83 km. Between about 83 and 88 km we could not distinguish electrons from ions. This was again possible above that height until the apogee was reached. For comparison, the results of a noon flight is presented. The afternoon flights made during January 1976 show that negative ions seem to have been confined to lower levels.

When the results of mass spectrometer measurements of water cluster ions are considered as an indication for the presence of water in the D-region, (quite some amount must be there in the summer season, otherwise one should not be able to see noctilucent clouds) and taking into account that water has powerful scavenging properties for free electrons and excited states of molecules expecially when clustered (e.g. SMITH et al., 1977) winter-anomalously high absorption may be the result of a seasonal depletion of this minor constituent which is quite abundant. Its seasonal variation of abundance in the lower atmosphere is well known.

The reduction of water vapour content as a probable cause for an increase of absorption was suggested before by FOLKESTAD (1970), FOLKESTAD et al. (1972), THRANE (1972) and REID (1970). The results of our guardring probe measurements show that this depletion seem to start in rather low heights (This was seen as an enhanced ion density in heights around 40 km under precursor conditions) and travels up into D-region heights within a time scale of a few days. The depletion of the scavengers (which might comprise other minor constituents also) changes the electron loss process from being attachment-like to recombination and allows by this the build-up of an enhancement of electron density which finally causes highly-winter-anomalous absorption . This state is ended by a re-injection of scavengers into the D-region from lower heights causing the re-formation of ledges in the electron density which may be found then in varying heights which are however, in general, lower than observed in summer. This mechanism might help to understand why correlations between winter-anomalously high absorption and strong stratospheric warmings exist (SHAPLEY and BEYNON, 1965) and why the significance for a correlation between winds measured in relatively low altitudes (72-74 km) and integral absorption is quite high. One would expect then significant correlations between wind and absorption also for lower levels but this analysis was not yet made.

Provided that the assumption that a change of abundance of water vapour in D-region heights changes the amount of short wave radio wave absorption is correct, it opens by principle the possibility to modify the D-region ionosphere by removing electrons in order to decrease absorption and, by this, lowering the L.U.F. locally. This could be tested by a relatively simple sounding rocket experiment. A certain amount of water should be carried into the D-region when radio wave absorption is winter-anomalous and is released in the most sensitive height region around 82-83 km in such a way that a flat disk is formed. This disk will be carried away with the wind and the reduction of electron density caused by the clouds should be observed as a decrease of absorption when it passes over suitably located A1 absorption sites. About 20 kg of water suitably deployed might produce a noticable effect. Smaller quantities might suffice when in-situ-measurements are preferred. In this case, the first rocket could carry and deploy the water in the desired heights, a second small rocket would follow short after the launch of the first one and measure the effect of electron density reduction. One should expect that the effect of electron density reduction is larger in winter and is less pronounced in the summer season provided that the cloud is generated always in the same height.

An experiment of this kind has been made by us already. However inadvertedly. One example is given in Fig. 22 which shows the telemetry record of the variation of the current/voltage characteristics of the guardring probe experiment around apogee of the rocket trajectory, recorded on 35 mm film. We separated there the payload from the rocket motor shortly before the apogee was reached to expose the rear end of our foil cloud canister. This was necessary to deploy the foil cloud used for wind and density measurements. Separation is done by igniting an explosive charge of a stochiometric mixture of potassium permaganate and magnesium powder. This moment is indicated in the telemetry record by a drop-out of the TM signal which is seen in the record as a noisy pulse. When the cloud of combustion products (which may contain a certain amount of unburnt particles also) the guardring probe which is mounted at the tip of the rocket, we see for a short moment an enhancement of electron density. After a time delay of 1,8 - 2,2 seconds, the container is opened by an overpressure
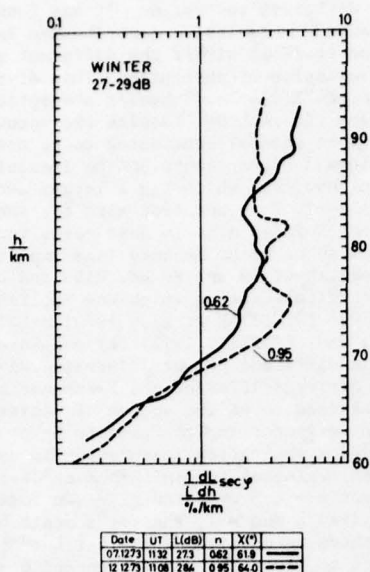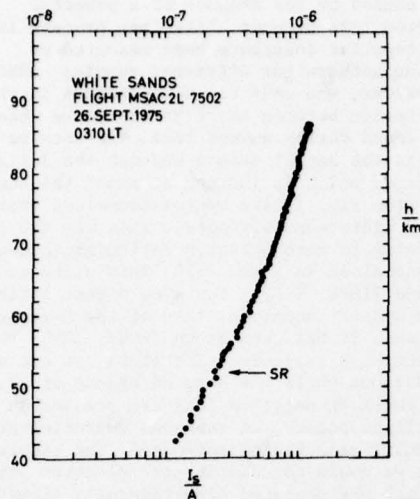
Fig. 21a
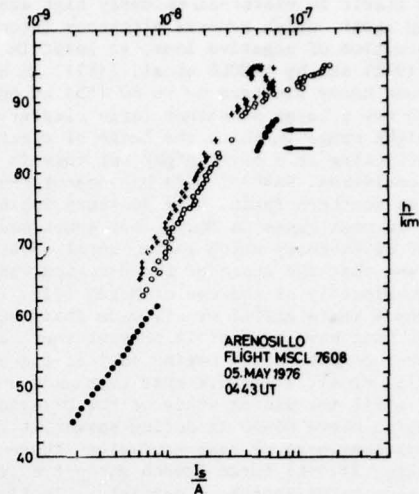
Fig. 21b
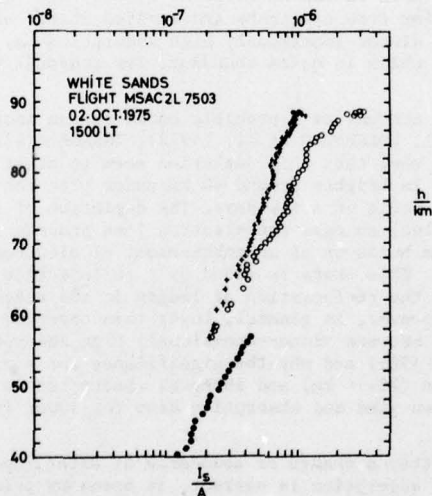
Fig. 21c

Fig. 21   Presence of negative ions in the D-region atmosphere at sunrise. Summer
conditions, right: noon measurement. The height region in which a layer
(two layers?) of negative ions was found coincides with that reported
by NARCISI et al. (Ref. 24).
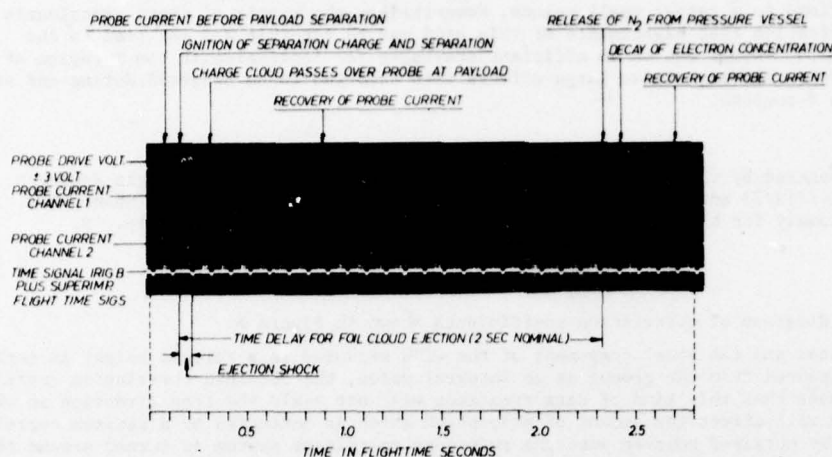
Fig. 22   A first qualitative experimental proof for the feasability of the suggested modification
experiment of the D-region atmosphere to increase locally the L.U.F. Fig. 22 shows a
print of the telemetry signals of the D-region probe experiment recorded on 35 mm cinefilm
(photographic positive). It shows the time interval between separation of the payload
from the rocket motor by ignition of an explosive charge and the expulsion of a cloud
of metallized ultralight plastic foils used for in-situ wind and air density measurements.
Both events occur near apogee of the rocket's flight between about 92 and 94 km. The
upper channel in the record displays the probe voltage waveform which varies linearly
with time between plus 3 Volt and minus 3 Volt and vice versa. The channel (channel 1)
below transmits the probe current/voltage characteristics in two sensitivities which
differ by a factor 100. The two sensitivities are alternated. Channel 2 transmits the
same probe current but with a difference of a factor 10 in sensitivity and with
reversed polarity to facilitate data evaluation when the two channels are accidentally
not wide enough separated in the analog record to prevent overlapping. At the outmost
left: current/voltage characteristics measured in the undisturbed atmosphere (electrons
produce a higher current than positive ions). Telemetry drops out when the explosive
charge is ignited. (TM transmitter jumps off frequency due to mechanical load on the
oscillator crystal caused by the separation shock.) The cloud of combustion products
(mostly of metallic nature, magnesium and potassium) causes locally a transient increase
of the electron density which is measured by the probe. After 2.1 seconds (this time
varies from payload to payload) the foil cloud is expelled by compressed nitrogen
which is contaminated by water vapour. The gas cloud causes a substantial decrease
of electron density in the vicinity of the probe when part of this gas cloud expands
over the probe. Because the gas jet which expels the foils is directed backwards
opposite to direction of flight the effect of electron density reduction lasts only
for a short time. Afterwards, as is seen at the very right of the record, the probe
current returns to its normal value. These effects were used as housekeeping data
to indicate proper function of the experiments. A quantitative evaluation was not
attempted due to the lack of measurements of relevant parameters.

of nitrogen. The foils are then exposed to the environs. Because the foils are packed into the container on the ground, the foils surely have absorbed quite some amount of water vapour which may be released during exposure. When the mixture of nitrogen gas and water vapour passed the probe we observed a marked decrease of electron density and often current/voltage characteristics normally found in lower heights which indicate the formation of negative ions. However, this depletion was not noticable in absorption measurements because the contribution to total absorption is very small at about 90-95 km and the effect is confined to a rather small volume. Nevertheless the result of these experiments may be taken as an indication that experiments of this kind may be feasible and may lead to the desired effect. That water vapour can be an efficient scavenger for ionisation in the F-region of the ionosphere has been proven already. Quite large effects were reported to be observed during and after the launches of Saturn V rockets.

ACKNOWLEDGEMENT

APPENDIX 1

Determination of beam diagrams of correlation coefficients shown in Figure 8:

When the meridional and the zonal component of the wind measured in a certain height is correlated with the absorption measured from the ground as an integral value, the obtained correlation coefficients are different. This means that this kind of data treatment will not yield the true direction in which a change of wind speed will affect the amount of absorption which is indicated by a maximum correlation coefficient. This can be obtained however when the reference coordinate system is turned around the compass card. Designating the meridional components of the wind in the original coordinate system (positive when going to north) as M_i and the zonal component (positive when going to east) as Z_i. The correlation coefficient between absorption and a wind going to direction α is then given by:

$$r(\alpha) = \frac{A \cos \alpha + B \sin \alpha}{(C \cdot \cos^2 \alpha + D \cdot \sin^2 \alpha + 2E \sin \alpha \cos \alpha)^{1/2}} \cdot \frac{1}{F^{1/2}}$$

with:

$$A = \Sigma M_i Y_i - \frac{1}{n} \Sigma M_i \Sigma Y_i$$

$$B = \Sigma Z_i Y_i - \frac{1}{n} \Sigma Z_i \Sigma Y_i$$

$$C = \Sigma M_i^2 - \frac{1}{n} (\Sigma M_i)^2$$

$$D = \Sigma Z_i^2 - \frac{1}{n} (\Sigma Z_i)^2$$

$$E = \Sigma M_i Z_i - \frac{1}{n} \Sigma M_i \Sigma Z_i$$

$$F = \Sigma Y_i^2 - \frac{1}{n} (\Sigma Y_i)^2$$

with Y_i being the relevant value of observation. By this, a beam diagram is obtained. Its maximum points into the direction of maximum correlation between wind and absorption.

REFERENCES

Armstrong, R.J., F. Lied and E.V. Thrane: A possible explanation of the winter-anomaly in ionospheric absorption at Kjeller, Physica Norvegica 4, 157-160, 1970.

Arnold, F. and D. Krankowsky: Mid latitude lower ionosphere structure- and compostition measurements during winter, submitted to J.Atm. Terr. Phys. 1978.

Arnold, F., J, Kissel, D. Krankowski, H. Wieder and J. Zähringer: Negative ions in the lower ionosphere: A mass spectrometric measurement, J. Atm. Terr.Phys. 33, 1169 - 1175, 1971.

Best, J.E. and I.A. Ratcliffe: Proc. Phys. Soc. 50, 233, 1938.

Beynon, W.J.G., and E.R. Williams: Electron density in the lower ionosphere and the winter anomaly in HF absorption. J. Atm. Terr. Phys. 32. 1325-1329, 1970.

Beynon, W.J.G., and E.R. Williams: Rocket measurements of D-region electron density profiles, J. Atm. Terr. Phys. 38, 1319-1325, 1976.

Bowhill, S.A., E.A. Mechtly, C.F. Sechrist and L.G. Smith: Rocket ionization on a winter day of high absorption, Space Res. VII, 246, 1967.

Dickinson, P.H.G., F.D.G. Hall, and F.D.G. Bennet: Rocket measurements of electron concentration in the lower ionosphere at two European locations. J.Atm.Terr.Phys. 28, 163 - 173, 1976.

Dieminger, W., G. Rose, and H.U. Widdel: In-situ measurements of electron concentration, neutral wind and air pressure compared with the winter anomaly, In: Lower Ionosphere Structure, 341-348 ed. K. Rawer, Akademie-Verlag, Berlin, 1974.

Folkestad, K.: Ionospheric studies by in-situ measurements in sounding rockets, NDRE Report No. 59, 1970.

Folkestad, K., and R.J. Armstrong: Interpretation of loos rates observed during auroral absorption in terms of a two-ion model of recombination, J. Atm. Terr. Phys. 32, 409-412, 1970.

Folkestad, K., E.V. Thrane, and B. Landmark: A study of ion-pair production rates and electron number densities in the ionospheric D-region: J. Atm. Terr. Phys. 34, 963-968, 1972.

Gregory, J.B.: Radio wave reflections from the mesosphere: I height of occurrence, J. Geophys. Res., 66, 429-445, 1961.

Gregory, J.B., and A.H. Manson: Seasonal variations of electron densities below 100 km at mid-latitudes II: electron densities and atmospheric circulation, J. Atm. Terr. Phys. 31, 703-729, 1969.

Gregory, J.B., and A.H. Manson: Seasonal variations of electron densities below 100 km at mid-latitudes III: stratospheric-ionospheric coupling, J. Atm. Terr. Phys. 32, 837-852, 1970.

Gregory, H.B. and A.H. Manson: Seasonal variations of electron densities below 100 km at mid-latitudes V: radiation temperatures and electron densities. J. Atm. Terr. Phys. 37, 645-653, 1975

Haug, A., and B.L. Landmark: A two-ion model of electron-ion recombination in the D-region, J. Atm. Terr. Phys. 32, 405, 1970.

Haug, A., and E.V. Thrane: The diurnal variation in the mid-latitude D-region. J. Atm. Terr. Phys. 32, 1641-1647, 1970.

Krankowski, D., F. Arnold, H. Wieder, J. Kissel, and J. Zähringer, Positive-ion composition in the lower ionosphere, Radio Sci. 7, 93-98, 1972.

Maehlum, B.: On the "winter-anomaly" in the mid-latitude D-region, J. Geophys. Res., 72, 2287, 1967.

Manson, A.H.: The concentration and transport of minor constituents in the mesosphere and lower thermosphere (70-110 km) during periods of anomalous absorption, J. Atm. Terr. Phys. 33, 715-721, 1971.

Mechtly, E.A., S.A. Bowhill, L.G. Smith, H.W. Knoebel: Lower ionosphere electron concentration and collision frequency from rocket measurements of Faraday rotation, Differential absorption and probe current. J. Geophys. Res., 72, 5239-5249, 1967.

Mechtly, E.A.: Accuracy of rocket measurements of lower ionosphere electron concentrations, Radio Sci. 9, 373-378, 1974.

Mechtly, E.A., and J.S. Shirke: Rocket electron concentration measurements on winter days of normal and anomalous absorption, J. Geophys. Res., 73, 6243-6247, 1968.

Narcisi, R.S., A.D. Bailey, L.E. Wlodyka, and C.R. Philbrick: Ion composition measurements in the lower ionosphere during November 1966 and March 1970 solar eclipses. J. Atm. Terr. Phys. 34, 647-658, 1972.

Rawer, K.: Der Einfluß der Dämpfung auf die Kurzwellen-Ausbreitung, Deutsche Luftfahrtforschung IB. Nr. 1872, Zentralst. f. wiss. Berichtswesen ZWB, 20.10.1943.

Reid, C.C.: Production and loss of electrons in the quiet daytime D-region of the ionosphere, J. Geophys. Res., 75, 2551-2562, 1970.

Rose, G.: Über die Bestimmung der D-Schicht-Absorption für eine 2000 km lange Meßstrecke und deren Endpunkte, Forschungsbericht des Landes Nordrhein-Westfalen, ed. L. Brandt, Westdeutscher Verlag, Köln-Opladen, 1965.

Rose, G., and H.U. Widdel: Experimental evidences for a transient ion layer formation in connection with sudden ionospheric disturbances in the height range 20-50 km, Planet. Space Sci. 20, 871-876, 1972.

Rose, G., and H.U. Widdel: D-region radio wave propagation experiments, their significance and results during the Western European Winter anomaly campaign 1975/1976, J. Geophys. 44, 15-26, 1977.

Rose, G., H.U. Widdel, A. Azcarraga, and L. Sanchez: A payload for small sounding rockets for wind finding and density measurements in the height region between 95 and 75 km. Phil. Trans. R. Soc. Lond. A 271, 509-528, 1972.

Rose, G., H.U. Widdel, A. Azcarraga, and L. Sanchez: Results of an experimental investigation of correlation between D-region neutral gas winds, density changes and short-wave absorption, Radio Sci. 7, 181-191, 1972.

Schmidtke, G.: Todays knowledge of the solar EUV output and the future needs for more accurate measurements in Aeronomy, XXth meeting of COSPAR, Tel Aviv, June, 1977.

Schwentek, H.: Regular and irregular behavior of the winter-anomaly in ionospheric absorption, J. Atm. Terr. Phys. 33, 1647-1650, 1971.

Schwentek, H., and Chr. Timpe: The applicability of method A3 for measurements of absorption in the ionosphere at 6 MHz using only the 1 F mode. J. Atm. Terr. Phys. 34, 867-876, 1972.

Sechrist, C.F.: Theoretical models of the D-region. J. Atm. Terr. Phys. 34, 1565-1589, 1972.

Sechrist, C.F.: Ionospheric D- and E-regions. Rev. Geophys. Space Phys. 13, 894-900, 1975.

Sechrist, C.F., E.A. Mechtly, J.S. Shirke, and J.S. Theon: Coordinated rocket measurements on the D-region winter anomaly. I. Experimental results. J. Atm. Terr. Phys. 31, 145-153, 1969.

Shapley, A.H., and W.J.G. Beynon: Winter anomaly in ionospheric absorption and stratospheric warnings, Nature 206, 1242-1243, 1965.

Smith, D., N.G. Adams, and D. Grief: Implications of some laboratory determination of No+ reaction rates to cluster ions formation in the D-region. J. Atm. Terr. Phys. 39, 513-521, 1977.

Thomas, L.: Recent developments and outstanding problems in the theory of the D-region. Radio Sci. 9, 121-136, 1974.

Thomas, L.: The summer to winter changes in the D-region and stratosphere. J. Atm. Terr. Phys. 37, 595-600, 1975.

Titheridge, J.E.: The stratification of the lower ionosphere. J. Atm. Terr. Phys. 24, 283–296, 1962.

Thrane, E.V.: On the diurnal and seasonal variations of the D-region and E-region above Kjeller, in: Magnetosphere-Ionosphere Interactions, K. Folkestad ed. Oslo University Press, 1972.

Thrane, E.V.: Ionospheric profiles up to 160 km - a review of techniques and profiles, in: Lower Ionosphere Structure, ed. K. Rawer, Akademie-Verlag, Berlin, 1974.

Widdel, H.U.: Correlations between atomic oxygen airglow and radio wave absorption in winter (J. Atm. Terr. Phys., accepted for publication)

Zimmermann, S.P., and R.S. Narcisi: The winter-anomaly and related transport phenomena. J. Atm. Terr. Phys. 32, 1305-1308, 1970.

VARIATION OF THE GREEN LINE OXYGEN AIRGLOW EMISSION RATE
AS A PRECURSOR INDICATIVE OF WINTERTIME ABSORPTION ANOMALY
OF HF RADIO WAVES.

H. Lauche
G.Lange-Hesse
Max-Planck-Institut für Aeronomie
Postfach 2o
D-3411 Katlenburg-Lindau 3
Federal Republic of Germany

SUMMARY

Airglow emission of the E-layer has been observed from the ground at nighttime during the Winter Anomaly Campaign at Arenosillo, Spain, winter 1975/76. A comparison of these optical data with the HF waves ionospheric absorption values of the following day indicates that obviously a special kind of variation of the airglow emission can be used as a "precurser indicative" for an increase of the ionospheric D-region absorption at the following day. However, these preliminary results need further confirmation.

The Wintertime Absorption Anomaly is a phenomenon which causes interference of HF radio waves communications by a pronounced increase of the LUF (lowest usable frequency). Therefore a prediction of the occurence of those absorption increases using typical "precursers indicative" would be of use. A precurser of this kind e.g. is a typical hight distribution of the electron concentration, also called precurser profile [WIDDEL, 1978]. However, the experimental equipment to measure this precurser profile is relatively extensive and can not be used for a continuous forcasting service.

Since the Winter Anomaly is controlled by the neutral atmosphere and not by solar wave or particle radiation [LANGE-HESSE, 1953], the authors therefore have looked to other parameters of the neutral high atmosphere which can be measured by equipments from ground and perhaps have special relations to the Winter Anomaly. During the Winter Anomaly Campaign at Arenosillo, southern Spain 1975/76 the red and green oxygen airglow emission from the upper atmosphere was measured continuously for this purpose from the ground at nighttime by means of a 4channel all-sky panorama photometer. Two of these channels were tuned to the emitted wavelength; the other channels were used to measure simultaneously the background continuum. The line channels and the background channels were matched to give the same response over a wide range of incident photon rate. The photon rate from the background channel was subtracted automatically.

Even when the background brightness was more than 20 times stronger than the line emission, it was possible to measure the line intensity. The sentitivity of this photometer was very stable and checked daily (29 ± 3 counts per Rayleigh *). In this way it was possible to make reliable observations even under hazy conditions close to full moon. The great number of measured points in the sky permitted a fairly good approximation to the transmission of the lower atmosphere. The loss of light can be recalculated when the vertical transmission is better than o.5.

The oxygen green light is emitted from ^1S state. This state is produced by the Chapman or the Barth mechanism. [Chapman, 1931; Barth et al, 1961]. Both mechanisms give approximately the same production rate of $O(^1S)$.

The concentration of atomic oxygen has a pronouced maximum near 95 km altitude and this is the region where $O(^1S)$ is mainly produced.

There is still a weak emission from the F-layer, but in most cases this contribution can be neglected.

During magnetic storms green line emission from the F-layer can be important. But in this case the emission of the red line is increased also. Redline emission in low latitudes is mainly produced by dissociative recombination at F-layer heights

$$O_2^+ + e \rightarrow O + O^* + 6,9 \text{ eV}$$
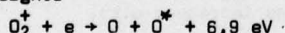
In principle it possible to exite $O(^1S)$ state but it was shown by ZIPF [1970] that this reaction mainly exites the ^1D state. That means: The green emission from the F layer is approximately 10% of the red emission. The red emission was observed simultaneously by the same photometer. At times of low magnetic activity the F-layer green emission was 4 to 7 R. While the observed total emission varied between 60 and 200 Rayleighs.

Due to the long lifetime of this state [$O(^1S)$:0.74s, see Fig. 1] exited atoms are partly quenched by collisions. Recent measurements have shown that atomic oxygen is the most important quencher [Offermann and Drescher, 1973; Slanger and Black, 1976]. Quenching by O_2 and N_2 can be neglected. The rate of emission $I_{\lambda = 557.7 \text{ nm}}$ obeys the following equation:

$$I_{\lambda = 557.7 \text{ nm}} = \frac{K_1 [O]^3}{1 + K_2 [O]} \text{ Photons cm}^{-3} \text{s}^{-1}$$

$$K_1 = 1.4 \cdot 10^{-30} \exp\left\{\frac{-1300}{RT}\right\} \text{ cm}^6 \text{ molecule}^{-2} \text{s}^{-1}$$

$$K_2 = 5 \cdot 10^{-11} \exp\left\{\frac{-610}{RT}\right\} \text{ cm}^3 \text{ molecule}^{-2} \text{s}^{-1}$$

Variations of the emission rate are caused by changes of either the oxygen density or the neutral gas temperature.

---

*) 1 Rayleigh = 1 R = 10^6 Photons/cm^2 s
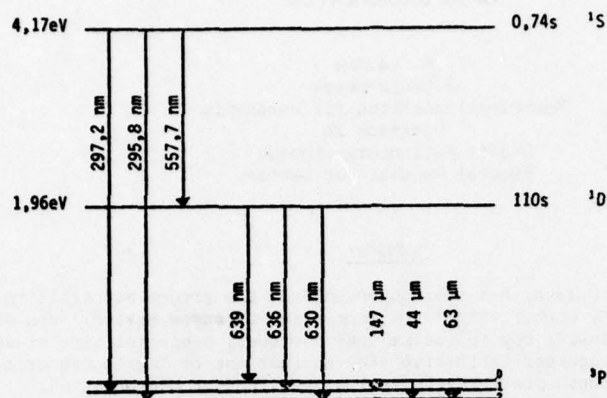
Fig.1 Exitation terms of Oxygen

Wavelength	Transition	Einstein coefficient
297,2 nm	$^1S \to {}^3p^1$	$7,8 \cdot 10^{-2}$ s^{-1}
295,8 nm	$^1S \to {}^3p^2$	$8,0 \cdot 10^{-4}$ s^{-1}
557,7 nm	$^1S \to {}^1D$	$1,28$ s^{-1}
639,2 nm	$^1D \to {}^3p^0$	$2,2 \cdot 10^{-6}$ s^{-1}
636,4 nm	$^1D \to {}^3p^1$	$2,2 \cdot 10^{-3}$ s^{-1}
630,0 nm	$^1D \to {}^3p^2$	$6,9 \cdot 10^{-3}$ s^{-1}
147,0 µm	$^3p^0 \to {}^3p^1$	$1,7 \cdot 10^{-5}$ s^{-1}
44,2 µm	$^3p^0 \to {}^3p^2$	$1,8 \cdot 10^{-9}$ s^{-1}
63,1 µm	$^3p^1 \to {}^3p^2$	$8,9 \cdot 10^{-5}$ s^{-1}

Fig. 1 Exitation terms of oxygen

When starting airglow observations at the beginning of the Winter Anomaly Campaign, we expected higher quenching after times of anomalous high absorption, due to heat flux from lower layers.

Upon comparing variations of airglow intensities and of HF radio wave absorption, correlated periodic variation of about 1 to 2 hours were observed with both methods, (see Fig. 3); the correlation coefficient was 0.73 with absorption lagging about 12 hours behind the airglow. This behaviour was observed during almost all nights of the Winter Anomaly Campaign, except the days of high magnetic activity. During that night the red emission from the F layer was increased also.

In the following section it is referred to an absorption value, called L_D mesured in dB (for definition see WIDDEL, 1978, in this volume). This is a characteristic value for the average absorption during the whole daylight hours.

In Fig. 2 a <u>continuous increase</u> of the airglow intensity occurs in the evening of January 20 and lasts until 1 hour UT. The airglow then remains on this level for the rest of the night. There are fairly good evidences that this pronounced increase of airglow intensity in the evening is a precursor indicative of an increase of HF radio wave avsorption at the following day. In this special example the absorption value L_D was equal to 35 dB on Jan.20. The L_D-value during wintertime on normal days, that means without Winter Anomaly, is of the order of 25 to 35 dB. The following day, Jan.21, an L_D-value of 68 dB was measured. That means extrem high absorption.

Another example is given in Fig. 3. The level of the airglow intensity in contrast to Fig. 2 is nearly constant during the whole night until 3 hours UT in the morning and no pronouced increase is observed in the evening. The L_D-value on Jan. 1 is 49, on Jan. 2: 50. That means no remarkable change in absorption.

A third example similar to the first is given in Fig. 4. A pronounced increase of airglow intensity is observed in the evening of Jan. 7. The L_D-value of this day is 50 dB, for the following day 66 dB. That means again a pronounced increase in HF-radio wave absorption in correlation with an increase of airglow intensity the night before.

A fourth example similar to the second is given in Fig. 5 . A nearly constant level of airglow intensity occurs during the whole night. The L_D-value for Jan.22 is 47, for Jan. 23: 5o. The increase in absorption is less than 10% and therefore within the statistical variation, that means it has no physical significance.

The results shown here indicate that obviously there is a possibility to use airglow observation of

the green oxygen line as a precursor indicative for an increase of HF-radio wave absorption during Winter Anomaly. However, this relation needs further confirmation since the result given here depends only on one campaign and one place. Additional experiments therefore should be carried out at other places.

For future experiments, ground-based equipments capabel of determing temperatures in the emitting region would be very helpful too.

REFERENCES:

Chapman, S., 1931, Proc. Royal Society, London, Ser. A 132, 353

Lange-Hesse, G. 1953, J.atm.terr.Phys., 3, 153-162

Barth, C.A., Hildebrandt, A.F., 1961, J.-Geophys.Res. 66, 985

Zipf, E.C., 1970, Bull.Am.Phys.Soc. 15, 418

Offermann, D., Drescher, D., 1973, "Atomic Oxygen Densities in the Lower Thermosphere as Derived from in Situ 5577 Å Night Airglow and Mass Spectrometer Measurement", J.Geophys. Res. 78, 6690-6700

Slanger, T.G., Black, G., 1976, The Journal of Chemical Physics, Vol. 64, Nr. 9

Rose, G., Widdel, H.U., 1978,   "D-Region Radio Wave Propagation Experiment, Their Significance and Results during the Western European Winter Anomaly Campaign 1975/76", J.of Geophysics, 44, 15-26

Lauche, H., 1978,   "Observations of the Oxygen Green Line Airglow during the Winter Anomaly Campaign 1975/76", J.of Geophysics 44. 35-38

Widdel, H.U., 1978,   "Winteranomaly of Radio Wave Absorption and D-Region Modification" in this Volume.
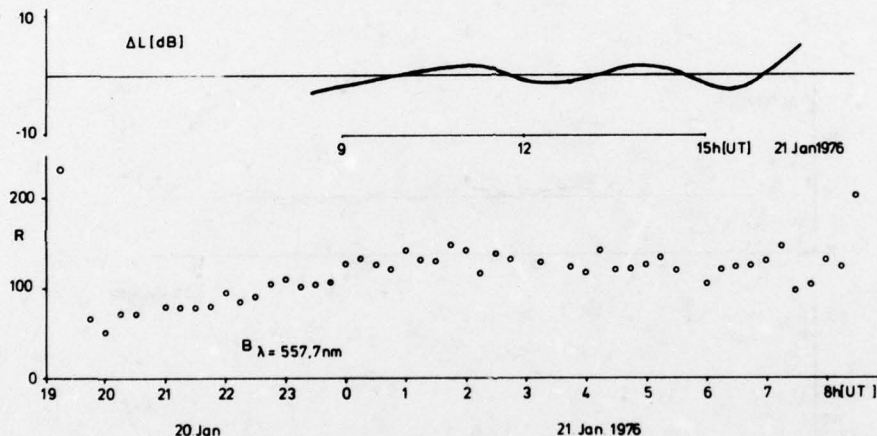
Fig.2 Periodic variation of green airglow intensity B in Rayleigh (R) and radio wave absorption L in decibel (dB) at Arenosillo, southern Spain.Radio wave absorption data L according to ROSE and WIDDEL (1978).For Jan. 20,1978:L_D=35 dB,for Jan.21,1978:L_D=68 dB.For definition of L see ROSE and WIDDEL (1978),for L_D see WIDDEL (1978) in this Volume.L_D-Values taken from WIDDEL and ROSE (1978) Fig.6.
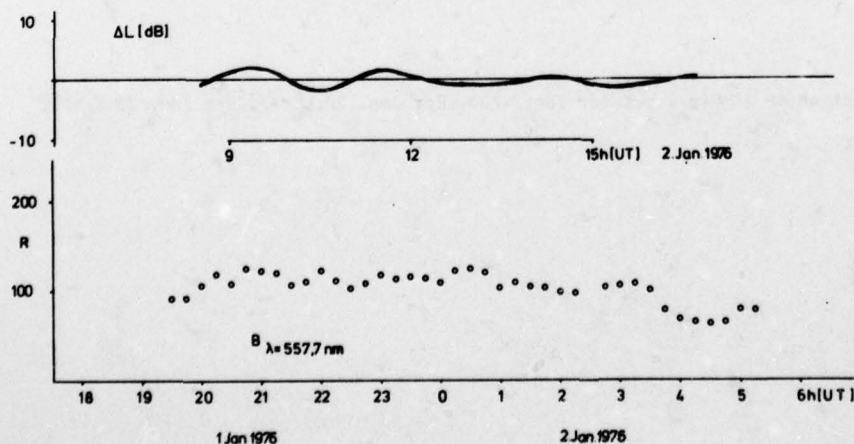
Fig.3 Similar representation as in Fig.2 but for Jan. 1/2, 1976. For Jan.1:L_D=49, for Jan.2:L_D=50.
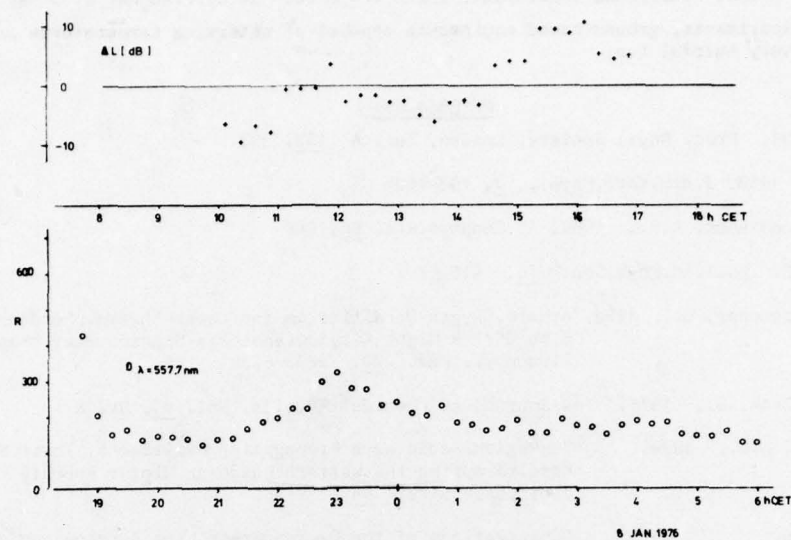
Fig.4 Similar representation as in Fig.2 but for Jan. 7/8, 1978. For Jan. 7:L_D=50, for Jan. 8:L_D=66.
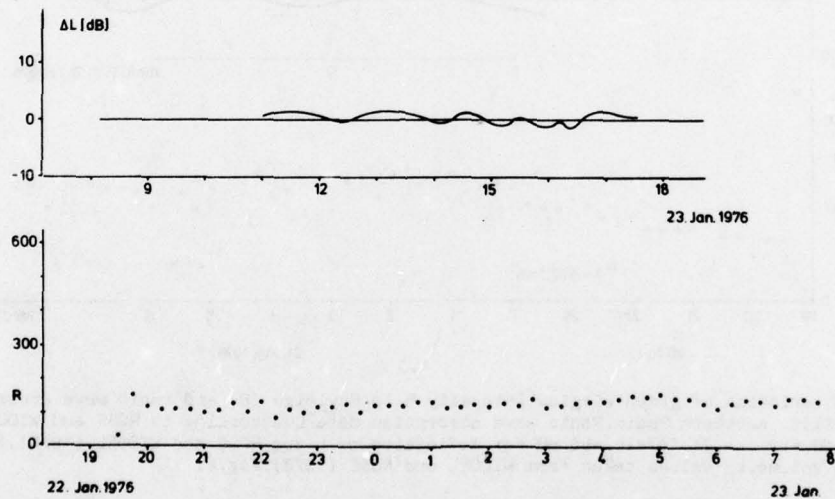
Fig.5 Similar representation as in Fig.2 but for Jan.22/23. For Jan. 22:L_D=47, for Jan. 23:L_D=50.

DISCUSSION

N.G.Gerson, US

Were there any large increases in the winter-time absorption without any evidence of increased green line airglow radiations (on the previous night)? What could be the cause of these discrepancies?

Author's Reply

Yes, they can occur since the correlation coefficient betwene airglow and absorption variation is 0.73.

CALCUL DE LA M. U. F. EN PRESENCE DE GRADIENTS
DE GRANDE ECHELLE

P. GOURVEZ   et   R. HANBABA

CENTRE NATIONAL D'ETUDES DES TELECOMMUNICATIONS

DEPARTEMENT M.I.R - LANNION

RESUME -

Le but de cette étude est de déterminer dans quelle mesure les gradients ionosphériques de grande échelle doivent être pris en compte dans les calculs de prévision de propagation des ondes décamétriques. La méthode d'analyse consiste en un calcul rigoureux de la propagation à travers une ionosphère représentée par un modèle tridimensionnel. Les premiers résultats concernent des cas de propagation H.F. dans l'ionosphère des basses latitudes magnétiques.

1 - INTRODUCTION

Les méthodes de prévision de propagation dans l'ionosphère pour les ondes de la gamme décamétrique (fréquence de 2 à 30 MHz) reposent généralement sur des méthodes simples. La trajectoire d'une onde est assimilée à une suite de segments de droites entre le sol et des couches ionosphériques réduites à des miroirs plans. La hauteur d'un point de réflexion est prise égale à la hauteur virtuelle de réflexion de l'onde de fréquence équivalente émise en incidence verticale (loi de la sécante). Les réflexions étant spéculaires, la trajectoire de l'onde est toute entière contenue dans un plan qui est celui du grand cercle terrestre joignant l'émetteur au récepteur. Dans cette formulation, la réfraction des rayons est donc ignorée ; et l'utilisation de la loi de la sécante suppose l'absence de gradients horizontaux d'ionisation. Autrement dit, la simplicité du modèle de propagation et corrélativement, celle du modèle d'ionosphère sont essentiellement dues à ce que la variation spatiale de l'indice de réfraction, découlant de celle de la densité d'ionisation, n'est pas prise en compte. Cette approximation peut être justifiée aux latitudes moyennes où les gradients de densité d'ionisation sont faibles. Par contre, elle s'avère irréaliste pour les régions où ceux-ci sont importants.

En effet, des études expérimentales concernant des liaisons transéquatoriales ont montré l'existence de modes de propagation se caractérisant par : des fréquences de travail relativement grandes (jusqu'à de l'ordre de 50 MHz), des affaiblissements peu élevés, sur des liaisons   pouvant atteindre plusieurs milliers de kilomètres (Nielson et Col., 1974 ; Crochet et Col. 1967). D'autres études, menées à l'aide d'émetteurs embarqués à bord de satellites, ont permis d'observer des modes de caractéristiques semblables, mais pour des directions d'émission Est-Ouest dans le voisinage de l'équateur magnétique (Garrara et Col., 1970). Une interprétation théorique de ces modes fut obtenue en leur attribuant pour origine physique l'effet des gradients d'ionisation présents dans la couche F équatoriale (Anomalie Equatoriale). Deux méthodes de calcul furent utilisées : l'une basée sur la théorie simple rappelée précédemment, mais dans laquelle les couches ionosphériques planes peuvent avoir une inclinaison fonction du gradient d'ionisation (Odoux, 1967 ; Crochet, 1969) l'autre consiste en la résolution numérique des équations de propagation dans l'approximation de l'optique géométrique, la densité d'ionisation étant fournie par un modèle déduit de l'observation (Kuriki et Col., 1974 ; Bertini et Col., 1976). Il en résulte que les modes observés correspondent à des trajectoires ne présentant pas de réflexion intermédiaire au sol et/ou située en partie en dehors du plan du grand cercle de la liaison (supermodes, modes "guidés").

1.0

4.5
5.0
5.6
6.3
7.1

2.8

2.5

3.2

2.2

3.6

1.1

4.0

2.0

1.8

1.25

1.4

1.6
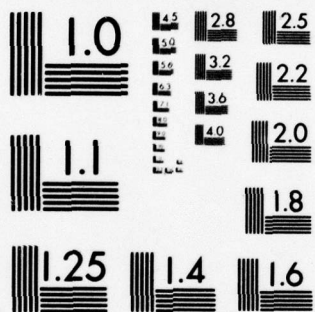
MICROCOPY RESOLUTION TEST CHART
NATIONAL BUREAU OF STANDARDS-1963-A

A la suite de ces résultats, des méthodes de prévision de propagation H.F. incluant l'effet des gradients horizontaux d'ionisation furent mises au point. Toutefois, même celles qui se limitent à l'application de la théorie simplifiée resteraient trop lourdes pour être utilisées facilement en exploitation de routine . Nous avons donc entrepris une étude systématique de l'effet des gradients d'ionisation de grande échelle sur le calcul de la M.U.F. Notre but est de déterminer dans quelles conditions il faut nécessairement en tenir compte.

Nous présentons ici la méthode envisagée et les modèles retenus, ainsi que quelques résultats préliminaires.

2 - METHODE D'ANALYSE

2.1 - Calcul de la propagation ionosphérique

Le but de l'étude nécessite qu'elle soit fondée sur une méthode rigoureuse de calcul des trajectoires d'énergie des ondes décamétriques dans l'ionsphère. En outre, nous nous intéressons à l'effet des gradients d'ionisation de grande échelle ; c'est-à-dire ceux qui n'entraînent qu'une faible variation de l'indice de réfraction sur des distances de l'ordre des longueurs d'ondes considérées. Le problème reste donc dans le domaine de validité de l'optique géométrique et les trajectoires vérifient en chaque point le système d'équations différentielles déduites par Haselgrove du principe de Fermat (Haselgrove, 1954).

Nous utilisons donc une méthode de tracé de rayons, qui est la détermination des trajectoires par intégration numérique du système d'équations de Haselgrove. A cette fin, nous avons employé un programme de calcul adapté de celui développé par Jones et Col. (1975). Dans ce type de méthode, l'indice de réfraction est calculé en chaque point d'intégration. Il faut donc connaître, en tout point de l'espace, le champ magnétique terrestre, la fréquence de collision électronique et la densité électronique. Pour les deux premiers, nous avons conservé des sous programmes de calcul standards (champ magnétique dipolaire, fréquence de collision combinaison de deux fonctions exponentielles de l'altitude). En revanche, nous avons recherché un modèle de densité électronique aussi réaliste que possible.

2.2 - Modèle de densité électronique ionosphérique

Un modèle de densité électronique approprié à notre étude doit satisfaire deux conditions : décrire correctement les variations spatiales et temporelles de la densité réelle ; ne pas demander des ressources informatiques (temps de calcul, allocations mémoires) telles que le tracé de rayons en deviendrait prohibitif. Nous avons opté pour le modèle actuellement recommandé par le C.C.I.R. (Rapport 340) qui répond aux deux critères de choix.

La distribution de densité électronique en fonction de l'altitude est déduite du modèle de Bradley et Col. (1973) (Figure 1). Ce modèle se compose de :

- une couche E parabolique dont l'altitude h_{mE} du maximum et la demi-épaisseur y_{mE} sont constantes, égales respectivement à 110 km et 20 km. La fréquence critique f_{OE}, est calculée à partir des équations empiriques de Muggleton (1975).

- un accroissement linéaire de la densité, depuis l'altitude h_{mE} jusqu'à l'altitude où la fréquence plasma est égale à 1.7 f_{OE}.

- une couche F2 parabolique dont l'altitude du maximum est h_{mF2}, la demi-épaisseur y_{mF2} et la fréquence critique f_{OF2}. h_{mF2} est calculée à partir d'une formule du type de celle de Shimazaki, corrigée pour tenir compte de l'ionisation sous-jacente à la couche F2. Dans cette formule intervient $M(3000)F2$. y_{mF2} est fonction de $M(3000)F_2$, $h'_{F,F2}$, f_{OE}, f_{OF2} et R_{12} ; $h'_{F,F2}$ est la hauteur virtuelle minimum de réflexion en incidence verticale sur la couche F_2.

Dans nos calculs, les valeurs données à h'$_F$,F2 sont tirées d'ionogrammes provenant des stations situées dans le voisinage de la zone pour laquelle l'étude de propagation est effectuée. D'autre part, M(3000)F2 et f$_{OF2}$ sont obtenus comme sommes des développements en série d'harmoniques sphériques (Jones W.B. et Col., 1969).

Les harmoniques sphériques sont des fonctions dont l'ensemble constitue une base sur laquelle sont développées les médianes mensuelles des paramètres ionosphériques. Les variables en sont : la latitude et la longitude géographiques, le temps universel, le numéro du mois de l'année, la moyenne sur 12 mois du nombre de taches solaires. Les coefficients des développements sont calculés à partir des valeurs des paramètres mesurées sur les ionogrammes provenant du réseau mondial de stations ionosphériques. La figure 2 montre un exemple de carte d'iso-fréquences f$_{OF2}$ (en MHz) obtenue par ce procédé numérique.

3 - RESULTATS

3.1 - Mise en oeuvre de la méthode de calcul

Une fréquence maximum utilisable (M.U.F.) est définie pour une liaison donnée. Sa détermination consiste à rechercher, pour une fréquence d'émission donnée, des trajets assurant la liaison. Dès que l'un deux a été trouvé, la fréquence est incrémentée et le processus de calcul réitéré. Et la M.U.F. est la fréquence la plus élevée pour laquelle un trajet est encore possible. Cette procédure implique donc le calcul d'un grand nombre de trajectoires. Aussi, dans un premier temps, nous avons choisi de fixer, non pas la liaison, mais la fréquence d'émission et de calculer la distance au sol atteinte en fonction de l'angle d'élévation à l'émission. En l'absence de gradients horizontaux d'ionisation, une même distance est atteinte pour deux élévations (l'une pour le rayon bas, l'autre pour le rayon haut) et il existe une distance minimum (correspondant à une élévation unique) pour laquelle la fréquence de travail est justement la M.U.F. En présence de gradients, nos calculs prouvent qu'il n'en est plus ainsi. Pour une même distance, il n'y a pas toujours coexistence d'un rayon haut et d'un rayon bas. En effet, pour les élévations faibles (≲ 10°) la propagation a lieu selon des modes particuliers. Nous en présentons maintenant deux exemples.

3.2 - Exemples de trajets particuliers dus aux gradients horizontaux d'ionisation

Nous nous plaçons dans le cas de la propagation des ondes H. F. dans l'ionosphère des basses latitudes magnétiques de la zone africaine, l'émetteur étant situé à Dakar (14.6°N, 342.5°E). Pour une période d'activité solaire moyenne (R$_{12}$ = 44,5) et le mois d'Août, nous choisissons une heure T.U. à laquelle l'anomalie équatoriale est au maximum de son développement au-dessus du continent africain, soit 18.00 T.U. La carte d'iso-f$_{OF2}$ (figure 2) déduite des développements en harmoniques sphériques permet de localiser les crêtes d'ionisation et de calculer un azimut d'émission pour lequel l'onde H.F. sera amenée à se propager dans une région de gradients. La valeur de l'azimut d'émission ainsi calculée est de 120°. Compte tenu de la valeur de 9.65 MHz pour la crête de f$_{OF2}$ considérée ici, nous fixons la fréquence d'émission à 15 MHz.

Dans ces conditions, la courbe calculée : élévation d'émission en fonction de la distance de bond ne présente pas la forme classique (cf. § 3.1). Nous évaluons alors les caractéristiques des trajectoires de l'onde à l'aide de deux types de présentation des résultats du calcul : la projection des trajectoires dans le plan vertical défini par les coordonnées de la station d'émission et l'azimut d'émission, d'une part ; leur projection au sol, d'autre part.

Pour les angles d'élévation à l'émission élevés (> 15°), les trajectoires (figure 3a) sont constituées d'une série de réfractions dans la couche F2 et de réflexions au sol. Pour une trajectoire donnée, la distance au sol atteinte lors d'un bond diffère notablement d'un bond à l'autre. Par contre, pour les angles d'élévation faibles (< 10°), les trajectoires sont constituées d'une suite de réfractions dans la couche F2, sans réflexion intermédiaire au sol.

D'autre part, les déviations azimutales des trajectoires par rapport au plan vertical de l'émission restent dans les deux cas inférieures à, ou de l'ordre de un degré. Toutefois, les trajectoires dont les angles d'élévation à l'émission sont élevés subissent des déviations plus importantes (figure 3b) que celles dont les angles d'élévation sont faibles (figure 4b).

Nous nous plaçons maintenant dans le cas de la propagation H.F. dans la zone équatoriale africaine aux heures de lever du soleil. Pour la même période (mois d'Août, indice d'activité solaire R_{12} = 44.5), mais à 06.00 T.U. Nous maintenons les mêmes valeurs pour les paramètres d'émission, en particulier un azimut égal à 120°. En effet, selon cette direction, la valeur de f_{OF2} (figure 5) passe de 3 MHz environ à la verticale de l'émetteur (14.6°N,342.5°E) à 7 MHz environ à celle du point de position 10°S, 30°E. Néanmoins, un premier calcul montre que la fréquence 15 MHz n'est pas réfléchie pour toute la gamme désirée d'élévations. Aussi fixons nous la fréquence à 12 MHz.

Les résultats sont semblables aux précédents, pour les angles d'élévation à l'émission élevés (figure 6a et 6b) comme pour les angles faibles (figure 7a et 7b). Cependant, les trajectoires d'angles d'élévation à l'émission faibles qui, antérieurement, ne retournaient pas au sol (figure 4a), connaissent ici des périgées à basse altitude, et, éventuellement, un retour au sol (figure 7a). De plus, les déviations azimutales des trajectoires peuvent être plus importantes (figure 6b comparée à la figure 3b).

En résumé, les cas traités à ce jour enseignent que les gradients horizontaux de densité électronique qui existent dans certaines régions de la couche F ionosphérique impliquent pour la propagation H.F. :

   - ou bien des trajectoires à plusieurs "bonds", la distance au sol pouvant différer notablement d'un bond à l'autre ;

   - ou bien des trajectoires ne présentant qu'une suite d'apogées dans la couche F et de périgées à plus basse altitude, avec ou sans retour final au sol.

De plus, dans les cas examinés pour l'instant, les valeurs calculées des écarts du plan de la trajectoire par rapport au plan d'émission sont faibles (inférieur à ou de l'ordre de 2 degrés).

CONCLUSION

Les premiers résultats de cette étude montrent que les modèles physiques entrant dans les calculs de propagation des ondes décamétriques dans l'ionosphère ne traduisent pas toujours fidèlement la réalité. Toutefois, les conséquences de l'hypothèse principale sur laquelle ces modèles sont bâtis, à savoir l'effet négligeable des gradients horizontaux d'ionisation, ne seraient pas toutes trop sévères.

En effet, le calcul rigoureux montre que la propagation pourrait rester à peu près confinée dans le plan du grand cercle de la liaison.

Par contre, notamment pour les faibles angles d'élévation (qui sont ceux correspondant aux cas pratiques), l'omission des gradients entraine qu'il n'est pas tenu compte de modes de propagation ne comportant que deux traversées des couches absorbantes, donc très efficaces pour les radiocommunications. De plus, ces modes pourraient présenter une régularité d'occurence appréciable puisque liés à l'existence de gradients d'ionisation qui eux-mêmes la présentent (Ex. : évolutions diurne, saisonnière, de l'anomalie équatoriale).

REFERENCES

BERTINI F., M.T. de GIORGIO, P.F. PELLEGRINI, "Ray-tracing in the ionosphere for long range propagation studies", Alta Frequenza, Vol. XLV, 474-480, (1976).

BRADLEY P.A., J.R. DUDENEY, "A simple model of vertical distribution of electron concentration in the ionosphere, J. Atmosph. Terr. Phys., 35 (12) 2131-2146 (1973)

CARRARA N., M.T. DE GIORGIO, P.F. PELLIGRINI, "Guided propagation of H. F. radio waves in the ionosphere", Space Sci. Rev. 11, 555, (1970).

C.C.I.R., Supplément au Rapport 252-2, "Deuxième méthode provisoire du C.C.I.R. pour l'évaluation du champ et de l'affaiblissement de transmission de l'onde ionosphérique pour les fréquences comprises entre 2 et 30 MHz, (1978), à paraitre.

C.C.I.R., Supplément n° 2 au Rapport 340, "Atlas C.C.I.R. des caractéristiques ionosphériques", (1978) à paraitre.

CROCHET M., C. GOUTELARD, "Phénomènes de propagation hors du grand cercle observé sur des liaisons à grande distance en ondes décamétriques", C. R. Acad. Sci. Paris 264, 348, (1967).

CROCHET M., Thèse de Doctorat ès Sciences, Fac. Sciences Paris, (1969).

HASELGROVE J., "Ray theory and a new method for ray tracing", in the Physics of the Ionosphere, The Phys. Soc., London, 355, (1954).

JONES W. B., R. P. GRAHAM, M. LEFTIN, "Advances in ionospheric mapping by numerical methods", E.S.S.A. Tech. Report ERL 107-ITS 75, Washington, (1969).

JONES R.M., J. J. STEPHENSON, "A versatile three dimensional ray tracing computer program for radio waves in the ionosphere", Tech. Report OT/ITS, (1975).

KURIKI I., KASUYA I., HOJO H., TANOHATA K., "Analysis of the maximum observed frequencies on oblique ionograms by ray tracing technique", J. Radio Res. Lab., 21, (105) 161, (1974).

MUGGLETON L.M., "Uneméthode pour la prévision de f_{OE} à un instant et en un lieu quelconques", J. des Telecom., 42 (7) 413, (1975).

NIELSON D. L., CROCHET M., "Ionospheric propagation of H. F. and VHF radio waves across the geomagnetic equator", Rev. Geophys. Space Phys., 12(4) 688, (1974).

ODOUX J., "Recherche d'une possibilité de calcul de la limite supérieure des fréquences réfléchies par la couche F2 en présence d'un faible gradient d'ionisation horizontal", Ann. Telecom., 22 (3-4) 77, (1967).
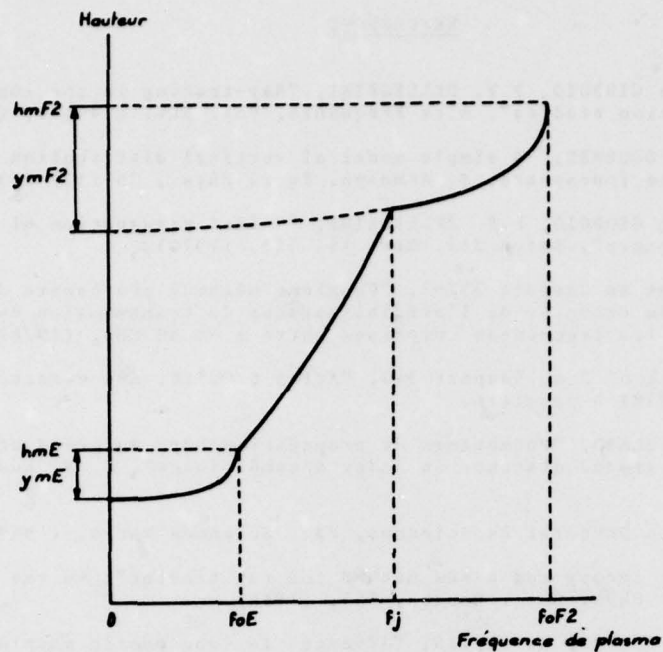
FIGURE 1 - Schéma de la distribution verticale de densité électronique
ionosphérique donnée par le modèle de Bradley et Col. (1973).
Les échelles des axes sont linéaires.
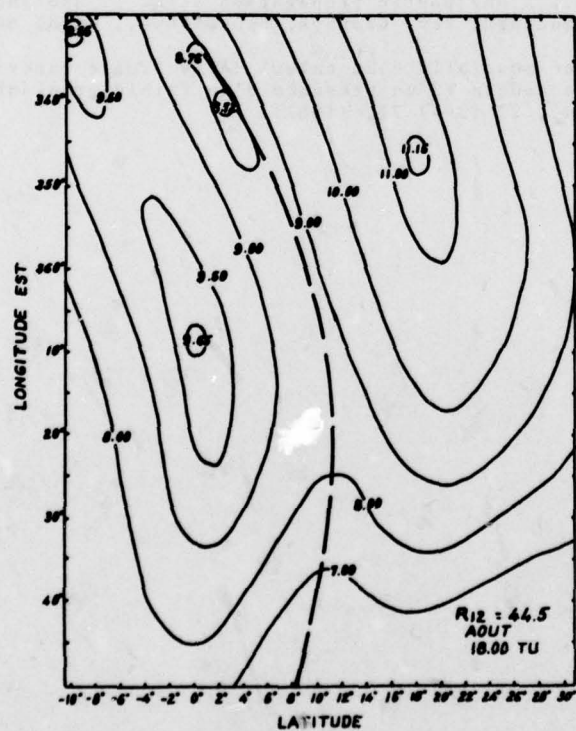
FIGURE 2 - Carte des iso-fréquences critiques f_{oF2} (en MHz) pour la zone
africaine des basses latitudes, au mois d'Août à 18.00 T.U. et
un indice d'activité solaire R_{12} = 44.5. La courbe en tiretés
représente l'équateur d'inclinaison magnétique.
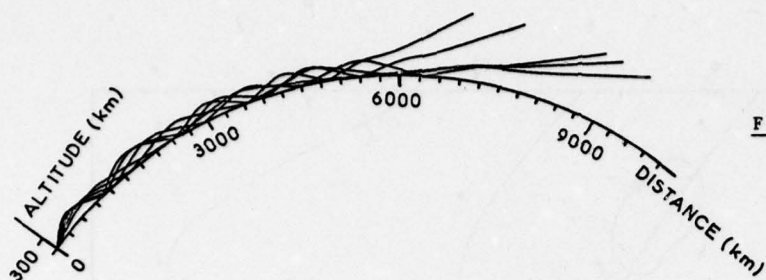
FIGURE 3a
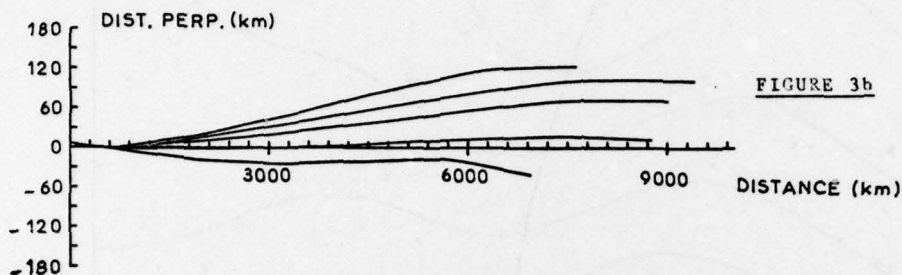
FIGURE 3b

FIGURE 3 - Pour le modèle de distribution géographique de f_0F2 donné par la fi-
gure 2, projection dans le plan d'émission (fig. 3a) et projection
au sol (fig. 3b) des trajectoires d'une onde telle que :
Fréquence d'émission : 15 MHz - Position de l'émetteur : 14.6°N, 342.5°E.
Azimut à l'émission : 120° - Elévations à l'émission : supérieures à 15°
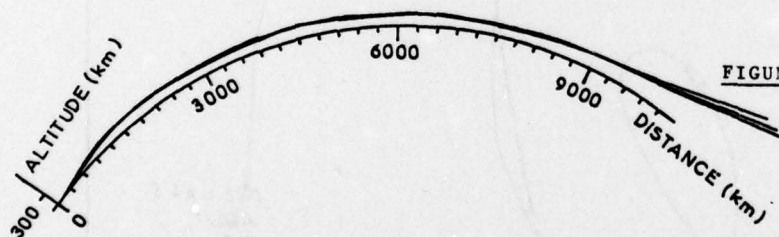
FIGURE 4a
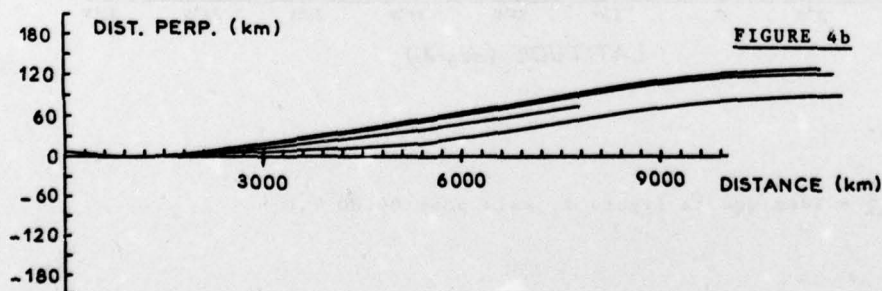
FIGURE 4b

FIGURES 4a et 4b : Idem, pour des élévations à l'émission inférieures à 10.
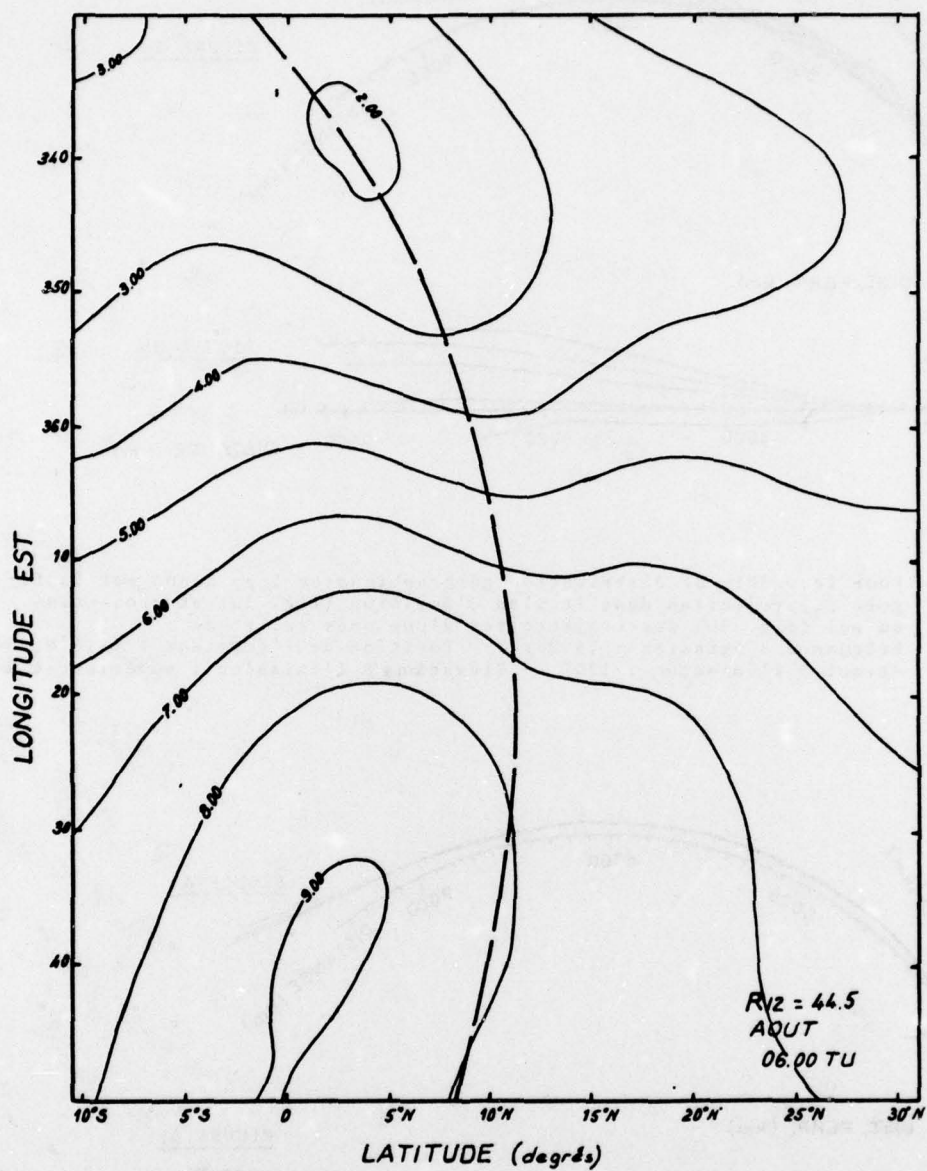
FIGURE 5 - Idem que la figure 2, mais pour 06.00 T.U.
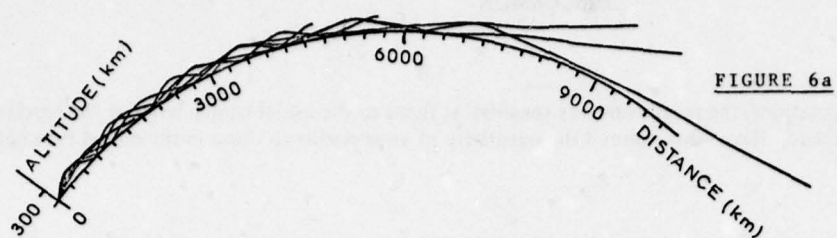
FIGURE 6a
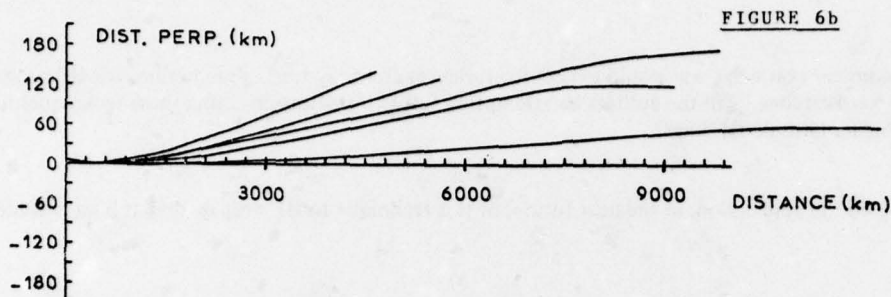
FIGURE 6b

FIGURE 6 - Pour le modèle donné par la figure 5, projection dans le plan
d'émission (fig. 6a) et projection au sol (fig. 6b)
des trajectoires d'une onde telle que :

Fréquence d'émission : 12 MHz - Position de l'émetteur : 14.6°N,342.5°E
Azimut à l'émission : 120° - Elévations à l'émission : supérieures à 15°
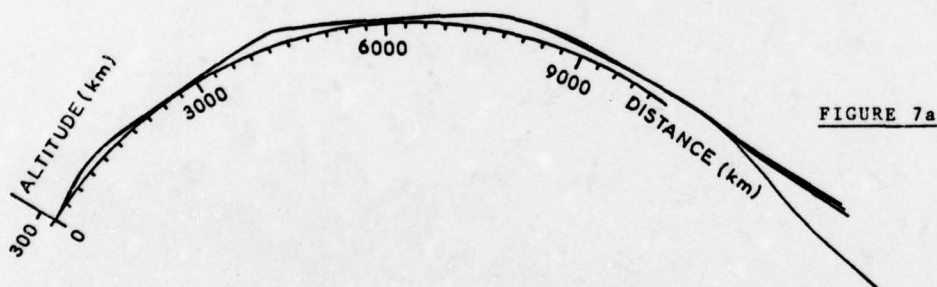
FIGURE 7a
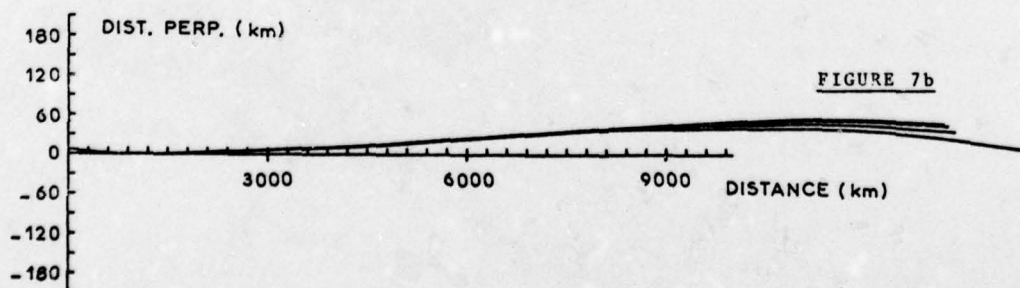
FIGURE 7b

FIGURES 7a et 7b - Idem, pour des élévations à l'émission inférieures à 10°.

DISCUSSION

N.M.Tomljanovich, US

With any ray tracing calculations, the results are very sensitive at times to the initial launch angle at the specific parameters of the ionosphere. Have you explored the sensitivity of your results to those in the model parameters at the initial conditions?

Author's Reply

In fact, the results obtained are very much dependent on the firing angle. The results presented have been selected from among all the trajectories obtained by systematically varying this angle from 1 to 20°.

J.R.Carlson, Canada

Would you care to comment on what one would expect for variances from ray tracing predictions for HF propagation paths in the higher latitudes. Will the authors be attempting future investigations using these techniques in application to any higher latitude HF lines?

Author's Reply

We have not considered the application, in the near future, of this technique to HF propagation at high latitudes.

N.G.Gerson, US

This very interesting paper presents an aspect that could be introduced into long-term models of ionospheric predictions. The basic mechanism involves the presence in the ionosphere of two refractivity gradients, the first of which would allow injection of a radio ray into an ionospheric duct and the second rejection of the ray from the duct to the ground. Three pairs of semi-permanent ionospheric gradients exist: (a) either side of the magnetic equator, (b) along the sunset-sunrise zone and (c) along the auroral zones. The first has been studied for VHF earlier and by Gourvez and Hanbaba in this paper. The second, termed antipodal propagation, has been examined by Gerson and by Banks. The third was investigated on a path that extended from the Northern to the Southern Polar Cap Regions (Gerson). In each case, MUF predictions for the paths involved failed drastically. The experiments showed much greater intensities and much longer durations than indicated by the predictions. It would seem appropriate, based on the results mentioned, to consider development of ionospheric prediction models for the refractivity pairs mentioned above.

SUMMARY OF SESSION IV

HF (SHORT TERM EMPHASIS)

by

Dr K.Davies
Session Chairman

This session concentrated on ionospheric predictions in the short term domain, i.e. predictions of ionospheric variations up to a few days. These are generally intended for operational needs, as contrasted to long-term predictions which are intended for the design of radio circuits.

Rush described some of the techniques employed by different groups around the world to forecast the ionosphere and radio propagation conditions on a short-term and long-term basis. Following the paper questions were raised concerning artificial modification of the ionosphere resulting from the proposed "power satellite". This involves a large solar collector ($\simeq 50$ km^2) in geostationary orbit. The energy is transmitted as microwaves ($\simeq 2400$ MHz). Two effects were discussed: (1) changes in electron densitites caused by ohmic heating, e.g. creation of irregularities that could scatter energy and (2) chemical modification because of the exhaust of rockets used to lift the material.

Jones was followed by **Dambolt** in describing passive systems for real-time updating of MUF predictions by recording radio reception from distant transmitters. In the period following these papers, the practicality of such techniques was discussed.

Röttger fourier analyzed the diurnal and seasonal variation of medium-scale Travelling Ionospheric Disturbances (TIDS) observed in the equatorial region. The significant spectral components were then used to model the occurrence of the TIDs. The paper generated a lot of discussion on the cause of evening irregularities in the equatorial zone. From seasonal variations of the occurrence of irregularities, Röttger concluded that gravity waves originated from cumulous clouds in the troposphere. His line of reasoning was questioned by several speakers but the possibility of the mechanism was appreciated.

IONOSPHERIC PREDICTIONS: METHODS AND RESULTS

Charles M. Rush
U.S. Department of Commerce
National Telecommunications and Information Administration
Institute for Telecommunication Sciences
Boulder, Colorado 80303

SUMMARY

Forecasting the state of the ionosphere and the variations in ionospheric structure that give rise to deleterious performance of ionospheric dependent propagation systems has been the objective of intense study since World War II. Originally geared toward long-term (monthly median) prediction of HF circuit performance, newer ionospheric forecasting techniques are directed toward the prediction and specification of the ionosphere on a time-scale of hours and days. Further, because of the increasing reliance upon satellite-based VHF/UHF propagation systems, greater emphasis is being placed on specifying the limitation induced by the ionosphere on VHF/UHF systems.

In this paper, we describe some of the techniques employed by different groups around the world to forecast the ionosphere and radio propagation conditions on a short-term and long-term basis. These techniques range from the highly statistical approach such as given in CCIR REPORT 252-2 for estimating skywave field strength for radio waves at frequencies greater than 2.0 MHz to the application of basic physical principles to forecast the ionospheric response to a solar disturbance. The agreement between both short-term and long-term ionospheric prediction techniques with observations of various ionospheric/radio propagation parameters will be described and methods for further improvement of the predictions will be addressed.

1. INTRODUCTION

The ionosphere can be defined as that region of the Earth's upper atmosphere where free electrons and ions exist in sufficient abundance to have a significant impact on the overall chemical and physical mechanisms at work in the atmosphere. For purposes of this discussion, it is assumed that the ionosphere extends from about 50 Km to 2000-3000 Km. Because of the presence of free electrons, the ionosphere refracts and slows down a radio wave that is incident upon it. It is this feature that enables the propagation of HF waves well beyond the optical horizon. Thus, in a very real sense, the ionosphere must be regarded as an integral part of an HF communication system for the existence of the ionosphere permits such a communication system to operate. The ionosphere will also affect radio waves that propagate through it in the Very High Frequency (VHF) and Ultra High Frequency (UHF) bands. The VHF/UHF waves will be slowed down by the total number of electrons (TEC) along the propagation path and will arrive at desired reception points in a slower time than if the waves propagated in free space. If there are irregularities in the structure of the ionosphere along the radio propagation path, the wave can be severely distorted, resulting in information loss at the reception point.

Because of the importance of the ionosphere to the performance of radio communications systems, efforts were undertaken as early as World War II to forecast ionospheric structure and radio propagation conditions (Lincoln, 1970). Because of changing requirements, efforts to forecast the ionosphere have taken various forms over the years, moving from a primarily military-applications motivation to a primarily civilian application to the present, which could be aptly described as a combination of military and civilian applications.

2. REQUIREMENTS FOR IONOSPHERIC FORECASTING

Other than for system planning exercises, most of the requirements for ionospheric forecasting pertain to specifying and forecasting ionospheric conditions on a varying time scale. Forecasts of impending geomagnetic disturbances and their associated ionospheric effects are needed to provide warnings of possible degradation in system performance. These geomagnetic disturbances produce effects that last from hours to a few days and can severely disrupt a communication system, particularly in the LF and HF band, although effects at the higher frequencies have also been observed.

Certain HF systems require knowledge of maximum usable frequency (MUF) and lowest usable frequency (LUF) that can be employed in transmitting information from point-to-point. These systems have the flexibility of changing frequencies in a time period that is short enough to adapt to changing ionospheric conditions. In addition, there is a community of HF communicators who need to know what the probability is that a certain class of service for specific frequencies will be maintained for the next 24 to 48 hours.

Navigational systems that employ VHF and UHF radio waves between satellites and the ground and satellites and aircraft will have to account for the time delay imposed on the radio signal by the electrons along the path of propagation. This time delay is a function of the frequency used in the system and is directly proportional to the total number of electrons along the path. Radars that are employed in space object identification must account for the refractive effects that the ionosphere imposes on the system. These imposed refractive effects are also directly proportional to TEC along the propagation path. Depending upon the operational scenario, both the navigational system and the space object identification radars will require information about the ionospheric structure (in this case TEC) on a time scale varying from one hour to one day.

Satellite communication systems can be subjected to rapid variations and fading in signal amplitude that are caused by the radio wave propagating through a region of intense ionospheric irregularity. These variations, known as scintillations, can give rise to bit error rates and even loss of information on a satellite to ground link. System designers must have a knowledge of the morphological behavior of ionospheric scintillation in order to provide adequate link margins. System operators and users will need to know the probability that scintillation will occur and the magnitude of the signal fading, in order to adapt their system to the observed environmental conditions.

At this conference, numerous presentations will address the requirements for ionospheric predictions and forecasts, and discussion will be given to the methods and capabilities that are currently employed to forecast the ionosphere, radio propagation conditions, and other related geophysical parameters. The International Radio Consultative Committee through its documents eminating from Study Group 6 describes the organizations involved in operational ionospheric forecasting. Further, these documents provide an indication of the type of and frequency of ionospheric forecasts made all over the world.

It should be pointed out that the need for ionospheric forecasts, particularly forecasts geared toward overall system performance, appears to be increasing. (Forecasts in this sense refer principally to the ability to specify the limitations on system performance that are imposed by the ionosphere and its variations.) One reason for this is that with increasing sophistication in hardware design and equipment component manufacturing, the limitations to electromagnetic system performance are not due to internal (i.e., equipment) sources but rather due to the medium (and its variations) in which the electromagnetic waves must propagate. Another reason why forecasts of the ionosphere are assuming increasing importance is that in the Fall of 1979, the International Telecommunications Union will call together a General World Administrative Radio Conference in Geneva. This conference, known as G-WARC, will address the radio regulations and frequency utilization and allocation. Many of the deliberations at G-WARC will be addressed to issues in which a knowledge of the ionosphere and its structure impact the utilization of the radio spectrum. An example is the deliberation concerning the possibility of sharing the HF spectrum between the Mobile, Fixed, and Broadcasting Services. The interference or potential for interference that one class of service operating on the same frequency as another class of service will cause, will depend on the HF propagation conditions that are determined by the ionosphere. Finally it should be mentioned that new systems are evolving that require ionospheric knowledge in order to assess system performance. Such systems include not only navigation and detection systems but also systems devoted toward the feasibility of developing energy alternatives. An example is the Solar Power Satellite system described by Glaser (1977).

Numerous organizations throughout the world are engaged in forecasting the state of the ionosphere and radio communications on both a long-term and short-term basis. For the most part these efforts are geared to specific purposes--this is particularly true of those ionospheric forecasting efforts geared toward military applications. However, a few organizations tend to be somewhat general in their capabilities to forecast the ionosphere and solar conditions. Table 1 provides a listing of those organizations engaged in short-term ionospheric forecasting of a general nature. It can be seen that the table reflects short-term ionospheric forecasting efforts the world over.

3.   CURRENT IONOSPHERIC FORECASTING EFFORTS

Most operational requirements that pertain to ionospheric forecasting and specification deal with the short-term (hours to days) changes in ionospheric structure. Although efforts are underway by a number of organizations that are involved in forecasting the ionosphere on a short-term basis, this section will address only selected topics. A more generalized account of ionospheric forecasting techniques can be obtained from the AGARD Conference Proceedings on Ionospheric Forecasting (1970).

Figure 1 provides an illustration of the electron density in the ionosphere as a function of latitude and height along a given longitude. Shown on the figure are contours of plasma frequency (in MHz) which can be related to electron density (N_e)/cm^3 through the relationship N_e(cm^{-3})=1.24 x 10^4 x f_p^2 (f_p in MHz). The electron density is a function of solar cycle, season, local time, location and geomagnetic activity. The contours shown in the figure were deduced using observed ionospheric parameters in conjunction with an ionospheric model described by Rush and Elkins (1975). The highest frequency (or equivalently, electron density) is denoted as the critical frequency of the F2 region, foF2.

A knowledge of the structure of the ionosphere such as depicted in Figure 1 is needed in order to properly determine or forecast the behavior of radio propagation systems that rely on the ionosphere. It is because of this that numerous efforts have been undertaken to develop models of the ionospheric electron density that can be used to determine radio propagation conditions. The models developed by Nisbet (1971), Bradley and Dudeney (1973), and Ching and Chiu (1973), for example, have proven to be particularly useful for assessing ionospheric impact on radio propagation systems.

The total electron content in a vertical column can be obtained directly from any of the aforementioned models. The TEC in this case, calculated by numerically integrating the electron density with height, is not the entire ionospheric TEC but rather the TEC up to an ionospheric height that corresponds to the upper limit of the model. Because of the increasing importance of TEC to radar and navigation systems, models of TEC have been developed specifically to account for radar range refraction and group path delay. The models given by Bent at el. (1975) and Klobuchar (1975) are examples of this type of ionospheric model.

Ionospheric parameters are measured at a number of locations on a routine basis around the globe. These parameters which provide information about the E, F1 and F2 regions of the ionosphere form the basis of median maps of ionospheric parameters given by the CCIR in Report 340. The mapping technique employed has been developed by Jones and Gallet (1962) and these maps of ionospheric parameters are used in the electron density models of Rush and Elkins (1975), Bradley and Dudeney (1973), and Nisbet (1971), the total electron content model of Bent et al. (1975), and HF propagation prediction programs given in CCIR Report 252-2 and subsequent supplements to that Report.

Because ionospheric parameters are observed at specific locations, efforts have been devoted to the development of techniques to extend and extrapolate the influence of an observation so as to be valid for an entire region. Work by Flattery and Ramsey (1975) and Rush and Edwards (1976) was directed to this end. Further, these efforts were directed toward providing an updated representation of ionospheric parameters, based on real-time or quasi-real-time data. Figure 2 provides an indication of how much improvement can be obtained using observations from about 27 stations scattered throughout the world when median maps are updated. In the top panel, ITS indication refers to the rms error between the median prediction and observations while the analysis indication shows the rms errors after updating. The lower three panels show the errors resulting after the updated maps were compared against data not used in the updating procedure. Further details are available from Edwards et al. (1975).

Not only must we be concerned with the spatial variability of the ionosphere, but we must also address the day-to-day variability. For a large number of HF-related applications, the day-to-day variability of the F2 region critical frequency (foF2) and the height of maximum density (hmF2) are the most important variations. Figure 3 provides an indication of the percentage changes in foF2 and hmF2 compared to the observed median values over the course of four months. It is readily apparent that foF2 shows a very strong diurnal dependence, being about twice as large during local night as during local day. The effects of such changes on the performance of HF circuits has been discussed in detail by Rush et al. (1974).

Because of the relative importance of foF2 in constructing electron density models, in determining total electron content, and in assuring propagation conditions at both HF and VHF, attention has been given to predicting foF2 on a daily-hourly basis. Figure 4 shows prediction errors at Moscow resulting from updating a monthly median prediction with data 1, 2, 3...6 hours old. The results are for solar maximum conditions. It can be seen that the amount of improvement in the prediction (smaller standard deviation) generally decreases with increasing time lag used in the updating process. There are times (0600 LMT in March and 0900 LMT in December) when the only improvement afforded is obtained using data 1 hour old while at other times, particularly during the midday period at equinox and most all hours during the summer solstice, data up to 4 hours old yield significant improvements in the prediction of foF2. During the winter solstice, it appears that data over 2 hours old applied in the manner as described above are of little use in reducing the prediction error.

The effect of short-term data in reducing the prediction error in foF2 clearly has a diurnal dependence. Data observed shortly before or at local sunrise are of little use in updating the median prediction except within 1 or 2 hours after sunrise. On the other hand, foF2 observed around 0900 LMT can be used to reduce the prediction error for a time period 3 to 6 hours in advance. At periods surrounding local sunset, a behavior comparable to that at sunrise is seen in the effectiveness of short-term observations of foF2 to reduce the prediction error. Generally, it can be said that when the ionosphere undergoes significant changes such as accompany the sunrise and sunset transitions, observations of foF2 before such transitions are of little value when applied to the updating scheme used here.

Figure 5 shows the comparison between the standard deviations obtained using the median foF2, the 5-day weighted mean foF2 and the 5-day weighted mean updated during the previous hour's observation for the 1964 data at Moscow. Generally, the 5-day weighted mean yields a better approximation to the observed daily hourly values than does the observed monthly median. It can be seen that in many instances updating the 5-day weighted mean with data only 1 hour old does not lead to a significant reduction in the standard deviations. In fact, in some instances (midday in December), such updating causes an increase in the standard deviation. The difference in the effect of short-term updating in foF2 that is observed between solar maximum and minimum is probably associated with the fact that the ionosphere during solar minimum is not subjected to as many of the large-scale perturbations that occur during solar maximum conditions. These perturbations, due to geophysical phenomena such as solar flares and geomagnetic storms, can lead to rapid changes in the ionosphere within a period of hours. Thus, data obtained over five days would be inherently more variable during solar maximum than during solar minimum. This would imply that data taken in hourly increments should have a larger effect on reducing the overall ionospheric variability during solar maximum conditions than during solar minimum conditions.

In addition to methods of predicting ionospheric parameters such as foF2 and hmF2, efforts have been undertaken to specify and forecast the occurrence of irregularities in electron density. These irregularities can give rise to spread-F on vertical incidence ionograms, to scattering of VHF signals and to scintillation on UHF satellite-to-ground signals. Figure 6 provides an idealized representation of the global and temporal behavior of ionospheric scintillation.

In recent years attention has been given to predicting scintillation of specific regions of the ionosphere such as at the polar and equatorial regions because of the large effects of ionospheric changes in those regions on the behavior of electromagnetic systems operating within and through those regions. For example, a summary of results pertinent to the equatorial region is given by Aarons (1977).

4.   CONCLUSIONS

The current efforts in ionospheric forecasting are geared toward specific system requirements. In many cases, operational requirements dictate that these efforts address the short-term prediction problem. Measurements of ionospheric parameters as well as correlated solar and magnetospheric observations that are used in any prediction scheme must be provided to a central location in a time period that ensures their usefulness (Rush, 1976). The cost of accomplishing this must be weighed against the improvement that is afforded in system performance and falls under the purview of the user of such improved information.

REFERENCES

Aarons, J., 1977, Equatorial scintillation - A review, IEEE Trans. on Antennas and Prop., 25, 729-736.

AGARD Conference Proceedings on Ionospheric Forecasting, 1970, AD-700896, No. 49, edited by Vaughn Agy.

Bent, R.B., S.K. Llewellyn, G. Nesterczuk and P.E. Schmid, 1975, The development of a highly-successful world-wide empirical ionospheric model and its use in certain aspects of space communications and world-wide total content investigation, Proceedings on the Effects of the Ionosphere on Space Systems and Communications, Naval Research Laboratory, edited by J.M. Goodman.

Bradley, P.A. and J.R. Dudeney, 1973, A simple model of the vertical distribution of electron concentration in the ionosphere, J. Atmos. Terr. Phys., 35(12), 2131-2146.

CCIR Report 252-2, 1974, CCIR interim method for estimating sky-wave field strength and transmission loss at frequencies between the approximate limits of 2 to 30 MHz, Geneva.

CCIR Report 340, 1974, CCIR Atlas of Ionospheric Characteristics, Geneva.

Ching, B.K. and Y.T. Chiu, 1973, A phenomenological model of glodal ionospheric electron density in the E, F1, and F2 regions, J. Atmos. Terr. Phys., 35(9), 1615-1630.

Edwards, W.R., C.M. Rush and D.M. Miller, 1975, Studies on the development of an automated objective ionospheric mapping technique, AFCRL-TR-75-0124, 5 March.

Flattery, T.W. and A.C. Ramsay, 1975, Deviation of total electron content for real time global applications, Proceedings on the Effects of the Ionosphere on Space Systems and Communication, Naval Research Laboratory, edited by J.M. Goodman.

Glaser, P.E., 1977, The potential of satellite solar power, Proceed. of the IEEE, 65(8), 1162-1176.

Jones, W.B. and R.M. Gallet, 1962, Representation of diurnal and geographic variations of ionospheric data by numerical methods, ITU Telecomm. J., 29, 129-149.

Klobuchar, J.A., 1975, A first order, worldwide ionospheric time delay algorithm, AFCRL-TR-75-0502, 25 September.

Lincoln, J.V., 1970, Ionospheric forecasting in the United States 1944-1966, AGARD Conference Proceedings on Ionospheric Forecasting, AD-700896, No. 49, edited by Vaughn Agy.

Nisbet, J.S., 1971, On the construction and use of a simple ionospheric model, Radio Sci., 6(4), 437-464.

Rush, C.M., 1976, An ionospheric observation network for use in short-term propagation predictions, ITU Telecomm. J., 43, 544-549.

Rush, C.M. and T.J. Elkins, 1975, An assessment of the magnitude of the F-region absorption on HF radio waves using realistic electron density and collision frequency models, ITU Telecomm. J., 42, 476-488.

Rush, C.M. and W.R. Edwards, Jr., 1976, An automated mapping technique for representing the hourly behavior of the ionosphere, Radio Sci., 11(11), 931-937.

Rush, C.M., D. Miller and J. Gibbs, 1974, The relative daily variability of foF2 and hmF2 and their implications for HF radio propagation, Radio Sci., 9(8,9), 749-756.

TABLE 1

Organizations Providing Short-Term Ionospheric Forecasts

Country	Organization	Address
Germany	FTZ	Forschungs Institut der DBP beim FTZ D6100 Dormstadt
Australia	IPS	Ionospheric Prediction Service P.O. Box 702, Darlinghurst 2010
United States	NOAA/SEL	Space Environment Services Center Boulder, Colorado 80303
France	CNET	Service des Ursigrammes Observortie de Paris F92190 Meudon
India	India Meteorological Organization	Kodaikanal Observatory
Japan	R.P.L.	Radio Research Laboratories Koganeishi, Tokyo, 184
United Kingdom	MRPS	Marconi Radio Propagation Services Great Baddow, ESSEX
Sweden		Central Administration of Swedish Telecommunications Stockholm
USSR	Hydrometeorological Service	Hydrometeorological Services Institute for Applied Geophysics Moscow

PLASMA FREQUENCY CONTOURS
21 MARCH 1966 1100 HRS GMT
0° LONGITUDE
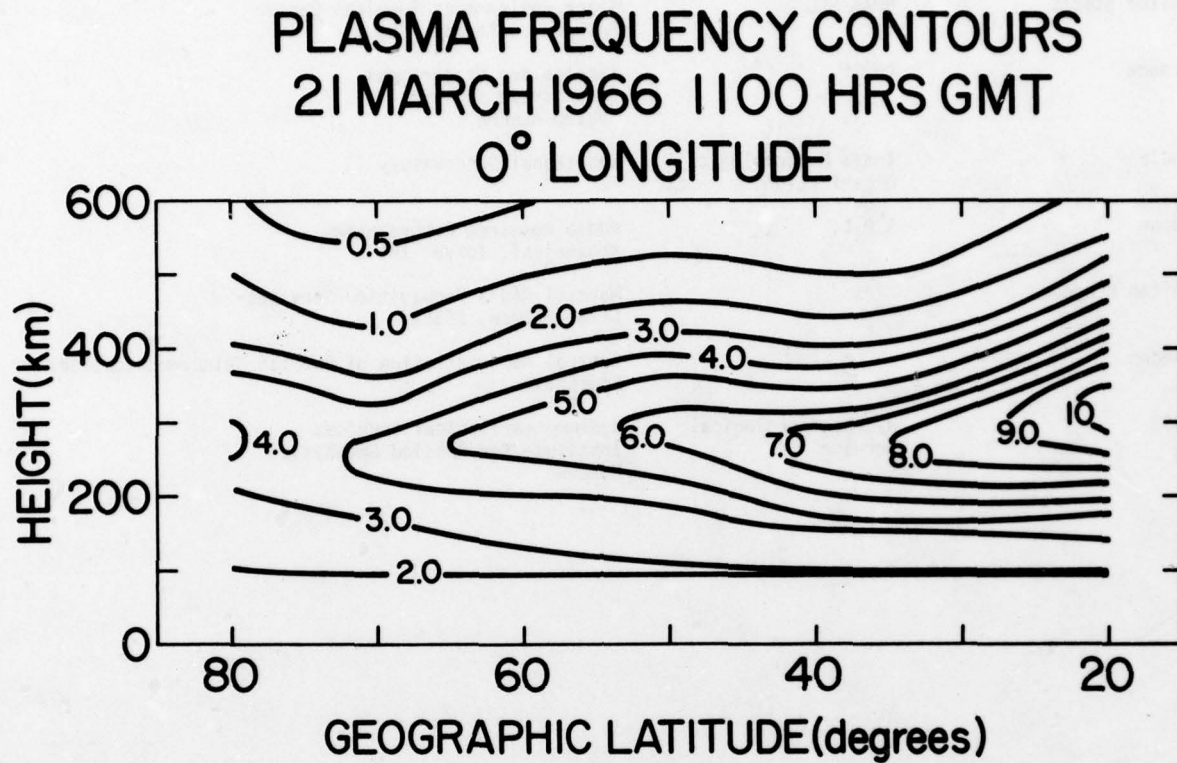
Figure 1: Contours of constant plasma frequency.
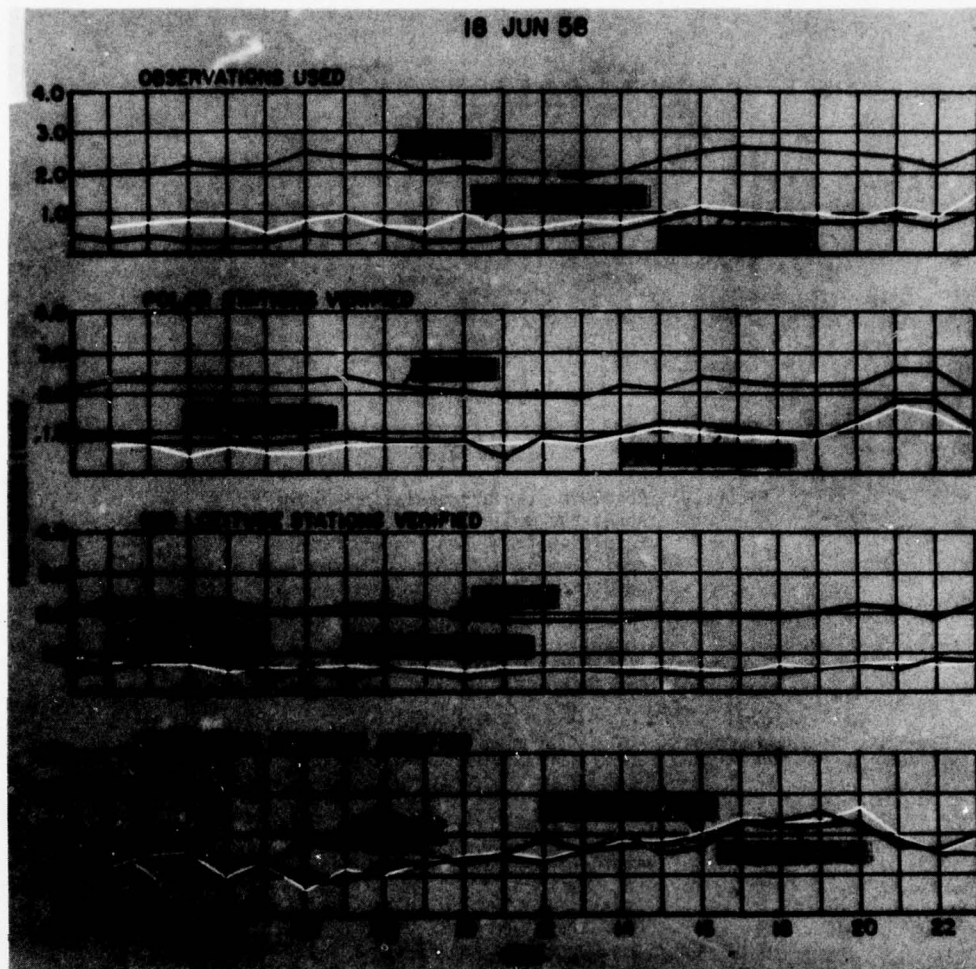
Figure 2: RMS errors between observed and forecasted values of foF2.
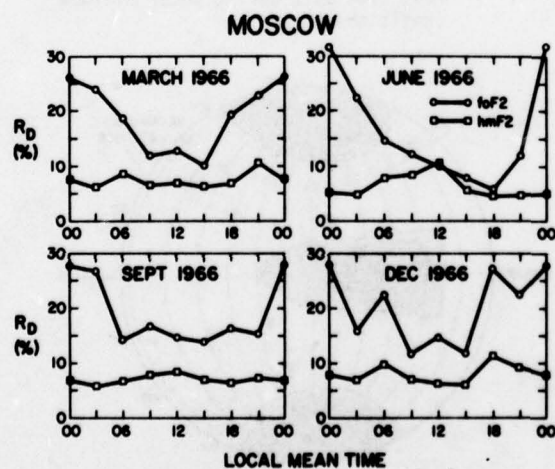
Figure 3: Percentage standard deviation of foF2 and hmF2 around the observation monthly median at Moscow.
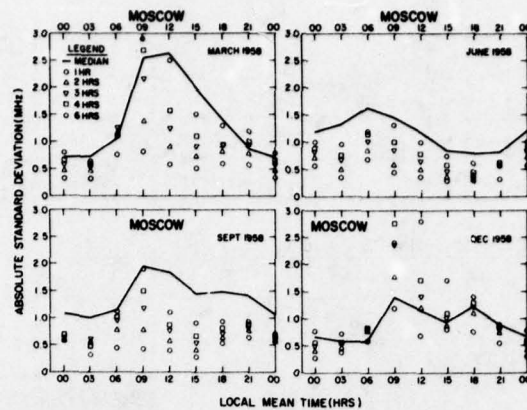
Figure 4: Absolute standard deviation of foF2 about the median and the deviation resulting from updating with quasi-real time data during solar maximum conditions.
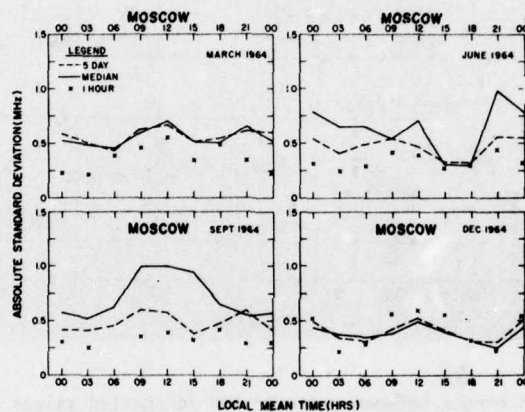
Figure 5: Absolute standard deviation of foF2 about the median and the deviation resulting from updating with quasi-real time data during solar minimum conditions.

DEPTH OF SCINTILLATION FADING (PROPORTIONAL TO DENSITY OF CROSSHATCHING)
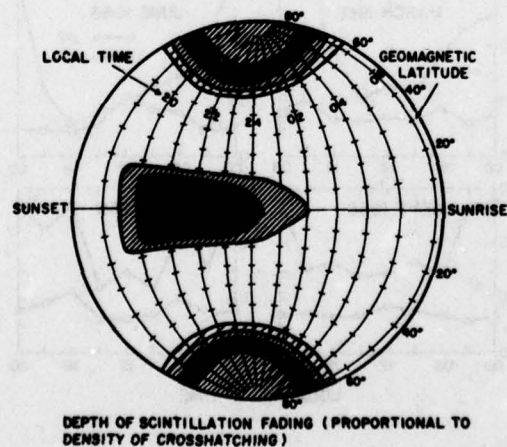
Figure 6: Idealized representation of the global behavior of scintillation.

DISCUSSION

K.Davies, US

You mentioned the fact that the morning MUF's being above the predicted values is no guarantee that the afternoon values will be above the predicted; this is true in parts of the world, other than Europe, and is one of the main reasons why it is difficult to update predictions more than about 6 hours in advance.

Author's Reply

Your comment is well taken. In fact, a number of workers have found that observations taken on one side of a terminator (such as sunrise) are of little value in predicting the ionospheric F2 region on the other side. I think that because the F2 region is controlled in large measure by dynamical processes (such as diffusion, drifts and winds, all of which have comparable time constants). Changes in ionospheric structure due to differences in the relative importance of each process, will render it difficult to forecast the ionosphere with any degree of accuracy beyond 4–6 hours.

REAL-TIME UPDATING OF MUF PREDICTIONS

T.B. Jones, C.T. Spracklen* and C.P. Stewart

Department of Physics
University of Leicester
Leicester, U.K.

1.   INTRODUCTION

The long-term accuracy of ionospheric predictions, using currently available programmes, is in general very good (1). In contrast, the short-term accuracy is poor, due principally to the variability of the ionosphere in the short term and the incidence of geophysical disturbances, e.g. magnetic storms. The operator using a longhaul circuit is thus faced with a difficult problem in that at any given time he is unable to determine the MUF accurately. He will therefore tend to select a frequency which is known to be well below the lowest MUF possible for the circuit. In practice the MUF could be considerably greater than the expected value and consequently the frequency selected could be several MHz below the optimum working frequency. In view of this difficulty, there is a need for a real time prediction system which will update the prediction programme according to the ionospheric conditions prevailing at the time when the MUF (or optimum working frequency) is requested.

The concept of real time evaluation of the propagation parameters is not new and prediction systems based on oblique sounding over the path have been developed commercially (2,3). These systems generally require suitable signals to be radiated at one end of the path and received at the other, so that measurements of the ionospheric parameters, usually in the form of an oblique incidence ionogram, can be obtained. The equipment is fairly costly and instrumentation of each path of interest is required unless these are similar in length and location. In some applications access is only available to one end of the path; moreover, a wide range of propagation paths, varying in length and in azimuth, may be of interest. In this paper a single station equipment is described which can evaluate the propagation conditions prevailing in a given region of the ionosphere and provide an improved forecast for any particular path and frequency of interest.

2.   PRINCIPLE OF OPERATION

In most prediction programmes the basic parameter to be determined is the path MUF. In order to assess the accuracy of the prediction, some method of measuring the MUF is required. Since we have control only of the receiving site, conventional sounding techniques cannot be applied. One can, however, monitor a number of broadcast transmitters (e.g. weather map stations) located in the general area for which the prediction is required.

The time variation of the MUF for a one-hop path is indicated by the solid curve in Fig. 1. This curve is typical of the data obtained from a prediction programme. Now let us assume that we are monitoring a transmitter of frequency f. Before time t_1 and after time t_2 no signals are received, since the working frequency exceeds the path MUF. Thus the signal strength recording for the transmitter would be as indicated in Fig. 2. Now, if the particular day considered is anomalous, the MUF curve might be displaced, as indicated by the dotted curve in Fig. 1. We have assumed the ionospheric electron density to be enhanced and the MUF values are consequently increased. It is now evident from Fig. 1 that the signal will be received at a time t_1^1, i.e. earlier than predicted, and that it will persist until time t_2^1, i.e. later than predicted. Thus the time at which the signal is first acquired (and the time when it is lost) provides a measure of the difference between the predicted MUF curve and the actual conditions prevailing at the time when measurements are made. The greater the time difference between the t and t^1 values the more the actual situation differs from the predicted conditions. The difference between the predicted (f^1 in Fig. 1) and measured MUF (working frequency) at the time t_1^1 can be used to modify the ionospheric model used in the prediction programme. This can then be used to forecast the MUF for other frequencies and propagation paths, provided reflection occurs in the same general area of the ionosphere. The more MUF transitions that can be measured the more accurately will the modified prediction (i.e. the forecast) fit the actual situation.

3.   EXPERIMENTAL ARRANGEMENT

The advent of micro-processor technology has made available low cost digital processing which is particularly suitable for process control. In the present system (see Fig. 3 for block diagram) a micro-processor is used as the main control element which receives high-level commands from a mini-computer. The micro-processor performs all control and error checking functions for a digitally controlled receiver. The receiver is tuned sequentially to a series of pre-programmed frequencies which are held in the micro-processor memory. The signal strength of the received signals is related to the AGC voltage and this is digitised and recorded into the memory. The data are averaged to minimise the effects of noise bursts and interference and is output, along with the time, to a floppy disc. This system can monitor up to 20 frequencies per second and 3 min averages of each frequency can be recorded onto the disc, which holds approximately two days data for 20 frequencies. The micro-processor can communicate with a mini-computer via a high speed serial interface. The mini-computer contains the prediction programme and enables high level language routines to be implemented. It also provides the link for operator control.

The receiver is tuned to a number of frequencies sequentially. These frequencies are radiated from transmitters in the general zone of interest and are used to determine MUF transition times. They are not specifically the frequencies for the propagation paths for which updated prediction (forecasts) are required. The micro-processor examines the signal strength recorded from each transmitter as stored on the disc and determines the time when the signal is first acquired (t_1^1) and finally lost (t_2^1) (see Fig. 2).

---

* Now at the Department of Applied Physics, University of Durham, Durham, U.K.

The mini-computer receives these MUF transition times from the micro-processor and calculates the predicted MUF for these times using the prediction programme contained in its memory. The time difference between actual and predicted MUF transitions are then determined. The mini-computer then revises the ionospheric model so that the two MUF times coincide for as many of the test circuits as possible; thus an updated ionospheric model appropriate to the conditions actually prevailing is obtained. The operator can now obtain a prediction from the mini-computer for any path frequency he desires using the new updated ionospheric model and so a 'forecast' is obtained. The system has been tested for a limited period and the preliminary results obtained are now discussed.

4.   RESULTS (preliminary)

Measurements have been made of the strength of the signals received from a number of weather map transmitters in western Europe. These were selected since they normally have omni-directional antennas and transmit continuously for 24 hours each day. Examples of the signal strength records showing clear MUF transitions are reproduced in Fig. 4. At the lower frequency a strong diurnal variation in signal level with a minimum value at noon, due to the effects of ionospheric absorption, is evident. At the higher frequencies no absorption effects are observed and the major signal amplitude changes are determined entirely by whether or not the frequency exceeds the MUF.

An attempt has been made to compare the measured MUF for a particular path with the predicted value. This can be done only at the time of the MUF transition, i.e. when the working frequency becomes equal to the path MUF. The measured MUF transition times for the 10.98, 13.37 and 15.95 MHz transmissions from Moscow are indicated in Fig. 5, which also shows the predicted MUF curve for this circuit. It is evident from the figure that in the morning the measured MUF curve occurs earlier than the predicted values, whereas in the afternoon the signals are received later than predicted. This situation could arise from enhanced F-region ionisation which results in a general increase in the MUF for any given time throughout the day.

A simple procedure for correcting the predicted MUF has been developed using the type of information contained in Fig. 5. In the morning, the lowest frequency (10.98 MHz) is received first and in the example of Fig. 5 this was acquired before the predicted time by some 30 minutes. The results so far examined suggest that if the lower frequency occurs earlier than predicted, then the two higher MUF transitions also occur earlier, i.e. the MUF curve is displaced, as indicated by the broken curve in Fig. 5. To obtain a quantitative measure of this displacement the predicted MUF at the 10.98 MHz transition time is determined. The ratio of the measured MUF (10.98 MHz) to the predicted value provides a multiplying factor by which the frequencies at any other time (i.e. the predicted MUF curve) are increased for the morning period. For the afternoon correction the ratio is based on the transition time of the 15.95 MHz signal since this occurs first and the MUF curve is multiplied by the ratio of 15.95 MHz to the MUF predicted at the time when this signal disappears. Thus, two multiplying factors, one for morning and one for the afternoon, are used to obtain a new MUF prediction for these periods. The success of this technique can be evaluated since measurements of the transition times for three frequencies are available (i.e. three points on the MUF curve). Since one transition time is required to obtain the correction factor, the other two can be employed to determine the difference between the revised MUF curve and the measured MUF transition time for these two frequencies. A measure of the improvement in the revised prediction is thus obtained and this is indicated in Table 1. In the morning an improved prediction is obtained in 63% of the cases when the 10.98 MHz transition time is used to obtain the multiplying factor. In the afternoon 85% of the predictions are improved when the 15.95 MHz transition time is used to obtain the correction factor. The lower success rate in the morning is attributed to the very steep rise in the MUF curve at this time when small errors in measuring transition times produce large differences in the predicted MUF.

In addition to the Moscow transmissions, a number of other European transmitters have been monitored (the frequencies and path lengths of these are given in Table 2). The ratio of the working frequency to the predicted MUF at the transition time, i.e. the time when the frequency is first received or finally lost, provides a measure of the accuracy of the prediction. If the predicted MUF curve is correct, then this ratio is clearly unity. The ratios have been determined at the times of MUF transition for the transmitters listed in Table 2 and the results for two typical days (16/2/78 and 25/2/78) are reproduced in Fig. 6.

In the morning of the 16/2/78 all the transmissions produce ratios greater than unity, apart from the short paths from Luxembourg and Offenbach (W. Germany) which yield ratios close to unity. In the afternoon the ratios are again greater than unity, apart from the southern path from Rome. During the morning of 25/2/78 ratios greater than unity were obtained for all transmissions, except for one of the Stockholm frequencies. In the afternoon, ratios less than unity are obtained for all frequencies apart from the northerly Oslo path which produces a ratio of 1.06. It would appear from the preliminary data obtained, that transmissions reflected from the same general area of the ionosphere behave in a similar manner, at least for the morning or evening periods. Thus, observations on one or more of these frequencies could provide a general indication of the expected behaviour of other frequencies reflected from the same general area of the ionosphere. More data need to be collected before this type of information can be formulated into a "forecast" procedure. However, these preliminary data indicate that real-time forecasting for a general region of the ionosphere may be possible.

5.   SUMMARY

A low cost system using micro-processor technology has been described which can monitor the MUF transition times for a large number of frequencies. By comparing the measured MUF transition times with those obtained from a prediction programme, the predicted MUF curve can be adjusted so as to provide a more accurate forecast of the MUF. The technique is successful when applied over a period of a few hours but it is found necessary to produce independent revised MUF curves for the morning and afternoon periods. The measured MUF transition times for several transmitters in western Europe suggest that the MUF for a given general area of the ionosphere may be generally "high" or "low". It would thus seem possible to

use two or three transmissions to assess the difference in the ionosphere from its predicted behaviour and to revise the predicted MUF curve accordingly for any desired circuit.

Further studies are now being undertaken to assess the improvement that can be achieved by application of updating techniques of this kind.

REFERENCES

1.	CCIR interim method for estimating sky-wave field strength and transmission loss at frequencies between the approximate limits of 2 and 30 MHz. Report 252-2, Geneva (1970).

2.	Daly, R.F., Felperin, K.D., Dayharsh, T.I. and Tupper, B.C. Curts phase II automatic frequency selection system-signal processing, application and evaluation. Stanford Res. Inst., May 1967.

3.	Barry, G. and Fenwick, R.B. Techniques for real time H.F. channel measurement and optimum data transmission. AGARD Conf. Proc., 1975.

TABLE 1

Time difference between measured MUF transition times and the
predicted and updated predicted values

Period 13 February 1978 to 4 March 1978, Moscow transmissions

a.m.		p.m.	
Time from original prediction	Time from revised prediction	Time from original prediction	Time from revised prediction
0.10	0.30	6.00	-2.27
-0.35	0.02	2.40	0.06
-0.45	-0.18	1.45	-2.15
-1.15	-0.45	2.30	0.50
-0.12	0.05	4.00	0.50
-0.16	0.08	0.50	-0.19
-1.35	-0.55	1.00	-2.30
-2.30	-1.35	0.50	-0.45
-0.25	-1.00	2.05	1.35
4.00	2.00	3.20	3.00
-0.25	-0.50	0.23	-0.15
-0.40	-1.20	1.20	0.50
-1.00	-1.05	0.35	-0.02
-0.57	-1.20	0.40	0.10
-1.15	-1.00	-1.40	-1.20
-1.30	-1.10	-0.30	-0.05
		3.00	2.30
		0.04	-0.10
		0.40	0.20
		-0.35	-0.10

+ Predicted MUF transition time earlier than measured time

- Predicted MUF transition time later than measured time

TABLE 2

Locations and frequencies of transmitters monitored
Path lengths to Leicester also shown

Location	Path length (km)	Frequencies (MHz)
Moscow	2490	10.980 13.370 15.950
Bracknell	348	4.782 8.040 9.203
Rome	1575	8.1466 13.600
Oslo	1049	5.945 8.0575 11.097
Stockholm	1172	6.901 8.0775
Offenbach	742	9.947
Rota (Spain)	1828	7.626 12.184
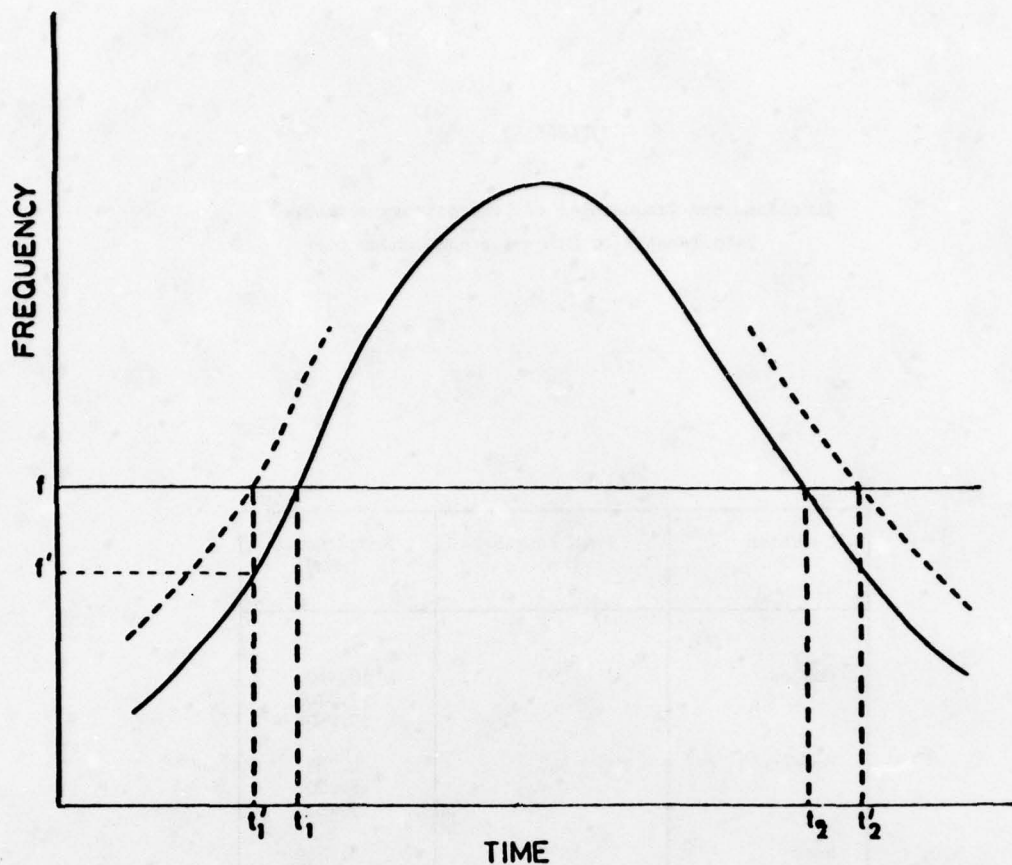
Figure 1   Typical variation of MUF with time for one-hop circuit. Full line indicates predicted
curve and broken curve actual values. f is the working frequency and f^1 the predicted MUF
at the time (t_1^1) when this frequency (f) is first received.
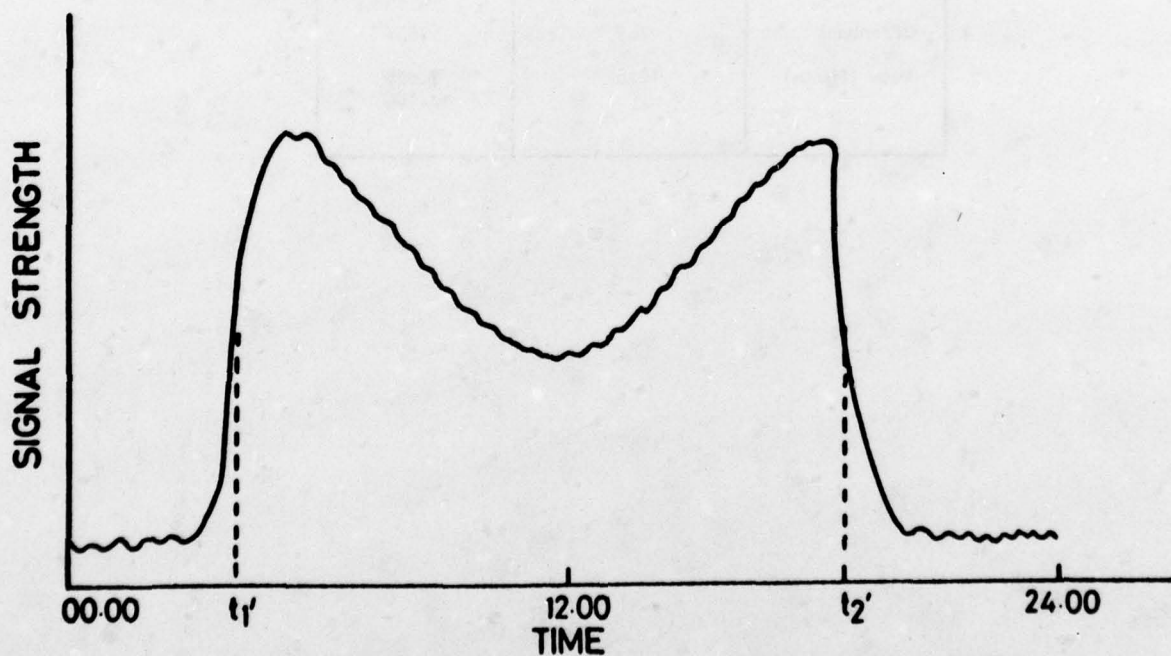
Figure 2   Typical variation of signal strength with time for a given frequency and propagation distance.
The times at which path MUF is equal to the working frequency are marked t_1^1 and t_2^1.
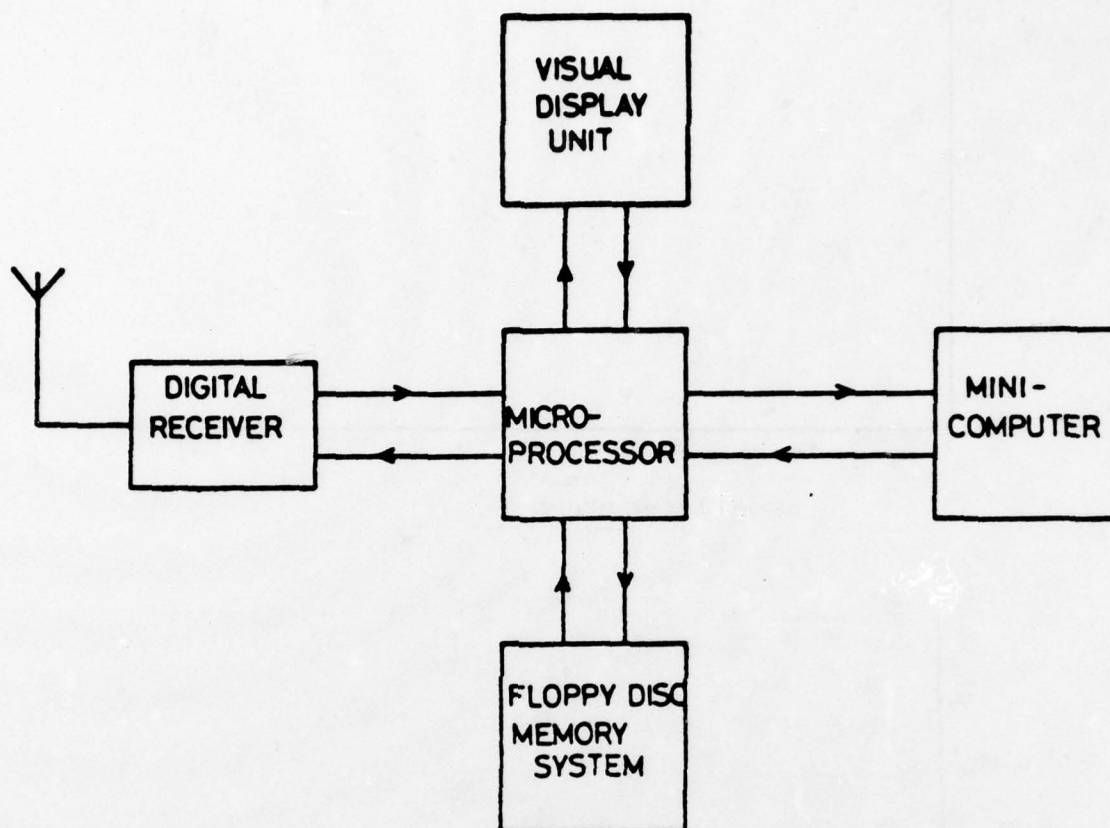
Figure 3   Block diagram of prediction system.

DBS

80

60

40

20

0

0   2   4   6   8   10   12   14   16   18   20   22

TIME GMT
BURGHCLASTE 3.985 MHZS DATE 11/03/77

DBS

70

60

50

40

30

20

10

0

0   2   4   6   8   10   12   14   16   18   20   22

TIME GMT
MOSCOW 15.950MHZS 12/11/777
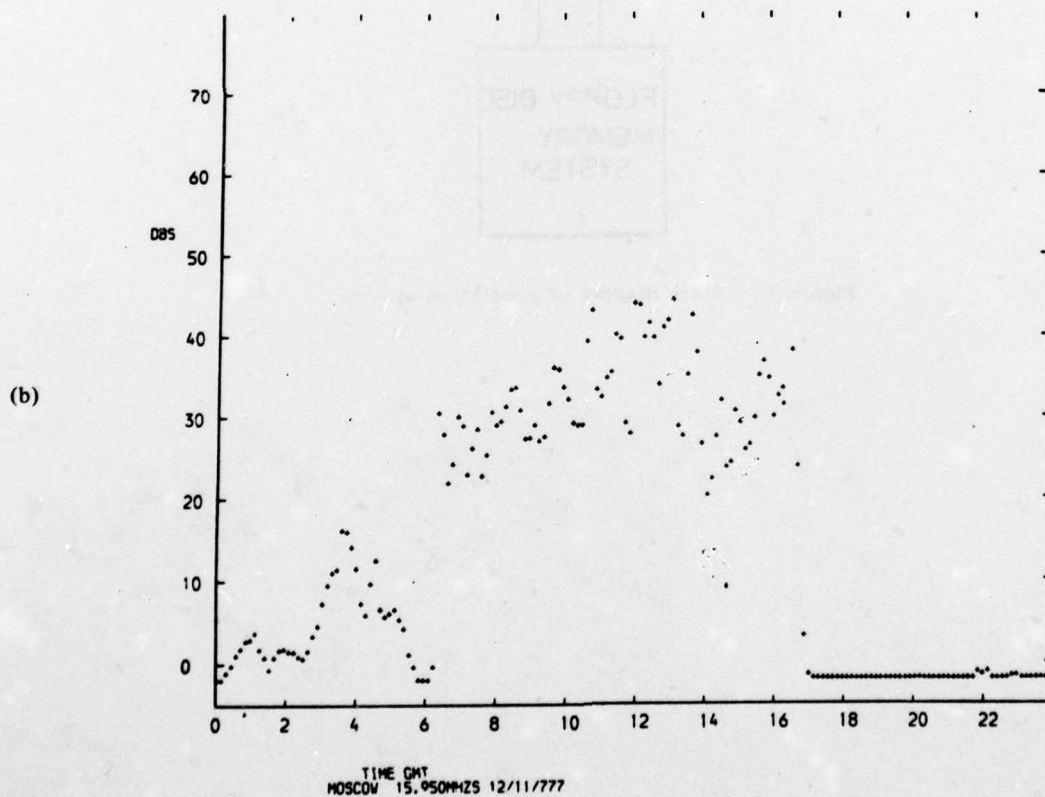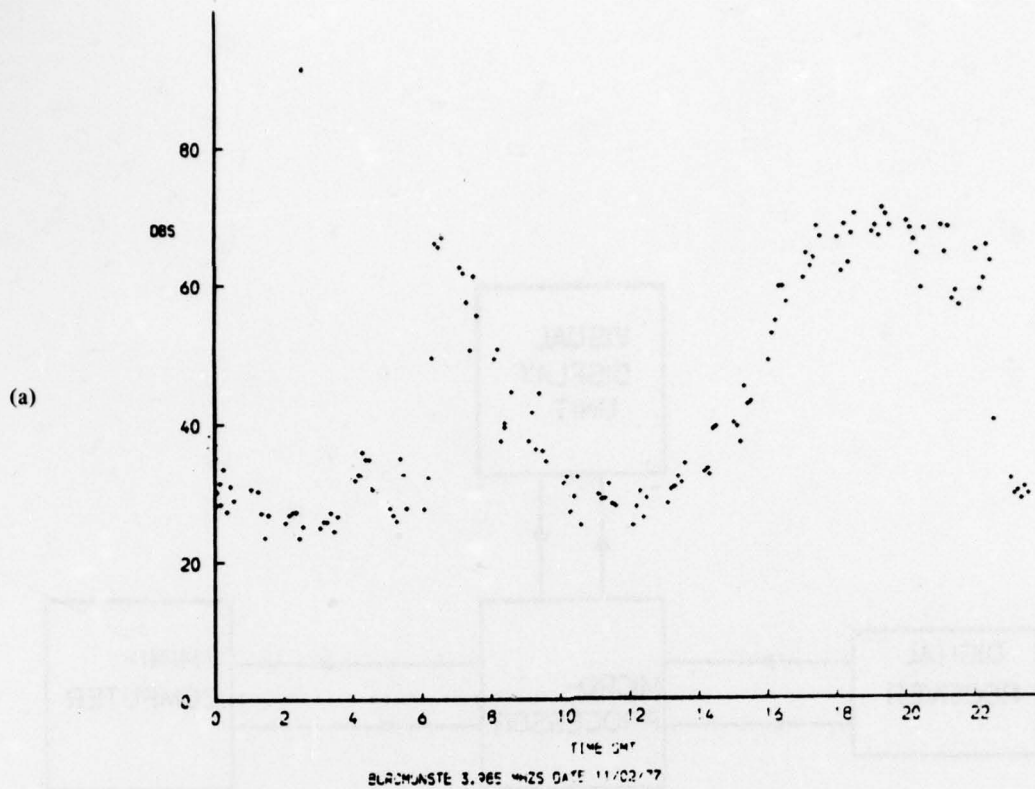
Figure 4   (a) Variation of signal strength with time. Lower frequencies exhibit minimum around noon
                due to absorption effects.

           (b) Variation of signal strength with time. At higher frequencies this is controlled mainly
                by MUF transitions.
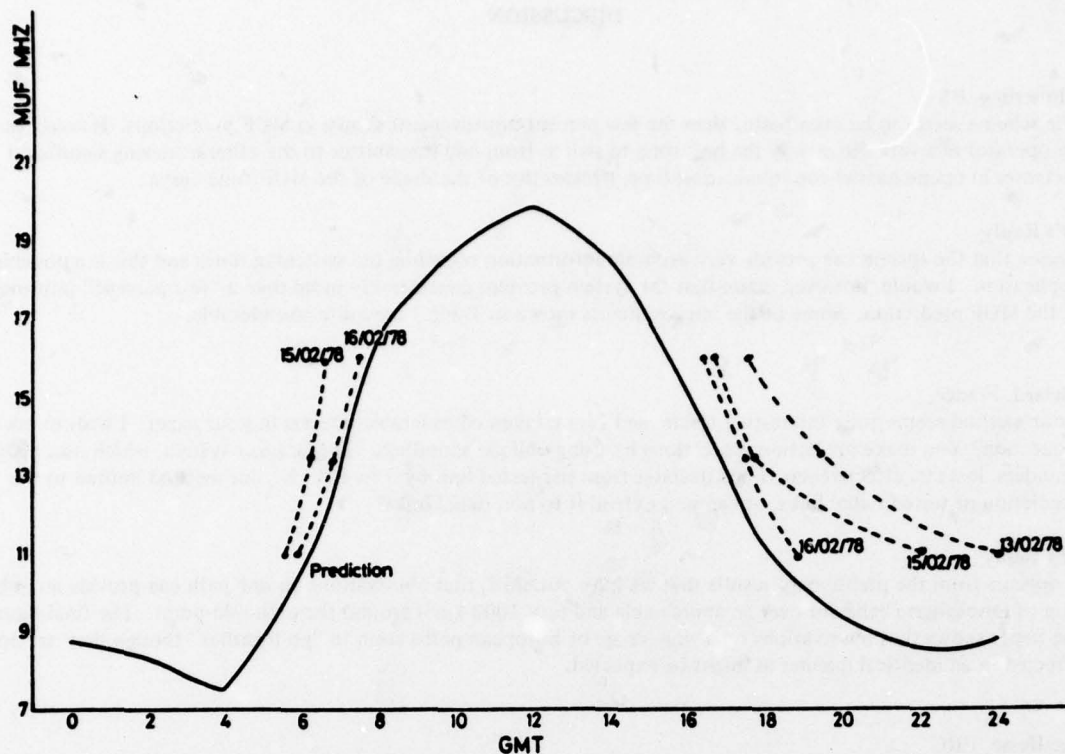
Figure 5 Predicted MUF curve for Moscow-Leicester path (full-line curve). Measured transition times for 13, 15 and 16 February 1978 are indicated by broken lines.
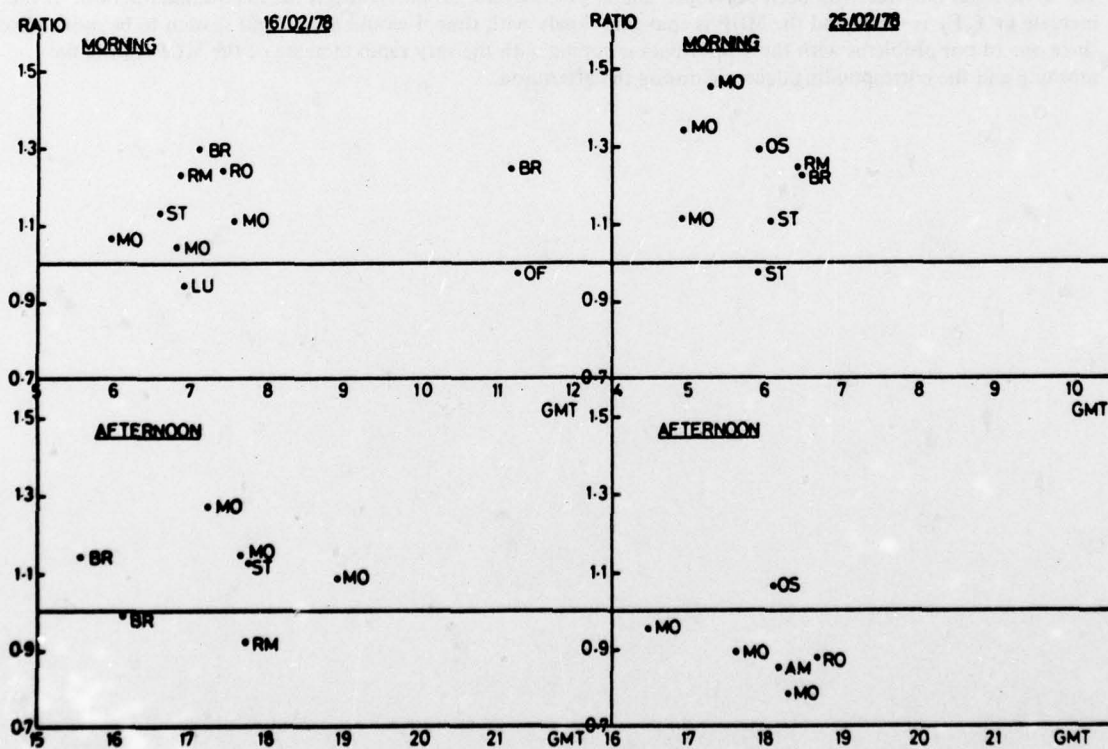
Figure 6 The ratios of (measured MUF)/(predicted MUF) for 16 and 25 February 1978. Morning and afternoon periods shown separately.

KEY: BR - Bracknell   MO - Moscow   RM - Rome   RO - Rota
      ST - Stockholm   OS - Oslo   OF - Offenbach

DISCUSSION

E.R.Schmerling, US

The scheme seems to be even better than the few percent improvement shown in MUF predictions. It *could* tell an operator in a very direct way the best time to switch from one transmitter to the other achieving significant increases in open-channel communication time, irrespective of the shape of the MUF/time curve.

Author's Reply

I agree that the system can provide very accurate information regarding the switching times and this is a possible application. I would, however, claim that the system provides considerably more than a "few percent" improvement in the MUF prediction. Some of the improvements shown in Table 1 are quite considerable.

C.Goutelard, France

Your method seems quite interesting to me, and I have taken considerable interest in your paper. I wish to ask you a question. You make prediction corrections by using oblique soundings. The Granger system, which uses bistatic sounders, loses its effectiveness if one deviates from the tested link by 5 to 10°. Is your method limited to the prediction of tested radial links, or can you extend it to non radial links?

Author's Reply

It appears from the preliminary results that we have obtained, that observations on one path can provide an indication of ionospheric behavior over an appreciable and (say 1000 km^2) around the path mid-point. The final figure in the paper shows that observations on a wide range of European paths seem to "go together" though they are not all affected in an identical manner as might be expected.

G.Lange-Hesse, FRG

The examples you have given are taken from winter-time and equinoctial seasons, when the increase of $f_o F_2$ in the morning is very strong. However, during summer-time conditions the $f_o F_2$ increase in the morning is very low. I should like to know whether your method can be used under these extreme conditions?

Author's Reply

The system has only recently been developed and as yet, we have no observations for the Summer period. If the increase in $f_o F_2$ is small, and the MUF is changing slowly with time, I would expect our system to be more effective since one of our problems with the Winter data is coping with the very rapid increase of the MUF during the morning and the corresponding decrease during the afternoon.

HF SHORT-TERM FIELD-STRENGTH PREDICTIONS
AND THEIR AGREEMENT WITH OBSERVATIONS

Th. Damboldt

FORSCHUNGSINSTITUT DER DEUTSCHEN BUNDESPOST

D-6100 DARMSTADT, P.O. BOX 5000

SUMMARY

The Research Institute of the Deutsche Bundespost makes daily HF field-strength predictions for two European and three overseas paths (Germany-England, -USSR, -USA, -Japan, and -Australia). These predictions are based on solar-geophysical data supplied by the Ursigram Service (these data are at least several hours old) and on real-time field-strength measurements of distant HF-transmitters on 26 frequencies. Also available are the geomagnetic variations indicated on a local magnetometer in real-time, the critical frequencies of the ionosonde at Lindau, solar observations from Wendelstein and geomagnetic observations from Wingst, all in near real-time. The method of estimating expected changes in propagation conditions is rather conventional and relies mainly on the experience of the forecasters.

The distinctive feature of the predictions is that they are forecast in the form of a quality figure which is related to the daily expected field strength (converted to 1 kW and referred to an omnidirectional antenna). All paths are monitored on four or five frequencies and the daily quality figure for each path is obtained by calculating the mean of the 24 hourly values of the field strength of that frequency having the highest field strength for each of the individual hours. This is done on the assumption that the optimum frequency would be used for communication. This value does not agree with the mean of the field strength of the five frequencies. The quality figure in steps of 0.1 (corresponding to 0.5 dB) is forecast for the above-mentioned 5 circuits on each workday before noon.

The choice of the forecast being made in terms of a field strength-related quality figure allows the forecast to be compared with the actually measured field strength. In retrospect, it is also possible to check the reliability of the forecasts. During the past three years in which this method has been in use, the average reliability amounted to 99% for deviations between predicted and measured quality figures up to $\pm$ 2.0 and to 90% for deviations up to $\pm$ 1.0. The reliability, of course, is different for the various paths and months, the worst case ocurred in March 1975 for the path Halifax-Germany with an agreement between forecast and observation of only 87% and 58% for deviations of 2.0 and 1.0, respectively.

1.   INTRODUCTION

The importance of HF radio communications has decreased considerably during the past decade. At the same time the interest in radio propagation predictions decreased but did not cease completely. A successful attempt was made in the Federal Republic of Germany to come to an agreement with various users of predictions (e.g. German Post Office, Ministry of Defense, Ministry of Foreign Affairs, Deutsche Lufthansa) who wanted a small prediciton service to be maintained. It was decided to continue to have the prediction group with the German Post Office (i.e. with the telecommunication administration). This group forms part of the Research Institute of the German Post Office in Darmstadt and makes both long-term and short-term predictions for the HF range on a routine basis. The long-term predictions and a comparison with measurements were described by Damboldt (1976). The short-term predictions and their agreement with observations are described in this paper. The short-term prediciton method has changed considerably in comparison with the previous method, described by Ochs (1970). Much of the information contained in the paper by Ochs, however, is still relevant.

2. FIELD-STRENGTH MEASUREMENTS

The prediction method decribed here relies mainly on continuous field-strength measurements of distant HF transmitters. The receivers are located in the northern part of West Germany at a receiving site with particularly low man-made noise level. The AGC-voltages of the receivers are sent to the office at Darmstadt over a telephone line. Here, most of the chart recorders (19 out of a total of 26) are installed in such a way that all recordings can be read simultaneously (Fig 1).

For recording purposes only radio stations transmitting 24 hours a day are suitable. A number of meteorological broadcast transmitters which meet this requirement was chosen. Information on these transmitters was taken either from ITU's International Frequency List (power, frequency, site) or from the "Nautischer Funkdienst" (contents of transmissions). Unfortunately, reliable details about transmitter powers and antennas usually are not available for all stations because most of them are operated by the military. At the present time the field strengths of the following stations are recorded:

Norfolk	(USA)
Tokyo	(J)
Canberra	(AUS)
Bracknell	(GB)
Moscow	(SU)

In order to evaluate the chart recordings, a fully automatic analyzer or a direct digitization of the AGC-voltage is not suitable because of the possible presence of interference. The proper trace on the chart characterized by certain features is marked by an experienced operator. This is possible because all transmitters use frequency shift keying (shift $\pm$ 400 Hz). Since the recordings are made with a receiver bandwidth of 100 Hz only, the trace on the chart shows characteristic changes from mark to space. The transmissions at the frequencies of each path recorded contain the same information. Therefore the changes from mark to space must be recognizable on all four of five chart recordings of that path (Fig 2). If a trace does not show these characteristics, there is either interference, technical trouble, or the frequency is above the MUF or below the LUF.

The strip charts are cut off every workday in the morning and hourly values of the measured receiver input voltage are read off the revised charts. The conversion from receiver input voltage into field strength is somewhat complicated because the receiving antennas are rhombic antennas of high directivity (Damboldt, 1977). The conversion is done by computer which stores all necessary data to yield a field strength normalized to a transmitter power of 1 kW and an isotropic transmitting antenna. These values are then tabulated and depicted in different suitable ways.

3. CALCULATION OF A QUALITY FIGURE

A daily quality figure is calculated for each circuit from the 24 hourly values of the received field strength of the transmitters recorded. For each hour the field strength of the frequency with the highest field strength is taken. This is done on the assumption that the optimum frequency would be used for communication. Now the quality figure is computed according to:

$$ Q = \frac{F_1 + F_2 + \ldots + F_{24}}{24} \, 0.2 + 6.0 $$

where the F_1 denote the hourly values of the field strength in dB related to $1\,\mu V/m$. It follows that a 24-hour average field strength of 0 dB ($\mu V/m$) corresponds to a quality figure of 6.0 and that an increase of the quality figure by 0.1 corresponds to a field-strength increase of 0.5 dB. This gives handy values and the quality figures for the paths monitored usually vary between 2.0 (equal to an average field strength of -20 dB related to $1\,\mu V/m$) during poor conditions on the long distance path Australia-Germany and 14.0 (equal to an average field strength of +40 dB ($\mu V/m$)) during good conditions on the short-distance path England-Germany (Fig 3).

Strictly speaking, the quality figure is not a direct measure of the field strength because it is the average of the logarithms of field strengths and therefore the physical meaning of this value is difficult to assess: i.e. the direct relation between quality figure and field strength is valid only if the 24 hourly values are equal. The application of the quality figure as a daily measure of propagation conditions has none the less proved its usefulness over the past three years.

Calculating the quality figure becomes somewhat complicated if, at some hours, reception of the proper transmitter is masked by interference (symbol S) or impossible because of technical problems (symbol C). In that case a value S or C is entered and the computer program checks whether - according to the long-term predictions - the signal intensity during the relevant time is predicted to be below the threshold of the receiver or not. If it is below the receiver threshold, it is compared with the measured signal intensity for the same hour at the day before the key-day. If this was also below the receiver threshold, the corrected value "G" is stored in the memory. G means: No value because the frequency used was above MUF or below LUF during this hour. If a signal was measured on the day before the key-day, the corrected value for the key-day is receiver threshold plus twice the last day's value divided by three. - A similar procedure is applied if the long-term prediction predicts a value above the receiver threshold. Therefore, in the case of interference or technical problems the measured field strength of the past days has some influence on the key-day's "corrected value". In the case of sudden changes of radio-propagation conditions together with accidental interference or technical problems (transmitter or receiver breakdown) this method may lead to an over - or underestimation of the quality figure, thus smoothing rapid changes in actual propagation conditions.

4. FORECASTING THE QUALITY FIGURES

Every workday the quality figures are forecast before noon. At that time the evaluated and corrected measurements of all 26 paths for the past 24 hours are available in different graphical representations (Fig 4). Also available at that time are the readings of a local magnetometer, the readings of the Geomagnetic Observatory Wingst (near Hamburg), hourly values of the vertical incidence critical frequencies for the past 24 hours from the ionosonde at Lindau and - weather permitting - a chart of sunspots from the observatory on Mount Wendelstein. Moreover, a variety of data measured in different parts of the world is received through the Ursigram Service. The disadvantage of these data is that they are at least several hours old. Further very useful information is supplied by the solar daily forecast (SDF) received regularly from Boulder. With all this information at hand, two experienced forecasters predict the quality figure for the 24-hour period ahead, also taking into account the 27-day recurrence tendency and the conservation trend as well.

Fig. 5 shows a sample prediction which is named "Daily Report". The Daily Report is made up of two parts. The first part comprises the review of the past 24 hours and the second part the expected development for the next 24 hours. Both parts are arranged in an identical way for simplicity. Most entries are self-explanatory. The quality figures are calculated and predicted according to the methodes described above.

5. CONTROLLING THE RELIABILITY OF THE PREDICTIONS

A record is kept of the daily predicted and measured quality figures. Table I shows an example of this record for the month of October 1976 which was the month with the most unsuccessful predictions. Whenever the deviation between the predicted and measured values is greater than $\pm$ 1.0 (or 5 dB) it is marked with the number i, whenever it is greater than $\pm$ 2.0 (or 10 dB), it is marked with the number ii. This method allows a current control of the accuracy of the predictions.

As mentioned previously, the predictions are issued on workdays only. This means that each week on Friday before noon a prediction is issued for the next three days. It is quite clear that these predictions for several days ahead are more likely to be incorrect than the predictions for only the following day. The result of this fact can

clearly be seen in Table I where of the 70 quality figures forecast for the weekends 14 were in error, whereas for the 85 quality figures forecast during the week only 5 were in error. The month of October 1976 was chosen only as an example. The "weekend effect" can be seen in nearly all other monthly tables.

At the end of each month the monthly mean of the reliability of the daily predictions is calculated for each path. The results are given in Table II which shows the monthly means for the years 1975 to 1977. It can be seen that the average reliability amounts to about 90% for differences between predicted and measured quality figures of less than $\pm$ 1.0 (or $\pm$ 5 dB) and to about 99% for differences of less than $\pm$ 2.0 (or 10 dB).

Another possibility to express the reliability of the predictions quantitatively - although of limited informativeness - is the correlation coefficient:

$$r = \frac{\sum (x_i - \bar{x}) \cdot (y_i - \bar{y})}{\sqrt{\sum (x_i - \bar{x})^2 \cdot \sum (y_i - \bar{y})^2}}$$

where $\bar{x}$ and $\bar{y}$ denote the average of the variables x_i and y_i.

For each year and path several correlation coefficients were calculated:

p/m   means the correlation coefficient between the daily values of the predicted and measured quality figures (predicted/measured)

my/mt   means the autocorrelation coefficient between the daily values of the measured quality figures with a time lag of one day (i.e. measured yesterday/measured today)

pt/my   means the correlation coefficient between the daily predicted quality figures and the quality figures measured a day earlier (predicted today/measured yesterday).

Table III shows these correlation coefficients for the different years and paths. The interpretation of Table III is quite difficult. It can be seen, however, that the correlation coefficient between predicted and measured values in most cases is higher than the autocorrelation coefficient with a time-lag of one day. This means that the predictions are better than those only based on the quality figure measured a day earlier, although the differences between these two values are small (the same is true for the weather forecast as generally known).

The difficulty of a correct interpretation of the correlation coefficient arises at this point. A confidence limit can hardly be given because the number of independent values cannot be determined. A conservation trend of about 6 to 10 days has to be taken into account. Therefore, in the course of one year, the number of independent values is 40 to 50, at most. With this small number the scatter of the predicted values in relation to the measurements has a large influence on the correlation coefficient. Most predictions deviate from the measurements only by a small amount. This would in practice still be regarded as a correct prediction.

It should also be borne in mind that, if propagation conditions change considerably (e.g. during a disturbance) and the trend is predicted correctly but predicted and measured quality figures are not identical, a low value of the correlation coefficient is obtained, especially if the number of values used for the correlation is small. This means that the effect of a few successful predictions of disturbances is masked by many small deviations of also successful - but less important - predictions during undisturbed conditions.

Another interesting fact can be seen in Table III:
The close correlation between predictions and the measurements made one day before. The interpretation of this fact is that the forecaster's decision apparently is strongly influenced by the previous day's propagation conditions.

6.   CONCLUSIONS

This paper describes the quality control of the daily radio propagation predictions comprising a quantitative index: the so-called quality figure. This quality figure can be predicted and also be determined afterwards from field-strength recordings. The comparison between predicted and measured values shows good agreement.

A disadvantage of the quality figure has become apparent, viz the mean of the logarithmic field-strength values tends to smooth extremes and this mean value has no physical meaning. Strictly speaking, the quality figure is connected directly with the field strength only if all 24 hourly values are identical. It is questionable whether the users of the predictions are satisfied with a value representing 24 hours of a day when traffic may have been possible during a limited time only (e g on long-distance paths). As a next step a new quality figure will be devised which consists of two parts. The first part gives the number of hours during which a particular path is available for communication (i.e. field strength above a certain threshold) and the second part gives the mean field strength during these hours.

7.   REFERENCES

Damboldt, Th., A Comparison between the Deutsche Bundes-
    post Ionospheric HF Radio Propagation Predictions and
    Measured Field Strength, AGARD Conference Proceedings
    173 (1976), paper 12

Damboldt, Th., Lüchow Receiving-Site Measurements:
    Conversion from r.m.s. Receiver Input Voltage to Sky-Wave
    field strength, C.C.I.R. IWP 6/1 Doc 54 (1977)

Ochs, A., The Forecasting System of the Fernmeldetechnisches
    Zentralamt (FTZ), AGARD Conference Proceedings 49 (1970),
    paper 43

TABLE I

Predicted and Measured Quality Figures for the Month of October 1976

		Pred Hal	Meas Hal		Pred Tok	Meas Tok		Pred Can	Meas Can		Pred Msk	Meas Msk		Pred Brk	Meas Brk	
Fri	1	8.0	7.8	.	6.0	5.7	.	4.3	5.1	.	13.0	13.1	.	13.2	14.0	.
Sat	2	8.2	7.5	.	6.0	4.9	i	4.3	4.8	.	13.0	13.9	.	13.2	13.5	.
Sun	3	8.4	8.4	.	6.0	6.3	.	4.3	4.9	.	13.0	13.4	.	13.2	13.4	.
Mon	4	8.2	10.1	i	6.1	6.4	.	4.7	5.5	.	13.4	14.9	i	13.5	14.9	i
Tue	5	9.4	9.7	.	6.2	5.8	.	5.1	5.1	.	14.4	13.9	.	14.5	14.3	.
Wed	6	9.5	8.4	i	5.8	6.1	.	5.0	5.5	.	13.8	14.5	.	14.2	13.8	.
Thu	7	8.4	8.5	.	6.0	6.6	.	5.1	5.3	.	14.2	14.6	.	13.8	14.5	.
Fri	8	8.5	9.0	.	6.5	6.8	.	5.2	5.9	.	14.3	14.7	.	14.3	15.1	.
Sat	9	8.5	10.1	i	6.5	6.8	.	5.2	5.8	.	14.3	14.7	.	14.3	15.2	.
Sun	10	8.5	9.9	i	6.5	7.6	i	5.2	5.8	.	14.3	13.9	.	14.3	15.1	.
Mon	11	9.5	10.2	.	7.4	7.0	.	5.5	6.0	.	14.2	13.6	.	15.0	15.1	.
Tue	12	9.4	9.1	.	6.2	6.7	.	5.6	5.5	.	13.5	14.0	.	14.6	15.1	.
Wed	13	8.6	8.9	.	6.6	5.9	.	5.5	5.2	.	14.0	14.1	.	14.8	14.5	.
Thu	14	8.4	9.5	i	5.8	5.8	.	5.0	4.8	.	14.0	14.0	.	14.5	15.0	.
Fri	15	9.5	8.1	i	6.0	5.8	.	4.8	5.5	.	14.0	14.5	.	14.8	14.8	.
Sat	16	9.5	7.2	ii	6.0	4.6	i	4.8	5.0	.	14.0	13.9	.	14.8	14.5	.
Sun	17	8.8	6.6	ii	5.4	4.6	.	4.8	4.6	.	14.0	12.7	i	14.8	14.1	.
Mon	18	6.6	7.3	.	4.5	4.9	.	4.5	4.7	.	12.8	12.8	.	14.0	13.6	.
Tue	19	7.8	8.0	.	5.4	5.2	.	5.0	4.4	.	13.4	12.7	.	13.8	13.9	.
Wed	20	8.4	7.7	.	5.5	4.4	i	4.6	3.9	.	13.0	12.0	.	13.9	13.6	.
Thu	21	8.0	8.6	.	5.0	4.9	.	4.4	4.7	.	12.2	13.1	.	13.6	14.1	.
Fri	22	8.8	8.1	.	5.2	5.2	.	4.8	4.8	.	13.2	13.2	.	14.0	14.3	.
Sat	23	8.8	8.9	.	5.2	5.9	.	4.8	5.6	.	13.2	13.2	.	14.0	14.4	.
Sun	24	8.8	9.5	.	5.2	5.8	.	4.8	5.6	.	13.2	13.2	.	14.0	14.2	.
Mon	25	9.5	8.8	.	5.8	6.1	.	5.5	4.3	i	13.2	12.2	.	14.2	13.9	.
Tue	26	8.8	8.8	.	5.9	5.7	.	4.5	5.0	.	12.5	13.3	.	13.9	14.3	.
Wed	27	8.5	9.6	i	5.8	5.8	.	5.0	4.9	.	13.0	12.3	.	13.9	14.2	.
Thu	28	9.2	9.3	.	5.8	5.8	.	4.9	4.4	.	12.8	12.9	.	14.0	14.1	.
Fri	29	9.0	8.4	.	5.8	5.9	.	4.6	4.8	.	12.8	13.5	.	14.0	14.2	.
Sat	30	9.0	8.5	.	5.8	5.9	.	4.6	4.6	.	12.8	13.0	.	14.0	13.9	.
Sun	31	9.0	7.9	i	5.8	4.6	i	4.6	4.7	.	12.8	12.0	.	14.0	14.2	.

TABLE II

Reliability of Short-term Field-strength Predictions in %

Year 1975 Month	Halifax +/- 5dB	10dB	Tokyo +/- 5dB	10dB	Canberra +/- 5dB	10dB	Mauritius +/- 5dB	10dB	Bracknell +/- 5dB	10dB	All +/- 5dB	10dB
Jan	83.9	100.0	93.5	96.8	100.0	100.0	100.0	100.0	80.6	96.8	91.6	98.7
Feb	82.1	96.4	75.0	96.4	96.4	100.0	85.7	100.0	85.7	96.4	85.0	97.9
Mar	58.6	87.1	77.4	100.0	93.5	100.0	83.9	100.0	74.2	96.8	77.4	96.8
Apr	80.0	96.7	93.3	100.0	100.0	100.0	73.3	96.7	86.7	100.0	86.7	98.6
May	74.2	100.0	71.0	100.0	93.5	100.0	83.9	100.0	90.3	96.8	82.6	99.4
Jun	93.3	100.0	83.3	100.0	96.7	100.0	90.0	96.7	96.7	100.0	92.0	99.3
Jul	93.5	96.8	93.5	100.0	100.0	100.0	87.1	100.0	100.0	100.0	94.8	99.4
Aug	67.8	93.5	83.9	100.0	96.8	100.0	96.8	100.0	100.0	100.0	89.3	98.7
Sep	73.3	96.7	86.7	100.0	100.0	100.0	83.3	96.7	100.0	100.0	88.7	98.7
Oct	90.3	100.0	90.3	96.8	100.0	100.0	83.9	96.8	100.0	100.0	92.9	98.7
Nov	76.7	100.0	93.3	100.0	96.7	100.0	93.3	100.0	93.3	100.0	90.6	100.0
Dec	71.0	90.3	93.5	100.0	100.0	100.0	77.4	100.0	100.0	100.0	88.4	98.1
mean:	78.7	96.5	86.2	99.2	97.8	100.0	86.6	98.9	92.3	98.9	88.3	98.1

Year 1976 Month	Halifax +/- 5dB	10dB	Tokyo +/- 5dB	10dB	Canberra +/- 5dB	10dB	Moscow +/- 5dB	10dB	Bracknell +/- 5dB	10dB	All +/- 5dB	10dB
Jan	74.2	93.5	87.1	100.0	96.8	100.0	93.5	100.0	96.8	100.0	89.7	98.7
Feb	82.8	96.6	96.6	100.0	96.8	100.0	93.1	100.0	100.0	100.0	93.8	99.3
Mar	90.3	100.0	90.3	100.0	100.0	100.0	80.6	96.8	93.5	100.0	91.0	99.4
Apr	76.7	96.7	70.0	86.7	100.0	100.0	93.3	100.0	100.0	100.0	88.0	96.7
May	96.8	100.0	77.4	93.5	96.8	100.0	100.0	100.0	100.0	100.0	94.2	98.7
Jun	90.0	100.0	83.3	100.0	96.7	100.0	100.0	100.0	100.0	100.0	94.0	100.0
Jul	100.0	100.0	83.9	100.0	100.0	100.0	100.0	100.0	87.1	100.0	94.2	100.0
Aug	100.0	100.0	83.9	100.0	100.0	100.0	100.0	100.0	93.5	100.0	95.5	100.0
Sep	93.3	96.7	86.7	100.0	100.0	100.0	96.7	100.0	100.0	100.0	95.3	99.3
Oct	67.7	93.5	83.9	100.0	96.8	100.0	93.5	100.0	96.8	100.0	87.7	98.7
Nov	86.7	100.0	93.3	100.0	96.7	100.0	93.3	100.0	93.3	100.0	92.7	100.0
Dec	Norfolk 100.0	100.0	74.2	100.0	100.0	100.0	90.3	100.0	96.8	100.0	92.3	100.0
mean:	88.2	98.1	84.2	98.4	98.4	100.0	94.5	99.7	96.5	100.0	92.4	99.2

Year 1977 Month	Norfolk +/- 5dB	10dB	Tokyo +/- 5dB	10dB	Canberra +/- 5dB	10dB	Moscow +/- 5dB	10dB	Bracknell +/- 5dB	10dB	All +/- 5dB	10dB
Jan	80.6	100.0	90.3	96.8	100.0	100.0	90.3	100.0	96.8	100.0	91.6	99.4
Feb	85.7	100.0	96.4	100.0	100.0	100.0	96.4	100.0	92.9	100.0	91.6	100.0
Mar	80.6	100.0	93.5	100.0	90.3	100.0	93.5	100.0	100.0	100.0	91.6	100.0
Apr	80.0	100.0	76.7	96.7	93.3	100.0	83.3	100.0	100.0	100.0	86.7	99.3
May	83.9	96.8	71.0	96.8	90.3	100.0	96.8	100.0	100.0	100.0	87.7	98.7
Jun	96.7	100.0	66.7	100.0	100.0	100.0	100.0	100.0	100.0	100.0	92.7	100.0
Jul	93.5	100.0	71.0	93.5	90.3	100.0	100.0	100.0	96.8	100.0	90.3	98.7
Aug	93.5	100.0	61.3	90.3	100.0	100.0	100.0	100.0	100.0	100.0	91.0	98.1
Sep	83.3	100.0	73.3	96.7	83.3	100.0	100.0	100.0	96.3	100.0	87.2	99.3
Oct	77.4	96.8	80.6	100.0	93.5	100.0	87.1	100.0	87.1	100.0	85.1	99.4
Nov	76.6	100.0	76.7	97.6	96.7	100.0	96.7	100.0	100.0	100.0	89.4	99.4
Dec	71.0	93.5	90.3	100.0	100.0	100.0	83.9	100.0	96.8	100.0	88.4	98.7
mean:	83.6	98.9	79.0	97.3	94.8	100.0	94.0	100.0	97.0	100.0	89.7	99.3

TABLE III

	1975			1976			1977		
	p/m	my/mt	pt/my	p/m	my/mt	pt/my	p/m	my/mt	pt/my
Halifax Norfolk	0.77	0.77	0.65	0.88	0.83	0.90	0.85	0.84	0.94
Tokyo	0.87	0.86	0.82	0.75	0.75	0.86	0.61	0.65	0.77
Canberra	0.90	0.89	0.93	0.83	0.83	0.89	0.71	0.70	0.83
Mauritius Moscow	0.63	0.73	0.83	0.82	0.74	0.89	0.81	0.80	0.90
Bracknell	0.82	0.82	0.88	0.58	0.54	0.70	0.94	0.92	0.97
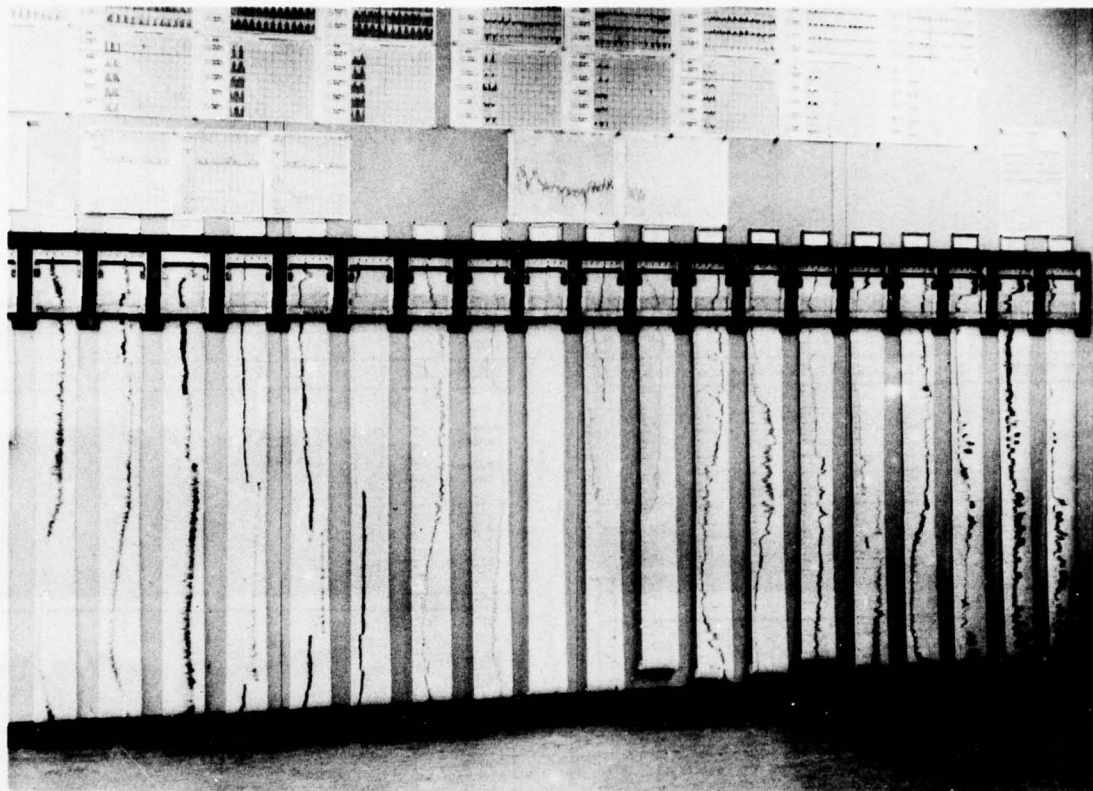
Fig.1   Wall with 19 chart recorders
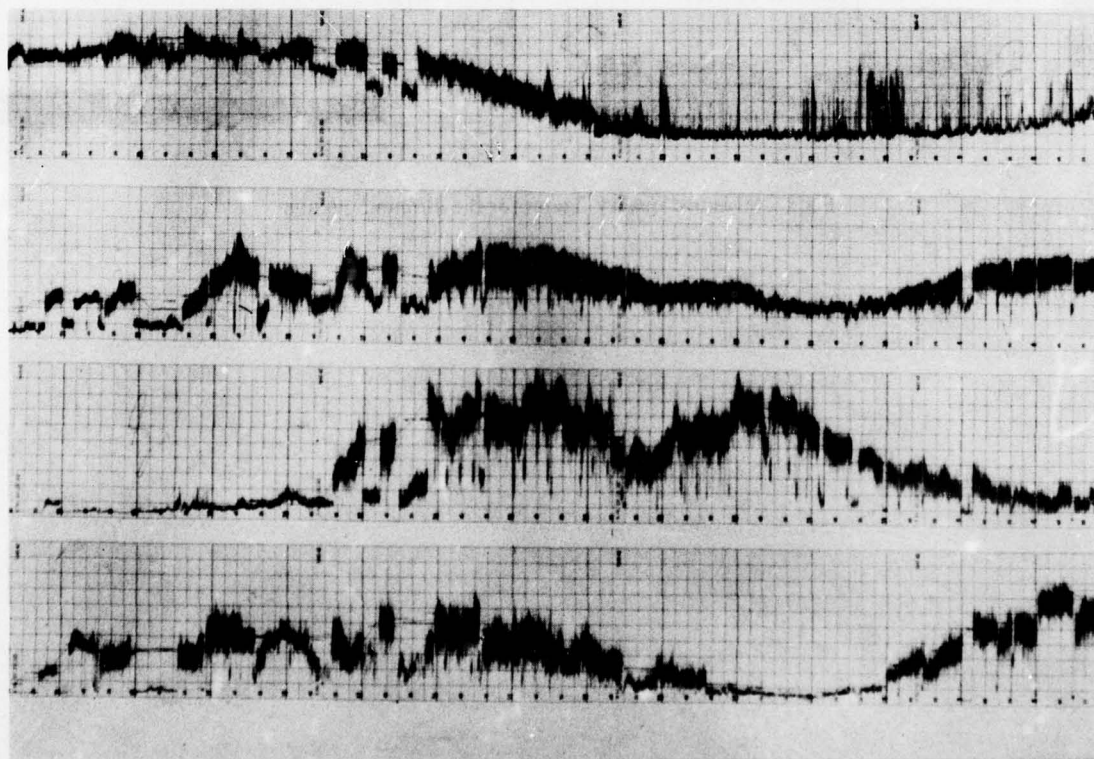
Fig.2   Typical recording of F1-transmissions if narrow
if-filters are used
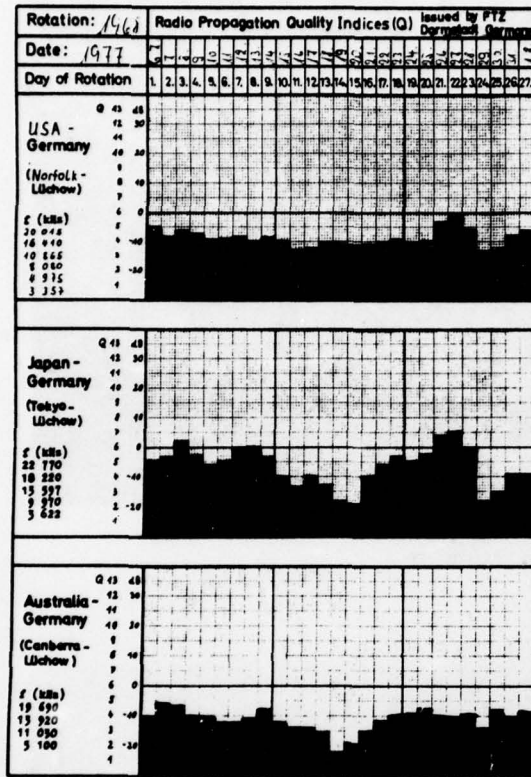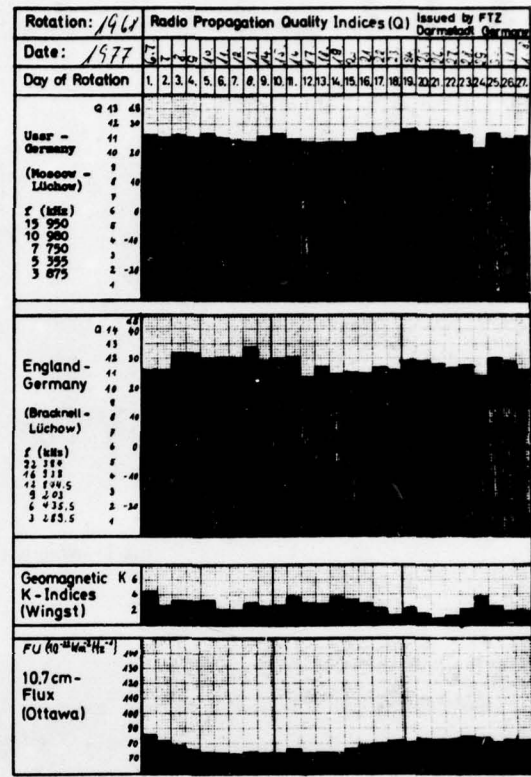
Fig.3 Measured quality figures for the different circuits
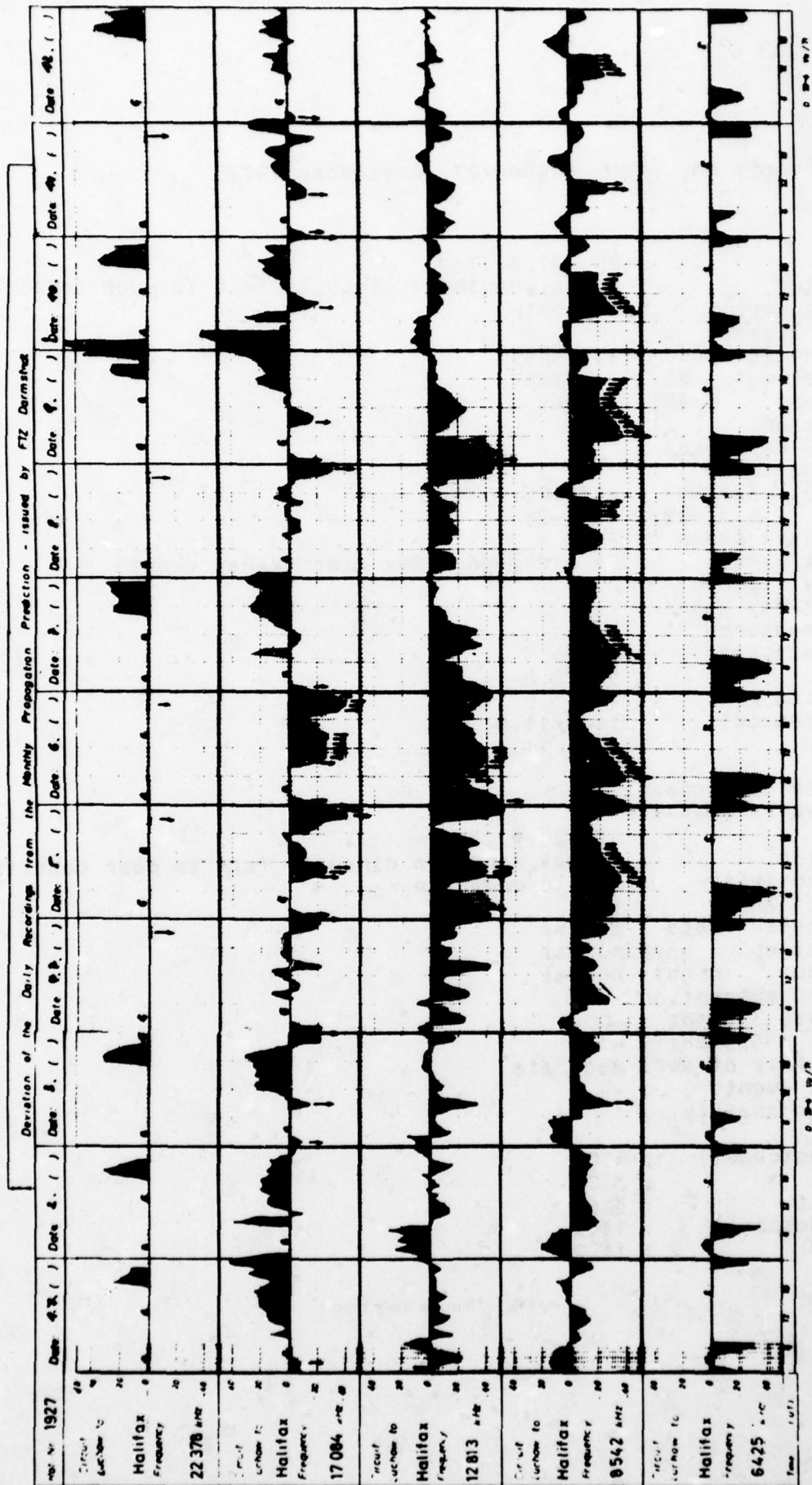
Fig.4 Hourly deviations of measured field strength from the long-term prediction

419209 ion d

daily report no. 186 issued 27. september 1977

review
======
period   : 26.-27.9.77
situation   : normal,northern circuits fair to poor conditions
solar activity   : moderate
10 cm ottawa   : 99
geomagnetic field : 23344454
vertical muf   day: + 0-1mhz
in europe   night: normal
absorption
last 27 day mean/
daily measured
bracknell 3.3 mhz : -15/-25
moscow   5.3 mhz : -16/-21
short wave fades : --
special events   : 26 0124z+26 0148z minor x-ray events
quality figures
last 27 day mean/
daily measured
usa (eastcoast)   : 5.3/4.1
japan   : 5.0/2.8
australia   : 4.6/3.8
ussr (moscow)   : 11.5/11.4
england   : 11.5/11.3

expected development
====================
period   : 27.-28.9.77
situation   : normal,northern circuits fair to poor conditions
solar activity   : low to moderate
10 cm ottawa   : 102
geomagnetic field : active
vertical muf   day: normal
in europe   night: normal
expected absorption
bracknell 3.3 mhz : -20
moscow   5.3 mhz : -17
probability of swf: moderate
special events   : --
expected quality
figures
usa (eastcoast)   : 4.0
japan   : 3.0
australia   : 3.6
ussr (moscow)   : 11.2
england   : 11.2

Fig.5   Sample daily report

MODELLING THE DIURNAL AND SEASONAL VARIATION

OF MEDIUM-SCALE TRAVELLING IONOSPHERIC DISTURBANCES

J. Röttger
Max-Planck-Institut für Aeronomie
D-3411 Katlenburg-Lindau 3, F.R.G.

SUMMARY

The diurnal and seasonal variation of medium-scale travelling ionospheric disturbances observed in the equatorial region is Fourier analyzed. The significant spectral components are used for modelling the occurrence of medium-scale TIDs.

The spatial resonance mechanism in the equatorial ionosphere can steepen the amplitudes of TIDs which then break up into ionospheric irregularities. The non-linear steepened TID pattern, giving rise to large-scale patches of the equatorial spread-F, is modelled by a Fourier series.

1. INTRODUCTION

Travelling ionospheric disturbances have a considerable influence on the radio wave propagation through the ionosphere. They cause quasi-periodical group- and phase-path changes as well as variations of the incidence angle. Since it is accepted that the macro-scale structure of the equatorial spread-F is, by means of the spatial resonance effect, influenced by travelling ionospheric disturbances, an impact to the variation of scintillations of satellite signals has also to be taken into account. This paper tries to model the occurrence of TIDs and the resulting patches of spread-F irregularities in the equatorial ionosphere.

2. TRAVELLING IONOSPHERIC DISTURBANCES

From an almost three-years period of HF-backscatter experiments (RÖTTGER, 1977), the diurnal and seasonal variation of the occurrence of medium-scale travelling ionospheric disturbances (TIDs) was evaluated. These HF-backscatter experiments were carried out in Tsumeb/Southern Africa transmitting northwards. The probed area was the southern part (5-10° S) of the equatorial ionosphere. Figure 1 shows the occurrence pattern of TIDs observed by this technique. Clear occurrence maxima are observed in the morning and evening hours. The dominant evening maxima are most pronounced in the southern summer months, whereas the morning maxima are strongest in southern winter. Almost no TIDs were observed around noon during southern summer. The periods of the TIDs are between 10 and 30 min and the horizontal wavelengths are up to several hundred kilometers.

The occurrence pattern is Fourier analyzed and the significant Fourier components are used to model the occurrence of TIDs as a function of season and time of the day. An appropriate formula to be applied in the model is:

$$N_m(t) = \frac{N_g}{N}(t,m) = N_{om} + \sum_n N_{nm} \exp(i\frac{2\pi n t}{T})$$

where $N_m(t)$ = mean significant occurrence probability of TIDs,
N_g = number of records showing TID structures,
N = total number of records,
t = time of the day in hours,
T = 24 hours,
n = Fourier index,
m = 1,...,12 = running number of months,
N_{om}, N_{nm} = Fourier components.

The values of the Fourier components, which are significant up to the third harmonic, are available in a tabulated form. The mean occurrence pattern N_m^*, as it is shown in the intensity print-out of Figure 1, is obtained by filtering the observed occurrence pattern N_m, taking only the three relevant Fourier components (diurnal, semidiurnal and terdiurnal components) to calculate N_m^*. The mean residual value then becomes $\varepsilon_N = \pm 0.19$, which is the statistical variation of the TID occurrence pattern N_m^*.

A significant correlation of the TID occurrence with rainfall activity is manifested (RÖTTGER, 1977), indicating that the sources of the atmospheric gravity waves, which cause these TIDs, are found in the tropical cumulonimbus convection in the equatorial region. Thus, knowing the rainfall variations at other equatorial regions, one has an appropriate indicator to predict the TID occurrence.

3. TRAVELLING PATCHES OF EQUATORIAL SPREAD-F IRREGULARITIES

Transequatorial propagation measurements (RÖTTGER, 1975a) and observations with an HF-CW-Doppler experiment operated in Peru (RÖTTGER, 1977) indicate the relation of travelling ionospheric disturbances and the structure of the premidnight equatorial spread-F. This relation is due to the spatial resonance mechanism (WHITEHEAD, 1971; BEER, 1972; RÖTTGER, 1973), which operates when an ionospheric plasma drift matches the phase velocity of atmospheric gravity waves. Because of resonance steepening TIDs can break up into small-scale ionospheric irregularities. The TID pattern can appropriately be described by a breaking wave field (e.g. RÖTTGER, 1975a), which theoretically was proved by KLOSTERMEYER (1978). During the post-sunset/premidnight hours optimum conditions for the spatial resonance mechanism exist in the

equatorial ionosphere (RÖTTGER, 1978), which makes it possible to explain some of the macro-scale features of the equatorial spread-F.

Due to the resonance effect an originally monochromatic TID breaks up into harmonics. A model using a Fourier series to describe the ionization disturbance N_e under spatial resonance was proposed by RÖTTGER (1975a) to explain results from transequatorial propagation experiments. A similar approach is given by the series (RÖTTGER, 1975b):

$$\Delta N_e = \delta_o \cdot N_{eo} \, (S_1 + S_2)$$

with S_1 = $\sin \underline{k}_1 \cdot \underline{r}$ ($\hat{=}$ original ionospheric disturbance),

     S_n = $\sum\limits_{n=2}^{\infty} n^{-\beta} \sin \underline{k}_n \cdot \underline{r}$ ($\hat{=}$ TID harmonics causing a steepening),

     $\delta_o \cdot N_{eo}$ = original amplitude of the TID, where N_{eo} is the undisturbed ionization distribution,

     $\underline{k}_1$ = wave vector of the original TID,

     $\underline{k}_n$ = wave vector of the n'th harmonic,

     n   = Fourier index,

     $\underline{r}$ = radius vector in the vertical x,z-plane,

     β   = spectral index, assuming an inverse power law spatial spectrum.

This formula, which gives the steepened TID disturbance at the time t = 0, was used to calculate the ionization distribution N_e and the growth rate γ of spread-F irregularities shown in Figure 2. The background ionospheric profile $N_{eo}(z)$ is a Chapman layer fitting to the post-sunset equatorial F-layer (h_{max} = 400 km with 50 km thickness at half the maximum electron density). The horizontal wavelength of the non-steepened TID is 200 km and the vertical wavelength is 40 km. The TID amplitude decreases exponentially with height from δ_o = 0.5 at the height h = 350 km to δ_o = 0.05 at the height h_{max} > 400 km of the electron density maximum. The Rayleigh-Taylor growth rate γ is assumed to be dependent on the height-varying collision frequency and the vertical gradient scale length of the electron density (HAERENDEL, 1973). The smaller the exponent β, the stronger the TID steepening is; β → ∞ means no TID steepening.

The print-out in the lower diagram of Figure 2 shows regions of enhanced growth rate of small-scale ionization irregularities caused by ionization gradients steepened by a breaking TID. These regions can be accepted as the leading edges of spread-F patches moving in the positive x-direction (east). The depletions of ionization caused by the steepened TID might be the source regions of spread-F bubbles moving upward to the topside ionosphere (SCANNAPIECO and OSSAKOW, 1976; WOODMAN and LA HOZ, 1976) and the corresponding ionization biteouts reported by McCLURE et al. (1977). The outlined model of the developing phase of spread-F patches, which are observed at the bottom-side of the F-layer (i.e. up to the height of the undisturbed layer maximum), does not apply to the succeeding bubble structure in the topside ionosphere. However, this mechanism can explain the steep gradients of electron density in the F-region valley, which are assumed as a source of weak equatorial spread-F echoes (BALSLEY and FARLEY, 1975). It also can explain the "swoopers" reported by DAVIES and CHANG (1968) and the airglow pattern observed by MALCOLM and MILES (1970) and WEBER et al. (1978).

It is evident that an aspect sensitivity of transequatorial radio propagation (e.g. RÖTTGER, 1973) results from the tilted patchy structure of the ionization irregularities (see Fig. 2). Also satellite signals passing transverse to or along these structures must be influenced in a different manner, i.e. will show a variation of scintillation with incidence angle.

It appears that the resonance-steepened structure shown in Figure 2 reasonably models the bottom-side structure of the equatorial spread-F patches. A model of TID occurrence in the equatorial region is introduced in this paper. The ionization drift necessary to excite the spatial resonance mechanism is known from measurements made over a long period (WOODMAN and CALDERON, 1976). The diurnal variation of the horizontal and vertical ionization drift would also allow a presentation by means of a Fourier series. This opens the possibility of providing a versatile model of TIDs as well as spread-F patches in the equatorial ionosphere by means of tabulated Fourier components.

REFERENCES

BALSLEY, B.B. and D.T. FARLEY, 1975, "Partial reflections: A source of weak VHF equatorial spread-F echoes", J. Geophys. Res. 80, 4735-4737.

BEER, T., 1972, "A new theory of equatorial spread F", in: Final Scientific Report on Ionospheric Research Using Satellites; An Interpretation of Ionospheric Faraday Rotation Observations at the Equator (edit. J.R. Koster and T. Beer), Chapter 6, Dept. of Phys., Univ. of Ghana, Legon, Accra.

DAVIES, K. and N.J.F. CHANG, 1968, "Radio-Doppler observations of the ionosphere near the magnetic equator", AGARD-CP 37, Part 2, paper 52.

HAERENDEL, G., 1973, "Theory of equatorial spread F", Manuscript, Max-Planck-Institut für Physik und Astrophysik, Institut für Extraterrestrische Physik, Garching, Fed. Rep. Germany.

KLOSTERMEYER, J., 1978, "Nonlinear investigation of the spatial resonance effect in the nighttime equatorial F-region", J. Geophys. Res. (in press).

MALCOLM, R. and C. MILES, 1970, "Airglow maps produced by University of Canterbury", New Zealand DSIR Progress Report, Contract 32.

McCLURE, J.P., W.B. HANSON and J.H. HOFFMAN, 1977, "Plasma bubbles and irregularities in the equatorial ionosphere", J. Geophys. Res. 82, 2650-2656.

RÖTTGER, J., 1973, "Wave-like structures of large-scale equatorial spread-F irregularities", J. Atmos. Terr. Phys. 35, 1195-1206.

RÖTTGER, J., 1975a, "Entwicklungsphasen des äquatorialen Spread-F", Kleinheubacher Berichte 18, 355-366.

RÖTTGER, J., 1975b, "Breaking-wave structure in the electron density profiles of the nighttime equatorial ionosphere", Paper, Session: Radio Waves and the Ionosphere, URSI XVIII General Assembly, Lima, Peru.

RÖTTGER, J., 1977, "Travelling disturbances in the equatorial ionosphere and their association with penetrative cumulus convection", J. Atmos. Terr. Phys. 39, 987-998.

RÖTTGER, J., 1978, "Drifting patches of equatorial spread-F irregularities - An experimental support for the spatial resonance mechanism in the ionosphere", J. Atmos. Terr. Phys. (to be published).

SCANNAPIECO, A.J. and S.L. OSSAKOW, 1976, "Nonlinear equatorial spread F", Geophys. Res. Lett. 3, 451-454.

WEBER, E.J., J. BUCHAU, R.H. EATHER and S.B. MENDL, 1978, "North-south aligned equatorial airglow depletions", J. Geophys. Res. 83, 712-716.

WHITEHEAD, J.D., 1971, "Ionization disturbances caused by gravity waves in the presence of an electro-static field and background wind", J. Geophys. Res. 76, 238-241.

WOODMAN, R.F. and C. CALDERON, 1976, "E-region electric fields: Observational aspects", Conference Digest, Fifth International Symposium on Equatorial Aeronomy, paper 6-1, James Cook University, Townsville, Australia.

WOODMAN, R.F. and C. LA HOZ, 1976, "Radar observations of F region equatorial irregularities", J. Geophys. Res. 81, 5447-5466.
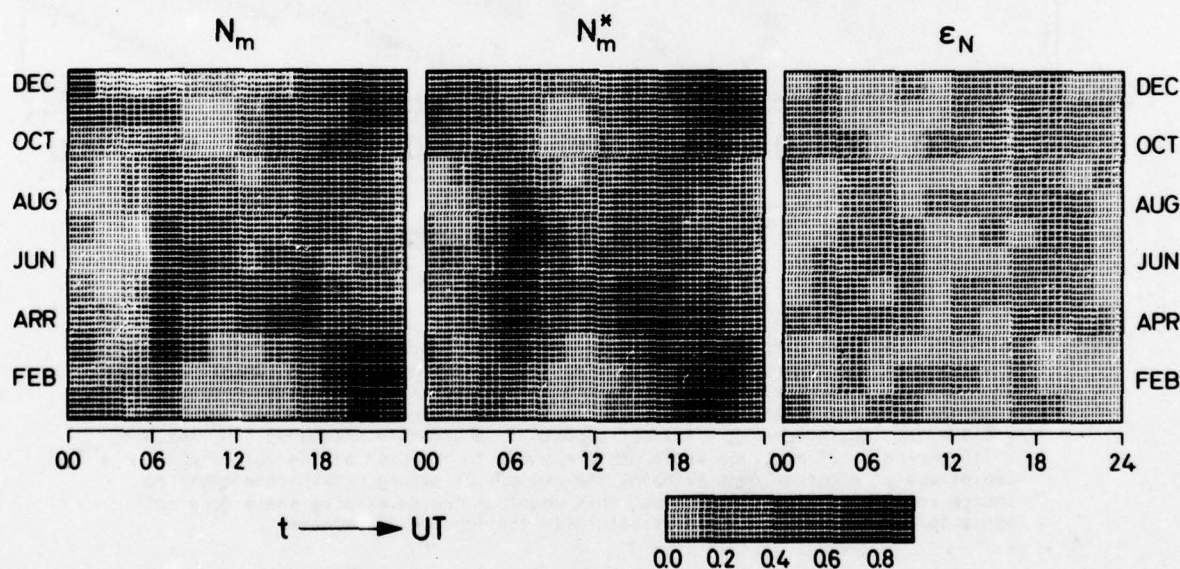
Fig. 1 Mean occurrence pattern N_m of TIDs near the equator (mean taken over 28 months of observations in 1969, 1971 and 1973 (RÖTTGER, 1977)). The gray scale gives the occurrence frequency between 0 and 1. N_m^* is the filtered occurrence pattern, taking the Fourier series up to the third harmonic where ε_N is the residual value. Local time is UT+1h.
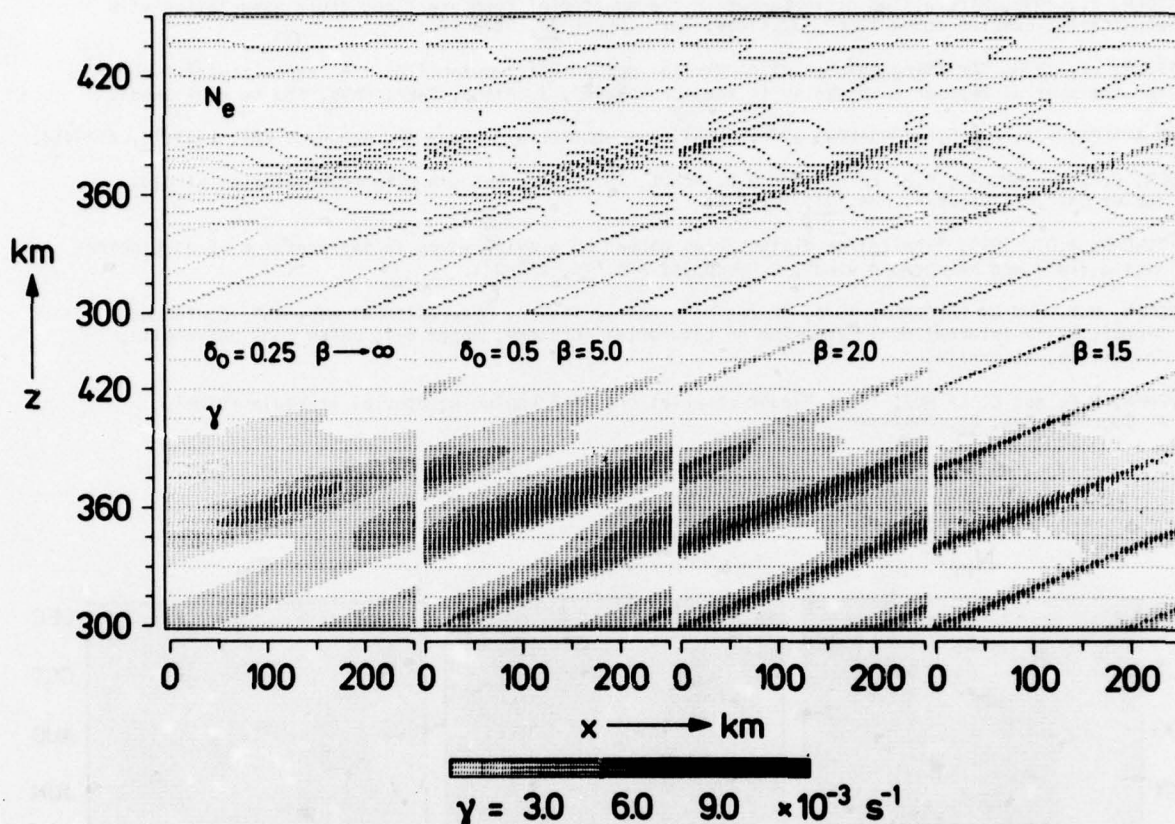
Fig. 2   Model of the developing phase of equatorial spread-F patches: The electron density
distribution N_e distorted by a steepening TID. x is the horizontal (east) and z is
the vertical direction. The growth rate γ of spread-F irregularities is deduced
from the vertical electron density gradient in the upper diagram. $\beta \rightarrow \infty$ gives an
undistorted TID, whereas $\beta = 1.5$ corresponds to a strongly steepened TID. Assuming
a TID period of 21 min, the whole pattern moves to the east at the velocity 160 m s^{-1}.
Depletions of electron density below the regions of strong growth rate might be
source regions of spread-F bubbles. This model of the developing phase does not
apply to the succeeding bubble structure in the topside ionosphere.

DISCUSSION

J.Aarons, US

In the growth phase of the plume, the motion is Westward according to new evidence.

Author's Reply

During the growth phase of the resonance mechanism, ionization is entrained into regions defined by the phase fronts of the steeping TID. This mechanism moves ionization away from other areas which are at the bottomside or near the maximum of the F-region where consequently the depletions of ionization form. From the tilt of the original TID with its top at the East, it then follows that the entrainment of ionization is in a Westward direction. At the gradients given by the ionization density contour lines, small-scale irregularities form which cause scintillations. Since the contour lines during the growth phase of the resonance mechanism are compressed in upward (at the bottomside) and a Westward direction, we correspondingly expect the irregularities to exhibit an apparent Westward motion. After this growth phase the irregularity patches move at about the background drift velocity to the East.

E.J.Fremouw, US

I believe there was an inconsistency between the gravity-wave tilts you described and the tilt of backscatter plumes observed at Jicamarca. The bottoms of the latter are observed prior to the tops. Thus, for an Eastward drift, they must be tilted from top-west to bottom-east.

Author's Reply

The resonance mechanism under discussion holds for TIDs which have tilted ionization contours. These tilts are so that first the upper portion of a contour moves overhead followed by the lower portions. This evidence can be observed at the bottomside structure of the spread-F maps obtained with the Jicamarca radar. A clear distinction has to be made between the bottomside structure and the plumes, which originate near the resonance depletions near the F-layer maximum. The direction of motion of these plumes or bubbles apparently is no more influenced by the originating TID. Thus, as mentioned in the paper, there is no inconsistency if one clearly separates between the triggering mechanism (which causes depletions of ionization by means of the spatial resonance) and the life history of a bubble following its generation phase.

SUMMARY OF SESSION V

TRANSIONOSPHERIC PROPAGATION

by

Dr H.Soicher
Editor

Two major effects in transionospheric propagation dominated the topics of presentations in this session. The first, was the effect of ionization distribution along the Ionospheric and/or Plasmaspheric propagation path on the signal's group delay (or phase); the second, was the amplitude and phase scintillations produced by the small-scale density structure in the ionosphere. The former is critical for precision satellite navigational and positioning systems, while the latter degrades signal performance.

Aarons, MacKenzie, and Bhavnans used a vast amplitude scintillation data base obtained through collaborative studies with various equatorial and high latitude observatories, to analytically model the average scintillations in the VHF and UHF bands. With given solar flux and magnetic activity as parameters, a user in these latitude ranges would have an indication of the mean scintillation to be expected.

In two related papers, Werstiuk and Winter followed by Muldrew and James described the SARSAT system and related ionospheric effects respectively. The Search and Rescue Satellite program (SARSAT) seeks to locate a downed aircraft by measuring the doppler frequency shift of the signal from the aircraft's emergency locator transmitter by the satellite and retransmitting (on a different frequency) to a central station. The ionospheric contribution to the doppler shift was discussed in detail.

Fleury and Cornec reported on Ionospheric Studies at Lannion, France, using beacon transmissions of the ATS-6. In particular, the absolute values and variability of the plasmaspheric electron content as well as of the amplitude scintillations on 40, 140, and 360 MHz, were shown.

Fremouw and Rino presented a signal-statistical and morphological model (and its limitations) of radio wave scintillations produced in the Ionospheric F Layer. In its most extensive form, the model, which contains a morphological model of irregular ionospheric structure and a two-component propagation routine that permits both focusing and diffractive scatter effects, usually outputs first-order signal statistical moments including intensity and phase scintillation indices.

Papet-Lepine discussed the refractive influence of the ionosphere on geodetic measurements using artificial satellites, taking into account ionospheric distribution models including gradients.

EQUATORIAL AND HIGH LATITUDE EMPIRICAL MODELS OF SCINTILLATION LEVELS

Jules Aarons
Air Force Geophysics Laboratory
Hanscom AFB, MA 01731

Eileen M. MacKenzie
Emmanuel College
Boston MA   02115

Krishin Bhavnani
Logicon, Inc.
Bedford MA   01730

SUMMARY

By making measurements of scintillations from VHF and UHF beacons on synchronous satellites, it was possible for AFGL to amass a data bank sufficient to obtain analytical models of average scintillation at high and equatorial latitudes. The data base, obtained in collaborative studies with various observatories, consists of 15 minute scintillation indices of 3 to 7 years of observations (differing for various stations). Observations were made at Sagamore Hill, Massachusetts, Goose Bay, Labrador and Narssarssuaq, Greenland. Equatorial data used was from Accra, Ghana and Huancayo, Peru. For both high and equatorial latitudes forcing functions are time of day, day of the year, magnetic index and solar flux. The resulting analytical models have been validated with one additional set of data at sub-auroral and auroral latitudes but remain to be validated at equatorial latitudes.

1.   INTRODUCTION

In order to provide scintillation levels both in the high latitude and the equatorial regions, the Air Force Geophysics Laboratory has developed an analytical model of scintillation excursions.

The data base is a series of measurements of the scintillations of synchronous satellite beacons, predominantly at 137 MHz, extending over several years.

The model provides mean scintillation excursions as a function of time of day, month, solar flux and magnetic index. With forecasting of solar flux and magnetic index, a user in the latitude range covered would have an indication of mean scintillation to be expected.

2.   DATA TECHNIQUES

Scintillations in amplitude can be characterized by a depth of fading index and a fading period. A useful index to compare scintillation data is the scintillation index, S_4, which is defined as the square root of the variance of received power divided by the mean value of the received power (Briggs and Parkin, 1963). An alternative, less rigorous quantitative measure of scintillation index was proposed by AFGL and adopted by the Joint Satellite Studies Group (JSSG) to ensure a standard method of data scaling in long-term statistical analysis.

The definition is: $SI_{JSSG} = P_{max} - P_{min}/P_{max} + P_{min}$ where P_{max} is the power amplitude of the 3rd peak down from the maximum excursion of the scintillations and P_{min} is the power amplitude of the 3rd peak up from the minimum excursion, measured in dB (Whitney et al., 1969).

The equivalence of selected values of these indices is indicated below.

S_4	dB_{JSSG}	SI_{JSSG}
.075	1	11 %
.17	3	32 %
.3	6	59 %
.45	10	81 %

3.   EQUATORIAL MODEL

3.1 Equatorial Data Base

In the equatorial case, observations of the scintillations of the ATS-3 and LES-6 satellite beacons at 137 and 254 MHz respectively form the data base. The data was reduced by the method outlined by Whitney et al. (1969). Scintillation excursions in dB for 15-min periods were used; these correspond approximately to the 1% percentile levels in the cumulative amplitude probability distribution function for the 15-min period. The dB excursions are convertible into S_4 indices by an empirical relationship, the results of which form the above table.

Two sets of data were used, one taken by the Instituto Geofiscio del Peru at Huancayo, Peru in a cooperative program with AFGL and the second by the University of Ghana at Accra, Ghana as furnished by John Koster.

Figure 1 maps the geographical paths to the satellites used from each of the stations. During the entire period of the data base, the satellite intersection point varied slightly for all of the satellites involved, usually within 2° of longitude while remaining at the same latitude.

Table 1 gives this range of intersections, as well as the range of related parameters.

3.2 Equatorial Data Base Creation and Modeling

Fifteen-minute samples of scintillation index (dB) data for the ATS-3 and LES-6 satellites from the above three stations have been augmented into complete data bases on tape. Data associated with each 15-minute sample include: Station ID, Satellite ID, Frequency, Date and UT, Scintillation Index (dB), 3-hourly magnetic index (Kp), 2695 MHz solar flux, (S_f), 4995 MHz solar flux, sub-ionospheric latitude and longitude, and corresponding geomagnetic latitude and magnetic local time.

Huancayo, Peru ATS-3	May 1969 - April 1976	
Huancayo, Peru LES-6	Dec 1970 - March 1976	
Accra, Ghana ATS-3	Oct 1971 - April 1976	

3.3 The Equatorial Forcing Functions

The forcing parameters include the following:

a) Planetary magnetic index, Kp. At equatorial latitudes it has been shown (Mullen, 1973) that changes in magnetic activity can increase or decrease scintillation activity. For Huancayo, the variation is a function of time and season. Magnetic activity however predominantly inhibits scintillation activity at Ghana (Koster, 1972).

b) Increasing solar flux, even when divorced from magnetic index variations, increased scintillation activity (Aarons, 1977). Whether the activity is changed in severity remains to be determined but the occurrence of deep scintillation fading increases dramatically with increases in solar flux. Utilizing the 2695 MHz solar measurements at Sagamore Hill, we separated observations into three regimes of solar flux units (S_f), (1) 0-95, (2) 96-120, (3) 121 and greater.

c) The seasonal occurrence patterns are clearly distinguishable all over the world. However, the patterns vary with longitude (Basu and Basu, 1976; Aarons, 1977). Between Accra, Ghana and Huancayo, Peru there are differences particularly during the December-January period even though the longitude differences were only approximately 65°.

d) The diurnal pattern is clear with start of activity shortly after local sunset and maximum activity before midnight. The rapid and dramatic onset of scintillation activity was difficult to reproduce in a simple analytical form. In order to compare the model with observations, the data were partioned into 12 months, 4 Kp, three solar flux (2.7 GHz) and 24 local time ranges. The date, Kp, S_f, and SI readings were averaged in each time block. The Kp ranges are 0-1+, 2-3+, 4-5+, and 6 up.

3.4 Equatorial Modeling

The equations have been developed to reproduce the mean scintillation excursions at each station. These are seen in Table 2. The forcing parameters are Kp, solar flux, day of the year and local time. A sample of the behavior of the data and the best fitting model equations can be seen in Figure 2 for Huancayo A3 and Figure 3 for Ghana A3 for differing solar flux and Kp groupings for one particular month (February).

Both Ghana and Peru data exhibit monthly maximum excursions in the Feb-Mar and Oct-Nov periods, while minimum excursions can be noted in June and July. Both sets of data show clear increases with increasing solar flux (at the same level of magnetic activity). However, both the data and the model indicate little variation with magnetic activity under the same solar flux conditions in Peru. Magnetic activity can be seen to inhibit scintillation excursions at Ghana.

3.5 Equatorial LES-6 Data

During the bulk of time available for this experiment, beacon transmissions from the satellite LES-6 were available at 254 MHz. One serious problem with observations from this satellite was that during the local time period ∿ 2200-2400 at Huancayo, a time period with great intensity of scintillations, the satellite's transmissions were radiated away from the earth and its signal was effectively lost. The resulting data has this omission; the equation tries to bridge the gap.

A second problem is the absence of a high signal to noise ratio resulting in a limiting value of approximately 16-19 dB excursions peak to peak; more recent experiments (Whitney et al, 1977) have shown peak to peak excursions at 254 MHz to at least 25 dB. However, this is less serious than the limited range of the 137 MHz system.

The best fitting equation found for the LES-6 data is also shown in Table 2. A graphing of data for February is illustrated in summary form in Figure 4; the hours 2200-2400 have been omitted.

For the period November thru March, the LES-6 data are of the order of .5 to .6 of the larger values of scintillation excursions of ATS-3.

The behavior of both sets of Huancayo data is similar though the ratio of scintillation levels between the frequencies varies seasonally. For example, the months of

Table 1

Station and Sat.	Date	Subion. Lat.	Subion. Long.	Geomag. Deg. of Intersection Pt. from Geomag. Eq.	El.	Az.	Iono. Z.A.
Huancayo, Peru A3	5/69-12/71	11.3°S	73.1-75.6°W	0°	51.7-75.9°	71.3-6.4°	36.0-13.9°
	1/72-4/76	11.3°S	74.9-75.1°W	0°	73.6-75.1°	31.8-20.1°	16°
Huancayo, Peru L6	12/70-3/76	11.3°S	72.1-72.7°W	0°	42.2-47.5°	73.5-76.0°	45-40°
Accra, Ghana A3	10/71-4/76	5.2°N	9.5-11.0°W	11°N	10.7-13.7°	268°	67-69°

Table 2

Equatorial Scintillation Index (dB) Models

Huancayo ATS3

$$SI(dB) = 1.+2[FA+FB+\{(-1.3FA+2.1FB)\cos(HL+.1-.25K_p)\}+FC\{\cos(2(HL+3.3))-.4\cos(3(HL+1.5))\}]$$

where $FD = \cos(DA-4.4)-.5\cos(2(DA-4))$ $FA = (-2.9+.6FD)As$ $FB = (.3+FD)+(.1-.2FD)K_p$ $FC = (1.6-.4FD)As+.2K_p$

Huancayo LES6

$$SI(dB) = 2[FA+FB+\{(-1.5FA+.8FB)\cos(HL-.2-.25K_p)\}+FC\{\cos(2(HL+3.3))-.4\cos(3(HL+1.5))\}]$$

where $FD = \cos(DA+1.3)-.6\cos(2(DA-4))$ $FA = (-2.7-.3FD)As$ $FB = (.2+FD)+(.1-.1FD)K_p$ $FC = (1.6+.7FD)As+.1K_p$

Ghana ATS3

$$SI(dB) = -.05+2[FA+FB+\{(-3.6FA+1.9FB)\cos(HL-.25K_p)\}+FC\{\cos(2(HL+3.3))-.4\cos(3(HL+1.2))\}]$$

where $FD = \cos(DA-10.3)-.5\cos(2(DA-4))$ $FA = (-.7+.2FD)As$ $FB = (.4+.5FD)+(0.)K_p$ $FC = (.7-.4FD)As+.15K_p$

DA - Day Number   As = $S_f/100$, where
HL - Local Time (hrs.) S_f - 2695 MHz Solar Flux

May, June and July are very low at both frequencies with increasing Kp bringing on increasing SI.

3.6 Equatorial Model: Average vs. Median Data

Figures 5, 6, and 7 show both the average and the median values of the data at each of the stations for one month. It is seen that no substantial differences occur between the average and median values.

In general, for low and medium levels of scintillation, the average data tends to be slightly higher than the median while at high scintillation levels, the median data is slightly higher than the average.

4. HIGH LATITUDE MODEL

4.1 High Latitude Model Data Base

The data from three stations were available. These stations with their trans-ionospheric positions in the sub-auroral thru auroral latitudes allowed a modest coverage of high latitude scintillations.

The 15-minute samples of scintillation index (dB) data for the ATS-3 satellite for the above 3 stations have been augmented into complete data bases on tape, as was performed with the 3 equatorial data bases. The data associated with each 15-minute sample include the same parameters described in the equatorial data base section. The dates of the data used for each station are:

Narssarssuaq	9/17/68 - 9/1/74
Goose Bay	1/1/72 - 12/31/74
Sagamore Hill	12/1/69 - 11/30/74

Goose Bay data for 1974 cover mainly November and December.

The three stations are situated near the 70° West meridian, and their propagation paths to the ATS-3 satellite are shown in Figure 8. Their geomagnetic and geometrical parameters are given in Table 3.

Table 3

Station	Inv. Lat.	El.	Az.	Iono. Z.A.
Narssarssuaq	63.2°	18.0°	208°	64°
Goose Bay	60.3°	28.8°	191°	56°
Sagamore Hill	53.5°	40.9°	178°	46°

4.2 The Forcing Functions at High Latitudes

In this initial development, a relatively simple equation was developed to reproduce the mean scintillation excursions at the three stations.

The forcing parameters were the following:

a) Planetary magnetic index, Kp. It has been shown that at high latitudes (which in this case include the Narssarssuaq and Goose Bay observations and, during severe magnetic storms, the Sagamore Hill observations) Kp is a forcing function (Aarons and Allen, 1971).

b) Early work by Aarons et al. (1971) showed that solar flux, even when divorced from magnetic index variations, had an effect on scintillation behavior. Utilizing the 2695 MHz solar measurements at Sagamore Hill, we separated observations into three regimes of solar flux units (S_f); (1) 0-95, (2) 96-120, and (3) 121 and greater. As will be shown scintillations do not in every month increase with increasing solar flux but vary as a function of season.

c) The seasonal parameter. A very dramatic minimizing of diurnal effects is shown in the Narssarssuaq observations over the winter (Basu, 1975). This would have to be reflected in the model.

d) The diurnal pattern would have to be shown. This would include the variations as a function of local time under magnetically quiet and disturbed conditions as modulated by the seasonal function.

Analyses were conducted separately for each station. The data were partitioned into 12 months, 7 Kp, 3 Solar Flux (2.7 GHz), and 24 UT ranges. The date, Kp, S_f and SI readings were averaged in each block. A compact file was thus made available for high speed iterative modeling studies. The seven Kp ranges are 0-1, 1+ to 2, 2+ to 3, 3+ to 4, 4+ to 5, 5+ to 6, 6+ and up. The three S_f ranges are 0 to 95, 96 to 120, 121 and up. Tables of the averaged SI are provided for each of the stations.

Out of a maximum possible 6048 blocks (12 x 7 x 3 x 24), the averaged files comprise the following:

Narssarssuaq	4985 blocks
Goose Bay	4217 blocks
Sagamore Hill	5065 blocks

The empty blocks generally correspond to the highest two Kp ranges, that is, 5+ and up,

and occasionally the highest S_f range.

4.3 Modeling at High Latitudes

A search was conducted to derive an empirical model of SI. Analytical forms of the model were preferred to ensure smooth transitions as a function of the driving functions, namely, day of year, Kp, S_f, and universal time. These forms also permitted use of regression techniques for least squares fitting to the averaged data file. In the course of the search for improved fits, special characteristics of the data were noted which suggested elaborations of the model form. Examples are the delayed peak in the diurnal SI variation with higher Kp, the seasonal effect on diurnal variation amplitude relative to the average SI, the seasonal effect on influence of Kp and S_f, and the need for higher harmonics to represent the diurnal variation.

Initially, separate models were developed for each station. These individual models approximate the actual data base as closely as possible while smoothing abrupt variations to fit an analytical form.

Table 4 presents the model for each station in terms of local time. The difference between universal time and local time at the sub-ionospheric point (350 km) was taken to be 3.4 hr at Narssarssuaq, 4.1 hr at Goose Bay, and 4.7 hr at Sagamore Hill. In the model equations, the cosine arguments (in radians) that include the terms for day number (DA) and hour (HL) assume a multiplicative term of $2\pi/365$ and $2\pi/24$ respectively. Though not shown in the equation for reasons of convenience, these must be included in the calculations.

In Figures 9 to 11 typical comprehensive comparative plots of the averaged data and the model are provided for each station. The model predictions used the actual averaged data, Kp and S_f for each hour, and are therefore absent when data are absent. These best fit models may occasionally predict small negative SI's; these are made to asymptotically approach zero by replacing a value V which is less than 0.5 by $e^{2(V-.85)}$. This ensures continuity in the predictions near 0.5 and introduces minimal distortion since only the very low scintillations are adjusted.

4.4 The Equations and the Data

To illustrate the behavior of the data and of the best fitting model equations, Narssarssuaq data is shown in Figure 9 for the month of March. One can note, for example, along the left-hand side for the solar flux set of 0 to 95, that scintillations increase with increasing Kp. The dotted line is the model equation and the continuous line connects 1-hr means of scintillation excursions.

Along any series of boxes with identical Kp one can note that the model and the data indicate that the general trend is for the scintillation excursions to increase with increasing solar flux.

The behavior of the Goose Bay data (solid line) and best-fitting model (dashed line) for March are shown in Figure 10. Within each particular solar grouping scintillations increase with increasing Kp. For the same Kp grouping, the scintillation excursions increase with increasing solar flux.

Behavior of the Sagamore Hill data and model for March are shown in Figure 11. For the low solar flux group (0 to 95), a very slight increase in scintillations associated with increasing Kp is seen. The same is true of the solar flux group 96 to 120 while for high solar flux, the increase with Kp becomes more noticeable. In general, within a particular Kp grouping, scintillation index increases with increasing solar flux.

4.5 Comprehensive Model

Two attempts to combine these individual models into more comprehensive latitudinal models were made. The first, a 3-station model, is restricted to use over the latitude range 53°-63°Λ. It attempts to reproduce the individual station observations at the station invariant latitude and interpolates at latitudes in between. This model, presented in Table 5, is a modified and corrected form of equation B2 in an earlier published version of the high latitude model (Aarons et al., 1976).

The sub-auroral to middle latitudes present a different morphology from the high latitude ionosphere except during periods of intense magnetic activity when auroral effects at F-layer heights extend into the sub-auroral region. Thus the inclusion of the Sagamore Hill data although serving to extend the model in latitude, does not provide a true picture of this entire scintillation region, since two differing morphologies are joined. Under high Kp cases auroral effects do take place at the latitude of Sagamore Hill in which case the 3-station model may be valid. Therefore a second model, more physically coherent, was postulated which would range over the latitudes 60°-63°Λ, including the Goose Bay and Narssarssuaq data bases but excluding Sagamore Hill which would then simply rely on its single station model. This model, is presented in Table 6 with a sample month, March, shown in Figure 12. As noted for the individual station models, additional multiplicative terms are assumed in this model.

The standard deviation between the 2-station model values and the individual station models (Aarons et al., 1976) is $\sigma \sim .7$, with the range of variation running +1-2, 0- -1 dB. However, the standard deviation between the actual data base and the individual station model runs from $\sigma \sim 1.5$ for Sagamore Hill to $\sigma \sim 2.8$ for Narssarssuaq, with the range of residuals being even higher, since the actual data contains highly variable scintillations, especially for disturbed magnetic conditions and high solar flux, in which the data base is limited.

Table 4

Scintillation Index (dB) Models for Local Time

Narssarssuaq

$$SI(dB) = -6.4+9.2(1-.2FD)[1+.23(1-.3FD)]cos(HL+2.0+.34K_p)+.03cos(2(HL-0.6))+.02cos(3(HL+3.0))]2[.14K_p(1+.12FD)+.09As(1+1.76FD)]$$

$$FD = cos(DA+15.6)+.56cos(2(DA-22.4))$$

Goose Bay

$$SI(dB) = -1.3+1.1(1-.77FD)[1+.5(1-.2FD)cos(HL+2.1-.6K_p)+.06cos(2(HL-2.1))+.02cos(3(HL+5.2))]2[.3K_p(1+.1FD)+.8As(1+1.2FD)]$$

$$FD = cos(DA+.5)+.2cos(2(DA-99))$$

Sagamore Hill

$$SI(dB) = 0.33+.02(1+.2FD)[1+1.2(1-.01FD)cos(HL-0.4-.15K_p)+.3cos(2(HL-0.8))-.1cos(3(HL+6.1))]2[.38K_p(1+.3FD)+3.1As(1-.2FD)]$$

$$FD = cos(DA+56)+.7cos(2(DA-143))$$

DA - Day Number

As - $S_f/100$

HL - Local Time (hours) at Sub-Ionospheric Point (350 km)

S_f - Solar Flux at 2695 MHz in Solar Flux Units

Table 5

Revised Mathematical Model

Narssarssuaq - Goose Bay - Sagamore Hill Based

$$SI = -2.0+1.2CL+6.5(1-.2FD)[1+.6(1-.16FD)(1-.45SL)cos(HL+2-.4K_p)+.05cos(2(HL-.9))+.02cos(3(HL+3.5))] \times 2^{[.32(PF-66.1)]}EXA$$

where $EXA = 2^{[.2K_p(1+.25CL)(1-.1XD)+As(1-.8SL)(1+.45FD)]}$

and $CL = cos((PF-54.4)\frac{\pi}{25})$ $CDL = 1+.75SL$ $SL = sin((PF-54.4)\frac{\pi}{25})$ $SDL = 1-3SL$

$PD = cos(DA+16) + .3cos(2(DA-30))$ HL = Local time
$FD = CDL \times PD$ $As = S_f/100$
$XD = SDL \times PD$ K_p = Magnetic index
PF = Invariant Latitude (in degrees) DA = Day number

Table 6

Narssarssuaq-Goose Bay Based

$$SI = -1.3-2.7CL+6.2(1-.17(1+2.6CL)FD)[1+.33(1-.35(1-.8CL)FD)cos(HL+2.1-.4K_p)+.05cos(2(HL-.9))+.02cos(3(HL+3.5))](1-.9CL)EXA$$

where $EXA = 2^{[.2K_p(1+.13FD)+.75AsCL(1+FD)]}$

$FD = cos(DA-2.6)+.2cos(2(DA-30))$ HL = Local time (hr.)
$CL = cos((PF-53.5)\pi/25)$ PF = Geomag. Lt. (deg.)
$As = S_f/100$ [$\frac{2\pi}{365}$ & $\frac{2\pi}{24}$ implied in all annual & diurnal periodic terms (see text)]

4.6 Limiting

A basic problem in the data and the modeling is the problem of limiting. Since the
attempt in this model was to find average excursions, the limited signal to noise ratio
of the recordings resulted in excursions at 137 MHz being at their maximum 16-19 dB
(depending on equipment). Thus for example if the 15 minute indices for 2200-2215 on
any month all showed excursions of 19 dB the average would be 19 dB. As has been shown
by other experiments with greater signal to noise ranges the excursions could have been
> 26 dB. Equipment limitations would not have indicated the higher values. Thus a
comparison with higher frequency data will possibly serve to indicate occurrence
patterns and the effect of various forcing functions; frequency dependence reductions
done with this model are of limited validity.

4.7 High Latitude Models: Averaged versus Median Data

In order to test if the averaged data were skewed by problems of limiting the mean
values were compared with medians. Figure 13 illustrates this for Narssarssuaq; it can
be seen that no substantial differences occur between the averaged and median dB values.
For low scintillation activity averaged values tend to be higher than median values.
Similar comparisons with roughly the same results were made with both Sagamore Hill and
Goose Bay data.

5.   DISTRIBUTION OF OCCURRENCE OF SCINTILLATION

Distribution analyses were conducted in both equatorial and high latitude data
files. This data is shown partitioned into 2 significant scintillation blocks, > 6 dB
and > 9 dB. The data then is divided into Night (17-05 LT) and Day (05-17 LT). There
is no breakdown of magnetic activity for Huancayo data. These distributions are as follows:

5.1 Equatorial Data

Percent Occurrence of Scintillation (Peak-to-Peak)

		Night (17-05LT)	Day (05-17LT)
Huancayo A3			
	$\geqslant$ 6 dB	22	1.3
	$\geqslant$ 9 dB	18	.9
Huancayo L6			
	$\geqslant$ 6 dB	14	.5
	$\geqslant$ 9 dB	11	.3
Ghana A3			
K$\approx$0-3	$\geqslant$ 6 dB	30.8	1.5
	$\geqslant$ 9 dB	15.9	.6
K$\approx$4-9	$\geqslant$ 6 dB	26.8	1.5
	$\geqslant$ 9 dB	11.7	.6

5.2 High Latitude Data

Percentage of Occurrence of Scintillation (Peak-to-Peak)

Narssarssuaq, Greenland   ATS-3   137 MHz

		Night (17-05LT)	Day (05-17LT)
$K = 0-3^+$			
	≥ 6 dB	46.3	14.5
	≥ 9 dB	29.4	6.2
$K = 4-9$			
	≥ 6 dB	78.8	47.2
	≥ 9 dB	61.8	31.0

Goose Bay, Labrador   ATS-3   137 MHz

		Night (17-05LT)	Day (05-17LT)
$K = 0-3^+$			
	≥ 6 dB	8.3	.5
	≥ 9 dB	3.9	.2
$K = 4-9$			
	≥ 6 dB	30.2	8.3
	≥ 9 dB	15.0	3.7

Sagamore Hill, Mass.   ATS-3   137 MHz

		Night (17-05LT)	Day (05-17LT)
$K = 0-3^+$			
	≥ 6 dB	5.4	.3
	≥ 9 dB	2.5	.1
$K = 4-9$			
	≥ 6 dB	6.9	.7
	≥ 9 dB	3.6	.3

6. FREQUENCY DEPENDENCE

In order to fully utilize both the equatorial and high latitude model, it is desirable to be able to extrapolate the model dB values resulting from the 137 MHz data base to model values for higher frequencies.

This entails the use of the spectral index η, where,

$$\eta = \frac{[\log (S_1/S_2)]}{[\log (f_1/f_2)]}$$

where the scintillation index is in terms of S_4 (Whitney, 1974). This expression is valid as long as scintillation index is a constant power-law function.

In order to accomplish this conversion, the spectral index η must be established. This relationship with S_4 is shown in Figure 14 for Ootacamund, India (Deshpande et al., 1977). These results are based on approximately 1 year of measurements (August 1975 - August 1976) of the ATS-6 satellite. For weak scintillations, the index η is essentially independent of S_4 with values ranging from $\sim$.8-1.4, with the median, shown here, at approximately 1.2. With stronger scintillations, the η value decreases and approaches saturation at $S_4 = 1.0$.

Figure 14 also shows the relationship of η and S_4 as determined from Huancayo, Peru 137/360 MHz data. This data base consists of 17 sets of two-frequency data (Whitney and Basu, 1977). The 360 MHz scintillations did not have the intensity to actually measure $\eta=0$ but it is expected that this could be achieved as a worst-case condition. This is considered characteristic of strong scattering when scintillations approach the saturated regime (Yeh et al., 1975). When the scattering is so intense that both 137 and 360 MHz scintillations are saturated, the scintillations are frequency independent. Under these conditions, the worst-case fading can be approximated by a Rayleigh distribution.

Under conditions of weak scattering, a $f^{-1.5}$ variation with S_4 indices is noted and is consistent with a 3-dimensional irregularity power spectral index of 4.

Recent observations (Fremouw et al., 1978) employing ten frequencies between 138 MHz and 2.9 GHz, transmitted from the same satellite DNA-002, show a consistent $f^{-1.5}$ behavior of S_4 for S_4 less than about 0.6.

These data were taken at both equatorial latitudes (Ancon) and high latitudes (Poker Flat, Alaska). In both cases the frequency dependence becomes less steep for stronger scintillation, saturating for values of S_4 approaching unity, as expected for "fully developed" intensity scintillation obeying a Rayleigh distribution.

7. GEOMETRICAL CONSIDERATIONS

7.1 High Latitudes

It has been noted that scintillations maximize both at low angles of elevation and when the signal propagation path is parallel to the lines of force of the earth's field. In order to fully examine the problem of geometry, a model would need to be developed in which the irregularity shape and elongation varied as a function of latitude, time and geomagnetic conditions.

Mikkelsen et al. (1978) has attempted to determine the theoretical scintillation index, S_4, when the irregularities are described by a power-law power spectrum. This utilizes the coordinates of the radio ray in the local coordinate system with set values for the elongation of the irregularities along and perpendicular to the magnetic field lines.

Mikkelsen assumed the approximate dividing line between weak and strong scintillation is $\sim$ 9 dB, with SI < 9 dB denoting the weak case. For this case, the geometric variation of S_4 is given by:

$$S_4 \propto \sqrt{z/\cos i \; f(\psi,\phi)}$$

where i = ionospheric zenith angle = angle between radio ray and irregularity layer

ψ = propagation angle = angle between the radio ray and the magnetic field direction,

ϕ = azimuth of the radio ray in local coordinate system of z-axis along the magnetic field and y-axis in the magnetic east-west direction

$f(\psi,\phi) = \alpha\gamma(\gamma^2\cos^2\phi+\sin^2\phi+\cos^2\psi(\cos^2\phi+\gamma^2\sin^2\phi)+\alpha^2\sin^2\psi)/[\gamma^2\cos^2\psi+\alpha^2\sin^2\psi$

$$x \; (\gamma^2\cos^2\phi+\sin^2\phi)]^{\frac{1}{2}}$$

z = reduced slant range to irregularity layer = $z_1(z_2-z_1)/z_2$

where z_1 = slant range to irregularity layer

z_2 = slant range to satellite

α = elongation of the irregularities along the magnetic field lines

γ = elongation of the irregularities in the magnetic east-west direction

Using his irregularity formulation he found the Narssarssuaq observations of the orbiting satellite, Nimbus-4, at an altitude of 1000 km a best fit of irregularity configuration with 2.5:1.3:1 where the first term is α, elongation of the irregularity along the lines of force of the magnetic field, the second is γ, orthogonal to the elongation along the lines of force, being in the magnetic east-west dimension, and the last term is orthogonal to the other two planes. At high latitudes this last term would lie in the north-south meridian.

Martin and Aarons (1977) interpreted synchronous satellite data in the Narssarssuaq-Goose Bay area using different irregularity equations (Gaussian). They found the dominating irregularities to be elongated along the magnetic field with a 5:2:1 configuration. Theoretically the irregularity model in the N-S meridian is of the order of the Fresnel dimension at 137 MHz and in such cases there is little difference between Gaussian and power-law spectrum for scintillation indices (Rufenach, 1975).

Livingston and Rino (1978) by observing the WIDEBAND satellite ($\sim$1000 km altitude) in Poker Flat, Alaska find evidence for L shell aligned, sheet-like irregularities with a lower bound to the configuration of 10:10:1.

In order to present a simplified solution to this problem, a correction factor for the three high latitude stations under the assumption of the elliptical column model of individual irregularities of 5 km along the lines of force of the earth's magnetic field, 2 km orthogonal to the lines of force (E-W) and of 1 km in the north-south meridian has been calculated. In the publication Aarons et al. (1976) we have illustrated geometrical corrections needed from the three high latitude sites. It was determined that the correction for the S_4 value derived from each index would be a factor $\sim$2.0 greater at the azimuth and elevation of the ATS-3 satellite from Narssarssuaq than at zenith. From Goose Bay the correction factor using the same model would be $\sim$1.3 and from Sagamore Hill it would be $\sim$1.4 assuming a Gaussian irregularity spectrum.

While the model of scintillation excursion does not incorporate these correction factors, these simple factors can be used to normalize the levels to overhead values. Until the irregularity configuration is settled in the scientific community final correction factors cannot be given. It is possible that the configuration changes as a function of latitude, solar and geomagnetic activity, and perhaps even local time. Factors given above are probably minimum reductions relative to overhead values.

7.2 Equatorial Latitudes

In the equatorial region, no quantitative attempt has been made to correct for the geometry of the observing situation. Two factors in the determination of the geometrical effects are the effective thickness of the irregularity region and the configuration of the individual irregularities producing the scatter.

Recently the thickness parameter has been more closely studied for the equatorial case using the backscatter Jicamarca observations. The thickness may vary from a few kilometers when weak scatter scintillations are noted to an effective thickness vertically of several hundred kilometers when the plumes are formed (Basu, 1977). However, since the patches of irregularities have dimensions resembling a book with magnetically N-S dimension of the order of 1000 km or more, E-W dimensions of 50-200 km and with the vertical extent ranging from a few kilometers to several hundred kilometers it will be difficult to establish a uniform model. The viewing situation would also affect the scintillations, even if a uniform model could be established. Scintillations at low angles will maximize along the north-south magnetic meridian. Also, even if the signal

does not travel along this meridian, the path may be such as to travel diagonally thru the irregularity patch rather than cutting straight across it, thus producing a longer path length in the irregularities themselves.

The dimensions of these individual small scale irregularities have not been established but they appear to be rod-like and of the order of 100:1:1 with a 50 or 100 factor along the lines of force of the earth's magnetic field, thus horizontally aligned at the geomagnetic equator. This could explain the varying effective thickness of the patches, where it could be considered that the patches were "built" by grouping of these rod-like structures, vertically to form a "book" shape as described above.

8.   DISCUSSION

In order to determine scintillation occurrence at both high and equatorial latitudes, models of scintillation excursion have been generated from an extensive 15-minute scintillation index (dB) data base. At high latitudes, this is composed of data obtained at Narssarssuaq, Goose Bay and Sagamore Hill. In the equatorial region, the data base is composed of observations at Huancayo, Peru of both VHF and UHF beacons and VHF observations from Accra, Ghana. In both regions, the forcing parameters of scintillation excursions considered were: time of day, season, magnetic index and solar flux. At high latitudes, the response of the data at each of the stations to the forcing functions showed similar trends, though the intensity of the reactions differed. Hence these individual station models were merged into two analytical models valid over the latitudinal extent 53°-63°Λ, and 60°-63°Λ for the 3- and 2-station models respectively, with the latter scientifically more valid. The equatorial data, representing two separate longitude sectors, at times differed in their response to the forcing parameters and therefore separate equations for each station and satellite were retained.

Distribution analyses were also conducted upon this data base. In the high latitude region, the nightly maximum is evident and within this, the increase of SI with magnetic index. This trend is more noticeable at the more northern station, Narssarssuaq, and is mitigated at lower latitudes.

In the equatorial region, the varying percentages of occurrence between the two satellites at Huancayo reflects the frequency dependence factor. The magnetic index is more important in the Ghana data than in Huancayo observations but was still not as influential as in the high latitude set of data.

9.   FUTURE MODEL STUDIES

Future work on this model is expected to include validation with other data, improvement of the simple analytical formulas given, and additional studies of frequency dependence and geometrical terms.

10.   ACKNOWLEDGEMENTS

We would like to acknowledge the care and application of those who took the observations and in many cases reduced the records. In particular, these are Prof. John Koster of the University College of Accra, Ghana, Ing. Alfredo Bushby and Ing. Jacinto Pantoja, Geophysical Institute of Peru, Huancayo, Peru and K. Damdgaard, of the Danish Meteorological Institute.

In addition many individuals at AFGL were involved in the observations, particularly Herbert Whitney, John Mullen and Harold Strick.

11.   REFERENCES

Aarons, J. (1977) Equatorial scintillations: A review, IEEE Trans. Ant. Prop., AP-25, 729-736.

Aarons, J. and Allen, R.S. (1971) Scintillation boundaries during quiet and disturbed magnetic conditions, J. Geophys. Res., 76:170-177

Aarons, J., Whitney, H.E., and Allen, R.S. (1971) Global morphology of ionospheric scintillations, Proc. IEEE., 59:159.

Aarons, J., Mullen, J., Whitney, H., Martin, E., Bhavnani, K., and Whelan, L. (1976) A high-latitude empirical model of scintillation excursions: Phase 1, AFGL-TR-76-0210, 17 Sept.

Basu, Sunanda (1975) Universal time seasonal variations of auroral zone magnetic activity and VHF scintillation, J. Geophys. Res., 80, 4725-4728.

Basu, Sunanda, Aarons, J., McClure, J.P., LaHoz, C., Bushby, A. and Woodman, R.F. (1977) Preliminary comparisons of VHF radar maps of F-region irregularities with scintillations in the equatorial region, J. Atmos. Terr. Phys., 39, 1251-1261.

Basu, S. and Basu, S. (1976) Correlated measurements of scintillations and in-situ F-region irregularities from Ogo-6, Geophys. Res. Lett., 3, 681-684.

Briggs, B.H. and Parkin, I.A. (1963) On the variation of radio star and satellite scintillation with zenith angle, J. Atmos. Terr. Phys., 25, 339.

Deshpande, M.R., R.G. Rastogi, H.O. Vats, G. Sethin, H. Chandra, R.V. Bhonsle, H.S. Sawant (1977) Scientific Report on ATS-6 Radio Beacon Studies, Physical Research Laboratory, Ahmedabad, India.

Fremouw, E.J., R.L. Leadabrand, R.C. Livingston, M.D. Cousins, C.L. Rino, B.C. Fair and R.A. Long (1978) Early results from the DNA Wideband satellite experiment — Complex signal scintillation, Radio Sci., 13, 167-187.

Koster, J.R. (1972) Equatorial scintillation, Planetary Space Sci., 20:1999-2014.

Livingston, R.C. and C.L. Rino (1978) Ionospheric irregularity anisotropy and drifts at high latitudes, presented at URSI, Boulder, CO.

Martin, E. and J. Aarons (1977) F-layer scintillation and the aurora, J. Geophys. Res., 82, 2717-2722.

Mikkelsen et al., (1978) Geometrical considerations of 136 MHz amplitude scintillation in the auroral oval, J. Atmos. Terr. Phys. (in press).

Mullen, J.P. (1973) Sensitivity of equatorial scintillations to magnetic activity, J. Atmos. Terr. Phys., 35:1187-1194.

Rufenach, C.L. (1975) Ionospheric scintillation by a random phase screen: spectral approach, Radio Sci., 10, 155.

Whitney, H.E. (1974) Notes on the Relationship of Scintillation Index to Probability Distributions and Their Uses for System Design, AFCRL-TR-74-0004, Hanscom AFB, MA.

Whitney, H.E., C. Malik, and J. Aarons (1969) A proposed index for measuring ionospheric scintillation, Planet. Space Sci., 17, 1069-1073.

Whitney, H.E. and S. Basu (1977) The effect of ionospheric scintillation on VHF/UHF satellite communications, Radio Sci., 12, 123-133.

Whitney, H.E., J. Aarons, J. Buchau, E.J. Weber and J.P. McClure (1977) The evolution of scattering equatorial F-region irregularities and resultant effects on trans-ionospheric radio waves, presented at the 24th Agard Panel Meeting, Aspects of Electromagnetic Scattering in Radio Communication, Cambridge, MA.

Yeh, K.C., C.H. Liu and M.Y. Youakim (1975) A theoretical study of the ionospheric scintillation behavior caused by multiple scattering, Radio Sci., 10, 97-106.
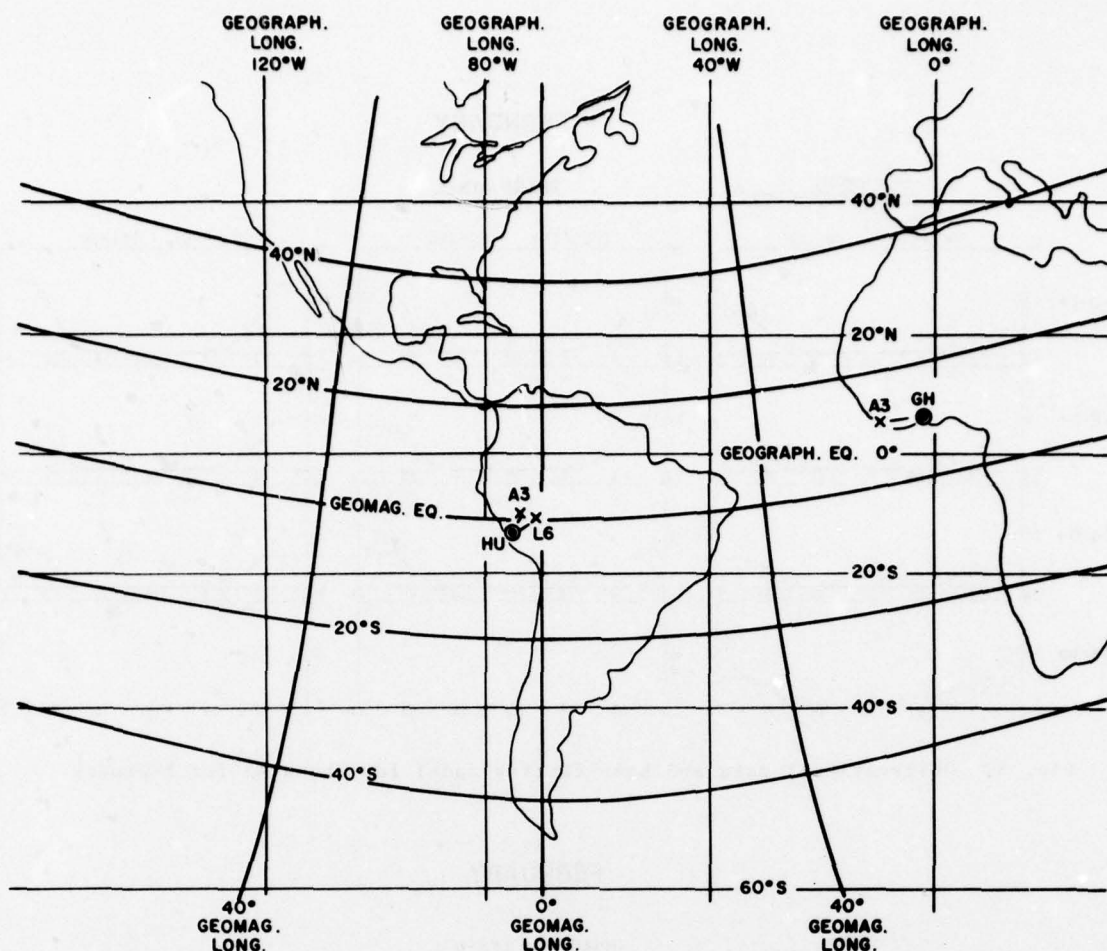
Fig. 1. Map of satellite intersections in equatorial region for Huancayo A3, Ghana A3, and Huancayo L6.
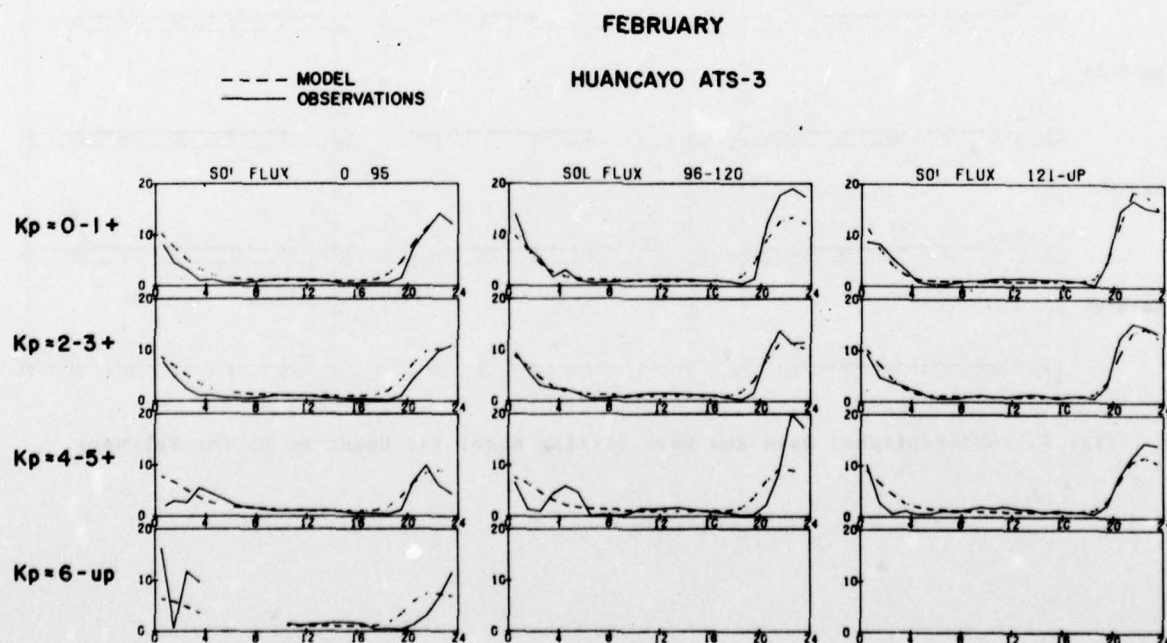
FEBRUARY

Fig. 2. Observational data and best-fitting model for Huancayo A3 for February.

FEBRUARY

MODEL
OBSERVATIONS

GHANA ATS-3
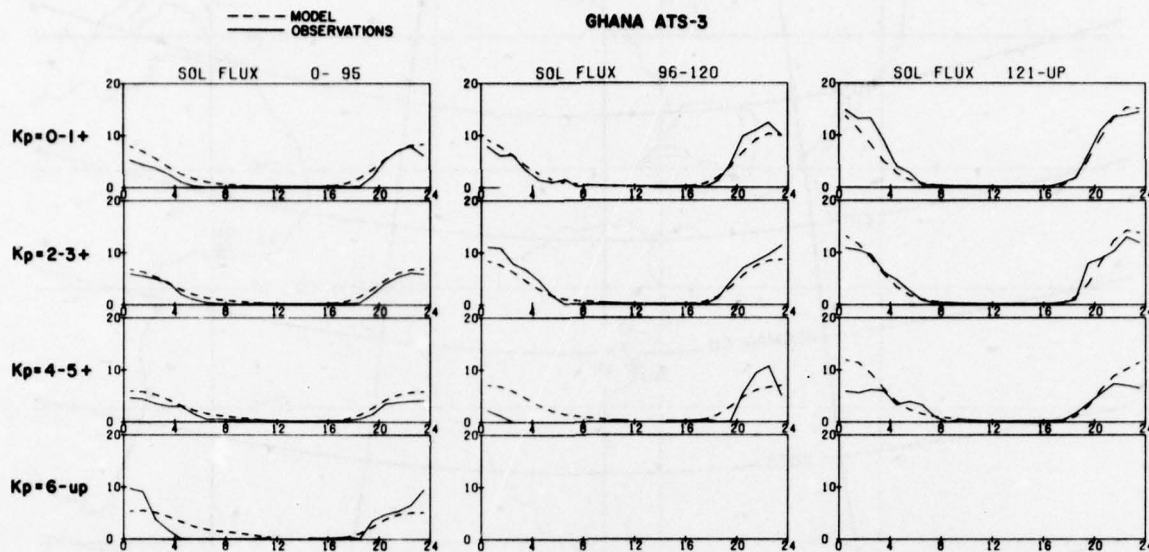
Fig. 3. Observational data and best-fitting model for Ghana A3 for February.

FEBRUARY

MODEL
OBSERVATIONS
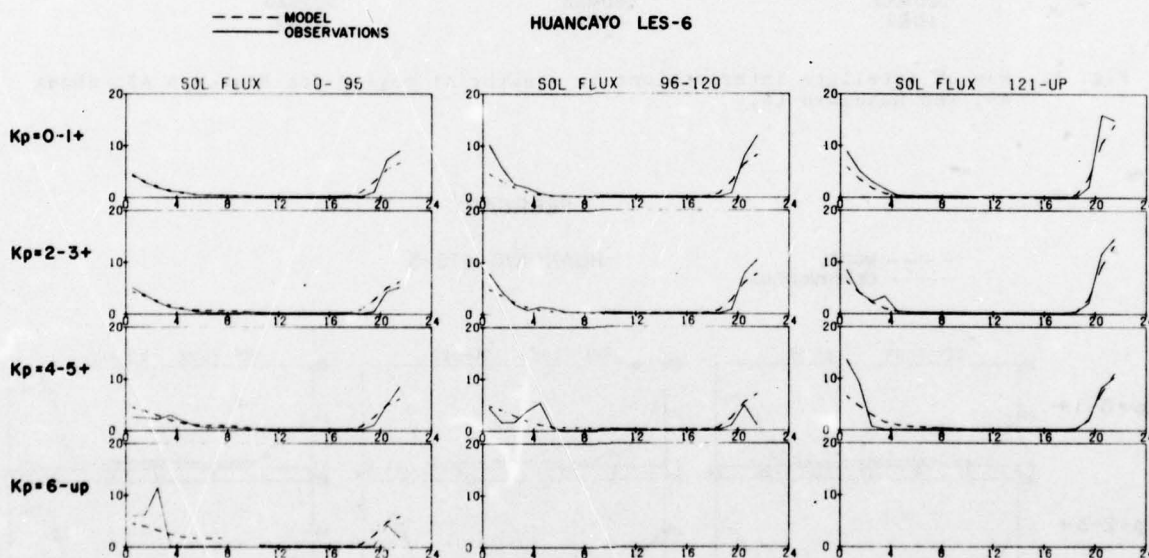
HUANCAYO LES-6

Fig. 4. Observational data and best-fitting model for Huancayo L6 for February.

HUANCAYO ATS-3
FEBRUARY
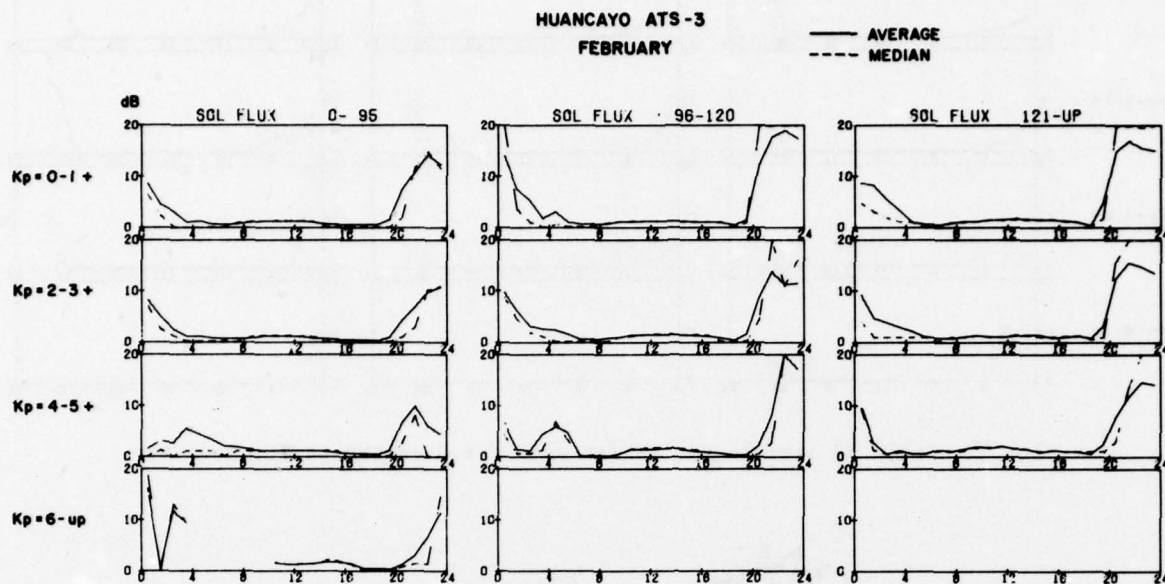
—— AVERAGE
---- MEDIAN

Fig. 5. Graph of average vs. median data for Huancayo A3 for February.

GHANA ATS-3
FEBRUARY
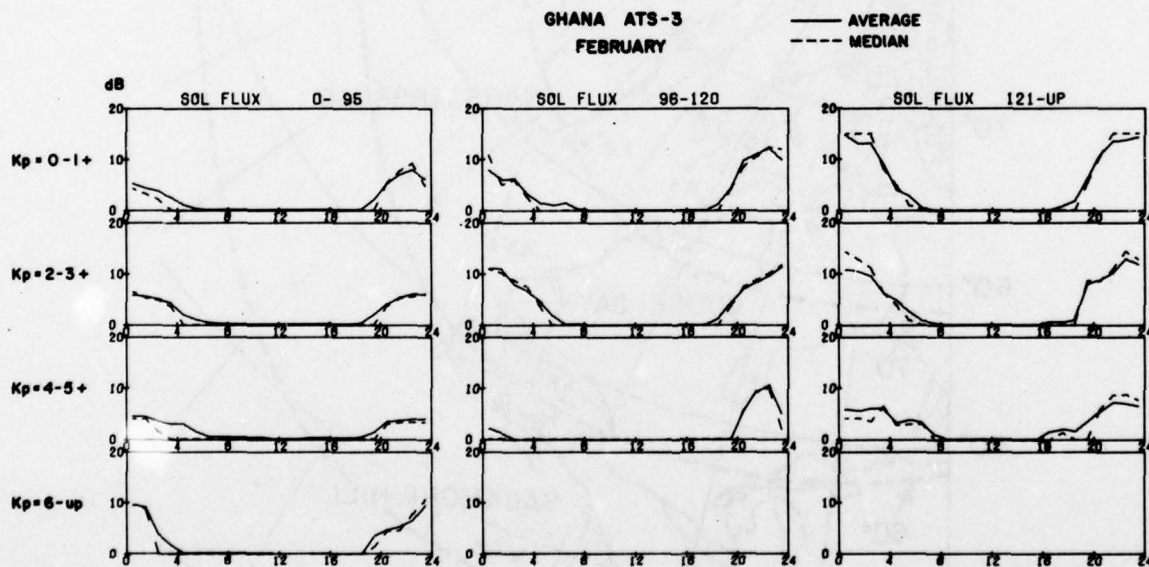
—— AVERAGE
---- MEDIAN

Fig. 6. Graph of average vs. median data for Ghana A3 for February.
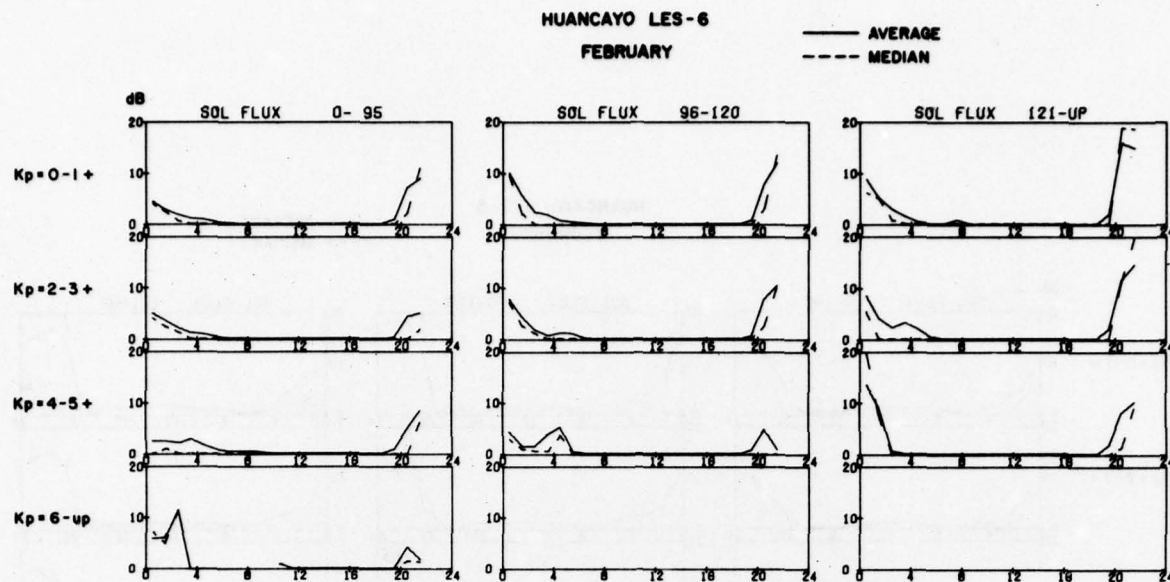
Fig. 7. Graph of average vs. median data for Huancayo L6 for February.
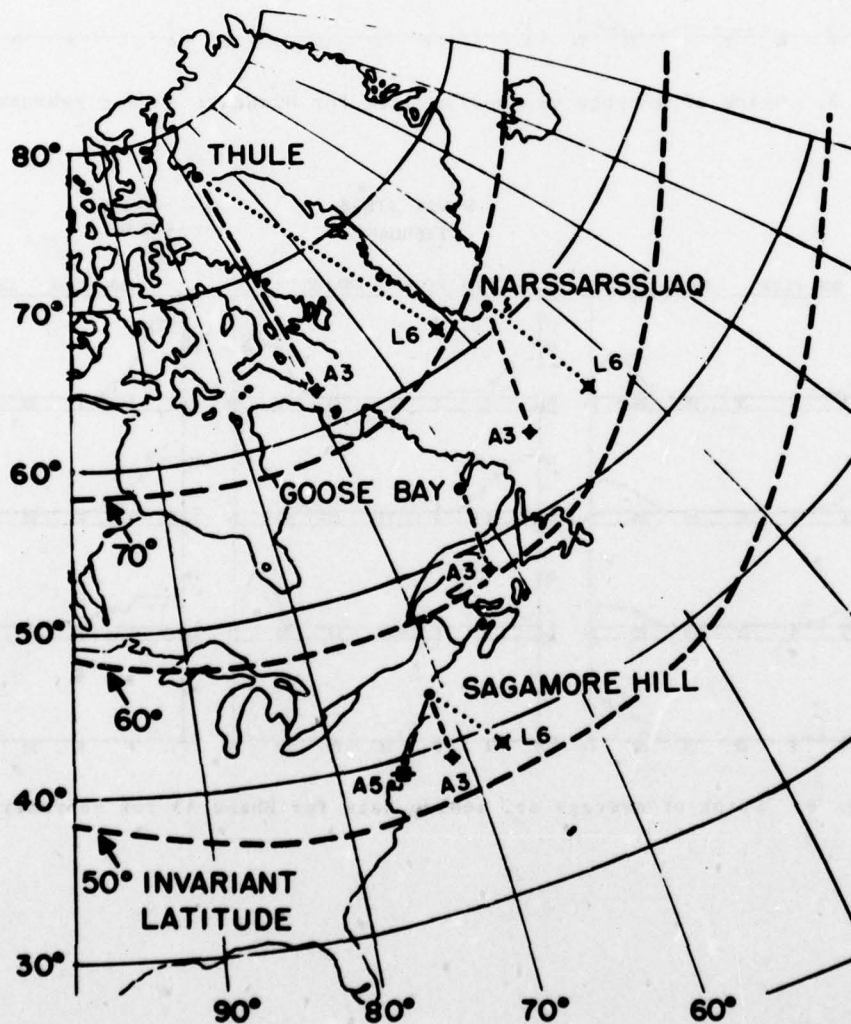
Fig. 8. Map of satellite intersections in the high latitude region for Narssarssuaq, Goose Bay and Sagamore Hill.

NARSSARSSUAQ MONTH 3
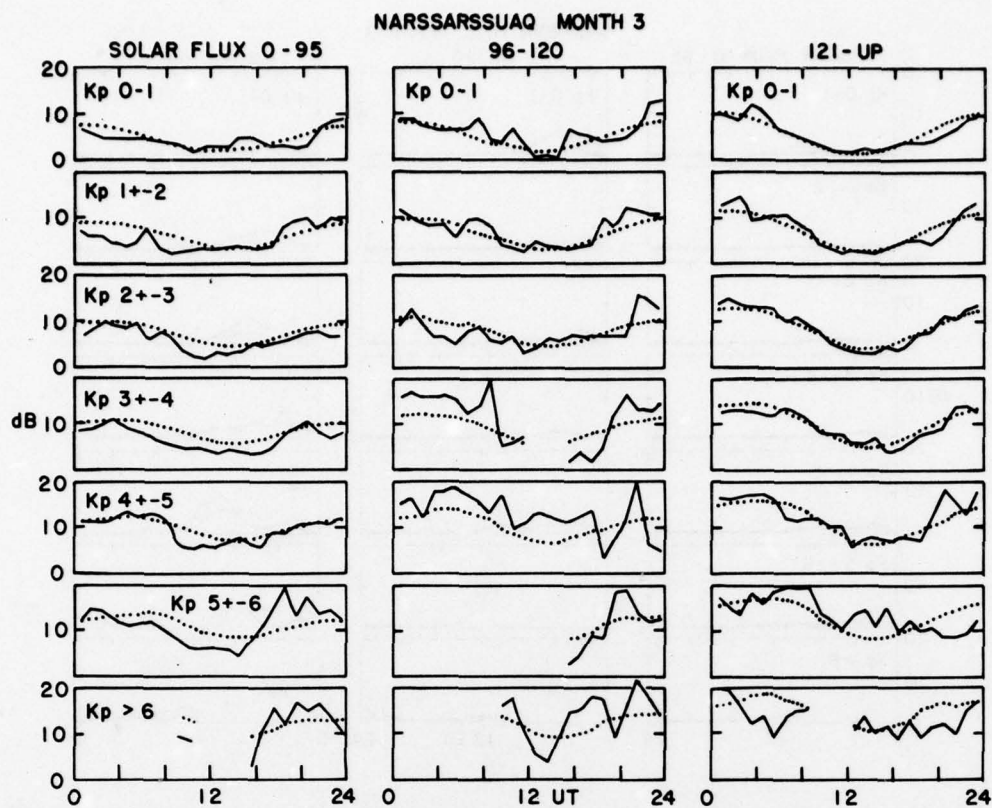
Fig. 9. Observational data and best-fitting model for Narssarssuaq A3 for March.

GOOSE BAY   MONTH 3
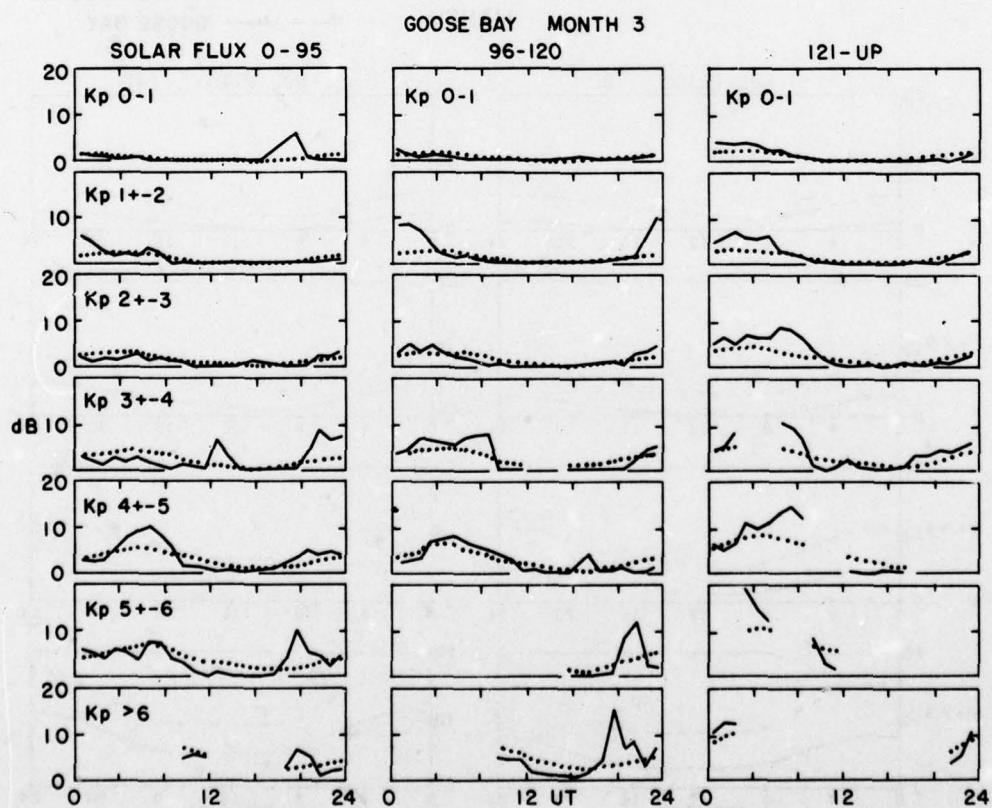
Fig. 10. Observational data and best-fitting model for Goose Bay A3 for March.
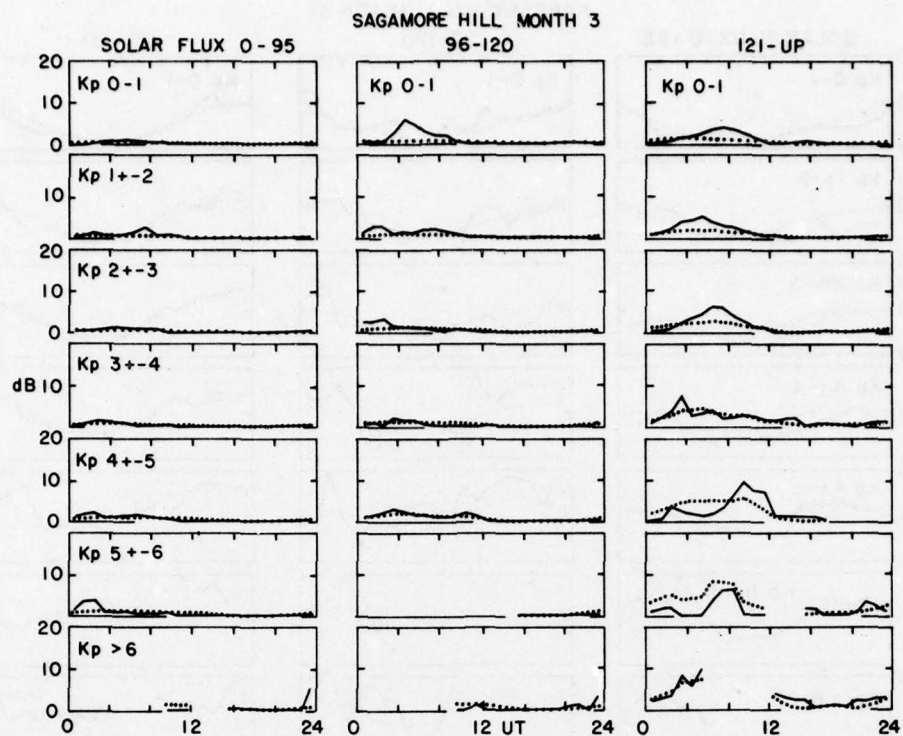
Fig. 11. Observational data and best-fitting model for Sagamore Hill A3 for March.
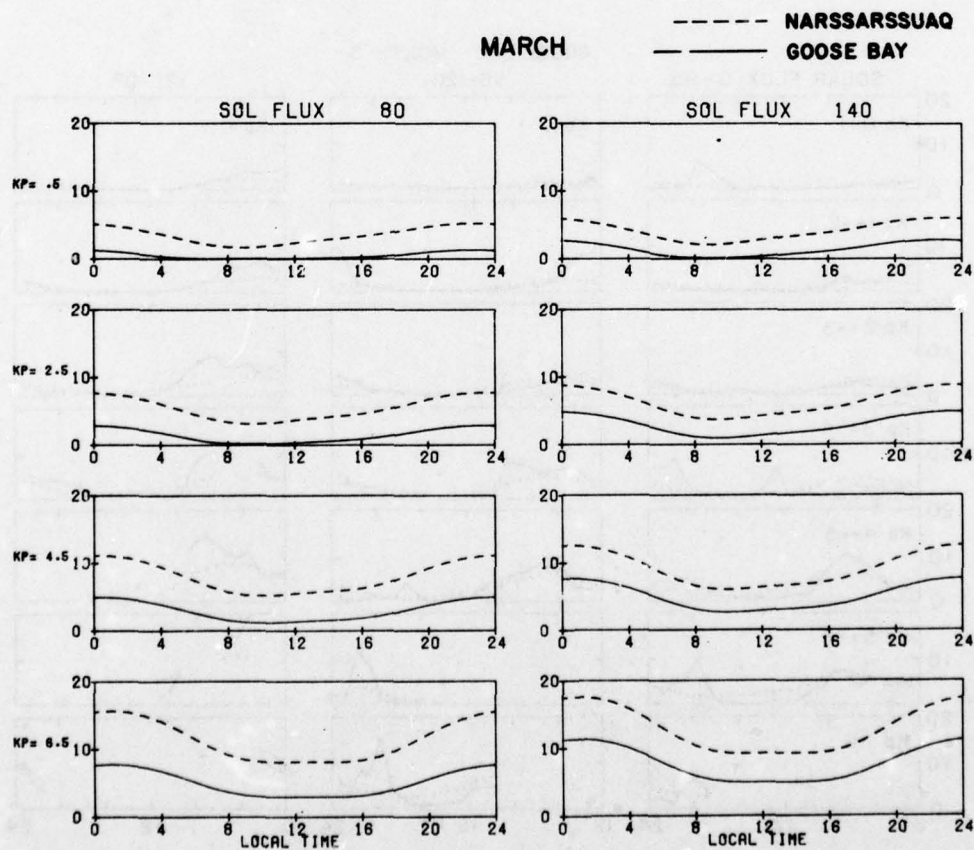
Fig. 12. Plots of mathematical model based on Narssarssuaq and Goose Bay (two station model) for March.

NARSSARSSUAQ   MARCH
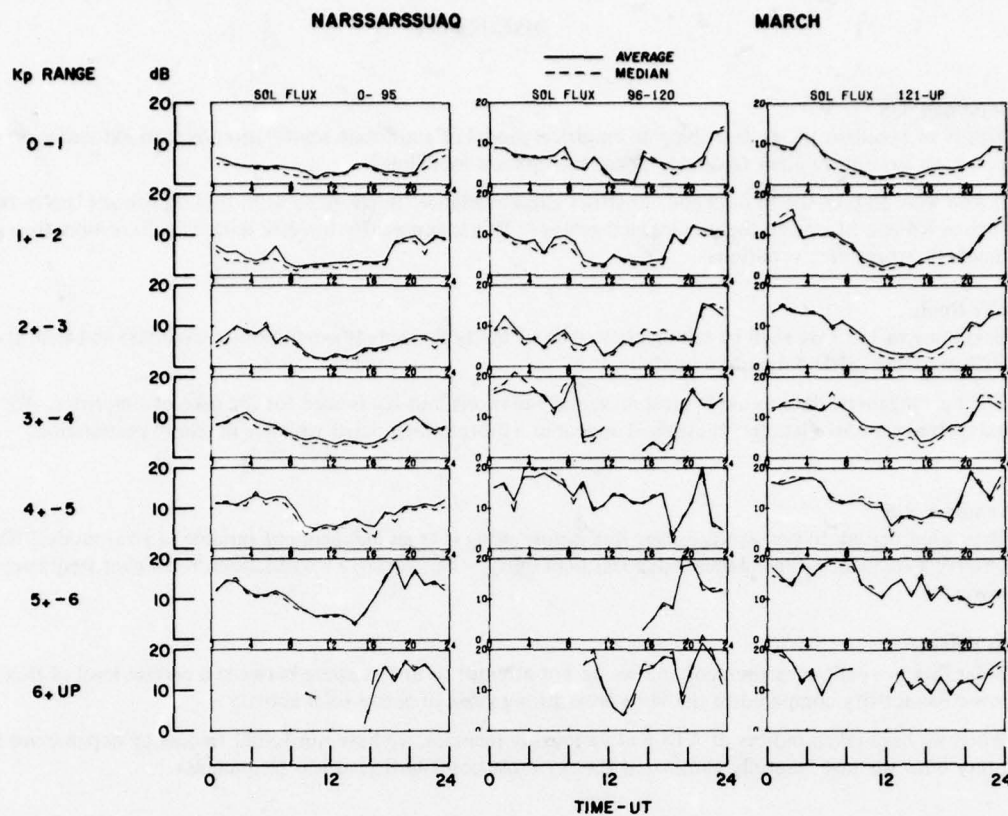
Fig. 13. Graph of average vs. median data for Narssarssuaq for March.
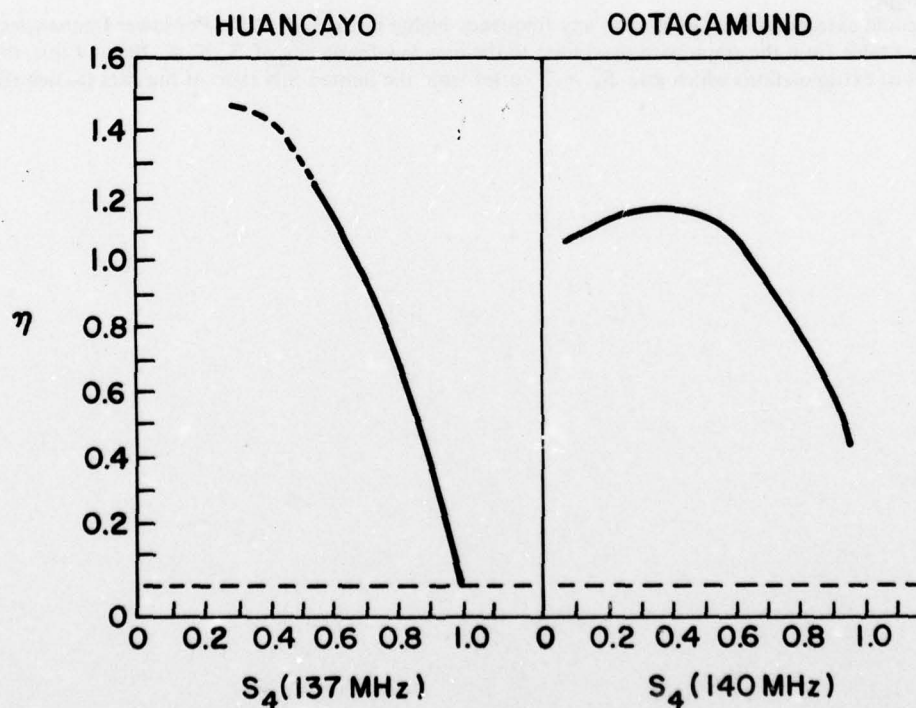
Fig. 14.   Relationship between spectral index η and S$_4$ as exhibited by ATS-6 observations at two equatorial stations, Ootacamund, India and Huancayo, Peru.

DISCUSSION

J.M.Goodman, US

This is an excellent paper describing an empirical model of amplitude scintillation over an extensive data base. Do you have any future plans to do any phase scintillation modeling?

If you were to take the SI data and construct autocovariance functions so as to find significant lags between solar flux or Kp and SI, would the picture change any? This is apparently the case with TEC in conjunction with magnetic storm time variations.

Author's Reply

Beginning in 1979 we shall be taking phase data of the type needed (synchronous satellites) and shall combine this with available (SRI) data into a model.

The best magnetic data to use is local magnetic variations, but Kp is used for the sake of simplicity. We have done extensive cross-correlations; these shall appear in a morphology paper which is in (slow) preparation.

E.J.Fremouw, US

Over what period do you average solar flux before using it as an independent variable in your model? Do you ever observe a frequency-dependence index less than unity — i.e., stronger scintillation on a higher frequency than a lower?

Author's Reply

Solar flux is a daily measurement and we do not attempt to differentiate between a certain level of flux in a year of low solar activity compared to the same level during years of active solar activity.

When we have taken indices of ATS-6 at various frequencies, we have not found frequency dependence less than unity once we have carefully eliminated the sky noise contribution at low frequencies.

N.G.Gerson, US

What is the greatest frequency range through which you would be willing to extrapolate your f vs SI curve? What, for example, would be the highest and lowest frequencies which you would accept.

Author's Reply

One could extrapolate at 136 MHz to any frequency higher until S_4 is $< .7$. For lower frequencies, one would make a table from the graph with maximum to the new low frequency of $S_4 < .4$. Beyond this, the curves can be used but extrapolations which give $S_4 > .7$ suffer from the limited S/N ratio of the data (as described in the text).
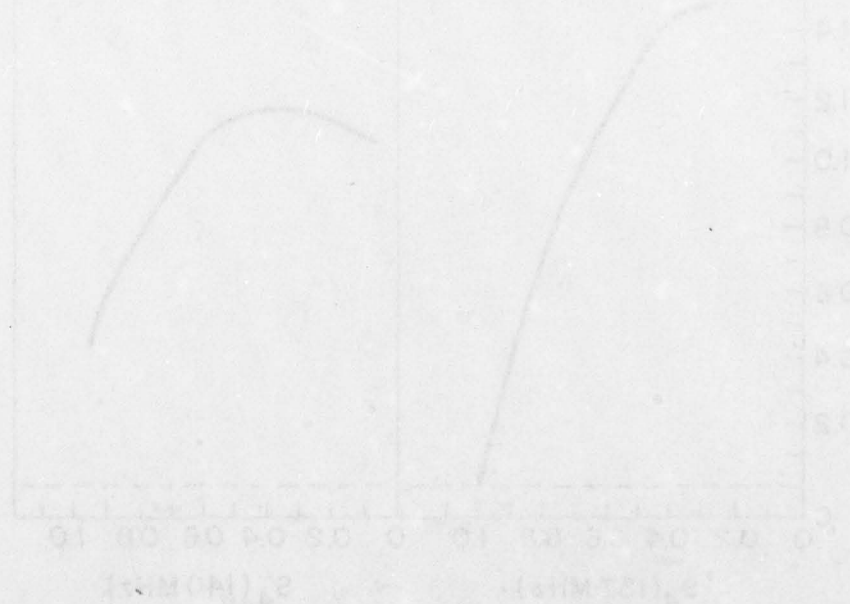
THE SEARCH AND RESCUE SATELLITE (SARSAT) SYSTEM PROJECT

H.L. Werstiuk and A.E. Winter
Communications Research Centre
Department of Communications
Ottawa, Canada

SUMMARY

For the past several years, Canada has been studying the application of satellite technology as an aid to search and rescue (SAR). The work has included examination of SAR requirements and the investigation of various system concepts culminating in proof-of-concept experiments using the AMSAT OSCAR satellites during 1975 and 1976. In the experiments, signals from simulated Emergency Locator Transmitters (ELTs) were received by the polar-orbiting OSCAR 6 satellite and relayed to a ground station at the Communications Research Centre (CRC). By the processing of Doppler information contained in this relayed signal, the position of the ELT could be determined with an accuracy of 5-15 km.

In the past SARSAT-related studies and experiments have been conducted separately by both Canada and the United States. In the fall of 1976 a joint program was proposed to demonstrate a satellite-aided search and rescue system. This joint program has been approved by both countries and calls for a pre-operational demonstration of the system commencing in 1981 using suitably-instrumented weather satellites operated by the National Oceanic and Atmospheric Administration (NOAA). France has recently taken a decision to participate in this project. The satellite system under consideration would be capable of detecting and locating ELTs and EPIRBs (Emergency Position-Indicating Radio Beacons) operating at 121.5, 243 and 406 MHz.

This paper will describe some of the experimental techniques and earlier results obtained in the Canadian program, and a companion paper (Muldrew and James, 1978), will describe the modeling of ionospheric effects relating to this experiment.

1. INTRODUCTION

Search and rescue (SAR) operation in remote areas can be costly and time-consuming. In Canada most search and rescue efforts are in aid of distressed aircraft, although a significant portion involve maritime searches as well. Commonly, a long period (up to several days) may elapse before a Rescue Co-ordination Centre (RCC) is alerted that a search is required.

To improve the effectiveness of search aircraft and reduce search time, the use of ELTs became mandatory for all general aviation aircraft in the U.S.A. in July 1974 and for all aircraft in Canada in January 1975. ELTs are low-powered emergency radio transmitters which are automatically activated in the event of an emergency. Some other characteristics of ELTs are given in Table 1. The current means of monitoring ELT emergency signals consist of limited monitoring by government facilities, usually at airports, and by overflying aircraft which monitor on a voluntary basis. The current effectiveness of ELTs is limited by the lack of an adequate continental monitoring system capable of receiving emergency signals from ELTs anywhere in Canada's search and rescue responsibility area.

TABLE 1

ELT/EPIRB CHARACTERISTICS AT 121.5/243 MHz

Parameter	Value
RF Signal	
Transmitter Power	75 mW (U.S.); 100 mW (Canada)
Transmission Life	48 hrs. minimum (U.S.); 100 hrs. minimum (Can.)
Temperature for Operation	-40°C to +55°C
Frequency	121.5/243 MHz
Frequency Tolerance	$\pm 5 \times 10^{-5}$
Polarization	Vertical
Modulation	
Modulation Type	Downward swept-tone modulated AM
Modulation Duty Factor	33% Minimum, 55% Maximum
Modulation Factor	85% minimum
Tone Sweep Rate	2-4 sweeps per sec.
Sweep Frequency Range	1600-300 Hz

In the maritime area, there is also a growing trend for vessels to carry emergency beacons. In Canada and in several other countries, towing vessels of five gross tons or larger must carry a float-free buoy with a radio beacon operating on 121.5 and 243 MHz. These devices, commonly called Emergency Position Indicating Radio Beacons (EPIRBs), are also extensively carried by many vessels on a voluntary basis. The reception of an EPIRB signal from a vessel in distress requires the fortuitous presence of another surface vessel within line-of-sight (within 30 km) or an overflying aircraft within range (within 250 km) which happens to have receivers tuned to these emergency frequencies.

The use of satellite technology to provide systematic distress monitoring of large areas of the earth's surface is receiving increased attention both in Canada and internationally. Any use of satellites for this task should be capable of providing a rapid emergency alert and of providing sufficient position location accuracy to permit rescue forces to quickly locate the distressed aircraft or ship without extended search times. The purpose of this paper is firstly to outline various system concepts which have been considered in the light of Canada SAR requirements; secondly, to describe a SARSAT "proof of concept" experiment; and finally, to discuss the proposed joint SARSAT demonstration system. In a companion paper, Muldrew and James (1978) describe the ionospheric effects on the SARSAT experiment.

2.   SYSTEM CONSIDERATIONS

2.1   Canadian SARSAT Requirements

The requirements that SAR users in Canada (primarily the Department of National Defence and the Coast Guard) place upon a potential SARSAT system can be summarized as follows:

(a) The system must provide coverage of the whole Canadian SAR Region.

(b) The system must provide the alert and location functions for existing ELTs operating at 121.5 and 243 MHz.

(c) The system location accuracy must be, with a high probability, within home-in range to an ELT by a search aircraft (approximately 50 km).

(d) The system must detect and locate the transmitting ELT within six hours of an emergency incident.

2.2   Orbit Choices

Two orbit types have been considered for use in a SARSAT system; the geostationary and the polar orbit. A Canadian requirement is that SAR coverage be provided over the full Canadian SAR region. As shown in Figure 1, this extends from approximately 40°W longitude to 140°W longitude, and from the U.S.A./Canadian border to the north pole. Figure 1 illustrates the well-known fact that northern coverage from a geostationary orbit is limited to approximately 80°N latitude and does not provide coverage for the full SAR region. Additionally, the distance from the earth's surface to geosynchronous orbit requires the development of a new, higher-powered ELT.

Figure 2 illustrates the coverage which would be provided by sequential passes of a polar orbiting satellite. On each pass, the satellite could receive signals from ELT/EPIRBs within the illustrated "orbit swath". This type of orbit, while providing intermittent coverage, does in fact cover the whole SAR region after about five passes. Three ground stations would be required for coverage of Canada's SAR region. Considerable overlap of coverage is provided by successive passes at northern latitudes. Multiple satellites are required to reduce maximum waiting time to an acceptable value. For example, two satellites will provide full earth coverage every six hours, three satellites every four hours, and so on. In maritime regions or over flat terrain, there would also be a high probability that an ELT would access the satellite on two consecutive passes, so that waiting time would be reduced to two hours maximum for a three satellite system. The shorter ELT-to-satellite range for a polar orbit is also compatible with the current low-powered ELTs.

2.3   Preferred System Concept

Consistent with requirements for coverage and operation with existing ELTs, a satellite-aided SAR system operates as shown in Figure 3. ELT signals are received by the satellite and retransmitted to a distant central station. The motion of the satellite introduces Doppler shift. At the ground station, the received ELT signal is analysed to extract an ELT position estimate from the Doppler shift information on the ELT carrier frequency. This estimate is passed to an RCC which dispatches search aircraft to the emergency site. The search aircraft then uses conventional "homing" techniques to pinpoint the exact ELT location.

3.0   SARSAT EXPERIMENTS

During 1975 and 1976, a series of experiments (Lambert and Winter, 1976) was carried out by the Communications Research Centre (CRC) to confirm the feasibility of locating ELTs by Doppler-signal processing using polar orbiting satellites. Additional objectives were to identify problem areas in the possible implementation of a SARSAT system, and obtain R&D information to aid in definition and specification of a SARSAT system.

The experiments, which emulated the operation of a satellite-aided ELT position-location system in all critical aspects related to position determination, were carried out using the OSCAR-6 amateur radio satellite. This satellite was kindly made available for these experiments by the Radio Amateur Satellite Corporation (AMSAT). OSCAR-6 is in a near-polar orbit, and has a transponder on an uplink frequency of

146 MHz near the international distress frequency of 121.5 MHz, and a downlink frequency of 29.5 MHz. As shown in Figure 4, the experiment was performed by deploying to a remote site a portable transmitter which simulated an ELT signal. This signal was received by the satellite and retransmitted to the CRC earth station where signal processing was performed to obtain position locations from the Doppler information.

OSCAR-6, being in a low-polar orbit similar to one which might be used in an operational system, causes considerable Doppler shift (approximately $\pm$ 3 kHz) of the ELT signal. A typical example of Doppler data obtained during the OSCAR-6 experiments is shown in Figure 5. The technique of obtaining position information from a curve of Doppler frequency shift versus time for a satellite pass involves several steps, as shown by the software flowchart in Figure 6. First, corrections must be applied to the received signal to compensate for Doppler on the downlink and to average out noise effects. Then the zeroDoppler, or point of closest approach of the satellite to ELT, must be determined with as much accuracy as possible. The slope of the Doppler curve at this point is used to calculate the range from satellite to ELT. The range is in turn used, along with satellite orbital data, to determine two initial estimates of possible positions on the earth's surface. These two positions are symmetrically located on each side of the satellite orbital track. One position is the true ELT location, while the other is a phantom location. In an operational SARSAT system, the resolution of the ambiguity would occur by modelling the small difference in the two Doppler curves due to the rotation of the earth, by using data from a second satellite pass, by a priori knowledge, or at worst, by a check of both indicated positions. The estimated ELT positions are used to compute predicted Doppler curves, and an iterative procedure is used to solve for a final position which produces the best fit of computed Doppler data to the measured Doppler curve.

3.1   Experiment Results

During the experiment, simulated ELT packages were sent to several locations in Canada, including Yellowknife in the northwest and Eureka in the far north. Data from over 150 satellite passes was obtained. As an example, Figure 7 gives the results of several experiments where simulated ELTs were actually located at CRC, near Ottawa. The scatter of points, most of which are within a ten mile radius, gives the actual positions which were estimated by data processing of the Doppler information. The results obtained show that it is routinely possible to locate ELTs within 10-20 km accuracy.

3.2   Location Errors

Figure 8 is a plot of the overall observed frequency error between measured Doppler and predicted Doppler frequency expected from the actual location of the simulated ELT. Degradation of the ELT location accuracy can occur due to factors such as orbit prediction error, ionospheric effects, measurement errors, and ELT frequency instability. The many reference satellite passes and resulting location predictions have shown that orbit prediction errors and ELT frequency drift are the most significant in the overall system performance.

Orbit error can be reduced to acceptable limits (about 1 km) by choosing an accurate enough earth-model, and frequently updating satellite orbital information (about every three days) from independent tracking systems (e.g. NORAD) or by ranging to the satellite.

Ionospheric effects and resulting errors are highly frequency dependent and are very significant at the 30 MHz OSCAR downlink frequency (Muldrew and James, 1978). From a system point of view these effects can be reduced by remodulating, in the satellite, the received ELT signals on to the downlink carrier to the ground station. Ionospheric effects at 121.5 and 243 MHz will still remain. Use of an ionospheric model for the Canadian region in the computer processing at the ground station will allow real-time reduction of these ionospheric effects.

Doppler curve measurement errors depend to a large extent upon the signal-to-noise ratio of the received carrier, the portion of the satellite pass which has been simultaneously visible to the ELT and the monitoring earth station, the spectral purity of the ELT signal itself, and the sophistication of the signal processor which extracts Doppler information prior to position estimation. The variability in the signal quality observable from current ELTs in the field has proven to be a troublesome problem in the design of a Doppler signal processor capable of operation with both "good" and "bad" ELTs.

Frequency instability of the ELT also has an important bearing on the location accuracy. Although a knowledge of the actual frequency of the ELT is not necessary for the position determination algorithm to function, frequency drift of the ELT during the course of a satellite pass could contribute frequency errors much larger than those shown in Figure 8. Fortunately this frequency drift, which is caused by aging, temperature, or other effects, is normally reasonably well-behaved during a pass, and simple modelling of a frequency drift parameter as a first-order effect during the data processing is capable of correcting most of the resulting error. Any ionospheric effects which appear as first order ELT frequency drifts are also corrected by the frequency drift parameter.

4.   PROPOSED SARSAT PROJECT

During the period that Canada was performing the OSCAR experiments (Winter, Lambert, Pearce and Werstiuk, 1976), NASA was also studying the application of space technology to search and rescue problems. The results of their studies led to system concepts similar to those which have evolved from the Canadian studies. Beginning late in 1976, a series of meetings were held between Canadian and U.S. officials to explore the feasibility of a joint Canadian/U.S. Search and Rescue Satellite Project. Such a joint project would include the necessary spaceborne equipment to be flown as an additional 'instrument' on board the U.S. TIROS-N/NOAA weather satellites. This project was subsequently approved in principle by both countries, followed by a decision by France to participate by supplying part of the SARSAT instrument.

The objective of the system would be to demonstrate a significant improvement in the distress monitoring coverage of remote areas, and to provide more rapid alerting and accurate position determination capability than is now available to SAR forces. This capability will be provided for existing ELT/EPIRBs operating at 121.5 and 243 MHz, as well as for new improved types of ELT/EPIRB test units operating in the 406 MHz band allocated for this purpose. The new ELT test units will operate in a burst transmission mode more suited for detection by satellites, and will transmit identification and status codes via the SARSAT system. The improved design of these new ELT test units should allow position determination with accuracy of 2-5 km, versus the 10-20 km accuracy expected for current ELTs.

4.1 Baseline System

The SARSAT space segment is planned to be implemented by including SAR instruments on-board the TIROS-N series series of spacecraft in a near-polar, 850 km orbits. It is expected that the last three spacecraft of the TIROS-N series (NOAA-E, F, and G) will be equipped with the SAR instrument. Signals from the SAR instrument will be received by Local User Terminals (LUTs) appropriately located to provide the desired coverage area. The system will provide two modes of operation, namely the regional coverage mode and the full-orbit coverage mode as described below.

(a) Regional Coverage Mode

The regional coverage mode is shown in Figure 9. ELTs and EPIRBs operating in all three bands will transmit their signals to the orbiting spacecraft. Within each band, there can be one or more simultaneous ELT/EPIRB emissions, as well as non-ELT/EPIRB emissions. This is especially applicable to the 121.5 and 243 MHz bands, which are also used for emergency voice communications. The spacecraft instrument will multiplex each band into a composite signal and relay the signal in real time to the LUTs which are in view at the time. At each LUT, the composite signal will be demultiplexed into the individual bands, and each ELT/EPIRB signal will be individually detected and processed to determine position location information. This information will be forwarded to the nearest Rescue Co-ordination Centre, where SAR forces are alerted and deployed. The regional coverage mode requires that the spacecraft is simultaneously visible to the LUT and the ELT/EPIRB for a sufficient length of time to permit a position determination (approximately 4 minutes).

(b) Full-Orbit Coverage Mode

The full-orbit coverage mode is illustrated in Figure 10. ELT/EPIRB signals at 406 MHz only will be received in the SARSAT on-board processor, where partial signal processing is performed. The processor will look for and accept only a valid ELT/EPIRB 406 MHz emission, subsequently decode the identification code (I.D.) and status code of the ELT, and measure the frequency of the Doppler-shifted signal. The frequency measurement, appropriately time-tagged and including the I.D. and status code, will be stored onboard the satellite for later transmission to a NOAA earth station. This allows ELT/EPIRB emissions to be received and partially processed when the satellite is not in view of the LUT. This data is subsequently read out by a NOAA Command and Data Acquisition Station (NOAA CDA) and passed on to a SAR mission control centre. The data is then further processed to compute position location of the distress, identify the person/vehicle in distress, and to display the status code message. (i.e. ship on fire, sinking, medical emergency, etc.).

4.1 Spacecraft SAR Instrument

Figure 11 is a functional block diagram showing the SAR instrument and its interface with the spacecraft. The antenna subsystem consists of three receiving antennas with nominal centre frequencies of 121.5, 243 and 406 MHz, and a transmitting antenna with a nominal centre frequency of 1543 MHz. The beamwidth of the antenna at 121.5 and 243 and 1543 MHz will correspond to approximately 120°, consistent with coverage provided by the 850 km orbital altitude. The antenna beam at 406 MHz will be shaped to some extent to compensate for increased range losses at lower elevation angles.

The repeater itself consists of redundant receivers at 121.5, 243 and 406 MHz, a transmitter at 1543 MHz, and associated frequency synthesizers, power supplies, switches, modulation controls, and telemetry and command circuits. The 406 MHz processor consists of a 406 MHz receiver and associated acquisition, measurement and demodulation circuits to receive the 406 ELT test unit signals and produce an output of time-tagged frequency and ELT/EPIRB identification and status data. The interface between the 406 processor and the data transmission on the 1543 MHz downlink will be via the TIROS spacecraft Manipulated Information Rate Processor (MIRP).

4.2 SARSAT Local User Terminal (LUT)

Figure 12 is a functional description of an earth station that is designed to be a local user terminal (LUT). The LUT consists of an antenna and control unit, a receiver/demodulator unit, and a signal processor. The antenna system will be a program tracking L-band antenna approximately 3 meters in diameter. The antenna position information will be generated in the LUT from spacecraft orbital elements transmitted from the NOAA CDA station.

Down conversion and demodulation from L-band to a low IF will be provided by the receiver and demodulator unit. In addition the frequency of the downlink carrier will be monitored to provide orbital update information. The signal processor will receive the signals at the low IF from the receiver and demodulator unit, process the information to produce Doppler-shifted frequency-curve data, identify the individual curves, and calculate the possible ELT/EPIRB positions for each curve. The signal processor for the 121.5 MHz and 243 MHz frequency bands is a critical development area due to the wide range of characteristics for ELTs currently in use.

The interactive console display section will provide the interface between the individual segments of the LUT and will provide for operator input when required. Data lines provide for such functions as the distribution of ELT/EPIRB position location data to the RCCs and acquisition of satellite orbital information.

4.3   Project Schedule

The current project schedule is shown in Figure 13. The SAR instrument engineering-model implementation will be underway by mid-1978, with integration of the first flight instrument on NOAA-E scheduled for 1980. Development of the LUT signal processor will be complete by the end of 1978, with the prototype LUT produced in 1979. Additional LUTs will be manufactured by mid-1980, with the ground segment readiness tests completed by early 1981, which is the earliest possible launch of NOAA-E carrying the first SAR instrument. NOAA-E will not, however, be launched until replacement of an earlier NOAA satellite is required, and this is expected to be in early 1982. The system will then enter a fifteen month checkout, demonstration, and evaluation phase, with active participation by potential North American SAR users and possibly other interested countries (for example USSR, Norway, France, Australia). Two additional SAR instruments will also be produced and integrated with NOAA-F and G spacecraft scheduled for launch in mid-1983 and early 1984. These additional instruments will permit transition to a pre-operational phase if the evaluation phase proves the system to be successful.

5.   ACKNOWLEDGEMENTS

6.   REFERENCES

Lambert, J.D. and A.E. Winter, 1976, "A Search and Rescue Satellite System (SARSAT) Experiment", presented at Communications '76 Conference, 8-11 June 1976, Brighton, England, and published in IEE Publication 139, pp. 351-355.

Muldrew, D. and G. James, 1978, "Ionospheric Effects on the Doppler Frequency for a Search and Rescue Satellite (SARSAT)", AGARD Symposium, Ottawa, 24-28 April 1978, this issue.

Winter, A.E., J.D. Lambert, J.L. Pearce and H.L. Werstiuk, 1976, "Satellite-Aided Search and Rescue", presented at the IEEE Conference, Montreal, Canada, 20-22 October 1976, and published in IEEE Publication 1126-2, pp. 101-102.
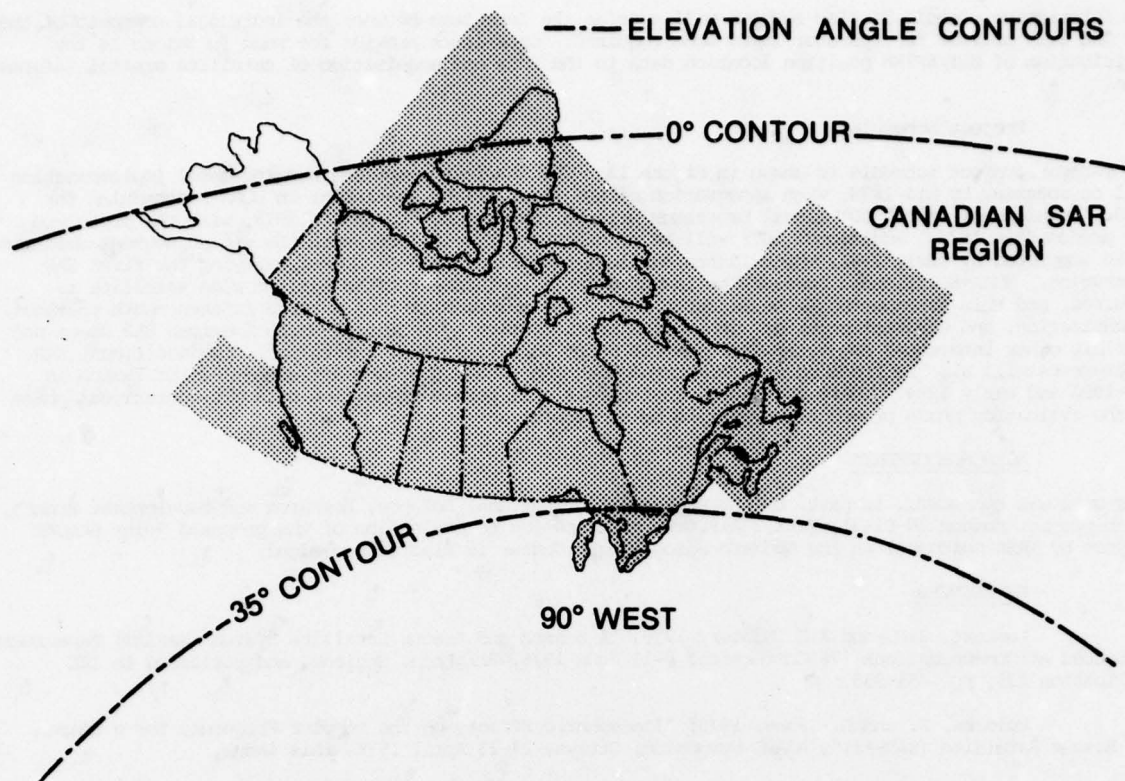
Figure 1   Elevation Angle Contours to a Geostationary Satellite at 90°W Longitude.
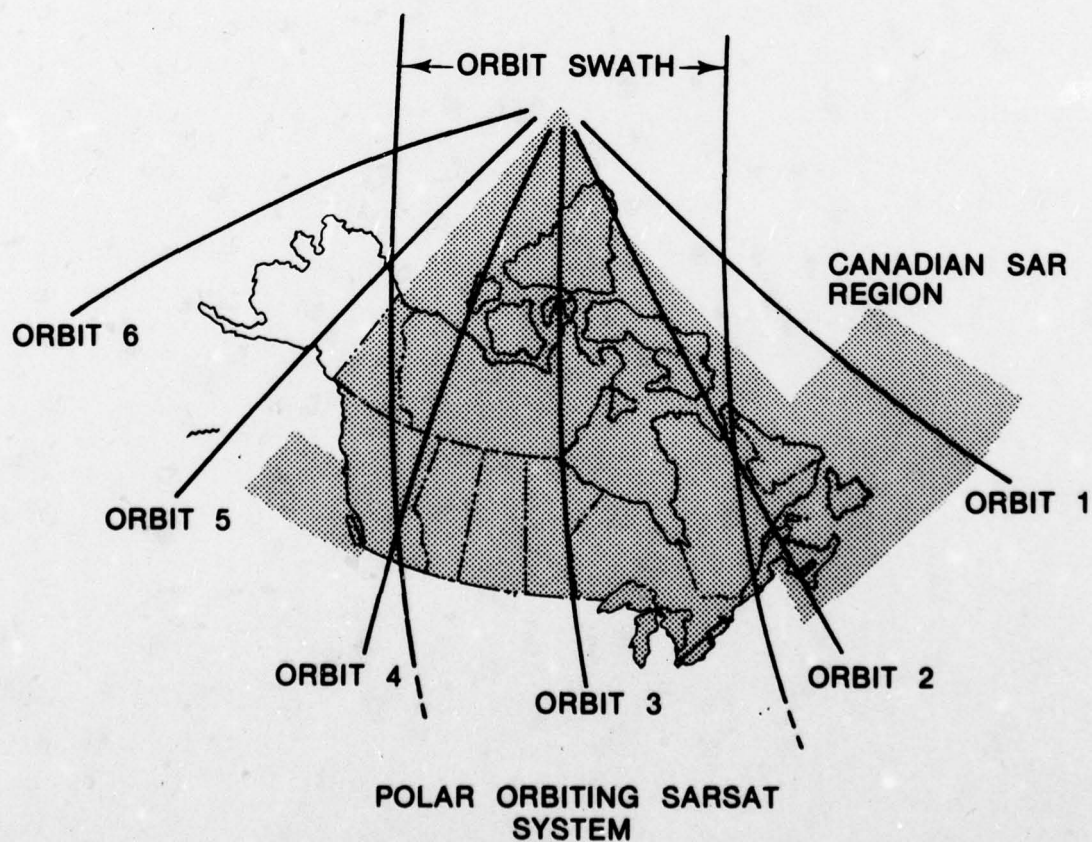
Figure 2   Orbit Subtracks for a Polar Orbiting SARSAT System.
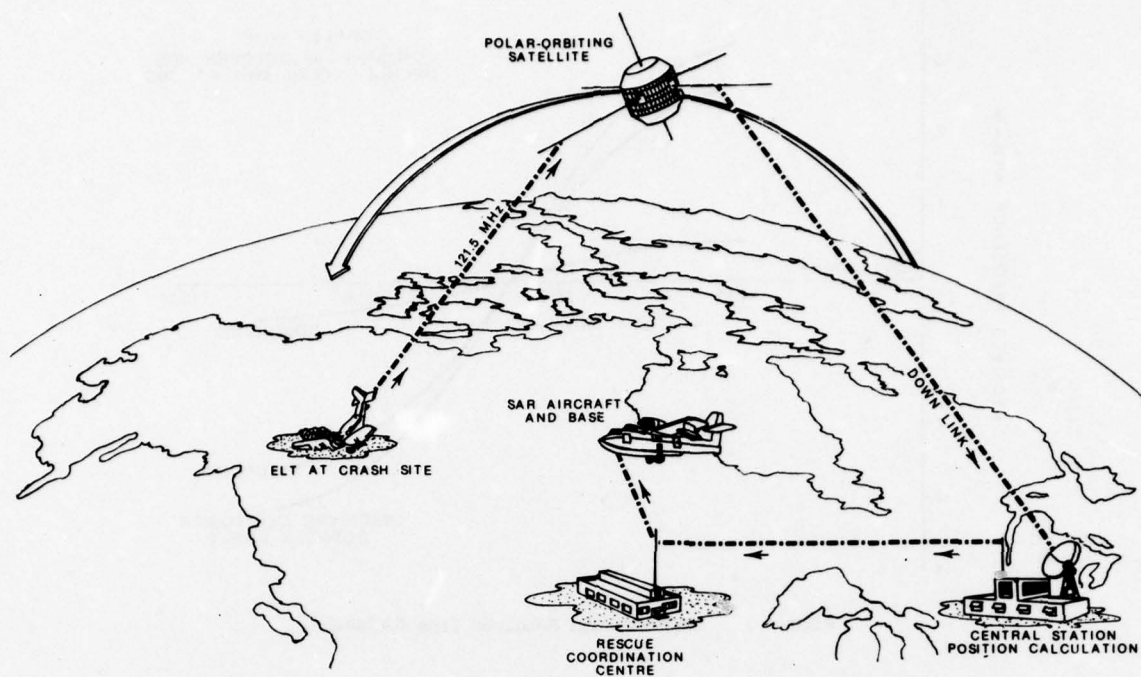
Figure 3   Satellite-Aided SAR System Concept.
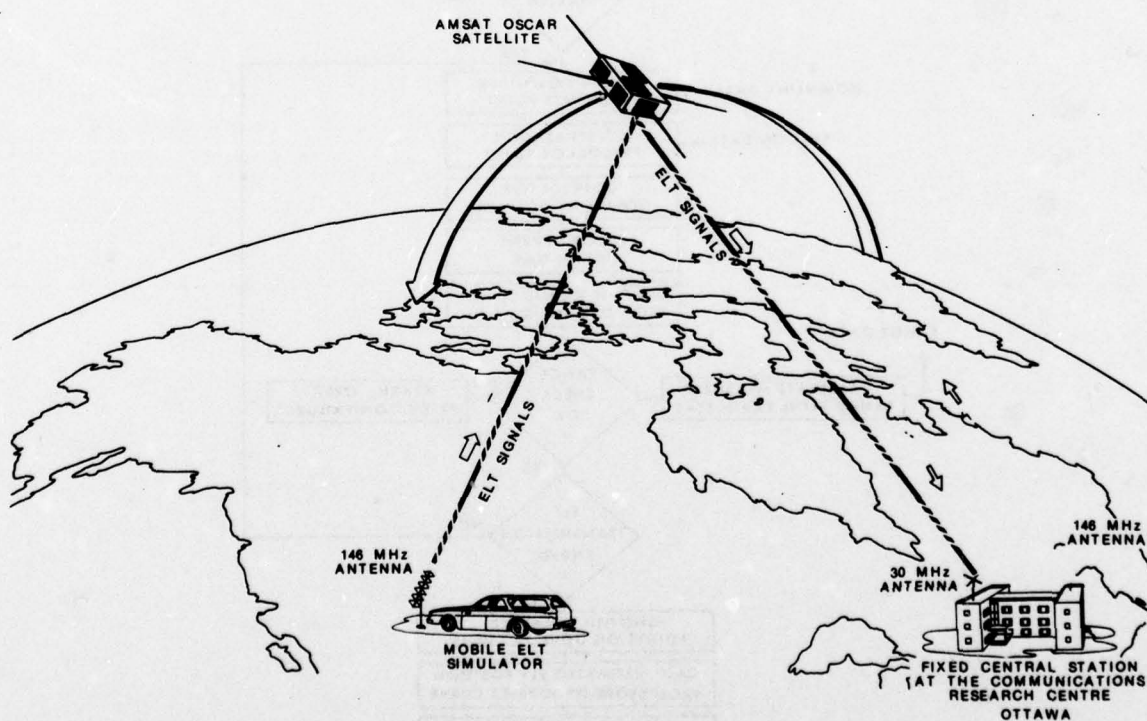
CRC SARSAT Experiment.
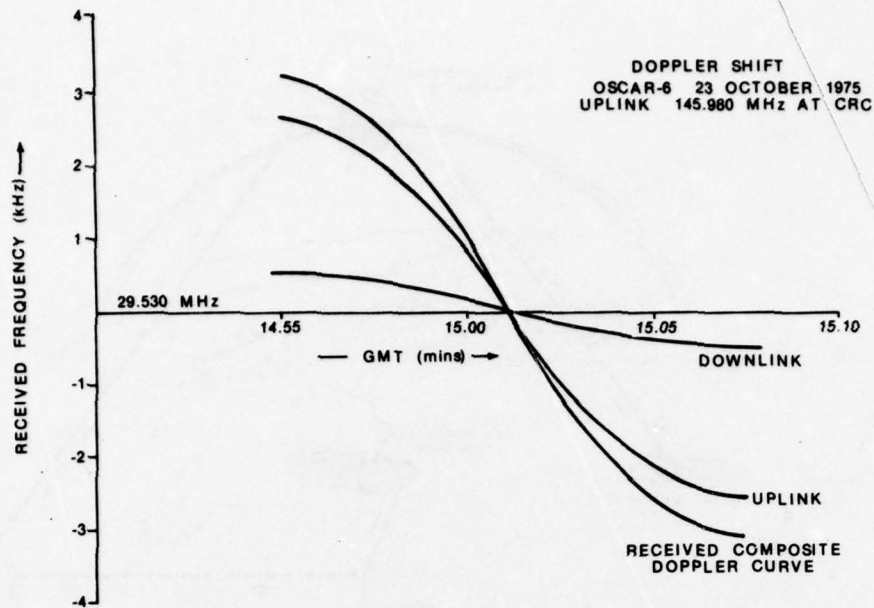
Figure 5   Doppler Data Received from OSCAR-6.
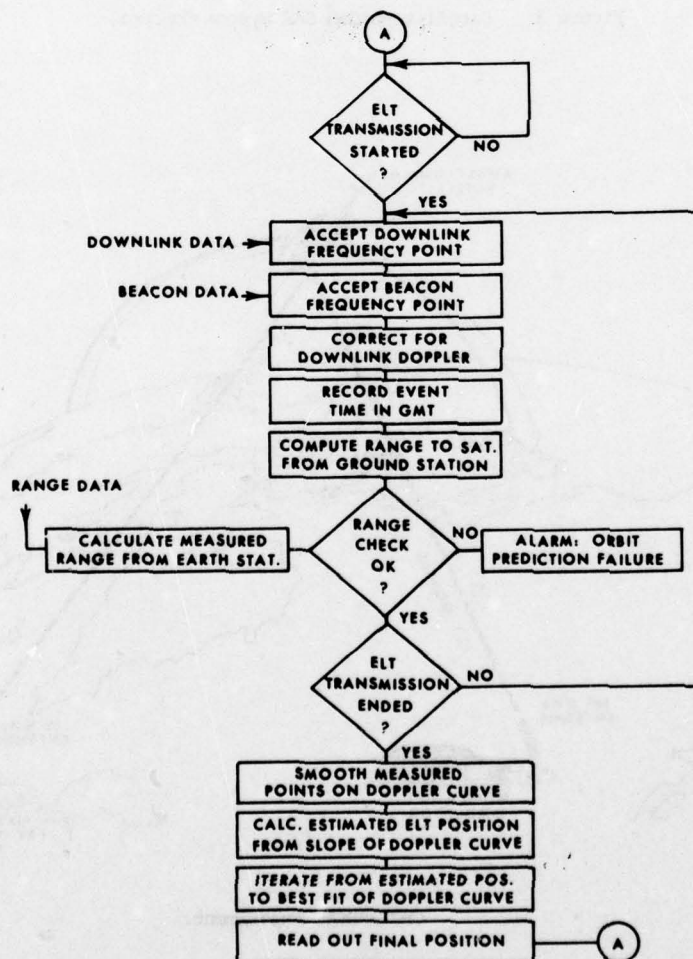
Figure 6   Software Flowchart.
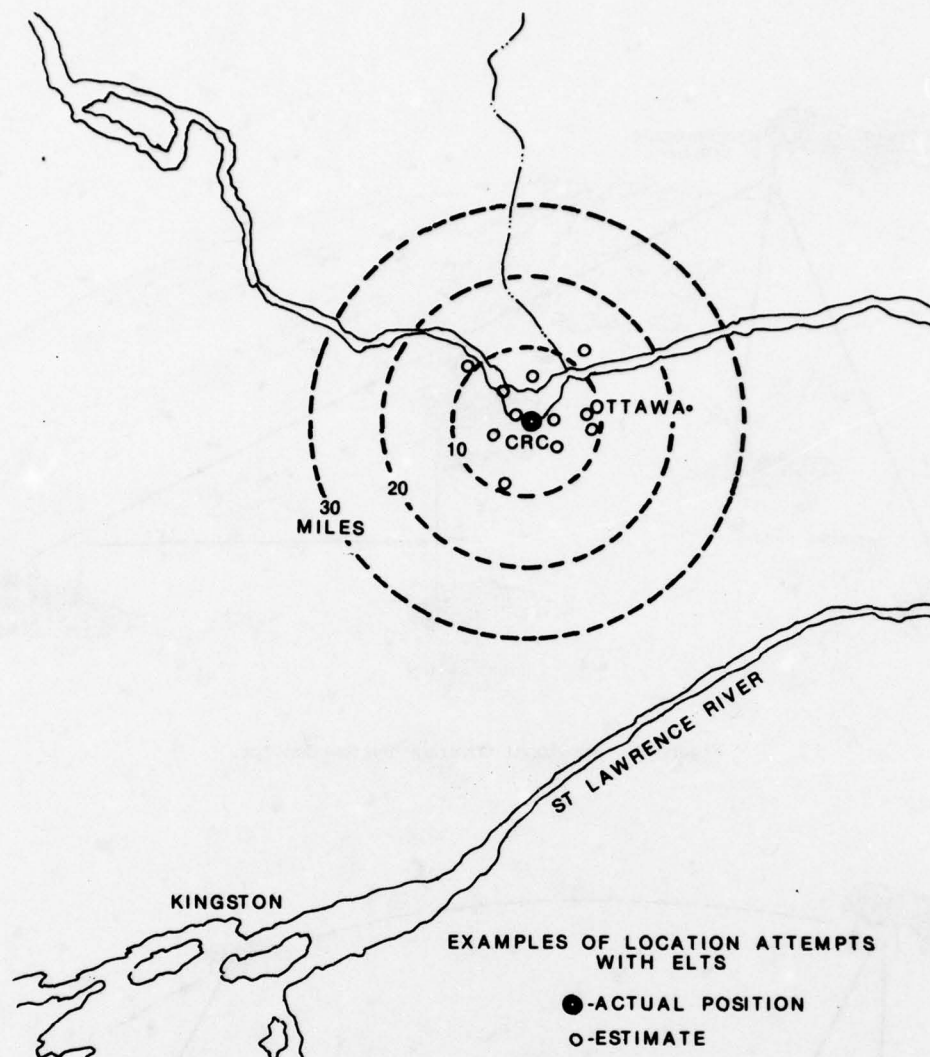
Figure 7   Examples of Experimental Results from the CRC SARSAT Experiment.

EXAMPLES OF LOCATION ATTEMPTS
WITH ELTS
●-ACTUAL POSITION
○-ESTIMATE

OSCAR 6, 6 JAN. 1976

DOPPLER FREQUENCY ERROR
(PREDICTED DOPPLER-MEASURED DOPPLER)

ACTUAL POSITION
45.380 LAT., 284.120 LONG.

ESTIMATE OF POSITION
45.384 LAT., 283.943 LONG.

UPLINK FREQUENCY
145.980477 MHz
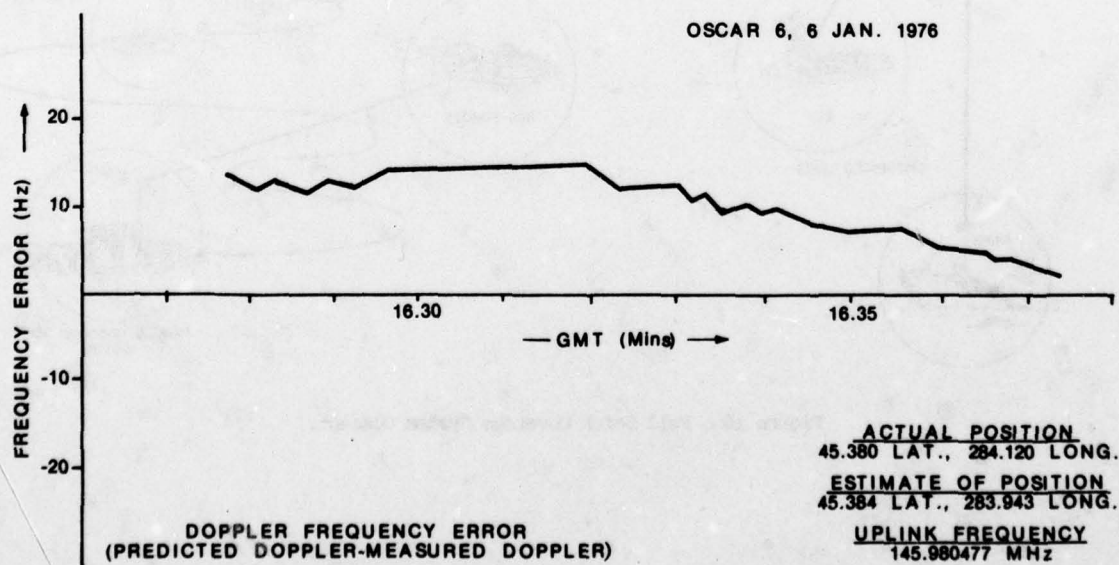
Figure 8   Residual Frequency Error After Optimization.
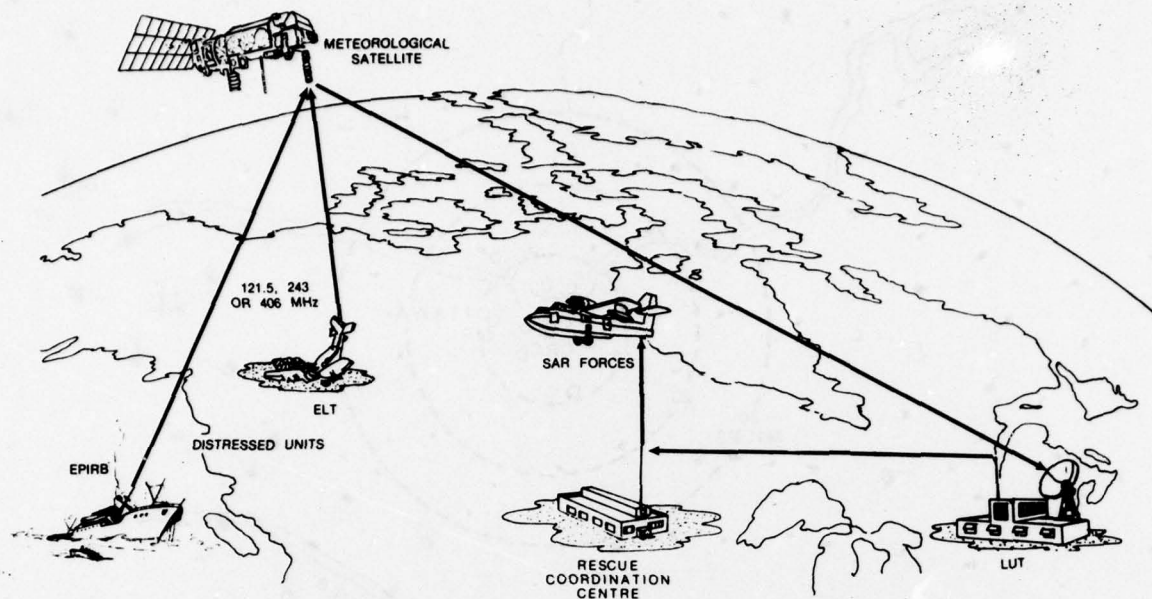
Figure 9   Regional Coverage System Concept.
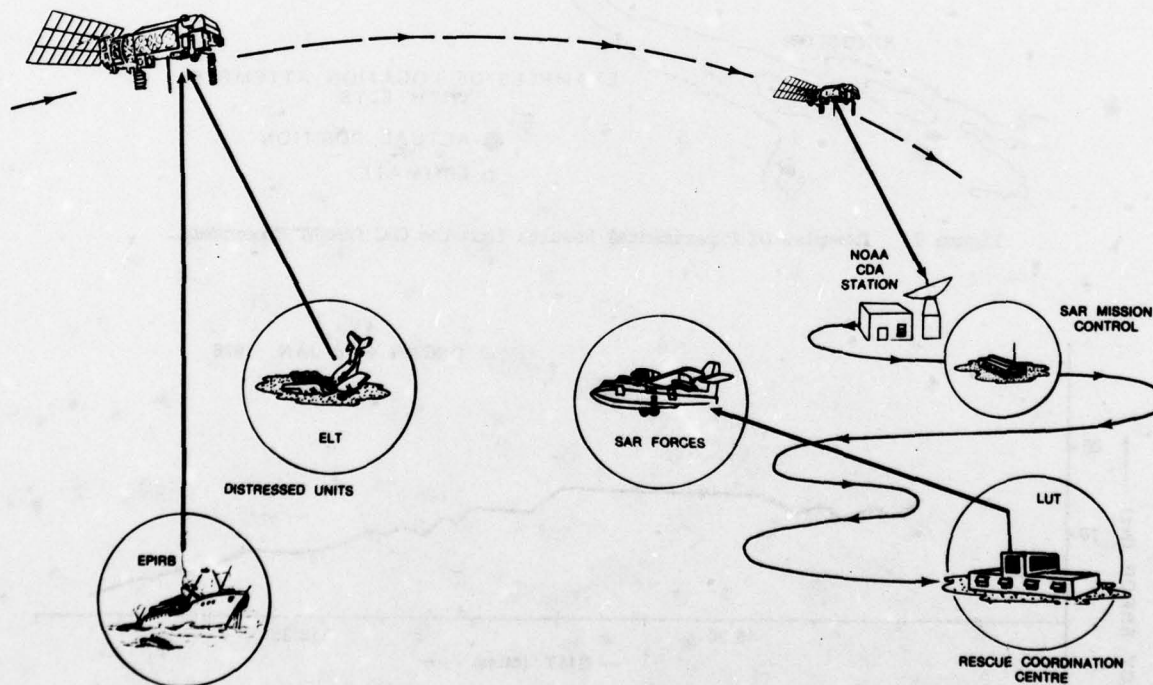
Figure 10   Full Earth Coverage System Concept.
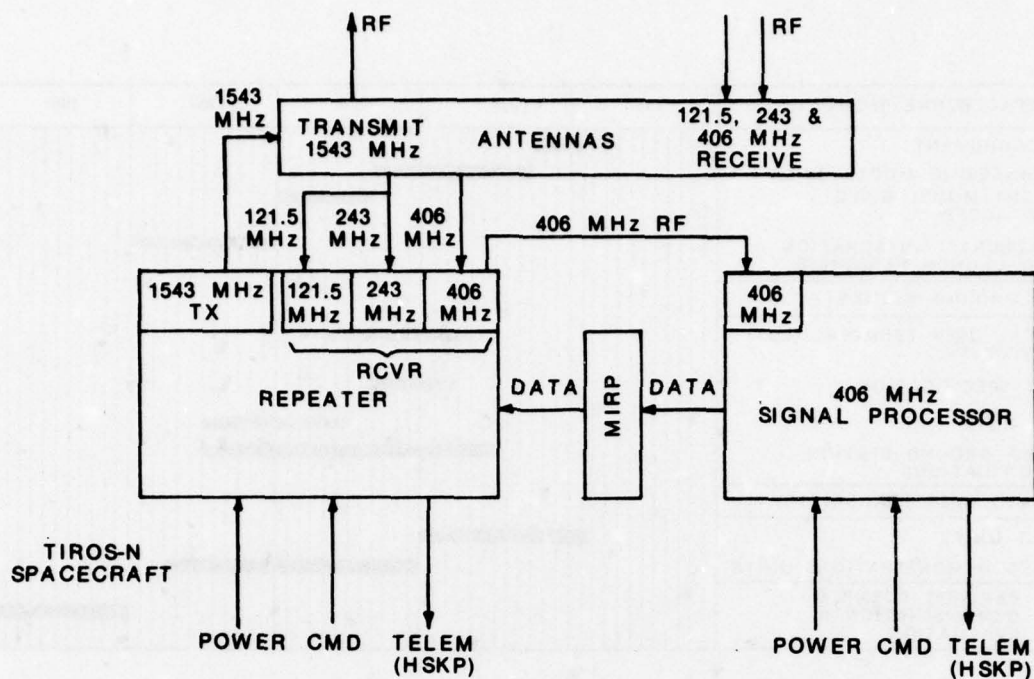
Figure 11 SAR Mission Instrument Functional Interface.
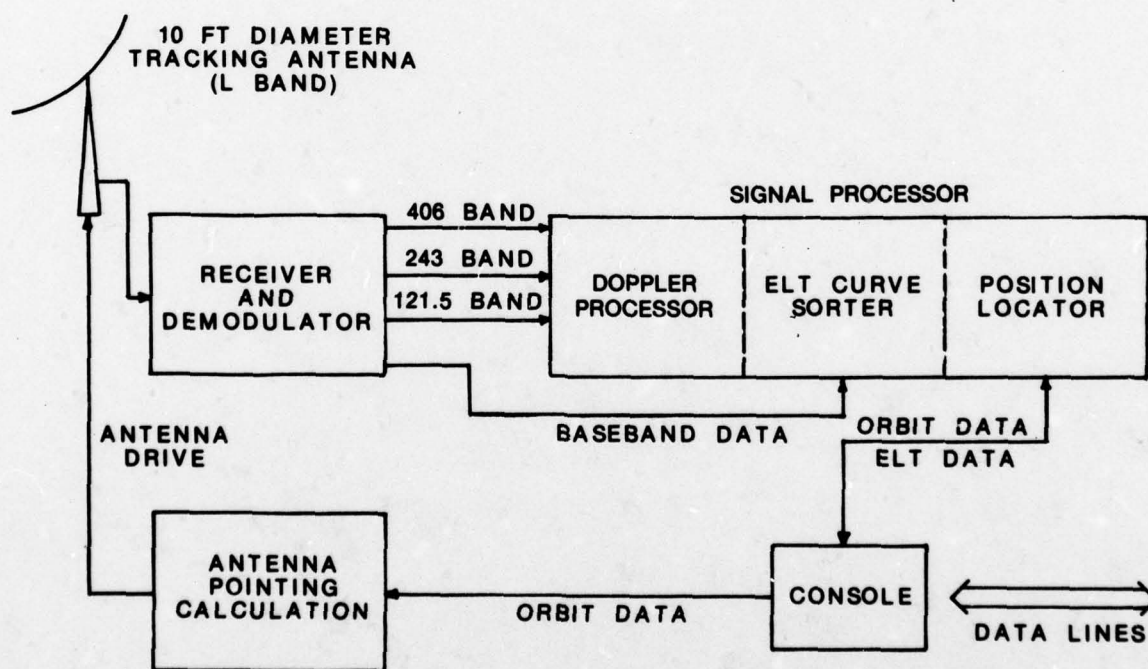
Figure 12 Functional Diagram of a SARSAT Ground Station.

SPACEBORNE SEGMENT	1977	1978	1979	1980	1981	82
PROCUREMENT						
ENGINEERING MODEL BUILD						
FLIGHT MODEL BUILD AND ACCEP.						
SPACECRAFT INTEGRATION AND LAUNCH READINESS						
GROUND SEGMENT						
LOCAL USER TERMINAL (LUT) PROTOTYPE						
LUT SPECIFICATIONS						
U.S. LUTs						
NOAA GROUND STATION MODIFICATIONS						
406 MHz USER TRANSMITTERS						
TEST UNITS						
FIELD DEMONSTRATIONS UNITS						
EARLIEST POSSIBLE DEMONSTRATION & EVALUATION						

Figure 13   Proposed Joint SARSAT Program Schedule.

IONOSPHERIC EFFECTS ON THE DOPPLER FREQUENCY

FOR A SEARCH AND RESCUE SATELLITE (SARSAT)

D.B. Muldrew and H.G. James
Communications Research Centre
Department of Communications
Ottawa, Canada

SUMMARY

The Doppler frequency shift of signals propagating from an Emergency Locator Transmitter (ELT) up to a search and rescue satellite (SARSAT) and down to a central station enables the position of the ELT to be determined (see companion paper). The Doppler frequency shift is affected by the ionosphere. Ionospheric effects are estimated for a proof-of-concept SARSAT experiment using the AMSAT OSCAR-6 satellite and a central station at Ottawa. For the downlink frequency of 30 MHz it is found that the daytime ionosphere with no horizontal gradients in electron density can change the Doppler frequency shift by a few hertz. Horizontal gradients of electron density can have more effect on the Doppler frequency than the vertical distribution of density. This is because the Doppler effect caused by the negative vertical density gradient in the topside ionosphere tends to cancel the Doppler effect caused by the positive gradient in the bottomside. However, in the late afternoon, evening and nighttime, large east-west troughs in the density distribution exist which can produce shifts of a few tens of hertz at 30 MHz.

1. INTRODUCTION

The Communications Research Centre is involved in the Search and Rescue Satellite program (SARSAT) to locate downed aircraft. The program is funded by the Department of National Defence who have the responsibility for search and rescue in Canada.

By measuring the Doppler frequency shift of the signal from an aircraft's Emergency Locator Transmitter (ELT), after it has been received by a satellite and retransmitted on a different frequency to a central station (Lambert and Winter, 1977; Werstiuk and Winter, 1978), the position of a downed aircraft can be located. Ignoring the effect of the ionosphere on the Doppler frequency will increase the error in estimating the location of the aircraft. This paper examines the ionospheric effect in some detail.

A proof-of-concept experiment has been carried out at the Communications Research Centre using the AMSAT OSCAR-6 satellite (Lambert and Winter, 1977). ELT signals, originating from known locations, were received by OSCAR-6, retransmitted at 30 MHz, and then received at Ottawa. Calculations in this paper are thus done for 30 MHz. In an actual SARSAT system the ELT frequency would probably be 121.5 MHz and the downlink frequency would be considerably more than 30 MHz.

The ionosphere has a small but significant effect on the Doppler frequency shift of a VHF signal propagating between a moving satellite and fixed ground station. The Doppler frequency shift, hereafter called "Doppler", is the same whether the signal travels from the satellite to the ground or vice versa. Although the 30 MHz OSCAR-6 signal is transmitted from the satellite and received on the ground, for convenience it will be assumed here that the signal is transmitted from the ground and received at the satellite. The Doppler is given by

$$f_D = -\frac{1}{2\pi} \underline{k} \cdot \underline{v} = -\frac{1}{2\pi} k \, v \cos \lambda \tag{1.1}$$

where $\underline{k}$ is the wave normal at the satellite of a VHF signal transmitted from the ground station and arriving at the satellite moving with velocity $\underline{v}$ and λ is the angle between $\underline{k}$ and $\underline{v}$ at the satellite. For reception at the satellite, if $\underline{k}$ has a component in the direction of $\underline{v}$, f_D is taken to be negative. For a satellite at a height well above the F2-layer peak, only the ionospheric effect on λ need be considered. Here the Doppler between the satellite and fixed station is calculated; in the SARSAT case the Doppler between the ELT and satellite must be added.

The theoretical background for calculating the Doppler frequency is given by Muldrew and James (1978), hereafter referred to as I, and this is reviewed in Section 2. In the present paper calculations based on specific ionospheric models are presented in Section 3.

2. DOPPLER FREQUENCY CALCULATIONS

The mathematics required for the Doppler frequency calculations, a listing of the main computer program and most of the subroutines, and a sample calculation (corresponding to the solid curve in Figure 9) are given in I. The Doppler is calculated for three possibilities: (1) no ionosphere, (2) an ionosphere consisting of a thick spherical shell of constant electron density with no horizontal gradients, and (3) a similar ionosphere with horizontal gradients.

2.1 No-Ionosphere Case

The geometry for the no-ionosphere case is shown in Figure 1 where the propagation is in a straight line from the ground station assumed to be Ottawa (45.36°N, 75.88°W) to the satellite at height h_s above the earth's surface. The earth is assumed to be spherical with radius R = 6371 km. The angle subtended at the centre of the earth by the ground station and satellite is Θ and Φ is the angle of incidence of the ray at the satellite. The latitude, longitude and height of the satellite are obtained using orbit

calculation programs and data supplied by NASA; the latitude and longitude of the station are given.

The z axis is the vertical through the satellite and the x axis is in the horizontal plane and is directed away from the fixed station. The (x, y, z) coordinate system at any instant is assumed fixed with respect to the earth. The Doppler frequency is

$$f_D = -\frac{f}{c} \ (v_x \sin \Phi + v_z \cos \Phi) \tag{2.1.1}$$

where f is the transmitter frequency, c is the free-space velocity of light, v_x and v_z are the x and z components of satellite velocity. The satellite velocity in (x, y, z) coordinates and the derivation of Φ are given in I.

To check the accuracy of the calculations in the fixed-earth system using (2.1.1), the Doppler was calculated independently using celestial coordinates. In one case, it was found that errors of about 0.1° in specifying the latitude and/or longitude of the fixed station resulted in errors of up to about one hertz. Also, the satellite velocity was required to be defined carefully. Calculating the satellite velocity from two satellite positions one second apart and applying this to one of the positions rather than the average position could result in errors of about one hertz.

2.2   Ionosphere Case, No Horizontal Gradients

As illustrated in Figure 2 the ionosphere is approximated by a thick spherical layer with a constant plasma frequency f_N between 200 and 500 km. The use of a more sophisticated model at the present time is not justified since any predicted value of f_N would not be sufficiently accurate. The 200 and 500 km values are based on experience from bottomside and topside ionograms. If a model ionosphere is capable of predicting better values for h_1 and h_2, the program can easily be changed to accommodate these values.

For a curved earth and an ionosphere composed of a spherically stratified thick layer, Snell's law can be stated

$$n \ (R + h) \sin \Phi = CONST \tag{2.2.1}$$

where n and Φ are respectively the refractive index and angle between the wave normal and the vertical at distance R + h from the centre of the earth. The refractive index above and below the layer is 1 and in the layer

$$n = n_o = [1 - f_N^2/f^2]^{\frac{1}{2}} \tag{2.2.2}$$

where f_N is the plasma frequency or critical frequency (foF2) of the slab and f is the ray frequency.

From (2.2.1) and (2.2.2) it is possible to obtain an implicit equation for Φ' given the positions of the station and satellite; this equation is given in I. All the other angles indicated in Figure 2 can then be determined. The Doppler frequency with no horizontal gradients of electron density is

$$f_{DI} = -\frac{f}{c} \ (v_x \sin \Phi' + v_z \cos \Phi') \tag{2.2.3}$$

The Doppler obtained from (2.2.3) was verified using the alternate equation

$$f_{DI} = -\frac{f}{c} \ \frac{d}{dt} \int nds \tag{2.2.4}$$

where ds is an incremental length along the ray path which, in this case, is the three lines A, B and C (Figure 2).

2.3   Ionosphere With Horizontal Gradients

To calculate the effect of horizontal gradients, it is assumed that the ray in the no-horizontal gradient case is a straight line from the station to the satellite. The deviation of the path from this straight line due to the horizontal gradient can then be calculated and this deviation applied, at the satellite, to the actual no-horizontal-gradient case illustrated in Figure 2 where the ray consists of 3 straight line sections.

If there is a horizontal gradient of electron density in the ionosphere, the portion of the ray in the ionosphere (see Figure 2) will not be a straight line but will be curved away from the direction of the gradient. Note that the refraction due to the vertical gradient at h_1 in Figure 2 is almost completely compensated at h_2 (cf. light passing through a pane of glass). This compensation does not occur with a horizontal gradient; hence a modest horizontal gradient can have a greater effect in total refraction on the ray than a large vertical gradient.

The radius of curvature R_c of the ray in the ionosphere, is given by another form of Snell's law [Storey, 1958]

$$\frac{1}{R_c} = -\frac{1}{n} \ (\nabla n)_\perp \tag{2.3.1}$$

where $(\nabla n)_\perp$ is the refractive index gradient perpendicular to the ray. The gradient ∇n is assumed constant between h_1 and h_2 and in the program is obtained by finding the average gradient along the ray between h_1 and h_2.

The ray path is shown in Figure 3 in a view looking vertically downward at Ottawa. The straight line OS is for no horizontal gradients. The path with horizontal gradients is broken into three parts,

A below the layer, B in the layer, and C above the layer ionosphere. A and C are straight lines, B has radius of curvature R_c. The deviation due to horizontal gradients, α, is very small so that to a good approximation the length of lines A, B and C can be obtained from Figure 2. The Doppler frequency for the horizontal-gradient case is determined by the angle Φ' derived assuming no horizontal gradients, from the angle α between $\underline{k}$ (wave normal at the satellite no horizontal gradient) and $\underline{k}'$ (wave normal at the satellite, horizontal gradient), and from the angle μ between the plane containing $\underline{k}$ and $\underline{k}'$ and the vertical plane through the station and satellite. The Doppler frequency, derived in I, is

$$f_{DIG} = -\frac{f}{c}\left[v_x(\cos\alpha\,\sin\Phi' - \varepsilon_o|\cos\mu|\sin\alpha\,\cos\Phi')\right.$$

$$+ v_y(\varepsilon_2|\sin\alpha\,\sin\mu|) \qquad (2.3.2)$$

$$\left. + v_z(\cos\alpha\,\cos\Phi' + \varepsilon_o|\cos\mu|\sin\alpha\,\sin\Phi')\right]$$

where $\varepsilon_o = \pm1$ and $\varepsilon_2 = \pm1$. The values of ε_o and ε_2 are determined by the geometry.

3.   EXAMPLES OF IONOSPHERIC EFFECTS ON DOPPLER CURVES

3.1   Description of Model

Doppler frequency shifts have been calculated for a variety of ionospheric density models and for three different OSCAR-6 orbits. One of the orbits passes almost vertically over the assumed 30 MHz ground receiver at Ottawa (45.36^{o}N, 75.88^{o}W) whereas the other two have subsatellite tracks that pass within a minimum great-circle distance (GCD) of about 2000 km of the receiver, one to the east and the other to the west. Ephemeris data for the passes were calculated using a satellite orbit package and NASA-supplied Brouwer mean orbital elements for the spacecraft. Various orbital details are given in Table 1.

Table 1

Date	Time interval Start	Stop	Closest GCD to subsatellite point	Direction	Label
6 Jan/76	1620 UT	1644 UT	2280 km	Southbound	"West"
16 Jan/76	1403	1427	30	Southbound	"Overhead"
16 Jan/76	1210	1234	2240	Southbound	"East"

The tracks of the subsatellite points for the three passes, in relation to the location at Ottawa of the ground receiver are shown in Figure 4. OSCAR-6 is in a roughly circular orbit, and its height during these passes varies between 1448 and 1461 km. The orbit is retrograde with an inclination of approximately 110°, so that on these three north-to-south passes, the subsatellite track has a westward component of motion and makes an angle with the equator of about 70°. The first two lines in Table 1 correspond to passes during which personnel from the Communications Research Centre carried out experimental ELT tests using a mobile transmitter and a receiver at Shirley Bay, whereas the "East" pass was not used for that purpose.

Ionospheric density distributions of various types have been modelled for the ray-tracing calculation of theoretical Doppler frequency shift on the satellite-to-ground 30 MHz signal. As mentioned above, the ionosphere was approximated by a spherical layer 300 km thick lying between 200 and 500 km altitude and within this layer the density could have horizontal gradients but no vertical gradients. In cases where the density varied along the ray path, the average density and horizontal gradient were obtained by averaging the values at 25 km-height intervals along the path.

Horizontal density gradients play an important role in determining ray paths and it was decided to include several values of density gradient in the Doppler calculations. The different models used are listed in Table 2. For figure 5 a constant foF2 was used to evaluate the refractive index and a zero or east-west gradient was used to calculate the curvature of the ray path.

It was not possible to obtain topside passes at the same time as the OSCAR passes. Hence ISIS II passes were chosen having the same season and local time as the OSCAR passes. The ISIS II passes were recorded about one year earlier than the OSCAR passes.

The difference in frequency between the Doppler shift calculated with the ionosphere present and the free-space shift, called the "ionospheric Doppler difference", is plotted as a function of the latitude of the OSCAR-6 satellite (Figures 5 to 9). The difference frequency, usually amounting to only several hertz in contrast to the total Doppler shift of a few hundreds of hertz, indicates the net effect of the ionosphere on the Doppler shift. The computer program starts calculating Doppler differences at 12 minutes before the instant of closest approach and proceeds at 50-second intervals through a 24-minute period. Near the beginning and the end of the pass, either the ionosphere reflects the rays or the satellite is out of range due to the earth's curvature and contact is no longer possible. The cutoff depends on the great circle separation of receiver and satellite and thus the latitude of cutoff is influenced by the longitude of the satellite. It will be seen that the low-latitude cutoff of the "west" pass is higher in latitude than that of the "east" pass.

Table 2

Figure No.	foF2	Horizontal gradient in foF2	Comments
5	8 MHz	None, 0.001 MHz/km eastward, 0.001 MHz/km westward	
6	Varies	Varying north-south gradient, from ionograms	Both foF2 and gradient scaled from ionograms recorded on an Ottawa ISIS II pass starting 75/004/1442 UT.
7	Varies	Varying north-south gradient, from ionograms	Both foF2 and gradient scaled from ionograms recorded on an Ottawa ISIS II pass starting 75/009/1557 UT.
8a,b,c	Varies	Varying north-south gradient, hypothetical trough	Both foF2 and gradient derived from a hypothetical distribution composed of a deep ionospheric trough centred at Ottawa superposed on constant southward gradient.
9	Varies	Varying north-south gradient, from ionograms, east-west gradient added	Constant eastward gradient of 0.0005 MHz/km is assumed. Both foF2 and north-south gradient are derived from ionograms recorded on an Ottawa ISIS II pass starting 75/003/1414 UT.

3.2 Results of Computations

The models represent typical ionospheric conditions that a polar-orbiting SARSAT is likely to encounter. The cases are discussed in sequence:

3.2.1 Figure 5

The no-horizontal gradient case, corresponding to the dotted curves in Figure 5, obviously illustrates the importance of vertical gradients only, and provides a baseline for comparison with the later cases. At high latitudes where the spacecraft has a velocity component toward the receiver, the Doppler shift without an ionosphere is greater than with an ionosphere because the ionospheric refraction acts to make the wave normal less nearly parallel to the spacecraft velocity vector than in the free-space case. The difference goes positive for algebraically similar reasons on the southern half of the pass. Reversing the direction of satellite motion would result in a difference curve that is reflected about the latitude axis.

At the extremities of the curves, the difference value tends to come back to zero. For the no-horizontal gradient case the ray path can be determined from Snell's law as given by (2.2.1) where, using Figure 2, the constant is R sin Φ_1. For the problem considered here, the ionosphere has only a small effect on the ray path between station and satellite and, for given station and satellite positions, the values of Φ_1 corresponding to the no-ionosphere and ionosphere cases would be within about 1°. At the extremities of the curves in Figure 5, the corresponding values of Φ_1 for the ionosphere and no-ionosphere cases are both near 90° so that sin Φ_1 is, to a good approximation, independent of Φ_1 and the constant in (2.2.1) is simply R. Hence as the satellite approaches the horizon the value of Φ', or λ in (1.1), becomes independent of the ionosphere and the ionosphere Doppler difference approaches the no-ionosphere value.

The reflection cutoff at the southern end of the passes occurs at a lower latitude on the east pass than on the west pass because the inclination of the satellite orbital trajectory is such as to allow the satellite to move farther south on the east pass before the great-circle distance reaches the cutoff value.

To obtain an estimate of the systematic east-west gradient, Ottawa ground ionosonde values of foF2 were plotted as a function of local time using data from the first half of January 1976. The OSCAR-6 local solar time was about 09 hr for the three southbound passes studied. The ionosonde data implied that eastward plasma frequency gradients of the order of 1 kHz/km existed in the ionosphere at 09 hr. Occasionally westward gradients of the same order of magnitude occured. Accordingly, the east-west gradient was set at plus and minus 0.001 MHz/km corresponding to the solid and broken curves respectively in Figure 5. For the 'East' pass, the amplitude of the ionospheric Doppler difference curve increases as the horizontal gradient direction changes from east to west. For the 'Overhead' pass there is no important dependence on the direction of the horizontal gradient. For the 'West' pass, the amplitude of the difference curve decreases as the gradient direction changes from east to west. This can be understood by realizing that the constant gradient experienced by the ray has the effect of bending the wave-normal directions away from the direction of the horizontal gradient. Otherwise there is no dramatic change from the no-gradient case.

The maximum latitude of the OSCAR-6 satellite is about 78.5^o; after reaching this latitude the satellite moves southward again. This explains the double values at the north extremity of the west passes.

3.2.2 Figure 6

The use of unsmoothed topside sounder data to model the north-south density distribution results in a more irregular Doppler curve. At the bottom of Figure 6 is the latitudinal profile of foF2 exhibiting strong southward gradients near Ottawa but a rather flatter distribution to the north and south. The figure illustrates that a ray crosses a region of the ionosphere at a latitude intermediate between the station and the satellite. The result is that the large excursions of the Doppler difference are

displaced in latitude with respect to the fluctuations in the foF2 profile that caused them. The letters spaced along the profile and the "West" difference curve just above it indicate the relationship. For instance, the "A" ray transmitted by OSCAR-6 at 25.5° latitude crosses the 350 km height in the ionosphere at a latitude of 34° and a positive Doppler difference of 4.8 Hz is calculated. The sharp positive peaks in the Doppler curve at A,E and I are seen to be caused by large southward density gradients.

In all the sets of curves, it is seen that the variations on the overhead Doppler curve are smaller than on the other two passes. This is due to the fact that the ray has a longer ionospheric path under the influence of the gradients on the oblique paths to the east or west orbits than it does on overhead paths.

3.2.3   Figure 7

The ISIS II sounder data, shown at the bottom of Figure 7, reduce to a latitudinal profile of foF2 which has a modest southward gradient north of Ottawa and a reasonably deep depression to the south. The comparatively large negative excursion of the Doppler difference around 35° latitude arises from the refractive effects of the depression. The displacement in latitude of the Doppler excursion with respect to the depression due to the obliquity of rays is again observed.

3.2.4   Figure 8a,8b,8c

The implementation of a deep trough in the foF2 profile centred at Ottawa has a dramatic effect on the Doppler difference frequency. The overhead pass in Figure 8b is plotted over the density profile, and the pairs of letters on the two curves show again that the largest effects correspond to rays that experience the largest north-south gradients while passing through the ionospheric layer. The depth of the trough (5 MHz) is representative of some of the deeper troughs observed by Muldrew (1965), and may be regarded as a typical upper limit. The total ionospheric Doppler difference of a few tens of hertz in Figures 8a and 8c is about as large as will ever be observed since the deep depression of foF2 was positioned at the most influential latitude: that of the receiver.

3.2.5   Figure 9

In the final example, a constant eastward gradient of 0.5 kHz/km was combined with foF2 and its southward gradient derived from the ISIS data profile at the bottom of Figure 9. This leads to the solid curve at the top of Figure 9. The central portion of the foF2 profile responsible for this curve is free of long scale systematic gradients but has small variations in foF2 which cause fairly large latitudinal fluctuations in the Doppler difference when the satellite is near Ottawa latitudes. The broken line was obtained by using the foF2 profile for the plasma frequency and setting all horizontal gradients to zero. Again, the results reveal that the small-scale gradients lead to differences of the order of a few hertz.

4.   CONCLUDING REMARKS

Ionospheric refraction will typically cause systematic and random errors of a few hertz at 30 MHz if no horizontal gradients are assumed between an ELT and SARSAT and between SARSAT and Ottawa. Large density gradients, including troughs, can exist in the F region and these will be responsible for the largest errors. Magnetically disturbed conditons occur occasionally and the main trough can then be centred near Ottawa; for the OSCAR-6 case errors of a few tens of hertz could result. For normal magnetic conditions, the main trough is north of Ottawa and errors of about 10 Hz for the OSCAR-6 case occur.

The plasma-frequency profile presented in Figure 9 applies to a local time of 0830 hr. Irregularities in f_N and north-south variations in this figure are fairly typical for morning and early afternoon conditions; the magnitude of f_N, however, will vary throughout the day. The main trough (Muldrew, 1965) is a regular feature of the ionosphere. It begins to form about 1500 hr local time and becomes very pronounced from about 1700-2100 hr. Between 2100 and sunrise it is still present but is not so well defined. In the afternoon it moves southward and from about 1800 hr to sunrise during normal magnetic activity it is located near 60° geomagnetic latitude or about 49° geographic latitude at the Ottawa longitude. During the night other troughs or rapid variations in f_N with latitude can occur throughout the high latitude ionosphere.

To use the computer programs effectively for operational ionospheric correction in the SARSAT system, a model of the ionospheric parameters for North America would be required. This model would give critical F-layer frequencies and horizontal electron-density gradients, and perhaps effective F-layer thickness, as a function of longitude, latitude, local time, month, sunspot number and magnetic-activity index (Kp). It is hoped that such a model will be completed in 1978.

Doppler difference curves have been calculated at frequencies other than 30 MHz. The conditions corresponding to the solid curve in Figure 9 were applied to frequencies of 121.5, 143 and 406 MHz which are of interest in a SARSAT system. The shapes of the resulting difference curves remained unchanged but their amplitudes were lower by a factor of approximately the inverse ratio of the frequencies. For instance, the solid 30-MHz curve in Figure 9 has a peak at 47° latitude of about 6.3 Hz, whereas the calculated 121.5 MHz maximum at that latitude is 1.3 Hz. This frequency dependence is expected, since Doppler frequency varies as f, and the refractive index deviation from unity varies as f^{-2}.

In the proof-of-concept studies at 30 MHz carried out at CRC, the error in locating an ELT was about 10 or 15 km (Werstiuk and Winter, 1978). For the ionospheric conditions studied perhaps half of this error was due to the ionosphere. At certain times when large ionospheric troughs occur at the appropriate latitude, ionospheric errors might be many times this value. In an operational system the main ionospheric effects would be due to the 121-MHz ELT-Satellite link and hence the ionospheric error would be reduced by about a factor of 4. Presumably the other errors would also be reduced in an operational system so that the ionospheric error would be one of the major sources of error.

5. REFERENCES

LAMBERT, J.D., and A.E. WINTER, 1976, "A Search and Rescue Satellite System (SARSAT) Experiment", IEEE Conference Publication 139, 351-355.

MULDREW, D.B., 1965, "F-Layer Ionization Troughs Deduced from Alouette Data", J. Geophys. Res., _70_, 2635.

MULDREW, D.B. and H.G. JAMES, 1978, "Ionospheric Effects on the Doppler Frequency Shift in SARSAT Propagation", CRC Report 1313, Communications Research Centre, Ottawa, Canada.

STOREY, L.R.O., 1958, "A Method to Interpret the Dispersion Curves of Whistlers", R.P.L. Report 23-4-1, p. 33, Defence Research Telecommunications Establishment, Ottawa, Canada.

WERSTIUK, H.L., and A.E. WINTER, 1978, "The Search and Rescue Satellite (SARSAT) System Project", paper 5-2, this issue.

Figure 1   Geometry for no-ionosphere case.

Figure 2   Geometry for ionosphere case with no horizontal gradients.
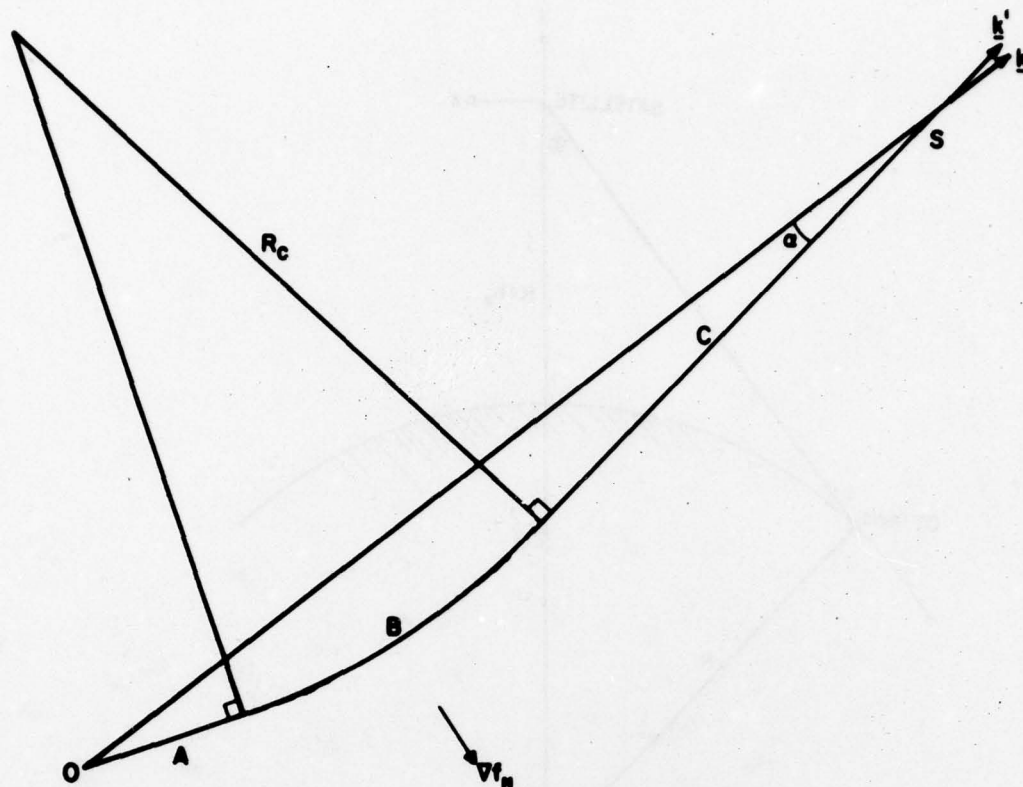
Figure 3 Plan view of ray-path deviation due to a horizontal gradient.
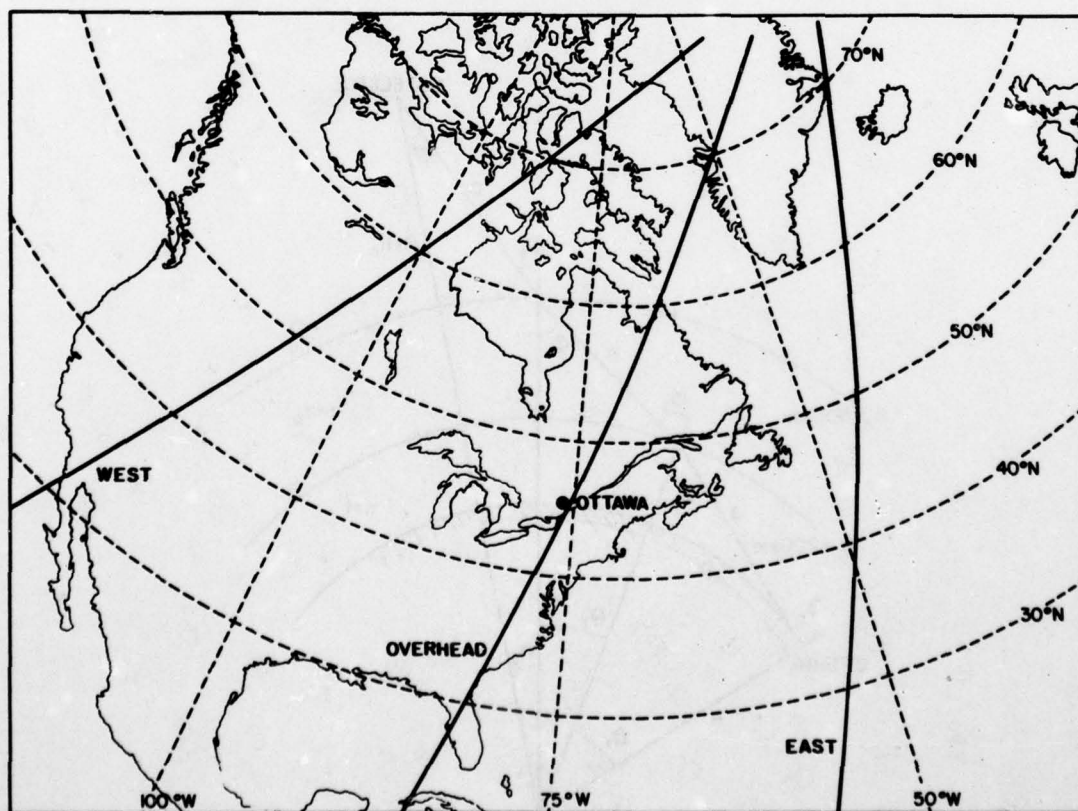
Figure 4 Subsatellite tracks of 3 OSCAR-6 passes, on a geographical coordinate frame.
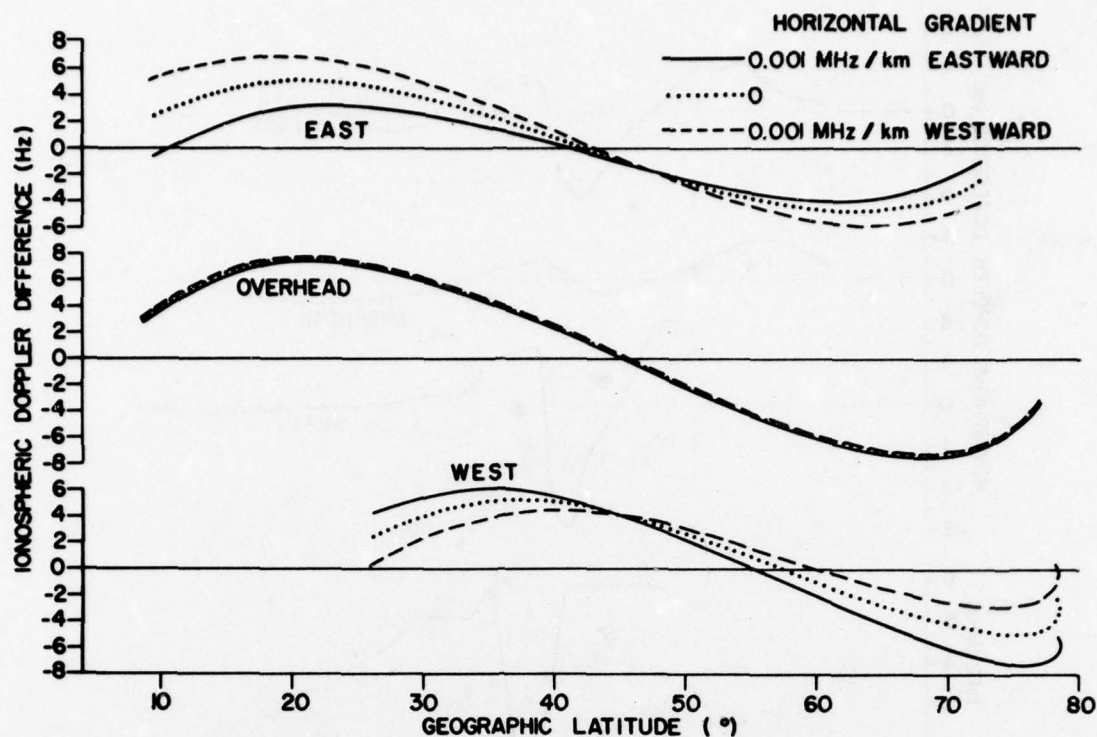
Figure 5 Calculated ionospheric Doppler difference curves as a function of geographic latitude for three OSCAR-6 passes. Cases with no horizontal gradient in foF2, with an eastward gradient in foF2, and with a westward foF2 gradient are presented.
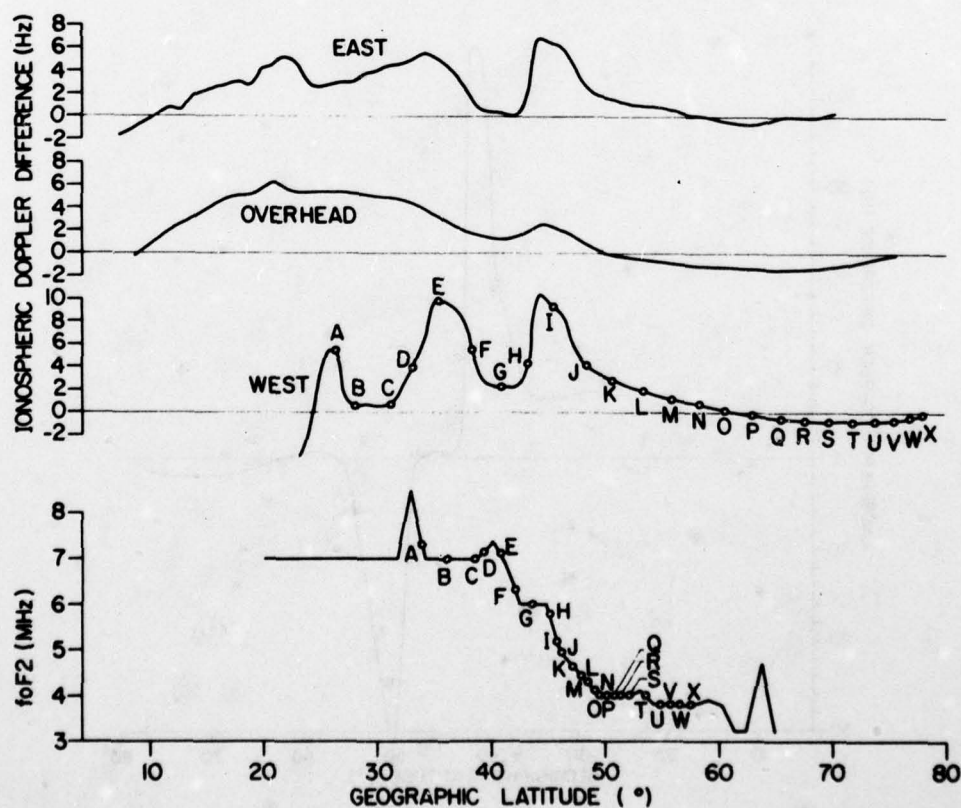
Figure 6 Calculated ionospheric Doppler difference curves for 3 OSCAR-6 passes and foF2 obtained from ISIS II data (1442 UT, Jan. 4, 1975) as a function of geographic latitude.
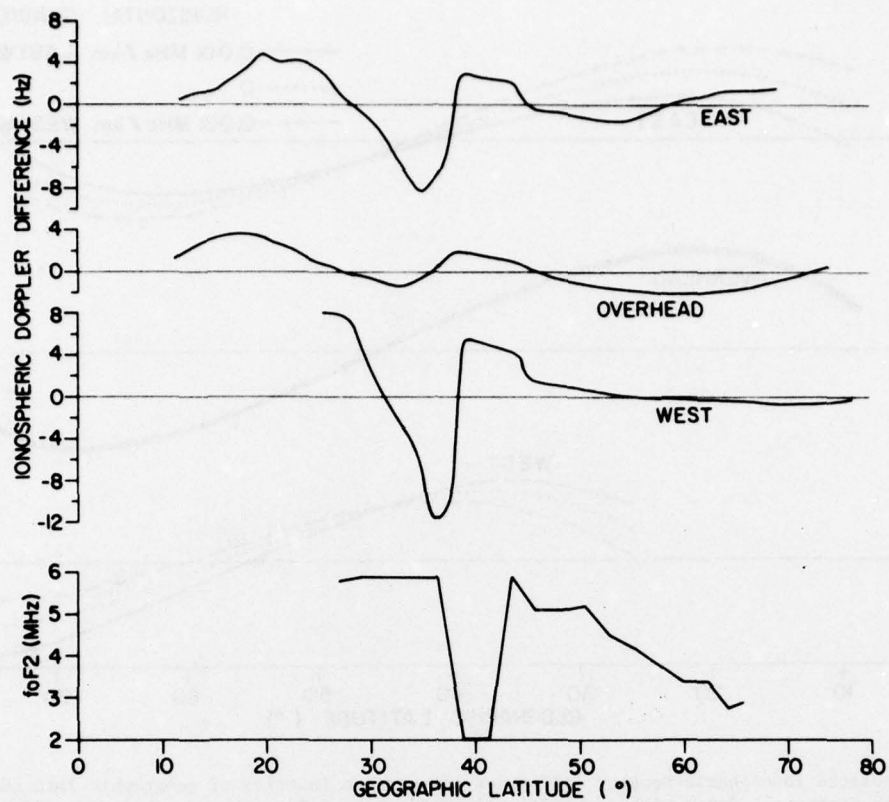
Figure 7 Same as 6 except ISIS II data recorded 1557 UT, Jan. 9, 1975.
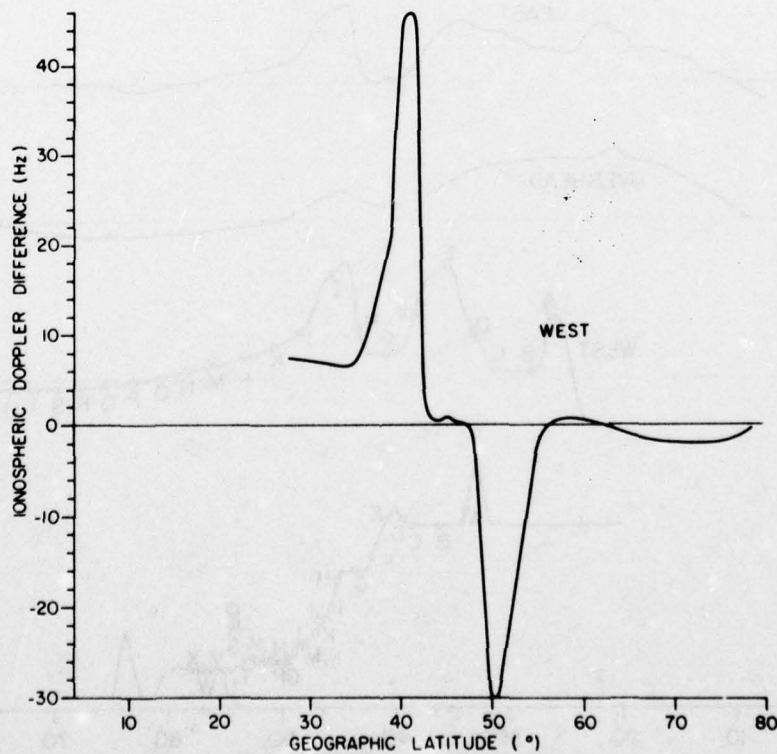
Figure 8a,8b,8c Calculated ionospheric Doppler difference curves as a function of geographic latitude for three OSCAR-6 passes and a hypothetical foF2 distribution as a function of geographic latitude.
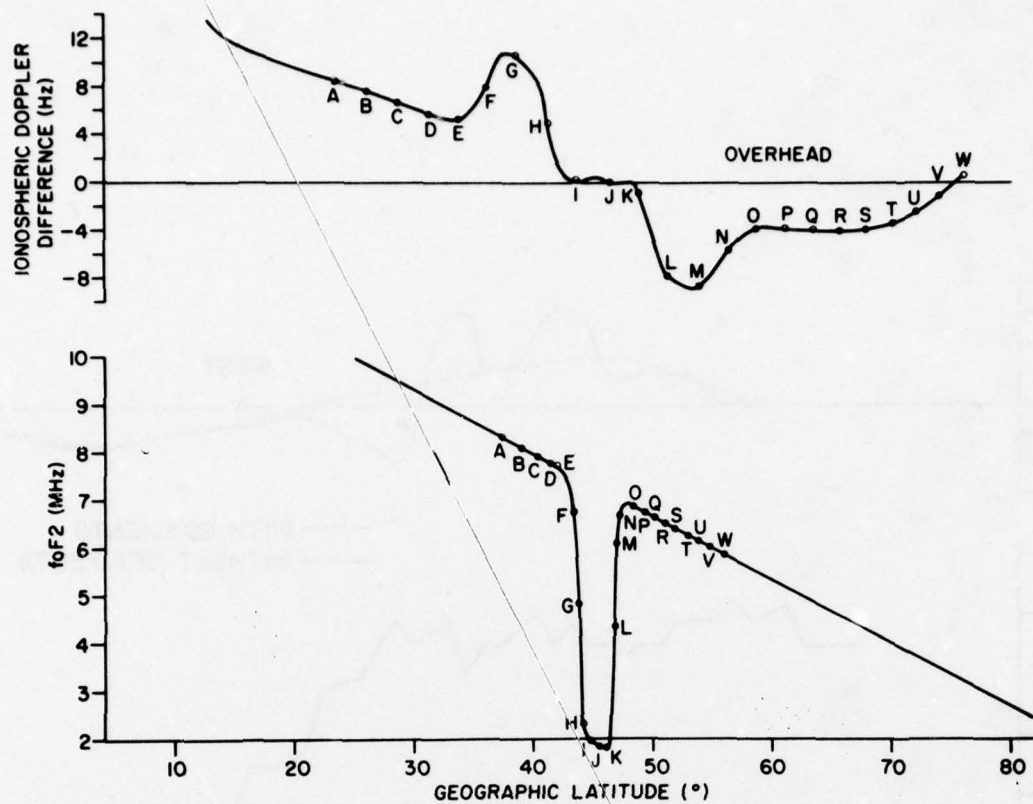
Figure 8(b)
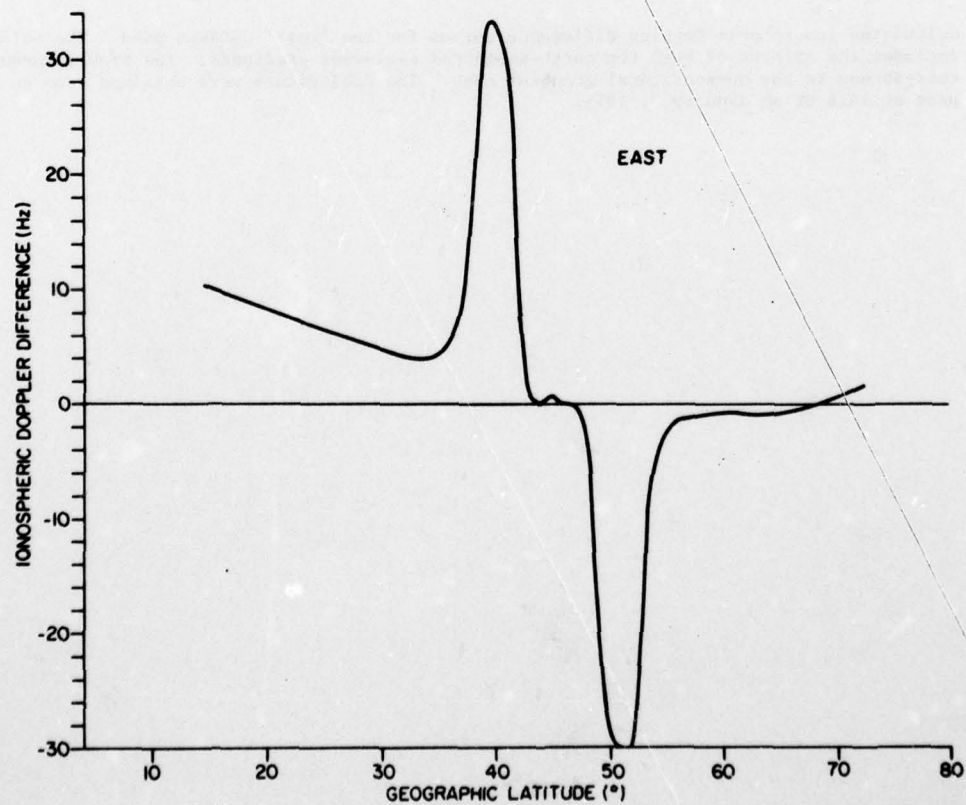
Figure 8(c)
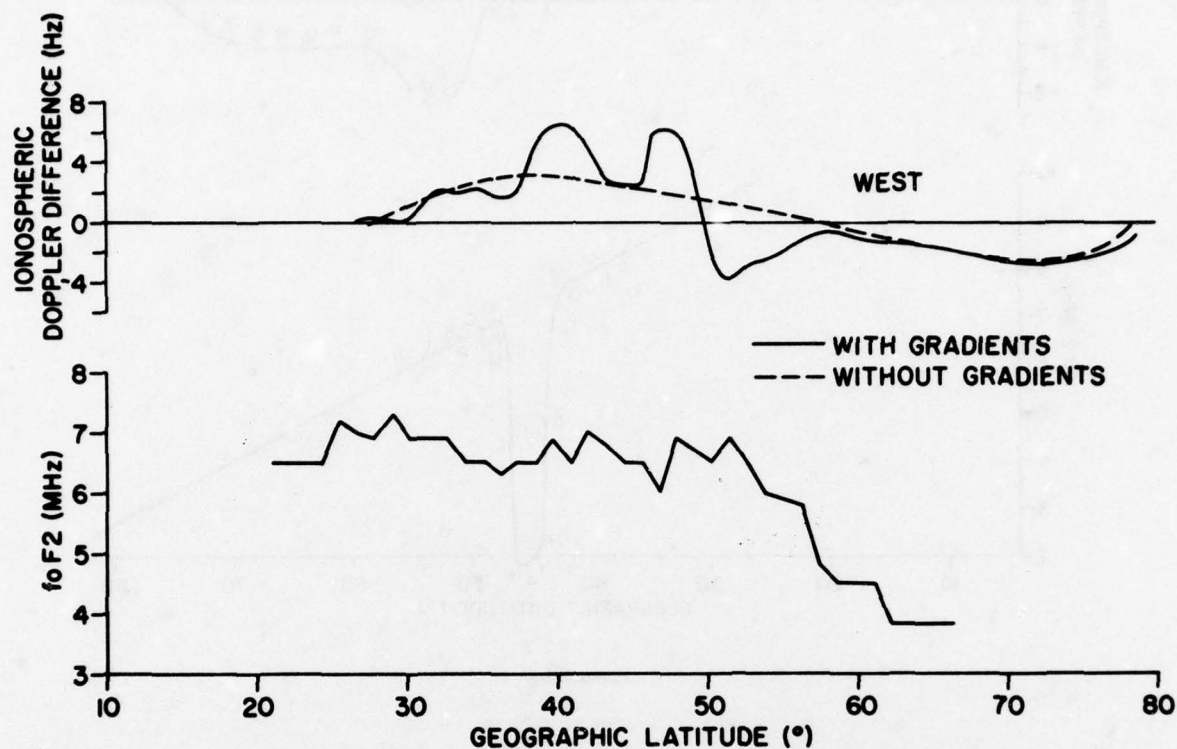
Figure 9 Calculated ionospheric Doppler difference curves for the 'west' OSCAR-6 pass. The solid curve includes the effects of both the north-south and east-west gradients. The broken curve corresponds to the no-horizontal-gradient case. The foF2 values were obtained from an ISIS II pass at 1414 UT on January 3, 1975.

DISCUSSION

R.J.Long, US

Why does the system proposed not use a dual frequency transmitter as in US Transit Navigational Satellite? Since the system proposed is only in design concept state, I believe it is necessary to look at the present status of navigational capabilities of Transit.

Author's Reply

Most light aircraft carry only a single-frequency ELT and it would be difficult and expensive to implement a two-frequency system. I agree that systems such as the Navy Navigational Satellite System using the Transit satellites should be investigated. Cost and implementation problems will have to be compared with effectiveness.

J.M.Goodman, US

Can you possibly use the processor described by Dr Tomljanovich to obtain the data you need for ionospheric correction without pursuing a modelling exercise?

Author's Reply

Other systems for producing an estimate of the ionospheric Doppler difference could, of course, be used. A study has not yet been carried out to see which system would be preferable in terms of effectiveness, cost, and convenience. The model presently being developed at CRC will have a large variety of uses, not only the one mentioned in this paper for calculating the ionospheric Doppler difference.

J.Aarons, US

I would suggest you might use 136-MHz observation of Wideband Satellite to validate your model. In addition, there are many 40-MHz doppler measurements available for this region.

Author's Reply

(No comment)

ETUDE DU CONTENU PLASMASPHERIQUE ET DES SCINTILLATIONS

A PARTIR DES SIGNAUX D'ATS-6 A LANNION

R. FLEURY ET J.P. CORNEC

CENTRE NATIONAL D'ETUDES DES TELECOMMUNICATIONS

DEPARTEMENT M.I.R. - LANNION

ABSTRACT

The amplitude and the phase of radio beacon signals received from ATS-6 have been studied at LANNION from January to August 1976.

The ionospheric content and the total electron content are deduced respectively from measurements of Faraday rotation and group delay. The plasmapheric content is given by the substraction of the former from the latter. During magnetically quiet periods, the ratio N_P/N_T shows a nocturnal maximum, about 45-55 %, and a daytime minimum at 10-15 %. The observations are fitted in an ionosphere-magnetosphere model ; that gives thus the electronic density distribution in terms of the altitude for two seasons (winter and spring).

As for the scintillations, it results from the recordings that, in summer, they are more frequent and stronger than in winter. During summer they are also more frequent in daytime, in connection with sporadic E-layers. Finally we study the dependence of the index S_4 on the frequency, the connection of scintillations with the magnetic activity and spread-F, and the recordings of isolated bubbles of irregularities.

1. INTRODUCTION

Nous présentons d'ici des résultats préliminaires concernant d'une part les contenus ionosphérique et plasmasphérique   et d'autre part les scintillations d'amplitude.

Ces résultats sont déduits des mesures faites à LANNION (48°, 75 N ; 3°, 45 W) entre Janvier et Août 1976 sur les signaux émis par un satellite géostationnaire (ATS-6), dont la longitude EST était 35°. Le satellite était vu sous une élévation de 23,1° et un azimuth à 133,4°.

Les aspects techniques de l'expérience ont été décrits par ailleurs (PAPET-LEPINE,1976).

Le rayon observateur-satellite atteignant les altitudes 150 et 300 km à la verticale des ionosondes de POITIERS et SAINT-SANTIN respectivement, nous avons utilisé les ionogrammes de la première station pour contrôler la présence de couches E sporadiques et déterminer la hauteur du maximum d'ionisation hmF2, et ceux de la deuxième station pour contrôler la présence de F diffus. La station de POITIERS a sondé quotidiennement pendant la durée des observations, tandis que celle de SAINT-SANTIN n'a fonctionné que 3 ou 4 jours par mois en simultanéité avec le sondeur à diffusion incohérente.

2. LE CONTENU PLASMASPHERIQUE

2.1. Equations

Le contenu plasmasphérique N_p est obtenu par différence entre le contenu total N_T et le contenu ionosphérique N_F. Ces deux derniers sont respectivement déduits à partir des mesures de phase et de rotation Faraday selon la méthode exposée par DAVIES et autres (1976). Nous rappelons ici brièvement les principales équations appliquées à la station de LANNION.

Le temps nécessaire à un signal émis d'un satellite S pour atteindre un récepteur R situé au sol est donné par la relation

$$ t = \int_0^S \frac{ds}{vg} = \frac{1}{C} \int_0^S n \, ds $$

où vg représente la vitesse de groupe du signal et n l'indice de réfraction du milieu. Cette relation permet de déduire la variation de phase. Le contenu total N_T est déterminé à partir des différences de phase des deux modulations 1 MHz sur les signaux 40 et 360 MHz, ce dernier étant pris comme signal de référence. Nous faisons également l'hypothèse que l'on peut remplacer la variation en altitude de la gyrofréquence électronique par sa valeur moyenne prise à 1 100 km (f_L = 0,60 MHz). Nous avons

$$ N_T = 3,536 \ 10^{13} \ \emptyset \ 41 $$

où $\emptyset\,41$ est exprimé en degrés et N_T en el/m^2

La rotation Faraday, exprimée en degrés d'un signal le long d'un trajet S est obtenue par la relation

$$\Omega f = 2{,}36 \; 10^4 \; x \; \frac{1}{f^2 - f_L^2} \; \int_0^S \; f_L \; N \; ds$$

Prenant f_L constante, égale à sa valeur à 380 km (f_L = 0,753 MHz) on obtient approximativement pour le contenu ionosphérique N_F jusqu'à une altitude de 2500 km

$$N_F = 5{,}378 \; 10^{14} \; \Omega \; 140$$

La différence entre les deux contenus précédents donne celui de la région comprise entre la haute ionosphère et le satellite. Cette région est constituée par la plasmasphère jusqu'à 5 rayons terrestres (selon les conditions magnétiques), par la plasmapause sa limite supérieure et par une partie de la magnétosphère, région où la densité électronique est très faible.

Pour calculer N_p nous introduisons le facteur de forme F qui correspond à une moyenne pondérée sur toute la trajectoire oblique de la gyrofréquence électronique.

$$F = \frac{\int_0^S \; Nf_L \; ds}{\int_0^S \; Nds} = -11{,}4557 \; \frac{\Omega \; 140}{\emptyset \; 41}$$

En supposant que F est indépendant de l'heure locale la relation suivante permet de calculer N_p.

$$N_p = N_T \; \left(1 - \frac{F}{0.753}\right)$$

Les premiers résultats ont montré que le contenu plasmasphérique était très faible par rapport au contenu total. Cela nécessite donc une très calibration des mesures effectuées pour accéder aux valeurs absolues. Pour ces raisons nous avons retenu dans notre étude des périodes de quelques jours au lieu de médianes mensuelles nécessitant une observation quasi continue dans le temps.

2.2. Résultats expérimentaux

Pour des conditions magnétiquement calmes nous avons retenu deux périodes, l'une en hiver l'autre au printemps : la période du 26 au 30 Janvier, située quelques jours après une légère agitation précède un orage graduel débutant le 30 vers 21 h TU ; la période du 18 au 21 Avril caractérisée par un indice planétaire K_p inférieur à 2 + est située 9 jours après la précédente perturbation.

Les variations diurnes de N_p sont semblables pour ces deux périodes et sont représentées par la figure 1 pour l'intervalle 26-30 Janvier. Elles présentent les caractéristiques suivantes :

- un maximum de nuit vers 04-06 heures locales. Le maximum d'hiver est supérieur de 2.5 unités de contenu (1 unité $\simeq 10^{16}$ el.m^{-2}) à celui du printemps,

- une décroissance rapide le matin, après le lever du soleil alors que N_F augmente,

- un minimum de jour vers 12-14 heures, d'amplitudes sensiblement égales pour les deux saisons (4.5 unités),

- une croissance plus lente avant le coucher du soleil pour atteindre le maximum le lendemain matin.

Les perturbations autour des moyennes respectives sont plus fortes le jour (20 %) que la nuit (10 %).

La variation diurne du rapport N_p / N_T est identique à celle de N_p (figure 2 pour la 2ème période). On observe un minimum de 12 % en hiver, 17 % au printemps entre 08 et 18 heures, un maximum de 50 % en hiver et 67 % au printemps vers 03 Heures. Cela reflète bien la plus grande importance du contenu plasmasphérique la nuit par rapport au jour dans le contenu total N_T.

En période magnétiquement perturbée, les premiers résultats observés lors de la phase I ont montré une augmentation de N_p avec N_F et un vidage de la plasmasphère lors de la phase négative de l'orage ionosphérique (SOICHER, 1975 ; POLETTI - LUIZZI et autres, 1977). Cette dernière conclusion apparaît sur la figure 1 représentant les variations de N_p en fonction de l'heure locale. Le contenu N_p présente un maximum d'ionisation en fin de période (nuit du 29 au 30). A partir de 15 TU le 30 nous observons sur l'indice électrojet AE une succession de sous-orages dans la zone aurorale qui vont donner naissance à un orage graduel le 31 (ALLEN et autres, 1977). Quelques heures après le déclenchement de la perturbation N_p décroît brutalement à une valeur moitié moindre de celle de la nuit précédente alors que le contenu ionosphérique ne subit pas de variations. Malheureusement une coupure à l'émission ne nous a pas permis de suivre l'évolution future de N_p. L'orage magnétique a début brusque du 7 février, débutant le matin 0928 TU permet de mettre en évidence une importante phase positive sur le contenu ionosphérique. En effet, de 10 h à 14 h N_F passe de 26.3

à 41.4 unités soit une diminution semblable à la variation diurne observée entre le 26 et le 29
janvier. Cela veut dire que la phase positive se produit principalement au dessous de 2 500 km
c'est-à-dire dans la haute ionosphère. L'examen de l'altitude du maximum d'ionisation à la station
de POITIERS ne montre aucune élévation de la couche F2 dans cet intervalle de temps. L'excès
d'ionisation peut donc être la conséquence d'un champ électrique magnétosphérique aube-crépuscule
(MENDILLO, 1973).

2.3. Discussion des résultats

La variation diurne décrite dans le paragraphe précédent est identique à celle observée
par d'autres auteurs, lors de la phase I en particulier (SOICHER, 1975 ; POLETTI - LUIZZI et
autres, 1977). Cependant KERSLEY et autres (1977) observent à ABERYSTWYTH, lors de la phase II
un minimum, la nuit et un maximum en fin d'après-midi, plus fort l'été que l'hiver. Il reste que
la variation diurne est peu importante et que les écarts mensuels observés peuvent provenir de
différentes conditions magnétiques et surtout de différents trajets dans la plasmasphère. La
faible amplitude de la variation diurne s'explique par le fait qu'elle n'est due qu'aux seuls
modes de diffusion étant donné l'absence de mécanismes de production et de pertes électroniques
à ces altitudes.

Les mesures expérimentales obtenues et certaines données supplémentaires décrites ci-
dessous sont utilisées pour évaluer les paramètres du modèle de KIMURA (1966) et ainsi déterminer
la distribution de la densité électronique en fonction de l'altitude.

La densité Ne est déterminée par le produit $Nr \times N\sigma$ où Nr et $N\sigma$ sont des fonctions respec-
tives de la distance radiale et de la colatitude. Nr est déduit du modèle à équilibre diffusif
D (III) de KIMURA (1966) dans lequel on tient compte de l'accélération centrifuge due à la rota-
tion de la terre. Ce modèle suppose que le plasma est en équilibre diffusif vertical au dessus
d'un niveau de référence pris à 1 000 km. ANGERAMI et THOMAS (1964) ont montré qu'en réalité
l'équilibre se fait le long des lignes de force du champ géomagnétique. En supposant une ionos-
phère stratifiée sphériquement (absence de gradients horizontaux) l'erreur introduite est peu
importante. $N\sigma$ représente la densité au niveau de référence. Au dessus de la plasmapause (prise
à L = 4.5) on adopte un modèle en R^{-4}. Nous supposons qu'à 1 000 km les ions dominants sont H^+,
He^+, O^+. Le fait de négliger les ions moléculaires NO^+ et O_2^+ entraîne une erreur sur la densité
de la couche F2 lorsque la hauteur de celle-ci est inférieure à 300 km (situation de jour).

Le fait de négliger la couche E sous-estime le contenu Faraday de jour et principalement
en été (DAVIES et autres, 1976).

La température moyenne du plasma à 1 000 km est déduite des figures 1 et 2 publiées par
TITHERIDGE (1976) et obtenues à partir de la sonde Alouette 1.

La hauteur du maximum de la couche F2 est déterminée à partir de la formule de BRADLEY
et DUDENEY (1973) donnant hm F2 à partir des données foF2, foE et M(3 000) F2 fournit par l'iono-
sonde de Poitiers. Le tableau N°1 résume les paramètres décrivant le profil.

SAISON PERIODE	$N\sigma$ el m^{-3}	N_p/N_T	hmF2 km	Composition ionique à 1000 km H^+	He^+	O^+	h_T km	N_{1000}/N_{400}	T Degrés	$\frac{N_p(1000)}{N_T}$	$\frac{N_p(3000)}{N_T}$
EQUINOXE JOUR	0.2028E11	18 %	250	0.008	0.001	0.991	2300	0.216	3000°	28.1 %	17.0 %
EQUINOXE NUIT	0.7185E10	65%	330	0.800	0.170	0.030	600	0.366	1700°	89.6 %	61.6 %
HIVER JOUR	0.11E11	19 %	256	0.005	0.000	0.995	2890	0.293	3700°	33.7 %	19.4 %
HIVER NUIT	0.48E10	47 %	316	0.730	0.120	0.150	825	0.120	1500°	58.1 %	46.6 %

Tableau N°1 - Paramètres du modèle de densité

Sur les figures 3 et 4 nous avons représenté les profils obtenus respectivement de jour et
de nuit pour le printemps.

Les ions O^+ prédominants au-dessous de 300 km sont maintenus la nuit par la diffusion des
ions H^+ de la plasmapause suivant la réaction

$$H^+ + O \rightarrow O^+ + H$$
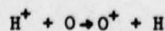
La hauteur de transition des ions $O^+ - H^+$ (altitude où les densités de O^+ et de H^+ sont égales) se situe vers 600 km. De jour, le phénomène s'inverse. Le mouvement des ions H^+ se fait vers le haut et on observe une altitude de transition à 2300 km. Le rapport N_p (h) / N_T pour les deux altitudes h = 1 000 et h = 3 000 km permet de constater que, dans cette tranche d'altitude le contenu est plus fort le jour que la nuit. C'est donc principalement cette région que joue le rôle de réservoir d'ions H^+.

2.4. Interprétation des résultats

Le temps de groupe et la rotation Faraday des signaux émis sur le satellite ATS 6 ont été enregistrés à LANNION lors de la phase II de l'expérience. Ces mesures permettent d'accéder respectivement au contenu total N_T jusqu'au satellite, au contenu ionosphérique N_F jusqu'à 2 500 km environ et par différence au contenu plasmasphérique. Cette technique permet de fournir des informations continues sur les variations de Np et peut être complémentaire des observations déduites des siffleurs. Elle nécessite une bonne calibration des mesures ce qui a limité notre étude à des périodes de quelques jours. En période magnétiquement calme, Np présente un minimum de jour et un maximum de nuit avant le lever du soleil. La variation diurne du rapport Np / N_T se situe entre 10 et 20 % le jour, supérieure à 50 % la nuit. Ce comportement permet de définir la règle qui régit les échanges ionosphère-protonosphère. De nuit, la plasmasphère est fortement ionisée et joue le rôle de réservoir : un mouvement vers le bas des ions H^+ principalement permet de maintenir une ionosphère de nuit. De jour, le mécanisme s'inverse et l'altitude de transition des ions $O^+ - H^+$ remonte. Durant les perturbations magnétiques, les processus d'interaction sont accrus. Lors de la phase initiale de l'orage le comportement de Np est encore mal défini ; lors de la phase principale la plasmasphère se vide soit dans le milieu magnétosphérique par convection soit dans l'ionosphère par un mouvement de diffusion vers le bas. Nous n'avons pas observé de processus de remplissage de la plasmasphère qui demande cinq à huit jours d'observations continues.

3. LES SCINTILLATIONS

3.1. Introduction

Les scintillations ont été étudiées sur les trois fréquences 40, 140 et 360 MHz pour lesquelles la disponibilité limitée du satellite et des difficultés techniques locales n'ont permis de recueillir des données que pendant respectivement environ 42 %, 22 %, et 32 % du temps. D'autre part, la période d'échantillonnage, 10 s, n'est adaptée à l'étude quantitative que d'un nombre restreint d'enregistrements. C'est pourquoi la majeure partie des résultats présentés ici proviennent d'une étude qualitative d'enregistrements graphiques.

3.2. Traitement des données

On constate sur les enregistrements de l'amplitude à 40 MHz la superposition de variations lentes de l'amplitude et des scintillations elles-mêmes (figure 5). Cette fluctuation lente, quoique non exactement reproduite dans sa forme, débute et s'arrête à des heures quasiment identiques d'un jour à l'autre. Elle est sans doute due à l'interférence du rayon direct issu du satellite avec un rayon réfléchi sur le sol, combinée au léger écart à la géostationnarité du satellite. Ce phénomène rend difficile le calcul d'un indice de scintillations à partir des graphiques sur une période supérieure à 10 mn. Le signal reçu sur 360 MHz a généralement un rapport signal sur bruit assez faible et seules les fortes scintillations ressortent sur les enregistrements. Le signal sur 140 MHz est exempt des défauts des deux autres fréquences.

Pour les études quantitatives les scintillations sur 40 et 360 MHz ont été extraites en filtrant les données sur 7 points (JENKINS et col., 1968), l'intervalle traité étant supérieur ou égal à une heure.

3.3. Caractères généraux des scintillations observées

Dans ce qui suit nous avons retenu comme cas de scintillations la totalité des observations sur 140 et 360 MHz tandis que sur 40 MHz seul ont été retenus les évènements tels que l'indice mesuré sur les enregistrements graphiques soit supérieur à 0,1. La principale caractéristique qui ressort de cette étude préliminaire est le niveau très différent de l'activité des scintillations sur les trois fréquences suivant la saison. Une autre conclusion particulière au signal sur 40 MHz, est la quasi permanence des scintillations. Elles ne furent totalement absentes que pendant environ 40 heures sur toute la période étudiée.

Pendant la période hiver - équinoxe (Janvier - Avril) elles ont été peu fréquentes, principalement nocturnes et assez faibles ; à 40 MHz elles ont été saturées ($S_4 = 1$) que pendant onze heures réparties en périodes longues d'une heure environ, en association avec du F-diffus. Sur cette même fréquence, les scintillations ont été absentes ou peu importantes ($S_4 < 0,1$) pendant une dizaine de jours, uniformément répartis sur toute la période. Par ailleurs, l'indice S_4 maximal observé sur 140 MHz n'a pas dépassé 0,14.
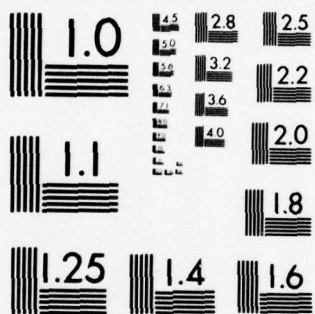
MICROCOPY RESOLUTION TEST CHART
NATIONAL BUREAU OF STANDARDS-1963-A

A onze occasions, sur 40 MHz, des scintillations d'indice supérieur à 0,2 ont été présentes de jour (0600 - 1800) pendant un temps allant de 1 heure à 6 heures. Au moment de ces scintillations les couches E sporadiques à POITIERS avaient une f_oE_S < 3MHz et le F-diffus était évidemment absent ; les irrégularités responsables de ces scintillations ne peuvent alors être situées qu'aux altitudes supérieures à celle du maximum de la région F.

Les scintillations d'été (Mai - Août) se caractérisent par leur permanence et par une fréquence d'apparition plus grande des scintillations fortes réparties également entre le jour et la nuit. La figure 6 montre un exemple de ces scintillations fortes sur 140 et 360 MHz. Les scintillations fortes se distinguent elles-mêmes par la relative soudaineté de leur apparition ; leur disparition peut être aussi soudaine mais se fait généralement plus graduellement. Leur durée est très variable. L'apparition est souvent accompagnée d'un évanouissement du signal encadré d'une (ou plusieurs) figure(s) de diffraction de Fresnel caractéristiques des "bulles" d'irrégularités que nous verrons plus loin (§ 6).

Par ailleurs, une période de scintillations fortes, et donc la zone d'irrégularités correspondante, est souvent très morcellée et discontinue, et parsemés de "bulles". (Figure 7). Tout se passe comme si des nuages comportant des irrégularités importantes, isolés et ayant un fort gradient sur leurs bords, traversaient la rayon satellite-observateur.

Pendant les mois d'été un maximum dans l'activité des scintillations apparaît entre 0900 h et 1300 h. Respectivement 50 et 54 % des cas de scintillations observées dans cet intervalle coïncidaient avec la présence sur les ionogrammes de POITIERS de couches E_S avec une f_oE_S supérieure à 4 et 5 MHz.

Cette association des scintillations diurnes avec les couches E_S pendant l'été a déjà été constatée et étudiée en moyennes latitudes (ANASTASSIADIS et col, 1970 ; DAS GUPTA et col, 1976).

Les études ont montré que dans la très grande majorité des cas analysés, f_oE_S est supérieure à un certain seuil, de l'ordre de 4 à 5 MHz et que les traces sur les ionogrammes sont du type "diffuses en altitude".

Notre étude n'a pas porté sur les caractéristiques des traces mais, comme nous l'avons vu plus haut ses conclusions confirment l'existence d'une fréquence seuil. On notera aussi que, comme en hiver, une grande partie de ces scintillations de jour doivent être provoquées par des irrégularités situées au-dessus du maximum de la région F2.

3.4. Dépendance en fréquence

L'étude quantitative a permis d'obtenir quelques valeurs de l'exposant n, tel que $S_4 \propto f^{-n}$. Ces valeurs sont réunies dans le tableau suivant.

Tableau N°2

Dépendance de l'indice de scintillations avec la fréquence

	Jour	Heure		f_1	f_2	S_{41}	S_{42}	n
1	21 Janv.	0450	0530	140	360	0,48	0,10	1,60
2	4 Fév.	1400	1430	40	140	0,4	0,06	1,48
3	5 Fév.	2030	2120	140	360	0,145	0,086	0,56
4	5 Fév.	2210	2300	140	360	0,136	0,053	1,01
5	5/6 Fév.	2300	0010	140	360	0,140	0,081	0,58
6	6 Fév.	0010	0130	140	360	0,089	0,055	0,51
7	7 Fév.	0130	0300	140	360	0,105	0,050	0,80

Les deux premières valeurs sont en accord avec les résultats de la théorie de la diffusion faible, qui attribue à n la valeur 1,5, quand on utilise une loi de puissance décroissante avec un indice spectral de 4 pour le spectre de puissance des irrégularités (RUFENACH, 1975 ; TAUR, 1974). On constate aussi que, bien que l'indice S_4 à 40 ou 140 MHz reste peu élevé, c'est-à-dire inférieur à la limite traditionnelle de la diffusion forte (S_4 = 0,5), l'exposant n décroît quand S_4 augmente. Cela peut alors indiquer que les signaux sont soumis à une diffusion multiple, en accord avec des résultats antérieurs théoriques ou expérimentaux (YEH et col.,1977 ; WHITNEY et col., 1977). Mais cela peut aussi signifier (exemples 3, 5 et 6) que l'origine des scintillations en 360 MHz n'était pas ionosphérique, mais peut-être troposphérique.

3.5. Liaison avec le F-diffus et l'activité magnétique

De Janvier à Août, la présence de F diffus fut constatée neuf fois sur les ionogrammes de nuit de SAINT-SANTIN, avec une durée allant de 1 heure à 6 heures. Dans 8 cas, cette présence fut accompagnée de scintillations sur les trois fréquences, très fortes sur 40 MHz ($S_4 = 1$). Dans 7 cas le F-diffus était également présent à POITIERS. Mais la corrélation scintillations-F-diffus a été plus faible pour cette station (33 % des cas).

En ce qui concerne la liaison scintillations-activité magnétique aucune tendance nette ne se dégage, si ce n'est pendant l'été, où les plus fortes scintillations furent enregistrées pendant les jours calmes ou très calmes.

3.6. Irrégularités isolées

La figure 8 a montre un exemple de figures de diffraction produite par des bulles d'irrégularités, isolées et périodiques, enregistrées sur 140 et 360 MHz le 22 Juillet. Il semble qu'il y ait un groupe de cinq figures de 17,3 mm de période et deux figures séparées par 15,3 mm.

De telles figures de diffraction ont été observées fréquemment et depuis longtemps sur l'amplitude des signaux en moyennes et basses latitudes (IRELAND et col., 1977 ; KELLEHER et col., 1975). Parmi d'autres caractéristiques, différentes méthodes d'analyse attribuent aux nuages d'irrégularités, responsables de ces figures, une altitude le plus souvent voisine de 100 km (c'est-à-dire dans la région E) (CLARK et col., 1975 ; KELLEHER et col., 1975) ou parfois une altitude située dans la région F (KELLEHER et col., 1975 ; HERON, 1976). D'autre part une étude menée par ELKINS et col. (1969) en zone sub-aurorale sur de tels groupes de bulles, leur attribue une vitesse horizontale d'environ 100 m/s et une direction préférentielle de déplacement proche de l'azimuth 170°.

Par ailleurs on peut raisonnablement déduire de la périodicité du groupe de la figure 8a, que les bulles d'irrégularités responsables de ce groupe ne sont pas indépendantes et qu'elles ont été produites par le même phénomène. En attribuant à ces bulles une vitesse de 100 m/s, on obtient pour le groupe de cinq bulles une longueur d'onde d'environ 100 km. L'origine d'un tel groupe reste à déterminer. D'autres exemples de figures de diffraction de Fresnel provoquées par des bulles d'irrégularités ont été réunis sur la figure 8b.

Nous avons enregistré 108 fois sur 40 MHz de telles bulles d'irrégularités pendant la période d'observation. Dans 76 % des cas, ces figures étaient isolées comme ci-dessus, c'est-à-dire qu'elles sont apparues indépendamment de scintillations. Dans tous les autres cas, elles ont été enregistrées à l'intérieur d'une période de scintillations, c'est-à-dire que la figure de diffraction de Fresnel a supplanté les scintillations pendant quelques minutes.

Les résultats de l'étude de la fréquence d'apparition de ces bulles d'irrégularités sont rassemblés dans le tableau ci-dessous. Les nombres qui y figurent sont des pourcentages ; chaque nombre de la ligne supérieure sert de référence aux pourcentages de la colonne correspondante.

Tableau N° 3

Observations de bulles d'irrégularités

	Totalité des observations				Bulles isolées		
	Janvier Août	Hiver Equinoxe	Eté		Janvier Août	Hiver Equinoxe	Eté
	100	22	78		100	27	73
0600-1200	41	17	48		37	9	47
1700-2400	47	58	44		50	64	45
1800-2100	36	50	32		37	55	30
f_oE_s 5 MHz	-	-	45		-	-	28
f_oE_s 6 MHz	-	-	30		-	-	25

On a défini dans ce tableau trois tranches horaires qui sont apparues typiques à l'examen des résultats ; la troisième tranche concerne plus particulièrement la période hiver-équinoxe.

On constate d'abord que la très grande majorité des observations a eu lieu l'été et que, quelle que soit l'époque de l'année, la moitié environ des bulles rencontrées apparaissent en début de nuit. On remarque ensuite l'augmentation de l'hiver à l'été, du nombre de cas enregistrés le matin. Enfin les deux dernières lignes indiquent, pour la saison d'été, le pourcentage d'observations, associées à des couches E sporadiques ayant une f_oE_s supérieure ou égale à 5 ou 6 MHz.

On note que ce sont surtout des bulles non isolées, c'est-à-dire incluses dans une zone d'irrégularités, qui sont associées à ces couches ; cela est normal car une E$_S$ productrice de scintillations a une étendue spatiale plus importante qu'une bulle isolée et a donc plus de chances de laisser une trace sur un ionogramme.

D'autre part aucune liaison n'a été constatée entre ces bulles et le F-diffus sur les ionogrammes des deux stations.

4. CONCLUSION

Nous avons représenté quelques résultats obtenus lors de la phase II de l'expérience ATS-6 lorsque ce dernier était positionné par 35° Est. Compte tenu des différentes fréquences et du fait qu'il était possible de faire des enregistrements continus dans le temps deux directions principales ont été élaborées :

- une étude du contenu ionosphérique et du contenu total à partir de la rotation Faraday et de la mesure du temps de groupe. Par différence il est possible d'obtenir le contenu plasmasphérique et d'étudier les échanges entre l'innosphère et la magnétosphère. De plus, un système de trois stations au sol couplé avec le sondeur à diffusion incohérente de SAINT-SANTIN a permis d'accéder aux principales caractéristiques des perturbations ionosphériques itinérantes qui se traduisent sur le contenu total par des fluctuations quasi sinusoïdale de l'ordre de 1 à 2 % (SIZUN et col., 1978).

- une étude des scintillations ionosphériques. On a établi la variation de leurs caractéristiques en fonction de la saison, leur dépendance avec la fréquence et leur liaison avec les différents paramètres géophysiques.

Ces résultats présentés concernent la partie décroissante et le minimum du 20ème cycle de l'activité solaire.

Malheureusement, de nombreuses difficultés inhérentes au satellite (questions d'énergie avec priorité accordée à d'autres expériences) et à la station de réception (difficultés liées à l'enregistrement et à la calibration des mesures) ont limité notre étude et nos résultats à quelques périodes favorables.

Il reste que le satellite géostationnaire reste un outil important dans l'étude scientifique de l'ionosphère du fait de ses possibilités d'enregistrements continus en différentes positions sur la Terre. Une connaissance du comportement statistique des irrégularités est nécessaire pour les prévisions à très court terme de la propagation des ondes radio. Les mesures continues obtenues en différentes stations permettent d'établir des cartes mondiales de contenu total complémentaires des cartes d'ionisation déduites des mesures d'ionosondes et utiles pour déterminer la réfraction des signaux radio émis par les satellites défilants. Cela nous incite à émettre le souhait qu'un futur satellite géostationnaire puisse être positionné dans une zone intéressant l'Europe, l'Asie et l'Afrique.

5. REFERENCES

ALLEN, J.H., ABSTON, C.A., MORRIS, L.R., 1977, Geomagnetic data for January 1976, world Data center A for Solar-Terrestrical Physics, Report UAG-60.

ANASTASSIADIS, M., MATSOUKAS, D., MORAITIS, G., 1970 "40 MHz ionospheric scintillation and the sporadic E layer", Radio sci., Vol. 5, pp. 953-957.

ANGERAMI,J.J. et THOMAS, J.O., 1964, The distribution of ions and electrons in the Earth's exosphere, J. geophys. Res., 69, 4537-4560.

CLARK, D.H., W., 1975, "Quasi periodic scintillation of radio-satellite signal", J. Atmos. Terrest. Phys., Vol. 37, PP 1277-1279.

DAS GUPTA, A., KERSLEY, L., 1976, "Summer day time scintillation and sporadic E, J. Atmos. Terrest. Phys. Vol. 38, pp 615-618.

DAVIES, K, FRITZ, R.B et GRAY, T.B, 1976, Measurements of the columnar electron content of the ionosphere and plasmasphere, J. Geophys. Res, 81, 2825 - 2834.

ELKINS, T.J., SLACK, F.F., 1969, "Observations of travelling ionospheric disturbances using stationnary satellites", J. Atmos. Terrest. Phys., Vol. 31, pp. 241-439.

HERON , M.L., 1976, "On the modelling of ionospheric irregulatities from Fresnel diffraction patterns", J. Atmos. Terrest. Phys., Vol. 38, pp. 1027-1032.

IRELAND, W., PREDDEY, G.F., 1967, "Regular fading of satellite transmissions",J. Atmos. Terrest. Phys., Vol 29, pp. 137-149.

JENKINS, G.M., WATTS, D.G., 1968, "Spectral Analysis and Its Applications", Holden-day, San Francisco, p. 300.

KELLEHER, R.F., MARTIN, P., 1975, "Fresnel-type fading on satellite records at low latitudes", J. Atmos. Terrest. Phys. Vol. 37, pp. 1109-1116.

KIMURA,I., 1966, Effects of ions on whistler-mode ray tracing, Radio Science, Vol 1 (new series.),3, 269-283.

MENDILLO, M., 1973, Magnetosphere convection at ionosphere heights, report AFCRL-TR-73-0358, 15 p.

PAPET-LEPINE, J., 1976, Utilisation des émissions ATS-6 dans différentes recherches géophysiques, Minutes of the thirteenth working group meeting of the Joint Satellite Studies Group, 71 - 81.

POLETTI-LUIZZI, D.A., YEH, K.C. et LIU, C.H., 1977, Radio beacon studies of the plasmasphere, J. Geophys. Res., 82, 1106-1114.

RUFENACH, C.L., 1975, "Ionospheric scintillation by a random phase screen : Spectral Approach", Radio Sci., vol. 10, pp. 155-165.

SIZUN, H. et WARET, M., La cassure de la tropopause : zone de génération des perturbations ionosphériques itinérantes de moyenne échelle. Annales de géophysiques (1978) à paraître.

SIZUN, H. et BERTEL, L., Observations des ondes atmosphériques de moyenne échelle à partir de mesures diversifiées. Note technique n° 4 ETN/MIR, CNET 1978.

SOICHER, H., 1977, Plasmasphère contribution to group path delay of transionospheric satellite navigation signals, AGAR Dograph CP 173.

SOICHER, H., 1976, Response of electrons in ionosphere and plasmasphere to magnetic storms, Nature, 259, 33-34.

TAUR, R.R., 1974, "Ionospheric scintillation at frequencies above 1 GHz", Comsat Tech. Rev., Vol. 4, pp. 461-476.

TITHERIDGE, J.E., 1976, Ion transition heights from topside electron density profiles, Planet. Space Sci. 24, 229-245.

UMEKI, R., LIU, C.H., YEH, K.C., 1977, "Multifrequency studies of ionospheric scintillations", Radio sci. Vol. 12, pp. 311-317.

YEH, KC., LIU, C.H, YOUAKIM, M.Y., 1975, "A theoretical study of the ionospheric scintillation behavior caused by multiple scattering", Radio Sci., Vol. 10, PP 97 - 105.
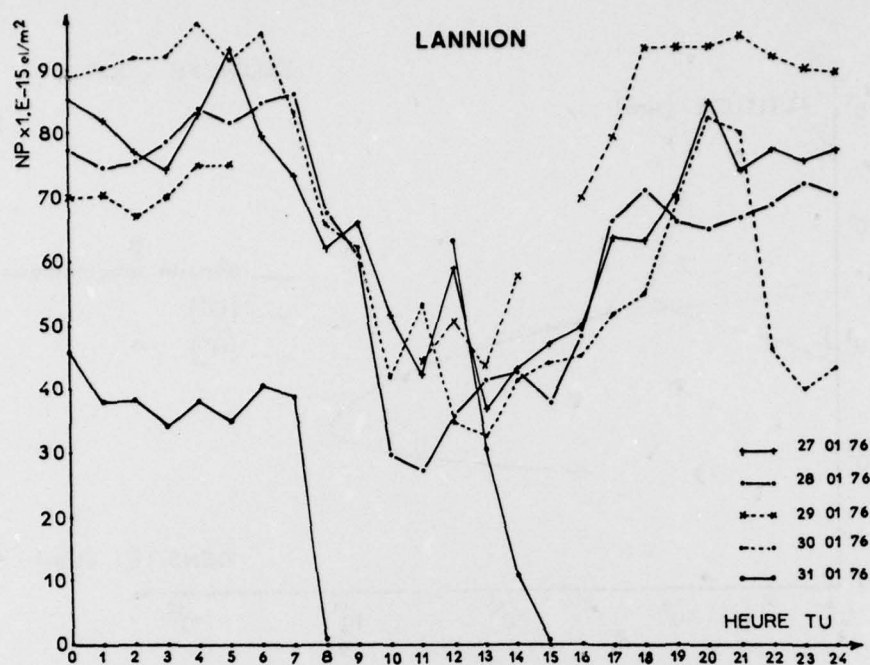
Figure 1 : Variations de N_p en fonction de l'heure TU pour la période 26-31 Janvier 1976.
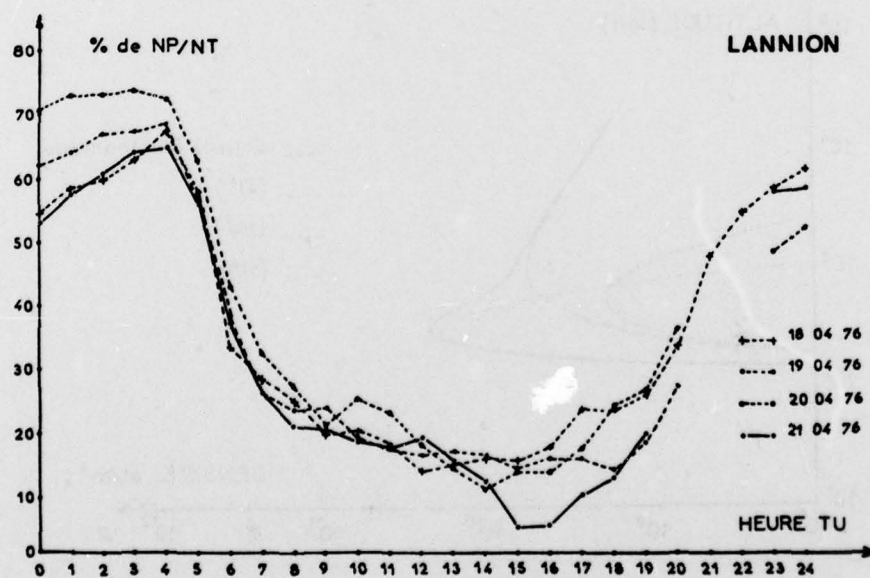
Figure 2 : Variations de N_p/N_T en fonction de l'heure TU pour la période 18-21 Avril 1976.
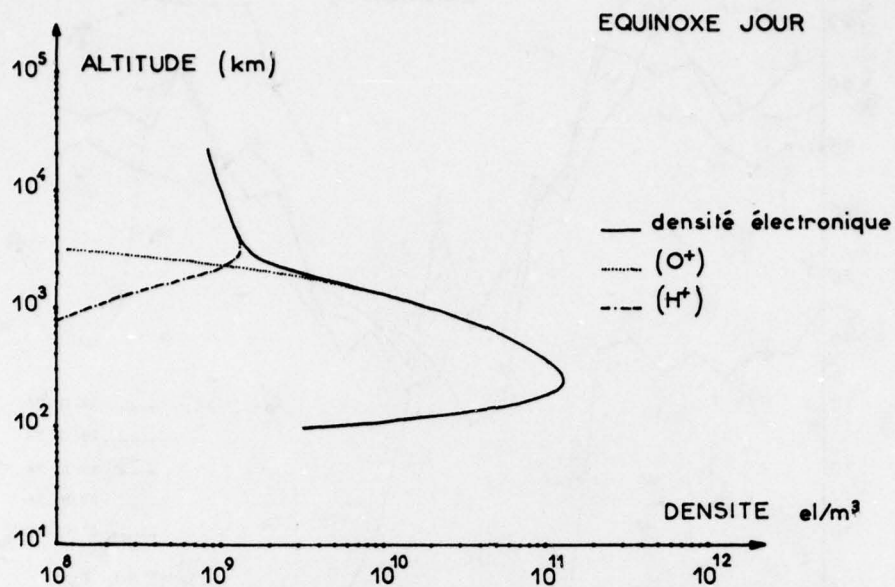
Figure 3   :   Profil de densité en fonction de l'altitude, l'équinoxe, de jour
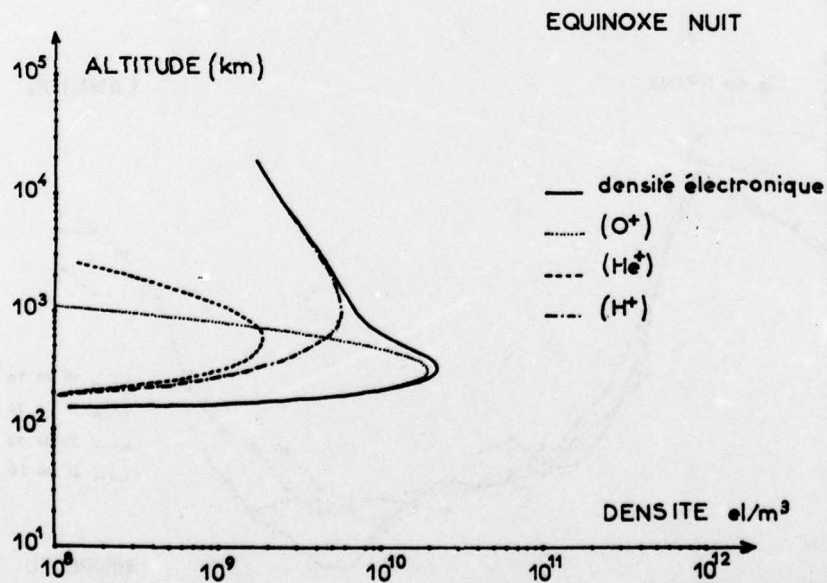
Figure 4   :   Profil de densité en fonction de l'altitude, l'équinoxe, de nuit

30 Mai 1976 — 40 MHz
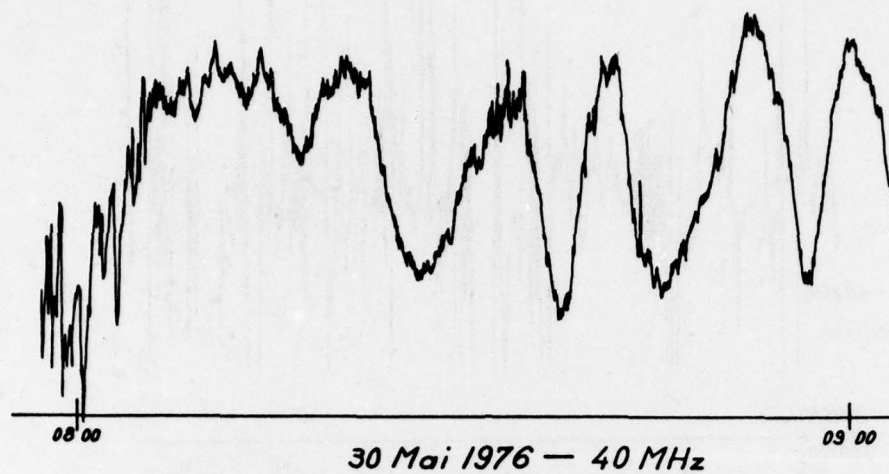
Figure 5 : Exemple d'enregistrement de l'amplitude du signal à 40 Mhz, montrant la superposition de la variation lente et des scintillations (30 Mai).

360 MHz

140 MHz
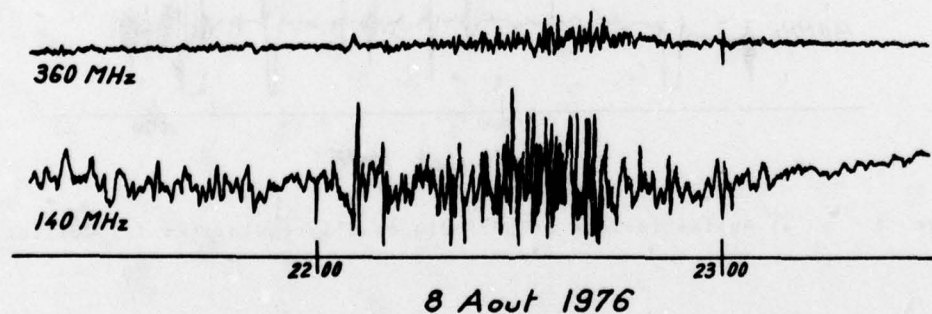
8 Aout 1976

Figure 6 : Exemple de scintillations forces pendant l'été sur 140 et 360 Mhz le 8 Août 1976.

40 MHz

360 MHz
140 MHz

19 00   20 00
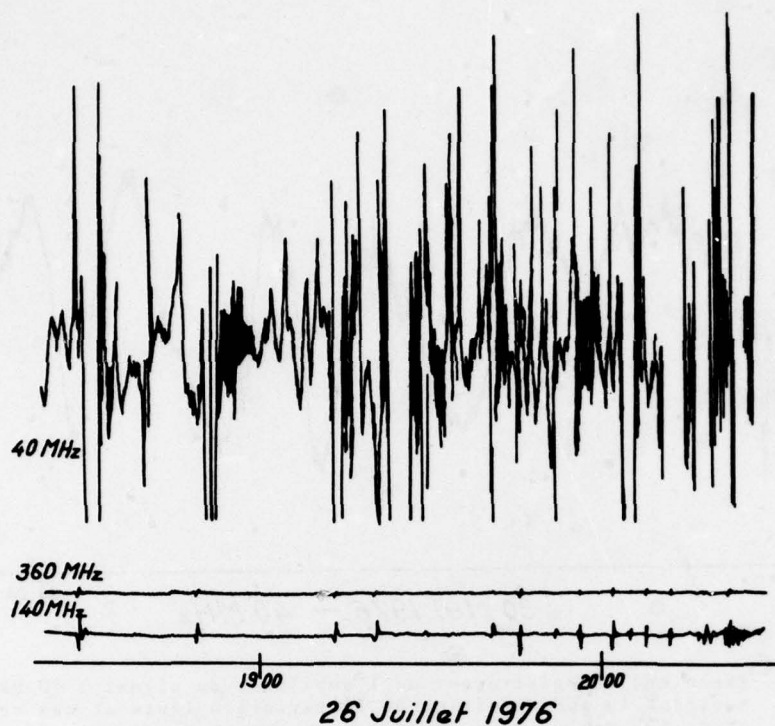
26 Juillet 1976

Figure 7 : Autre exemple de scintillations fortes d'été sur les trois fré-
quences (26 Juillet).

360 MHz

140 MHz

19 00   20 00
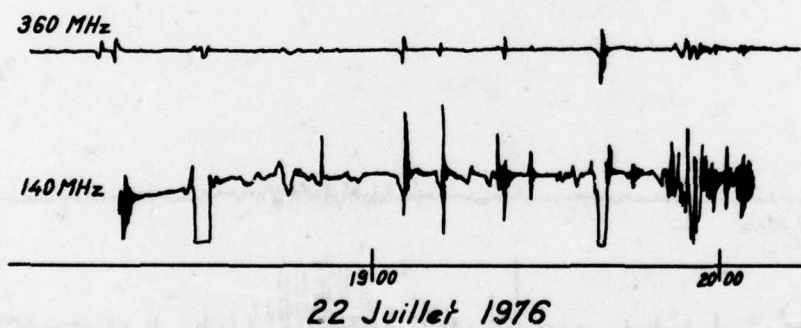
22 Juillet 1976

Figure 8 : a) Bulles isolées et périodiques d'irrégularités (22 Juillet)

40 MHz

360 MHz

360 MHz

140 MHz

140 MHz

09 40   09 50

10 20   10 30

10 40   10 50

15 Avril 1976

3 Aout 1976

8 Aout 1976
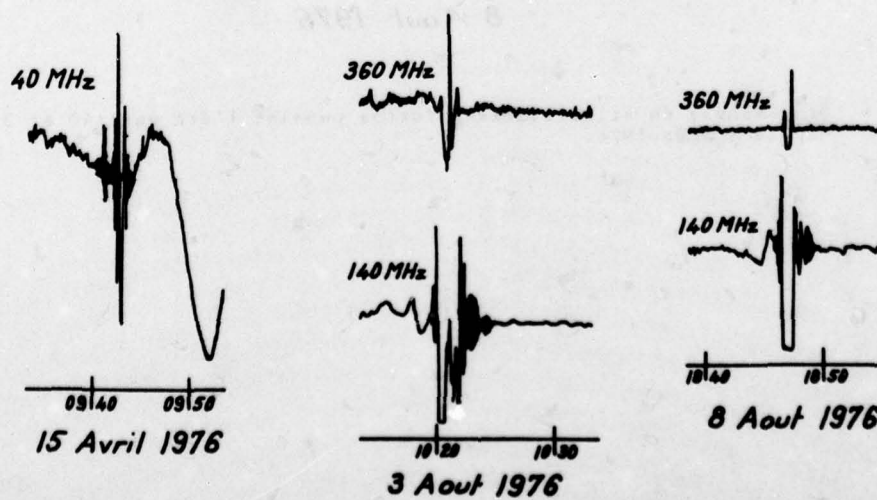
b) Figures de diffraction de Fresnel typiques enregistrées sur les
3 fréquences (15 Avril, 3 Août et 8 Août).

DISCUSSION

H.Soicher, US

N_p values seem rather high as compared to measurements in the American Sector! What is the equivalent vertical N_p for the Lannion station?

Author's Reply

The results presented give the value of the oblique plasmapheric content. The satellite was observed from an elevation angle of less than $20°$; it did not seem possible to us to convert them into vertical values by the methods generally used for the total ionospheric contents. In fact, we have noted that N_p increases before the beginning of a storm; however, the results we have obtained are not numerous enough to be significant.

E.J.Fremouw, US

I was interested in your observation of isolated scintillation features. You referred to them as resulting from ionospheric "bubbles", which implies an electron-density depletion. I think they result instead from electron-density enhancements, since they produce central defocuses. In our observations of complex-signal scintillation, we find the amplitude features to be associated with phase advances, which correspond to increases in phase velocity and therefore, to an electron-density enhancement.

Author's Reply

In the language generally used in this field, the word "bubble" means that the electronic density offers a discontinuity area, the edges of which have a high gradient, without specifying the sign of this gradient. As for the rest, we agree on what you say.

P.Bernhardt, US

I was interested to hear that both plasmaspheric content (satellite beacon measurement) and whistler measurements are used to derive your O^+ and H^+ ionospheric models. Do you have simultaneous plasmaspheric and weather measurements? If so, how do these measurements compare?

Author's Reply

Similar measurements from the beacon satellite, on the one hand, and from the "whistlers" on the other, have not been systematically provided for. However, the few measurements which have been made indicate a certain amount of correlation between the two methods.

INFLUENCE DE L'IONOSPHERE SUR LA PRECISION
DES MESURES EN GEODESIE PAR SATELLITE ARTIFICIEL

J. PAPET-LEPINE
CENTRE NATIONAL D'ETUDES DES TELECOMMUNICATIONS
DEPARTEMENT M.I.R - LANNION

INTRODUCTION

Il est d'un grand intérêt en géodésie de mesurer avec une grande précision la distance entre un satellite et un observateur au sol. Par des moyens radioélectriques, il est possible d'utiliser la mesure du temps de groupe en émettant une fréquence modulée, puis, après passage par un récepteur de réémettre la modulation vers l'émetteur d'origine. La mesure de la différence de phase entre la fréquence de modulation et la fréquence du pilote permet la mesure du temps de groupe recherché. Malheureusement, on sait que l'ionosphère apporte une erreur lorsqu'on utilise une seule fréquence radioélectrique pour déterminer la distance séparant un satellite, à un instant donné, d'une station au sol. On parvient toutefois à corriger fortement cette erreur en utilisant des modèles d'ionosphère et des mesures journalières des paramètres ionosphèriques.

Cependant, dès que la précision exigée atteint des ordres de grandeurs importants, par exemple 1 m sur une distance de 5 000 km, ou 1 mm par seconde pour la mesure de la vitesse par effet Doppler, aucun modèle n'est capable à ce jour d'atteindre de telles précisions. Le problème peut-être résolu en temps réel en utilisant l'action dispersive de l'ionosphère. C'est ainsi qu'en prenant plusieurs fréquences judicieusement choisies et en combinant les effets de chacune d'elles, on arrive à des précisions inférieures à celles qui sont demandées.

Le but de la présente communication est de montrer les ordres de grandeur des erreurs résiduelle dues à l'ionosphère lorsqu'on utilise au moins deux fréquences. On supposera par la suite que les erreurs de mesure expérimentale sont d'un ordre de grandeur très inférieur à la précision exigée.

PREMIERE PARTIE : ERREURS RESIDUELLES SUR LA MESURE DES DISTANCES

1 - GENERALITES

1 - Méthode utilisée pour le calcul des distances

On sait que pour les fréquences élevées (f > 100 Mhz), la formule d'APPLETON-LASSEN donnant l'indice de réfraction de l'ionosphère peut être simplifiée. Son développement limité aux deux premiers termes, donne pour la valeur de la phase :

$$\phi_1 = \frac{\omega_1}{c} \left[S_1 - \frac{aN_1}{f_1^2} \right] \qquad (1)$$

où S_1 désigne le chemin optique entre le satellite et une station au sol, le contenu total d'électrons le long de ce chemin, ω la fréquence de la porteuse et a une constante.

Si l'on utilise une deuxième fréquence, on obtient une relation identique à la précédente :

$$\phi_2 = \frac{\omega_2}{c} \left[S_2 - \frac{aN_2}{f_1^2} \right] \qquad (2)$$

Du fait de la réfraction, les trajets de phase suivis par les deux fréquences sont différents ainsi que les contenus totaux obliques. Faisons l'hypothèse que le fait d'utiliser des fréquences élevées, réduit l'influence de la réfraction ; on peut donc écrire :

$$S_2 - S_1 = D_V \qquad (3)$$

avec D_V désignant la distance géométrique entre le satellite et la station au sol. De même, on obtiendra :

$$N_2 - N_1 = \bar{N} \qquad (4)$$

en désignant par N le contenu total d'électrons rencontré entre les trajets des deux ondes. On obtient ainsi, à partir des formules 1 et 2, un système de deux équations à deux inconnues qui permettra d'évaluer la distance D_V en éliminant le contenu total moyen.

Si maintenant, pour des raisons de cohérence de phase, on se sert d'une troisième fréquence, pour le retour vers la station d'origine et si, d'autre part, f1 = αfe et f2 = βfe, on trouve par une combinaison linéaire :

$$D_V = \frac{\alpha^2 (1 + \beta^2) D_1 - \beta^2 (1 + \alpha^2) D_2}{\alpha^2 - \beta^2} \qquad (5)$$

formule dans laquelle D_1 et D_2 représentent les distances correspondant aux mesures des phases ϕ_1 et ϕ_2.

Il s'agit donc d'évaluer les erreurs engendrées par les hypothèses qui ont permis d'écrire les relations 3 et 4.

2. - Calcul des trajets optiques

Il existe actuellement des équations rigoureuses qui régissent la propagation d'une onde de fréquence supérieure à 1 Mhz, dans un milieu ionisé dont l'indice de réfraction est fonction à un instant donné des trois dimensions géométriques, en présence du champ magnétique terrestre (anisotropie). En partant des équations de l'optique hamiltonnienne, HASSELGOVE a établi un système de 6 équations en coordonnées sphériques qui résolvent théoriquement le problème. La seule hypothèse introduite est celle qui suppose la variation lente du milieu par rapport à la longueur d'onde.

Pour les ondes de fréquences supérieures à 100 Mhz, les effets de l'anisotropie du milieu sont inexistants. Il est donc possible de négliger l'influence du champ géomagnétique sur les trajectoires (la normale à l'onde est confondue avec la direction de propagation). En conséquence, cela permet de simplifier les programmes, donc la durée des calculs (HANBABA, 1968).

L'indice de réfraction utilisé dans les calculs est donné par la formule :

$$\mu^2 = 1 - \frac{X}{1 + Y \cos \Theta} \qquad (6)$$

qui correspond à l'onde ordinaire de la formule d'APPLETON-LASSEN, avec :

$$X = \frac{foF2}{f}^2 \cdot g(h), \quad Y = \frac{fH}{f} \qquad (7)$$

formules dans lesquelles foF2 désigne la fréquence critique du maximum d'ionisation, fH la gyrofréquence électronique, f la fréquence et g(h) la forme attribuée à l'ionosphère.

Le champ géomagnétique est calculé à partir du développement en harmoniques sphériques du dipode magnétique terrestre pour une station située à 45° de latitude Nord et pour une longitude 0°.

Dans les calculs de simulation on prend directement la racine du carré de l'indice de la relation 6, sans faire de développement en série de la valeur sous la racine.

3. - Simulation

Pour une simulation de ce genre il n'est pas nécessaire d'introduire des profils réels obtenus par des sondages ionosphériques verticaux, d'autant plus qu'au-dessus du maximum d'ionisation le profil sera obligatoirement approximé. Un calcul de simulation montre que si l'on modifie la forme du profil, tout en restant dans des limites réalistes par rapport au maximum de densité envisagée, le résultat est modifié au maximum de 20 % ; c'est-à-dire qu'une erreur de 50 cm pourrait varier dans des limites maximales de 40 à 60 cm dans ces conditions, on suppose une ionosphère constituée de deux profils de Chapman superposés. L'un représente la région F, la hauteur et la valeur du maximum d'ionisation. La hauteur d'échelle de la région F est reliée au contenu total d'électrons vertical par une relation de proportionnalité : le rapport contenu total sur maximum est proportionnel à la hauteur d'échelle. Dans la région E, on utilise le maximum d'ionisation de la région, la hauteur maximale et une hauteur d'échelle moyenne adaptée à cette région. En résumé, le modèle employé utilise les paramètres suivants :

- le contenu total d'électrons
- les hauteurs des couches E et F
- les fréquences critiques de ces couches

Si l'on se donne les valeurs de ces paramètres, le programme de tracé de rayons permet de calculer deux mesures "vraies" en calculant le trajet de phase pour chacune des fréquences utilisées (400, 2 000 et 1 500 MHz). Ces mesures sont dites vraies parce qu'elles sont obtenues, pour une géométrie déterminée, sans aucune approximation et en tenant compte des différents accroissements de parcours dus à la réfraction sur chacune des fréquences. Le résultat de ces mesures simulées est ensuite introduit dans l'équation 5. Connaissant la valeur vraie de la distance satellite observateur et la valeur calculée par l'équation 5, la différence entre ces deux valeurs donnera l'erreur résiduelle sur le calcul de cette distance.

II - RESULTATS

4. - Choix des valeurs des paramètres utilisées

D'après les mesures qui ont été faites depuis une quinzaine d'années du contenu total d'électrons (CTE), on possède des ordres de grandeurs des extremums en fonction de l'activité solaire. Mais ces mesures sont trop peu nombreuses dans le temps et sur la surface du globe pour pouvoir établir une statistique globale significative.

Nous avons donc choisi une valeur très élevée du CTE (99.10^{16} électrons par mètre carré) qui n'est que très rarement dépassée. En effet, cette valeur ne peut être observée que vers midi aux basses latitudes, pour des périodes de très forte activité solaire. La figure 1 montre l'évolution du CTE mesuré à KINGSTON à la Jamaïque, au mois de Mars 1972, c'est-à-dire en période de moyenne activité solaire. En première approximation, on peut admettre que la valeur maximale du CTE au cours d'une journée est égale à :

$$Ne \ (1 + b \ IR_5) \qquad (8)$$

Les coefficients Ne et b dépendent de la saison et de la latitude géomagnétique de la zone de traversée de l'ionosphère. b est de l'ordre de 8.10^{-3}, Ne est compris entre 4.10^{16} (pour les latitudes élevées) et 50.10^{16} électrons par mètre carré (pour les basses latitudes, aux équinoxes). On voit que pour un indice IR_5 égal à 125 (très forte activité solaire) la valeur 100.10^{16} est atteinte. Le graphique de la figure 2 donne une prévision de l'indice d'activité IR_5 pour le prochain cycle solaire.

5. - Résultats en l'absence de gradient

Les erreurs résiduelles sur les mesures de distances en prenant des profils ionosphériques identiques sur les 3 fréquences sont données dans le tableau 1.

Les valeurs utilisées sont les suivantes :

TEC : 99.10^{16}, FoE : 4 MHz, FoF_2 = 15 MHz, hE = 115 km et hF = 300 km.

TABLEAU 1

E(degré) = 5	10	15	20	25	30	35	40	45	50	55
Δd(cm) = 20,2	- 13,2	- 5,7	- 1,5	1,6	2,8	4,0	4,0	5,0	5,0	6,0

Dans le cas d'une ionosphère moyenne les résultats sont donnés dans le tableau 2, avec les valeurs suivantes :

TEC : 20.10^{16}, foE = 4 MHz, foF_2 = 7,5 MHz

TABLEAU 2

E(degré) = 5	10	15
Δd (cm) = - 0,9	0,2	0,8

Au dessus de 15° les résultats sont sans signification compte tenu de la précision de l'ordinateur.

6. - Introduction des gradients de densité

Dans la réalité la densité électronique est une fonction des coordonnées d'espace et du temps. On suppose en général l'ionosphère stationnaire pendant la durée d'un passage d'un satellite défilant. Jusqu'à maintenant on a supposé la densité d'électrons uniquement fonction de l'altitude. En fait, il existe plusieurs sortes de gradients horizontaux. La densité d'électrons est une fonction lente de la latitude, mais il vient se superposer des variations plus ou moins rapides et qui sont dues à la présence d'irrégularités isolées provoquant des variations de phase importantes. Elles sont dues à des variations de densité assez faibles mais sur des distances relativement courtes. Les perturbations ionosphériques itinérantes dues à des ondes atmosphériques ont des amplitudes importantes mais leur période (onde de moyenne échelle) supérieure à 20 minutes sont sans effet sur la mesure de distance. En revanche, il en sera question dans les mesures de vitesse.

Nous ne possédons malheureusement que peu de renseignements sur la morphologie des irrégularités (HANBABA 1971). Pour effectuer la simulation, nous avons supposé que la densité électronique intégrée le long d'un trajet est différente de la densité intégrée le long de l'autre trajet. C'est donc la résultante des variations de densité rencontrées le long de chacun des trajets. En pratique on calcule donc un trajet avec un CTE de l'ordre de 100.10^{16}, puis le second trajet avec un CTE de 2 % inférieur. La combinaison des deux trajets donne l'effet du gradient ainsi introduit. La valeur de 2 % a été choisie dans le même esprit que le CTE maximal, c'est donc une valeur extrême. De ce fait, étant donné que l'influence d'un gradient constant n'est pas réaliste (l'influence à la verticale du lieu doit être quasiment nulle), on pondère donc cette influence en fonction de l'élévation. La loi la plus simple qui se rapproche de la réalité est de considérer une variation du type cosécante de l'angle d'élévation. La fonction de pondération choisie est la suivante :

$$2 \ \frac{\sin 5°}{\sin E} \ \% \tag{9}$$

7. - Résultats en présence de gradients importants

On utilise donc deux profils ionosphériques distincts :

- l'un pour l'onde à 400 MHz
- l'autre pour les ondes à 1 500 et 2 000 Mhz

a) Forte activité ionosphérique

Les profils utilisés dans ce cas sont les suivants :

- profil 2 : TEC = 99.10^{16}
  - E = 4 MHz
  - F_2 = 15 MHz
  - hE = 115 MHz
  - hF = 300 MHz

- profil 1 : obtenu à partir du profil 2 par introduction d'un gradient correspondant à un accroissement de 2 % du CTE.

Le tableau 3 donne les résultats obtenus en attribuant le profil 1 à la fréquence de 400 MHz et le profil 2 aux deux autres.

Le tableau 4 donne les résultats obtenus en intervertissant les profils.

TABLEAU 3

E(degré) =	5	10	15	20	25	30	35	40	50
Δd(cm) =	- 111,5	- 92,4	- 75,7	- 62,2	- 51,7	- 44,7	- 39,1	- 34,6	- 28,4

	55	60
	- 26,2	- 24,4

TABLEAU 4

E(degré) =	5	10	15	20	25	30
Δd(cm) =	70,1	68,0	65,6	60,0	54,9	50,3

Pour tenir compte de l'écartement moindre des chemins optiques on modifie le profil 1 de façon à ce que l'accroissement correspondant du TEC diminue quand l'élévation E augmente. On obtient ainsi les résultats du tableau 5 pour lequel la formule 9 donne 2 % pour E = 5°.

TABLEAU 5

E(degré) =	5	10	15	20	25	30	35	40	45	50
Δd(cm) =	- 111,5	- 52,1	- 29,1	- 17,0	- 9,4	- 5,5	- 2,8	- 0,8	0,6	1,5

b) Activité ionosphérique moyenne

Les profils utilisés dans ce cas sont les suivants :

- profil 2 : TEC = 20.10^{16}
  f_oE = 4 MHz
  f_oF_2 = 7,5 MHz
  hE = 115 Km
  hF = 300 Km

- profil 1 : accroissement du TEC de 2 % constant.

Le tableau 6 donne les résultats obtenus en attribuant le profil 1 à la fréquence de 400 MHz et le profil 2 aux deux autres.

Le tableau 7 donne les résultats obtenus en intervertissant les profils.

TABLEAU 6

E(degré) =	5	10	15	20	25	30
Δd(cm) =	- 19,3	- 16,5	- 13,7	- 11,7	- 9,7	- 8,9

TABLEAU 7

E(degré) =	5	10	15	20	25	30	35	40
Δd(cm) =	17,4	16,1	14,6	13,7	11,8	10,5	10,2	10,1

L'ensemble des résultats donnant les erreurs résiduelles sur la mesure des distances est donné par les courbes de la figure 3.

8. - Evaluation du contenu total d'électron en partant des mesures de distances

Le système d'équations permettant d'obtenir une évaluation de la distance satellite-observateur donne également une estimation du CTE.

$$D1 = D_V + \frac{1}{2} \frac{40,3}{fe^2} No 1 + \frac{1}{\alpha^2}$$

$$D2 = D_V + \frac{1}{2} \frac{40,3}{fe^2} No 1 + \frac{1}{\beta^2}$$

d'où $$No = \frac{2fe^2}{40,3} \frac{\alpha^2\beta^2}{\alpha^2 - \beta^2} (D_2 - D_1) \qquad (10)$$

D_1 et D_2 sont les résultats des mesures sur 2 000 et 400 MHz, D_V la distance géométrique estimée, donnée par la relation 5.

La valeur N_o ainsi obtenue représente la densité électronique intégrée le long du parcours satellite observateur, c'est-à-dire le CTE oblique. Pour avoir le CTE vertical N_V, la valeur oblique doit être projetée sur une verticale appropriée. Pour un profil ionosphérique donné, on détermine, cette verticale de façon à ce que l'erreur sur N_V soit nulle pour l'élévation maximale considérée dans le cas d'une propagation ne faisant pas intervenir de gradient, (voir figure 4).

Pour $\alpha_T = 60°$, α_o est telle que $N_V \cos \alpha_o = N_o$, d'où :

$$h_o = R_T \frac{\sin \alpha_T}{\sin \alpha_o} - 1$$

Dans tous les autres cas de mesure, pour le profil considéré, N_V sera évalué comme la projection de N_o sur la verticale coupant le trajet BS à l'altitude h_o.

Résultats :

1er cas : CTE = 99.10^{16} FoE = 4 MHz foF_2 = 15 MHz, sans gradient

Avec E = 30°, on obtient h_o = 303,759 km, d'où les résultats du tableau 8 :

TABLEAU 8

E(degré) =	5	15	20	25	30
N_V en 10^{16} el/m^2 =	104,66	100,55	99,66	99,26	99,00

2ème cas : CTE = 99.10^{16} foE = 4 MHz foF_2 = 15 MHz, avec un gradient de 2 % pour l'onde à 400 MHz. Les résultats sont donnés dans le tableau 9.

TABLEAU 9

E(degré) =	5	10	15	20	25	30
N_V =	106,80	104,28	102,62	101,71	101,26	101,03

3ème cas : Même valeur des paramètres que dans le 2ème cas, mais le gradient est appliqué aux ondes à 1 500 et 2 000 MHz. Les résultats sont donnés dans le tableau 10.

TABLEAU 10

E(degré) =	5	15	20	25	30
N_V =	104,58	100,48	99,59	99,15	98,93

Dans le cas où l'on pondère l'effet du gradient par la formule 9, les résultats sont identiques à ceux du tableau 8.

Les résultats obtenus montrent la difficulté bien connue de passer du contenu total oblique au contenu total vertical. La précision entre le contenu total oblique obtenu par la formule 10 et le contenu total oblique vraie est bien meilleure que celle obtenue sur les contenus verticaux. Quoiqu'il en soit c'est une méthode qui permet de savoir le degré de prise en compte des erreurs ionosphériques.

DEUXIEME PARTIE : ERREURS RESIDUELLES SUR LA MESURE DES VITESSES

Le problème de la simulation des mesures de vitesse est beaucoup plus compliqué que celui posé dans le cas des mesures de distances. On se trouve confronté aux choix suivants : soit utiliser une méthode analytique simplifiée pour éviter les erreurs introduites par la dérivation numérique, soit utiliser une méthode plus complexe basée sur le tracé des rayons, mais introduisant des erreurs numériques dans son emploi. Nous allons montrer maintenant les résultats obtenus par ces deux procédures.

I - METHODE ANALYTIQUE

9. - Principe de la méthode de calcul

On obtient la mesure de l'effet Doppler total en dérivant par rapport au temps les équations 1 et 2. Si l'on utilise une troisième fréquence, comme dans le cas des mesures de distance, on trouve par une combinaison linéaire :

$$V = \frac{\alpha^2 (1 + \beta^2) V_1 - \beta^2 (1 + \alpha^2) V_2}{\alpha^2 - \beta^2} \qquad (11)$$

dormule dans laquelle V_1 et V_2 représentent les vitesses correspondant aux mesures des effets Doppler sur les fréquences f_1 et f_2.

Par un raisonnement analogue à celui développé dans le §.1, il s'agit de calculer l'influence de l'ionosphère sur les mesures donnant V_1 et V_2, puis connaissant la vitesse géométrique Vg, d'évaluer l'erreur entre Vg et V calculée par la formule 11.

10. - Calcul de l'effet Doppler géométrique

L'effet Doppler géométrique peut s'écrire :

$$Vg = \frac{dS_g}{dE} \cdot \frac{dE}{dt} \qquad (12)$$

Nous supposons que le satellite décrit une orbite plane circulaire d'altitude h. D'après la figure 4, et en utilisant quelques formules élémentaires on peut établir la relation suivante :

$$\cos (E + \theta) = \frac{R}{R + h} \cos E \qquad (13)$$

Dans le cas général où le satellite passe en vue de l'observateur avec une élévation maximale E_o, nous pouvons choisir cette position pour référence. Soit z l'angle géocentrique correspondant, il est minimal pour :

$$\cos (z + E_o) = \frac{R}{R + h} \cos E_o$$

D'après la figure 5, le plan xoy est perpendiculaire au plan de l'orbite. Soient A la position de l'observateur et S une position courante du satellite, le triangle sphérique ARS est rectangle en R, d'où :

$$\cos \theta = \cos \beta \cos z$$

De cette dernière formule, nous tirons :

$$d\theta = \frac{\sin \beta}{\sin \theta} \cos z \, d\beta$$

et de la formule 13, nous tirons :

$$dE = \frac{\sin (E + \theta) \, d\theta}{\frac{R}{R+h} \sin E - \sin (E + \theta)}$$

soit finalement :

$$\frac{dE}{dt} = \frac{\sin (E + \theta)}{\frac{R}{R+h} \sin E - \sin(E +\theta)} \frac{\sin\beta}{\sin\theta} \cos z \frac{d\beta}{dt} \qquad (14)$$

D'autre part, si g_o désigne l'accélération de la pesanteur au sol, on a :

$$\frac{d\beta}{dt} = - \frac{R}{R + h} \frac{g_o}{R + h} \qquad (15)$$

De même, on obtient pour dSg/dE :

$$\frac{dSg}{dE} = \frac{R_S}{\cos^2 E} \quad (\frac{R_T}{R_S} \frac{\sin E}{\sin(E+\theta)} - 1) \cos \theta \cos E + \sin \theta \sin E \quad (16)$$

Finalement, nous obtenons la vitesse cinématique en introduisant dans la relation 12 les formules 14, 15 et 16. Ce qui donne, après simplification :

$$V_g = \frac{d\theta}{dt} R_T \cos E$$

11. - Calcul de l'effet Doppler ionosphérique

En présence de l'ionosphère la vitesse est donnée par l'équation suivante :

$$V_i = - \frac{d\theta}{dt} \int_{(S_i)} \mu_i \, dS_i$$

où μ désigne l'indice de réfraction et S_i le parcours optique à la fréquence f_i.

Il n'est pas possible d'obtenir directement la dérivée analytique de l'expression 18, puisque μ et S ne sont pas des fonctions simples du temps de déplacement du satellite. Un certain nombre de simplifications sont nécessaires si l'on désire néanmoins la valeur de la dérivée en tous points. Si l'on suppose que le champ géomagnétique à une influence négligeable et si l'on admet que l'orbite est circulaire seul l'élément ds est une fonction du temps. En prenant pour ds l'expression fournie par la loi de Bougner, on obtient :

$$V_i = - \frac{1}{2} R_T^2 \sin 2\alpha_T \frac{d\alpha_T}{dt} \int_0^{h_s} \frac{\mu_i (R_T + h) \, dh}{\{\mu_i^2 (R_T + h)^2 - R^2 \sin^2 \alpha_T\}^{3/2}} \quad (19)$$

où R_T est le rayon terrestre, h_s l'altitude du satellite et α_T l'angle zénithal au sol du trajet optique. L'angle α_T est différent du complément à l'angle d'élévation E à cause de la réfraction. L'angle géocentrique θ est lié à α_T par l'équation :

$$\theta = R_T \sin \alpha_T \int_0^{h_s} \frac{1}{\{\mu_i^2 (R + h)^2 - R_T^2 \sin^2 \alpha_T\}^{1/2}} \frac{dh}{(R+h)} \quad (20)$$

La dérivée de cette expression par rapport à α_T s'écrit :

$$\frac{d\theta}{d\alpha_T} = R_T \cos \alpha_T \int_0^{h_s} \frac{\mu_i (R_T + h) \, dh}{\{\mu_i^2 (R_T + h)^2 - R_T^2 \sin^2 \alpha_T\}^{3/2}} \quad (21)$$

En combinant les formules 19 et 21, ont obtient :

$$V_i = R_T \frac{d\theta}{dt} \sin \alpha_T \quad (22)$$

puisque : $\quad \frac{d\alpha_T}{dt} = \frac{d\alpha_T}{d\theta} \cdot \frac{d\theta}{dt}$

12. - Calcul de l'angle zénithal en présence de l'ionosphère

D'une façon générale et sans introduire de simplifications, il est relativement aisé de résoudre l'équation 20 à l'aide d'une méthode numérique itérative et d'obtenir α_T avec une grande précision quelque soit le profil utilisé pour μ (BERTHEL et GESLIN, 1972).

Si l'on désire un ordre de grandeur de l'erreur introduite par l'ionosphère, il est possible d'effectuer un calcul approché de α_T en supposant l'observateur dans le plan de l'orbite et en supposant négligeable l'influence du champ géomagnétique.

Dans la formule 20 on développe l'indice de réfraction d'une part et d'autre part, on écrit que :

$$\alpha_T = \alpha_T' - \Delta\alpha_T \qquad\text{avec}\qquad \Delta\alpha_T << \alpha_T'$$

en désignant par α_T' l'angle zénithal géométrique, complément de l'angle d'élévation E et $\Delta\alpha_T$ la déviation due à la réfraction.

On trouve :

$$\Theta = R_T \sin \alpha_T' \int_{R_T}^{R_S} \frac{dR}{R_A} - \frac{R_T^3}{2} \Delta\alpha_T \sin^2 \alpha_T' \sin \alpha_T' \int_{R_T}^{R_S} \frac{dR}{R_A^3}$$

$$+ \frac{a}{2f^2} R_T \sin \alpha_T' \int_{R_T}^{R_S} \frac{NRdR}{A^3} - R_T \cos \alpha_T' \Delta\alpha_T \int_{R_T}^{R_S} \frac{dR}{R_A}$$

+ termes d'ordre supérieur.

Relation dans laquelle N désigne la densité des électrons, f la fréquence et a une constante et pour laquelle :

$$A^2 = R^2 - R_T^2 \sin^2 \alpha_T$$

et

$$\mu^2 = 1 - \frac{aN}{f^2}$$

D'autre part, on sait que d'une façon classique :

$$\Theta = R_T \sin \alpha_T' \int_{R_T}^{R_S} \frac{dR}{R \sqrt{R^2 - R_T^2 \sin^2 \alpha_T'}} = R_T \sin \alpha_T' \int_{R_T}^{R_S} \frac{dR}{RA}$$

En négligeant les termes d'ordre supérieur à 1, on en déduit :

$$\Delta\alpha_T \cos \alpha_T' \int_{R_T}^{R_S} \frac{dR}{RA} \left[1 + \frac{R_T^2 \sin^2 \alpha_T}{A^2} \right] = \frac{a}{2f^2} \sin \alpha_T' \int_{R_T}^{R_S} \frac{RNdR}{A^3}$$

Soit :

$$\Delta\alpha_T = \frac{a}{2f^2} \operatorname{tg} \alpha_T' \frac{\displaystyle\int_{R_T}^{R_S} \frac{RNdR}{A^3}}{\displaystyle\int_{R_T}^{R_S} \frac{RdR}{A^3}}$$

Si l'on suppose que N est prise en moyenne, on trouve :

$$\Delta\alpha_T = \frac{a\bar{N}}{2f^2} \operatorname{tg} \alpha_T' \tag{23}$$

en désignant par $\bar{N}$ la densité moyenne de l'ionosphère ; c'est-à-dire :

$$\bar{N} = \frac{1}{R_S - R_T} \int_{R_T}^{R_S} NdR = \frac{\mathcal{N}}{R_S - R_T}$$

où $\mathcal{N}$ est le contenu total d'électrons pris à la verticale.

D'après la formule 22 les mesures sur les fréquences 1 et 2 sont données par les relations suivantes :

$$V_i = \frac{d\theta}{dt} R_T \sin \alpha'_T - \frac{d\theta}{dt} R_T \Delta\alpha_i \cos \alpha'_T$$

$$\text{avec :} \quad \Delta\alpha_i = \frac{aN_i}{2f^2} \text{ tg } \alpha'_T \qquad\qquad (23 \text{ bis})$$

Si l'on multiplie la première mesure par k^2 avec $kf_2 = f_1$, et si l'on soustrait les résultats on trouve :

$$\frac{k^2 V_1 - V_2}{k^2 - 1} = V_g - \frac{d\theta}{dt} R_T \cos \alpha'_T \quad \frac{k^2 \Delta\alpha_1 - \Delta\alpha_2}{k^2 - 1}$$

On en déduit l'erreur relative sur la vitesse :

$$\frac{\delta V_g}{V_g} = \frac{k^2 \Delta\alpha_1 - \Delta\alpha_2}{k^2 - 1} \text{ cotg } \alpha'_T$$

Soit, d'après les relations 23 bis :

$$\frac{\delta V_g}{V_g} = \frac{a \Delta\bar{N}}{2f_2^2 (k^2 - 1)} \qquad\qquad (24)$$

Si l'on suppose que la fréquence 1 a rencontrée une densité moyenne supérieure de 2 % à celle rencontrée par la fréquence 2, et pour une densité moyenne de 4.10^{11} correspondant à une très forte activité ionosphérique et à un contenu total de 10^{18} électrons par mètre carré, on trouve : $\delta V_g/V_g = 8.10^{-8}$. Si maintenant la vitesse radiale du satellite est de l'ordre de 5 km.s^{-1} pour E = 10° l'erreur sur la mesure de cette vitesse sera de l'ordre de 0,4 mm.s^{-1}.

13. - Résultats obtenus par la méthode analytique

Le profil de densité électronique utilisé possède les caractéristiques suivantes :

- contenu total d'électrons 99.10^{16} em^{-2}
- maximum d'ionisation ($f_oF_2 = 20$ MHz) $N_{max} = 5.10^{12}$ em^{-3}
- hauteur du maximum $h_m = 300$ km

Les tableau 11 à 15 donnent l'erreur résiduelle sur les distances obtenues par cette méthode et l'erreur résiduelle sur les vitesses pour un observateur situé dans le plan de l'orbite. Dans le cas présent les erreurs de distances sont déduites de l'indice de phase qui correspond mieux à l'esprit de la méthode utilisée, alors que celle qui ont été obtenues dans la première partie sont déduites de l'indice de groupe, toutefois, on trouve le ΔD correspondant dans la colonne 4.

TABLEAU 11

Profil unique pour les 3 fréquences

E	Δd_m	Δv mm/s	ΔD
5	0.17	- 0.49	- 0.52
10	0.12	- 0.42	- 0.35
20	0.053	- 0.20	- 0.16
30	0.027	- 0.097	- 0.081
40	0.016	- 0.052	- 0.047
50	0.010	- 0.029	- 0.031
60	0.0078	- 0.017	- 0.023
70	0.0063	- 0.010	- 0.019
80	0.0056	- 0.004	- 0.017

TABLEAU 12

Gradient de - 2 % sur 400 MHz.

E	Δd_m	Δv mm/s	ΔD
5	- 0.74	0.17	0.40
10	- 0.70	0.52	0.47
20	- 0.57	0.65	0.46
30	- 0.46	0.54	0.40
40	- 0.38	0.42	0.35
50	- 0.33	0.32	0.31
60	- 0.30	0.23	0.29
70	- 0.28	0.15	0.27
80	- 0.27	0.074	0.26

TABLEAU 13

Gradient de + 2 % sur 400 MHz

E	Δd_m	Δv mm/s	ΔD
5	1.09	1.16	- 1.45
10	0.93	1.36	- 1.17
20	0.67	1.05	- 0.78
30	0.51	0.73	- 0.57
40	0.42	0.52	- 0.45
50	0.36	0.38	- 0.38
60	0.32	0.27	- 0.33
70	0.30	0.17	- 0.31
80	0.28	0.083	- 0.29

TABLEAU 14

Même profil pour les 3 fréquences, mais f_oF_2 = 15 MHz

E	Δd_m	Δv mm/s	ΔD
5	0.081	0.34	- 0.24
10	0.051	0.18	- 0.15
20	0.025	0.083	- 0.074
30	0.013	0.044	- 0.040
40	0.0082	0.025	- 0.025
50	0.0056	0.015	- 0.017
60	0.0043	0.009	- 0.013
70	0.0035	0.005	- 0.011
80	0.0031	0.002	- 0.0094

TABLEAU 15

Contenu total $= 50.10^{16}$ $f_o F_2 = 15$ MHz

Profil identique sur les 3 fréquences.

E	Δd_m	Δv mm/s	ΔD
5	0.042	0.12	- 0.13
10	0.028	0.10	- 0.084
20	0.013	0.048	- 0.038
30	0.0064	0.023	- 0.019
40	0.0038	0.012	- 0.011
50	0.0026	0.007	- 0.0076
60	0.0019	0.004	- 0.0056
70	0.0015	0.002	- 0.0046
80	0.0014	0.001	- 0.0041

II - METHODE NUMERIQUE

14. - Principe de la méthode numérique

Pour calculer la dérive numérique une seconde méthode est possible en introduisant un polynome sur les mesures de distance obtenue dans la première partie. En effet, le tracé de rayons fournit la valeur des mesures D_1 et D_2, de la distance géométrique S_g pour diverses valeurs de l'élévation E. L'approximation par des arcs de paraboles glissantes, par exemple permet d'obtenir les courbes F_1, F_2, F_g représentant $D_1(E)$, $D_2(E)$, $S_g(E)$.

Il reste à relier E au temps t, et nous aurons :

$$V_1 = \frac{dD_1}{dE} \cdot \frac{dE}{dt}$$

$$V_2 = \frac{dD_2}{dE} \cdot \frac{dE}{dt}$$

$$V_g = \frac{dS_g}{dt} \cdot \frac{dE}{dt}$$

avec dE/dt fournie par les formules 14 et 15.

15. - Résultats obtenus par la méthode des polynomes du second degré

Le profil ionosphérique de référence sera toujours celui correspondant à une très forte activité ionosphérique :

$$f_o E = 4 \text{ MHz}, \quad f_o F_2 = 15 \text{ MHz}, \quad CTE = 99.10^{16}$$

Les résultats sont rassemblés sur la figure 6 pour laquelle les courbes en trait continu ont été obtenues avec le même profil pour les 3 fréquences, et les courbes en tireté avec une augmentation de 2 % sur le profil utilisé à 400 MHz.

Sur la figure 7 les courbes en trait continu ont été obtenues avec une augmentation de a % sur le profil utilisé à 400 MHz, pondéré par la formule :

$$a = 2 \frac{\sin 5°}{\sin E} \tag{25}$$

tandis que les courbes en tireté ont été obtenues avec une pondération deux fois plus petite. Enfin, les courbes en tireté fin donnent les résultats obtenus pour une activité ionosphérique plus faible.

Les nombres en degré accompagnant chaque courbes donnent la valeur de l'angle d'élévation au temps de distance minimale.

16. - Gradients discontinus

Nous pouvons ainsi supposer les profils variant de manière arbitraire autour du profil suivant l'élévation. Les résultats obtenus varient alors très fortement suivant le choix des profils à chaque élévation et selon les valeurs de E servant à l'interpolation.

A titre d'exemple les tableaux 16 et 17 en faisant varier le profil P_o de 5° en 5° et en utilisant des polynomes du 3ième degré :

TABLEAU 16

Profil moyen pour toutes valeurs de E à 1500 et 2 000 MHz et pour 400 MHz augmenté de 2 % à 400 MHz à 10° et 20°.

Ex	90°	60°	30°
5°	- 20.0	- 19.3	- 15.7
8°	- 2.5	- 2.4	- 1.9
10°	5.0	4.7	3.7
13°	8.9	8.5	6.3
15°	6.1	5.8	4.1
18°	- 7.4	- 6.9	- 4.6

TABLEAU 17

Profil moyen à 1 500 et 2 000 MHz à 10 et 20° avec un gradient de + 2 % à 5 et 15° et pour 400 MHz profil moyen à 5 et 15° et + 2 % à 10 et 20°

Ex	90°	60°	30°
5°	- 41.7	- 40.1	- 32.7
8°	- 6.5	- 6.2	- 4.9
10°	8.5	8.1	6.3
13°	16.5	15.6	11.6
15°	10.9	10.3	7.3
18°	- 16.2	- 15.2	- 10.1

17. - Utilisation d'un polynome du premier degré

La vitesse est évaluée comme une variation de distance ramenée à l'unité de temps :

$$V = \frac{\Delta R \ (t_1, t_2)}{\Delta t}$$

avec $\Delta R = S_1 - S_1$

et $\Delta t = t_1 - t_1$

De cette manière nous déterminons :

$$V_1 = \frac{\Delta D_1}{\Delta t} \quad , \quad V_2 = \frac{\Delta D_2}{\Delta t} \quad , \text{ et } V_g = \frac{\Delta S_g}{\Delta t}$$

Pour $\Delta t = 5$ secondes et pour le profil classique défini au §.13 nous obtenons les résultats des tableaux 18 et 19. Ceux du tableau 19 sont en outre pondérés par la formule 25.

TABLEAU 18			TABLEAU 19	
E	Δv		E	Δv
5°	0.5		5°	1.4
15°	1.1		10°	1.0
20°	0.2		15°	1.4
25°	0.4		20°	0.4
30°	0.3		25°	0.5
			30°	0.4

TROISIEME PARTIE : INFLUENCE DES FLUCTUATIONS IONOSPHERIQUES

18. - Les scintillations ionosphériques dans les bandes métrique et décimétrique

On sait que la présence d'irrégularités de la densité électronique de l'ionosphère se traduisent par l'apparition de scintillations sur la phase et l'amplitude d'un signal radioélectrique traversant cette zone de fluctuations (CORNEC, 1976).

Si les scintillations sur les signaux émis par des satellites artificiels dans la bande des ondes métriques sont maintenant bien connues, l'observation de scintillations dans la bande des ondes décimétriques et même centimétriques est relativement récente.

Elles ont été enregistrées principalement dans la région équatoriale (TAUR, 1973, WERNIK et LIU, 1974) et, c'est la région la mieux étudiée de ce point de vue, moins fréquemment dans la zone aurorale (POPE et FRITZ, 1971) et, très récemment, à une latitude moyenne (BROWN et Coll. 1976). Les fréquences auxquelles on a constaté leur présence vont de 1,5 à 8 GHz.

Les variations maximales observées de l'intensité du signal reçu ont atteint 6 dB (avec des pointes à 20 dB) en région équatoriale et 3 dB dans les autres régions.

Tout comme les scintillations observées dans la bande métrique aux latitudes équatoriales, celles de la bande décimétrique sont un phénomène essentiellement nocturne, débutant vers 17 H locales et finissant vers 5 H avec un maximum d'activité vers 20 H. Les mesures sur 4 et 6 GHz montrent que des fluctuations supérieures à 0,5 dB sont présentes environ 0,6 % du temps (le pourcentage pour 1 dB est identique).

Dans les régions aurorales les scintillations sont présentes à toute heure, le maximum d'activité se produisant vers 2 H. Les résultats publiés indiquent que des fluctuations supérieures à 0,5 dB et 1 dB se rencontrent respectivement pendant 65 % et 10 % du temps la nuit, les chiffres correspondant pour le jour étant 42 % et 5 % (1).

Il n'est pour l'instant pas possible de donner une variation générale des scintillations SHF avec la latitude. On peut seulement signaler qu'elles se rencontrent surtout, d'une part, entre 30° Nord et 30° Sud magnétiques avec une plus grande probabilité d'apparition à l'équateur magnétique et, d'autre part, en ce qui concerne les points subionosphériques à 350 km, dans l'oval auroral.

Par ailleurs, dans la zone équatoriale, il semble que l'on doive s'attendre à un maximum d'activité aux longitudes atlantiques.

Au cours de l'année, toujours à l'équateur, la plus forte activité se rencontre aux équinoxes, les fluctuations supérieures à 0,5 dB pouvant alors être présentes environ une heure par jour ; la plus faible activité se situe au moment des solstices, la durée totale journalière des scintillations pouvant descendre jusqu'à moins de cinq minutes. Aucune donnée pour la variation saisonnière n'est disponible pour les autres latitudes (les résultats relatifs aux latitudes élevées concernent l'équinoxe de printemps).

---

(1) Les chiffres tirés de ces articles ne concernent qu'un faible nombre d'observations et doivent donc être généralisés avec prudence.

Les premières observations publiées ont eu lieu un peu après le dernier maximum de l'activité solaire et les informations ci-dessus ne concernent donc que la partie déclinante du cycle de l'activité solaire.

A l'équateur on a constaté la présence de scintillations en bande métrique quand des scintillations en bande décimétrique étaient présentes, l'inverse n'étant pas toujours vérifié. Il en est de même aux latitudes aurorales, les scintillations en bande métrique étant alors très fortes. D'autre part, à l'équateur, les fluctuations d'amplitude sur deux fréquences voisines (1,5 - 3 GHz) sont assez bien corrélées (coefficient de corrélation de l'ordre de 0,4) (CRANE 1974), la variation de l'indice de scintillation (défini comme étant la valeur quadratique moyenne des fluctuations de l'intensité du signal reçu) avec la fréquence f suit une loi en f^{-1}, entre 1,5 et 4 GHz et une loi en f^{-2} entre 4 et 6 GHz. En zone aurorale, il a été trouvé une loi en $f^{-0,85}$ pour la variation de l'indice de scintillation entre les bandes métrique et décimétrique.

Les résultats obtenus portent surtout sur des scintillations d'amplitude. Il existe très peu de données sur les scintillations de phase sauf quelques résultats épars, par exemple CRANE (1977) qui donne une distribution statistique gaussienne pour les scintillations de phase.

19. - Considérations théoriques

Considérons un satellite émettant sur deux fréquences que nous supposerons dans ce qui suit dans un rapport harmonique simple et issu par synthèse d'un oscillateur commun.

L'effet Doppler mesuré sur les deux fréquences peut s'écrire :

$$\Delta \omega_1 = \frac{\omega_1}{c} \frac{ds}{dt} + 2\pi \frac{a}{f_1} \frac{d}{dt} + E_1$$

$$\Delta \omega_2 = \frac{\omega_1}{c} \frac{ds}{dt} + 2\pi \frac{a}{f_2} \frac{d}{dt} + E_2$$

Formules dans lesquelles f désigne la fréquence, s le chemin entre le satellite et l'observateur, le contenu total d'électron pris sur le même chemin, a et c des constantes, enfin E désigne une fonction qui contient les erreurs dues aux hypothèses faites sur la réfraction, le développement en série limité aux deux premiers termes, etc....

Puisque les deux fréquences sont d'un rapport connu, tel que $f_1 = k f_2$, il est possible de multiplier $\Delta \omega_1$ par k, puis de faire la différence entre les deux mesures, on trouve :

$$\delta \omega = \frac{b}{c} \frac{ds}{dt} + E_2 - k E_1$$

La combinaison des erreurs E a été étudiée par ailleurs, il s'agit donc ici d'évaluer les erreurs dues aux fluctuations sur les mesures.

On écrira donc :

$$\frac{\delta (\delta \omega)}{\delta \omega} = \frac{\delta v}{v} \tag{26}$$

L'erreur relative sur la mesure de l'effet Doppler géométrique est égale à l'erreur relative sur la mesure de la vitesse. Si l'on se donne une erreur de 0,5 cms^{-1} sur la vitesse, une vitesse de 5 kms^{-1} un $\Delta \omega_1$ de 100 KHz (f = 2000 MHz) et un $\Delta \omega_2$ de 20 KHz (f = 400 KHz), on trouve que l'erreur sur la mesure ne devra pas excéder 0,04 Hz.

Si l'on désigne par $\sigma_{\phi'1}$ l'écart quadratique moyen sur la dérivée de la phase à la fréquence 1 et $\sigma_{\phi'2}$ l'écart quadratique moyen sur la dérive de la phase à la fréquence 2, on devra donc évaluer :

$$\delta \sigma_{\phi'} = \sigma_{\phi'2} - k^2 \sigma_{\phi'1} \tag{27}$$

20. - Caractéristiques accessibles à la mesure

Lorsque dans le cas d'un satellite on a accés uniquement à la densité de probabilité de la phase et de son écart type, on peut utiliser la notion de fréquence de scintillation ν_ϕ, défini comme étant le nombre moyen de fois que le signal coupe la valeur moyenne. A partir des densités de probabilité de la phase et de sa dérivée qui sont de même forme avec des paramètres différents, on obtient f_s en fonction de σ_ϕ' et σ_ϕ. Dans le cas d'une densité gaussienne, on a :

$$\sigma_\phi' = \pi \; \nu_\phi \; \sigma_\phi \tag{28}$$

Si l'on ne mesure pas directement ν_ϕ, mais puisque l'on mesure le spectre de phase des scintillations, on a :

$$\nu_\phi^2 = \frac{\int_{-\infty}^{+\infty} \nu^2 \; P_\phi \; (\nu) \; d\nu}{\int_{-\infty}^{+\infty} P_\phi \; (\nu) \; d\nu}$$

Si l'on connaît la loi en fréquence de la variation de ν_ϕ et σ_ϕ, le problème est résolu. Dans le cas d'un écran diffractant semi-transparent, on suppose que celui-ci contient des irrégularités de toutes dimensions dans une épaisseur petite par rapport à la distance entre cet écran et l'observateur et pour lequel on puisse appliquer l'approximation de Born (diffusion simple). Dans ce cas on trouve que la valeur quadratique moyenne des scintillations de phase s'écrit :

$$\overline{(\Delta \; \phi)^2} = g_\phi(r) \quad \overline{(\Delta \; \phi_o)^2} \tag{29}$$

où $g(r)$ est une fonction de la géométrie entre la couche d'irrégularités et l'observateur et $\overline{(\Delta \; \phi_o)^2}$ est la valeur quadratique moyenne de la phase à la sortie de la couche.

D'après Booker (1975), on trouve pour $\overline{(\Delta \; \phi_0)^2}$:

$$\overline{(\Delta \; \phi_0)^2} = a \; r_o^2 \; \lambda^2 \; \overline{(\Delta \; N)^2} \; L \; \Delta \; h \; \sec \; \alpha_T' \tag{30}$$

où a est une constante valant $\pi^{1/2}$ pour une distribution gaussienne, λ la longueur d'onde émise, $\overline{(\Delta N)^2}$, la valeur quadratique moyenne de la densité d'électrons dans la couche Δh à l'altitude h_e, L désigne l'échelle de taille des irrégularités et $\sec \; \alpha_T'$ la sécante de l'angle entre la direction de propagation et la verticale du lieu, enfin r_o est le rayon classique de l'électron.

La distance au-delà de laquelle se développe les scintillations d'amplitude est donnée par la distance de Fresnel :

$$Z_f = \gamma \; L^2/\lambda \tag{31}$$

$\gamma = \pi$ dans le cas d'irrégularités isotropes.

Si l'on suppose comme le fait CRANE (1977) que le milieu contient des irrégularités de toutes dimensions, l'observateur se trouve toujours dans la zone de Fresnel pour la fréquence émise :

$$Z_f = Z = \frac{h_e \; (h_s - h_e)}{h_s} \tag{32}$$

h_s distance à la verticale entre le satellite et l'observateur. De ce fait, L est une fonction de la longueur d'onde.

D'autre part, la fréquence de scintillations est également une fonction de la fréquence par l'intermédiaire de L. D'après RUFENACH (1971), on trouve :

$$\nu_i = \frac{v_i \; (h)}{\pi \; \lambda \; Z} = \frac{v_i \; (h)}{\pi L} \tag{33}$$

où $v_i(h)$ représente la vitesse de déplacement de la couche.

Cette grandeur est inconnue mais il est possible de la mesurer à partir des spectres des fluctuations. La théorie de la diffusion faible relie ces spectres au spectre des fluctuations de la densité électronique. Il en ressort que le spectre de phase est directement proportionnel au spectre des irrégularités, tandis que le spectre d'amplitude s'en déduit par multiplication par une fonction de la fréquence, appelée pour cette raison fonction de filtrage. La forme de cette fonction change suivant que l'on accorde ou non une épaisseur appréciable à la couche d'irrégularités, mais ses principales propriétés ne changent pas.

D'autre part, il est possible d'exprimer les erreurs de vitesse en terme de fluctuations de l'angle zénithale optique. BOOKER (1958) a montré que la valeur quadratique moyenne des fluctuations de cet angle pouvait s'exprimée par la relation :

$$\overline{\Delta\alpha^2} = 2 \left(\frac{\lambda}{2\pi 1}\right)^2 \overline{\Delta\phi^2} \tag{34}$$

où 1 représente la longueur de corrélation des irrégularités et telle que :

$$\nu_1 = \nu_i$$

ce qui donne d'après la relation 33 :

$$1 = \pi L \tag{35}$$

21. - Résultats sur les mesures des distances et des vitesses

A partir des relations 27 et 28, on trouve :

$$\delta s = \frac{\lambda_2}{k^2 - 1} (k^{3/4} - 1) \sigma_{\phi_2} \tag{36}$$

pour les erreurs de distance et pour les erreurs de vitesse :

$$\delta V = \frac{\lambda_2}{k^2 - 1} (k^{5/4} - 1) \nu_2 \sigma_{\phi_2} \tag{37}$$

avec $k\lambda_1 = \lambda_2$; σ_{ϕ_1} et σ_{ϕ_2} sont obtenues à partir des relations 29, 30 et 32, et ν par la formule 33.

De même, à partir des relations 23 bis et 24, on trouve :

$$\frac{\delta V}{V} = \frac{\sigma_{\alpha_2}}{2\pi(k^2 - 1)} (k^{1/4} - 1) \tag{38}$$

D'après les relations 34 et 35, on a :

$$\sigma_\alpha = 2^{-1/2} \frac{\lambda}{\pi^2 L} \sigma_\phi$$

D'après SMITH (1966) la valeur maximale de l'écart type sur la densité électronique est de 1 % de la densité, ce qui correspond aux valeurs obtenues par le sondeur à diffusion incohérente du CNET (VIDAL-MADJAR et Coll., 1975). Si l'on se donne une densité maximale de 5.10^{12} on prendra $\sigma_N = 5.10^{10}$ ce qui est une valeur très forte. En ce qui concerne la fréquence de scintillations ν on possède peu de valeurs expérimentales. Si l'on prend la valeur donnée par RUFENACH (1971) 20 mHz pour $\lambda = 17,50$ m, on a (à 400 MHz) $\nu_2 = 4$ mHz. Ce qui donne pour une épaisseur réduite de 100 km et un angle d'élévation de 10° une erreur $\delta V = 0,95$ mms^{-1} en utilisant la relation 37. Si maintenant on utilise la relation 38 pour laquelle seuls interviennent σ_N et Δh en paramètres, on trouve en la combinant avec 36 et 37 :

E	σ_{ϕ_2}	σ_{α_2}	ν_2	ν_1	δv	δs	ν_i	L	Z
10°	1.17 rad	$2,6.10^{-4}$ rad	17 mHz	7,6 mHz	4 mms^{-1}	8.10^{-2} m	13,6 ms^{-1}	240 m	240 km

22. - Interprétation des résultats

Lorsqu'on admet des caractéristiques ionosphériques très fortes l'erreur sur la mesure des distances est négligeable. Il n'en est pas de même avec la mesure des vitesses. Même avec une activité ionosphérique faible cette erreur reste importante aux sites bas. Toutefois, on peut considérer que le manque de données expérimentales sur les scintillations de phase ne permet pas d'évaluer avec certitude les erreurs lorsqu'on utilise la théorie de la diffusion faible.

En effet, les insuffisances de la théorie de l'écran diffusant simple proviennent essentiellement du fait que la couche d'irrégularités n'est pas mince ; elle peut même se composer de plusieurs couches, et que le plus souvent, surtout en ondes métriques, la diffusion est forte et corrélativement, multiple. En effet, quand l'épaisseur de la couche ne peut plus être négligée, le facteur de filtrage change, mais n'entraîne pas des modifications fondamentales dans les résultats obtenus par la théorie de l'écran mince. En revanche, lorsque la diffusion est forte, la théorie se complique sensiblement. Il se produit, en effet, un phénomène de focalisation des intensités diffusées par plusieurs irrégularités. Le problème théorique se complique et il n'est pas possible de trouver une solution analytique. Des résolutions numériques existent et ont été proposées par plusieurs auteurs, mais les bases expérimentales sont encore insuffisantes pour que ces théories puissent être utilisées dans le cas qui nous intéresse.

CONCLUSIONS

En l'absence d'irrégularités l'influence de l'ionosphère sur les erreurs résiduelles affectant les mesures de distance et de vitesse est négligeable, même pour une très forte activité ionosphérique. Il n'en est pas de même si l'on prend en considération la présence d'irrégularités dans la répartition spatiale de la densité électronique de l'ionosphère.

Dans les deux premières parties nous avons utilisé sous le nom de gradient une répartition de la densité différente pour chacune des fréquences, les chemins optiques empruntés par elles étant également différents. Il est bien évident que les valeurs utilisées sont très fortes et ne se rencontrent que pour des maximums de cycles solaires forts et dans quelques régions du globe bien localisées. Malheureusement, on ne possède que des résultats de mesures fragmentaires et il est donc impossible d'en obtenir une statistique sérieuse.

En ce qui concerne plus particulièrement les mesures de vitesse, les résultats de la seconde partie montrent que l'utilisation des mesures de distance approximées par des polynomes pour obtenir par dérivation les mesures de vitesse introduit des erreurs considérables surtout lorsque les mesures sont faites à des pas de durée importante. En revanche, lorsque l'on effectue la mesure directe de l'effet Doppler, à condition d'introduire des erreurs expérimentales relatives inférieures à 10^{-7}, les erreurs résultantes sur la mesure des vitesses deviennent très petites.

En définitive, les erreurs résiduelles sont négligeables la plupart du temps et dans presque toutes les régions du globe. Toutefois, il y a lieu de se prémunir en mesurant le contenu total d'électrons par la relation 10. Si cette valeur est trop forte les valeurs obtenues aux sites peu élevés seront entachés d'erreur surtout les mesures de vitesse et devront donc être rejetées.

Il en est de même avec l'influence des scintillations sur les mesures de vitesse (elle est négligeable sur les mesures de distance). Les fréquences utilisées étant élevées, l'influence des scintillations n'est pas permanente et n'existe pas dans toutes les régions du globe. On trouvera dans la monographie d'AARONS (1973) une tentative de modélisation des scintillations.

Enfin, l'influence de la troposphère sur les erreurs introduites dans la mesure des distances et des vitesses a été faite par ailleurs (AZOULAY (1976 et 1977).

REFERENCES

AZOULAY,A., 1976 - Etude de l'influence de la troposphère sur la mesure de distance Terre-Satellite. Note technique NT/EST/APH/34 CNET-Issy-les-Moulineaux.

AZOULAY,A., 1977 - Etude de l'influence de la troposphère sur la mesure de la vitesse radiale d'un satellite NT/TCR/APH/40.

AARONS,J ., 1973 - Scintillation studies. AGARDograph n° 166 p. 55.

BERTHEL, L. et GESLIN, D. (1972) - Nouvelle méthode pour calculer le chemin optique dans l'ionosphère. C. R. des Sciences, tome 274. p.721.

BOOKER, H.G., 1958 - The use of radiostars to study irregular refraction of radio-waves in the ionosphere. P.I.R.E. janvier 1958. p. 298-314.

BOOKER, H.G., 1975 - The role of the magnetosphere in satellite and radiostar scintillation. J.A.T.P., 37, p. 1089.

BROWN, W.E., HAROULES, G.G. et THOMSON, W.I., 1976 - Mid-Latitude ionospheric scintillation fading of microwaves signals. Nature vol. 259, p. 294.

CHIVERS, H.J.A., 1963 - Radiostar scintillation and spread F., J.A.T.P. 24, p. 468-472.

CORNEC, J.P., 1976 - Les scintillations et les irrégularités de la densité electronique ionosphérique. Note Technique Interne 33 TMA/MIR - CNET - MIR/LANNION.

CRANE, R.K., 1974 - Morphology of ionospheric scintillations. A.I.A.A. 12 th Aerospace Sciences Meeting, P. 52.

CRANE, R. K., 1977 - Ionospheric scintillation. P.I.E.E.E. 65, n° 2.

DAVIS, R.M., 1970 -Numerical map of spread-F occurences. Dep. Of Commerce, Boulder, Colorado, U.S.A.

HANBABA, R., 1967, - Trajectoires des ondes électromagnétiques émises par les satellites artificiels à travers une ionosphère anisotrope. Thèse de 3 ème cycle - Faculté des Sciences de Paris.

HANBABA, R., 1971 - Etudes des irrégularités de la densité électronique de l'ionosphère par la mesure des effets Faraday et Doppler différentiels des satellites balises. Thèse de Doctorat d'Etat - Faculté des Sciences de Paris.

KLOBUCHAR, J.A. and SEEMAN, D.R., 1973 - Total electron content of the ionosphere-data from the three world ionospheric regions. AGARDograph n° 166, p. 31.

POPE, I.H. et FRITZ, R.B., 1971 - High latitude scintillations effects on VHF and S-Band satellite transmissions. I. Pure and Appl. Phys. vol. 9, p. 593.

RUFENACH, C.L., 1971 - A radio scintillation method of estimating the small-scale structure in the ionosphere. J.A.T.P. 33, p. 1941.

SMITH, P.G. 1967 - Atmosphere distortion of signals originating from space source I.E.E.E. Trans, vol. 3 n° 2, p. 207-216.

TAUR, R.R. , 1973 - Ionospheric scintillations at 4 and 6 GHz. Comsat technical Review vol. 3, p. 415.

VIDAL-MADJAR, KOFMAN, D., et LEJEUNE W., G. - 1975 - Mesure de la raie n° 2 de plasma par diffusion incohérente à NANCAY. Ann. Géeophys. t. 31 p. 227-234.

WHITNEY, H.E., AARONS, J., ALLEN, R.S. et SEEMAN, D.R., 1972 - Estimation of the cumulative amplitude probability distribution function of ionospheric scintillations Radio Science, 7, p. 1095-1104.

WERNIK, A.W. et LIU, C.H., 1974 - Ionospheric irregularities causing scintillations of GHz radio signal. J.A.T.P., 36, p. 871.
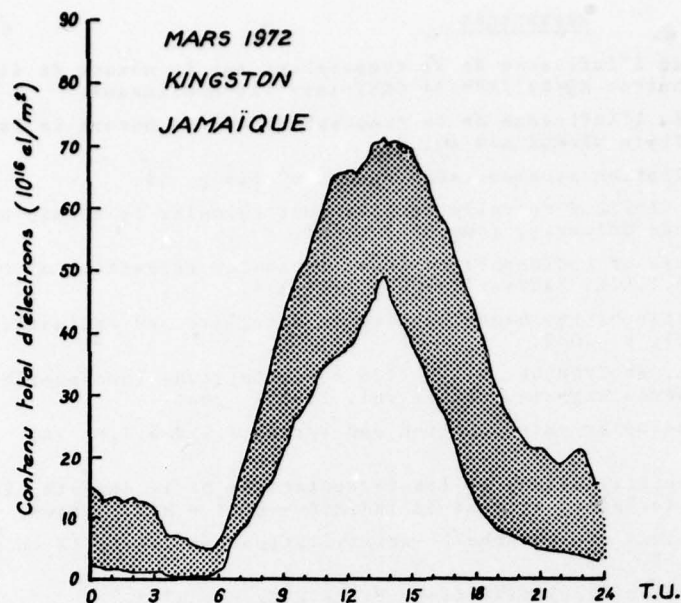
FIGURE 1 - Extremums des variations journalières du contenu total d'électrons
mesurées à KINGSTON pendant le mois de Mars 1972 pendant une pé-
riode de moyenne activité solaire.
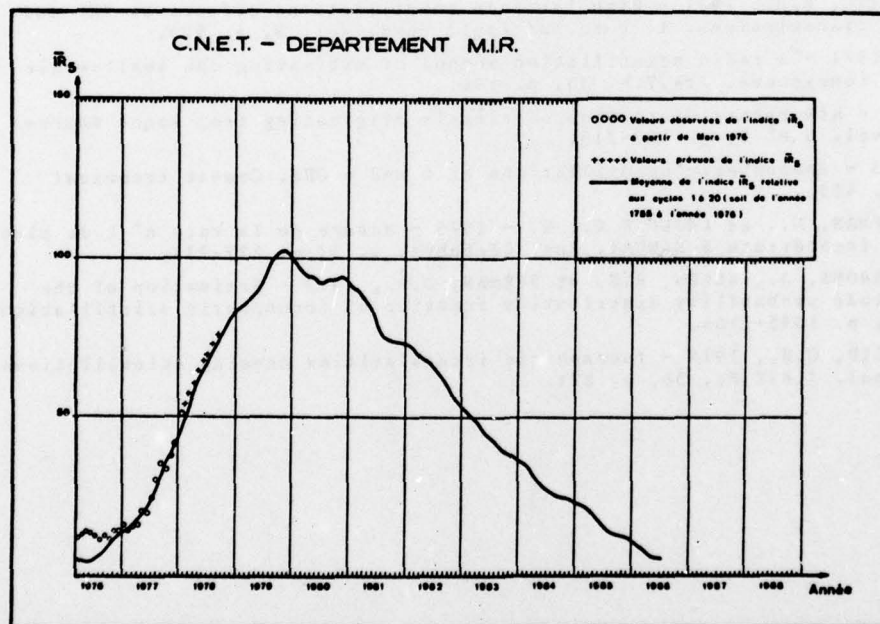
FIGURE 2 - Prévision de l'indice d'activité solaire pour le cycle solaire
actuel. L'indice $\overline{IR_5}$ est obtenu par la moyenne sur 5 mois des
indices mensuels.

ERREURS RESIDUELLES Δd SUR
LES MESURES DE DISTANCE

- - - - - CTE = 20.10¹⁶, foE = 4 MHz, foF2 = 7,5, sans gradient
- · - · - · CTE = 20.10¹⁶, foE = 4 MHz, foF2 = 7,5 MHz, gradient = 2 %
- - - - CTE = 99.10¹⁶, foE = 4 MHz, foF2 = 15 MHz, sans gradient
- · · · · · CTE = 99.10¹⁶, foE = 4 MHz, foF2 = 15 MHz, gradient = 2 %
———— CTE = 99.10¹⁶, foE = 4 MHz, foF2 = 15 MHz, gradient = 2 sin(5)/sin(E) %
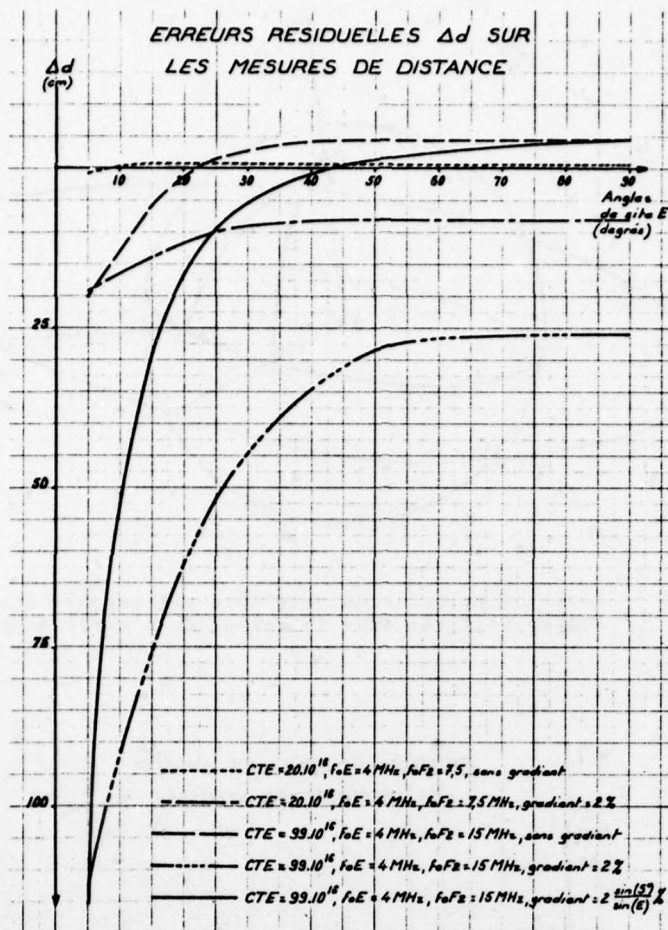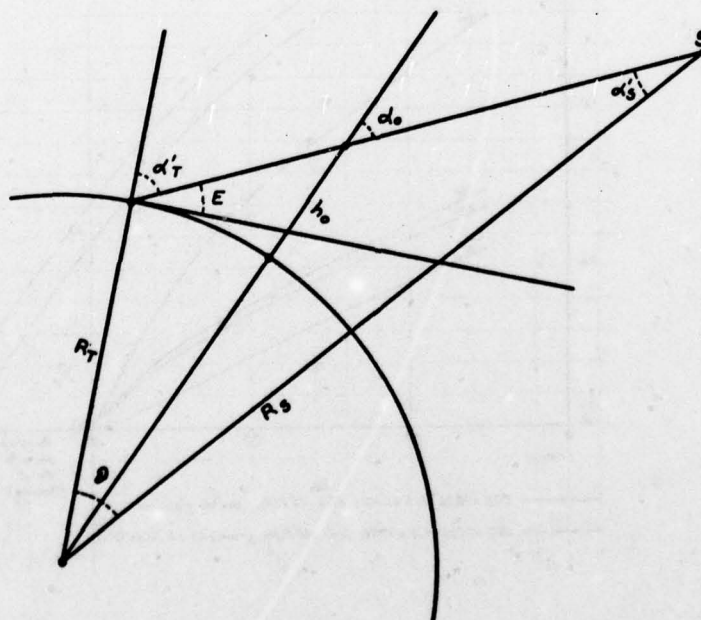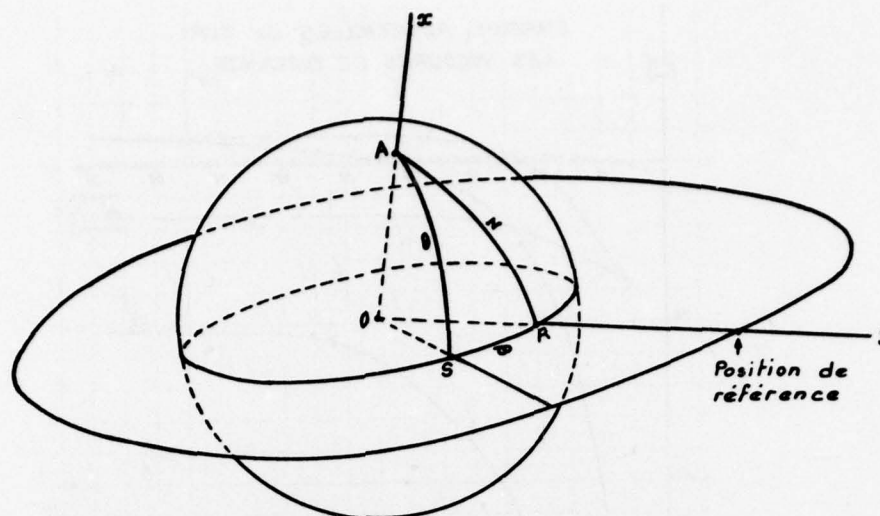
FIGURE 3 -

FIGURE 4 -

FIGURE 5 - Position relative du satellite par rapport à l'observateur.
Angles utilisés dans le calcul de l'effet Doppler géométrique.

FIGURE 6 -

ERREURS RESIDUELLES ΔV SUR
LES MESURES DE VITESSE
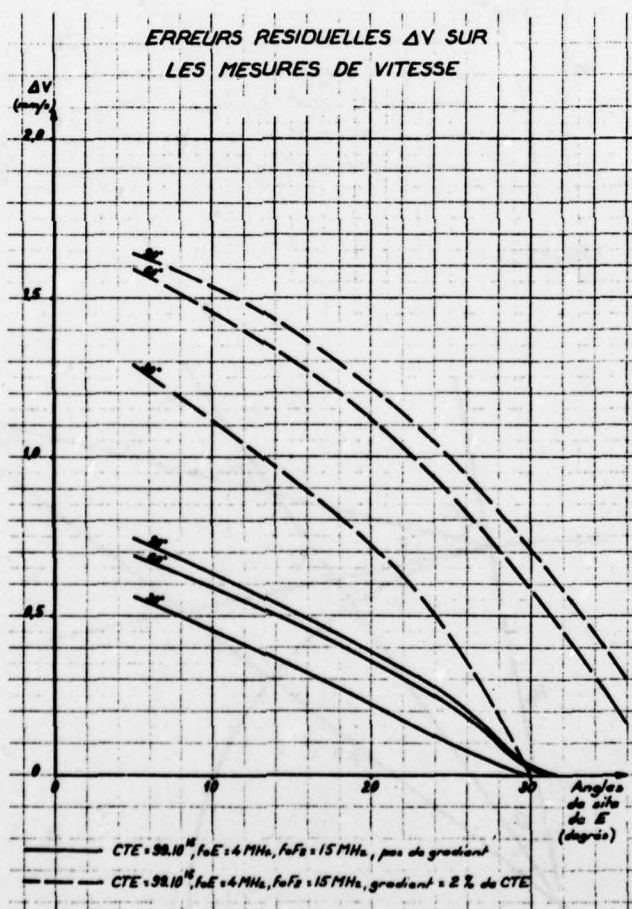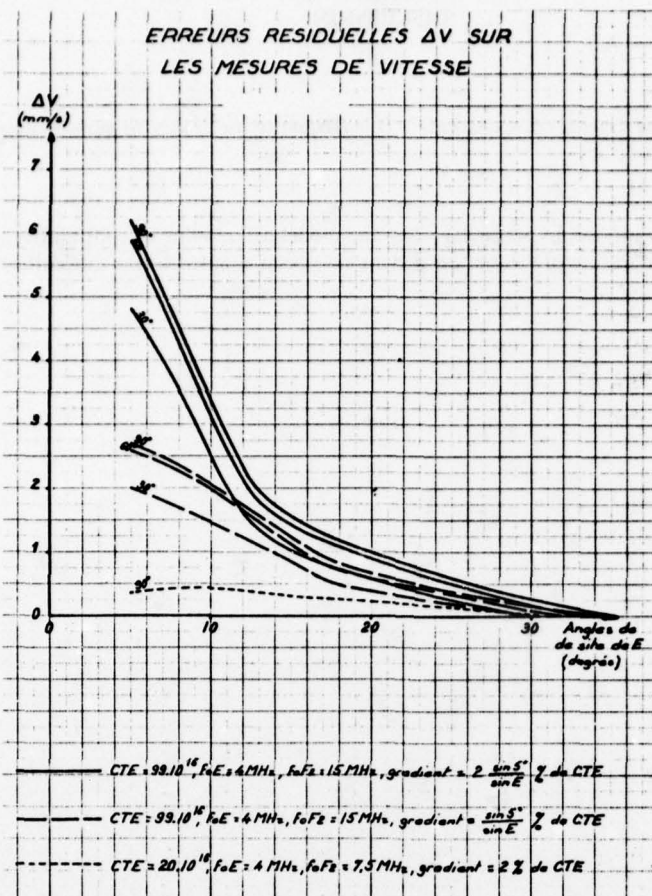
FIGURE 7 -

DISCUSSION

N.G.Gerson, US

How accurate were your ray-tracing computations? It is frequently necessary to employ double-precision for these calculations; did you do so?

Author's Reply

In fact, we have taken precautions, in particular when the model offers some discontinuities; the numerical methods used for the solution of the differential equation system have been adapted to the difficulties encountered.

A SIGNAL-STATISTICAL AND MORPHOLOGICAL
MODEL OF IONOSPHERIC SCINTILLATION
by
E. J. Fremouw
Physical Dynamics, Inc.
P. O. Box 3027
Bellevue, Wa. 98009 USA
and
C. L. Rino
SRI International
Menlo Park, Ca. 94025 USA

ABSTRACT

A signal-statistical and morphological model of radio wave scintillation produced in the F layer has been developed and committed to two user-oriented computer codes. The more extensive of the two codes, IONSCNT, contains a morphological model of irregular ionospheric structure and a two-component propagation routine that permits calculation of both focusing and diffractive scatter effects. The usual outputs of IONSCNT are first-order signal-statistical moments, including intensity and phase scintillation indices. The auxilliary code, DIST, employs some of the results from IONSCNT as inputs and permits the user to calculate first-order probability distributions of phase and amplitude, including fade-margin curves. A second operational mode of IONSCNT permits calculation of second-order signal-statistical moments, namely the spatial and temporal autocorrelation functions for intensity and phase and the two-frequency correlation coefficient for intensity. The structural description included in IONSCNT is a three-dimensional statistical model that allows for elongation along the geomagnetic field and, in the case of irregularities poleward of the subauroral scintillation boundary, for elongation in a second dimension (along L shells). The spatial spectrum employed is a power law, having a one-dimensional (i.e., in-situ) κ^{-2} form for electron-density squared. Morphologically, the model is of "average" or representative conditions for a given latitude, time of day, season, and epoch of the solar cycle.

1. INTRODUCTION

Ironically, the increasing sophistication of military and civilian systems for communication, navigation and positioning, and surveillance can render them more susceptible to performance degradation by the propagation medium than simpler systems. For instance, decreased signal margin in some broadband systems increases vulnerability to the effects of multipath fading. In other cases, exploitation of enhanced phase stability makes the inherent instability of the medium more important. Both kinds of effect can arise from ionospherically produced scintillation. Furthermore, employment of very wide bandwidths may either worsen or mitigate scintillation effects depending upon whether a wide coherence bandwidth is needed or frequency diversity can be exploited.

The foregoing considerations call for an integrated approach to modeling ionospheric scintillation, and several research groups have undertaken the task. For instance, early progress was made by the AFGL group to unify a large collection of morphological information on intensity scintillation (AARONS, WHITNEY, and ALLEN, 1971) and to provide an empirically realistic description of first-order amplitude statistics under scintillation conditions (WHITNEY, AARONS, and SEEMAN, 1972). In the present work, we have committed morphological and signal-statistical (both first- and second-order) information about complex-signal scintillation to a pair of computer codes intended for use in systems planning and design.

The encoded computations are firmly based on the theory of scattering from anisotropic irregularities in refractive index, including multiple scatter, and results have been tested against the best complex-signal scintillation data available, primarily from the DNA-002 multi-frequency, coherent radio beacon. The theory and resulting signal statistics are presented in Section 2, and the morphological model employed is described in Section 3. An overview of the two computer codes, IONSCNT (the main code) and DIST (an auxilliary code providing first-order, signal-statistical details), is given in Section 4. We present our conclusions in Section 5, including a description of the main limitations of the model.

2. SIGNAL STATISTICS AND PROPAGATION THEORY

2.1 Heuristic Description

The transionospheric communication channel may be regarded as a linear filter, the transfer function of which varies temporally and spatially. Fundamentally, the ionosphere behaves as a dispersive, phase-shifting network for all radio waves. The gross carrier phase shift, group delay, and dispersion introduced all are proportional to the integral of electron density along the principal raypath of a communication link. This integral, the "total electron content" (TEC), displays trend-like variations with location on the earth, time of day, season, and the level of solar/geophysical activity. These trends take place on very large spatial scales (hundreds and thousands of kilometers) and long time scales (tens of minutes and hours), and the communication-channel effects associated with TEC are best treated deterministically. Models of TEC behavior and effects (e.g., KLOBUCHAR, 1975) are available for application to the design and operation of communication and navigation systems and of radars.

The present work addresses effects of smaller-scale (tens of meters to tens of kilometers) ionospheric structure on link performance over shorter time scales (fractions of a second to minutes). Unlike the deterministic effects of TEC, the intensity and phase scintillations produced by the small-scale structure are best described in terms of signal statistics. The signal-statistical model described here is complementary to existing TEC models, in terms of time scale and spatial scale, and in terms of link effects.

The large-scale structures identified as trends in TEC produce pure phase trends in CW signals, whereas the unambiguous signature of smaller-scale, scintillation-producing structure is well-developed intensity fluctuation, accompanied by phase variations. The slowest intensity scintillations typically are observed to be relatively weak and to be accompanied by relatively strong phase scintillation.

An example of complex-signal scintillation is presented in Figure 1. The data presented are from the DNA Wideband satellite (FREMOUW et al, 1978). Phase (TEC) trends with Fourier periods greater than 10 s have been removed, as have intensity trends (due to changing range to the satellite, etc.). The complex-signal scintillation clearly is dominated by phase variations, but intensity fluctuations also are present on all Fourier frequencies greater than 0.1 Hz, as is demonstrated in Figures 2 and 3.

Figure 2 illustrates those scintillations contained in Figure 1 that have Fourier periods between 2.5 and 10 s, isolated by means of filtering intensity and phase. The weak intensity variations present are correlated with the strong phase variations that dominate the complex-signal scintillation in this period range. The correlation is evident in the complex-plane scatter plot at the top of the figure; that is, there is a marked tendency for a phase advance to be accompanied by a weak fade and for a phase retardation to be accompanied by weak signal enhancement. This is the behavior that would be expected in the geometric-optics (near) zone of large, lenslike ionospheric irregularities.

The scintillations with Fourier periods shorter than 2.5 s are illustrated in Figure 3, which shows that most of the intensity scintillation occurs in this period range, accompanied by relatively weak phase fluctuation. The statistical behavior illustrated is consistent with diffractive scatter by smaller-scale irregularities and with the complex-signal behavior inferred from amplitude-only data (FREMOUW and RINO, 1975; RINO, LIVINGSTON, and WHITNEY, 1976). Figure 1 and 2, however, demonstrate that the signal statistics describing the well-developed amplitude fluctuations and relatively fast phase fluctuations do not provide a complete representation of complex-signal scintillation.

The behavior typified by Figures 1, 2, and 3 has prompted us to postulate that the complex envelope, E, of a scintillating signal may be characterized in terms of the following two-component, signal-statistical model (FREMOUW and RINO, 1976):

$$E = E_s E_f = (x_s + iy_s) \exp (\chi_f + i\phi_f) \tag{1}$$

where x_s and y_s are jointly Gaussian variates, as are χ_f and ϕ_f. It is supposed that E_s (the "scatter" component) and E_f (the "focus" component) are statistically independent. Thus, the first-order statistics of E are totally specified by six (co)variances: σ_x^2, σ_y^2, σ_{xy}, σ_χ^2, σ_ϕ^2, $\sigma_{\chi\phi}$. The "six sigmas" and their second-order generalizations are related to structural parameters of the ionosphere by means of the propagation theory described in Section 2.2.

There have long been two intuitive notions about the complex-signal statistics to be expected for a scintillating signal. The first is based on the conceptual model of summation of "randomly phased" contributions from a large number of scattering centers (RATCLIFFE, 1956). This notion leads to the suggestion of RICE (1945) statistics or a generalization thereof (BECKMAN and SPIZZICHINO, 1963), in which the quadrature components of the signal are possibly correlated Gaussian variates with possibly different variances (RINO and FREMOUW, 1973; RINO, LIVINGSTON, and WHITNEY, 1976). The second notion is of a radio wave propagating in essentially straight paths along which the phase is randomly increased and decreased in such a way that the output phase is a Gaussian variate (BRAMLEY, 1955). A natural extension of this view is to suppose that the real and imaginary parts of the logarithm of the signal are normal variates.

The two-component model defined above is simply a unification of the foregoing two notions in a way suggested by the first definitive complex-signal scintillation data to become available. The two components are multiplicative because they were isolated experimentally by a process equivalent to a coherent AGC circuit. Heuristically, the components might be expected to be multiplicative because they stem from additive perturbations of the imaginary part of the complex logarithm (i.e., phase). A partial formalizing of the two-component propagation theory is described in Section 2.2.

Our propagation calculations employ (1) the phase-screen approach to describing the wave perturbation imposed by ionospheric structure, subject to the Markov approximation, and (2) the parabolic wave equation for calculating propagation effects, which is appropriate for all narrow-angle scatter problems. The unique feature of the approach is partitioning of the ionospheric spatial spectrum into two scale-size regimes (of no geophysical significance) to permit efficient computation and to incorporate the empirically derived two-component signal-statistical model. In essence, the computations are divided into one that accounts fully for diffractive scatter by relatively small-scale irregularities and one that employs the ray-optics approximation appropriate for efficient evaluation of focusing and defocusing by larger-scale irregularities.

A heuristic picture of the two-component model might be of a wave encountering a scattering layer, emerging with a scattered and a non-scattered part, and then passing through a region of larger phase-perturbing structure. The phase of both the scattered and non-scattered parts would be spatially modulated by the second region. Statistically, at least, the results would be the same if the positions of the two perturbation processes were interchanged or if they occurred in the same region. In this heuristic view, one might suppose that only the coherent (nonscattered) part of the scatter component would produce focuses after propagating through the large-scale, phase-perturbing screen. There is some evidence to support this supposition in data from the DNA Wideband satellite, and we have imposed a focusing limit in the model.

2.2 Mathematical Development

To develop a mathematical formalism that will allow us to relate the parameters that characterize the signal statistics to the irregularities that cause scintillation, we first consider the parabolic-wave

equation,

$$\frac{\partial E(\vec{r},z)}{\partial \mathit{l}} = -i \frac{\lambda}{4\pi} \nabla_T^2 E(\vec{r},z) + i r_e \lambda \Delta N(\vec{r},z) E(\vec{r},z) \quad . \tag{2}$$

employing the notation given in Table 1. By making the partition,

$$\Delta N = \Delta N_s + \Delta N_f \tag{3}$$

in Eq. (2), where ΔN_s gives rise to the scatter component (E_s) and ΔN_f gives rise to the focus component (E_f) and substituting $E = E_s E_f$ from Eq. (1) into Eq. (2), we obtain the coupled differential equations,

$$\frac{\partial E_s}{\partial \mathit{l}} = -i \frac{\lambda}{4\pi} \nabla_T^2 E_s + i r_e \lambda \Delta N_s E_s - i \frac{\lambda}{2\pi} \left(\frac{\nabla_T E_f}{E_f} \right) \nabla_T E_s \tag{4a}$$

and

$$\frac{\partial E_f}{\partial \mathit{l}} = -i \frac{\lambda}{4\pi} \nabla_T^2 E_f + i r_e \lambda \Delta N_f E_f \quad . \tag{4b}$$

The second equation is solved for the phase, ϕ_f, of E_f by using the phase-screen and ray-optics approximations, respectively:

$$\phi_f \cong r_e \lambda \sec \theta \int_0^L \Delta N_f \left(\vec{\rho}_s + \tan \theta \, \hat{a}_{k_T} z, z \right) dz \tag{5a}$$

and

$$\frac{\partial \chi_f}{\partial \mathit{l}} \cong \frac{1}{2k} \nabla_T^2 \phi_f \tag{5b}$$

where

$$\vec{\rho}_s = \vec{\rho} - \tan \theta \, \hat{a}_{k_T} z \quad . \tag{6}$$

Defining

$$R_{\chi\phi}(\vec{\Delta\rho}) \overset{\Delta}{=} \left\langle \chi_f(\vec{\rho}) \phi_f(\vec{\rho}+\vec{\Delta\rho}) \right\rangle \tag{7a}$$

$$R_{\chi}(\vec{\Delta\rho}) \overset{\Delta}{=} \left\langle \chi_f(\vec{\rho}) \chi_f(\vec{\rho}+\vec{\Delta\rho}) \right\rangle \tag{7b}$$

and

$$R_{\phi}(\vec{\Delta\rho}) \overset{\Delta}{=} \left\langle \phi_f(\vec{\rho}) \phi_f(\vec{\rho}+\vec{\Delta\rho}) \right\rangle \tag{7c}$$

it follows from Eq. (5) that

$$R_{\chi\phi}(\vec{\Delta\rho}) \approx \left(\frac{\lambda z \sec \theta}{4\pi} \right)^2 \left[a_{11} \frac{\partial^2 R_\phi}{\partial \Delta\rho_x^2} + 2a_{12} \frac{\partial^2 R_\phi}{\partial \Delta\rho_x \partial \Delta\rho_y} + a_{22} \frac{\partial^2 R_\phi}{\partial \Delta\rho_y^2} \right] \tag{8}$$

and that

$$R_{\chi}(\vec{\Delta\rho}) \approx \frac{\lambda z \sec \theta}{4\pi} \left[a_{11}^2 \frac{\partial^4 R_\phi}{\partial \Delta\rho_x^4} + 4a_{12} \frac{\partial^4 R_\phi}{\partial \Delta\rho_x^3 \partial \Delta\rho_y} + \left(4a_{12} + 2a_{11}a_{22} \right) \frac{\partial^4 R_\phi}{\partial \Delta\rho_x^2 \partial \Delta\rho_y^2} \right.$$
$$\left. + 4a_{12}a_{22} \frac{\partial^4 R_\phi}{\partial \Delta\rho_x^2 \partial \Delta\rho_y^3} + a_{22}^2 \frac{\partial^4 R_\phi}{\partial \Delta\rho_y^4} \right] \tag{9}$$

where the coefficients a_{ij} are given in Table 1 and where R_ϕ, the phase autocorrelation function is given by

$$R_{\phi}(\vec{\Delta\rho}) = \left(\sigma_f^2 L \right) \sqrt{1 + Q^2/2\beta_f^2} \frac{K_1\left(2\beta_f/\alpha_f \sqrt{1 + Q^2/2\beta_f^2} \right)}{K_1\left(2\beta_f/\alpha_f \right)} \tag{10}$$

where $K_1(x)$ is the modified Bessel function and

$$Q^2 = \frac{C\Delta\rho_x^2 - B\Delta\rho_x \Delta\rho_y + A\Delta\rho_y^2}{AC - B^2/4} \tag{11}$$

The coefficients A, B, and C depend on the propagation geometry and the anisotropy of the irregularities, as given by RINO and FREMOUW, (1977). The functional form for R_ϕ given in Eq. (10) arises from description of the random medium by a three-dimensional spatial power spectrum having a power-law form with a one-dimensional (i.e., in-situ) κ^2 behavior.

The "three sigmas" that specify the first-order statistics of the focus component are obtained by evaluating Eqs. (8), (9), and (10) for zero lag ($\Delta\rho = 0$), with σ_ϕ adjusted for propagation according to Eq. (23) and with σ_χ and $\sigma_{\chi\phi}$ limited to permit focusing only by the nonscattered part of E_s.

The scatter component is more difficult because the near-zone (ray-optics) approximation cannot be made. Moreover, we must also consider the coupling term in Eq. (4a). We assume, however, that the partitioning in Eq. (3) is such that the scale for changes in $\nabla_T E_f/E_f$ (i.e., $\nabla_T \ln E_f$) is much larger than the scale for changes in $\nabla_T E_s$. Then Eq. (4b) can be solved as if the $\nabla_T E_f/E_f$ term were constant. In this case, it can be shown that the gradient term makes no contribution to the second-order moments of E_s. If we make the further assumption that E_s is Gaussian, the second-order moments completely specify the statistics of E_s. It follows that the $\nabla_T^2 E_f/E_f$ term has no effect on the statistics of E_s -- that is, E_s and E_f are statistically independent.

By this argument, we can neglect the coupling term in Eq. (4a), which is then solved for ϕ_s using the phase-screen approximation. The scatter component is then given by

$$E_s\left(\vec{\rho}, z\right) = \iint F\left(\vec{\rho} - \vec{\rho}'\right) \exp\left\{i\ \phi_s\left(\vec{\rho}'\right)\right\} d\vec{\rho}' \tag{12}$$

where $F(\vec{\rho} - \vec{\rho}')$ is the free-space diffraction kernel for a wavefield scattered through narrow angles. Because E_s is Gaussian, its statistics are completely specified by the second-order coherence functions

$$R_s(\vec{\Delta\rho}) \overset{\Delta}{=} \left\langle E_s(\vec{\rho}) E_s^*(\vec{\rho} + \vec{\Delta\rho})\right\rangle \tag{13a}$$

and

$$B_s(\vec{\Delta\rho}) \overset{\Delta}{=} \left\langle E_s(\vec{\rho}) E_s(\vec{\rho} + \vec{\Delta\rho})\right\rangle. \tag{13b}$$

When R_s is computed using Eqs. (12) and (13a), the diffraction kernel becomes a delta function so that R_s does not vary with z and the following analytic expression results:

$$R_s(\vec{\Delta\rho}) = \exp\left\{-\sigma_s^2\ L\left[1 - Q^2 K_1(Q^2)\right]\right\} - \exp\left\{-\sigma_s^2\ L\right\} \tag{14}$$

The (complex) "assymetry" coherence function, B_s, which describes all diffraction effects, must be obtained by numerical evaluation of an integral very similar to Eq. (12). Details have been given by RINO et al (1977).

The "three sigmas" that specify the first-order statistics of the focus component are obtained by evaluating $R_s(\vec{\Delta\rho})$ and $B_s(\vec{\Delta\rho})$ for zero lag and employing the relationships

$$\sigma_x^2 = \tfrac{1}{2}\left|R_s(0) - \text{Re}\left\{B_s(0)\right\}\right| \tag{15a}$$

$$\sigma_y^2 = \tfrac{1}{2}\left|R_s(0) + \text{Re}\left\{B_s(0)\right\}\right| \tag{15b}$$

$$\sigma_{xy} = \tfrac{1}{2}\ \text{Im}\left\{B_s(0)\right\} \tag{15c}$$

To summarize, so long as E_s is Gaussian and the scale for changes in $\nabla_T \ln E_f$ is very large compared to the scale for changes in $\Delta_T E_s$, we can relate the multiplicative scatter and focus components to disjoint and therefore statistically independent spectral regimes of the contributing irregularities. From these relations we can calculate the signal moments that describe the field as a function of parameters that characterize the spectrum of the ionospheric irregularities. This constitutes the formal basis of all the propagation computations used in the IONSCNT code.

3. SCINTILLATION MORPHOLOGY

3.1 Controlling Parameters

As will be outlined in Section 4, two computer codes have been developed in this work. There are two operational modes in the main code, IONSCNT, one to provide first-order signal-statistical parameters and one to provide second-order quantities. The ultimate outputs of the first-order mode are the six sigmas that characterize the two-component model and the scintillation indices for phase, ϕ, and intensity, I, which are defined respectively as follows:

$$\phi_{rms} \overset{\Delta}{=} \left[\langle\phi^2\rangle - \langle\phi\rangle^2\right]^{1/2} \tag{16}$$

$$S_4 \overset{\Delta}{=} \frac{\left[\langle I^2\rangle - \langle I\rangle^2\right]^{1/2}}{\langle I\rangle} \tag{17}$$

According to the two-component model, the phase and intensity scintillation indices for the composite signal are given in terms of those for the scatter and focus components as:

$$\phi_{rms}^2 = \phi_{rmss}^2 + \phi_{rmsf}^2 \tag{18}$$

and

$$S_4^2 = \left(S_{4s}^2 + 1\right)\left(S_{4f}^2 + 1\right) - 1. \tag{19}$$

The component indices are obtained as follows. The most complicated is the phase scintillation index for the scatter component. It is obtained by performing the following two integrations:

$$\left\langle\phi_s\right\rangle = \int_o^{2\pi}\ \phi_s\ P_h\left(\phi_s;\ \sigma_{x_s},\ \sigma_{y_s},\ \sigma_{x_s y_s}\right) d\phi_s \tag{20a}$$

and

$$\left\langle\phi_s^2\right\rangle = \int_o^{2\pi}\ \phi_s^2\ P_H\left(\phi_s;\ \sigma_{x_s},\ \sigma_{y_s},\ \sigma_{x_s y_s}\right) d\phi_s \tag{20b}$$

over P_H, the Hatfield phase distribution for a signal with complex Gaussian statistics. The Hatfield distribution (HATFIELD and RINO, 1975) is specified by the three sigmas given in Eq. (15), with

$$R_s(0) = 1 - e^{-\sigma_s^2 L} \tag{21}$$

where σ_s^2 is a scattering coefficient per unit depth in a layer of thickness L [see Eq. (32)], and $B_s(0)$ is obtained from numerical evaluation of the diffraction integral. The quantities in Eq. (15) also are used

to calculate the intensity scintillation index for the scatter component, as follows:

$$S_{4s}^2 = 4\sigma_\chi^2 \left(1 - R_s(0) \right) + \left| B_s(0) \right|^2 \tag{22}$$

The phase and intensity scintillation indices for the focus component are calculated, respectively, as

$$\phi_{rmsf}^2 = \sigma_\phi^2 = \sigma_f^2 \, L - \sigma_\chi^2 \tag{23}$$

and

$$S_{4f} = e^{\sigma_\chi^2} - 1 \tag{24}$$

where $\sigma_f^2 L$ is the variance of the phase perturbation imposed by a layer of thickness L [see Eq. (31)], and σ_χ^2 is obtained from numerical evaluation of Eq. (9) for $\Delta\rho = 0$.

The propagation equations that govern $B_s(0)$, σ_χ^2 and $\sigma_{\chi\phi}$ [the latter obtained from Eq. (8)] depend upon the observing geometry relative to a horizontally stratified ionospheric layer and to a geomagnetic field model and upon several parameters that characterize the size and shape of ionospheric irregularities. The three-dimensional spatial power spectrum employed to describe the irregularities has a power-law form with a spectral index of minus four, corresponding to an in-situ (one dimensional) spectrum of κ^{-2}. Provision is made for anisotropy in two dimensions, one along the magnetic field and one perpendicular to the field. The spectrum over which the variance of ionospheric electron density, $\langle (\Delta N)^2 \rangle$, is modeled is limited by an outer-scale parameter, α_f, and the spectrum is divided into two components by means of an inner-scale cutoff for the focus component, β_f, and an outer-scale parameter for the scatter component, α_s.

3.2 Behavior of Axial Ratios, Scale Sizes, and Height

The axial ratios, a (along the field) and b (perpendicular to the geomagnetic meridian plane), were set to reproduce known geometrical characteristics of scintillation. Interferometer observations have shown that scintillation-producing irregularities are highly elongated along the magnetic field near the geomagnetic equator (e.g., KOSTER, KATSRIKU, and TETE, 1966). Recent studies by MARTIN and AARONS (1977) and by RINO (1977) indicate that high-latitude irregularities are somewhat elongated perpendicular to the geomagnetic meridian as well as along the magnetic field (i.e., that they are sheet-like along L-shells rather than axially symmetric along the field).

To include the foregoing experimental characteristics, the axial ratios a and b have been modeled as functions of geomagnetic latitude, λ_m, as follows:

$$a = 30 - 10 \left(1 + \mathrm{erf}\, \frac{\lambda_m - 20°}{3°} \right) \tag{25}$$

and

$$b = 1 + 2.5 \left(1 + \mathrm{erf}\, \frac{\lambda_m - \lambda_b}{3°} \right) \tag{26}$$

where λ_b demarks the geomagnetic latitude of the scintillation boundary between the midlatitude ionosphere and the subauroral ionosphere. Eq. (25) provides an along-field axial ratio of 30 near the geomagnetic equator, switching to 10 fairly abruptly at a geomagnetic latitude of 20°. Eq. (26) describes axial symmetry at latitudes equatorward of the scintillation boundary. Poleward of the boundary there is an additional elongation in the geomagnetic east-west direction, with a ratio of 6:1 (b = 6) relative to the remaining cross-field dimension.

The three scale parameters α_f, β_f, and α_s were established by iterative testing against signal-statistical samples obtained from passes of the DNA Wideband satellite. The most satisfactory fits were found to be different at different latitudes. (No data were available from the polar caps.) Variation of the scale-size parameters with geomagnetic latitude, λ_m has been modeled as follows:

$$\alpha_f = 900 + 850 \left(1 + \mathrm{erf}\, \frac{\lambda_m - 20°}{3°} \right) \text{ meters} \tag{27}$$

$$\beta_f = \alpha_f/2.5 \tag{28}$$

and

$$\alpha_s = \alpha_f/4 \tag{29}$$

Eq. (27) provides an outer scale (transverse to the magnetic field) of just under 1 km (i.e., approximately equal to the Fresnel-zone radius for VHF waves in the F layer) near the geomagnetic equator and of about 2.6 km poleward of 20° geomagnetic latitude. It is to be noted that the actual outer scale of ionospheric irregularities probably is considerably greater than one or a few kilometers; the present model accounts only for irregularities that produce scintillation, defined in terms of intensity fluctuation. Eqs. (28) and (29) are used to maintain effective continuity (between the focus and scatter components) of the spatial spectrum employed, while also safeguarding validity of the ray-optics approximation used for calculating propagation of the focus component of the perturbed wave.

The reason for employing a smaller outer scale in the equatorial region than elsewhere is that we have consistently observed with the DNA Wideband satellite that the ratio of S_4 to σ_ϕ is larger (unless, of course, S_4 is near its limiting value of approximately unity) in the equatorial region than elsewhere, for data processed in identical fashion. In terms of the phase-screen model, this observed fact means that a given level of phase perturbation (within the spatial spectrum admitted by 10-s detrending) results in stronger propagation effects (focusing and diffraction) near the equator than at higher latitudes. Employing a smaller outer scale for a given level of $\langle (\Delta N)^2 \rangle$ is one way of accounting for such behavior. A sys-

tematic decrease in the spectral index with decreasing latitude also could account for this effect. A variable spectral index, however, greatly complicates the computer code. Thus, we have not incorporated this option.

A greater propagation distance (i.e., employing a greater scattering-layer height) also increases the level of intensity scintillation. There is evidence from backscatter observation (WOODMAN and LA HOZ, 1976), for development of fine structure from the bottomside to the topside of the equatorial ionosphere. We have incorporated a simple latitude dependence of scattering-layer height in the model, as follows:

$$H = 500 - 75 \left(1 + \mathrm{erf} \frac{\lambda_m - 20°}{3°} \right) \mathrm{km} \tag{30}$$

which places the center of the layer at 350 km at geomagnetic latitudes greater than about 20° and at 500 km near the magnetic equator.

3.3 Behavior of Scattering Strength

Once geometrical and signal-statistical behavior is modeled by choice of axial ratios, scale sizes, and height, the worldwide morphological behavior of scattering strength is the dominant consideration for scintillation modeling. The total disturbance imposed on the wave consists of the wavefront perturbation imparted by both the focus and scatter portions of the spatial spectrum whose integral is $\langle (\Delta N)^2 \rangle$. For the focus component, the variance of the phase perturbation imposed by a layer of thickness L is given by

$$\sigma_f^2 L = r_e^2 \lambda^2 \frac{ab \sqrt{\alpha_f \beta_f} \langle (\Delta N)_f^2 \rangle}{G \cos \theta} L \sec \theta \left[\sqrt{2\pi} \frac{K_1 \left(2\beta_f / \alpha_f \right)}{K_2 \left(2\beta_f / \alpha_f \right)} \right] . \tag{31}$$

The corresponding quantity for the scatter component is

$$\sigma_s^2 L = r_e^2 \lambda^2 \frac{ab\alpha_s \langle (\Delta N)_s^2 \rangle}{G \cos \theta} L \sec \theta \tag{32}$$

where θ is the incidence angle on the layer, G depends on details of the scattering geometry through the anisotropy of the irregularities*, r_e is the classical electron radius, λ is the radio wavelength, and the K's denote modified Bessel functions.

All the geophysical parameters in Eqs. (31) and (32) were discussed in Section 3.2, except L and $\langle (\Delta N)^2 \rangle = \langle (\Delta N)_s^2 \rangle + \langle (\Delta N)_f^2 \rangle$. In conjunction with the latitudinal dependence of layer height, the layer thickness also was modeled as a simple function of geomagnetic latitude, as follows:

$$L = 200 - 50 \left(1 + \mathrm{erf} \frac{\lambda_m - 20°}{3°} \right) \mathrm{km} \tag{33}$$

With α_f and α_s set, the relative amount of perturbation assigned to the focus and scatter components is that required for their respective spectra to be asymptotically continuous. The condition is

$$\langle (\Delta N)_f^2 \rangle = \frac{\alpha_f}{\alpha_s} \langle (\Delta N)_s^2 \rangle . \tag{34}$$

Finally, observed morphological characteristics of intensity and phase scintillation were invoked to write the following mean, morphological description of $\langle (\Delta N)^2 \rangle$

$$\langle (\Delta N)_s^2 \rangle^{\frac{1}{2}} = \Delta N_m \left(\lambda_m, T \right) + \Delta N_h \left(\lambda_m, T, K_p \right) + \Delta N_a \left(\lambda_m, T, K_p \right)$$
$$+ \Delta N_e \left(\lambda_m, \lambda_g, T, D, R \right) . \tag{35}$$

The first two terms and the last term on the right of Eq. (35) account for behavior at, respectively, middle, high, and equatorial latitudes, as functions of geomagnetic latitude, λ_m, geographic latitude, λ_g, local time of day in hours, T, day of the year, D, mean sunspot number, R, and the planetary magnetic activity index, K_p. The third term in Eq. (35) accounts for scintillation associated with the auroral oval.

The midlatitude term, centered at a geomagnetic latitude of 32.5°, contains only a simple diurnal variation, as follows:

$$\Delta N_m = 1.3 \times 10^9 \left(1 + 0.33 \cos \frac{\pi T}{12} \right) \exp \left[\frac{\left(\lambda_m - 32.5° \right)^2}{\left(15° \right)^2} \right] . \tag{36}$$

The high-latitude term,

$$\Delta N_h = 3 \times 10^9 \left(1 + \mathrm{erf} \frac{\lambda_m - \lambda_b}{\lambda_h} \right) \mathrm{el/m}^3, \tag{37}$$

dominates poleward of the scintillation boundary, the geomagnetic latitude and width of which vary with magnetic activity and time of day as follows:

$$\lambda_b = 68.5 - 1.8 K_p - \left(5 + 0.5 K_p \right) \cos \frac{\pi T}{12} \mathrm{deg} \tag{38}$$

---

* $G = \sqrt{(AC - B^2/4)}$; see RINO and FREMOUW (1977)

$$\lambda_h = 5 + 0.2 \lambda_b \text{ deg} \quad . \tag{39}$$

Superimposed on the high-latitude term is the following auroral-oval term:

$$\Delta N_a = 3.2 \times 10^8 \ K_p \exp\left[-\frac{\left(\lambda_m - \lambda_a\right)^2}{\left(1.1 \ K_p\right)^2} \right] \text{el/m}^3 \tag{40}$$

where

$$\lambda_a = 74 - 1.8 \ K_p \cos \frac{\pi T}{12} \text{ deg} \quad . \tag{41}$$

The most complicated term in the morphological model is the following one describing behavior near the geomagnetic equator:

$$\Delta N_e = 2.3 \times 10^9 \ (1 + 0.04R) \left\{ \exp\left[-\frac{\left(\lambda_m - 10°\right)^2}{(10°)^2} \right] + \exp\left[-\frac{\left(\lambda_m + 10°\right)^2}{(10°)^2} \right] \right\} \tag{42}$$

$$\left\{ 1 - 0.4 \left[\cos \frac{\pi(D + 10)}{91} + \frac{\lambda_g}{15°} \cos \frac{\pi(D + 10)}{182} \right] \right\} \ \left\{ \exp\left[-\frac{(T + 1.5)^2}{(6)^2} \right] + \exp\left[-\frac{(T - 22.5)^2}{T_R^2} \right] \right\} \text{el/m}^3$$

where

$$T_R = \frac{3}{6} \text{ if } T \lessgtr 22.5 \quad . \tag{43}$$

Eq. (42) describes a region of disturbance that peaks some 10° on each side of the geomagnetic equator. This somewhat speculative morphological behavior has been invoked to account for a very persistent feature of scintillation observed at Ancon, Peru and Kwajalein, Marshall Islands (both within a few degrees of the magnetic equator) on signals from the DNA Wideband satellite. The persistent behavior is an increase in scintillation near the ends of satellite passes that is stronger than we have been able to account for on the basis of any purely geometrical feature of the model.

Eq. (42) also includes a linear increase of scintillation activity with increasing sunspot number and a diurnal peak somewhat before local midnight, with activity increasing rather rapidly after F-layer sunset and decaying more slowly after the peak. The seasonal variation includes equinoctial peaking but with a "filling in" of activity in the local summer season (i.e., centered on the December solstice in the geographic southern hemisphere and on the June solstice in the geographic northern hemisphere). This somewhat complicated behavior is consistent with differences in seasonal patterns observed at Kwajalein and at Ancon and reproduces reasonably well the equinoctial peaking observed by KOSTER (1966) and KOSTER, KATSRIKU , and TETE (1966) for observations at a station near the geographic equator in Africa; it is untested at other locations, however.

4. COMPUTER CODES

Two user codes were developed in this work: IONSCNT for calculating first-order and second-order signal-statistical moments, including scintillation indices for intensity and for phase and several correlation functions; and DIST for calculating first-order, probability-density functions for intensity and phase and the corresponding cumulative distribution functions.

Figure 4 shows a simplified, overall flow diagram for IONSCNT. The user inputs a set of selected ionospheric state parameters plus a description of his intended operational geometry. The code then calculates the appropriate ionospheric structure parameters from the morphological model contained in subroutines RMSDN and MDLPRM. The quantities relevant to the scatter and focus components are passed to routines for calculating diffraction and geometric-optics propagation effects, respectively.

The outputs from IONSCNT always include the intensity and phase scintillation indices, S_4 and ϕ_{rms}, and the six sigmas that describe the two-component, first-order, signal-statistical model. If the user has selected operating Mode II, second-order statistical counterparts are put out as well, including the temporal autocorrelation functions of intensity and phase, analogous information on the spatial autocorrelation function, and (if requested) the correlation coefficient for intensity fluctuations on two user-selected frequencies.

The temporal autocorrelation functions are computed from the calculated spatial autocorrelation function, using a velocity that accounts both for line-of-sight motion through the F layer and an assumed drift of otherwise unchanging ionospheric structure. The drift velocity is eastward at a speed given by the following geomagnetic-latitude-dependent model:

$$V_d = 50 - 15 \left(1 + \text{erf} \frac{\lambda_m - 20°}{3°} \right) + 40 \left(1 + K_p \right)\left(1 + \frac{\lambda_m - \lambda_b}{3°} \right) \tag{44}$$

which yields 50 m/s in the equatorial zone, 20 m/s at middle latitudes, and upwards of 100 m/s poleward of the subauroral scintillation boundaries depending on the level of geomagnetic disturbance.

An example of the Mode-I output of IONSCNT is presented in Figure 5. The increase in scintillation early in the second half of the pass arises from a combination of (1) geometric enhancement by sheet-like irregularities as the line of sight grazes the L-shell through the station, and (2) a contribution from the auroral term in Eq. (35). Graphs of S_4 and ϕ_{rms} for a representative pass of the Wideband satellite observed at Poker Flat, Alaska under the specified conditions are shown in Figure 6 for comparison. Note

that the pass illustrated was one of those used in iterative testing of the model; it was chosen as one representative of scintillation in Alaska under the specified conditions (including moderate magnetic activity). A range of scintillation behavior presumably would be observed for the same set of specified state parameters, and the model does not account for such variations.

In addition to the scintillation indices, the output illustrated in Figure 5 gives relatively subtle signal-statistical information, in the form of the six sigmas (four variances and two covariances) that characterize the two first-order, signal-statistical components. They appear in the six columns following the transmitter latitude and longitude and the angle (PSIBP) between the line of sight and the geomagnetic field. Taking point 8 in Figure 5 as an example, we have $\sigma_x^2 = 0.055$, $\sigma_y^2 = 0.271$, $\sigma_{xy} = -0.005$, $\sigma_\chi^2 = 0.000$, $\sigma_\phi^2 = 6.839$, $\sigma_{\chi\phi} = -0.002$.

By comparison, the corresponding values for a 30-s data segment (starting at 0217:35) recorded during a geometrically similar portion of the satellite pass illustrated in Figure 6 are 0.06, 0.27, -0.02; 0.01, 4.40, and -0.07. Similarities between the calculated and observed values suggest that the existing model would be useful for calculating the joint pdf of intensity and phase, if the joint statistics should be of interest for, say, optimal system design. Such a capability has not been incorporated in the present computer programs but could be added to the DIST code.

The DIST code now available permits calculation of distributions for amplitude (square root of intensity) and phase, separately. Examples are presented in Figure 7, using the six sigmas from point 8 of Figure 5 as inputs to DIST. As has been described fully by RINO et al (1977), the method of using DIST is to input the results of an IONSCNT calculation.

Figure 8 illustrates second-order outputs from IONSCNT, again using point 8 from Figure 5; the format is fully described in RINO et al (1977). The information provided can be used to characterize the spatial structure of the field as well as the temporal structure of intensity and phase. Figures 9, 10, and 11 are included to provide further information on the morphological behavior (and frequency dependence) of scintillation as characterized by IONSCNT. The reader will note that the code returns values of S_4 slightly larger than unity, which is the value corresponding to Rayleigh statistics, under extreme conditions. The two-component, signal-statistical model does permit values greater than unity in the presence of substantial focusing. The ray-optics approximation employed for calculating propagation of the focus component is not always fully satisfactory, and a limit on it has been incorporated in the code for conditions of strong scatter. It is to be noted that S_4 values up to 1.2 are observed occasionally, at least at VHF near the geomagnetic equator.

5. CONCLUSION

This paper summarizes work (reported more fully by FREMOUW et al, 1977) that began as an attempt to collate previously existing and highly fragmented scintillation data into a form useful for systems application. During the course of the work, both experimental and theoretical work on trans-ionospheric radio propagation progressed considerably. The major experimental development was the advent of complex-signal data from coherent radio beacons on the Navy navigation (Transit) satellites, ATS-6, and P76-5 (the DNA Wideband beacon). The theory of propagation in a random medium advanced both analytically and by application of numerical calculation to strong-scatter problems.

Availability of the coherent-beacon data has yielded much insight into the complex-signal statistics of scintillation, and this insight has been incorporated in our work to provide a signal-statistical model that is complementary to deterministic models of TEC effects. Our ability to incorporate the new experimental findings has been limited, however, by the theoretical framework we have employed. Signal-statistically, the most fundamental limitation of the present model is its heavy reliance on choice of an outer scale to describe scintillation-producing ionospheric structure. It is very likely that the outer scales invoked in the model (900 m in the equatorial region and 2.6 km elsewhere) have no geophysical significance; rather they represent the largest scales that contribute to intensity scintillation on the paths employed in collection of the data we used for quantitative calibration and iterative testing of the model. The paths employed were mainly between satellites in high-inclination, moderate-altitude (1000-km) orbits and the ground.

The main caution to be employed as a result of the outer-scale dilemma arises in application of the model to phase-sensitive systems where long-term stability is important, especially in the equatorial region. The user must always keep in mind that the rms phase fluctuations described by the code are those produced by ionospheric structures on the order of a kilometer and smaller in east-west extent near the equator (30 km and smaller in north-south extent). Phase trends due to larger-scale structure must be accounted for separately. For geostationary systems, this translates into time scales substantially longer than 20 s.

Morphologically, the most important limitation of the model is that it does not account for night-to-night departures of scintillation conditions on a given communication link during the same season, at the same local time, and under the same solar and geomagnetic conditions, which can be substantial. The model describes only the "expectation level" of scintillation for a specified set of observing conditions. Data now being accumulated could be employed to include a description of departures from mean scintillation conditions, but the present model stops short of doing so. Mean morphological limitations of the model include some uncertainty over long-term trends in activity during a solar cycle and virtual absence of any data from the polar caps for use in establishing the model.

Despite the foregoing limitations, the model described in this report is the most extensive computer-coded assimilation of scintillation information presently available for systems planning. It will provide systems-relevant characterization of scintillation for a wide range of operating circumstances. Hopefully it also can serve as a baseline for analysis of existing and forthcoming scintillation data, in attempts to understand the nature and dynamics of ionospheric structure.

REFERENCES

AARONS, J., H.E. WHITNEY, and R.S. ALLEN (1971), "Global Morphology of Ionospheric Scintillation", Proc. IEEE, Vol. 59, No. 2, pp. 159-172.

BECKMAN, P., and A. SPIZZICHINO (1963), The Scattering of Electromagnetic Waves from Rough Surfaces, pp. 119-136, Pergamon Press, New York, N.Y.

BRAMLEY, E.N. (1955), "Some Aspects of the Rapid Directional Fluctuations of Short Radio Waves Reflected at the Ionosphere", Proc. IEEE, Vol. 102, pp. 533-540.

FREMOUW, E.J. and C. L. RINO (1975), "Ionospheric and Tropospheric Scintillation as a Form of Noise", in AGARD Conference Proceedings No. 159 on Electromagnetic Noise Interference and Compatibility.

FREMOUW, E.J. and C.L. RINO (August, 1976), "Continued Modeling of Transionospheric Radio Propagation", Quarterly Technical Report 4, Contract F30602-75-C-0236, SRI Project 4259, SRI International, Menlo Park, CA.

FREMOUW, E.J., C.L. RINO, A.R. HESSING, and V.E. HATFIELD (July, 1977), "A Transionospheric Communication Channel Model", Quarterly Technical Report 7, Contract F30602-75-C-0236, SRI Project 4259, SRI International, Menlo Park, CA.

FREMOUW, E.J., R.L. LEADABRAND, R.C. LIVINGSTON, M.D. COUSINS, C.L. RINO, B.C. FAIR, and R.A. LONG (1978), "Early Results from the DNA Wideband Satellite Experiment - Complex-Signal Scintillation", Radio Science, Vol. 13, No. 1.

HATFIELD, V.E. and C.L. RINO (January 1975), "Non-Rician Statistics and Their Implications for Modeling Effects of Scintillation on Communication Channels", in The Effect of the Ionosphere on Space Systems and Communications, J.M. Goodman, ed., Naval Research Laboratory, Washington, D.C.

KLOBUCHAR, J.A. (September 25, 1975), "A First-Order Worldwide, Ionospheric, Time-Delay Algorithm", Report AFCRL TR-75-0502, Air Force Cambridge Research Laboratory, Hanscom AFB, Mass.

KOSTER, J.R. (1966) "Equatorial Studies of the VHF Signal Radiated by Intelsat II, F-3; 1. Ionospheric Scintillation", Progress Report No. 3, Contract No. F61052-67-C-0027, University of Ghana-Legon, Accra, Ghana.

KOSTER, J.R., I. KATSRIKU, and M. TETE(1966), "Studies of the Equatorial Ionosphere Using Transmission from Active Satellites", Annual Summary Report 1, Contract AF61(052)-800, University of Ghana-Legon, Accra, Ghana.

MARTIN, E. and J. AARONS (1977), "F Layer Scintillations and the Aurora", J. Geophys. Res., Vol. 82, No. 19, pp. 2717-2722.

RATCLIFFE, J.A. (1956), "Some Aspects of Diffraction Theory and Their Application to the Ionosphere", Repts. Prog. Phys., Vol. XIX, pp. 188-207.

RICE, S.O. (1945), "Mathematical Analysis of Random Noise", Part III, Bell Syst. Tech. J., Vol. 24, No. 1, pp. 47-159.

RINO, C.L. (1977), "Evidence of Sheet-Like Irregularity Structures in the Diffuse Aurora", paper presented at IAGA/IMAP Meeting, Seattle, WA., August 22-September 3.

RINO, C.L. and E.J. FREMOUW (1973), "Statistics for Ionospherically Diffracted VHF/UHF Signals, Radio Science, Vol. 8, No. 3, pp. 223-233.

RINO, C.L. and E.J. FREMOUW (1977), "The Angle Dependence of Singly Scattered Wavefields", J. Atmos. Terr. Phys., Vol. 39, pp. 859-868.

RINO, C.L., R.C. LIVINGSTON, and H.E. WHITNEY (1976), "Some New Results on the Statistics of Radio Wave Scintillation 1. Empirical Evidence for Gaussian Statistics", J. Geophys. Res., Vol. 81, No. 13, pp. 2051-2057.

RINO, C.L., A.R. HESSING, V.E. HATFIELD, and E.J. FREMOUW (July, 1977), "Two FORTRAN Programs for Calculating Global Ionospheric Amplitude and Phase Scintillation", Quarterly Technical Report 8, Contract F30602-75-C-0236, SRI Project 4259, SRI International, Menlo Park, CA.

WHITNEY, H.E., J. AARONS, and D.R. SEEMAN (1972), "Estimation of the Cumulative Amplitude Probability Distribution Function of Ionospheric Scintillations", Radio Science, Vol. 7, pp. 1095-1104.

WOODMAN, R.F. and C. LA HOZ (1976), "Radar Observations of F-Region Equatorial Irregularities", J. Geophys. Res., Vol. 81, No. 31, pp. 5447-5466.

ACKNOWLEDGEMENT

TABLE 1

Symbol	Definition
$\Delta N(\vec{r}, z)$	*Local electron density perturbation*
$\vec{\rho} = \vec{r} + \hat{a}_z z$	*Distance from origin of coordinates*
$\vec{r}$	*Component of $\vec{\rho}$ parallel to layer*
z	*Component of $\vec{\rho}$ normal to layer*
$\vec{k}$	*Principal propagation vector*
$\vec{\ell}$	*Distance vector in $\vec{k}$ direction*
λ	*Wavelength*
θ	*Incidence angle of $\vec{k}$*
ϕ	*Azimuth angle of $\vec{k}$ (measured from geomagnetic meridian plane)*
$\vec{k}_T (\theta, \phi)$	*Transverse component of $\vec{k}$*
$a_{11} = 1 + \tan^2\theta \cos^2\phi$	
$a_{12} = \tan^2\theta \sin\phi \cos\phi$	*Geometric coefficients*
$a_{22} = 1 + \tan^2\theta \sin^2\phi$	
σ_f^2	*Lineal phase-perturbation coefficient*
σ_s^2	*Lineal scattering coefficient*
L	*Layer thickness*
r_e	*Classical electron radius*
$A(\theta, \phi, \psi, a, b, \delta)$	
$B(\theta, \phi, \psi, a, b, \delta)$	*Geometrical coefficients defined by RINO and FREMOUW (1977)*
$C(\theta, \phi, \psi, a, b, \delta)$	
ψ	*Magnetic dip angle*
a	*Elongation parameter along magnetic field*
b	*Elongation parameter transverse to magnetic field*
δ	*Inclination angle of transverse irregularity axis*
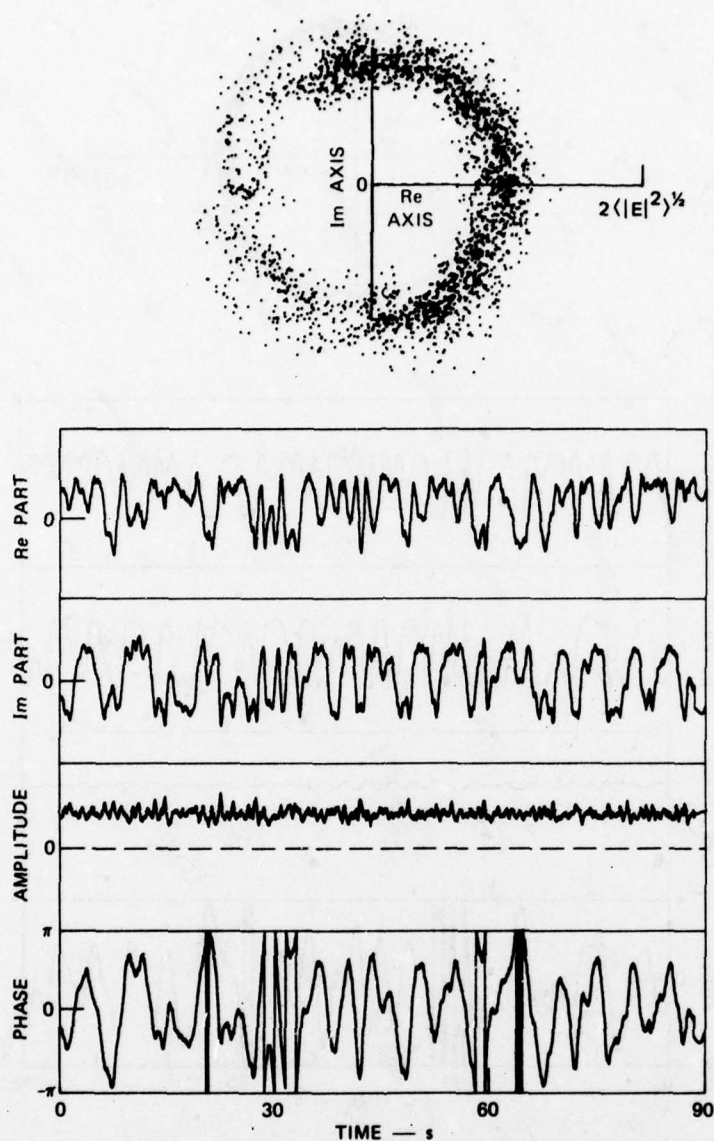
Fig.1   Three representations of VHF (138 MHz) complex-signal fluctuations during 90 s of a satellite pass over Stanford, California. Top to bottom: Scatter plot on complex plane; real and imaginary parts of complex signal; amplitude and phase of complex signal. Intensity and phase scintillation indices are $S_4 = 0.28$ and $\sigma_\phi = 1.58$ rad, respectively
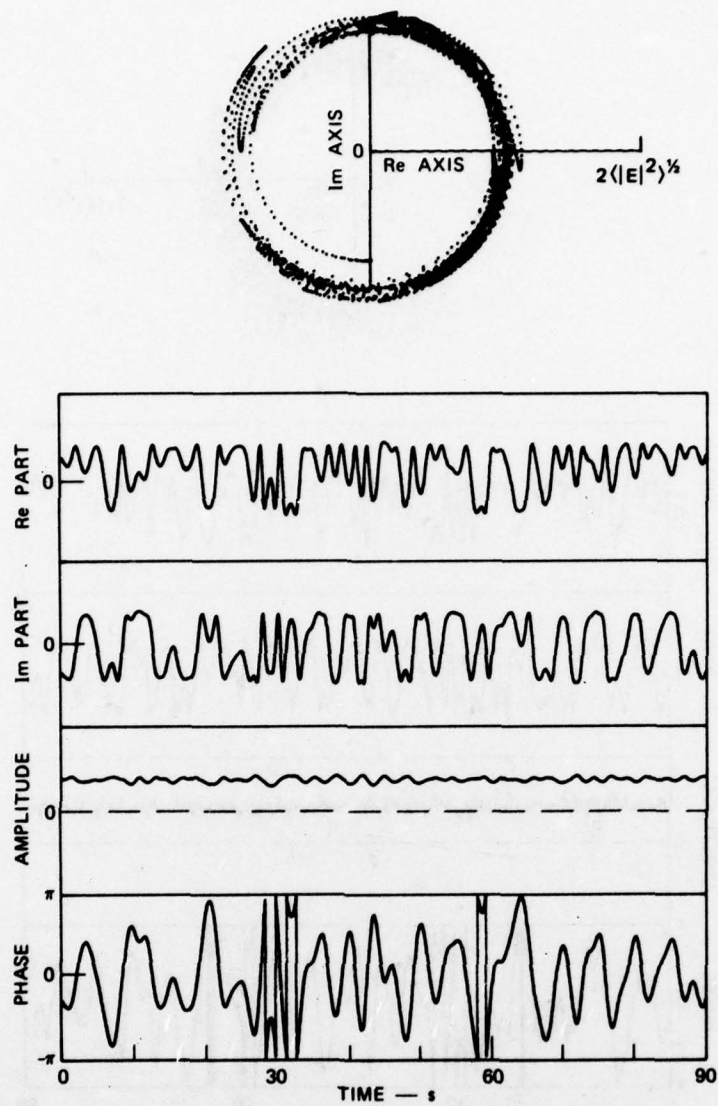
Fig.2 The focus component (containing intensity and phase fluctuations with Fourier periods between 2.5 and 10 s) of the complex-signal scintillation presented in Figure 1
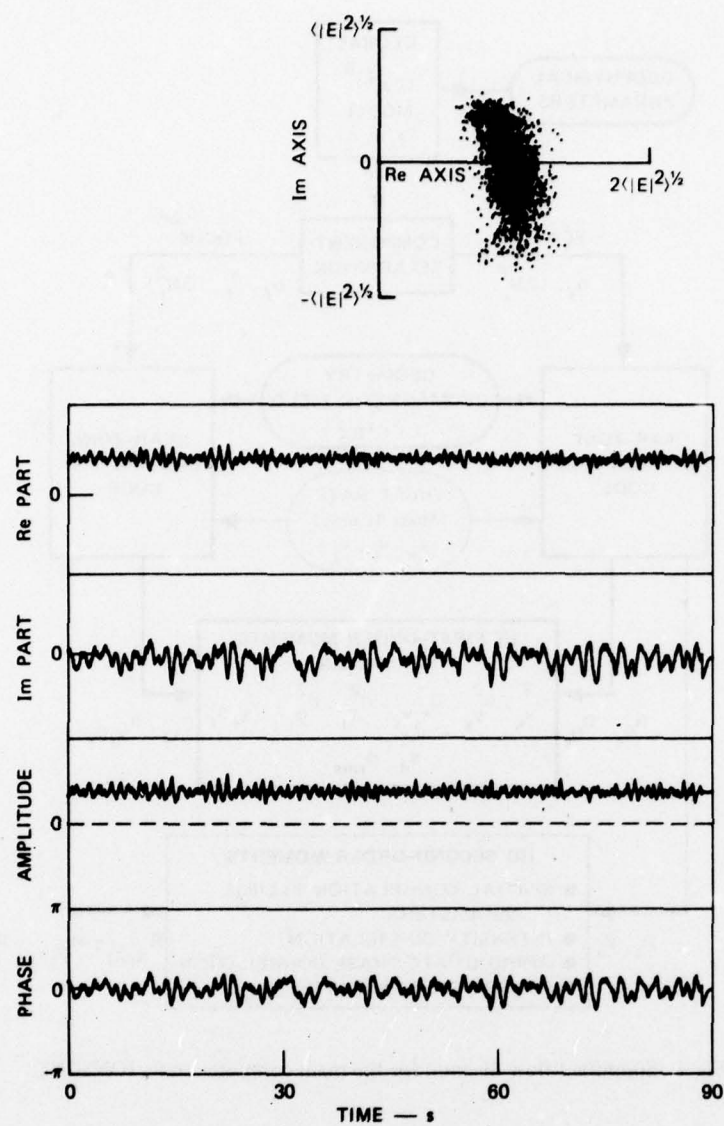
Fig.3 The scatter component (containing intensity and phase fluctuations with Fourier periods shorter than 2.5 s) of the complex-signal scintillation presented in Figure 1
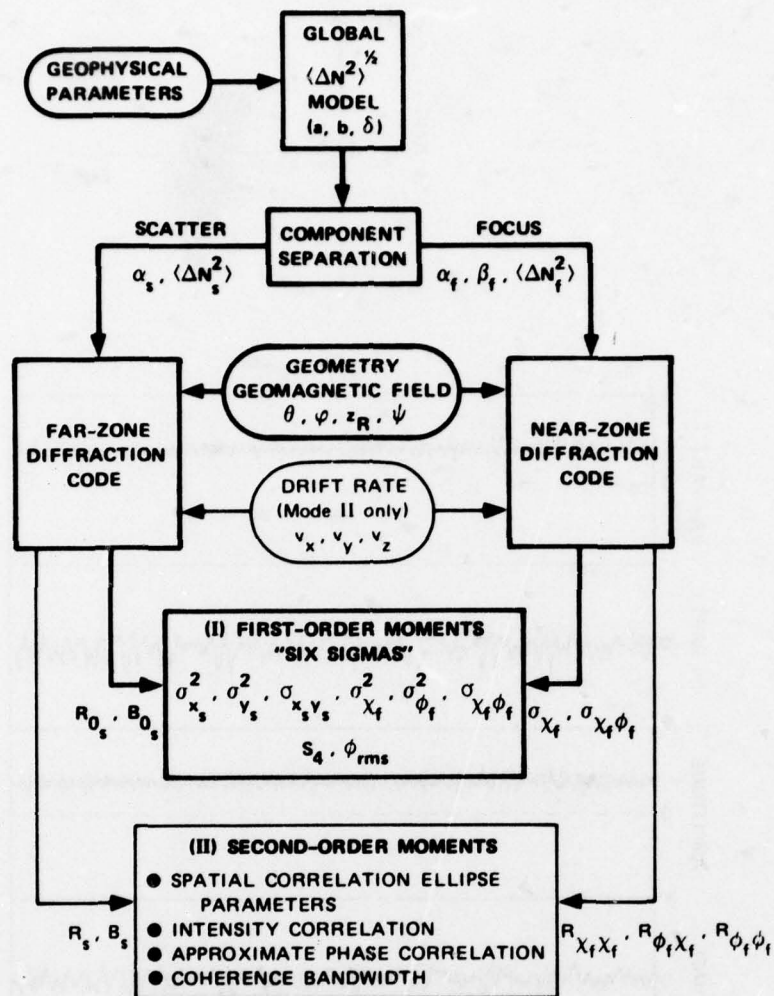
Fig.4 Simplified flow diagram for the main computer code, IONSCNT

F-LAYER PRODUCED VHF-UHF SCINTILLATION

CALCULATED FROM A MODEL DEVELOPED BY STANFORD RESEARCH INSTITUTE,
MENLO PARK, CALIFORNIA.

AURORAL

INPUT CONDITIONS USED FOR THIS CALCULATION WERE :

FREQUENCY= 137.68 MHZ   SUNSPOT NO.= 50.   DAY 150, OUT OF 365   KP INDEX = 5.00   TIME= 2.30 LMT AT RECEIVER

RECEIVER COORDINATES   LAT= 65.13 DEG   LONG=-147.49 DEG   ALT= .195 KM
TRANSMITTER COORDINATES   LAT= 79.00 DEG   LONG= -80.30 DEG   ALT= 1000.000 KM   FOR FIRST ORBIT POINT

(FOR THIS RUN, THE CHANGING PARAMETERS WERE: TRANSMITTER LATITUDE AND LONGITUDE ALONG ORBIT)

#	T-LAT	T-LONG	PSIBP	SGX2	SGY2	CRXY	SGLA2	SGPH2	CRLAPM	S4	PRMS
1	79.393	-86.332	76.364	.07756	.31279	-.00032	.00001	8.59309	-.00323	.63904	171.489
2	80.042	-95.056	75.875	.07066	.30171	-.00019	.00001	8.08837	-.00286	.60189	166.357
3	80.249	-104.801	74.875	.06357	.28934	-.00408	.00000	7.55634	-.00251	.58323	160.803
4	79.909	-117.478	73.317	.05706	.27697	-.00398	.00000	7.05897	-.00422	.55859	155.399
5	79.294	-125.035	71.158	.05191	.26636	-.00391	.00000	6.65264	-.00199	.53750	150.865
6	78.243	-138.900	68.364	.04890	.25972	-.00393	.00000	6.40872	-.00186	.52541	148.079
7	76.919	-147.012	64.967	.0911	.25992	-.00012	.00000	6.21886	-.00187	.5271	148.156
8	75.398	-152.593	61.064	.05458	.27097	-.00467	.00000	6.03920	-.00214	.5487	152.963
9	73.735	-158.937	57.024	.07024	.24985	-.00593	.00001	7.99800	-.00301	.60492	165.425
10	71.968	-163.316	53.303	.10933	.35111	-.00856	.00002	10.71388	-.00580	.71192	191.679
11	70.126	-166.951	50.524	.20584	.42735	-.01260	.00011	17.41688	-.01740	.86501	245.460
12	68.228	-170.010	49.081	.36895	.48433	-.01151	.00027	33.32540	-.0551	.58650	339.896
13	66.287	-172.620	48.924	.36639	.48413	-.01123	.00066	33.00260	-.05055	.98001	338.262
14	64.313	-174.875	49.656	.27195	.45839	-.01246	.00015	22.75736	-.0201	.9271	281.021
15	62.313	-176.849	50.801	.21471	.43300	-.01164	.00006	18.11635	-.0128	.6775	250.226
16	60.292	-178.595	51.992	.18077	.41259	-.01140	.00003	15.62494	-.00919	.8701	232.278
17	58.254	179.845	52.997	.15357	.39148	-.01140	.00002	13.69480	-.00748	.7906	217.190
18	56.202	177.438	53.690	.12548	.36547	-.01170	.00002	11.72445	-.00641	.7484	200.869
19	54.140	177.158	54.009	.09571	.32973	-.01197	.00002	9.62259	-.00056	.67958	181.572
20	52.068	175.985	53.926	.06829	.28620	-.01211	.00002	7.60016	-.00491	.5917	161.260
21	49.988	174.903	53.436	.04777	.24080	-.01276	.00002	5.91220	-.00086	.5019	142.242

* INDICATES ACCURACY OF VALUE MAY BE QUESTIONABLE DUE TO POOR INTEGRATION CONVERGENCE

Fig.5   Example of mode-I output for IONSCNT. The intensity and phase scintillation indices (S4 and PRMS, respectively) appear in the rightmost two columns
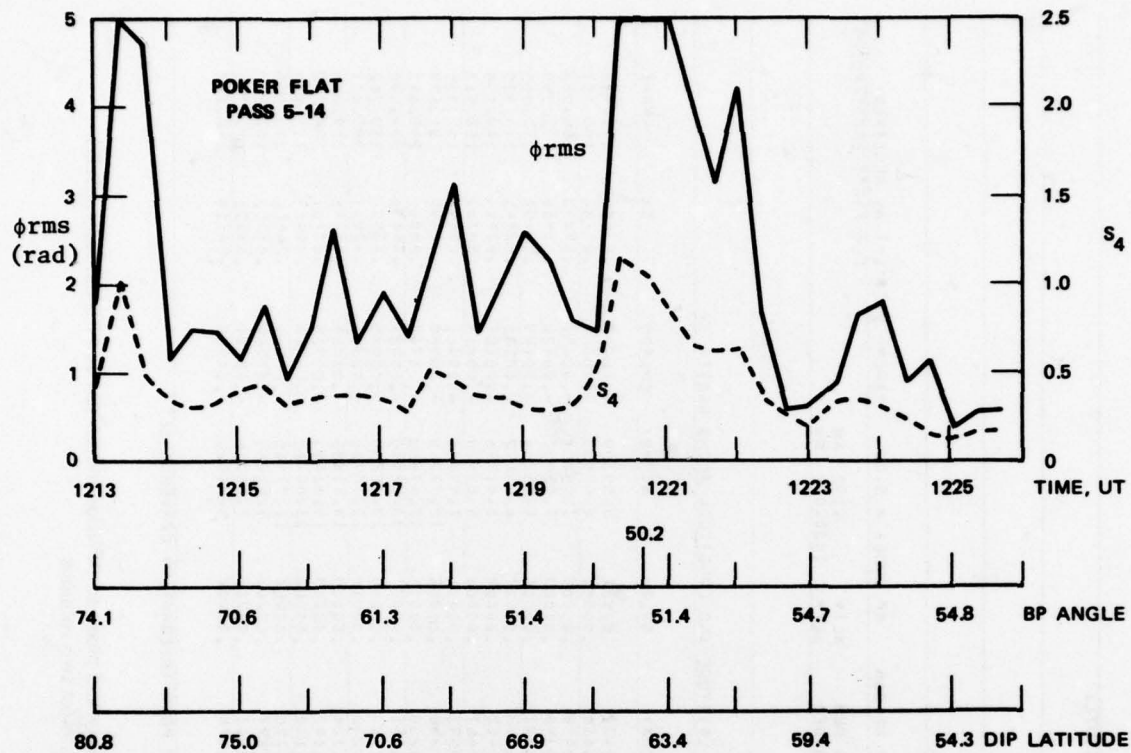
Fig.6 Standard summary display of VHF (138 MHz) intensity and phase scintillation indices
(S_4 and σ_ϕ, respectively) observed in Alaska on a particular satellite pass under conditions
approximated by the input conditions for the calculation illustrated in Figure 5

PARAMETERS FOR THE TWO-COMPONENT SCINTILLATION MODEL

S0X2= .05456 S0Y2= .27097 CRX0= -.00467 S0LA2= .00000 S0PH2= 6.03920 CRLAPH= -.00216

PROBABILITY DENSITY, P(A), VS. AMPLITUDE/UNDISTURBED AMPLITUDE

S0X2= .055 S0Y2= .27 CRX0= -.005 S0LA2= .000 S0PH2= 6.04 CRLAPH= .00

A	P(A)	A	P(A)	A	P(A)	A	P(A)	A	P(A)	A	P(A)
.00	.000	.05	.001	.10	.002	.15	.006	.20	.012	.25	.025	.30	.049	.35	.079
.40	.132	.45	.208	.50	.311	.55	.445	.60	.607	.65	.701	.70	.905	.75	1.173
.80	1.338	.85	1.462	.90	1.533	.95	1.544	1.00	1.495	1.05	1.395	1.10	1.255	1.15	1.092
1.20	.920	1.25	.753	1.30	.000	1.35	.447	1.40	.356	1.45	.267	1.50	.197	1.55	.144
1.60	.104	1.65	.075	1.70	.052	1.75	.037	1.60	.026	1.65	.018	1.50	.013	1.65	.009
2.00	.005	2.05	.003	2.10	.002	2.15	.001	2.20	.000	2.25	.000	2.30	.000		

(a)

PROBABILITY DENSITY, P(A)

AMPLITUDE/UNDISTURBED AMPLITUDE
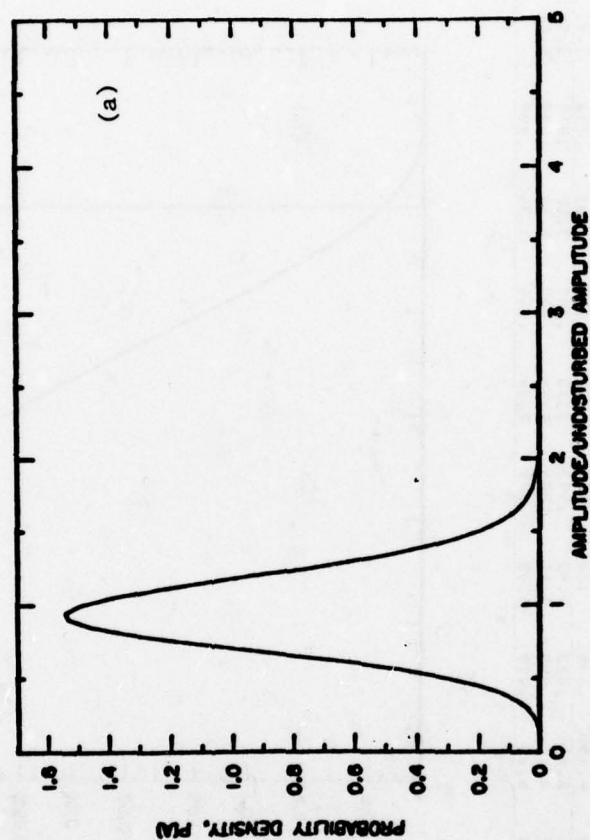
S0X2= .055 S0Y2= .27 CRX0= -.005 S0LA2= .000 S0PH2= 6.04 CRLAPH= .00

(a) Probability density function for amplitude

Fig.7 Example of outputs from dist code, using IONSCNT results from point 8 in Figure 5 as inputs

CUMULATIVE PROBABILITY: CPF, VS. SIGNAL STRENGTH IN DB RELATIVE TO UNDISTURBED LEVEL

SGX2= .055 SGY2= .27 CRXY= -.005 SGLA2= .000 SGPH2= 6.84 CRLAPH= -.00

DB	CPF	DB	CPF	DB	CPF	DB	CPF	DB	CPF	DB	CPF	DB	CPF	DB	CPF
-20.02	.000	-26.00	.000	-16.66	.000	-13.98	.001	-12.04	.002	-10.46	.003	-9.12	.006	-7.96	.012
-8.94	.020	-6.02	.033	-5.19	.033	-4.44	.078	-3.74	.113	-3.10	.157	-2.50	.211	-1.94	.274
-1.41	.344	-.92	.419	-.45	.496	.00	.573	.42	.645	.83	.711	1.21	.770	1.58	.820
1.96	.862	2.28	.896	2.61	.923	2.92	.963	3.23	.959	3.52	.970	3.61	.979	4.08	.965
4.35	.989	4.61	.992	4.86	.995	5.11	.996	5.34	.997	5.58	.998	5.80	.998	6.02	.999
6.24	.999	6.44	.999	6.65	.999	6.85	.999	7.04	.999	7.23	.999				

(b) Cumulative probability function for amplitude

SGX2= .055 SGY2= .27 CRXY= -.005 SGLA2= .000 SGPH2= 6.84 CRLAPH= -.00

Figure 7 continued

PROBABILITY DENSITY, P(PHI), VS. PHASE ANGLE IN RADIANS

SGX2= .055 SGY2= .27 CRXY= -.005 SGLA2= .000 SGPH2= 6.84 CRLAPH= -.00

PHI	P(PHI)	PHI	P(PHI)	PHI	P(PHI)	PHI	P(PHI)	PHI	P(PHI)	PHI	P(PHI)	PHI	P(PHI)	PHI	P(PHI)
-5.00	.0258	-4.90	.0277	-4.80	.0296	-4.70	.0316	-4.60	.0338	-4.50	.0360	-4.40	.0383	-4.30	.0408
-4.20	.0433	-4.10	.0459	-4.00	.0485	-3.90	.0513	-3.80	.0542	-3.70	.0571	-3.60	.0601	-3.50	.0632
-3.40	.0663	-3.30	.0695	-3.20	.0727	-3.10	.0760	-3.00	.0794	-2.90	.0827	-2.80	.0861	-2.70	.0895
-2.60	.0929	-2.50	.0963	-2.40	.0996	-2.30	.1030	-2.20	.1063	-2.10	.1095	-2.00	.1127	-1.90	.1159
-1.80	.1189	-1.70	.1219	-1.60	.1247	-1.50	.1275	-1.40	.1301	-1.30	.1326	-1.20	.1350	-1.10	.1372
-1.00	.1392	-.90	.1411	-.80	.1428	-.70	.1443	-.60	.1456	-.50	.1468	-.40	.1477	-.30	.1484
-.20	.1490	-.10	.1493	-.00	.1494	.10	.1493	.20	.1490	.30	.1485	.40	.1478	.50	.1468
.60	.1457	.70	.1444	.80	.1429	.90	.1412	1.00	.1394	1.10	.1373	1.20	.1351	1.20	.1328
1.40	.1303	1.50	.1277	1.60	.1250	1.70	.1221	1.80	.1192	1.90	.1161	2.00	.1130	2.10	.1058
2.20	.1065	2.30	.1032	2.40	.0999	2.50	.0965	2.60	.0931	2.70	.0897	2.80	.0863	2.90	.0830
3.00	.0796	3.10	.0763	3.20	.0730	3.30	.0697	3.40	.0665	3.50	.0634	3.60	.0603	3.70	.0573
3.80	.0544	3.90	.0515	4.00	.0488	4.10	.0461	4.20	.0435	4.30	.0409	4.40	.0385	4.50	.0362
4.60	.0340	4.70	.0318	4.80	.0298	4.90	.0278	5.00	.0259						

SGX2= .055 SGY2= .27 CRXY= -.005 SGLA2= .000 SGPH2= 6.84 CRLAPH= -.00

(c) Probability density function for phase

Figure 7 concluded

SECOND-ORDER OUTPUT FOR POINT 8

		SCAN			DIFFRACTION PATTERN		
		VEFF= 583.93 M/SEC			AXIAL RATIO= 3.53		
		AZ. OF SCAN= 28.55			AZ. OF MAJOR AXIS= -8.17		
LAG	LAG	PHASE AUTOCORRELATION FUNCTION			INTENSITY AUTOCORRELATION FUNCTION		
SEC	M	SCATTER	FOCUS	COMPOSITE	SCATTER	FOCUS	COMPOSITE
0.00	0.00	1.00000	1.00000	1.00000	1.00000	1.00000	1.00000
.30	319.51	.92913	.95629	.97264	.86940	.93938	.86940
.60	639.01	.81013	.98536	.97582	.70070	.78393	.70070
.90	958.52	.68558	.95774	.95237	.54864	.59396	.54844
1.20	1278.03	.56962	.94421	.92381	.43110*	.42615	.43109*
1.50	1597.53	.46736	.91573	.89132	.34282	.30942	.34282
1.80	1917.04	.37992	.88330	.85585	.27623	.24517	.27623
2.10	2236.55	.30667	.84740	.81843	.22487	.21963	.22446
2.40	2556.05	.24615	.81042	.77969	.18419	.21666	.18419
2.70	2875.56	.19668	.77164	.74034	.15127	.22310	.15127
3.00	3195.06	.15655	.73226	.70091	.12422	.23031	.12422

Fig.8 Example of mode-II output from IONSCNT. The temporal (lag shown in first column) and one-dimensional spatial (lag along drift direction of diffraction pattern shown in second column) auto-correlation functions of phase and intensity are shown in the fifth and eighth (rightmost) columns, respectively. Other columns give similar information for the focus and scatter components of the scintillating signal, individually. Geometrical information is given at the top
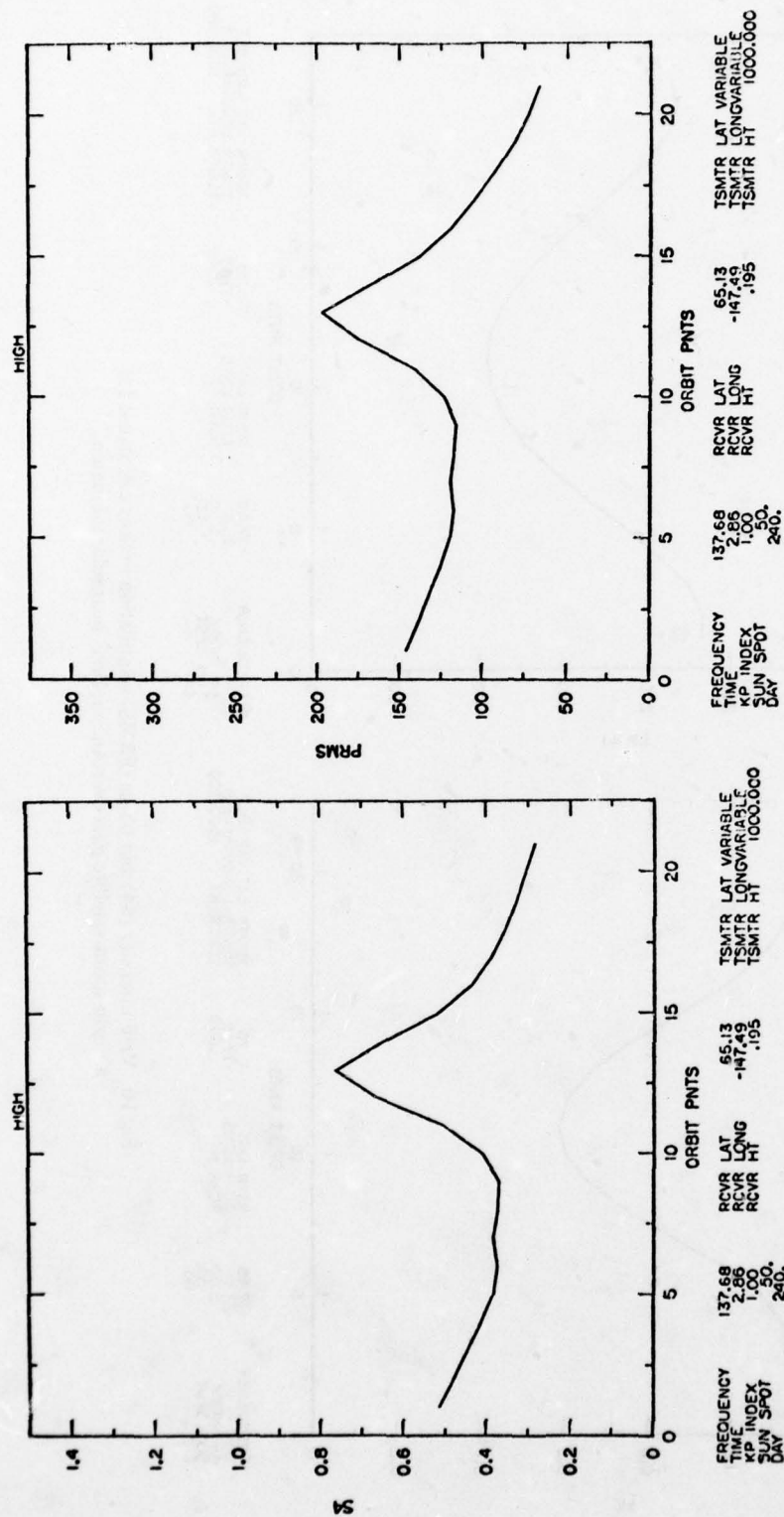
Fig. 9 VHF intensity (S4) and phase (PRMS) scintillation indices calculated for a satellite pass over Poker Flat, Alaska, under quiet geomagnetic conditions. In this case, the scintillation enhancement after mid-pass is primarily a geometric effect stemming from propagation nearly along sheet-like irregularities supposed to be aligned along L-shells
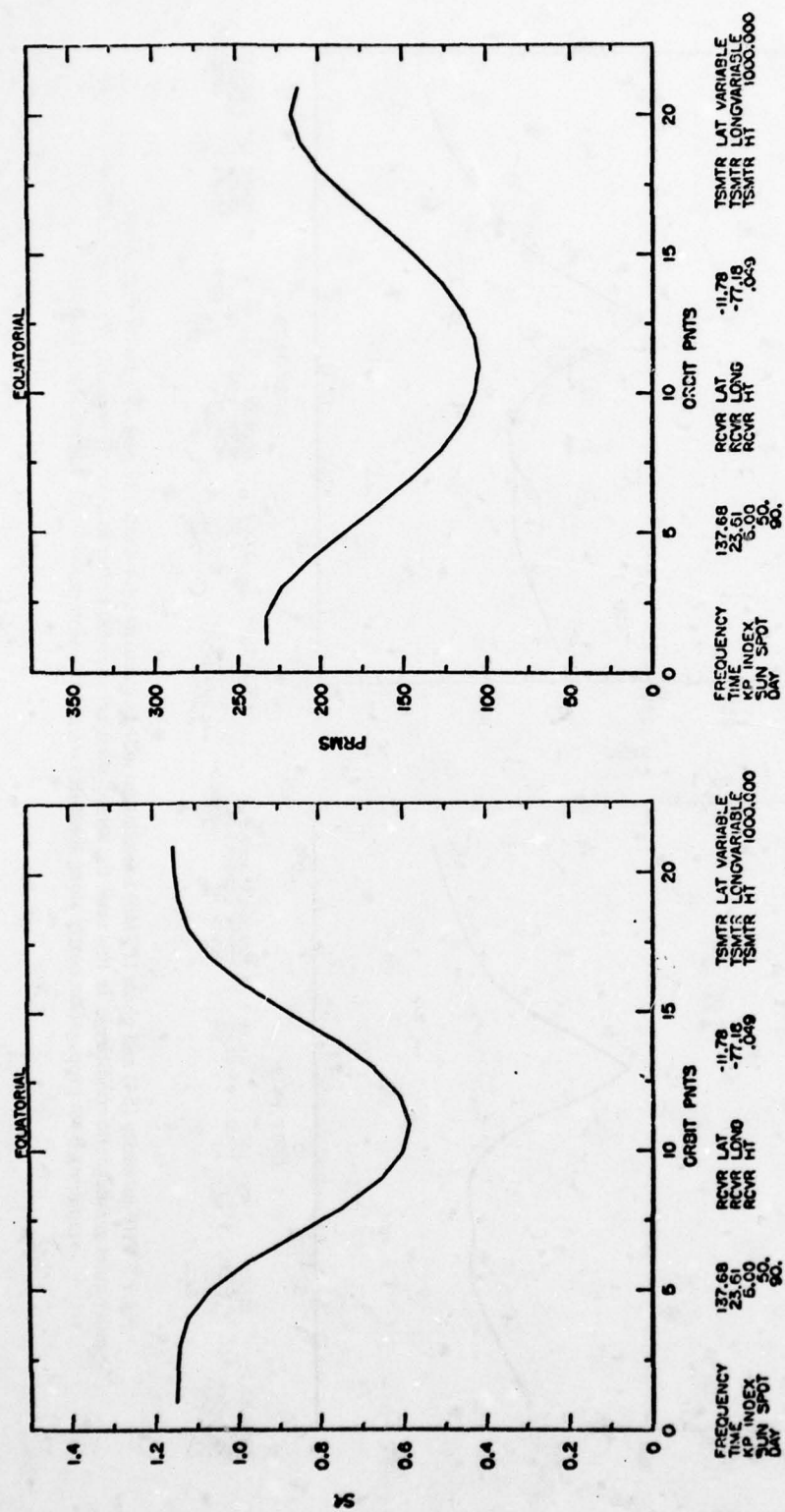
Fig.10 VHF intensity (S4) and phase (PRMS) scintillation indices calculated for
a north-south satellite pass over Ancon, Peru, near solar minimum

Fig.11 Calculated frequency dependence of average nighttime scintillation in the equatorial region near an equinox during a year of elevated solar activity. The code would predict Rayleigh statistics ($S_4 = 1.0$) under these conditions for frequencies below 50 MHz. The phase scintillation index (PRMS varies approximately as f^{-1})

DISCUSSION

J.Aarons, US

Since the scatter and focus components are both "multiplied" by the morphology terms, how do we know that both these components have the same morphology (or physics)?

Author's Reply

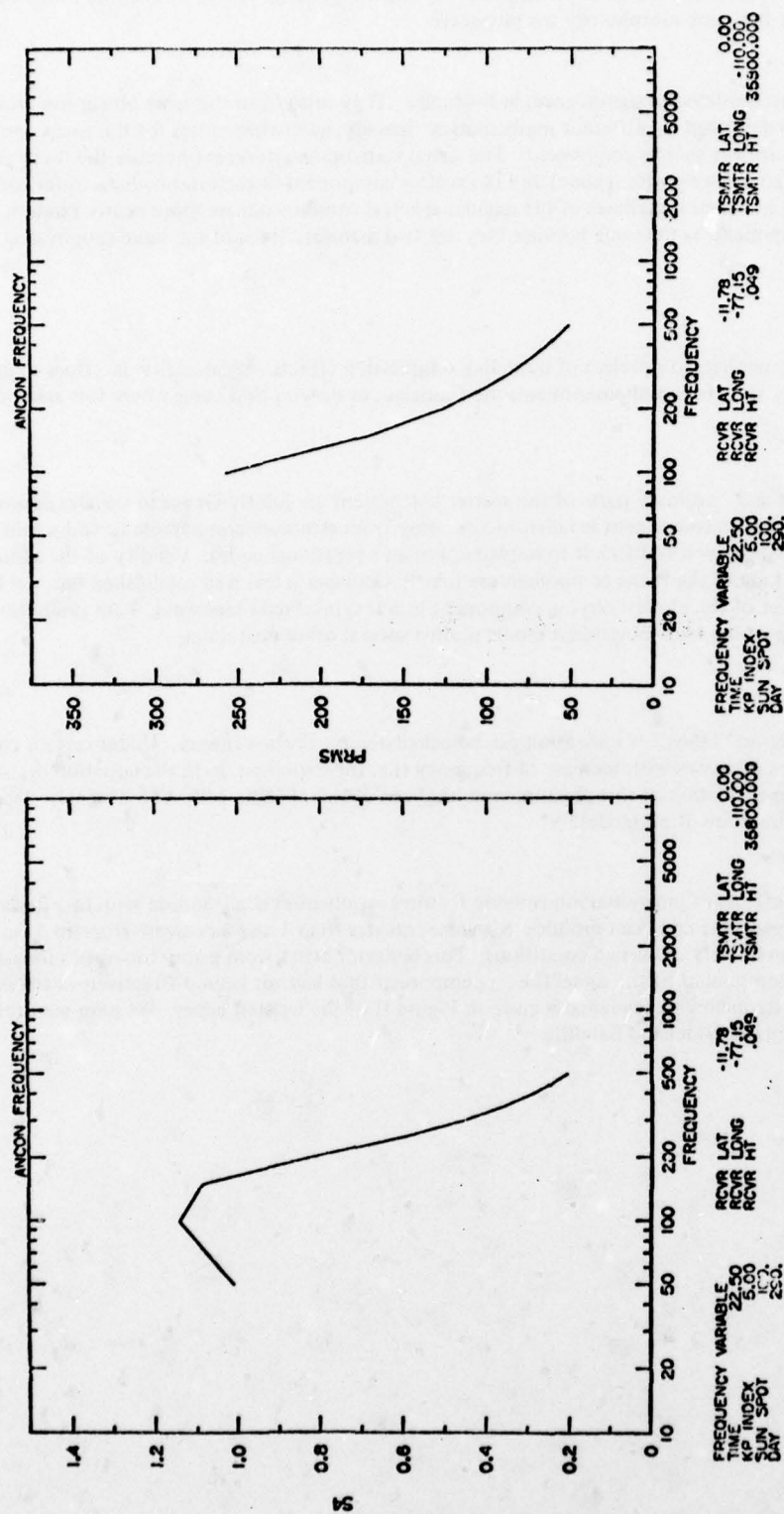The two components have no geophysical significance, individually. They arise from the same power-low irregularities, but their propagation is described by different mathematics: namely, geometric optics for the focus component and Fresnel diffraction for the scatter component. The signal statistics are different because the focus component is observed in the near zone (ray-optics regime) and the scatter component in the intermediate-to-far zone (Fresnel-diffraction regime), in which the phases of the angular-spectral components are more nearly random. The morphology of the two components is the same because they are two manifestations of the same geophysical phenomenon.

J.Röttger, FRG

I like your approach to the complicated problem of modeling scintillation effects. My question is: Does your assumption generally hold that the focussed components are Gaussian, or do you find cases where this assumption has to be modified?

Author's Reply

The assumption that the real and imaginary parts of the scatter component are jointly Gaussian variates seems to be quite good, especially if the scatter component is taken to arise only from structure comparable to and smaller than the first Fresnel zone (which, however, is difficult to implement in an operational code). Validity of the assumption that the phase and log-amplitude of the focus component are jointly Gaussian is less well established because there are fewer independent samples of this slowly varying component in our typical data segments. I am presently doing systematic hypothesis testing of the two-component model against several other postulates.

K.Davies, US

Deep fading produced by intense "blobs" of ionization can be calculated by Fresnel theory. Under certain conditions the calculated S_4 index increases with increase of frequency (i.e. the exponent n in the equation $S_4 \propto f^{-n}$ is negative). Experimental confirmation of this phenomenon has been found at India with ATS-6 signals. Does this phenomenon appear in the Fremouw-Rino model?

Author's Reply

The model does not address effects of individual ionospheric features – only effects of random structure described by a power-law spectrum. However, the code can produce S_4 values greater than 1 and a decrease (toward 1) in S_4 with decreasing frequency, under very disturbed conditions. This behavior arises from geometric-optics focusing and defocusing of a "coherent" component of the signal (i.e., a component that has not been diffractively scattered). An example of the resulting frequency dependence is given in Figure II of the written paper. We have seen this kind of behavior in some data from the Wideband Satellite.

CORRELATION AND PREDICTION OF TRANSIONOSPHERIC
SIGNAL TIME DELAYS AT WIDELY SEPARATED LOCATIONS

H. Soicher
DRDCO-COM-RF
US Army CORADCOM
Fort Monmouth, NJ 07703

ABSTRACT

Excess time delays of transionospheric radio signals introduce ranging errors in satellite-navigation and radar systems, which are directly proportional to the total electron content (TEC) along the propagation path. Correlations of TEC values (based on linear regression analysis) at Fort Monmouth, NJ (40.18°N, 74.06°W), Richmond, FL (25.60°N, 80.40°W) are determined. The correlation analysis is performed at daily intervals for equinoctial and winter periods during the quiet phase of the solar cycle.

Average regression lines obtained by the analysis are then used to try to determine TEC at Richmond, assuming the availability of TEC in Fort Monmouth. In most cases, the "predicted" TEC was within one standard deviation of actual observed data.

INTRODUCTION

The effects of ionization along the satellite-to-ground signal-ray-path on the propagation time of such a signal was previously discussed. (H. Soicher, September 1977). The excess time delay introduced by the ionization is directly proportional to the total electron content (TEC) along the signal path. In view of the stringent accuracy requirement of modern satellite-navigation and radar systems, the excess time delay must be compensated for either by real-time measurement or through empirical modeling techniques. The former requires that the user possess dual-frequency reception capabilities, while the latter (which utilizes a single frequency) depends on how well TEC and its temporal and spatial variability can be modeled and/or predicted. For improved accuracy, the forecasting techniques should be supported by periodic updating of data (preferably in real-time) at specified locations. The question arises as to the extent of the geographic area, surrounding a station having real-time TEC-determinating capabilities, within which TEC values could be interpolated with acceptable accuracy. In other words, could TEC be determined at location A if a real-time measurement was taken at a different location, B, and what would be the geographic constraints on A and B?

To this end, a specific investigation designed to determine the correlation (based on linear regression analysis) between TEC values at Fort Monmouth, NJ (40.18°N, 74.06°W), and at Richmond, Florida (25.60°N, 80.40°W), was undertaken. (H. Soicher, March 1978). Beacon transmissions from the geostationary Applications Technology Satellite ATS-6 (K. Davies, R.B. Fritz, and T.B. Gray, June 1976, and H. Soicher, Jan 1975) were used to determine the TEC at the two stations by means of the Faraday rotation technique.

The subionospheric points for the two stations i.e., the geographic locations where the ray paths to the ATS-6 (located at 94°W) intersect a "mean" altitude of 420 Km were 36.5°N, 76.6°W and 23.60N, 81.6°W, respectively. Thus, the "representative" TEC for the two stations was separated by ∿13° in latitude and by 5° in longitude (corresponding to a 20-minute difference in local time.)

Figure 1 indicates the variation of the maximum daily correlation coefficients for September 1974 and January, February, March, April and May 1975. These were arrived at by comparing the TEC daily data sets at Fort Monmouth and Richmond. At first, the correlation coefficient was calculated for identical UT times. Then, the Richmond data was shifted in time with respect to the Fort Monmouth data at 15-minute intervals in the forward (+) direction and in the backward (-) direction. Correlation coefficients are calculated for up to ten shifts in the forward or backward direction. The maximum correlation coefficient as well as the number of shifts for which the maximum correlation coefficient is attained are indicated in the figure, as are the shifts' monthly averages. In addition, the number of data pairs available for the correlation analysis for each day (maximum of 96 data pairs, since the data is available at 15-minute intervals) is also shown in the figure.

In general, the correlation coefficients ranged between ∿0.9 and ∿1.0 with relatively few falling below 0.9. The lower values of the coefficients did not necessarily coincide with the sparsity of the available data. On the average, the coefficient was maximum for no shifts in September, for ∿1 shift in January, and for >(-1) shift for the other months. While most maximum coefficients occurred for ±1-hour shifting (± fifteen-minute shifts), shifts of two hours and more were observed occasionally.

The next phase of the investigation was the effort to determine whether it is possible to accurately predict TEC at Richmond from TEC at Fort Monmouth, using average regression lines obtained for the two data sets. The technique employed was as follows: Average monthly regression lines were computed. From these an average overall line of regression was obtained. Having determined the average regression line, TEC at Richmond was calculated for a given TEC at Fort Monmouth. The deviation (D_i), of the calculated TEC at Richmond from its actual value at a particular time is then determined. This deviation, D_i, is then divided by the monthly TEC standard deviation value at the same time. The average absolute value of this ratio, i.e., $\frac{|D|}{\sigma} = \frac{1}{N} \sum_{i=1}^{N} \frac{|D_i|}{\sigma_i}$ (N≤96), was then computed for each day. The results are shown in Fig. 2. Also shown in Fig. 2 is the number of data points available for the analysis for each day (data is available at 15-minute intervals; ninety-six data points signifies a full day's data availability. Data is sometimes missing, due to turn-off of the satellites beacons).

The results using average regression lines, but for the time period 1300-2100 UT, when the maximum diurnal TEC values occur are shown in Fig. 3.

DISCUSSION

As Fig. 2 indicates, the daily average of the ratios $\frac{|D|}{\sigma}$ is, for the most part, smaller than one, i.e., on the average, the deviation of the computed Richmond TEC values, is, in general, within the monthly standard deviation of the Richmond data. The diurnal behavior of the ratio is such that the ratio is higher during the night (when σ is small) than during the day. Some of the high values of this ratio are attributable to ionospheric effects during magnetically active periods, e.g., on September 15 & 18, 1974, large enhancements of TEC were observed in response to magnetic sudden commencements; the results of the figure also indicate that the ratio appears larger during the equinoctial period (September, March) than during the winter and spring months. This is observed despite the fact that the standard deviation during the equinoctial months was considerably higher than during the other months.

Since total signal time-delays are largest during the day and thus, introduce significant errors in navigation and radar systems, it is appropriate to examine the ratio $\frac{|D|}{\sigma}$ during the time when TEC is diurnally larger, i.e., between 1300 and 2100 UT. During the day $|D|$ and σ are generally larger than during the night. Figure 3 indicates that the ratios $\frac{|D|}{\sigma}$, obtained by an average regression line for the day period, are substantially lower than the corresponding ratios for the full diurnal periods (Fig. 2). The fact that the bulk of the data indicates that the ratio falls below 1 is encouraging since both correlation methods yield "predicted" TEC values that fall within the monthly standard deviation of the data during the time period when the presence of TEC poses the source of largest error.

CONCLUSIONS

The high correlation of signal time-delay variation at two locales separated by $\sim 13°$ in latitude and $\sim 5°$ in longitude, prompted the examination as to whether time-delay data at one locale may be "predicted" if continuous corresponding data were available at the other locale. The correlation is high, in part, due to the 24 hour periodicity of the data. It is precisely this periodicity, however, that gives the "prediction" technique employed here its accuracy. The variation of the time-delay is the highly correlatable quantity, and thus, the whole data set--if available, should be used in the prediction scheme.

The average of monthly averaged regression lines was used in the analysis. The slopes of the average monthly regression lines were almost identical for September, April, and May, but differed within ±20% from this value for January, February, and March. The average intercepts of the line of regression were considerably more scattered.

For the most part, the deviation of the "predicted" data from the observed data was within one standard deviation of the monthly data set. For daytime periods, when the error introduced by the time-delay is greatest, the ratio $|D|/\sigma$ was even lower. The ratio is often high during time periods characterized by ionospheric disturbances.

Since the monthly value standard deviation is $\sim 25\%$ of the absolute value of the time delay, the method of prediction outlined here appears to have the capability of correcting the time delay due to the ionosphere to within $\sim 25\%$. Future efforts will be directed towards evaluation of correlation and prediction of ionospheric signal time-delays at stations of greater geographic and local time separation.

REFERENCES

H. Soicher, "Ionospheric and Plasmaspheric Effects in Satellite Navigation Systems," IEEE Trans. Antennas & Propagation, Vol. AP-25, No. 5, pp 705-708, September 1977.

H. Soicher, "Spatial Correlation of Transionospheric Signal-Time-Delay," IEEE Trans. Antennas & Propagation, March 1978 (In the Press).

K. Davies, R.B. Fritz, and T.B. Gray, "Measurement of Columnar Electron Contents of the Ionosphere and Plasmasphere," J. Geophysical Research, Vol. 81, p. 16, June 1, 1976.

H. Soicher, "The ATS-6 Radio Beacon Experiment," Nature, Vol. 253, pp. 252-254, January 24, 1975.

DAILY CORRELATIONS
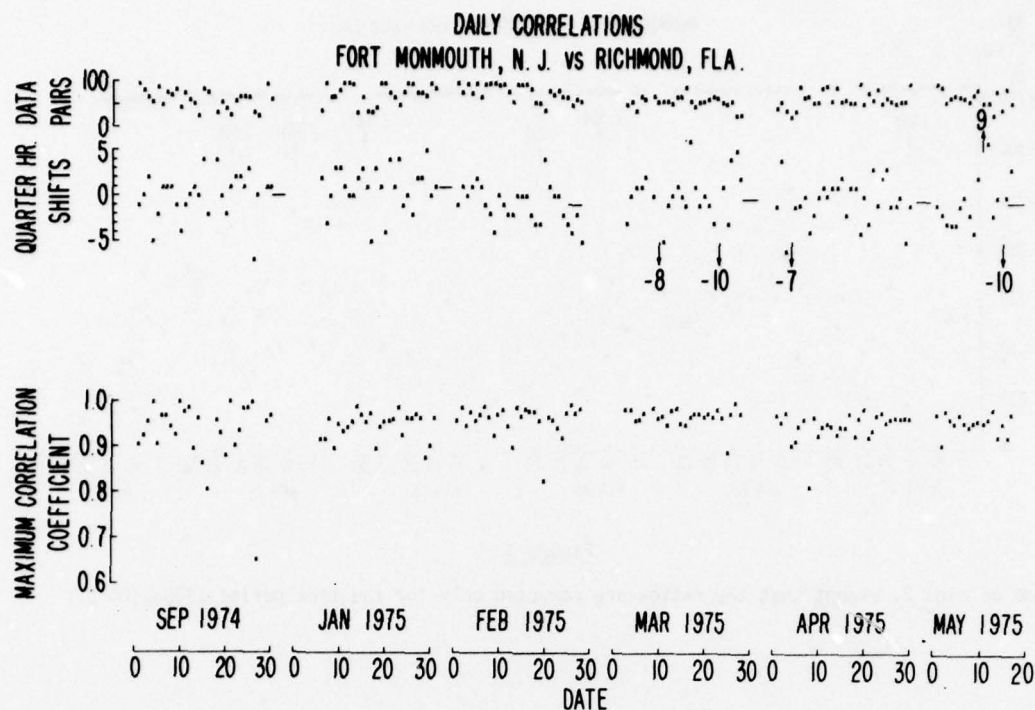## FORT MONMOUTH, N. J. vs RICHMOND, FLA.

Figure 1

Variations of the maximum correlation coefficients of the Fort Monmouth, NJ, and Richmond, FL, daily data sets. Also indicated are the time shifts for which these were attained, their averages (–), and the number of data pairs used in the analysis.
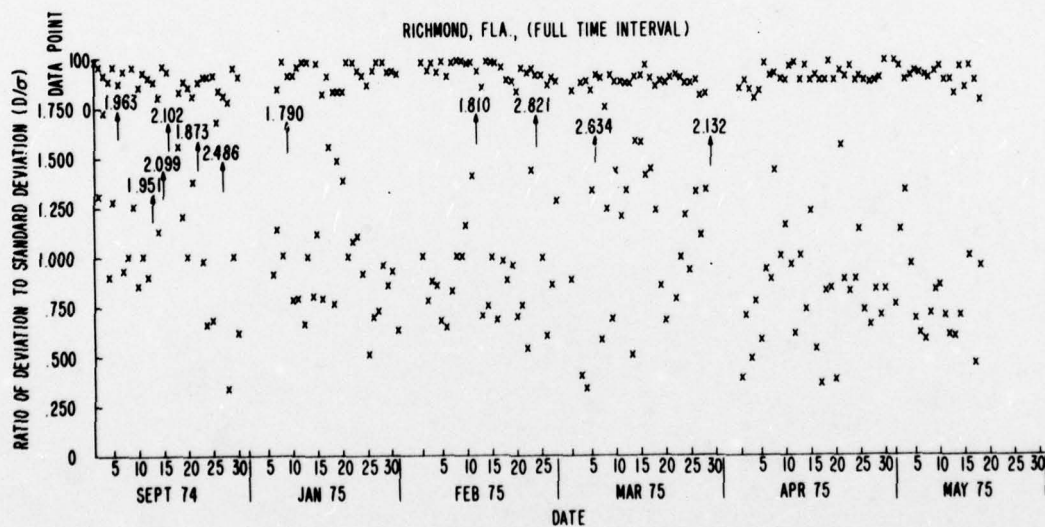
Figure 2

The variation of the ratio $|D|/\sigma$ for Richmond, Florida, for the time period September 1974, and January 1975– calculated for full diurnal periods by average regression line obtained from Fort Monmouth, NJ– Richmond, Florida data sets. ($|D| \equiv$ diurnal average of the deviations of the computed TEC values from observed ones; $\sigma \equiv$ monthly standard deviation of the Richmond data). Also indicated are the number of TEC values at 15-minute intervals used in the analysis.

Figure 3

Same as Fig. 2, except that the ratios are computed only for the time period 1300-2100 UT.

SUMMARY OF SESSION VI

SOLAR TERRESTRIAL EFFECTS

by

Dr G.Lange-Hesse
Session Chairman

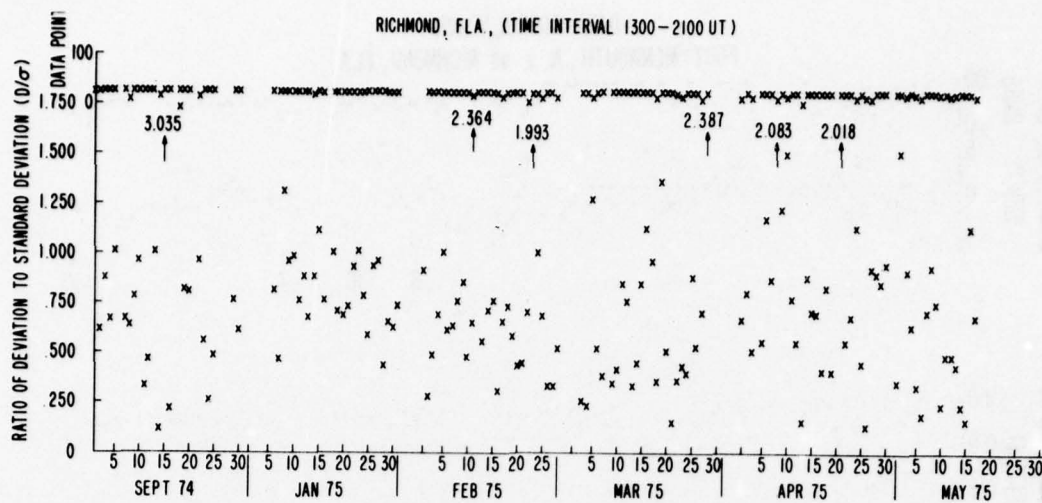Measurements of the temporal and spectral variability of solar X-ray, EUV and particle emission — carried out by the NRL SOLARD 11 satellite system — have formed the basis for prediction and assessment of ionospheric disturbances affecting military communications, surveillance and navigation systems.

Applications of real time measurements of solar X-ray and EUV emission fall into two rather broad and interrelated areas. The first is in assessment of the ionospheric electron density and from it calculation of parameters such as the LUF and MUF in real time. Such assessments can directly support day to day management of HF communications. In a disturbed period, realtime monitoring can be employed to assess the actual propagation conditions on various HF paths and give the communicator some flexibility in rerouting traffic over those paths which may be less affected.

Ionospheric disturbances also affect VLF navigation systems. Real-time monitoring of the solar flare X-ray and particle emission therefore can be used to correct position measurements should those be made during a disturbed period, or at least serve as a warning that the position determination is probably inaccurate.

Disruptions to communications, resulting from solar-terrestrial disturbances, can be minimized by forecasting the disturbances or at least by providing early notification of solar disturbances and their consequent effects in space and in the vicinity of the earth. Both functions rely on real-time solar-terrestrial data, which is now available through the cooperation of several US agencies and through international data exchange agreements. The Space Environment Laboratory is a central point for the collection, processing and dissemination of such data and for forecasts of solar-terrestrial conditions.

An improvement of the prediction technique by detection of fast solar wind streams at long distances from the earth up to 0.3 AU has become possible since the launch of the two solar probes HELIOS-1 and -2. Solar wind data measured by these probes were compared with data measured near the earth using the IMP satellites. Arrival time predictions of fast solar wind streams at the earth can be made on this basis with an accuracy of a few hours at least as long as the large scale conditions on the sun are relatively stationary as observed near the time of solar minimum. However, the latitudinal extent of the respective high speed streams is found to be important for making quantitative predictions. Coronal data sufficient for locating the sources of high speed streams can improve the precision of these predictions.

Since solar probes such as HELIOS-1 and -2 are not of permanent lifetime, another method was developed by **Roelof** and **Gold**. The technique they are applying depends on a combination of measurements of solar wind velocities with energetic particle fluxes on the same near-Earth spacecraft. By combining these measurements the coronal emission profile of both plasma and particles can be displayed as a function of heliographic longitude. With direct telemetry from spacecraft plasma detectors in the solar wind, such "mapping" of the coronal emission profile could be done in real time. Four examples of coronal structure of plasma and energetic particles has been shown. They illustrate the wide variety of time histories of particle events at Earth which can be produced by essentially the same coronal injection profile in the corona. They offer a brief scenario of how the decay history of these four events could have been predicted using simultaneous real-time solar wind and energetic particle measurements.

To be independent of satellite measurements another method was developed by **Houminer** on the basis of daily observations of the scintillation of a number of radio sources lying at widely separated positions. Observations of this kind provide a way for predicting geomagnetic activity associated with large scale features of the solar wind. By observing suitable sources lying to the east of the Sun it is possible to forecast, up to six days in advance, geomagnetic storms associated with corotating solar wind streams. Geomagnetic disturbances caused by interplanetary shock waves associated with solar flares may be predicted some 8—24 hours in advance, when using observations at UHF frequencies (300—400 MHz).

SOLAR TERRESTRIAL ENVIRONMENT MONITORING AND FORECASTING
AT THE
NOAA, SPACE ENVIRONMENT LABORATORY, BOULDER, COLORADO

A. G. Jean
G. R. Heckman
C. E. Hornback
Space Environment Laboratory
National Oceanic and Atmospheric Administration/ERL
Boulder, Colorado 80303, USA

SUMMARY

The Space Environment Laboratory of NOAA carries on an extensive program of monitoring solar geophysical data including both ground-based and satellite borne sensors. These data are used in the preparation of forecasts of ionospheric and geomagnetic disturbances that have direct influences on radio wave propagation. Such effects include sudden phase anomalies, that affect VLF navigation systems, LORAN, etc.; short wave fadeouts; polar cap absorption events and ionospheric storms.

A survey is given of the Space Environment Laboratory Data Acquisition and Display System (SELDADS) and of the forecasting and warning services provided by the Space Environment Services Center and the applications of these data to radio propagation in such areas as communications, navigation and surveillance.

1.0 INTRODUCTION

It is of historical interest to note that a component of the Department of Commerce has been concerned with solar-terrestrial relations for the past 36 years; first, the Interagency Radio Propagation Laboratory (IRPL) was formed in 1942 in the National Bureau of Standards, under Dr. J. H. Dellinger (who related radio fadeouts with solar eruptions). IRPL's formation was stimulated by an aircraft disaster in Europe in WWII, which was attributed to failure of HF radio communications with aircraft during a magnetic storm. The Central Radio Propagation Laboratory (CRPL) was formed in 1946 from IRPL in order to provide services for civilian and military needs in radio communications. The Space Disturbances Laboratory (SDL) was formed in 1965 with the creation of Environmental Science Services Administration (ESSA) to provide services and research in upper atmosphere and space. The Space Environment Laboratory (SEL) was formed in 1971 as part of NOAA's Environmental Research Laboratories and is the current segment of the Department of Commerce carrying on the solar-terrestrial research and services tradition. Currently, the SEL, in conjunction with the United States Air Force, Air Weather Service (AWS), operates a real-time solar terrestrial environment monitoring system and a forecasting service at Boulder, Colorado. Each of these two services: the Space Environment Laboratory Data Acquisition and Display System (SELDADS) and the Space Environment Services Center (SESC), will be briefly discussed.

2.0 SELDADS

The SEL Data Acquisition and Display System (Williams, D. J., 1976) is shown schematically in Figure 1. A variety of ground-based and satellite sensors furnish data to SELDADS. Three inputs which are not yet operational are:

--The U. S. Navy's SOLRAD 11 Satellite Program

--The National Science Foundation chain of magnetometers being implemented as as part of the U. S. International Magnetospheric Studies (IMS)

--The NOAA TIROS-N Satellite Program

The SOLRAD 11 satellite unfortunately developed problems which have inhibited the data flow; at the time of writing about two-thirds of the proposed chain of 25 magnetometers were functioning in the IMS program, and the TIROS-N satellite is scheduled for launch in September 1978.

The communications system is made up of:

--The USAF Astrogeophysical Telecommunications Network (ATN)

--A USN line providing direct SOLRAD 11 telemetry to SEL

--Dedicated commercial communication lines

--A dedicated meteorological line to Moscow

--The International Ursigram World Days Service (IUWDS) network

--The U. S. Defense Communications Network (AUTODIN)

The ATN network is used for the bulk of the ground-based data received by the real-time data base, whereas the bulk of the satellite data at this time is obtained by direct satellite telemetry to SEL.

Solar activity and event reports from a solar patrol network operated by the USAF/AWS and NOAA/SEL are transmitted through the ATN to SELDADS as they occur. The USAF/AWS is proceeding with the establishment of a new Solar Observing Optical Network (SOON) which will greatly enhance the global monitoring facilities and data flow (Air Force Tech order 31M1-2 FM67-1, to be published).

Real-time X-ray, proton and vector geomagnetic field measurements are available from the NOAA SMS/GOES geostationary weather satellite series (Grubb, R. N., 1969, 1975a). Data from two satellites of this series are simultaneously received by direct satellite telemetry at SEL and immediately converted, processed, recorded on magnetic tape and inserted into the real-time data system. Data in the data base are kept as 1-minute averages for the most recent four days and as 5-minute averages for 32 days.

Near real-time data of polar cap solar proton fluxes are received from a Solar Proton Monitor (Cashion, R. E., and Gary, S. A., 1969; Brown, S. R., 1975) carried aboard the NOAA low-altitude polar-orbiting weather satellite series ITOS and TIROS. These data arrive at SEL through the ATN and are inserted directly into the real-time data base. Plots of solar proton fluxes across the polar caps are maintained for the most recent 8 days, with polar cap averages being maintained for 1 calendar month.

Ground station data from the High Latitude Monitoring Station (HLMS) in Anchorage, Alaska are transmitted to SEL through the ATN and incorporated directly into the real-time data system. Vector ground-based magnetometer information is relayed from Thule, Greenland by teletype link to the HLMS and transmitted to SEL each minute. These data along with data from a chain of 8 riometers are collected by the HLMS and transmitted to SEL once every 15 minutes. These data rates reflect the line capacity of that portion of the ATN that is dedicated to the HLMS use.

The incoming data are received and processed at Boulder, Colorado by two mini-computers, each of which is capable of maintaining the real-time data base as well as performing a variety of specialized operations on the data. The real-time data base consists of the previous 32 days' worth of data and is maintained in two 58 megabyte discs. In many cases, time resolution will vary throughout the 32-day period of the data base, with finer time resolution existing for the most recent data.

Display capabilities for data residing in the real-time system include:

--interactive and call up CRT displays

--strip-charts

--word messages

--printer output

Normal data dissemination procedures include:

--direct computer-to-computer links with the real-time data system

--user terminals

--telephones

--teletype reports and forecasts

--a weekly summary of solar-terrestrial environment activity (issued by the SESC)

--special requests

Data available in SELDADS is summarized in Figure 2 and the SELDADS users are listed in Figure 3.

3.0 SPACE ENVIRONMENT SERVICES CENTER

The Space Environment Services Center (SESC), located in Boulder, Colorado, is a joint operation of the USAF/AWS and the SEL. The AWS is responsible for providing operational space environment support to the Department of Defense through its center at Global Weather Central (GWC) at Offutt AFB, while SESC provides a similar service for the civilian scientific and technical community. The SESC is concerned primarily with providing solar and geophysical information, leaving responsibility for ionospheric products to the GWC. The flow of space environment services for operational purposes are shown in Figure 4. The major users of the SESC output are listed in Figure 5.

Though SESC does not make ionospheric forecasts specifically, it provides a range of real-time services in direct support of systems that operate in, near, or through the ionosphere. Those services are described in the following sections.

3.1 Solar Geophysical Indices

A common tendency among operational users of space environment support is the use of various indices to simplify communication about the state of solar or geomagnetic

disturbances. Though some of the indices in current use have been used for decades, most of the recent advances in improved services have been in the introduction of new indices or the refinement of existing ones.

Sunspot Number

Sunspot numbers are only indirectly related to ionospheric systems, but a number of long-term (months and years) prediction models of HF radio propagation conditions and satellite orbit decay rely on sunspot numbers as an approximation for extreme ultra-violet (EUV) radiation levels. The fortuitously good correlations between EUV fluxes and sunspot numbers, when smoothed over months and years, and the observed quasi-periodicity of the sunspot numbers, enables useful predictions for model input to be made. Because there are still no operational satellites making solar EUV flux measurements, a number of system operators also rely on the day-to-day sunspot number as an approximation to the short-term EUV flux level despite the lower correlation of the daily values (Donnelly, R. F., 1977). When SOLRAD data are calibrated, EUV fluxes will be available in real-time, but the satellite must be operated for a number of years for the atmospheric models themselves to be calibrated sufficiently to make best use of the EUV fluxes.

3.2 Solar Flare Indices

The traditional method of classifying solar flares relies on a measure of the flare-area in an optically visible line, generally Hydrogen-alpha (6563Å), and on the brightness of the flare in that line. Beginning in 1969, personnel of the SESC (Baker, D. M., 1970) began classifying solar flares according to their emission in the 1 to 8 Å soft X-ray band as measured on the NRL SOLRAD satellites. The SESC now uses the 1 to 8 Å emission as the basic flare classification parameter. The X-ray classification system is shown in Figure 6.

3.3 Geomagnetic Indices

Though the usefulness of alternative indices of geomagnetic activity such as the time rate of change of the field at a particular location (Anderson, C. W., et al., 1974) or rapid field pulsations (Jacobs, J. A., 1970) have been described for some specific geophysical applications, the most widely used indices in real-time continue to be the 24 hour A and three hour K-indices, derived for individual stations. Planetary values of these indices are also derived, using data from several stations around the world.

The SESC is currently working on implementing a system of classifying substorms for near real-time use that would include the east and west boundaries of substorms, along with their time and some measure of their intensity (Pythe, T., et al., 1976).

3.4 Proton Event Indices

The primary definition of a "proton event" in the SESC services is a flux of 10 protons $(cm^2\text{-sec-sterad})^{-1}$ with energy greater than 10 MeV. For polar cap absorption, the definition of an event is a daytime absorption of 2 dB or 0.5 dB nighttime absorption at 30 MhZ.

4.0 SESC SERVICES

Figure 6 is a summary of the services provided by SESC. These services are described in the same order below.

4.1 Long-Range Predictions

Using the method of McNish and Lincoln (1948), the National Geophysical and Solar Terrestrial Data Center of NOAA predicts monthly smoothed sunspot numbers. This method relies on a comparison of annual mean sunspot numbers from the cycle being predicted to the annual means of previous cycles. The method is subject to considerable variability early in the cycle when the sample for comparison is small. The SESC provides and uses real-time observations of sunspot numbers to enable a more accurate prediction over the period of a few months. Predictions of the general level of solar activity and of geomagnetic activity (low, moderate, high) are made seven and twenty-seven days in advance.

4.2 Three-Day Forecasts

SESC makes forecasts for the next three days of:

--levels of geomagnetic activity (Fredericksburg A indices)

--solar radio flux at 2700 MhZ

--solar proton events

--class X and class M flares

The predictions for proton events and for flares are cast as the probability of the occurrence of each particular type of event for each universal (Greenwich) day. The

accuracy of the class M flare forecasts made for a 24-hour period one day in advance are shown in Figure 8. About 5,000 active regions are born on the sun during one solar cycle. Ten percent of these regions produce class M flares, one percent produce class X flares. The accuracy of the class M flares for a 24-hour period made one day in advance are shown in Figure 8. The left half of the figure shows that the forecasters have a high ability to separate the regions that produce class M flares from those that do not. The right half shows that the forecasters have a much lower ability to predict which days those 10 percent of the regions will produce class M flares.

4.3 Alerts of Events

In lieu of a satisfactory capability of predicting solar-geomagnetic disturbances, about 40% of SESC customers rely on rapid alerts of events once the event is detected. Categories and thresholds for these alerts are shown in Figure 9. The alerts have varying thresholds and the user of the service may specify at what level he wishes to be notified.

In addition to the alerts shown in Figure 8, there is another category of service that is intermediate between prediction and alert. The prediction of flare consequences such as proton events and geomagnetic storms can be greatly improved once a flare has occurred by using measures of the flare energy such as optical, radio or C-ray emission. A proton prediction program by Smart (Smart, D. F., and Shea, M. A., 1977) uses a combination of physical and heuristic models to predict the time, flux intensity and spectral parameters of a flare-induced proton event using any of several flare emission parameters. The Smart program is used as an operational prediction tool in the SESC. Similar models for flare-produced magnetic storms can also be used, though the model techniques for these are not as advanced as for the proton event modeling.

4.4 After-The-Fact Summary

Summaries of solar and geomagnetic activity are distributed daily in the teletype messages "Joint AFGWC/SESC Primary Report of Solar and Geophysical Activity" and "Joint AFGWC/SESC Secondary Report of Solar and Geophysical Activity."

The Preliminary Report and Forecast of Solar Geophysical Activity, published and mailed weekly by SESC, contains lists of solar flares, solar active regions, radio flux levels and selected plots of proton events, X-ray flare profiles and magnetograms.

4.5 Technical Needs

To provide improved service to the users of the SESC, several technical improvements are needed. Direct satellite monitoring of EUV fluxes rather than continued reliance on correlative parameters should improve the accuracy of both ionospheric and upper atmospheric density models.

There is at present no operational EUV satellite monitoring system and none is presently being built, though as indicated earlier, SOLRAD 11 could be the source of such data if it is operated for a sufficiently long period into the future. As indicated in Figure 8, the primary source of error in the class M flare forecasts is an inability to predict the time of the flare. This is generally true of all the flare predictions made by the SESC. Exceptions are for proton events and magnetic storm predictions, where the error in the predicted intensity or particle flux is generally as great or greater than the error in the predicted times. Monitoring of solar wind parameters outside the magnetosphere would give an improved prediction of magnetic storm times and intensities.

Better spatial resolution in the measurements or improved extrapolation from existing measurements for localized magnetospheric/geomagnetic phenomena such as substorms would improve existing ionospheric models. If the real-time space environment centers should be called upon to provide regular support for spacecraft operating anomalies, such as charging, there is the same need for higher resolution information than is now available.

Finally, in the data currently monitored, specific indices could be developed that more closely relate the measurements to particular operating systems or models. The C-M-X flare classification system was developed to provide such an improvement. The geomagnetic A and K indices are examples of gross indices that continue to be used in a wide variety of applications with widely varying time dependencies. On the other hand, the continuation of gross indices such as A and K has enabled the SESC to fulfill the important role of being a general information source to which operators of advanced technology systems can go to get a rapid first indication of whether solar and geomagnetic activity may be the source of some unexplained anomaly in their system. In several past instances, this has been the case and the result has led to further studies by the operators and enabled them to gain better understanding of environmental effects on their systems. Development of new systems in the future will presumably provide continued opportunities for the same service.

5.0 CONCLUSIONS

Disruptions to communications, transportation and utilities, resulting from solar/terrestrial disturbances, can be minimized by forecasting the disturbances and/or by providing early notification of solar disturbances and their consequent effects in space

and in the vicinity of the earth. Both functions rely on real-time solar/terrestrial data, which is available through the cooperation of several U. S. agencies and through international data exchange agreements. The Space Environment Laboratory is a central point for the collection, processing and dissemination of such data and for forecasts of solar terrestrial conditions.

REFERENCES:

Anderson, C. W., Lanzerotti, L. J. and MacLennan, C. G., 1974, Outage of the L-4 System and the Geomagnetic Disturbance of August 4, 1972", Bell System Technical Journal, Vol. 53, 1817.

Baker, D. M., 1970, "Flare Classification Based Upon X-ray Intensity", AIAA Paper No. 70-1370.

Brown, S. R., 1975, "Operational Processing of Solar Proton Monitor Data", NOAA Tech. Memo. NESS 73, National Technical Information Service, Springfield, Va.

Cashion, R. E., and Gary, S. A., 1969, "TIROS Solar Proton Monitor Test Procedures and Equipment", TG 1052, JHU/Applied Physics Laboratory Report, Silver Spring, Md.

Donnelly, R. F., 1977, The Solar Output and Its Variation, Colorado Associated University Press, Boulder, 320.

Grubb, R. N., 1975a,"The SMS/GOES Space Environment Monitor Subsystem", NOAA Tech. Memorandum ERL SEL-42, SEL, Boulder, Colo.

Grubb, R. N., 1969,"Justification and Outline Proposals for Space Environment Monitoring from GOES, MKI", Attach. to internal ESSA (now NOAA) document describing ERL requirements for GOES, March 1969, Boulder, Colo.

Jacobs, J. A., 1970, Geomagnetic Micropulsation, Springer-Verlag, Heidelberg, Berlin.

Mangis, S. J., 1975, "Introduction to Solar-Terrestrial Phenomena and the Space Environment Services Center", NOAA Tech. Report ERL 315-SEL 32, National Technical Information Service, Springfield, Va.

Pythe, T., McPherron, R. L., and Kokubun, S., 1976, "The Ground Signatures of the Expansion Phase During Multiple Onset Substorms", Planetary Space Sci., Vol. 24, 1115-1132.

Smart, D. F., and Shea, M. A., 1977, "Application of Elementary Coronal Propagation and Co-Rotational Concepts to Solar Proton Event Prediction", Proceedings 15th International Cosmic Ray Conference, Vol. 5, 131.

"Watch Upon A Star", 1977, published by U. S. Department of Commerce, National Oceanic and Atmospheric Administration, Boulder, Colorado, NOAA/PA 77002.

Williams, D. J., 1976, SELDADS; An Operational Real-Time Solar-Terrestrial Environment Monitoring System, NOAA Tech. Report ERL 357-SEL 37.
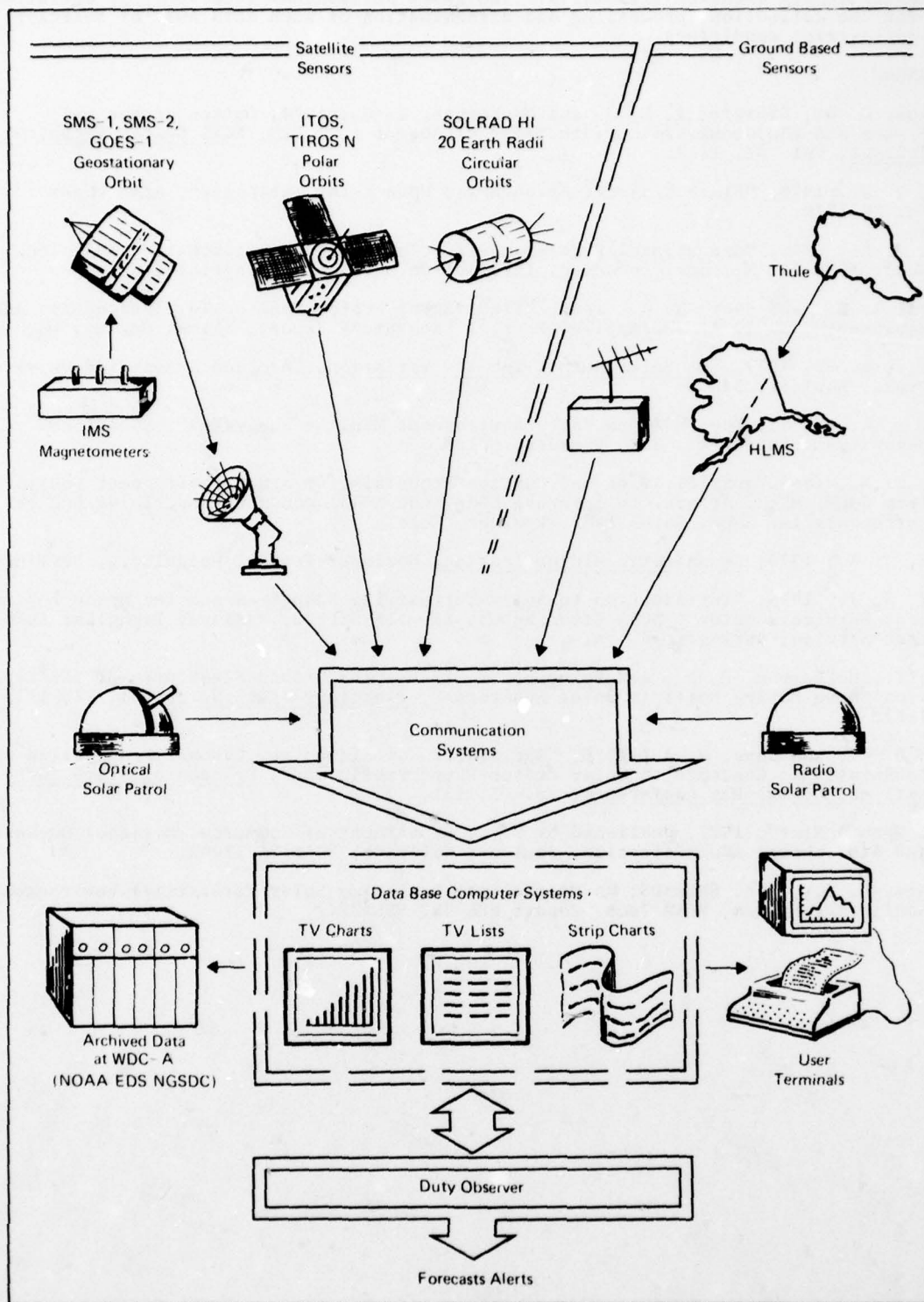
Fig. 1 Schematic of SELDADS

TYPE	WAVELENGTH	TIME RESOLUTION	PRIMARY SOURCES
X-ray Patrol	1-8Å	One-minute values	SMS/GOES Satellites
Optical Patrol	H-alpha	Approximately one minute	U.S.Air Force Observatories at Teheran, Ramey, Palehua, Holloman. NOAA/IPS Joint Observatory Culgoora. Boulder (part time). International Ursigram World Days Service (IUWDS) network.
Radio Patrol	Decametric through Centimetric	Approximately one minute	Quiet time flux levels event reports from Sagamore Hill, Ottawa, Boulder, Manila, Culgoora (CSIRO) IUWDS.
Particle Patrol	0.6-500 MeV protons		SMS/GOES
	≥ 2 MeV electrons		SMS/GOES
	4.0-329 MeV alpha particles		SMS/GOES
	>10, >30, >60 MeV protons		NOAA 5
	Additional data from Vela and Meteor (USSR) satellites		
Geosynchronous Magnetometer Patrol	Three Field Components		SMS/GOES satellites
Geomagnetic Indices	A, K		18 stations
Total Electron Content		Hourly	
Auroral Back-scatter Radar		15 minutes	
High Latitude Riometers	30 MHZ	15 minutes	5 Alaskan stations plus
Ionosonde Observations	FOF2,M3000,FMIN	One hour or six hours	Approximately 30 stations

Fig. 2 Data Available in SELDADS

DEDICATED LINES

SPACE ENVIRONMENT SERVICES CENTER

AIR FORCE GLOBAL WEATHER CONTROL

NAVAL OCEAN SYSTEMS CENTER

REGULAR DIAL-UP USERS (DAILY BASIS)

NESS SATELLITE OPERATIONS CONTROL CENTER

NAVAL RESEARCH LABORATORY

GENERAL TELEPHONE AND ELECTRONICS/SYLVANIA

ST. CLOUD STATE UNIVERSITY

KITT PEAK OBSERVATORY

UNIVERSITY OF NEBRASKA

RCA GLOBAL COMMUNICATIONS

EDS NATIONAL SOLAR GEOPHYSICAL DATA CENTER

SEL

PLUS APPROXIMATELY 20 ADDITIONAL USERS ON A
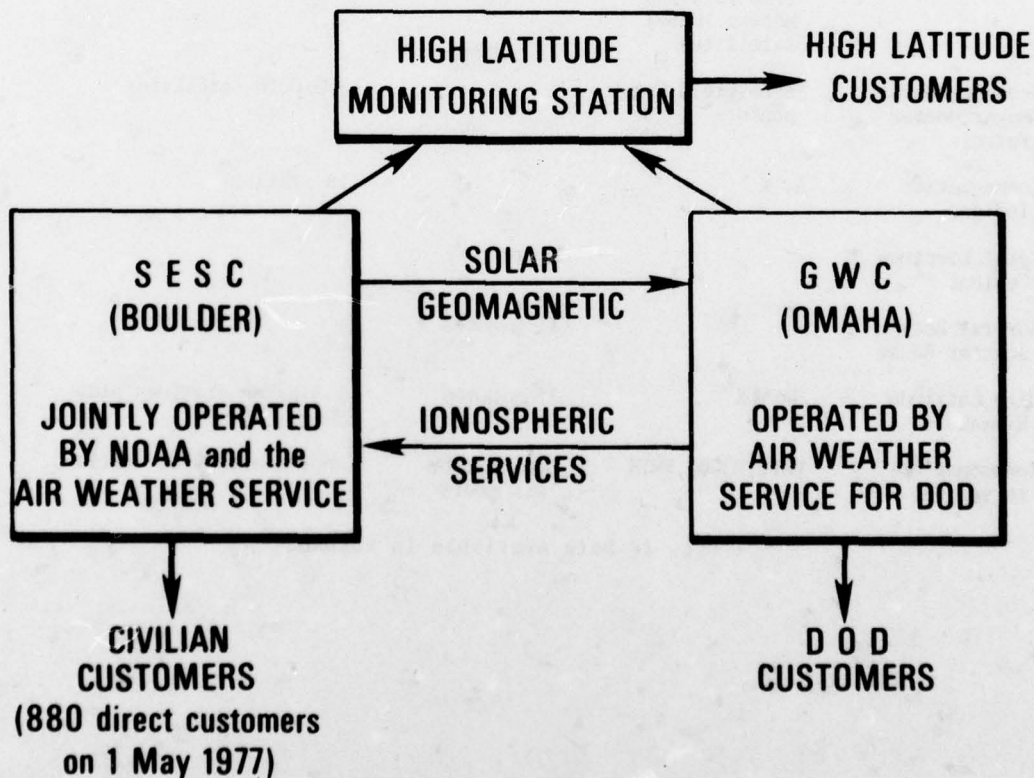FEW SELDADS CALLS PER WEEK BASIS.

Fig. 3   SELDADS Users

Fig. 4   NOAA/AWS Disposition of Services

MILITARY

        HF COMMUNICATION

        SATCOM COMMUNICATION

        RECONNAISANCE

        NAVIGATION

CIVILIAN OPERATIONAL

        HF COMMUNICATION

        A/C POLAR FLIGHTS

        GEOPHYSICAL EXPLORATION

        SATELLITE COMMUNICATION AND OPERATIONS

        A/C MID-LATITUDE COMMUNICATION (VHF)

        A/C HIGH-LATITUDE COMMUNICATION (HF)

        A/C NAVIGATION

        NUCLEAR POWER INDUSTRY MONITORING

        ELECTRIC POWER COMPANIES

        LONG-LINE TELEPHONE COMMUNICATION

        ERDA COMMUNICATION

CIVILIAN RESEARCH

        MAJOR SATELLITES

        ROCKET LAUNCHES

        SOLAR RESEARCH

        GEOPHYSICAL RESEARCH

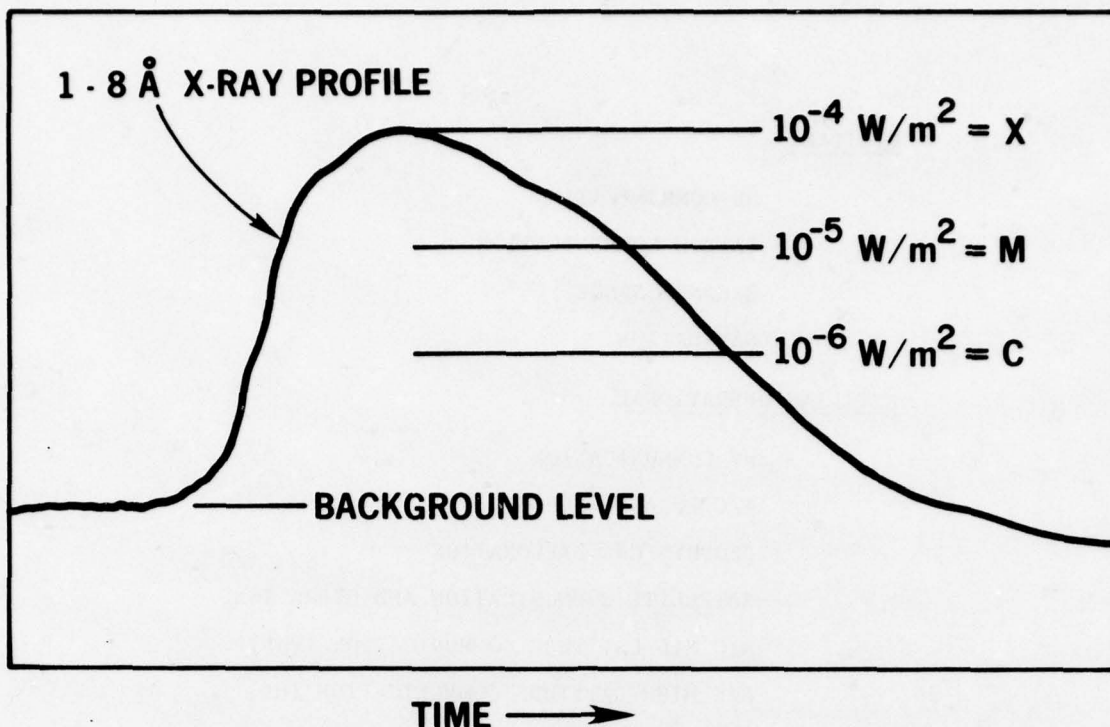   INTERNATIONAL AGREEMENTS

Fig. 5 Major Users of SESC Output

1 - 8 Å X-RAY PROFILE

10^{-4} W/m^2 = X

10^{-5} W/m^2 = M

10^{-6} W/m^2 = C

BACKGROUND LEVEL

TIME ⟶

Fig. 6 SESC Flare Classes

TYPE	TIME OF APPLICABILITY	PHENOMENA OF INTEREST
FORECAST	10 YEARS 6 MONTHS, 7 and 27 DAYS	SUNSPOT NUMBER GENERAL LEVEL OF SOLAR and GEOMAGNETIC ACTIVITY
FORECAST	1, 2, 3 DAYS FORECAST	FLARES, PROTON EVENTS, GEOMAGNETIC INDICES, SOLAR FLUX INDEX
FORECAST	30 MINUTES	FLARES
ALERT	IMMEDIATE	X-RAY, RADIO, OPTICAL EMISSION FROM FLARES
FORECAST	30 MINUTES - 100 HOURS	PROTON EVENT, GEOMAGNETIC STORM, SUBSTORMS
ALERT	IMMEDIATE	PROTON EVENT, GEOMAGNETIC STORM, SUBSTORMS
DATA (SELDADS)	REAL-TIME	ALL DATA
DATA (SUMMARY)	DAILY and WEEKLY	SELECTED DATA

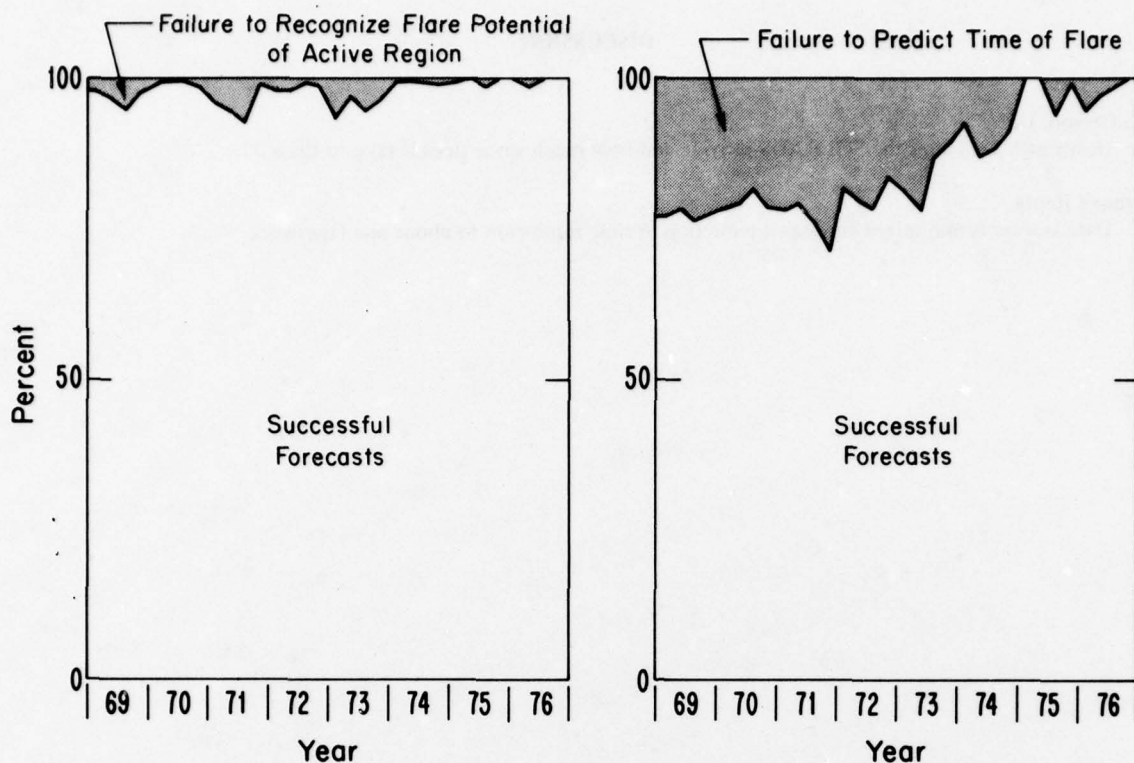Fig. 7 Distribution of SESC Services

Fig. 8   Class M Flares

SOLAR FLARES

    X5 (1-8Å X-ray Classification)
    X1
    M5
    3B (Optical Classification)
    2B
    1B

MAGNETIC DISTURBANCES

    A $\geq$ 50 (real time A measured at Boulder)
    A $\geq$ 30
    A $\geq$ 20
    K $\geq$ 6 (real time K measured at Boulder)
    K $\geq$ 5 observed in successive three-hour intervals
    K $\geq$ 5
    K $\geq$ 4
    SUDDEN COMMENCEMENT

RADIO BURSTS/NOISE STORMS

    10CM RADIO BURST GREATER THAN 100 FLUX UNITS
    245 MHZ OR NOISE STORM
    TYPE II AND/OR TYPE IV DECAMETRIC EMISSION

PROTON EVENTS

    PROTON FLUX (E>10MEV)>10CM^{-2}-SEC^{-1}-STERAD^{-1}

    Fig. 9   SESC Alert Categories and Thresholds for
               Issuing Alerts

DISCUSSION

N.G.Greson, US

How much data does the SOLRADS provide and how much space does it take to store it?

Author's Reply

Data storage is minimized through a reduction in time resolution to about one tape/week.

IONOSPHERIC DISTURBANCE FORCASTING THROUGH
USE OF X-RAY AND EUV MEASUREMENTS
FROM THE NRL SOLRAD SATELLITES

Robert W. Kreplin and Donald M. Horan
E. O. Hulburt Center for Space Research
Naval Research Laboratory
Washington, D.C. 20375

SUMMARY

Measurements of the temporal and spectral variability of solar X-ray, EUV and particle emission form the basis for prediction and assessment of ionospheric disturbances affecting military communications, surveillance and navigation systems. The NRL SOLRAD 11 satellite system has provided these measurements in real-time to the Naval Ocean Systems Center (NOSC) and the National Oceanic and Atmospheric Administration (NOAA) since July 1976.

The 1-8 Å X-ray flux transmitted to NOSC is used as input data by a computer terminal at the Naval Communications Station near San Francisco. Although solar activity was very low during the first year of operation the terminal provided an extremely useful tool in the management of Naval Communications in the Eastern Pacific.

This paper describes the spacecraft system, telemetry, and ground station which make possible real-time dissemination of the data. The NRL developed X-ray sensors and data processing techniques are also described.

Applications of other SOLRAD 11 measurements include derivation of the solar X-ray spectral distribution, assessment of F-region ionospheric disturbances, and prediction of periods of solar flare activity.

1.   INTRODUCTION

Since 1960 the Naval Research Laboratory has instrumented and successfully operated ten spacecraft for the purpose of monitoring the sun's X-ray and EUV emission. There now exists an almost continuous record of this emission covering a period from 1964 to the present (Kreplin, R.W., 1970; Kreplin, R.W., et al. 1977). All measurements have been made with standardized ionization chamber photometers. This body of data has been used to determine the role played by solar X-ray emission in ionospheric disturbances and to develop methods of forcasting periods of high flare activity and most recently, the ionospheric effects of such flares.

Sudden Ionospheric Disturbances (SID's) are a direct threat to military communications, surveillance and navigation systems. For this reason, the most recent SOLRAD spacecraft system was designed to satisfy the requirements of real-time monitoring and prediction.

2.   SYSTEM DESIGN CONSIDERATIONS

Providing a real-time assessment of the X-ray, UV, and particle radiation from the sun dictates conditions on the choice of orbit, design of the spacecraft, the telemetry link, the ground station, and the data processing and dissemination system.

Continuous real-time coverage requires that a spacecraft be in view of a telemetry station at all times. A low-orbiting satellite would require a large number of ground stations connected with surface or satellite communication links to satisfy the real-time requirements. The cost of such an array of ground stations would be prohibitive; far offsetting any advantages of the reduced requirements on the telemetry link. And, of course, it would not be possible to measure solar particle emission from that altitude.

At synchronous altitude a monitoring spacecraft would be in view of the ground station at all times. Unfortunately, such an orbit is in the center of the outer radiation belt. However, the SMS and GOES spacecraft (Grubb, R.N., 1975) have demonstrated that it is possible to monitor 0.5-4 Å and 1-8 Å X-ray radiation from synchronous orbit with magnetic protection of the X-ray sensors. But one might expect that during the period of solar maximum there may be times when the X-ray emission measurements would be masked by a high particle background. However, the SMS and GOES sensors are working very well during the present period of low solar activity. It is questionable whether or not the longer wavelength X-ray photometers carried by SOLRAD could operate in this environment. And it is, of course, impossible to measure the undisturbed solar particle fluxes from this orbit since they would be strongly modified by the earth's magnetic field.

Freedom from the earth's magnetic field and the trapped radiation environment requires an orbit in which the spacecraft is beyond the magnetopause for a maximum period of time. Consequently, an orbit of approximately 20 earth radii (126,000 km) was chosen as the best compromise between the requirements of maximum time in view of a ground station, freedom from trapped radiation, and reasonable RF signal strength at the ground station. In such an orbit one spacecraft would be in view of a single ground station for 11 to 13 hours with an orbit inclination of 28°. The original concept required three spacecraft and two widely separated ground stations to provide continuous monitoring of the sun's charged particle emission and X-ray and ultraviolet radiation. Because of budget considerations and launch vehicle capability the system realized consisted of two identical spacecraft, stationed 180° apart in the orbit. From a single ground station it has been

possible to monitor X-ray and ultraviolet radiation 90% of the time and solar charged particles 60% of the time undisturbed by the earth's magnetosphere. The system concept is illustrated in Figure 1.

2.1.   Description of Spacecraft

The two SOLRAD 11 spacecraft are cylinders approximately 1.4 meters in diameter and 0.4 m in height with a hole in the center of about 0.5 m diameter into which a solid propellent motor is installed. There are four solar panels extending from the outer circumference which are folded parallel to the cylinder axis during launch. Folding, four-element, turnstile antennas are mounted on the anti-solar faces and all of the sensors measuring solar X-ray and EUV radiation are on the opposite face. Two views of the spacecraft are shown in Figure 2. Each spacecraft weighs about 182 kg without the apogee or perigee solid motors.

The spacecraft were launched as a unit bolted together in a stack with the surfaces containing the solar sensors facing one another. The nozzles of the apogee and perigee motors pointed in opposite directions outward along the axis of the combined assembly.

The SOLRAD 11 A/B spacecraft assembly was launched from Cape Canaveral on 15 March 1976 by a Titan IIIC rocket. They were ejected as a unit at synchronous altitude and placed in their final orbit by perigee and apogee solid motors. They were separated and oriented facing the sun in final orbit about seven days after launch. The on-board hydrazine control system was then used to position the satellites 180° apart in orbit and then maintain this station. This system also controls the spin axis of each spacecraft so that they are constantly pointed toward the sun to within 1°.

2.2.   Telemetry System

One of the most serious problems of operation in a high altitude orbit is telemetry. Real-time data acquisition requires continuous operation of the transmitter. This, and the requirement of high output power, place great demands on the spacecraft power and thermal control systems. Directional antennas aboard the spacecraft would be a great advantage but one which must be paid for by the complexity of a 3 axis stabilization system. A simple omnidirectional turnstile antenna was chosen for SOLRAD 11 A/B compatible with the one axis stabilization system.

A five watt transmitter produced an effective radiated power of from +25 to +35 dbm in the 136-137 MHz telemetry band. The path loss over 126,000 km is 177 db which required an antenna gain on the ground of +24 dbi to provide a +10 db signal-to-noise ratio.

The modulation system and data rates were also chosen with a view toward improvement of the signal-to-noise ratio. The telemetry down-link modulation is PCM-PM with a data rate of 102.4 bps. To realize an additional improvement of about 3 db, convolution encoding (Viterbi, constraint 7, rate ½) is used (Viterbi, A., 1971). The encoded signal is then transmitted at 204.8 bps in a bi-phase level format. The ground station block diagram is shown in Figure 3. Note that because of the variation of polarization in the radiation pattern of the turnstile antenna the receiving system accepts both polarizations and selects the strongest signal automatically with a diversity combiner.

The data is transmitted in a format consisting of 32 twelve-bit words per frame. One complete frame is transmitted in 3.75 seconds. The first word of each frame is a synchronization pattern and the second word identifies the frame number. The remaining 30 words contain experiment data and housekeeping and status information from the spacecraft and experiments. Monitoring most solar emissions does not require a time resolution of 3.75 seconds so not all experiment outputs appear in every frame. They are submultiplexed to a rate which is sufficient to reproduce the most rapidly varying signal levels. These rates are listed in Tables I, II and IV describing the solar sensors. A period of two minutes is required to sample the 32 frames in which all experiment outputs are present.

2.3.   Data Processing and Distribution

The digital telemetry stream is directed to an on line computer in the ground station which decodes the telemetry, converts the data words into engineering units, and re-transmits the data via a 150 baud teletype line to the Naval Ocean Systems Center installation at La Posta, CA. This system is illustrated in Figure 4. The ground station computer also generates an archival digital tape, maintains an ephemeris file, and manages intercomputer communications with two computers located at NRL, one of which is able to transmit the NOSC data stream should the ground station unit fail for any reason.

The real-time data distribution network is shown in Figure 5. It has been in continuous operation since June 1976 with the exception of the line between NOAA/SESC and the Air Force Air Weather Service installation at Omaha.

The signals received at NOSC, La Posta are processed by another on-line computer to provide HF circuit assessments and predictions for the Naval Communications Station at San Francisco. This service will be described in another paper at this conference. X-ray data from the NOAA GOES and SMS spacecraft can also be transmitted on this line so that NOSC has sufficient data resources for 24 hour operation.

3.   DESCRIPTION OF THE SOLRAD 11 SENSORS AND APPLICATIONS

The sensors aboard SOLRAD 11 can be broadly classified into three catagories. Except for small differences, mainly in calibration constants, the sensors on both spacecraft were identical. In the first catagory are the standardized photometers for monitoring X-ray and EUV emission. These have changed only slightly from the designs flown in earlier satellites of the SOLRAD series. The 1-8 Å ionization chamber photometer was flown aboard SR-1 in 1960. The data from these sensors forms the base for a description of the sun's X-ray emission over more than one solar cycle. A specific description of the catagory I sensors aboard SOLRAD 11B appears in Table I. The 11A sensors are similar.

The X-ray radiation monitored by the SOLRAD 11 catagory I sensors is directly responsible for D- and E-region electron production during solar flares. It is this radiation which produces the disturbances to HF and VLF radio propagation observed as sudden short wave fadeouts (S-SWF) and sudden phase anomalies (SPA), thus it has direct application to HF radio propogation and VLF communication and navigation systems. NOSC has demonstrated that observations of the 1-8 Å X-ray flux can be directly related to the lowest observed frequency (LOF) on any HF radio path traversing the ionosphere. In addition to these direct effects the assembly of X-ray detectors can be used to measure the temperature and emission measure of the region producing the radiation and from those quantities a probability for flare occurrence can be estimated.

The EUV monitors are relatively new sensors and while the importance of these bands is understood in F-region models there is not yet sufficient data on which to develop prediction techniques.

In the second catagory, Table II, are sensors which have been flown in earlier spacecraft such as those of the OGO or OSO series launched by NASA. The results of these early experiments confirmed their relevance in ionospheric processes or to the characterization of the solar events that contribute to those processes. The scintillation and pro-portional counters measure the most impulsive portion of the solar flare X-ray emission spectrum. Although this penetrating X-ray radiation affects the lowest part of the D-region it is probably more useful as an indicator of the non-thermal processes in flares which accelerate protons capable of producing long lasting disturbances in the polar ionosphere.

The NRL Bragg crystal spectrometer aboard OSO-6 demonstrated that the relative intensity of spectral lines from the ions Mg XI and Mg XII are a sensitive indicator of flare activity (Doschek, G.A. and Meekins, J.F., 1978). The He-like ion Mg XI is quite strong in active regions where it is produced in plasma whose temperature is near one million degrees. The appearance of the H-like Mg XII indicates the presence of plasma with a temperature ten times greater. In large flares the intensity of Mg XII can exceed that of Mg XI so the ratio of these two lines can be used as an indicator of flare conditions within an active region.

The UV spectrometer covers the most intense line in the solar ultraviolet spectrum, Hydrogen Lyman-α, at 1216 Å. This line is the major contributor to D-region ionization during solar minimum. This experiment together with 1080 to 1350 Å sensors of the catagory I experiments were designed to determine the long term variability in the Lyman-α line and in the solar spectrum up to 1800 Å.

The particle sensors described in Table III are new to the SOLRAD series spacecraft since the earlier satellites orbited at low altitude where they only occasionally encountered the charged particles of the earth's trapped radiation belts. In fact, the particle sensitivity of the X-ray photometers was considered undesirable and they were protected from interference with large magnets which deflected the low energy electrons. These sensors provide a complete description of the particle streams emitted by the sun at those times when the satellites are outside the magnetosphere. With two operational spacecraft about 60% of the time one or the other will be in position to monitor the sun's particle emission. The particle sensors have been provided by groups outside of NRL and are based on experiment designs flown in earlier spacecraft.

While particle acceleration is thought to occur in most solar flares, only in a few of them do particles reach the vicinity of the earth because of the guidance of the solar magnetic fields. The highest energy protons may reach the earth within an hour of the start of the flare. They are, however, of minor geophysical importance compared to the increasing numbers of lower energy protons which arrive somewhat later. The peak total energy flux of these protons may occur two to three days after the flare. Because of their lower magnetic rigidity they are guided into the polar cap regions to produce an ionospheric effect known as a Polar Cap Absorption or PCA. This phenomena can be re-sponsible for loss of HF radio communications over periods as great as several days. Disruptions to the Omega Navigation System may also result. The omnidirectional proton experiment aboard SOLRAD 11 is designed to detect the arrival of the initial high energy proton stream while the low energy proton spectrometer measures the energy and flux of the protons producing the major ionospheric distrubances. Other experiments, designed to measure the spectra, intensity and direction of arrival of charged particles aid in our understanding of the particle propogation process. These measurements also provide in-formation necessary to our understanding of the acceleration processes in solar flares. The solar wind experiment measures the persistent flow of low energy particles which are present as a background upon which the flare particle streams are impressed. The solar wind interacting with the earth's magnetic field causes the variability which is detected by surface magnetometers and is the major source of particles responsible for the aurora.

The third catagory of sensors listed in Table IV is almost purely scientific. These experiments have been designed to provide information on fundamental scientific problems such as particle acceleration in solar flares, interaction of solar and stellar wind particles with the earth's atmosphere and the newly discovered gamma-ray burst phenomena.

X-ray polarization, if detectable in solar flare X-ray emission would provide proof of non-thermal processes and particle acceleration. This could be a useful index of potential PCA disturbances.

The stellar auroral X-ray sensors can provide information on the interaction of streams of energetic particles with the earth's upper atmosphere and the geocoronal-extra-terrestrial EUV sensors can also provide similar information.

4. DATA ANALYSIS AND INTERPRETATION

To calculate ionospheric electron densities it is necessary to know both the absolute intensity and wavelength distribution of the ionizing radiation.

It is quite difficult to design instruments which make measurements of absolute intensity with both high spectral resolution and high time resolution. The SOLRAD sensors are a compromise. They have been chosen to fulfill the goal of absolute flux measurement with high time resolution, sacrificing spectral and spatial resolution. Spectral information adequate for ionospheric applications can be derived from the response of photometers with adjacent or overlapping wavelength ranges.

The X-ray spectrum below 50 Å shows great variability over periods as short as a few tens of seconds during solar flares. Consequently great dynamic range is required of both the photometer and its associated electronic circuits. In a large solar flare the X-ray flux below 8 Å can change by a factor of 1000. At longer wavelengths and in the EUV the changes are much smaller.

The band sensitive photometers used aboard SOLRAD 11 are essentially gas filled diodes whose wavelength sensitivity is determined by the window material and thickness and by the type and pressure of the gas filling. These ionization chambers generate very small currents. Consequently, sensitive and very stable electrometer amplifiers are used to amplify the signal to a level compatible with the requirements of the telemetry system A/D converters.

The major sources of error in the X-ray photometer measurements arise from problems in photometer calibration and from the assumption of a sometimes unrealistic spectral distribution of the solar X-ray flux.

4.1 Sensor Calibration

The techniques used in calibration the SOLRAD 11 X-ray photometers have been described by Meekins et al. (1974) and by Unzicker and Donnelly (1974) so they will not be discussed in this paper. We present here only the results for the 1-8 Å X-ray photometer. The experimentally determined efficiency $\epsilon(\lambda)$ is plotted in Figure 6. There are two curves. The solid one is the best fit to the experimental points of the theoretical efficiency function

$$\epsilon(\lambda) = T_W(1-T_G) \tag{1}$$

where T_W and T_G are the transmission of the window and gas filling respectively.

$$T = \exp(-\mu_m \rho x) \tag{2}$$

μ_m is the photoelectric mass absorption coefficient and ρx is the area density of the window material. The absolute accuracy of the calibration is $\pm10\%$ near the peak efficiency, about 3 Å. The dashed curve represents the theoretical response of the photometer based on calculated values of T_W and T_G. The theoretical response was used to reduce data from the X-ray sensors flown aboard SOLRAD satellites prior to SOLRAD 11.

4.2 Derivation of Flux from Photometer Current

The second source of error in the calculation of X-ray flux is the assumption made in selecting the spectral distribution of the incident radiation. A single photometer can provide no information about the spectral distribution of the incident radiation and an emission spectrum must be assumed. The graybody approximation has been quite useful and all SOLRAD data have been reduced using this assumption from 1960 to the present. This has resulted in a uniform description of the solar variability in X-rays over one and one half solar cycles. In this method of analysis it is assumed that the emission spectrum can be approximated by a blackbody distribution with a diluted total energy emission, i.e.,

$$E_{GB}(\lambda,T) = (2\pi hc^2 D)\lambda^{-5}[\exp(c_2/T\lambda)-1]^{-1} \tag{3}$$

where $C_2 = hc/k$; h is Plancks' constant, c the velocity of light and k is the Boltzmann constant. D is a dilution factor. Since a single temperature T will not adequately describe the solar spectrum over a broad wavelength range various temperatures are used

in the calculation, e.g., $T = 2 \times 10^6$K is used for the 1-8 Å band and 10×10^6K for the 0.5-3 Å band.

The 1-8 Å flux data currently transmitted in real time from NRL to NOSC is calculated with this graybody assumption but these values are easily converted to flux values based on other spectral distributions.

Over the past decade a great deal has been learned about the solar spectral distribution in the X-ray region. Horan (1970) applied Culhane's (1969) theoretical description of the X-ray spectrum in the calculation of flux values using the ratios of the 1-8 Å and 0.5-3 Å photometer responses.

Using this ratio a temperature is derived which describes the assumed isothermal emitting plasma. A good approximation of the actual spectrum can be derived from this temperature using equations from Culhane and Acton (1970) for continuum emission and using equations of Tucker and Koren (1971) to derive the line emission. These spectra are illustrated in Figure 7 for temperatures 2, 8 and 32 million degrees K.

It is also possible to correct the earlier graybody fluxes to the more accurate single temperature spectral distribution using the equations and tables published by Dere, Horan and Kreplin (1974a). They found that the calculated 1-8 Å graybody fluxes were about a factor of 3 lower than the more accurate single temperature distribution for temperatures of 2×10^6K and at very high temperatures they were about 3 times greater.

A further refinement of the flux derivation problem was developed by Dere et al. (1974b) and termed the multi-thermal analysis. This technique uses a number of ionization chamber photometers with overlapping wavelength bands to calculate a quantity called the emission measure as a function of temperature. The emission measure is defined as the product of the square of the electron density and the differential volume. The multithermal model is more realistic than the single temperature description but the differences are probably not great enough to be of importance in ionospheric electron density calculations. Their calculation also requires considerable computer time which limits the application of the technique in any real-time assessment system.

5.   PRESENT AND PLANNED APPLICATIONS

Applications of real time measurements of solar X-ray and EUV emission fall into two rather broad and interrelated areas. The first is in assessment of the ionospheric electron density and from it calculation of parameters such as the LOF and MUF in real-time. Such assessments can directly support day to day management of HF communications. In disturbed periods, real-time monitoring can be employed to assess the actual propogation conditions on various HF paths and give the communicator some flexibility in rerouting traffic over those paths which may be less affected. Ionospheric disturbances also affect VLF navigation systems. Real-time monitoring of the solar flare X-ray and particle emission can be used to correct position measurements (Argo, P.F., 1975) should those be made during a disturbed period, or at least serve as a warning that the position determination is probably inaccurate.

5.1   Applications to Ionospheric Propogation

A specific example of the application of solar monitoring in the assessment of ionospheric conditions has been described in Rothmuller (1978). His group at NOSC has correlated the observed 1-8 Å flux measured by SOLRAD 10 with the lowest observed frequency (LOF) as measured by a network of oblique ionospheric sounders and has developed a model from which the LOF can be assessed, in real-time, over any path in the sunlit hemisphere directly from the 1-8 Å X-ray flux measurements. This model is now a part of the PROPHET computer system which serves the Naval Communications station at Stockton, CA as a frequency management tool.

Another application, but one not yet realized, is in the real-time assessment of the maximum useable frequency (MUF). While F-region models are available which might be used to compute the F-region electron density, and from it the MUF, and while the required EUV measurements are now being made by the SOLRAD 11 satellite, this program has not yet been implemented. At least two areas of work must be undertaken to make practical a real-time assessment of the MUF based on SOLRAD EUV data. One is the absolute calibration of the EUV sensors and the other is the development of a simpler model for computation of the MUF from the EUV measurements. Although programs are now available they require large computers and would not be practical in a real-time assessment system. Although absolute EUV fluxes are not yet available, EUV enhancements during solar flares are observed from the sensors aboard SOLRAD 11 B. The relative increases in small flares vary from less than 1% to 10% in the 700-1030 Å band. The largest enhancement so far observed occurred Sept. 18, 1977 at 0052 UT and amounted to an approximate increase of 30% over the pre-flare level.

All of the EUV bursts so far examined show rather slow variations. There have been no observations of the rapid fluctuations which should be required to produce the F-region ionospheric disturbances studied by Donnelly (1973). But it should be noted that in this period of solar minimum there have been very few flares capable of producing ionospheric distrubances. The role of EUV enhancements in F-region ionospheric disturbances will continue as an object of great interest in the ascending portion of this solar cycle.

5.2 Prediction of Solar Activity

The second area of application of X-ray and EUV real-time measurements is in prediction of those solar events and conditions which produce ionospheric disturbances. It is only through such predictions that it will become possible to predict ionospheric disturbances with a lead-time of a few hours.

NRL began making informal predictions of solar activity based on real-time measurements of X-ray flux in 1966. These predictions were used by the Naval Communications Command for several years until NOAA and the Air Force established formal forcasting centers. Our last predictions were used by the Navy Department, CNO(OP-986), in 1973. The predictions were based on the demonstrated sensitivity of X-ray radiation as an index of solar activity. A set of simple criteria were established, i.e., the 1-8 Å flux exceeding 0.001 erg $cm^{-2} sec^{-1}$, the 8-16 Å flux exceeding a level of 0.02 erg $cm^{-2} sec^{-1}$ and the 0.5-3 Å band showing fluctuating levels generally greater than 0.00001 erg $cm^{-2} sec^{-1}$. Experience showed that when these three criteria were met flares producing SID's were four times more likely to occur than when the conditions were not met.

Currently SOLRAD 11 data from the various X-ray sensors is analyzed to compute temperatures and emission measures of active regions. It has been shown that it is possible to predict the presence of a flaring region one to two days before it appears on the visible hemisphere of the sun. Sharp increases in active region temperatures deduced from X-ray flux measurements have been observed prior to flare activity but it is too early and too few flare periods have been investigated to tell whether this will become a reliable prediction tehcnique. Other SOLRAD X-ray measurements also offer promise in the development of flare prediction techniques. The sensitivity of the Mg XI and Mg XII ratio has been mentioned earlier but has yet to be investigated with a view toward development of a prediction technique.

6. CONCLUSIONS

The SOLRAD 11 A and B spacecraft provided nearly continuous monitoring of solar X-ray, EUV and particle emission from launch to December 1976 when the loss of a critical timing circuit in 11 B eliminated data from the particle sensors. The X-ray and EUV sensor operation was not affected. In June 1977 a failure of the telemetry modulation system aboard 11 A eliminated acquisition of all solar data from that spacecraft. The X-ray, EUV and solar wind experiments on 11 B continued to produce data up to February 1978 when the solar wind experiment failed leaving only the X-ray and EUV sensors operational. Fortunately, it is just these sensors which are necessary for applications to ionospheric assessment and prediction services. Consequently the flow of data to NOSC continues and with the assistance of NASA's network of tracking stations data acquisition in real-time is still possible for 12 to 16 hours every day.

The telemetry system and ground station have worked quite well and have generally satisfied the design requirements. However, one element of the turnstile antenna on 11 B failed to deploy producing an unsymmetrical radiation pattern. This is probably responsible for some of the synchronization problems present at times of low signal to noise ratios. High noise levels are also a problem when the sun is active and happens to fall within the main or side lobes of the ground station antenna.

In conclusion the SOLRAD 11 A/B system has demonstrated that real-time monitoring and dissemination of solar radiation measurements is practical and that they can be effectively employed in management of ionosphere dependent military systems.

7. REFERENCES

Argo, P.E., 1975, Modeling Omega PCA Phase Advances, Naval Electronics Laboratory Center, Report TR 1950.

Culhane, J.L. 1969, Thermal Continuum Radiation from Coronal Plasmas at Soft X-Ray Wavelengths, Mon. Not. Roy. Astr. Soc., 144, 375.
Culhane, J.L. and Acton, L.W., 1970, A Simplified Thermal Continuum Function for the X-Ray Emission from Coronal Plasmas, Mon. Not. Roy. Astr. Soc., 151, 141.

Dere, K.P., Horan, D.M. and Kreplin, R.W., 1974a, The Spectral Dependence of Solar Soft X-Ray Flux Values Obtained by SOLRAD 9, J.A.T.P., 36, 989.

Dere, K.P., Horan, D.M. and Kreplin, R.W., 1974b, A Multithermal Analysis of Solar X-Ray Emission, Solar Phys., 36, 459.

Donnelly, R.F., 1973, Ground-Based Observations of EUV Flare Emissions in High Energy Phenomena on the Sun, ed. Ramaty, R., and Stone, R.G., NASA publication, NASA SP-342, 242.

Doschek, G.A. and Meekins, J.F., 1973, Soft X-Ray Flare Spectra, in High Energy Phenomena on the Sun, ed. Ramaty, R., and Stone, R.G., NASA publication, NASA SP-342, 262.

Grubb, R.N., 1975, the SMS/GOES Space Environment Monitoring Subsystem, NOAA Technical Memorandum ERL SEL-42.

Horan, D.M., 1970, Coronal Electron Temperatures Associated with Solar Flares, Ph.D. Thesis, Catholic University of America, University Microfilms, 70-22133.

Kreplin, R.W., 1970, The Solar Cycle Variation of Soft X-Ray Emission, Ann. Geophys. 26, 567.

Kreplin, R.W., Dere, K.P., Horan, D.M., and Meekins J.F. 1977, The Solar Spectrum Below 10 A, in The Solar Output and its Variation, ed. White O.R., Colorado Associated University Press, Boulder, CO.

Meekins, J.F., Unzicker, A.E., Dere, K.P. and Kreplin, R.W., 1974, Absolute Calibration of X-Ray Ionization Chambers, Naval Research Laboratory, Report 7698.

Rothmuller, I.J., 1978, Real Time Propogation Assessment: Initial Test Result, Paper 5-2 in Proceedings of the 1978 Symposium on the Effect of the Ionosphere on Space and Terrestrial Systems, sponsored by NRL and ONR, Jan. 24-26.

Tucker, W.H., and Koren, M., 1971, Radiation from a High-Temperature, Low-Density Plasma: The X-Ray Spectrum of the Solar Corona, Ap. J. 168, 283; erratum 170, 621.

Unzicker, A.E., and Donnelly, R.F., 1974, Calibration of X-Ray and Ion Chambers for the Space Environment Monitoring System, NOAA Technical Report, ERL 310-SEL 31, Nov. 1974.

Viterbi, A., 1971, Convolution Codes and Their Performance in Communication Systems, IEEE Trans. on Communications Technology, COM-19, No. 5, 751.

TABLE I

SOLRAD 11 A/B Category I

Wavelength Band	Det. Type	Sampling Period	Expt. No.
X-RAY MONITORS			
1 to 8 Å	Ionization Chamber	7.5 sec	4
8 to 16 Å	Ionization Chamber	15	5
44 to 60 Å	Ionization Chamber	30	6
0.5 to 3 Å	Ionization Chamber	7.5	12
2 to 10 Å	Ionization Chamber	15	13
EUV MONITORS			
100–500 Å	LiF photo surface + Be filter	7.5	7A
500–800 Å	LiF photo surface + Sn filter	7.5	7B
700–1030 Å	LiF photo surface + In filter	7.5	7C
1080–1350 Å	NaCl photo surface + MgF filter	15	8B
1080–1350 Å	Ionization chamber	15	8A

TABLE II

SOLRAD 11 A/B Category II

X-RAY AND EUV SENSORS

Energy/Wavelength	Det. Type	Channels	Sampling Period	Expt. No.
15 to 150 keV	Scintillation Counter	4/1	7.5/1.875	1
3 to 60 keV	Proportional Counter	4/1	7.5/1.875	2
9.2 and 8.4 Å	Bragg Spectrometer	3	60	3
1175 to 1800 Å	UV Spectrometer	–	94 sec/12.5 min	9

TABLE III

SOLRAD 11 A/B Particle Sensors

NAME	ENERGY RANGE	CHANNELS	EXPT NO.	INSTITUTION
Solar Protons	< 9.5 MeV > 9.5 MeV (P)	2	14	Aerospace
	< 38 MeV > 27 MeV (a)	2		
Antisolar Protons	< 9.5 MeV > 9.5 MeV (P)	2	23	Aerospace
	< 38 MeV > 27 MeV (a)	2		
Omnidirectional Protons	5 to 116 MeV (P)	5	17A	Aerospace
	25 to 385 MeV (a)	5	17A	
Proton Telescope	20 to 500 KeV (P)	5 DIFF	17D	
	0.5 to 1.5 MeV (P)	3 INT	17D	
Heavy Ions	> 0.5 MeV/nucleon Z 1 to 18+	5	17C	
Proton-Alpha Telescope	1.3 to 100 MeV (P)	10	20	AFGL
	22 to 100 MeV (a)	3		
Low Energy Proton Spectrometer	97 KeV to 6 MeV	11	21	AFGL
Solar Flare Electrons	12 KeV to 1.6 MeV	12	22	AFGL, Aerospace
Solar Wind	0.2 to 5 KeV (+ ions)	24	15	MIT
	20 to 120 ev (e)	4		
	direction, velocity and temperature			

TABLE IV

SOLRAD 11 A/B Category III

Name	Energy/Wavelength Range	Channels	Sampling Period	Expt. No.
Thomson X-Ray Polarimeter	10 to 22 keV		30 sec	10
	22 to 60 keV		30 sec	
Bragg X-Ray Polarimeter	2.8 Å		2 min	11
Stellar Auroral X-Rays	1 to 8 Å		16 min	16
Geocoronal	100 to 1400 Å	6	2 min	18
Extraterrestrial EUV	100 to 1400 Å	6	2 min	19
X-Ray Background	0.5 to 20 keV	256	16 min	24
Gamma Rays	0.2 to 2 MeV	5	14.6 msec	25
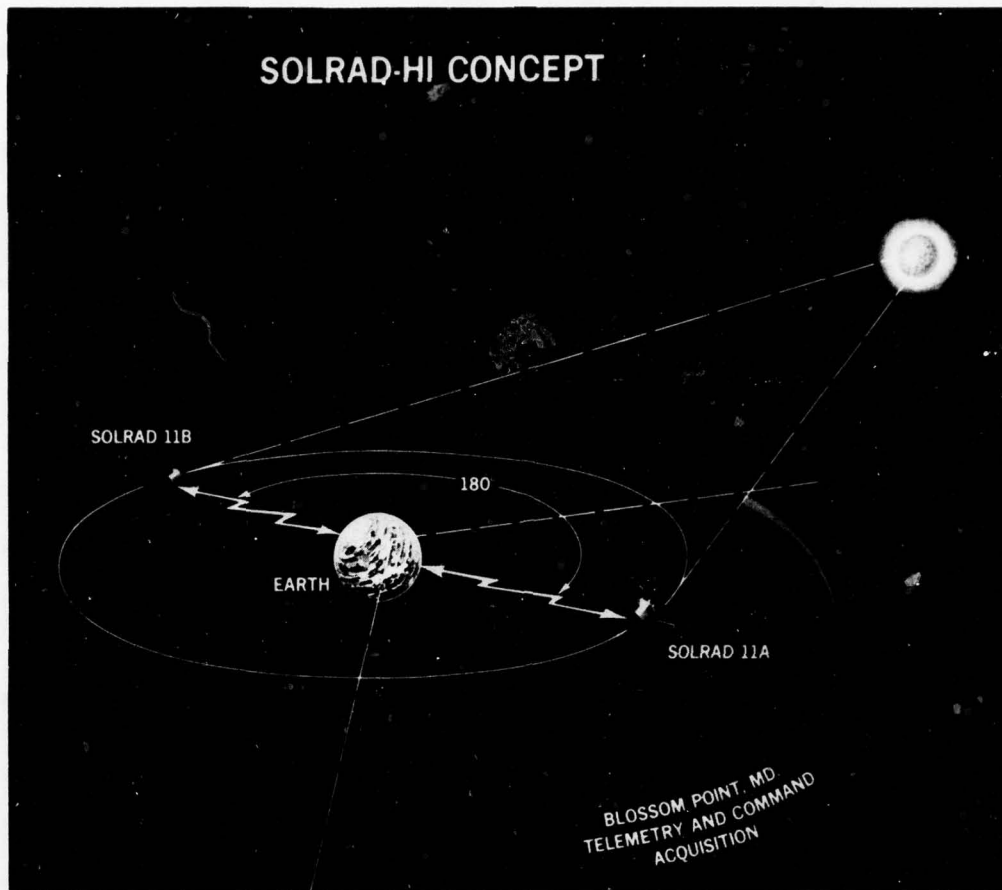
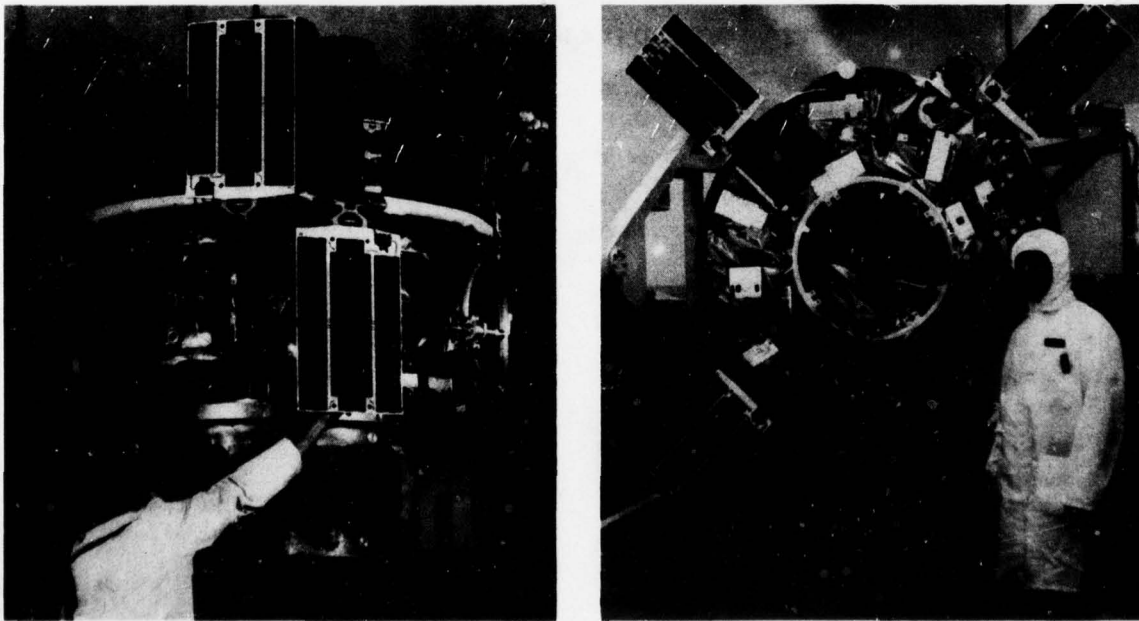Fig. 1   The SOLRAD 11 A/B monitoring concept

Fig.2   Two views of the SOLRAD 11 A/B spacecraft. At the left the two spacecraft are
shown in launch configuration and on the right one of the spacecraft is shown with
solar panels extended. This view shows the sun-facing surface where the various
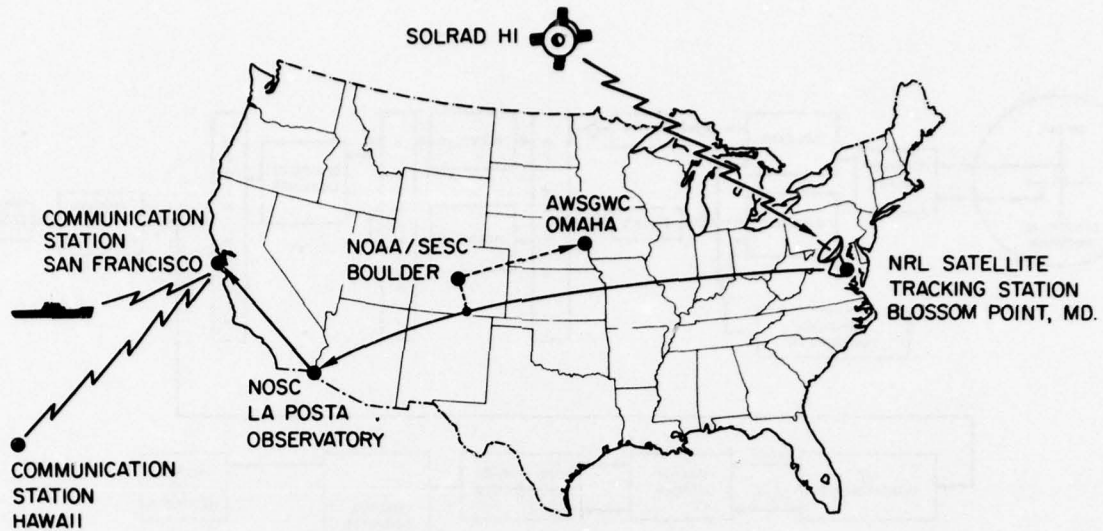X-ray and UV sensors are mounted

Fig.3   Block diagram of the SOLRAD 11 ground station at Blossom Point, Maryland

Fig.4   Block diagram of the SOLRAD 11 computer installations at Blossom Point and at NRL.
The NOSC data line can be driven from either Blossom Point or from NRL

Fig.5   SOLRAD data distribution network. The NOAA to Air Weather Service link
has not been implemented to transmit SOLRAD data between those two points
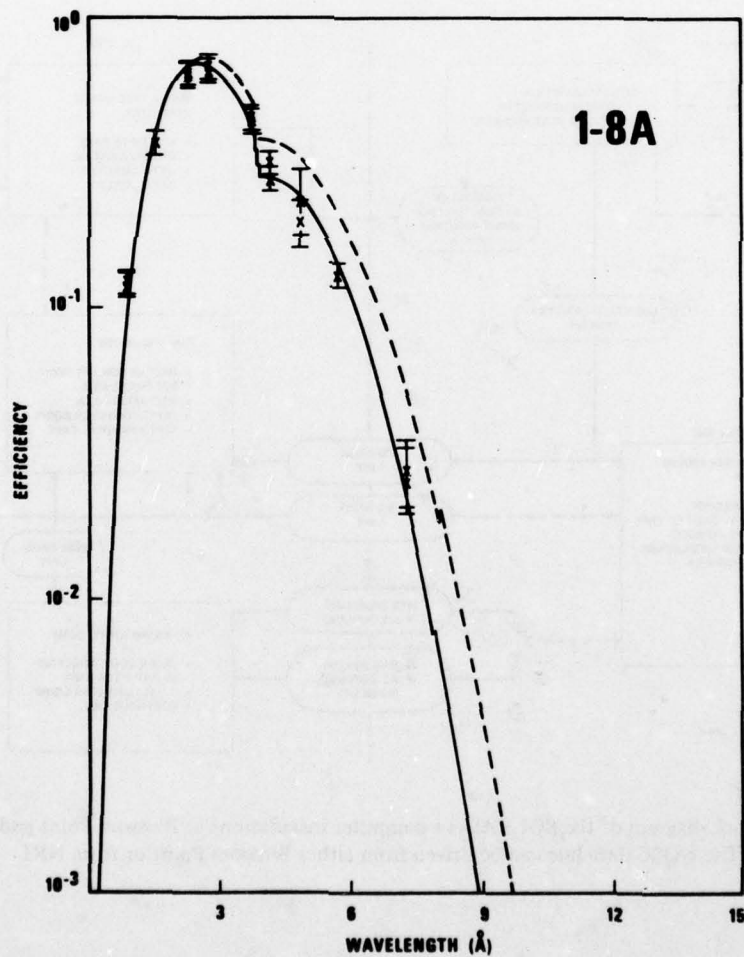
Fig.6   Experimentally determined wavelength response of the SOLRAD 11 1−8 Å photometer.
The crosses are the individual measurements. The solid line is the fitted wavelength response
while the dashed curve represents the theoretical response
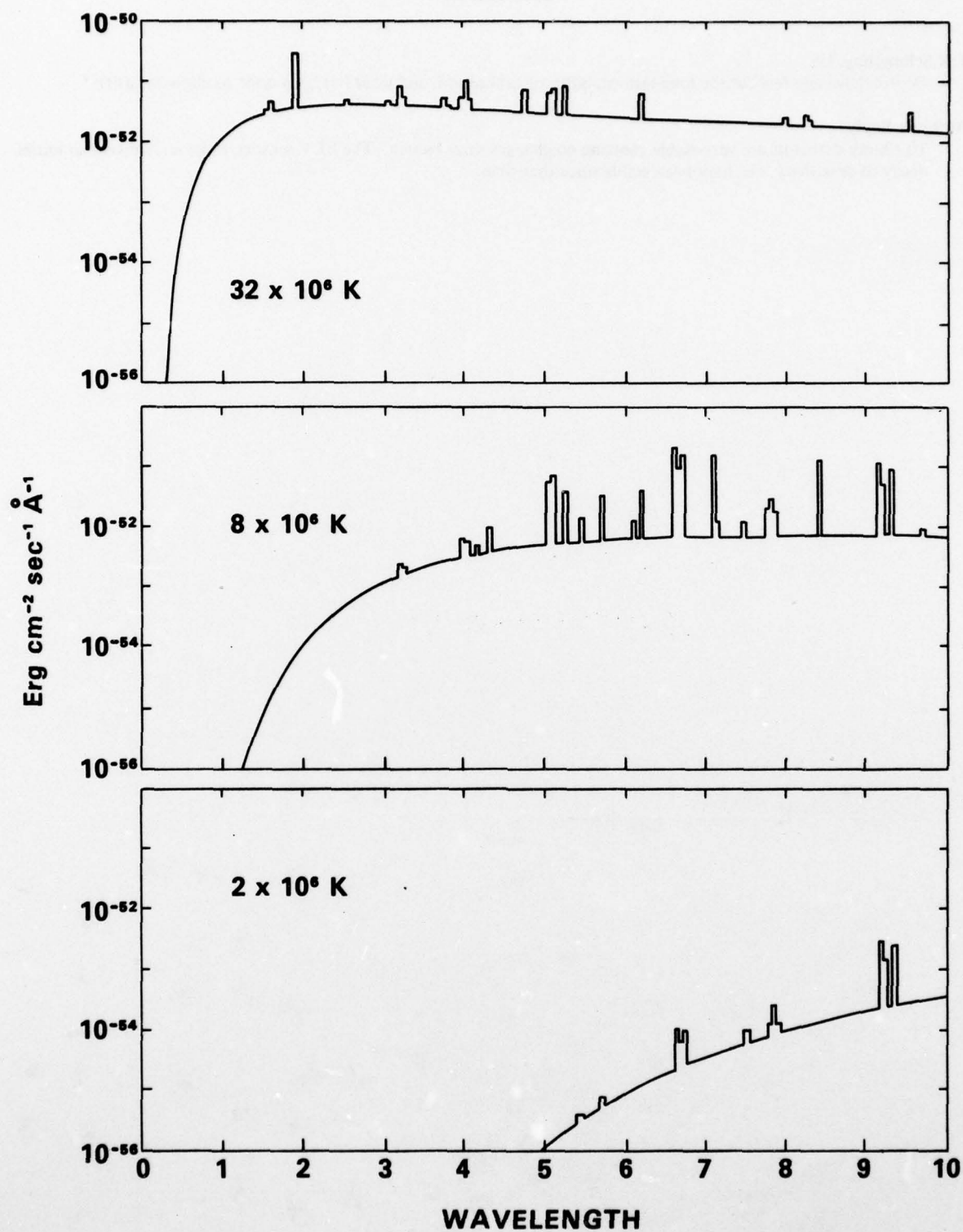
Fig.7 Solar X-ray spectra below 10 Å derived from the ration of 0.5−3 Å and 1−8 Å photometer responses. The ordinant units are ergs cm⁻² sec⁻¹ Å⁻¹ for unit emission measure. The amplitude of the line represents the energy contained in the line and not its peak intensity

DISCUSSION

E.R.Schmerling, US

Do you have any feel for the long-term stability of calibration, and what has been done to allow for drifts?

Author's Reply

The X-ray detectors are very stable showing no changes since launch. The EUV sensors, however, showed an initial decay of sensitivity, but have been stable since that time.

PREDICTION OF SOLAR ENERGETIC PARTICLE EVENT HISTORIES USING
REAL-TIME PARTICLE AND SOLAR WIND MEASUREMENTS
E. C. Roelof/R. E. Gold
The Johns Hopkins University
Applied Physics Laboratory
Laurel, Maryland 20810

SUMMARY

The comparatively well-ordered magnetic structure in the solar corona during the decline of Solar Cycle 20 has revealed a characteristic dependence of solar energetic particle injection upon heliographic longitude. When analyzed using solar wind "mapping" of the large scale interplanetary magnetic field line connection from the corona to the Earth, particle fluxes display an approximately exponential dependence on heliographic longitude $\exp(\phi/\phi_o)$, where $\phi_o \sim 10$ degrees. Since variations in the solar wind velocity (and hence the coronal connection longitude) can severely distort the simple coronal injection profile, the use of real-time solar wind velocity measurements can be of great aid in predicting the decay of solar particle events. Although such exponential injection profiles are commonplace during 1973-1975, they have also been identified earlier in Solar Cycle 20 (e.g., 1967 and 1969), and hence this structure may be present during the rise and maximum of the cycle, but somewhat obscured by greater temporal variations in particle injection.

1.   INTRODUCTION

Our continuing investigation of the prediction of solar energetic particle events and geomagnetic disturbances has led us into a comprehensive study of these phenomena for all of Solar Cycle 20 (1964-1976). To no one's surprise, solar-terrestrial phenomena showed distinctive changes in character from one phase of Solar Cycle 20 to another. For instance, during the declining phase of the cycle (1973-1976), the solar corona (and hence the interplanetary plasma and magnetic field), was considerably more well-ordered than other phases. This was to be expected, since it is a fact well-established early in this century that recurrent geomagnetic disturbances (the Bartel's M-regions) become more clearly defined in the last quarter of each solar cycle. Thus prediction of geomagnetic disturbances could degenerate to mere anticipation of 27-day recurrences during 1973-1976. However, if history repeats itself, we will again have to resort to more sophisticated prediction techniques for the rise and maximum of Solar Cycle 21 (1977-1984).

None-the-less, the decline of Solar Cycle 20 has provided information which will have direct application to prediction work during Solar Cycle 21. We have had the growing conviction that coronal structure is relatively ordered (on a global scale) throughout the solar cycle, but that the manifestation of this order is obscured throughout the rise and maximum of the cycle by temporal (non-recurrent) events which decline in frequency late in the cycle. This conviction is based on our success in occasionally identifying a structure in particle and plasma events which occurred early in Solar Cycle 20 (e.g., 1967 or 1969), which exhibits the same coronal signatures we find so much more obviously defined in the events from 1973-1976.

In this paper, we present the technique we are applying to all our data from Solar Cycle 20. By combining solar wind velocities with energetic particle fluxes (measured on the same spacecraft wherever possible), the coronal emission profile of both plasma and particles can be displayed as a function of heliographic longitude. Even if there is appreciable temporal evolution during events, heliographic longitude (fixed on the sun) is the natural coordinate system for interplanetary observations.

In Section 2, we illustrate our solar wind "mapping" technique and demonstrate its capability to unfold coronal structure from near-Earth interplanetary observations. With direct telemetry from spacecraft plasma detectors in the solar wind, such "mapping" could be done in real time. Section 3 presents four examples of coronal structure of plasma and energetic particles. These four events from 1973 illustrate the wide variety of time histories of particle events at Earth which can be produced by essentially the same coronal injection profile in the corona. Following a brief discussion of each event, we offer a brief scenario of how the decay history of these four events could have been predicted using simultaneous real-time solar wind and energetic particle measurements. Section 4 sets forth our recommendations for improved prediction techniques.

2.   SOLAR WIND MAPPING OF ENERGETIC PARTICLE FLUXES

The mapping of the large-scale interplanetary field does not depend on a stationary solar wind pattern. All that is required is that each packet of plasma carry "frozen-in" magnetic field lines out from the corona to 1 AU, and that the plasma not suffer any anomalous acceleration or deceleration during transit. The foregoing conditions are usually satisfied except right at the stream-stream interactions of fast-slow streams (due to either transient or co-rotating velocity gradients). Outside of the influence of stream-stream interactions, the transit time is approximately r/V, where $r = 1$ AU at Earth and V is the instantaneous solar wind velocity. The "mapped" heliolongitude L_C of plasma and field longitude is then given to sufficient approximation by $L_C = L_E + \Omega_{SID} r/V$, where L_E is the Earth's heliolongitude and Ω_{SID} is the sidereal rotation rate of the sun (Nolte and Roelof, 1973a, 1973b).

For purposes of illustration, we take the simplest case of a stationary corotating fast stream, depicted schematically in Figure 1. In panel (a) we sketch the stream velocity profile as a function of heliographic longitude. The resulting stationary streamlines (which will also be the large-scale interplanetary field lines), are shown in (b) in a plot of radius (R) vs longitude (ϕ) in the ecliptic plane. In such an R-ϕ plot, Archimedean spirals are straight lines. In the rising velocity portion of the fast stream at Earth, the connection longitude "sweeps" rapidly eastward across a wide longitude range on the sun in a short time (< 1 day). On the other hand, in the rarefaction following the peak of the stream at Earth, the connection longitude "dwells" at nearly the same location on the sun for a long time (1-5 days). These variations in connection longitudes of the interplanetary field lines to Earth are summarized in panel (c) of Figure 1.

Now consider the effect of such solar wind stream structure on a stationary solar energetic particle injection profile across the sun. We show in the upper panel, Figure 2 a smooth particle injection profile. If the logarithm of the intensity were plotted, this would be a longitude profile of the form $\exp(\phi/\phi_0)$ with $\phi_0 > 0$. We shall neglect any temporal evolution of the injection profile, but as we shall see in Section 3, this is actually a justifiable approximation for energies ~ 1 MeV/nucleon. The middle panel of Figure 2 repeats the mapping of connection longitudes by the stationary stream structures of Figure 1b. The lower panel of Figure 2 then gives directly the severe distortion of the coronal profile when it is observed as the time history at Earth while this plasma/particle structure co-rotates past the Earth. A little thought will reveal that the same distortion would be caused by a temporal solar wind disturbance having the same time history at Earth as the co-rotating examples of Figure 1, so the result of Figure 2 has considerably more general implications than just the distortion due to stationary solar wind structure.

Two further examples illustrating the identification of, and the compensation for, the distortions introduced into the flux histories by variations in the solar wind and interplanetary magnetic field are shown schematically in Figure 3. For a uniform solar-wind, the time history of solar particle fluxes (j) measured from a symmetric, steady coronal injection profile would be given by (a). The bottom panel shows the linear trace of the heliographic connection longitude (ϕ) as a time function ($\phi = -\Omega_{SYNOPIC}t$) through the coronal flux distribution $j_0(\phi)$. However, if there is a high speed solar wind stream above the western (early) portion of the coronal flux profile (b), then the trace of the connection longitude "sweeps" rapidly eastward from longitudes 1 to 3, "dwells" near 3 during the decay of the stream, and then continues uniformly through the rest of the profile (4 and 5). The result is a rapid rise and broad maximum for the fluxes which mimic rather well the profile of an impulsive flare particle event. Another possible distortion (out of the many possible for even this simple coronal injection profile), occurs when a stream occurring late in the event abruptly cuts off the observed fluxes (c), by rapidly "sweeping" the connection longitude eastward to a region of reduced fluxes in the corona (and therefore also in the interplanetary medium). The general possibility of these types of flux distortions was first mentioned by *Reid (1964)* but application to observations was not attempted for nearly a decade *(Roelof and Krimigis, 1973)*. We shall see in Section 3 actual events which exhibit very much the same types of solar wind and particle intensity histories as those diagrammed in Figures 3a–c when the IMP-7 JHU/APL particle and MIT solar wind measurements are mapped back to the corona.

There remains a crucial point which we have glossed over. What is the relationship between the intensity of particles at Earth and the corona on the same field line? Multispacecraft observations of solar protons $\leqslant 10$ MeV have established that there is negligible transport across interplanetary field lines, and moreover that the intensity gradient along field lines in the decay of these events is small (< 100%/AU) and tends to be positive (when it is measurable). Our experience leads us to make the approximation that intensities are comparable along field lines from the corona to Earth, and therefore we take, as a first approximation, the mapped-back fluxes to be the actual coronal injection profile *(Roelof, 1976; Roelof and Krimigis, 1977)*.

With regard to prediction of the decay of solar energetic particle events, Figures 2 and 3 contain an interesting implication. If we began with the observed (and distorted) particle history at Earth, and if we had real-time solar wind velocity measurements, we could reconstruct the relatively simple coronal injection profile. If its solar longitude dependence (in these cases either a simple one or two-sided exponential) became evident early in the decay, one could then predict the remainder of the decay, particularly if one had reliable predictions of solar wind stream structure to the east of Earth. Obtaining such solar wind predictions may well be feasible through a combination of solar magnetic field observations and the monitoring of interplanetary radio scintillations of compact radio sources. Global estimates of chromospheric magnetic polarity structure are prepared in Hα Synoptic Charts for each solar rotation under the supervision of P. S. McIntosh (NOAA/ERL). In collaboration with W. M. Cronyn and S. D. Shawhan of the University of Iowa, we are now studying the feasibility of synoptic monitoring of electron turbulence in the interplanetary medium using scintillation observations at 34.3 MHz taken with the COCOA-Cross radio array located at the University of Maryland Clark Lake Radio Observatory in Borrego Springs, California *(Cronyn et al., 1976, 1978; Roelof et al., 1975, 1976; Erskine et al., 1978; Gotwols et al., 1978)*. D. G. Mitchell of JHU/APL is carrying out theoretical studies of the interpretation of these line-of-sight observations *(Mitchell and Roelof, 1976; Mitchell, 1978)*.

3. MAPPED SOLAR ENERGETIC PARTICLE EVENTS

3.1 19 March 1973 (Day 78). See Figure 4

This event (Figure 4a) has a "classic" profile in 0.4 and 3 MeV protons, 3.5 MeV alphas and 2 MeV/nucleon medium nuclei. However, the lack of onset velocity dispersion and the very similar time histories among all the species and energies suggests that we are seeing predominantly coronal structure and not interplanetary propagation effects. When we examine the solar wind velocity (Figure 4b), the very close time coincidence between the stream and particle rises buttresses the suggestion of coronal structure. However, the near-constant solar wind velocity after day 78 makes it impossible to separate definitively temporal decay from spatial structure. Thus the mapped particle fluxes (Figure 4c) cannot be interpreted unambiguously as a spatial structure. None-the-less, if there were no temporal evolution during days 78–84, the e-folding angle for this nearly exponential longitude dependence is 8.7° (since the flux drops three orders of magnitude in 60°). We shall see below that this value is consistent with that obtained in other events in which temporal evolution can be shown to be negligible. The corona breadth of the peak of this solar wind stream (Figure 4d) is one of the largest in Solar Cycle 20. Since the solar wind velocity remained nearly constant throughout this particle event, it corresponds closely to the example in Figure 3a.

Prediction Scenario — The intimate association of the non-dispersive rise in fluxes with the onset of the solar wind stream would have alerted the real-time observer to the possible spatial nature of this event. Examination of the steadily steepening coronal profile of the mapped fluxes (Figure 4c) on days 79 and 80 would suggest the approach to an exponential profile. An extrapolation of the profile at the end of day 81 would have predicted the eastern boundary of the profile at $\sim 210°$, so if the solar wind velocity did not change, the event would not end before day 85. Since the solar wind velocity was already above 700 km sec^{-1}, the most likely change would have been a decrease, which would have probably extended the event past day 85.

3.2   2 June 1973 (Day 153). See Figure 5

The slow, similar rise of all species (Figure 5a) suggests coronal structure, consistent with the containment of this event within a large solar wind stream (Figure 5b). When the particles are mapped (Figure 5c), it becomes apparent that we are observing a near-stationary coronal injection profile, symmetric about ~ 0° heliographic longitude. This is precisely the situation diagrammed in Figure 3b. The increase in fluxes in days 159-160 when the connection longitude "back-tracked" 5° (Figure 5d) falls right on the point for day 157, and there is similar agreement between days 158 and 160. The e-folding longitude for the exponential gradient between 335° and 355° is 8.3°, close to that obtained assuming that the 19 March event was also predominantly a coronal injection profile.

Prediction Scenario — The broad profile (Figure 5c) traced out during the two-day solar wind "sweep" over 75° on days 153-154 (Figure 5d) would have alerted an observer to the spatial nature of the event. The drop from maximum flux on day 155 would signify that the connection longitude was now on the eastern wing of the profile, and symmetry (as a first guess) would put the eastern boundary of the profile at ~ 320°. If the solar wind velocity had remained near 700 km sec^{-1}, the predicted termination of the event would have been before day 159. However the solar wind began to decrease and the eastern slope of the profile would have been revealed by day 157 to be steeper than the western, so a revised estimate still would have had the event termination about day 160.

3.3   10 July 1973 (Day 191). See Figure 6

The extremely slow rise of all species in this particle event (Figure 6a) immediately suggests a coronal structure. The rapid drop-off of particle intensities on day 196 coincides precisely with the sharp rise in solar wind velocity to 700 km sec^{-1} (Figure 6b). When mapped in coronal longitude, however, the flux intensities assume a simple form (Figure 6c). If one fits an exponential in longitude $\exp(-\phi/\phi_0)$ to either side of the profile, one obtains $|\phi_0| \simeq 10°$, a value again comparable to the events of 19 March and 2 June. It is obvious that the abrupt flux drop-off on day 196 is due to the rapid 30° "sweep" of the connection longitude from 205° to 175° during the rise of the solar wind stream (Figure 6d). This was just exactly the situation sketched in Figure 3c.

Prediction Scenario — Estimating from the western wing of the flux profile (Figure 6c) and the maximum at the beginning of day 195, symmetry would have predicted an event termination late on day 199 if the solar wind velocity remained constant ~ 400 km sec^{-1}. However it had been rising since day 194, and if the assumption had been made that a 700 km sec^{-1} stream was nearing the Earth, the prediction would have been for an event termination no later than day 197.

3.4   7 September 1973 (Day 250). See Figure 7

This is the only event of the four we present which is clearly flare-associated. The flux increase (Figure 7a) resulted from an importance 2B flare (x-ray importance C1), 1212 UT, 7 September, S18°, W46° (heliographic longitude 188°). The similarities of the time histories of all species is striking, and the spatial nature of the variations is demonstrated by the lack of velocity dispersion on a one-hour time scale between the 0.4 MeV and 3 MeV protons (which have transit times of about 4 hours and 1 hour per AU, respectively). Since IMP-7 was in the magnetotail on days 250-253, solar wind data began on day 254 (Figure 7b). Fortunately, these data are sufficient to reveal that the rapid flux drop-offs on days 255 and 258 were both associated with rapid rises in solar wind velocity. Despite the flare origin of these fluxes, they reveal an exponential coronal injection profile when mapped back to the sun (Figure 7c) just as was demonstrated in the example given in Figure 2. The nearly stationary temporal dependence of the fluxes is evident when the connection longitude "dwells" near 130° for more than a day (Figure 7d). Between days 254 and 261, the fluxes drop 3.83 orders of magnitude over 90°, obeying an $\exp(-\phi/\phi_0)$ dependence with $\phi_0 = 10°$. This is the characteristic value obtained in all these four events, March-September 1973. As we show in Figure 7c, even the > 0.22 MeV electrons in this event display the same exponential gradient in longitude some 8 days after the flare. In fact, about 80% of the ~ 1 MeV solar proton events observed 1972-1976 exhibited this characteristic exponential coronal longitude profile during their decay phases *(Gold et al., 1977a)*.

Prediction Scenario — The monotonic decrease in the mapped coronal profile (Figure 7c) on days 253-255 would have defined the characteristic e-folding parameter $\phi_0 \simeq 10°$. The reasonable assumption of a steady decrease in solar wind velocity to 300 km sec^{-1} by day 258 would have predicted that fluxes would be still a factor ~ 30 above their pre-flare level at that time. If the solar wind had remained at 300 km sec^{-1}, the predicted termination of the event would have been day 263. However, since any rise in solar wind velocity would "sweep" the connection longitude eastward, the observed rise during day 258 would alert the observer to a probable early end of the event before day 260.

4.   RECOMMENDATIONS

The lession of the scenarios of Section 3 is that prediction of the decay of solar energetic particle events using real-time particle and solar wind data involves an understanding of the individual contributions of two processes.

(1) Inference of the particle injection longitude profile. This is accomplished by watching the "unfolding" of the mapped particle fluxes as in Figures 4c-7c. It appears that exponential profiles of the form $\exp(-|\phi-\phi_1|\phi_0)$ with $\phi_0 \simeq 10°$ provided a good working model for particles ~ 1 MeV/nuc during the decline of the cycle. The similar behavior of all particle species was helpful in identifying this common class of event. The exponential profile was usually evident after the fluxes had decayed by a factor of 5.

(2) Inference of solar wind emission profile. This is the crucial element, since if the particle injection profile is inferred, then the decay of the event is determined (for quasi-stationary particle population) by the subsequent history of the coronal connection longitude of the interplanetary

field lines. Prediction of subsequent solar wind velocity dependence from its previous variation is straight-forward only when a rarefraction or "dwell" of a high speed stream has just begun (as on day 156 in Figure 5d), or when a rise or "sweep" has just begun (as on day 194 in Figure 6d).

Reliable real-time prediction, once these quasi-stationary events have been identified, really requires good estimates of the solar wind velocities for the next several days, as we mentioned at the end of Section 2. Using interplanetary radio scintillations as a probe of solar wind disturbances appears to be the most promising technique. However, much progress has also been made in identifying likely source regions of high speed solar wind by their characteristic open coronal magnetic field structure, the clearest, but not the sole example of which, is the "coronal hole" (*Krieger et al., 1973; Nolte et al., 1976, 1977*). Along the same line, we have found characteristic coronal magnetic structures which enhance coronal transport and interplanetary injection of energetic particles: high lying magnetic "arcades" over long filaments dividing weak-field regions of opposite polarities; (*Gold and Roelof, 1976; Roelof et al., 1977*) and large scale (~ 100°) active region "magnetic complexes" which organize the interplanetary "access probabilities" of energetic particle populations (*Roelof et al., 1974; Gold et al., 1977; Nolte and Roelof, 1977*).

The indirect information of coronal magnetic structure therefore complements the more direct information from interplanetary scintillation observations. Inference of coronal magnetic structure (and its effect on solar wind and energetic particle emission), requires the deduction of simple rules from many examples. Fortunately, almost the whole of Solar Cycle 20 is well documented with solar wind and particle data. Some periods of the cycle are covered by Mariner and Pioneer spacecraft well-separated from Earth (1965, 1967, 1969, 1972-76). These "networks" of spacecraft facilitate the separation of temporal evolution from the underlying spatial structure, a separation particularly important during solar maximum.

We therefore recommend the dual course of incorporating the latest results of the interpretation of interplanetary scintillations into prediction techniques while also proceeding with a comprehensive study of plasma, magnetic field and energetic particle data from the last solar cycle and on into the current cycle. One could not ask for more fruitful circumstances for developing prediction techniques: the study of Solar Cycle 21 in "real-time" while making direct comparison with the rich archives of Solar Cycle 20.

REFERENCES

Cronyn, W. M., S. D. Shawhan, F. T. Erskine, A. H. Huneke and D. G. Mitchell, 1976, "Interplanetary Scintillation Observations with the COCOA-Cross Radio Telescope", *J. Geophys. Res., 81,* 695.

Cronyn, W. M., F. T. Erskine, S. D. Shawhan, B. L. Gotwols and E. C. Roelof, 1975, "Prediction of Ionospheric Effects Associated with Solar Wind Disturbances Using Interplanetary Scintillation Observations at 34.3 MHz" in *Effect of the Ionosphere on Space Systems and Communications,* ed. J. M. Goodman, Naval Research Laboratory, U. S. Government Printing Office (Washington, D. C.), 223.

Erskine, F. T., W. M. Cronyn, S. D. Shawhan, E. C. Roelof and B. L. Gotwols, 1978, "Interplanetary Scintillation at Large Elongation Angles: Response to Solar Wind Density Structure", *J. Geophys. Res., 83,* in press.

Gold, R. E. and E. C. Roelof, 1976, "A Prediction Technique for Low Energy Solar Proton Fluxes Near 1 AU" *Space Research XVI,* ed., M. J. Rycroft and R. D. Reasenberg, Akademie-Verlag (Berlin), 791.

Gold, R. E., S. M. Krimigis and E. C. Roelof, 1977a, "Spatially Dominated Solar Particle Events 1972-1976", *Proc. 15th International Cosmic Ray Conference (Plovdiv, Bulgaria), 5,* 119.

Gold, R. E., E. P. Keath, E. C. Roelof and R. Reinhard, 1977b, "Coronal Structure of the April 10, 1969 Solar Flare Particle Event", *Proc. 15th International Cosmic Ray Conference (Plovdiv, Bulgaria), 5,* 125.

Gotwols, B. L., D. G. Mitchell, E. C. Roelof, W. M. Cronyn, S. D. Shawhan and W. C. Erickson, 1978, "Synoptic Analysis of Interplanetary Radio Scintillation Spectra Observed at 34 MHz", *J. Geophys. Res., 83,* in press.

Krieger, A. S., A. F. Timothy and E. C. Roelof, 1973, "A Coronal Hole and Its Identification as the Source of a High Velocity Solar Wind Stream," *Solar Phys., 23,* 123.

Mitchell, D. G., 1978, "Analysis of Interplanetary Scintillation Spectra at Large Elongation Angles", *J. Geophys. Res., 83,* in press.

Mitchell, D. G. and E. C. Roelof, 1976, "A Mathematical Analysis of the Theory of Interplanetary Scintillation in the Weak-Scattering Approximation", *J. Geophys. Res., 81,* 5071.

Nolte, J. T. and E. C. Roelof, 1973a, "Large-Scale Structure of the Interplanetary Medium. I: High Coronal Source Longitude of the Quiet-Time Solar Wind", *Solar Phys., 33,* 241.

Nolte, J. T. and E. C. Roelof, 1973b, "Large-Scale Structure of the Interplanetary Medium. II: Evolving Magnetic Configurations Deduced from Multispacecraft Observations," *Solar Phys., 33,* 483.

Nolte, J. T. and E. C. Roelof, 1977, "Solar Wind, Energetic Particles and Coronal Magnetic Structure: The First Year of Solar Cycle 20", *J. Geophys. Res., 82,* 2175.

Nolte, J. T., A. S. Krieger, E. C. Roelof and R. E. Gold, 1977, "High Coronal Structure of High Velocity Solar Wind Streams", *Solar Phys., 51,* 459.

Reid, G. C., 1964, "A Diffusive Model for the Initial Phase of a Solar Proton Event", *J. Geophys. Res., 69,* 2659.

Roelof, E. C., S. M. Krimigis, W. M. Cronyn, S. D. Shawhan and P. S. McIntosh, 1975, "Observation Using Interplanetary Scintillations at 34.3 MHz of the Effect of a Solar Wind Distriburbance on a Solar Energetic Particle Event", *Proc. 14th International Cosmic Ray Conference (Munich), 5,* 1692.

Roelof, E. C., 1976, "Solar Particle Emission", in *Physics of Solar Planetary Environments, Proc. of the International Symposium on Solar-Terrestrial Physics (Boulder),* ed. D. J. Williams, *American Geophysical Union (Washington, D. C.), 1,* 214.

Roelof, E. C. and S. M. Krimigis, 1973, "Analysis and Synthesis of Coronal and Interplanetary Energetic Particle, Plasma and Magnetic Field Observations Over Three Solar Rotations", *J. Geophys. Res., 78,* 5375.

Roelof, E. C. and S. M. Krimigis, 1977, "Solar Energetic Particles Below 10 MeV", *Proc. of the L. D. De Feiter Memorial Symposium on Study of Travelling Interplanetary Phenomena,* ed. M. A. Shea and C. S. Wu, D. Reidel (Dordrecht), in press.

Roelof, E. C., J. A. Lezniak, W. R. Webber, F. B. McDonald, B. J. Teegarden and J. H. Trainor, 1974, "Relation of Coronal Magnetic Structure to the Interplanetary Proton Events of August 2-9, 1972, " in *Correlated Interplanetary and Magnetospheric Observations,* ed. D. E. Page, D. Reidel (Dordrecht), 563.

Roelof, E. C., S. M. Krimigis, W. M. Cronyn, S. D. Shawhan and P. S. McIntosh, 1975, "Solar Wind and Energetic Particle Events of June 20-30, 1974 Analyzed Using Measurements of Interplanetary Radio Scintillations at 34.3 MHz", *Space Research, XVI,* ed. M. J. Rycroft, Akademie-Verlag (Berlin), 727.

Roelof, E. C., R. E. Gold, and E. P. Keath, 1977, "Evaluation of a Prediction Technique for Low Energy Solar Particle Events", *Space Research XVII,* ed. M. J. Rycroft and R. D. Reasenberg, Akademie-Verlag (Berlin), 545.
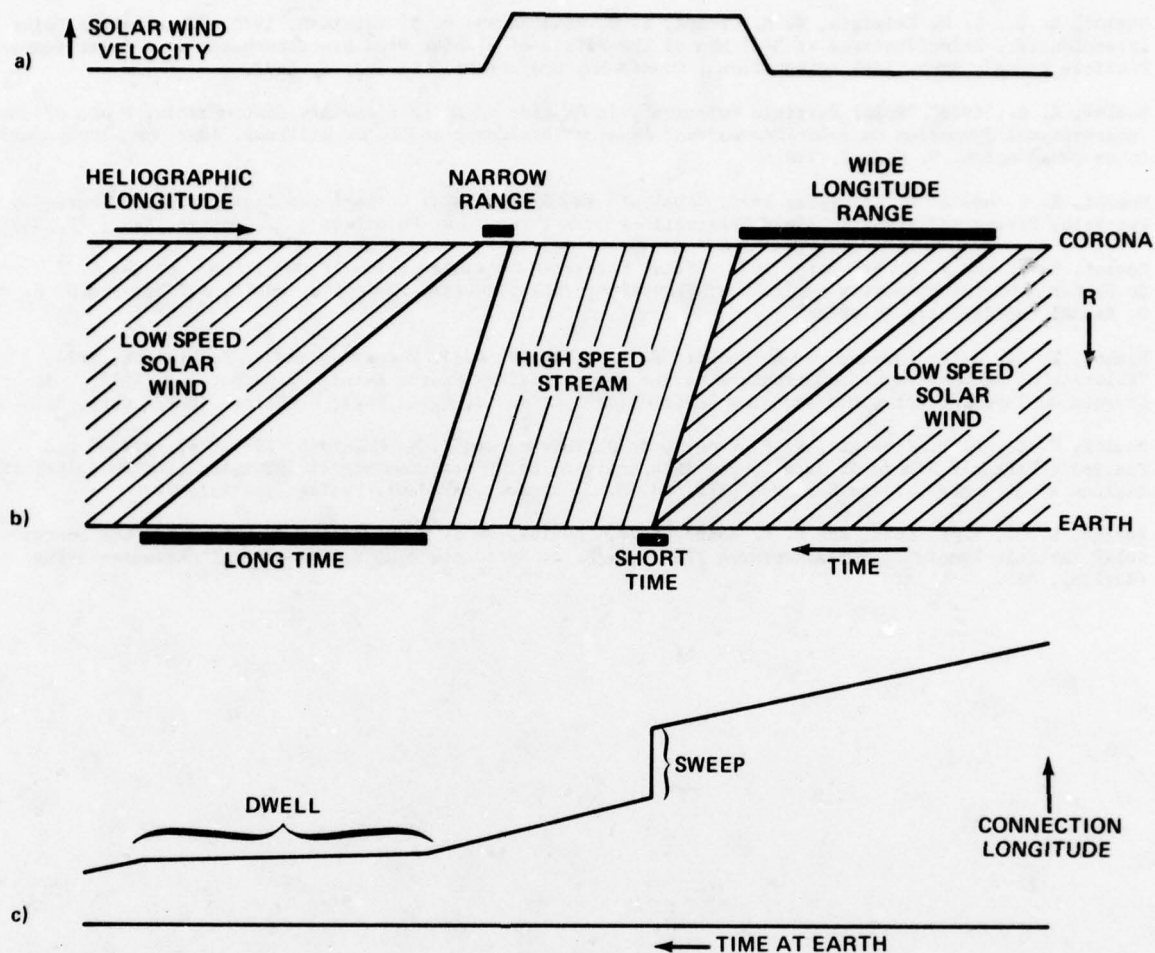
FIGURE 1 Schematic representation of a stationary solar wind stream and connection longitudes. The solar wind velocity profile is shown in (a) as a function of heliographic longitude, while in (b) an r-φ (radius-longitude) plot of constant-velocity stream lines in the ecliptic plane gives the large-scale configuration of the interplanetary magnetic field. As sketched in (c), during the rise of the interplanetary high speed stream, the coronal connection longitude "sweeps" across a wide longitude range in a short time, while in the rarefaction following the interplanetary velocity peak, the connection longitude "dwells" in a narrow longitude range for a long time.
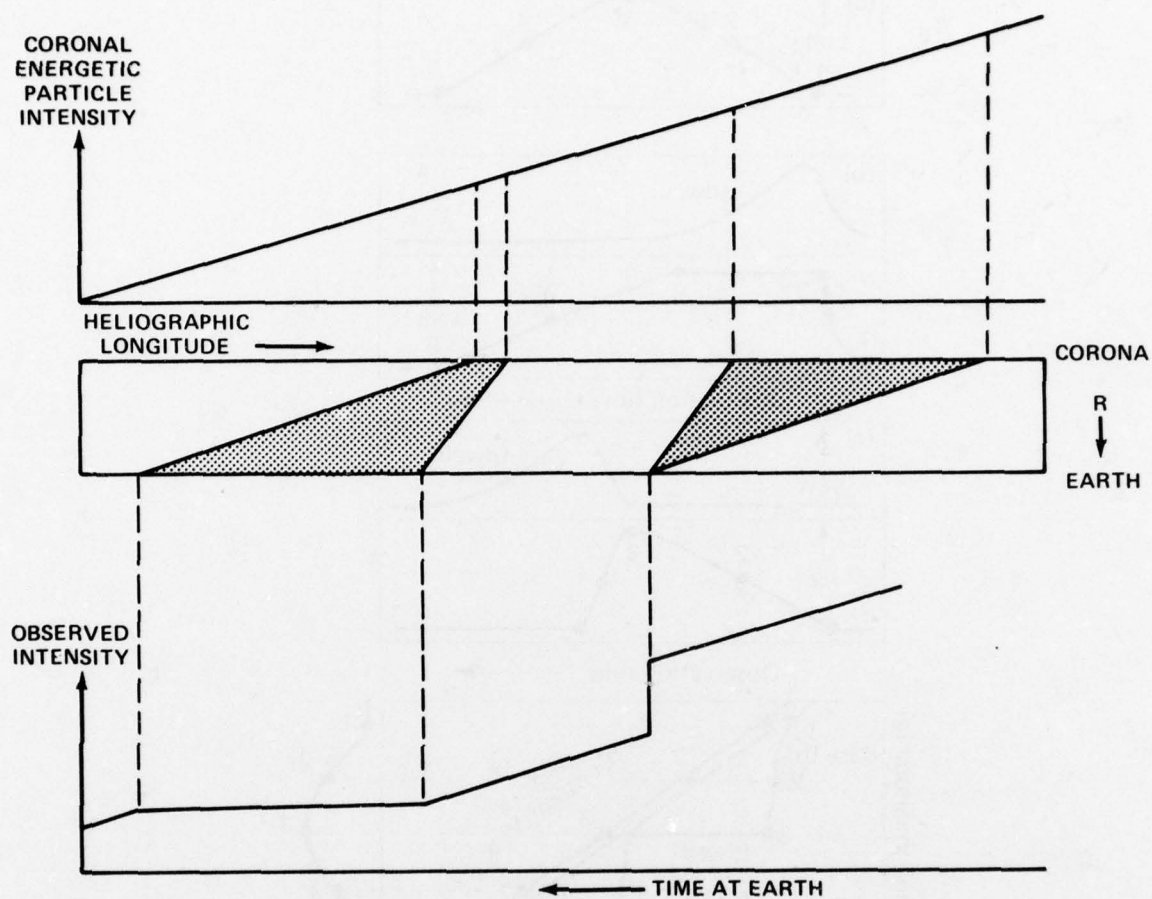
FIGURE 2 The distortion of an energetic particle coronal injection profile (upper panel) by a stationary solar wind stream structure (middle panel) like that of Figure 1. The observed intensity (lower panel) observed at Earth, although monotonically decreasing, is severely distorted by the "sweep" and "dwell" of the solar wind stream.
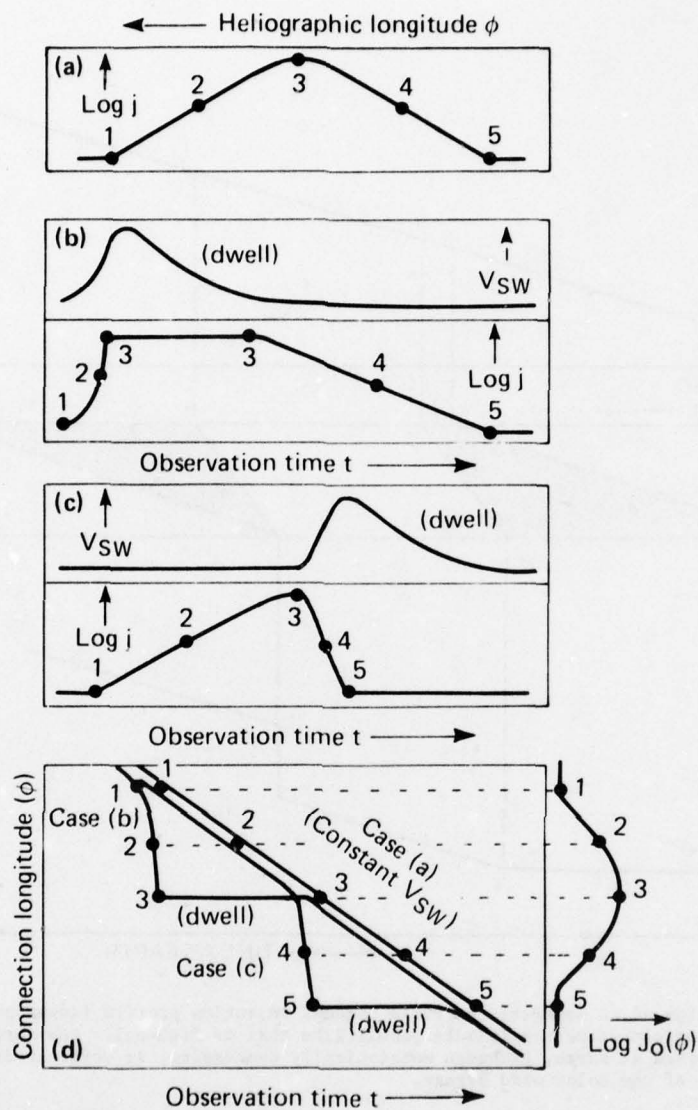
FIGURE 3 Examples of solar-wind/connection-longitude effects on a steady symmetric coronal particle injection: (a) velocity constant; velocity rise (b) early or (c) late in particle event. Lower panel (d) gives solar connection longitude at observation times t = 1, 2, 3, 4 and 5 days.

END
DATE
FILMED
3-79

DDC

MICROCOPY RESOLUTION TEST CHART

NATIONAL BUREAU OF STANDARDS-1963-A
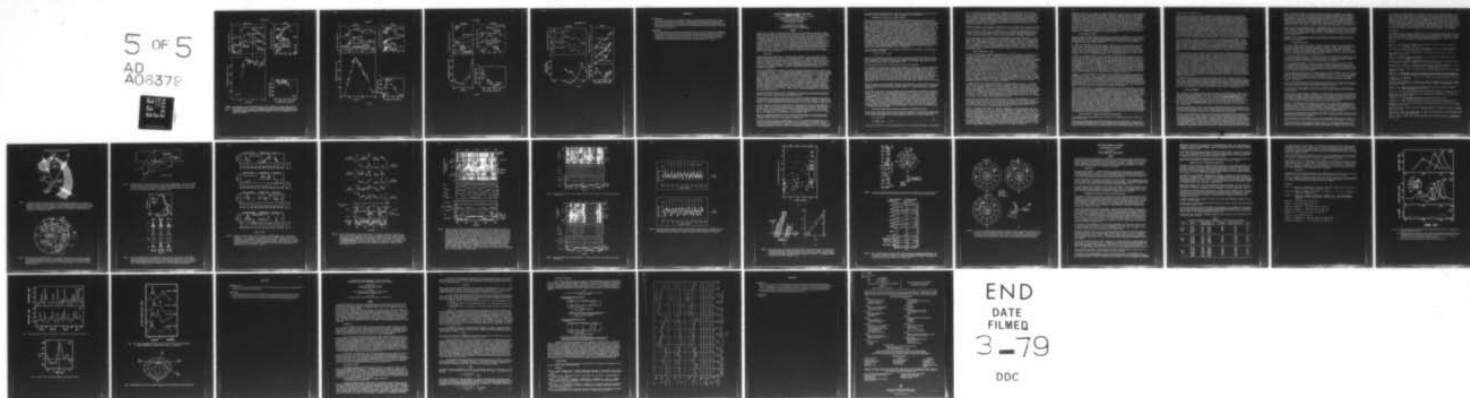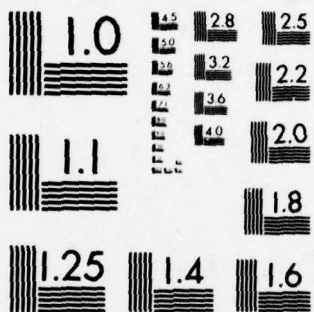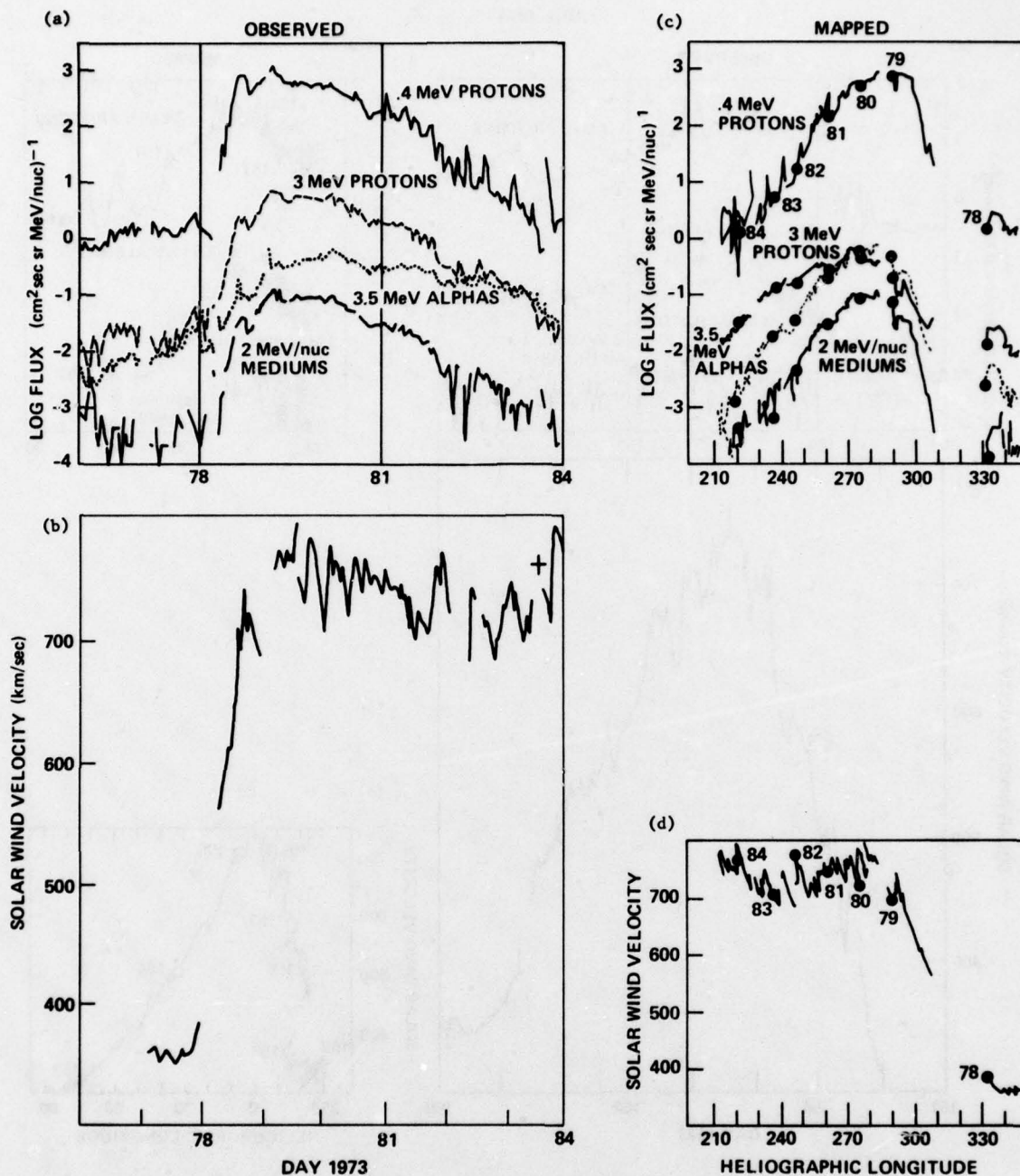
FIGURES 4, 5, 6 and 7 — Time histories of (a) solar energetic particle fluxes (JHU/APL) and (b) solar wind velocities (MIT) observed on IMP-7 in 1973. When mapped back to their coronal emission longitudes, the particles (c) exhibit an exponential dependence (sometimes two-sided) on heliographic longitude, and the solar wind streams (d) exhibit the characteristic "dwell" at the eastern edge of the stream source region.
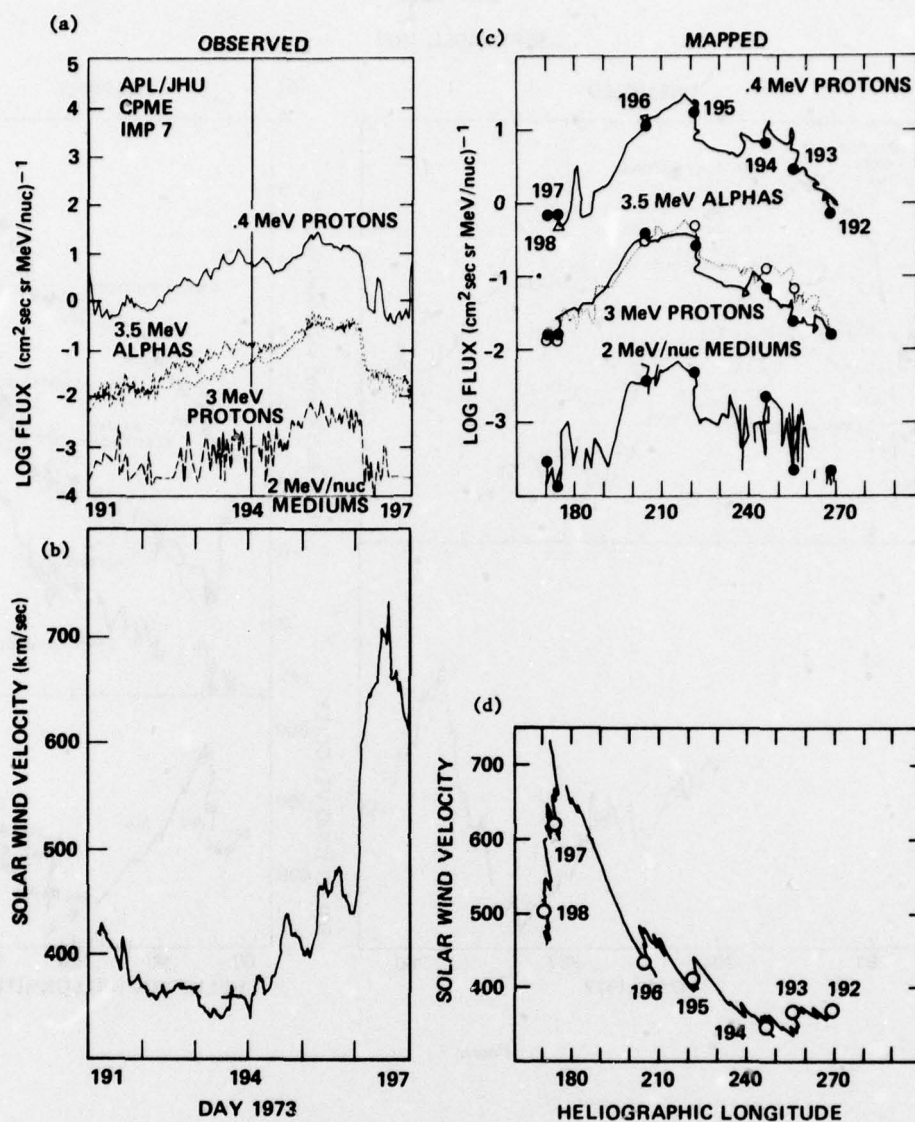
JUNE 1973
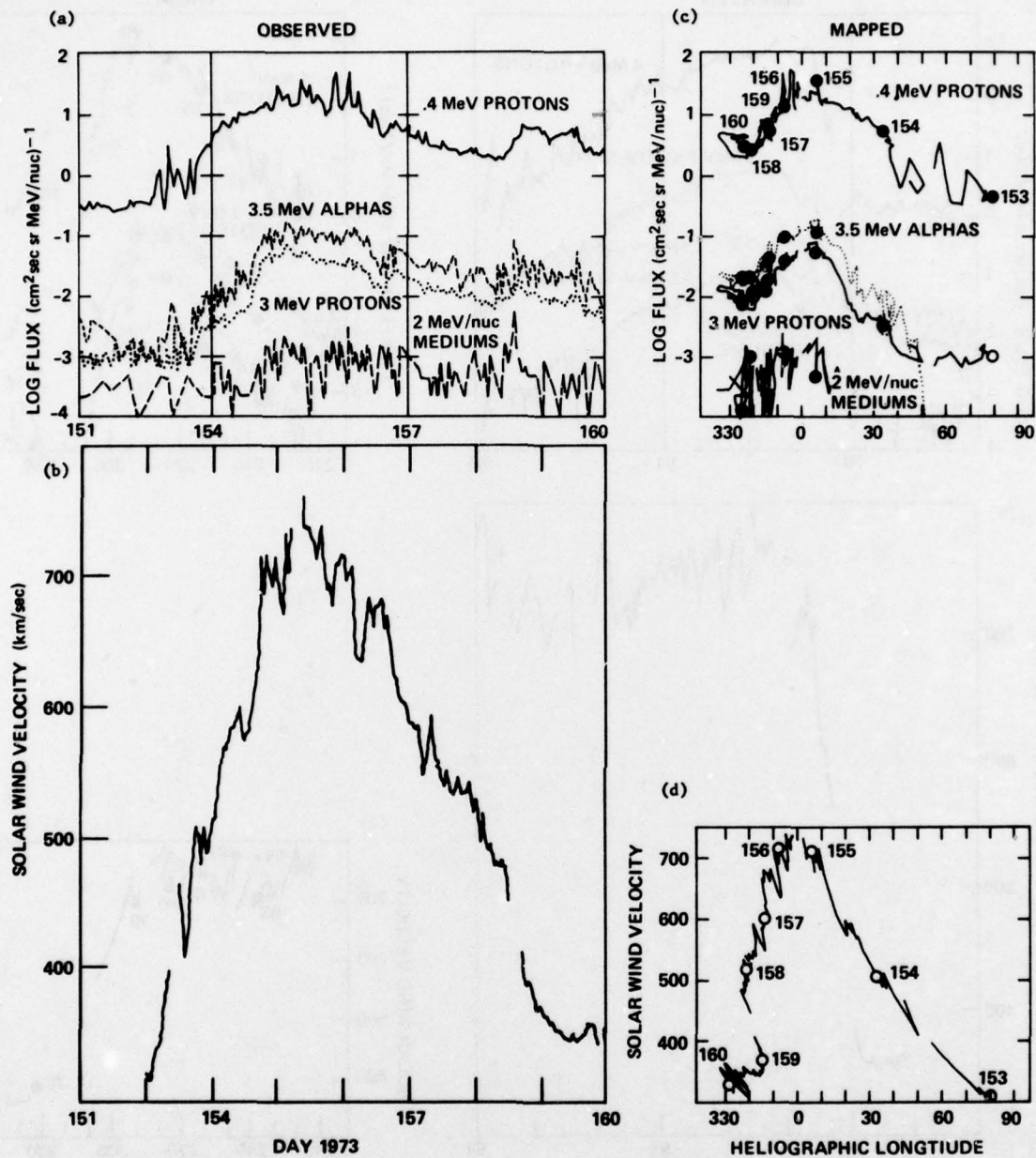
Figure 5
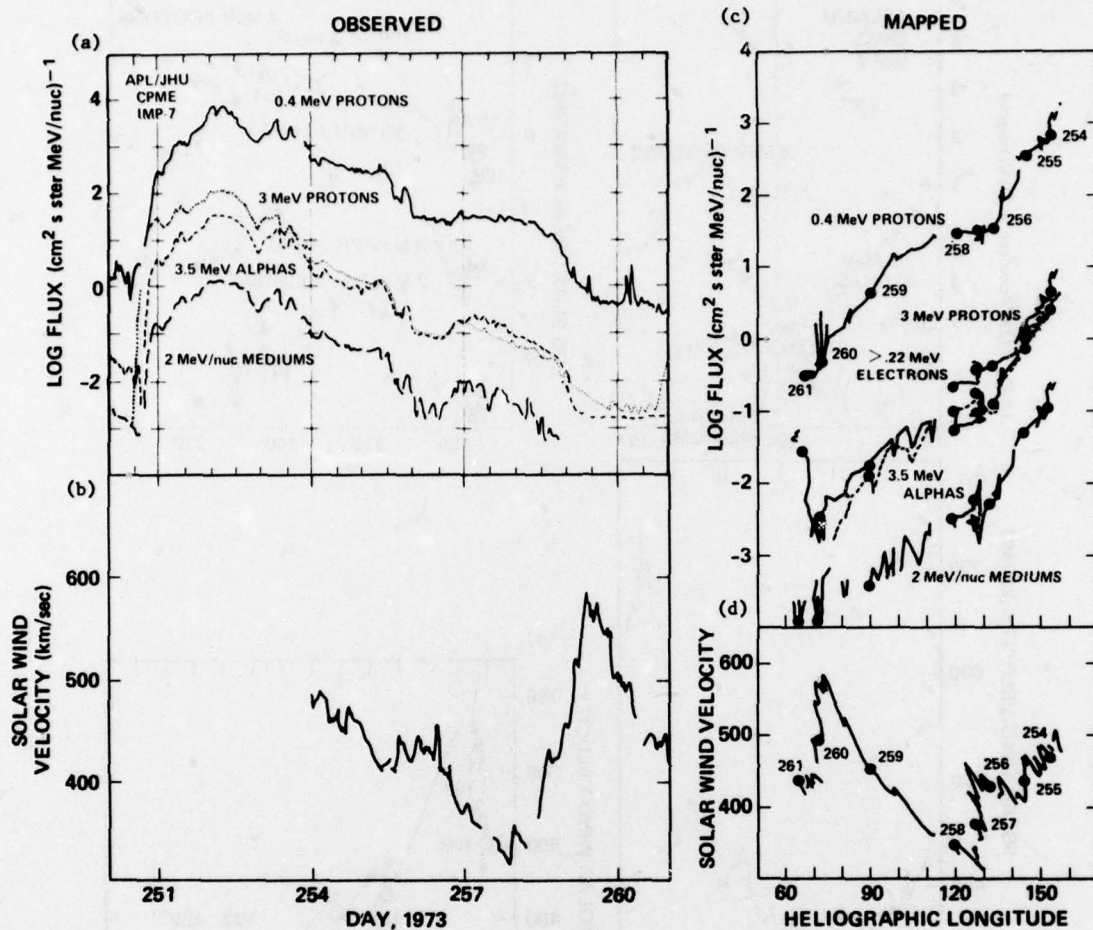
JULY 1973

Figure 6

Figure 7

DISCUSSION

E.J.Fremouw, US

Your paper is very interesting. I was particularly interested in your final point about a broadening of the spectrum. I can see three possible reasons for such a change: (1) enrichment of the fine-scale structure of the solar-wind plasma along the line of sight; (2) a decrease in the Fresnel radius at the effective distance of the plasma (implying a decrease in that distance); and (3) an increase in speed of the irregularities producing the scintillation. Do you know which of these effects is dominant?

Author's Reply

Yes, it is your alternative (2), at least in the event described of Day 181–183, 1976. J.Harmon of the UCSD group kindly provided us with velocity estimate from inter planetary scintillations observed at 74 MHz only for 3C48. The velocity derived at 74 MHz showed no increase on Day 182–194 while on the other hand both the 34 MHz and 74 MHz spectra were broadened. We therefore concluded that it was the increase in the Fresnel frequency with decreasing distance to the scattering region which broadened the spectrum (Gotwols, et al., 1978).

IPS ACTIVITY OBSERVED AS A PRECURSOR OF SOLAR INDUCED
TERRESTRIAL ACTIVITY

W. M. Cronyn, S. D. Shawhan, J. J. Rickard, and D. G. Mitchell
Department of Physics and Astronomy
University of Iowa, Iowa City, Iowa 52242
and Clark Lake Radio Observatory
Borrego Springs, CA 92004

E. C. Roelof and B. L. Gotwols
The Johns Hopkins University Applied
Physics Laboratory, Laurel, Maryland 20810

SUMMARY

Although there is currently intensive monitoring of solar disc and near-solar disc phenomena from radio emission to x-ray emission, and near-earth and terrestrial disturbances, there is very little systematic synoptic measurement within the vast region from the sun to the earth. The University of Iowa Cocoa Cross radiotelescope is a unique remote sensing instrument designed to exploit the IPS (interplanetary scintillation) technique and locate, map and track solar wind disturbances which result in geomagnetic disturbances, thereby also providing a forecast capability. Although the telescope has not yet been used to its maximum capability either operationally or scientifically we have already: found evidence for a precursor signal in the IPS activity with a 1-2 day lead time with respect to density enhancements which frequently give rise to geomagnetic activity; identified a spectral broadening signature which also serves as a precursor of geomagnetic activity; identified out-of-the-ecliptic plasma density enhancements which were not detected by near-earth, ecliptic-plane spacecraft; detected 12 co-rotating density enhancements; found over 80 sources which give detectable scintillation of which 45 have been used for detailed synoptic analysis and 9 for spectral analysis; and measured 0-lag coefficient of 0.56 between density and IPS activity enhancements.

1.   INTRODUCTION

Microscale ($\leqslant$ 500 km) irregularities in the electron density component of the solar wind cause small angular diameter natural radio sources ($\sim$ a few arcseconds or less) to display diffractive intensity fluctuations (interplanetary scintillation, or IPS) with time scales of $\sim$ 1 second. Enhancements in IPS activity are caused directly by enhancements in turbulence but, as we shall show, these are closely associated with enhancements in density. Since density enhancements are associated in turn with the onset of a variety of geomagnetic disturbances, the discovery, mapping and tracking of regions of enhanced IPS activity can be an important component of an operational geomagnetic forecasting program. By using background natural celestial radio sources as "probes" of solar wind conditions such a program can, in principle, be implemented.

We report on measurements and correlations of IPS data taken with 2 large radio telescopes located at the Clark Lake Radio Observatory. The scintillation index measurements were taken on the Cocoa Cross telescope of the University of Iowa. It is an instrument designed to exploit the IPS technique (Cronyn et al., 1976). Its low frequency, 34.3 MHz, and large electronically steerable collecting area of $\sim 7 \times 10^4$ m^2, comparable to the effective collecting area of the Arecibo dish, make it particularly sensitive to the weakly scattering solar wind at large elongation angles ($60° < \epsilon < 180°$). With the capability of observing a large number of scintillating sources each day, the Cocoa Cross telescope can be used to examine three scale lengths for density turbulence in the solar wind. The IPS is caused by microscale irregularity structure $\leqslant$ 500 km. Intercomparison of individual source-to-source responses can reveal scale sizes of variations in turbulent activity over a few degrees ($\sim 10^7$ km). The averaging of responses from many sources in different longitude and latitude regions emphasizes gross solar wind turbulence structures within which the earth is immersed, such as spiral streams and traveling plasmoids. (See, for example, Hundhausen, 1972, for review of solar wind properties.) Some of the Cocoa Cross index measurements are based in part on the work reported in the Ph. D. thesis of Erskine (1976). The index measurements were taken primarily during the latter half of 1974.

The spectral measurements were conducted on the University of Iowa Cocoa Cross radio telescope during the summer of 1976 (17 May - 25 August) and were supplemented by observations on the University of Maryland TPT radio telescope (Erickson and Fisher, 1974) during June 1976.

We have analyzed our observations in the context of a variety of ground-based geomagnetic and solar disc observations as well as in situ spacecraft measurements of solar wind density, velocity, and magnetic field. The width of the temporal power spectrum for a grid of compact radio sources is compared to the macroscopic features of the solar wind measured by near-earth spacecraft for a 39 day period during the summer of 1976.

It will be shown that as the density enhancement at the leading edge of a solar wind stream approaches earth, the temporal power spectrum broadens, reaching a maximum breadth on the day that the stream engulfs the earth. This is consistent with weak-scattering for an extended turbulent medium. The broadening with the approach of the turbulence is a result of both Fresnel diffraction and source angular diameter effects. Associated with the broadening, i.e., with the approach of the turbulent, high density leading edge of an on-coming stream, is an enhancement in total fluctuation power.

Figure 1 is a schematic illustration of the utilization of the IPS technique to observe, map and track large scale dynamic features of the solar wind, and emphasizes the importance of a coordinated synoptic measurement program involving both IPS and spacecraft observations.

In Section 2 we discuss briefly the instrumentation, source lists and data processing procedures. In Section 3 we present essential theoretical background. Synoptic observations of IPS index is discussed in 4 and the cross-correlation analysis of these measurements is presented in 5. Corotating events and evidence for an eastern precursor are reviewed in 6, and the spectral measurements are in 7. Observational conclusions are presented in 8 and an overview of future planning is summarized in 9. We have attempted

to provide sufficient background material in this paper to convey some understanding of the relationships underlying IPS behavior, particularly with regard to geomagnetic activity prediction.

2. INSTRUMENTATION, SOURCE LIST, AND DATA PROCESSING

The physical and electrical parameters of the Cocoa Cross telescope, the receiving system and the associated signal processing circuitry, the general mode of operation and sample chart record data are described in a previous paper (Cronyn et al., 1976) and, in detail, in a technical report (Cronyn and Shawhan, 1975). Additional information about the spectral analysis hardware and software may be found in Gotwols et al. (1978). Briefly, a large grid of sources is observed at meridian transit each day. Initially we began with a group of 33 IPS sources in May, 1974, which was expanded to more than 125 in July, 1974. More than 80 displayed IPS. Of the remainder, some are control sources, picked because their large angular diameter precludes IPS and allows us to determine whether ionospheric scintillation (to which all sources in our observing program are subject) can have scintillation power components are observed on the Cocoa Cross in the 0.1 - 1.5 Hz frequency range. The rest are sources chosen for basic astronomical observing programs. Most of the sources were chosen from a catalog of IPS sources compiled at a higher frequency of 81.5 MHz (Readhead and Hewish, 1974). A subset of 45 scintillators proved to be useful for synoptic analysis. These sources, most of which are radio galaxies or quasars, are identified by their '3C' or '4C' catalog numbers in Figure 2. We present the sources in ecliptic longitude (0° being the direction of the vernal equinox) and ecliptic latitude. Although the ecliptic latitude may differ considerably from the heliographic latitude of the point of closest approach to the sun of the line of sight from Earth, and the latter is useful in ordering IPS observations at small elongation angles (where it gives the direction from the sun to the dominant scattering region), heliographic latitude is not as appropriate as ecliptic latitude for the large elongation angles ($\geq 60°$) of our observations where scattering comes from an extended region closer to the earth than to the sun (see Figure 3).

A basic IPS parameter measurement which we discuss in the first part of this paper is the observed scintillation index, m, defined as:

$$m = \left(\int_{\nu_L}^{\nu_H} P(\nu)\, d\nu \right)^{1/2} = \Delta I / \langle I \rangle \tag{1}$$

where $\langle I \rangle$ is the average source intensity, ΔI is the rms intensity fluctuation for frequency components between ν_L and ν_H, $P(\nu)$ is the power spectrum of the intensity scintillations, and $\nu_L = 0.1$ Hz, $\nu_H = 1.5$ Hz. The quantities $S = m^2 \langle I \rangle^2$ and $\langle I \rangle$ are measured in real time using simple analog circuitry (Cronyn et al., 1976) and scaled directly from paper chart records.

The digital data are acquired at a 10 sps sample rate and Fourier-transformed.

When displayed on a log-log plot the spectra typically displayed a flat plateau from very low frequencies to a turn-over into a nominal power-law slope, the turn-over occurring at anywhere from less than 0.1 Hz up to 0.5 Hz (see Figure 3). Day to day variations in both the turn-over frequency and the rate at which the spectrum turns over into the power-law provide information about the velocity of the scattering medium and its density turbulence profile. Therefore, the spectra are parameterized by recording the power-law slope (α), the frequency at which the smoothed spectrum drops to 3 dB below the plateau (ν_3), and the frequency at which it drops to 6 dB below the plateau (ν_6). We are principally concerned with ν_3 and ν_6 in this paper; α will not be discussed here since many of the spectra analyzed did not have a signal-to-noise ratio which was sufficient to provide a good estimate of α. However, Mitchell (1977) using a small subset of the data presented here (with a higher than average signal-to-noise ratio) discusses the use of α.

There are occasional spectra which differ significantly from the majority. The most common deviant spectra exhibit an enhancement at low frequencies (≤ 0.2 Hz), flatten into a well defined plateau at intermediate frequencies, and turn-over again at higher frequencies (Figure 4). We will discuss these two component spectra later.

We have taken several steps to cast out observations that are contaminated by interference of terrestrial origin. The 10 sample per second high-pass filtered data from which the power spectrum was calculated is plotted for every observation. Having inspected similar plots for a number of cases of known interference, we were frequently able to identify terrestrial interference in the observations. To further validate the measurements we plot 2.5 s and 50 s averages of the main beam response and the scintillation power (Figure 2b). The main beam response is the raw signal from the receiver as the source moves through the radio telescope beam. For a detailed description see Cronyn et al., 1976 and Erickson and Fisher, 1974. The scintillation power is obtained by digitally band-pass filtering the main beam response over the 0.1 to 1.5 Hz range, and squaring the resultant time series. The peak in scintillation power must approximately coincide with the peak in the main beam response, and on the fine time scale the fluctuations in scintillation power must be reasonably distributed throughout the passage of the source through the beam, or the observation will be rejected.

3. RELATIONSHIP BETWEEN INDEX AND DENSITY FLUCTUATIONS, AND DELINEATION OF ACTIVITY

The variability in IPS activity which we shall discuss must be examined in the context of the ambient IPS level. First, we shall briefly review the basic intensity relationships. For weak scintillation, defined by the condition that a point source at infinity displays an index $m_o \ll 1$ (Cohen and Cronyn, 1974),

$$m_o \sim r_e \lambda\, \Delta n \sqrt{\ell L}$$

$$\Delta n^2 = \int_{k_o}^{\infty} dk\, F_n(k) \qquad k_o \sim \ell^{-1} \tag{2}$$

where $r_3 = 2.8 \times 10^{-13}$ cm, λ is the observing wavelength, L is the effective path length, ℓ is the effective

scale for IPS response, and Δn is the rms density fluctuation due to irregularities with wave numbers $k > k_o \sim \ell^{-1}$ in the density power spectrum $F_n(k)$. The response scale is $\ell \approx r_f/3$, where r_f is the radius of the first Fresnel zone, $r_f \sim \sqrt{\lambda Z}$, and Z is the distance to the irregularities. The observational index m of Equation (1) differs from the true index m_o by the absence of fluctuation components less than ν_L. Since density irregularity spatial wave number components k translate into temporal fluctuation frequency components ν through the relationship $\nu = kU_\perp/2\pi$, where $U_\perp$ is the solar wind velocity component transverse to the telescope-source ray trajectory, a progressively increasing fraction of the IPS energy is shifted into frequencies $< \nu_L$ at elongation angles $\gtrsim 90°$. The reduction of m relative to m_o is not severe until $\epsilon \gtrsim 160°$ for a point source.

Although the dependence of m_o on $\Delta n \sqrt{\ell L}$ is linear only if $m_o \leqslant 0.7$, we have found in practice that there is very little difficulty with ambiguity in the response of m (Erskine et al., 1978; Gotwols et al., 1978).

The m vs Δn behavior is mapped out in a characteristic m vs ϵ curve (where the elongation angle ϵ is the sun-earth-source angle). As ϵ decreases m increases because the distant integrated columnar turbulence increases. At some critical elongation angle ϵ_t, m will turn over and decline with further decreases in ϵ. The double-valued dependence of m on Δn will be restricted primarily to elongation angles near ϵ_t.

In Figure 5a we show the run of scintillation index with time for a low ecliptic latitude (0.1°) source, 3C225. The systematic, long term variation due to the changing elongation angle (bottom panel) is modulated by large, irregular day-to-day variations which we shall identify as 'activity'. The measured index behavior for a somewhat higher latitude source, 3C147 (+26.4°) is shown in Figure 5b; its elongation dependence is similar to 3C225, but comparison of indices on the same day often reveals marked differences due to the separation of 56.3° of ecliptic longitude between the two sources. Finally, in Figures 5c and 5d we show the behavior of the sources 3C280 and 3C380 at ecliptic latitudes of +47.9° and +71.8° which do not display as large systematic long term variation in index since ϵ does not change as much for these high latitude sources.

4. SYNOPTIC OBSERVATIONS -- INDEX

In Figure 6 are presented the normalized scintillation index curves for a cluster of six sources covering an ecliptic latitude range of 9° and a longitude range of 57°. Over the time period 1974, days 231 to 296, this cluster was west of the sun. IMP 7 and 8 (near the Earth) solar wind density and velocity measurements (from the Los Alamos Scientific Laboratory detectors), the planetary A_p index and the inferred interplanetary magnetic field polarity at the Earth are also provided. There is good qualitative agreement between the occurrence of density enhancements (which are often, but not always, associated with the magnetic sector boundaries and which are followed by velocity peaks), and the occurrence of increases in the scintillation index for each of the sources individually. This correlation is expected because of the increase in scattering associated with the density increase along the line of sight. We will show in later sections that this density association is a characteristic feature of IPS. However, the quantitative correlation of index response from source-to-source varies. For the enhancement on days 256-259 all sources exhibit approximately the same increase in index. For days 231-234, however 3C68.2 barely responds in comparison to the other sources. Also, 3C125 and 3C153 increase significantly less on days 285-289 than the other sources. These observations of distinct source-to-source differences within a source cluster suggest spatial variations in the electron density turbulence on the scale of 2-10° and/or temporal variations on a scale of 3-16 hours. Although there is no a priori reason to expect a relationship, it is interesting to note that this scale size for density structure is similar to velocity structure deduced, for example, by Rhodes and Smith (1976). From autocorrelation of the velocity difference between two spatially separated satellites they found a longitudinal coherence time of ~ 18 hours (10°) and significant changes on the scale of a few degrees in latitude.

It is apparent from Figure 6 that missing observations obscure the pattern over the sky on a given day. A further difficulty is encountered when we attempt to intercompare different sources on a given day; how are the IPS responses of different sources to be normalized? In Figure 6 the normalization to peak values is really arbitrary, since there is no assurance that each source line-of-sight contained the same turbulence on the peak days. Therefore we developed a non-parametric ranking scheme (Erskine et al., 1978) and also grouped adjacent sources in clusters (to minimize the effects of missing observations). Briefly, for each of the 3 extended observing periods in 1974 a distribution function of index m was computed for each source. The m's were then quantized according to $q_i = 2$ (top quartile for source i), $q_i = 1$ (next-to-top) and $q_i = 0$ (lower half). The observations were then weighted for each source by an error estimate, and an average over-all weighted index Q calculated for each box.

We selected 45 of the most reliable scintillating sources for a source 'clustering analysis'. As shown in Figure 2, we chose 10 regions or 'boxes' in the sky, each containing up to 8 radio sources, with the sources spaced no more than about 30° from any other source in the same box. The 10 sky boxes span nearly all ecliptic longitudes. Most of the boxes are centered at mid-northern ecliptic latitudes (from 20° to 50°). However, Box 5 is just south of the ecliptic, while Box 3 (the single source 3C161) is at -29° latitude. Box 9 is centered at a rather high latitude of about 70°.

With the set of weighted box responses for each day of observations, we studied the general large scale pattern of scintillation over the sky. One graphical representation of the box-averaged, Q_i is given for the three observational periods in Figures 7, 8, and 9. Four levels of shading are used in Figures 7-9 to display the high, moderate, low or missing IPS activity estimates for each sky box, each day, with the darkest shading indicating 'high', and no shading indicating 'missing observation'. The boxes are arranged from top to bottom in order of decreasing ecliptic longitude. At the bottom of Figures 7-9 are displayed correlative interplanetary and geomagnetic data in a format similar to Figure 6 (see captions for Figures 7-9). The solar wind measurements are from the Los Alamos Scientific Laboratory (LASL) detector on IMP 7 and 8, and the magnetic field from the University of Iowa plasma wave search coil detector on the IMP 8 spacecraft. In addition, we have computed the average 'all-sky IPS activity index', $\langle Q \rangle$, over all boxes. We also compute $\langle Q \rangle_{east}$ and $\langle Q \rangle_{west}$ for each day, using only the eastern and western sky boxes. We show that $\langle Q \rangle$, $\langle Q \rangle_{east}$, $\langle Q \rangle_{west}$, and $\langle Q \rangle_{high\ lat.} = Q_9$ vs time at the centers of Figures 7-9.

Examination of Figures 7-9 for evidence of a spatial-temporal pattern of IPS activity reveals the presence of vertical bands of high and moderate IPS activity. These bands encompass nearly all ecliptic longitudes and appear to be most prominent near times of solar wind density increases. The plots of $\langle Q \rangle$, $\langle Q \rangle_{east}$, $\langle Q \rangle_{west}$, and $\langle Q \rangle_{high\ lat.}$ all peak at approximately the same time. The peaks of IPS activity appear to coincide well with peaks in solar wind proton density, and for the most part, $|B_{xy}|$ also. The peaks in geomagnetic A_p occur several days later than the peaks in IPS activity. There were 17 sector crossings in the interval 1974, days 150-362. We observed widespread IPS enhancements at the times of all 13 crossings for which the telescope was operating. However, there were also widespread IPS enhancements at several times which do not coincide well with sector crossings: 1974, days 270-275 and 335-338. On the other hand, there was a slight increase of proton density on day 269 (maximum $\sim$ 18 cm^{-3}) and a distinct elevation of density for days 334-338 (maximum $\sim$ 51 cm^{-3}). Thus it may be more appropriate to call these IPS enhancements 'all-sky density events' because they correspond to near-earth solar wind density increases. In our judgement, the dominant class of IPS disturbances during May-December 1974 exhibited a high degree of recurrence and were definitely not flare associated.

5.   CROSS-CORRELATION ANALYSIS

In order to examine the temporal relationship between the 34.3 MHz IPS enhancements and correlative ground based geomagnetic, solar disc observations, and in situ spacecraft solar wind data, we have performed a standard time series cross-correlation analysis between $\langle Q(t) \rangle$ the all-sky IPS activity index and various correlative variables covering days 150 through 362. Days with no observations were not filled, but were simply deleted from the cross-correlation.

Two sample cross-correlation functions are presented in Figure 10, $\langle Q \rangle$ vs solar wind proton density and $\langle Q \rangle$ vs velocity. Our estimates of the 90% confidence limits (taking into account that the points are not all statistically independent) are also indicated. Both correlations indicate two sets of peaks, separated by 12-15 days, that exhibit an approximate 27-day recurrence over five solar rotations. This result confirms the qualitative impression of recurrence obtained from Figures 7-9. Also the recurrence pattern is consistent with the asymmetric two sector solar wind magnetic field structure that persisted throughout 1974. (See, for example, Hansen et al., 1976; Gosling et al., 1976.)

Of all the cross-correlations carried out, the IPS index Q correlated best with the proton density: 0.56 at 0 days lag. This good correlation suggests that the turbulence causing the scintillation is proportional to the density as has been suggested in other IPS observations (Houminer and Hewish, 1974). The good correlation is also in agreement with in situ spacecraft measurements which show little variation of the ratio $\Delta n/n$ (Δn = rms density fluctuation, n = average density) as a function of solar wind velocity, density, temperature or structure (Neugebauer, 1977). That is, high turbulence (giving rise to enhanced IPS) accompanies high density; the converse is also true. The 0 day lag is evidence that the scattering is occurring close to the earth. An average correlation significantly less than 1.0 is expected because from Figure 11a it is only when the density exceeds $\sim$ 10 cm^{-3} is the IPS index enhancement well correlated with the density. The IPS activity anticorrelates (0.52) with solar wind bulk velocity at a -2 day lag and positively correlates (0.38) at +3 days. These are the normal lags between the velocity minima preceding the density maxima and velocity maxima following as is apparent in Figures 7-9.

Although it is clear from Figures 7-9 that density increases usually result in IPS events, a quantitative comparison is instructive. In fact, it will lead us to an indication of the latitude structure of the density regions. In Figure 11a, we have plotted the peak (hourly average) solar wind proton density vs Q_9 (the ranking index for the high latitude box), for each day of IPS observations during the three data periods. We use Q_9 because the high latitude sources should respond more uniformly to local density disturbances than the low latitude sources (which may see the density structure approaching from the east or receding towards the west). Figure 11a reveals not only that high densities ($N > 10$ cm^{-3}) tend to accompany high latitude activity ($Q_9 \gtrsim 1.0$), but also that the density is low when Q_9 is low, thus confirming the importance of density structures in producing local scintillation enhancements.

There is also direct evidence of non-local density effects since there are a number of days on which there is high latitude activity $Q_9 \sim 2.0$ accompanied by low densities ($N < 10$ cm^{-3}). Days 247 and 294 exhibit a very high scintillation index accompanied by a low solar wind density at Earth. This behavior in Figure 11a is interpreted to be indicative of a high latitude turbulent plasma passing above the Earth but not extending down to the ecliptic plane. On the other hand, the sequence of days 175-180, 187-189 and 285-290 (which are labeled and connected with lines in Figure 11a) include at least one day of high Q_9 but low density embedded between days of high Q_9 and high density. This behavior could be interpreted as the density structure depicted in Figure 11b which would give the idealized N vs Q_9 response of Figure 11c. The high Q_9, low N on day 3 comes about because there is a significant density (turbulence) enhancement well out of the ecliptic above the Earth. The high N on day 4 could result from a second density structure making up the striated two-piece "curtain-like" structure of Figure 11b or by a folding down of the original density structure across the ecliptic on day 4. A slanting density structure as depicted in Figure 11b may be geometrically similar to a slanting sector boundary which has been shown by Suess and Feynman (1977) to be a natural consequence of the solar wind latitude velocity gradient (Rhodes and Smith, 1976; Coles and Rickett, 1976). Although the data in Figure 11 do not enable us to deduce the actual configurations of the density structures, we believe the distribution of points in the N vs Q_9 plot is good evidence for strong latitude variations of density enhancements in solar wind streams and that the IPS technique can eventually be used to deduce models of the structures.

6.   COROTATING EVENTS -- EVIDENCE FOR AN EASTERN SOURCE PRECURSOR

We now consider a very simplified geometrical configuration for corotating density events viewed by the lower latitude sources.

Since we are dealing primarily during 1974 with pronounced recurrent structures (Hansen et al., 1976; Gosling et al., 1976) we would expect to observe corotating density structures first in the eastern sources with solar ecliptic longitudes $\leq 135°$ (the nominal direction of corotating stream fronts), then in all sources (as the density structure envelopes the earth) and finally in the anti-sunward and western sources

with solar ecliptic longitudes $\geq 135°$.

We have examined our synoptic data for the signature of the approach rotation of three of the density events for which we have the best coverage east of the sun in terms of the number of sources and their reliability. We have assumed the 'density events' were associated with enhanced turbulence in solar wind density compression regions with centers situated along ideal Archimedes spirals which crossed over earth at 1974 days 161.5, 177.0 and 187.5 (the approximate times of density maxima and all-sky increases in Figure 7). The ecliptic longitude directions in which an earth-bound observer would look, expecting to see enhanced IPS activity, as the spirals approach earth, are indicated by the pairs of solid curved lines labeled '3' (300 km/s ideal spiral) and '9' (900 km/s ideal spiral) in Figure 7. The assumption is that the IPS index is enhanced when looking approximately tangent to a very thin spiral density compression region relative to looking in other directions (Houminer, 1971; Coles et al., 1974). Because our 'grid' of sources was rather sparse in the east after 1974 July, we have not drawn corresponding 'tangent direction' loci on Figures 8 and 9. The dominant features in Figures 7-9 are the 'density events' near times of recurrent sector crossings. From Figure 7 we see that there is no definitive indication that the IPS activity is preferentially high or moderate in the directions predicted by the solid curves. Bame et al. (1976) found that the high speed streams in 1974, at the end of solar cycle 20, were very broad compared to those earlier in the cycle. The large stream widths may contribute to the lack of distinct spiral IPS structure.

We also note that there tends to be a 'trough' of moderate and low IPS activity approximately 1-2 days earlier than the times of predicted enhanced activity due to the approaching eastern spirals. It would appear that there was a comparatively non-turbulent or low density region west of the density structure, probably the rarefaction of the preceding stream. The occurrence of such a trough allows the approaching density structure to be defined more clearly by line-of-sight measurements. The trough most evident in Figure 7 is that in the eastern sources (boxes 5-8) on days 156-159. Even though we are limited by incomplete coverage and somewhat noisier data during this initial period of our observations, that data still permit a more detailed examination of the cluster analysis for the duration of the event, days 156-163.

Plotted in the left-hand column of Figure 12 are the Q_1 for each day when observations were available. Since 3C161 was not observed at this time, there are no data for Q_3. At the top and bottom of the column are the LASL solar wind densities (3-hour averages). The orientation of the sky-boxes relative to the sun is shown in the right half of the figure. Boxes 5-7 display low Q-values on days 156-158 while box 4 is low on day 157 but shows a moderate enhancement (Q = 0.9) on day 158. Box 4 would be the first group of sources to detect a corotating structure. The eastern onset of the event is clear on day 159 in box 6 and may appear in box 5 (no observations for box 4), while boxes 7 and 8 (covering solar ecliptic longitude between 90° and 150°) remain at Q = 0. The solar wind density peaks at N = 25 cm^{-3} early on day 161, and an 'all-sky' event occurs on day 162. The enhanced Q-indices are sustained through day 163 in boxes 7-10 (viewing sources at longitude west of the direction of a stream front at earth), while box 1, the closest western box to the sun, shows an increase on that day. By contrast, boxes 2 and 4, just east of the sun, have dropped to Q = 0 on day 163, suggesting that the disturbance now appearing in the west has passed over the earth and is no longer visible east of the sun. A sketch of a density structure consistent with these observations is offered in Figure 12. The enhancement in the western box 1 on days 156-157 may be a response to plasma ejection from MPR 12972 which was in the western hemisphere on the sun and produced an importance 1B flare on day 155 (S14, W13) and a 3B flare on day 157.7 (S16, W48). Both flares were accompanied by type II-IV bursts.

We compared our results with those of another line-integrated measurement, columnar electron content (Croft, 1971) to study differences and similarities in morphology. It is of interest that each of the two line-of-sight integrated measurement techniques, columnar content and IPS, yields the same rather ambiguous result with respect to observation of a space-time signature appropriate to a corotating feature (density or turbulence). Of course the ambiguity may be resolved if sector structure is a consequence of an ordering of the solar magnetic field in a coordinate system whose axis is tipped with respect to the solar spin axis, and a sector boundary is, in fact, a near-equatorial neutral sheet (cf., Smith et al., 1977).

7. SPECTRAL MEASUREMENTS

Daily values of ν_3 for a number of radio sources for the period of days 166-199, 1976 are shown in Figure 13. For comparison we also display the solar wind velocity, density, and most probable thermal speed measured by the MIT plasma instrument on the IMP-7 and 8 spacecraft (Solar Geophysical Data). A number of cases of spectral broadening can be seen, some of which are correlated with solar wind streams as revealed by spacecraft data. There is no reason to believe that any of these broadenings are due to flare associated bast waves, since solar activity was at a very low level during this entire period. In fact, as reported in Solar Geophysical Data, for both June and July there were no observed Type II or Type IV radio bursts, no confirmed H_α flares greater than sub flare importance, and no high energy electron or proton events.

The spectral measurements in Figure 13 show a definite broadening both before and during the rise of the high speed stream of day 182. Since our data coverage was best for this event we will concentrate on it; the circumstances and parameter variations of the other activity periods are consistent with the 182 period but there is too little data from these periods to draw any definitive conclusion from.

A period of enhanced IPS activity began late on day 181. This occurred several hours before the solar wind velocity measured at earth started to rise due to the approaching corotating high speed stream, about 5 hours before the onset of a sudden commencement on day 182, and at a time when the solar wind density at earth had already reached an enhanced level. In order to study the temporal and spatial evolution of the scintillation power spectrum we plot in Figure 14 quantized values of ν_3 in geocentric ecliptic coordinates with the sun located at the top of each panel. The sequence of observations begins at the sun and runs in a counterclockwise direction. Figure 14a shows that all sources for which we had data displayed spectra of average width. In Figure 14b, the first source observed, 3C196, continues this trend and shows no signs of detecting the approaching corotating solar wind stream. Approximately one half hour later the situation

changes significantly when 3C216 shows a broad spectrum which reflects the approach of the oncoming stream. The different response of 3C196 and 3C216 implies a large spatial gradient in the strength of the turbulence of this stream. All other sources shown in Figure 14b displayed unusually broad spectra except 3C263.1 which had a two component spectrum, the second component of which was broad. Figure 14c shows the return of scintillation activity to normal; while 3C196 is broadened, 3C216 and 3C254 have returned to their average width. Confusing the simple picture of the event terminating as abruptly as it had begun is the enhanced width of the eastern radio source 3C270.1. This behavior may simply indicate a spatial structure in the turbulence. In any case it is clear from Figure 13 that the scintillation spectra of all other sources return to average or below average width approximately by the end of day 183.

Another aspect of the scintillation activity on day 182 which is not brought out in Figure 14 is the large number of usually non-scintillating sources (at 34 MHz) that scintillated on that day. Because they were rarely observed to scintillate we were unable to classify their spectra based on their own past performances. This "all-sky" enhancement of IPS in association with an enhancement in solar wind density (which precedes the velocity maximum) makes it clear that the event under discussion is similar to the "all-sky" events discussed earlier.

Additional analysis (Gotwols et al., 1978) of one case (3C48 on day 182) made it clear that the close proximity (~ 0.1 AU) of enhanced turbulence, and not an increase in velocity, was the cause of the observed spectral broadening.

8. OBSERVATIONAL CONCLUSIONS

1) We have looked for enhanced IPS index on sources east of the sun during the times approximately one week prior to earth-crossing of spiral solar wind density compression regions. We find some rather tenuous evidence that IPS index is preferentially enhanced on sources at ecliptic longitudes which lie approximately tangent to the approaching compression region. Even more tantalizing is evidence for a "trough" of depressed IPS activity preceding to corotating enhancement by 1-2 days. Such a trough would provide a 3-4 day lead time for enhanced-density associated geomagnetic activity. This effect is easiest to see when the interplanetary medium is relatively quiet.

2) We have observed twelve days out of seven months of data in which nearly every scintillating source in our grid showed enhanced IPS activity. Solar wind proton density is also strongly enhanced on these "all-sky" event days, demonstrating that this is the IPS signature of an interplanetary density structure (usually associated with a stream-stream interaction) sweeping over the Earth.

3) The IPS spectrum broadens as a corotating solar wind stream sweeps over or very near to the earth. This broadening could be caused by the relative closeness of the scattering medium and/or the higher velocity associated with the stream. In one case (3C48 on day 182) it was possible to show that it was the distance to the scattering region rather than the velocity which accounted for the broadening. This is consistent with the enhanced turbulence occurring at the leading edge of the stream where the velocity shows no increase but the density is enhanced.

4) Cross-correlation functions have been calculated between 34.3 MHz IPS 'activity index' $\langle Q \rangle$ and in situ plasma and field measurements as well as solar and geomagnetic activity. There is evidence for 27-day recurrence in all the cross-correlations over 5 solar rotations. The IPS 'activity index' $\langle Q \rangle$ correlates best (r = 0.56) with solar wind proton density at zero lag and velocity (r = -0.54) at -2 days lag. The only other significant correlations are with SSC's and with indicators of solar wind stream-stream structure: $|B_{xy}|$ and A_p.

5) Out of the ecliptic density enhancements have been detected which have been unassociated with simultaneous ecliptic plane enhancements. We have made synoptic observations of IPS index on a dense 'grid' of small angular diameter radio sources during 1974 May - December at 34.3 MHz.

6) Over 80 sources widely dispersed over the Northern Celestial Hemisphere, out of 150 monitored have displayed detectable interplanetary scintillations at 34.3 MHz, of which 45 proved useful for detailed synoptic analysis.

With this paper we have demonstrated the capability to observe significant IPS activity near the Earth and at large elongation angles, leading to identification of "all sky density enhancement" IPS events and to the detection of significant density enhancement regions out of the ecliptic. Synoptic observations of a large number of IPS sources for scintillation index and for scintillation spectrum as well as refinements in the analysis techniques guided by careful modeling should produce better resolution of solar wind density structure (and the underlying plasma processes) in and out of the ecliptic.

It cannot be over-emphasized that the observations described in this paper are merely suggestive of the potential of the IPS technique. The observations were carried out in the face of difficult operational problems which made continuous, 24 hour/day observation (which is essential to the understanding of the structure and evolution of solar wind activity) impossible for more than a few weeks at a time. The extensive data acquisition and analysis task carried out on the 1974 data involved hand-scaling wide dynamic range data from chart records and transferring it to punched cards for computer analysis.

The telescope has undergone extensive upgrading in every respect -- physical, electronic (signal-to-noise ratios are significantly higher now than during either of the 2 observing periods described in this paper), data acquisition (now digital) and analysis.

Thus, the prospects for future geomagnetic activity forecasting, measured against results to date as summarized in the above section using an instrument whose potential was barely tapped, are bright indeed.

Along with digital data acquisition carried out under control of a dedicated microprocessor which also controls the telescope we are implementing software so that we can, on a quasi-real time basis (i.e., hourly if we so choose), upline the data to a NOVA 2/10 minicomputer for analysis. Thus we will shortly

have the capability of having a nearly real time map of activity in the interplanetary medium, at least in the sense that our meridian transit telescope sweeps around the Northern Celestial Hemisphere once every 24 hours viewing background source scintillation. We will be developing a "radar screen" type of display in which the "targets" will be the various background scintillating sources, the intensity will represent the relative level of IPS activity (in comparison with, say, the previous day or the average of the previous week), and color might represent spectral width. Such a display can be used by itself as a forecasting tool or made available for cooperative analysis and forecasting using other techniques. On the basis of spectral broadening and index enhancement measurements made to date, we anticipate at least a 1-2 day forecast capability for corotating activity. Such a capability should be particularly relevant to the onset of increased solar activity when new corotating density enhancements will be developing within one solar rotation period and therefore cannot be predicted on the basis of prior appearance.

ACKNOWLEDGMENTS

REFERENCES

Bame, S. J., J. R. Asbridge, W. C. Feldman, and J. T. Gosling, "Solar Cycle Evolution of High-Speed Solar Wind Streams", Astrophys. J., 207, 977, 1976.

Coles, W. A., B. J. Rickett, and V. H. Rumsey, "Interplanetary Scintillations", Solar Wind Three, Ed. C. T. Russell, University of California, Los Angeles, 351, 1974.

Coles, W. A. and B. J. Rickett, "IPS Observations of the Solar Wind Speed out of the Ecliptic", J. Geophys. Res., 81, 4797, 1976.

Croft, T. W., "Corotating Regions in the Solar Wind, Evident in Number Density Measured by a Radio-Propagation Technique", Radio Sci., 6, 55, 1971.

Cronyn, W. M., and S. D. Shawhan, "A Decametric Wavelength Radio Telescope for Interplanetary Scintillation Observations", University of Iowa Res. Rept. 75-12, Iowa City, Iowa, 1975.

Cronyn, W. M., S. D. Shawhan, F. T. Erskine, A. H. Huneke, and D. G. Mitchell, "Interplanetary Scintillation Observations with the Cocoa Cross Radiotelescope", J. Geophys. Res., 81, 695, 1976.

Erickson, W. C. and J. R. Fisher, "A New Wideband Fully Steerable Decametric Array at Clark Lake", Radio Science, 9, 387, 1974.

Erskine, F. T., Interplanetary Scintillation Observations with the 34.3 MHz Cocoa Cross Radiotelescope, unpublished Ph. D. thesis, Dept. of Physics and Astronomy, The Univ. of Iowa, Iowa City, December, 1976.

Gosling, J. T., J. R. Asbridge, S. J. Bame, and W. C. Feldman, "Solar Wind Speed Variations: 1962-1974", J. Geophys. Res., 81, 5061, 1976.

Gotwols, B. L., D. G. Mitchell, E. C. Roelof, W. M. Cronyn, S. D. Shawhan, and W. C. Erickson, "Synoptic Analysis of Interplanetary Radio Scintillation Spectra Observed at 34 MHz", J. Geophys. Res. (submitted for publication), 1978.

Hansen, R. T., S. F. Hansen, and C. Sawyer, "Long-Lived Coronal Structures and Recurrent Geomagnetic Patterns on 1974", Planet. and Space Sci., 24, 381, 1976.

Houminer, Z., "Corotating Plasma Streams Revealed by Interplanetary Scintillation", Nature, 231, 165, 1971.

Houminer, Z. and A. Hewish, "Long-Lived Sectors of Enhanced Density Irregularities in the Solar Wind", Planet. Space Sci., 20, 1703, 1972.

Hundhausen, A. J., Coronal Expansion and Solar Wind, Springer-Verlag: New York, 1972.

Neugebauer, M., "Constancy of Relative Density Fluctuations in the Solar Wind", EOS, 58, 1224, 1977.

Readhead, A. C. S. and A. Hewish, "The Structure in Radio Sources at 81.5 MHz -- III. The Survey", Mem. R. Astr. Soc., 78, 1, 1974.

Rhodes, E. J. and E. J. Smith, "Evidence of a Large-Scale Gradient in the Solar Wind Velocity", J. Geophys. Res., 81, 2123, 1976.

Smith, E. J., L. Daris, B. T. Tsurutani, and J. H. Wolfe, "Observed Properties of the Interplanetary Neutral Sheet: Pioneers 10, 11", EOS, 58, 1226, 1977.

Suess, S. T. and J. Feynman, "Sector Boundary Distortion in the Interplanetary Medium", J. Geophys. Res., 82, 2405, 1977.
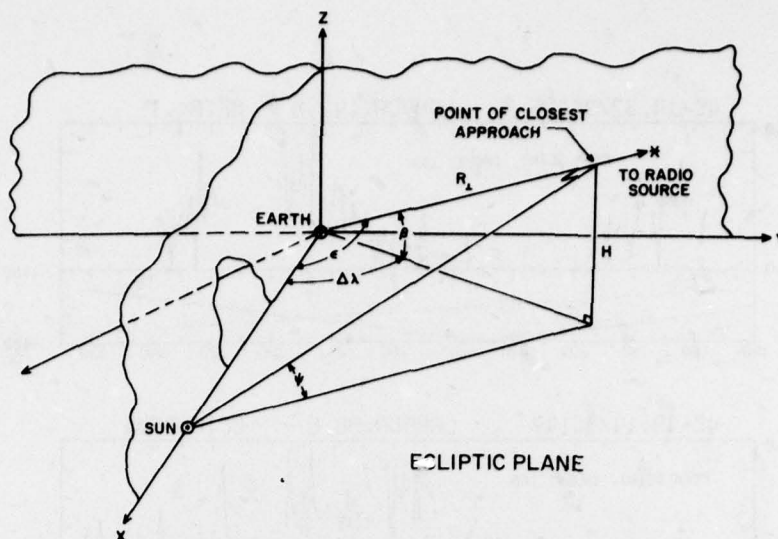
COCOA CROSS RADIO TELESCOPE MEASUREMENTS

FIGURE 1   A schematic illustration of the use of the 34.3 MHz Cocoa Cross radiotelescope to attempt ob-
servations of large scale dynamic features of the interplanetary medium such as transient plasma
disturbances following some solar flares and corotating plasma associated with solar wind streams.
Comparison of ground based interplanetary scintillation measurements with in-situ spacecraft ob-
servations of the solar wind is an important step in the interpretation of the scintillation
observations.   (From Erskine, 1976).

FIGURE 2   Radio sources displaying usable IPS over the synoptic period clustered for IPS sky-box analysis.
For this geocentric all-sky projection the azimuthal coordinate is ecliptic longitude (degrees)
and the radial coordinate is ecliptic latitude (degrees).   The position of the sun (⊙) between
days 156 and 200 is also shown, along with locus of elongation angles of 40° and 80° on day 182,
identified as ϵ_{182}.

FIGURE 3   Observing geometry for IPS observations. We define the following angles: Radio source ecliptic
latitude, β; solar ecliptic longitude of source $\Delta\lambda$; solar elongation angle ϵ; and heliocentric
ecliptic latitude, ψ, of the point of closest approach (PCA) along the line of sight from earth
to source. We also define the distances H = height of PCA above or below the ecliptic plane,
and $R_\perp$ = distance of PCA from earth. (From Erskine, 1976).
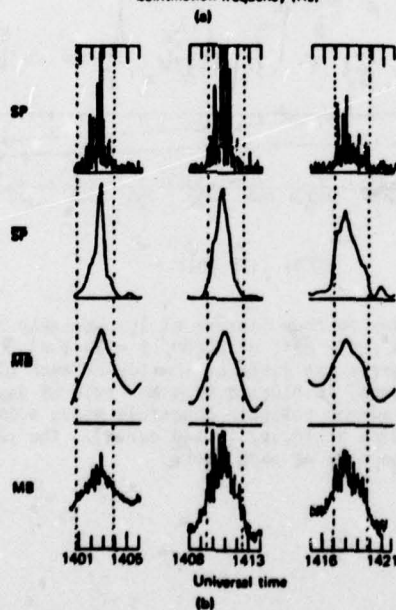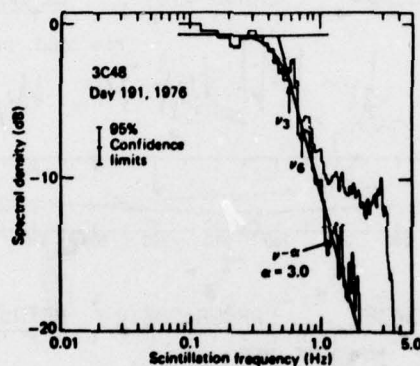
FIGURE 4   (a) Power spectrum of the scintillating radio source 3C48 taken with the Cocoa-Cross radio-
telescope on 1976, day 191. The confidence limits apply to the upper curve. (b) Scintillation
power (SP) and main beam response (MB) for the three transits of 3C48 shown in (a). The three
sets of dashed lines indicate the periods which were spectrally analyzed. Unbarred variables
are 2.5 second averages, and barred variables are 50 second triangle weighted averages.

1974 UT DAY
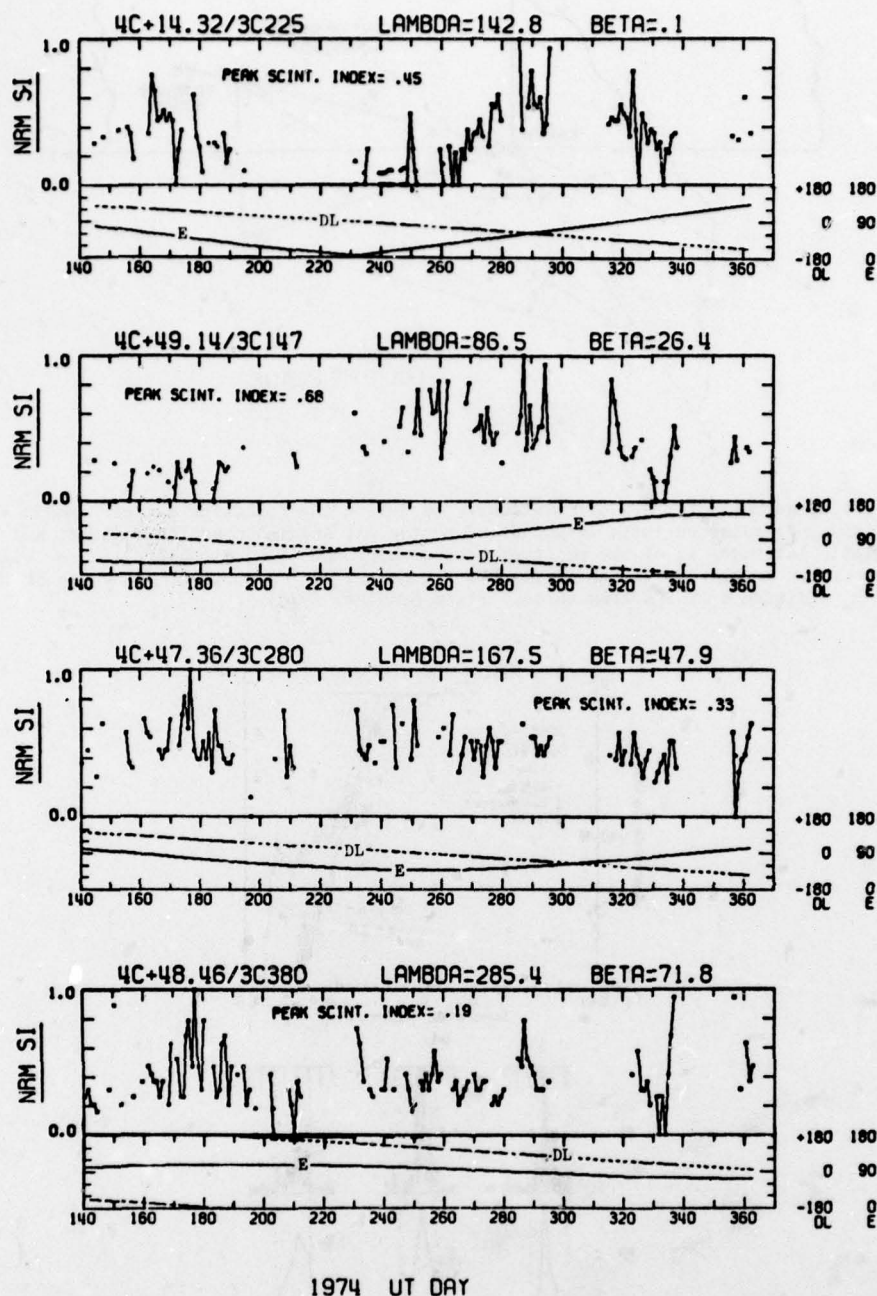
FIGURE 5 Synoptic 34.3 MHz IPS index on four sources at increasingly higher ecliptic latitudes, β:
a) 3C225, β = 0°; b) 3C147, β = 26°; c) 3C280, β = 48°; d) 3C380, β = 72°. Source ecliptic
coordinates (λ, β) in degrees are given at the top of each plot. Normalized (to peak) scin-
tillation index (solid lines) is plotted vs time (1974 UT day). Plotted below IPS index are
2 geometric parameters: source ecliptic longitude minus solar ecliptic longitude, DL, (dashed
curve); and solar elongation angle, ε, (solid curve). The peak value of index used in the
normalization given in the body of each plot.
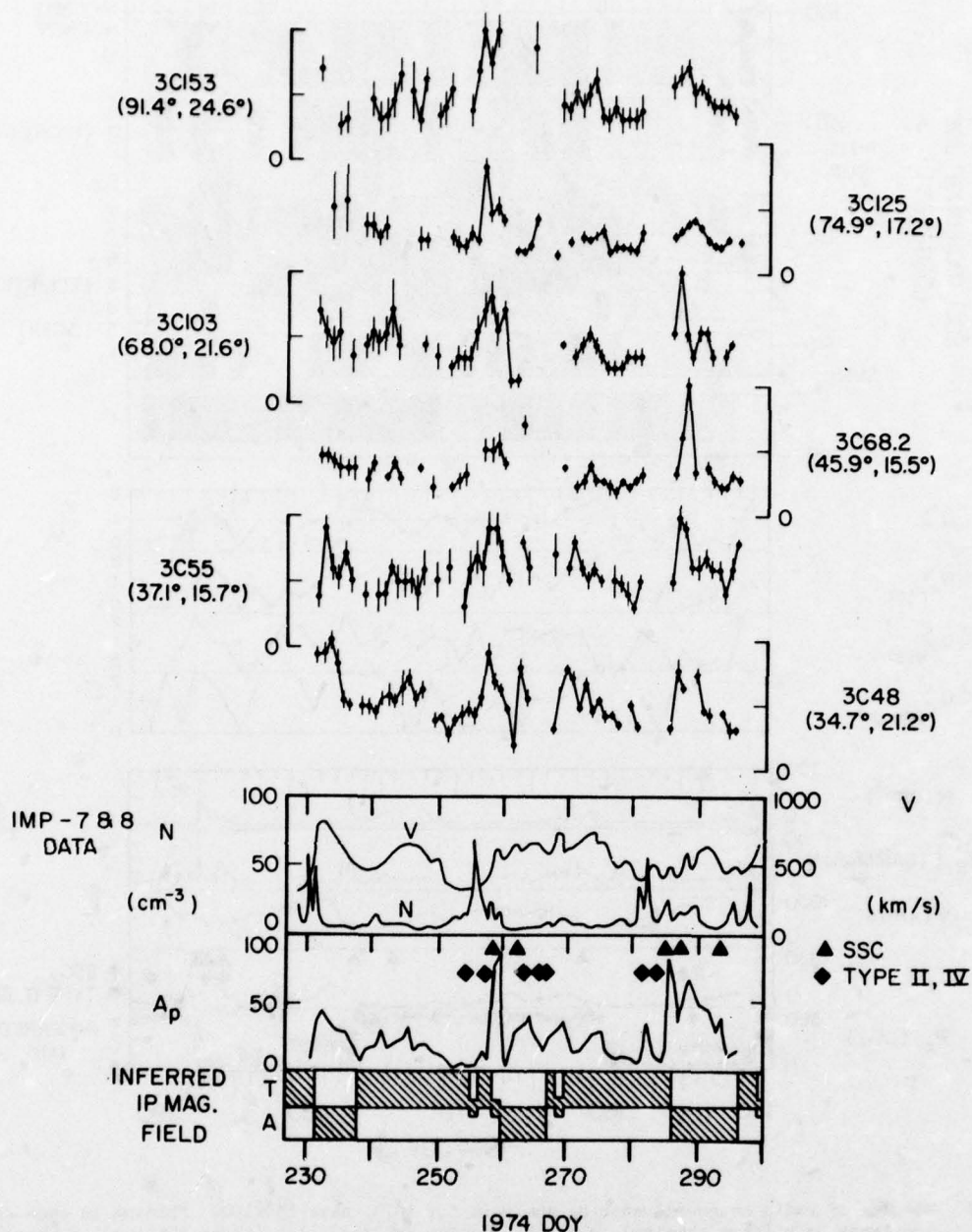
FIGURE 6   Synoptic observations of 6 scintillating sources in a region of dimensions 9° (ecliptic lati-
tude) x 57° (ecliptic longitude). Also shown are the following: IMP-7 and 8 solar wind proton
density velocity (Los Alamos Scientific Laboratory); Geomagnetic A_p index, and the occurrences
of geomagnetic sudden commencements (SSC) and Type II and IV solar bursts in close association
(Solar Geophysical Data); and inferred interplanetary magnetic field direction (Svalgaard, 1975).
At periods of density enhancements the source exhibits an increased scintillation index but
the significant source-to-source differences in response are indicative of density structure
with a scale of 2°-10°.
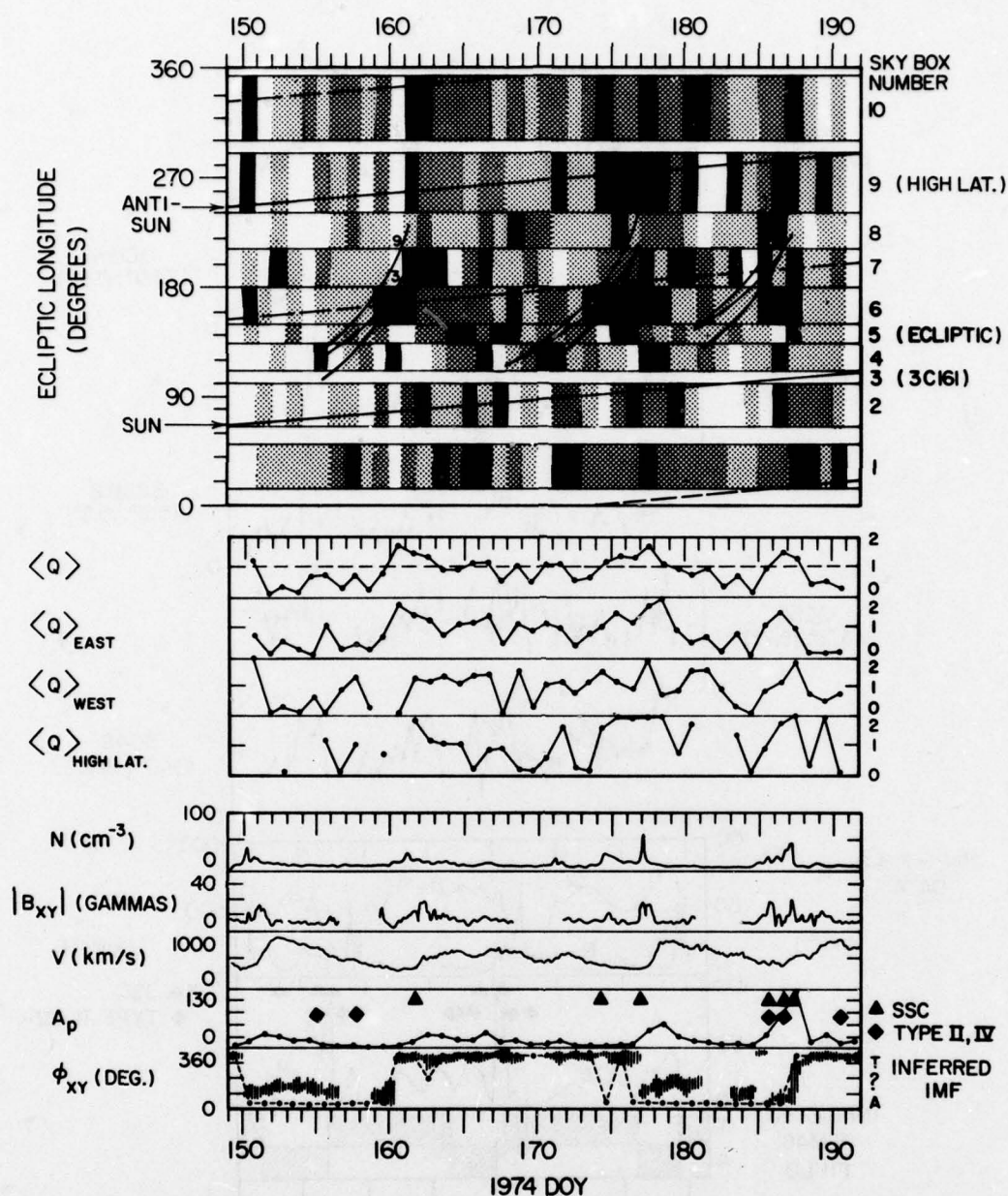
FIGURE 7   Results of radio source clustering analysis for 1974, days 150-190. Shading in each sky-box indicates high (dark shading), moderate (medium shading), low (light shading), or missing (no shading) IPS index. Heavy lines running diagonally in the body of the plot of ecliptic longitude vs time represent the position of the sun and the direction 180° from the sun (anti-sun). Dashed lines running diagonally in body of each plot are drawn at 90° ecliptic longitude east and west of the sun. At the center are plots of IPS 'activity index' for the following cases: all 10 boxes averaged together, $\langle Q \rangle$; eastern sky boxes only, $\langle Q \rangle_{east}$; western sky boxes only, $\langle Q \rangle_{west}$; high latitude box 9 only, $\langle Q \rangle_{high\ lat.}$. At the bottom of the plot are the following correlative data: IMP-7 and 8 spacecraft solar wind proton density and velocity; interplanetary magnetic field magnitude $|B_{xy}|$ and solar ecliptic direction φ_{xy}; Geomagnetic A_p index; inferred interplanetary magnetic field (Svalgaard, 1975) (dots with dashed lines). Model co-rotating spiral tangent directions are indicated for 300 km s⁻¹ and 900 km s⁻¹ solar wind speeds by symbols 3 and 9 respectively. Spirals cross earth on 1974, days 161.5, 177.0, and 187.5. Note particularly the increases in the activity indices at times of density enhancements and the 27-day recurrence of these increases.
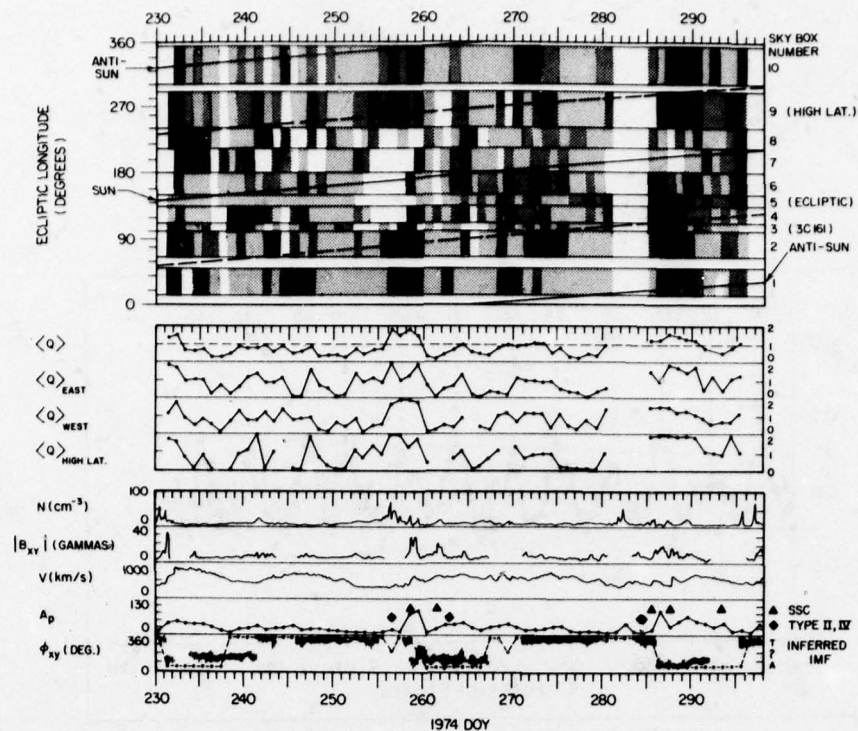
FIGURE 8   Results of radio source clustering analysis for 1974, days 231-295.   The format is the same as for Figure 7.
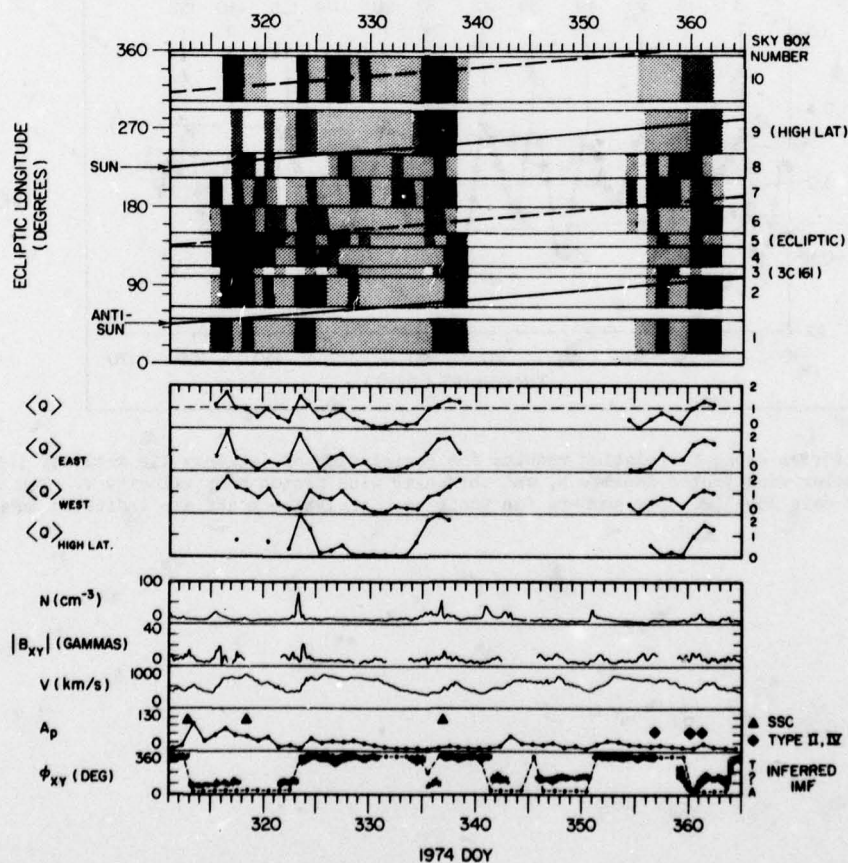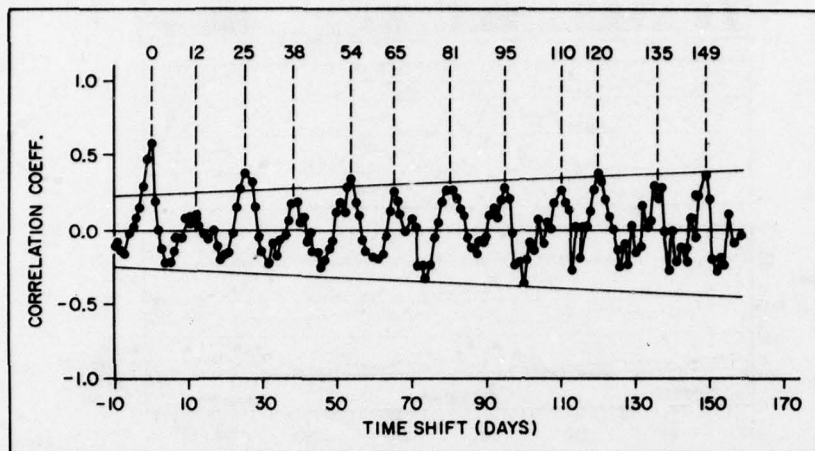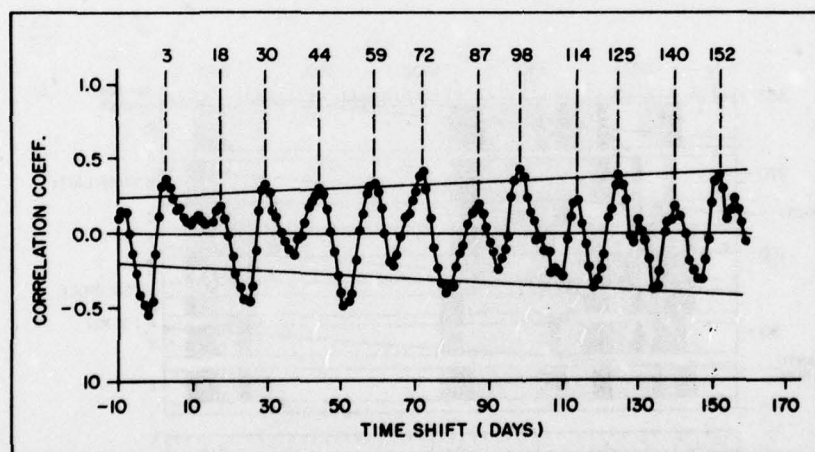

FIGURE 9   Results of radio source clustering analysis for 1974, days 315-362.   The format is the same as for Figure 7.
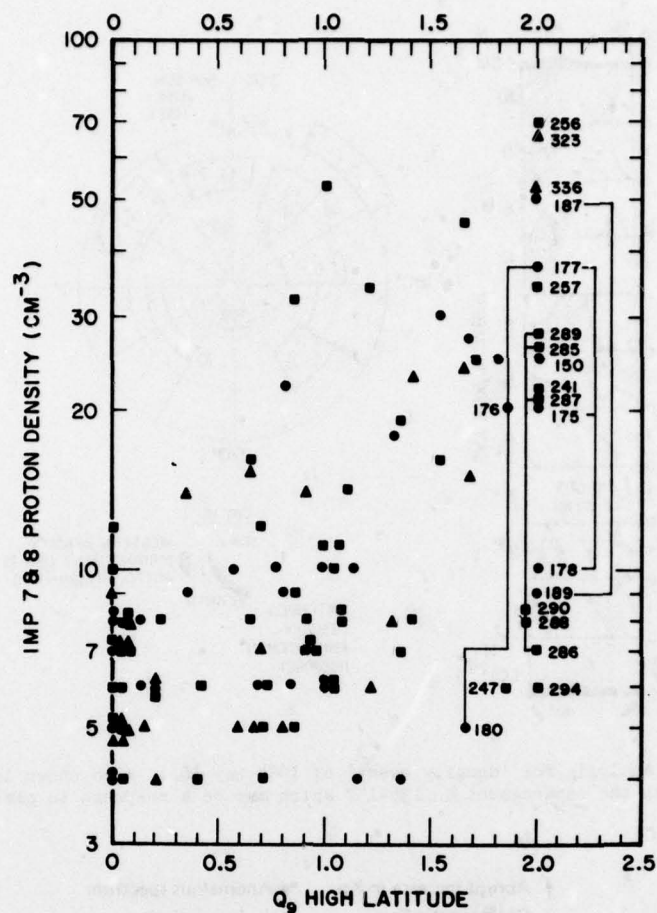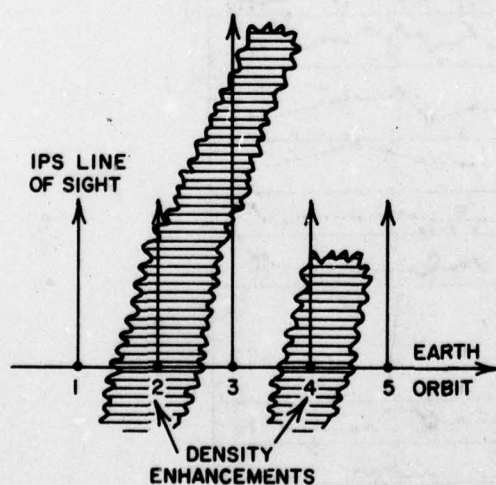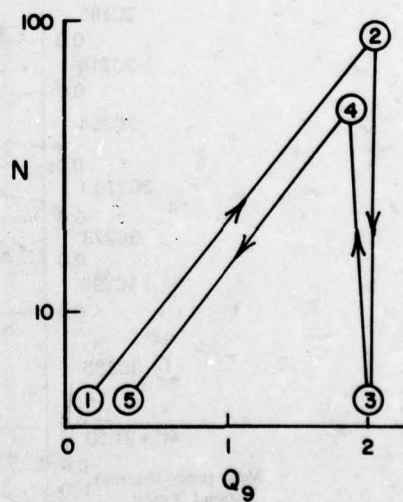
FIGURE 10 Time series cross correlation results for correlation of 'all-sky IPS activity index' (Q) versus the solar wind proton density N, and the solar wind proton bulk velocity V. The data base is 1974, days 150-362. Day numbers for positive correlation peaks are indicated in each plot.

(a)

(b)

(c)

FIGURE 11 a) Peak solar wind proton density (hourly average) from IMP-7 and 8 spacecraft vs high latitude IPS activity index, Q_9. Data Periods (1974): circle = Days 150-190, square = Days 231-295, triangle = Days 315-362. b) Pictorial representation of density structure in ecliptic latitude vs longitude coordinates along Earth orbit for a sequence of five days. c) Schematic behavior of N vs Q_9 for the density structure in (b).
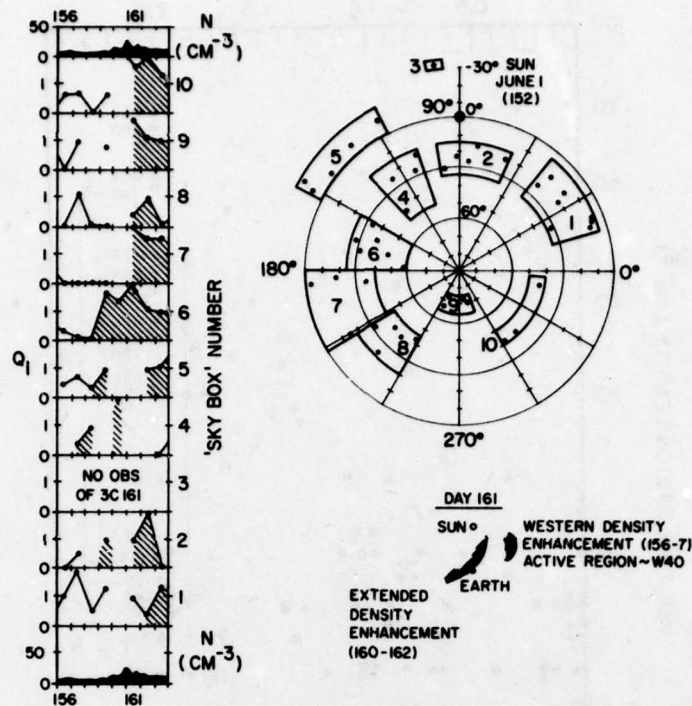
FIGURE 12 IPS 'sky box' analysis for 'density event' of 1974 Day 161. Also shown is a density structure
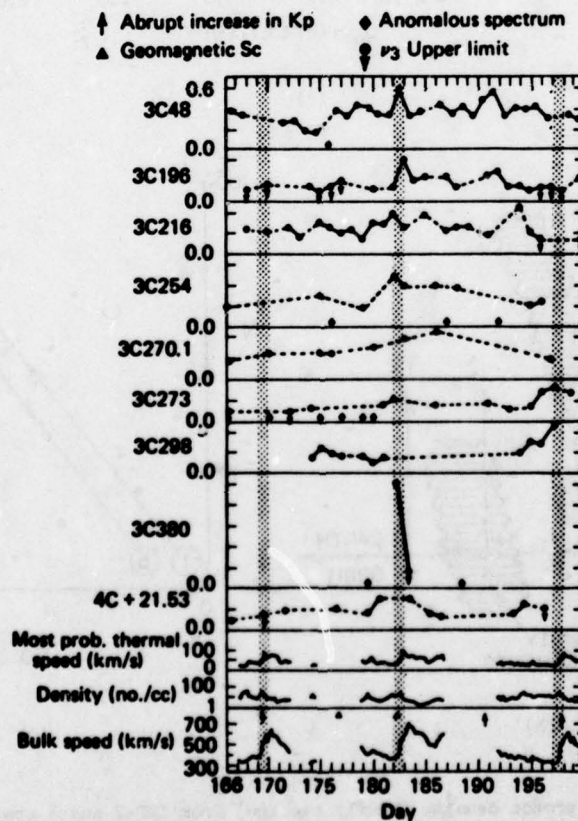consistent with the enhancement on 156-157 which may be a response to plasma from MPR 12972.

FIGURE 13 Top: ν_3 versus time for 9 sources, Bottom: solar wind probe data (Solar Geophysical Data, 1977).
The start of the three known solar wind streams is highlighted by shading. On those days when
a two component spectrum was present, or the spectrum was ambiguous, the data is omitted and a
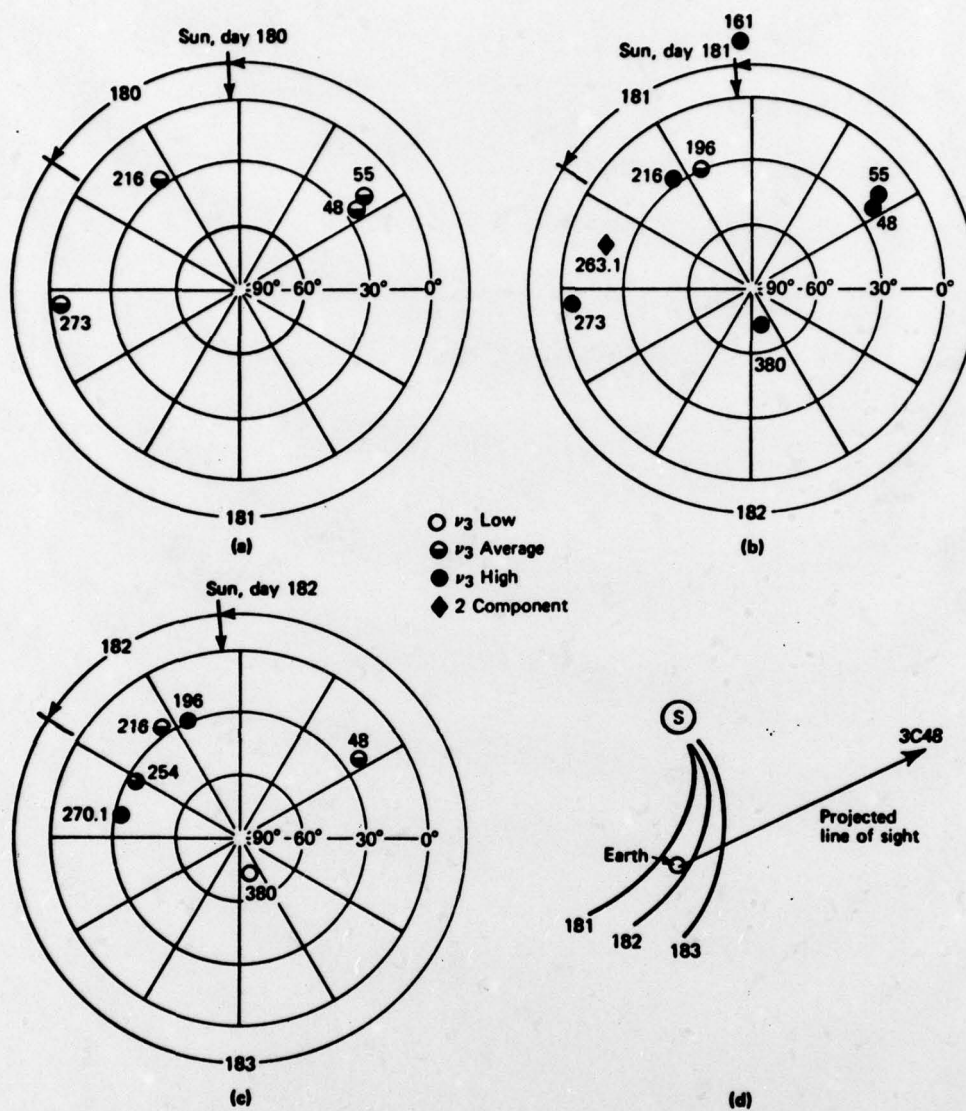diamond is plotted near the bottom of the relevant curve.

FIGURE 14 (a-c) ν_3 for a number of sources, plotted in geocentric ecliptic coordinates. The "day cut" is at the sun, and the observations proceed in a counterclockwise sequence. The threshold for low and high is one standard deviation from the average. (d) Line-of-sight to 3C48 projected onto the ecliptic plane on 1976, day 182. Also shown is the approximate shape of the center of a corotating density enhancement for days 181, 182 and 183 at the time when 3C48 was observed.

PREDICTION OF GEOMAGNETIC DISTURBANCES

BY INTERPLANETARY SCINTILLATION

Z. Houminer
National Committee for Space Research
Radio Observatory, Haifa, Israel.

SUMMARY

Daily observations of the scintillation of a number of radio sources lying at widely separated positions provide a way for predicting geomagnetic activity associated with large scale features of the solar wind. By observing suitable sources lying to the east of the Sun it is possible to forecast, up to six days in advance, geomagnetic storms associated with corotating solar wind streams. Geomagnetic disturbances caused by interplanetary shock waves associated with solar flares may be predicted some 8 - 24 hours in advance, when using observations at UHF frequencies (300-400 MHz).

1.   INTRODUCTION

Radio waves from extragalactic or galactic sources are scattered by irregularities of plasma density in the interplanetary medium. If the radio sources are compact so that they illuminate the plasma with sufficient coherence, the interference of the scattered waves produces a diffraction pattern at the Earth. This diffraction pattern drifts across the Earth as the solar wind blows the irregularities outwards, so that the radio source appears to scintillate when observed from one place.

Extended observations of interplanetary scintillation of a grid of sources suitably disposed about the Sun, provide a valuable method for monitoring the behaviour of the solar plasma. Such observations show large day-to-day variations in scintillation index which are closely associated with large scale features of the solar wind such as corotating streams and shock waves associated with solar flares.

It has been shown that the enhancements in scintillation are strongly correlated with geomagnetic activity (Houminer and Hewish, 1974; Cronyn et al, 1975; Erskine et al, 1976). In this paper I shall discuss the possible predictions of geomagnetic disturbances associated with either co-rotating streams or shock waves, using daily observations of the scintillation of a large number of radio sources.

2.   GEOMAGNETIC DISTURBANCES ASSOCIATED WITH COROTATING STREAMS

Interplanetary scintillation observations of radio sources at widely separated elongations exhibit large enhancements in scintillation which last for several days and are strongly correlated with the velocity structure of the solar wind (Houminer and Hewish, 1972; Watanabe and Kakinuma, 1972; Coles et al, 1974). These enhancements in scintillation are mainly caused by small scale density irregularities in the compressed plasma regions between fast and slow velocity solar wind streams (Houminer and Hewish, 1972). Further evidence that enhanced scintillation results from compression of the solar plasma may be drawn from the high correlation shown to exist between scintillation index and plasma density (Houminer and Hewish, 1974; Erskine et al, 1976).

Houminer (1971) showed that the time displacements of the scintillation enhancements for radio sources lying in different directions were consistent with a simple model of corotating sectors of enhanced density irregularities. The model was based on Readhead (1971) who showed, for a spherically symmetrical distribution of irregularities about the Sun, that the scintillation observed at elongations ε < 90° was mainly due to those irregularities located in the region where the line of sight passes nearest to the Sun. For ε > 90° the effect of Fresnel filtering becomes important and the main scattering region is located about 0.2 - 0.3 a.u. from the Earth. The scintillation index F varies as $F \propto \Delta N \, \ell^{1\frac{1}{2}}$ where ΔN is the r.m.s. fluctuation of electron density and ℓ the scale size of the irregularities, and it has been shown that enhanced scintillation is caused by an increase of ΔN within a spiral sector of angular width ϕ at the Sun (Houminer and Hewish, 1972).

The theoretical time displacements of the scintillation enhancements as a scintillation sector of width ϕ = 25° rotates past lines of sight of sources at elongations of 45°, 80° and 120°, are shown in Fig.1a. The larger enhancement in scintillation, e.g. for elongations between 80° - 120°, occur when the lines of sight are roughly parallel to the corotating spiral (Houminer, 1971).

The observed variations of scintillation index obtained with the 81.5 MHz array at Cambridge during the passage of a particular sector of enhanced density irregularities are shown in Fig.1b. The geometry of the corotating sector at 2 day intervals together with the lines of sight to the different sources are shown in the upper left corner of Fig.1b. The very good agreement between the observed and predicted time displacements confirms that the sector is aligned along the corotating spiral as assumed in the theoretical model.

The scintillation sector reached the Earth on June 25, 1971, as can be seen from the large enhancement in scintillation for the radio source 3C 298. Enhancements in scintillation could be observed several days before that as the sector rotated passed the lines of sight of 3C 190, 3C 237, 3C 263.1 and 3C 273. The scintillation enhancement for 3C 190 occurred on June 19, i.e. six days before the sector reached the Earth. The more pronounced enhancements for 3C 237, and 3C 263.1 were observed 2-3 days prior to June 25.

Thus by observing radio sources suitably disposed to the east of the Sun, the arrival at the Earth of a corotating scintillation sector can be predicted some 2-6 days in advance.

The three-hour values of the geomagnetic Kp indices for the period June 15 - 28, are shown in Fig.1c. It can be seen that the geomagnetic disturbance on June 25, coincides with the arrival time of the corotating sector at the Earth. In order to study the relation between scintillation enhancements and geomagnetic

disturbances, scintillation index measurements for the period January - April, 1971, were compared with geomagnetic Ap indices for the same period. The scintillation results which were obtained from observations of many sources at different elongations were first corotated to the Earth, in the manner described by Houminer and Hewish (1972).

The corotated scintillation results and the Ap indices for the period January - April, 1971, are shown in Fig.2. The crosscorrelation between the two sets of data is shown in Fig.3, indicating a strong correlation of 0.6 at a time shift of 0.5 ± 1.0 days. Similar correlation between scintillation enhancements and geomagnetic disturbances were obtained by Erskine et al. (1976).

We may conclude that by observing suitable scintillating radio sources, it is possible to forecast geomagnetic activity associated with corotating solar wind streams up to six days in advance.

3. GEOMAGNETIC ACTIVITY ASSOCIATED WITH SOLAR FLARES

Observations of the scintillation of a number of radio sources lying at widely separated positions, show occasional increases in scintillation index which cannot be ascribed to corotating features since they occur almost simultaneously for radio sources located on opposite sides of the sun. These increases which are short-lived in comparison to corotating streams and typically last for one or two days only, are shown to be related to interplanetary shock waves associated with solar flares (Wiseman and Dennison, 1972; Cronyn et al., 1975; Ricket, 1975; Houminer, 1976).

An example of such a scintillation enhancement occurring almost simultaneously for several sources, is shown in Fig.4. (Houminer, 1976). In comparison, an enhancement in scintillation which shows time displacements for the different sources consistent with a corotating feature, is also seen in the same figure. The enhancement marked A lasts for 1-2 days and can be explained only if the disturbance causing enhanced scintillation propagates over a wide front. The possible configuration of such a disturbance is shown in Fig.5 together with the lines of sight to the various sources.

Houminer (1976) examined scintillation index observations of many radio sources at 81.5 MHz during the period January - August 1971, in order to study flare associated scintillation enhancements. During this period only 3 scintillations enhancements occurred simultaneously for sources on both sides of the Sun.

The enhancements observed during 26-27 January could be associated with an importance 3 solar flare which started at 23:10 UT on January 24 and which appeared on the solar surface at 19°N and 49°W. The enhancements observed during 16-17 May could be related to an importance 2 flare which started at 14:20 UT, 14 May at 4°N and 10°E on the solar surface. No major solar flare could be clearly related to the enhancements on 14-15 April.

All three disturbances causing enhanced scintillation also caused sudden commencement geomagnetic storms, followed by Forbush decreases.

The radio sources for which enhanced scintillation were observed during the passage of the flare associated disturbances, are listed in Table I.

For each source the date and time of observation is given together with the elongation and the radial distance from the Sun of the point where the shock disturbance intercepts the line of sight. Also shown in Table I is the ratio F_m/F where Fm is the maximum value of scintillation index during the passage of the disturbance and F is the average undisturbed scintillation index.

The dates and times of the sudden commencement geomagnetic storms associated with the shock wave disturbances are also given in Table I.

TABLE I

Scintillation Observations During the Passage of the Flare Associated Disturbances

EVENT	SOURCE	DATE and TIME of observation (UT)		ELONGATION	RADIAL DISTANCE (au)	Fm/F
26 - 27 January 1971	3C 48	27/1	17:15	86°	1.02	2.9
	3C 147	27/1	21:18	131°	1.15	3.5
	3C 298	27/1	05:56	262°	1.04	4.0
	3C 459	26/1	14:54	43°	0.68	2.8
	Earth	27/1	04:30		1.0	
14 - 15 April 1971	3C 138	14/4	15:52	55°	0.82	2.9
	3C 147	14/4	16:12	64°	0.90	2.2
	3C 273	14/4	23:00	159°	1.19	2.9
	3C 298	15/4	00:50	160°	1.19	2.5
	3C 468.1	14/4	10:22	302°	0.85	2.6
	Earth	14/4	12:43		1.0	
16 - 17 May 1971	3C 161	16/5	14:48	49°	0.78	1.8
	3C 190	16/5	16:26	63°	0.92	2.2
	3C 196	16/5	16:38	62°	0.90	2.5
	3C 273	17/5	20:50	130°	1.14	2.9
	3C 298	17/5	22:40	147°	1.18	3.0
	3C 459	17/5	07:38	295°	0.88	2.3
	Earth	17/5	06:30		1.0	

It is seen from Table I that enhancements in scintillation were observed up to 16 hrs before the sudden commencements geomagnetic storms. However, it is not possible to determine whether an enhancement in scintillation is due to a flare associated shock wave before more observations on both sides of the Sun are gathered. From the data presented in Table I, it is seen that conclusive evidence about the nature of the disturbances causing enhanced scintillation could only be determined after the onset of the sudden commencement geomagnetic storms.

We may conclude that though, in principle, it is possible to predict geomagnetic disturbances associated with solar flares by observing scintillating sources at widely separated elongations, it is not possible to forecast such storms on the basis of scintillation observations alone at 81.5 MHz.

Interplanetary scintillation observations at higher frequencies, say, 300-400 MHz, can probe the solar plasma closer to the Sun. At these frequencies the cutoff in scintillation due to the finite size of the source occurs at about 0.2 a.u. from the Sun, in comparison to 0.5 a.u. for 81.5 MHz. As the average velocity of a shock front is about 0.4 a.u. per day, observations at such frequencies may enable us to monitor the enhancements in scintillation about a day earlier than at 81.5 MHz and thus forecast geomagnetic storms associated with solar flares some 8-24 hr in advance.

4. CONCLUSIONS

Interplanetary scintillation observations of suitably disposed radio sources provide a way of forecasting geomagnetic activity associated with corotating solar wind streams some 2-6 days in advance.

Prediction of geomagnetic storms associated with solar flares cannot be predicted when using observations at 81.5 MHz. However, observations at higher frequencies, which can probe the solar plasma closer to the Sun, may enable the prediction of such storms some 8-24 hours in advance.

REFERENCES

Coles, W.A., Ricket, B.J. and Rumsey, V.H.: 1974, in C.T. Russel (ed.), Solar Wind Three, University of California Press, Los Angeles, California, p.351.

Cronyn, W.M., Erskine, F., Shawhan, S.D., Gotwols, B.L. and Roelof, E.C.: 1975, in Proc. Ionospheric Effects Symp., Virginia 1975.

Erskine, F.T., Cronyn, W.M., Shawhan, S.D., Roelof, E.C. and Gotwols, B.L.: 1976, "Interplanetary Scintillation at Large Elongation Angles: Response to Solar Wind Density Structure". (preprint).

Houminer, Z.: 1971, Nature Phys. Sci. 231, 165.

Houminer, Z.: 1976, Planet. Space Sci. 24, 951.

Houminer, Z. and Hewish, A.: 1972, Planet. Space Sci. 20, 1703.

Houminer, Z. and Hewish, A.: 1974, Planet. Space Sci. 22, 1041.

Readhead, A.C.S.: 1971, Mon. Not. R. Astr. Soc. 155, 185.

Ricket, B.J.: 1975, Solar Phys. 43, 237.

Watanabe, T. and Kakinuma, T.: 1972, Publ. Astron. Soc. Japan 24, 459.

Wiseman, M. and Dennison, P.A.: 1972, Proc. Astron. Soc. Aust. 2, 79.
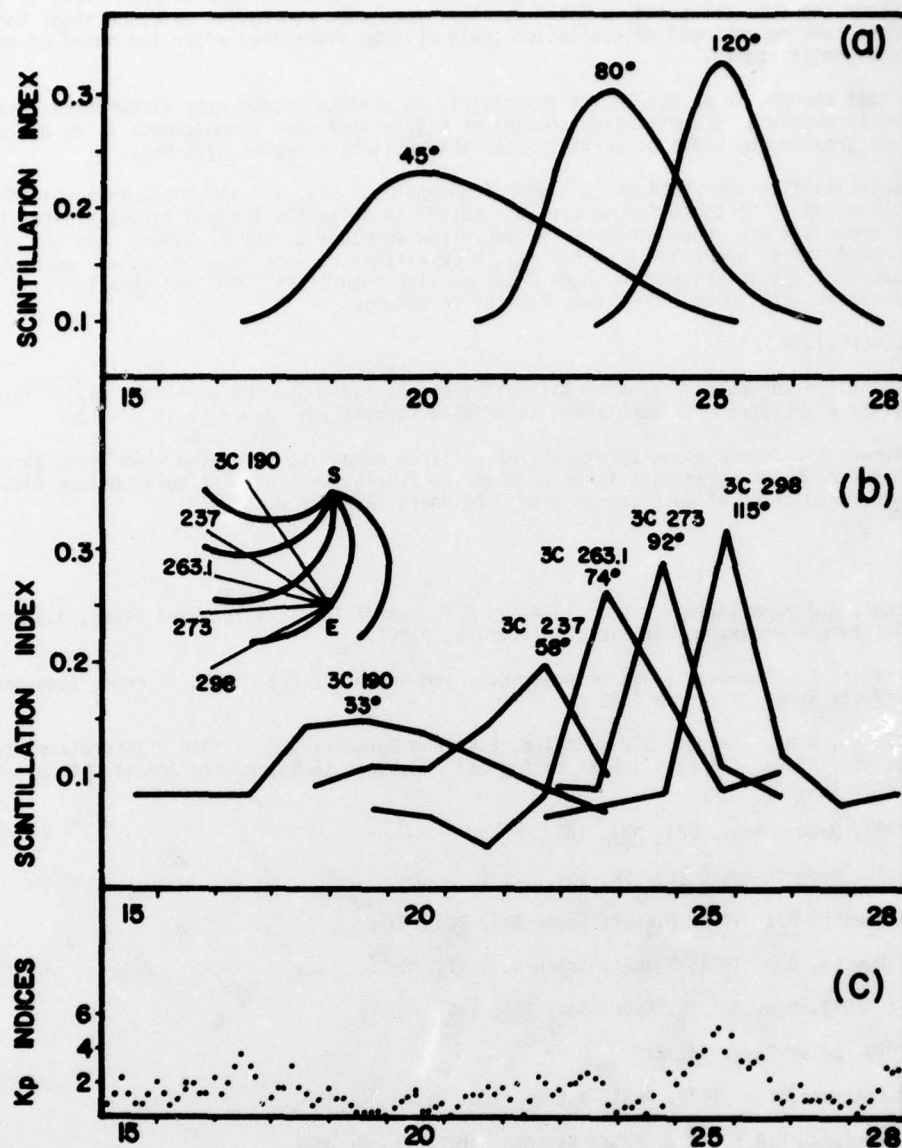
JUNE 1971

Fig.1 (a) Theoretical scintillation index variations for an enhanced sector of width $\phi = 25°$ computed for elongations of 45°, 80° and 120°

(b) Observed scintillation index variations for the enhanced sector which passed the Earth on June 25th. The geometry of the corotating sector at 2 days intervals together with the lines of sight to the various sources are shown in the inset at the upper left corner.

(c) Three-hour values of the geomagnetic Kp indices for the period June 15–28
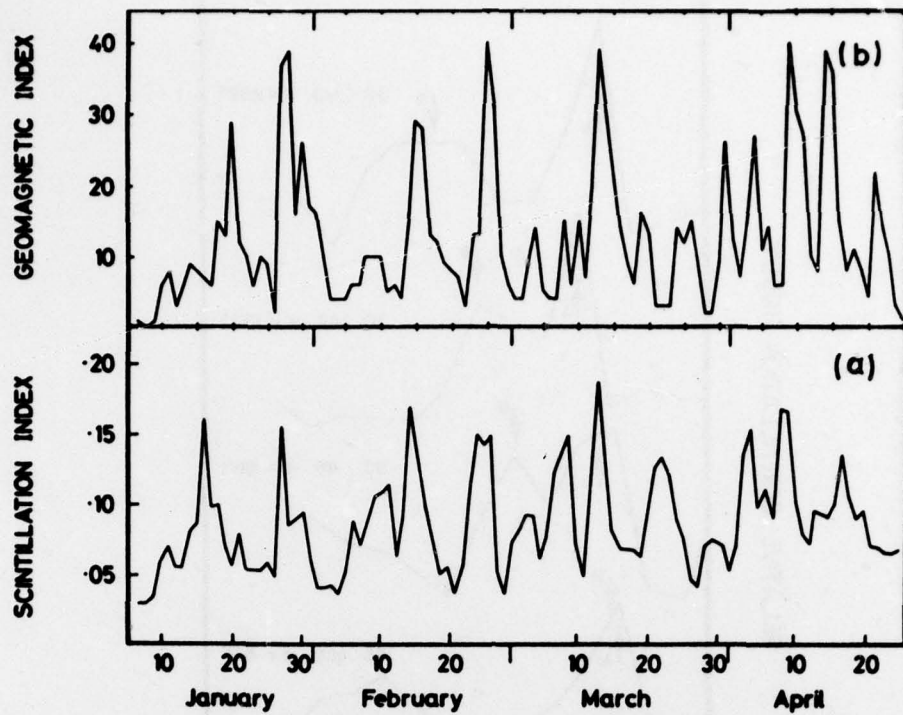
Fig.2 (a) Scintillation index results and (b) geomagnetic Ap indices, for the period January – April, 1971
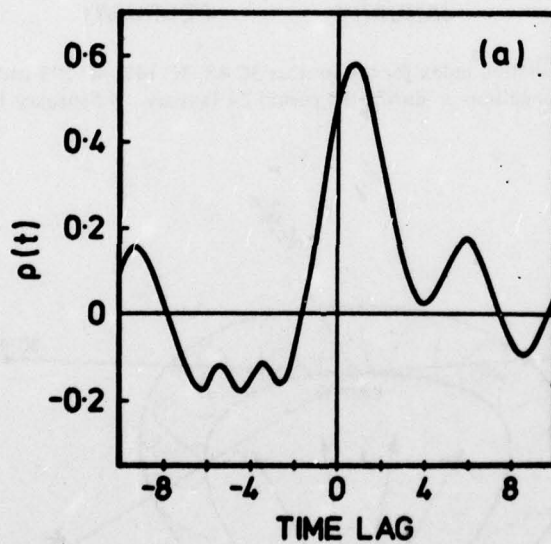

Fig.3 Crosscorrelation between the scintillation and Ap indices of Figure 2
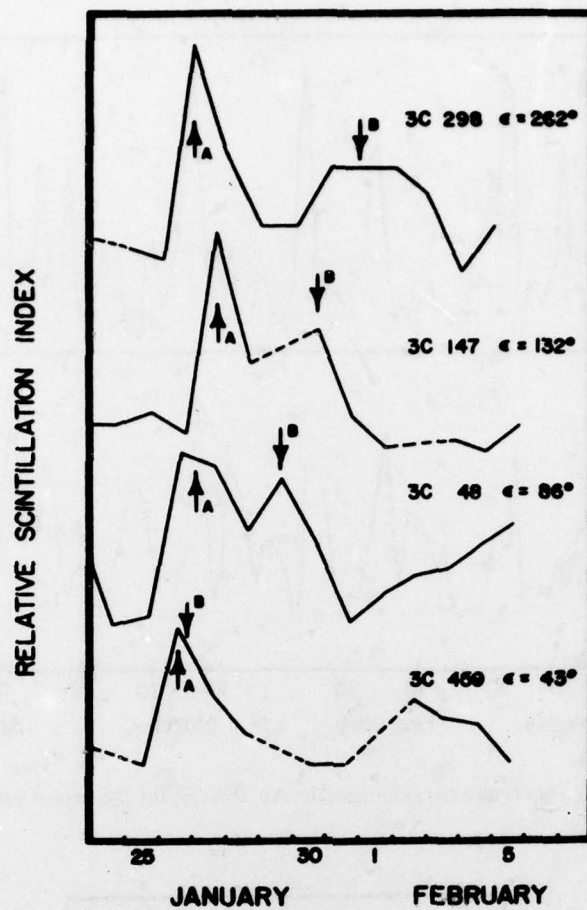
Fig.4 Daily values of scintillation index for the sources 3C 48, 3C 147, 3C 298 and 3C 459 observed at different elongations ϵ during the period 24 January – 5 February 1971
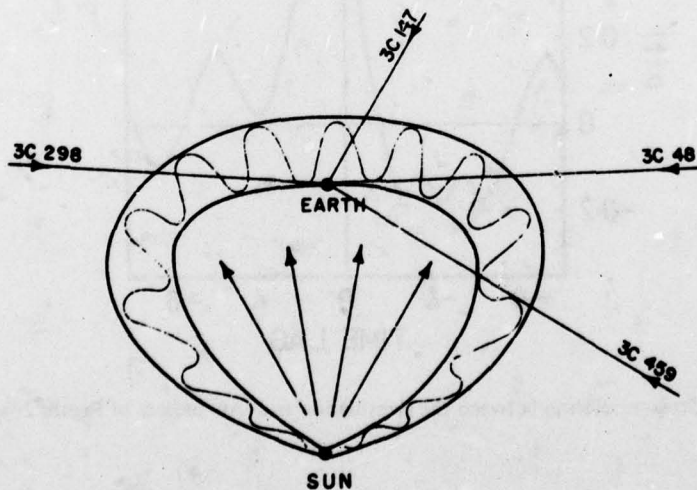

Fig.5 The configuration of a shock wave disturbance together with the lines of sight to the various radio sources

DISCUSSION

H.Rosenbauer, FRG

Do you see differences in the scintillation spectrum from shock/fronts and fronts of fast streams. The physical conditions seem to be rather different in the two cases.

Author's Reply

No, we do not see any differences. It is the rms density variations which cause IPS. We found good correlation between scintillation enhancements and density peaks at the compressed plasma regions between fast and slow velocity solar wind streams. However, it is not clear how the small-scale density irregularities are generated.

THE PREDICTION OF FAST STREAM FRONT ARRIVALS AT THE EARTH
ON THE BASIS OF SOLAR WIND MEASUREMENTS AT SMALLER SOLAR DISTANCES

H. Rosenbauer
Max-Planck-Institut für Aeronomie
D-3411 Katlenburg-Lindau 3, F.R.G.

R. Schwenn
Max-Planck-Institut für extraterrestrische Physik
D-8046 Garching b./München, F.R.G.

S.J. Bame
Los Alamos Scientific Laboratory, Los Alamos, N.M. 87545, U.S.A.

SUMMARY

It is well established that the arrival of high speed solar wind at the earth often leads to disturbed magnetospheric conditions, as indicated by enhanced Kp-values. Associated with such conditions are increased auroral activity and changes in the ionosphere which, in turn, lead to changes in RF-communication links in some wavelength regions.
We will discuss the problems involved in the prediction of the arrival of fast solar wind streams at the earth on the basis of measurements made by space probes in the region between 0.3 and 1 AU. Experience in such predictions has been gained by comparing solar wind data measured using the HELIOS-1 and -2 solar probes with data measured near the earth using the IMP satellites. It is shown that arrival time predictions accurate to within a few hours can be made at least as long as the large scale conditions on the sun are relatively stationary as observed near the time of solar minimum. However, the latitudinal extent of the respective high speed streams is found to be important for making quantitative predictions. Coronal data sufficient for locating the sources of high speed streams can improve the precision of these predictions.

1.   INTRODUCTION

Since the pioneering work of Bartels (1948) it was suspected and since the Mariner 2 measurements (SNYDER et al., 1963) it is known that plasma emission from the sun and its fluctuations causes a major part of the geomagnetic activity. Especially it was found by the Mariner 2 measurements and confirmed by many subsequent observations (see e.g. SHEELEY et al., 1977) that the Kp index is strongly correlated with solar wind speed, in particular a sharp rise of Kp is observed everytime the front of a "fast solar wind stream" arrives at the subsolar point of the earth's magnetosphere.

It is not the aim of this paper to deal with the complex physical processes that are set on upon the arrival of a stream front and cause "magnetospheric storms", affect the particle populations in the magnetosphere, produce enhanced ionospheric activity and auroral arcs, and finally disturb radio communication in certain wavelength regions. The principal idea is, however, that the frontside magnetosphere moves inward as the dynamic pressure of the solar wind increases. This way, electric fields are induced in the magnetosphere which drive currents along the magnetic field lines and through the ionosphere connecting the footprints of the field lines. These currents together with enhanced injection of particles into the magnetosphere and an energization of particles in the compressed magnetic field lead to increased particle precipitation into and onset of instabilities in the ionosphere. The direction of the interplanetary magnetic field (IMF) also plays an important role, indicating that merging of IMF and terrestrial magnetic field lines may take place during this process.

In this paper we studied whether and to what accuracy predictions can be made about the arrival time of fast streams at the earth on the basis of plasma measurements performed aboard the solar probes HELIOS-1 and -2. The two HELIOS spacecraft are in ecliptical orbits with perihelions of approximately 0.3 AU and aphelions of 1 AU. Our plasma instruments measure the three-dimensional distributions of the solar wind ions. All fluid parameters as density, bulk velocity (as a vector) and temperature (as a tensor) can be derived from these measurements. The observed structures were compared to those measured by similar plasma instruments aboard the earth-orbiting satellites IMP 7/8.

2.   THE PREDICTION PROBLEM

The problem of predicting the arrival time of fast solar wind streams at the earth on the basis of plasma measurements made anywhere in interplanetary space is a complex one. We shall therefore first regard an assumed idealized situation. If we had a spacecraft with plasma instruments aboard, situated exactly between the sun and the earth at a convenient distance, e.g. 0.8 AU, the situation could be regarded as ideal. Since the solar wind expands very nearly radially at heliographic distances under discussion here, the spacecraft would monitor the plasma which would hit the earth's magnetosphere about one day later. For a correct prediction of the arrival time of a fast stream at the earth, we would have to solve only two problems described by the questions:
       (1) How can the front of a fast stream be accurately identified
       (2) How fast does that structure move

As the characteristic signature of the onset of a fast stream we chose the density peak produced as a consequence of the fast stream ramming into the preceding slower plasma. Such density peaks are always correlated with steep rises of velocity and temperature and can therefore easily be identified. Two examples of such peaks are shown at the positions of the vertical dashed lines in Fig. 1. The question of when the plasma making up the density peak will arrive at the position of the earth is more difficult to answer, since the velocity gradients in the vicinity of such peaks are extremely large. According to our experience, the velocity of radial propagation of a stream front is slightly underestimated if one takes the velocity of the plasma in the density peak as a measure of the propagation of the front.

Because of these difficulties we assumed that the interaction region between the slow and the fast plasma moves such that the dynamical pressures from both sides (thermal and magnetic pressures are neglected) just balance, we get as a first order approximation a simple equation for the radial velocity v_3 of the interaction region:

$$v_3 = \frac{\rho_1 v_1 + \rho_2 v_2}{\rho_1 + \rho_2} \tag{1}$$

where ρ_1 and ρ_2 are the mass densities of the slow and the fast plasma respectively and v_1 and v_2 are the corresponding radial velocities. We applied this equation in all cases in which ρ_1, v_1 and ρ_2, v_2 could be determined reliably, and found that the accuracy of prediction increased by a factor 2 to 3 on the average as compared to using the actually measured speed of the plasma in the density peak.

If we now leave the assumed idealized situation and regard the real problem of making predictions on the basis of HELIOS measurements, we have to be aware of no longer monitoring the plasma elements which later on pass by the earth. Predictions are therefore only possible if assumptions are made, and the following additional questions have to be regarded:

(3) Are the large scale conditions in the source regions of the solar wind approximately stationary.

(4) What are the effects of the measurement being made at solar longitudes different from that of the earth.

(5) What are the effects of differences in solar latitude between the point of observation and the earth.

Question (3) is crucial, since predictions from measurements at different heliographic longitudes must be based on the assumption that large scale structures observed in the solar wind are mainly due to a sampling effect of plasma produced by different sources (e.g. "coronal holes" for fast streams) in the corona. If these sources remain stationary it can be assumed that observed structures "corotate" with the sun. As already proven by the Mariner 2 measurements (NEUGEBAUER and SNYDER, 1966) large structures, as extended fast streams, often do not change much over several solar rotations. It depends on the phase of the sunspot cycle how stationary the conditions really are (SHEELEY et al., 1977). Fast streams are very persistent in the declining part of the solar cycle. Since the HELIOS measurements reported here were made during such a period (1975 to 1976) we assumed stationary conditions on the sun for our evaluations. It has to be kept in mind, however, that the results obtained are only representative of periods in this part of the solar cycle.

The question of the effect of differences in heliographic longitude (4) between the point of observation and the earth is trivial as long as the above assumption of stationary conditions in the corona holds true, and the heliographic latitudes are equal. The delay time of a structure (at 1 AU heliographic distance) is then:

$$\Delta t = \frac{\Delta\varphi}{\omega_{syn}}$$

with $\Delta\varphi$ being the difference in heliographic longitude between the earth and the observing s/c, and ω_{syn} the synodical angular velocity of the equatorial region of the sun.

Since the rotation axis of the sun is tilted against the ecliptic the observing probe and the earth will generally not be at equal heliographic latitudes. This means that the solar wind structures observed at the spacecraft "rotate" by the earth northward or southward. Only in case the interaction regions of fast streams are oriented exactly north-southward (in a heliographic coordinate system) no problems arise. Unfortunately, this is rarely true since the boundaries of fast streams near the ecliptic often seem to be directed more east-west rather than north-south. This predominant directionality is probably due to the fast streams being generated in "coronal holes" extending equatorward from the solar polar regions and terminating near the equator. By comparison of HELIOS and IMP measurements we could show that sometimes solar wind structures are completely different if the observations are made at positions only a few degrees apart in solar latitude (SCHWENN et al., 1978). If the direction of the interaction front can be determined at the position of the monitoring spacecraft (which in principle is possible on the basis of stream deflection measurements) a first order correction can be made to the calculated stream arrival time at the earth.

As the times for the radial propagation of the stream front from the heliocentric distance of the monitoring spacecraft to the distance of the earth and the time necessary for the structure to rotate over the differential angle in heliographic longitude ($\Delta\varphi$) have simply to be added, the expected time delay between the observation and the arrival at the earth can be written as follows:

$$\Delta t = \Delta r \cdot v_3 + \frac{\Delta\varphi}{\omega_{syn}} \tag{2}$$

As pointed out above, this equation is valid only if the propagation velocity of the stream front is constant over Δr and the conditions on the sun are stationary for the time $\Delta\varphi/\omega_{syn}$. If we insert equ. (1) we obtain

$$\Delta t = \frac{\Delta r (\rho_1 v_1 + \rho_2 v_2)}{\rho_1 + \rho_2} + \frac{\Delta\varphi}{\omega_{syn}} \tag{3}$$

A first order correction for oblique directions of the fronts can be made by calculating the resulting phase shift of the structure. This phase shift is proportional to the difference in heliographic latitude $\Delta\phi$ between the earth and the observing spacecraft and $\tan\gamma$. Gamma is the angle between the lines of interception with a heliocentric sphere (at the position of the spacecraft) of a meridional plane and the stream front. This correction can be included in equ. (3)

$$\Delta t = \frac{\Delta r (\rho_1 v_1 + \rho_2 v_2)}{\rho_1 + \rho_2} + \frac{\Delta\varphi + \Delta\phi \tan\gamma}{\omega_{syn}} \tag{4}$$

3.   RESULTS AND CONCLUSIONS

The results of this study based on a major part of the HELIOS results of the years 1975/76 are given in table 1. In most cases the propagation speeds of the stream fronts were assumed to be identical to those of the compressed regions in front of the streams. Probably for this reason, the predicted time delays are slightly too large on the average. Application of equ. (3) for a few appropriate cases resulted in a considerable improvement of the prediction in these cases but did not largely affect the mean prediction accuracy because of the relatively small number of cases in which equ. (3) could reasonably be applied.

<div align="center">

Table 1

Correlations HELIOS/IMP of fast-stream front passages
75 cases in 1975/76

</div>

a. Corotation time less than 6 days
   25 cases total

Correlation	No correlation	$\Delta \emptyset$ (Lat.)
22	2	$0° - 3°$
1		$5.4°$
23	2	

Accuracy of prediction:
   $2.1° \pm 5°$ solar longitude*
or 4 hr ± 10 hr*

Accuracy of prediction if radial velocities of inter-
action regions are calculated where appropriate:
   $1.0° \pm 4.6°$ solar longitude
or 2 hr ± 9 hr

b. Corotation time more than 10 days
   50 cases total

Correlation	No correlation	$\Delta \emptyset$ (Lat.)
9	2	$0° - 3°$
7	4	$3° - 6°$
3	5	$6° - 9°$
6	14	$9°$
25	25	

Accuracy of prediction:
   $3.9° \pm 7.5°$ solar longitude
or 7 hr ± 13.6 hr

* Nomenclature: Positive solar longitudes and times respectively mean
   that the stream is early at the earth relative to the prediction.

In table 1 the results are subdivided into two categories of relatively small (< 6 days) and large (> 10 days) corotation times respectively. As one should expect, the prediction accuracy is considerably better for the cases with small corotation times than for the other group. It is not clear, however, whether the decrease of prediction accuracy with larger separations in heliographic longitude is mainly due to temporary changes in the corona (which must be expected to play a more important role when the observations are further apart in time) or whether the separation in heliographic latitude which was naturally larger on the average for the group with larger separations in longitude played the dominant role. The increase with increasing latitudinal separation of the relative number of cases without correlation between IMP and HELIOS observations indicates that the latitudinal separation of observations limits the possibility of predictions much more than the separation in longitude does. A more extensive study in which we try to include correction terms (as in equ. (4)) for latitudinal differences and take into account changes in the corona as derived from coronograph observations is presently under way.

4.   ACKNOWLEDGEMENTS

5.   REFERENCES

BARTELS, J., 1948, "Erdmagnetismus II: Zeitliche Variationen, Beziehungen zur Sonnenphysik, zum Polarlicht, zur Ionosphäre", In: Naturforsch. u. Medizin in Deutschland 1939-1946, 17, 39-91, hg. J. Bartels, Wiesbaden.

NEUGEBAUER, M. and C.W. SNYDER, 1966, "Mariner 2 observations of the solar wind, 1, average properties", J. Geophys. Res. 71, 4469-4484.

SCHWENN, R., M.D. MONTGOMERY, H. ROSENBAUER, H. MIGGENRIEDER, K.H. MÜHLHÄUSER, S.J. BAME, W.C. FELDMAN, and R.T. HANSEN, 1978, "Direct observation of the latitudinal extent of a high speed stream in the solar wind", J. Geophys. Res. 83, 1011.

SHEELEY, N.J., Jr., J.R. ASBRIDGE, S.J. BAME and J.W. HARVEY, 1977, "A pictorial comparison of interplanetary magnetic field polarity, solar wind speed, and geomagnetic disturbance index during the sunspot cycle", Solar Phys. 52, 485-495.

SNYDER, C.W., M. NEUGEBAUER, and U.R. RAO, 1963, "The solar wind velocity and its correlation with cosmic-ray variations and with solar and geomagnetic activity", J. Geophys. Res. 68, 6361-6370.
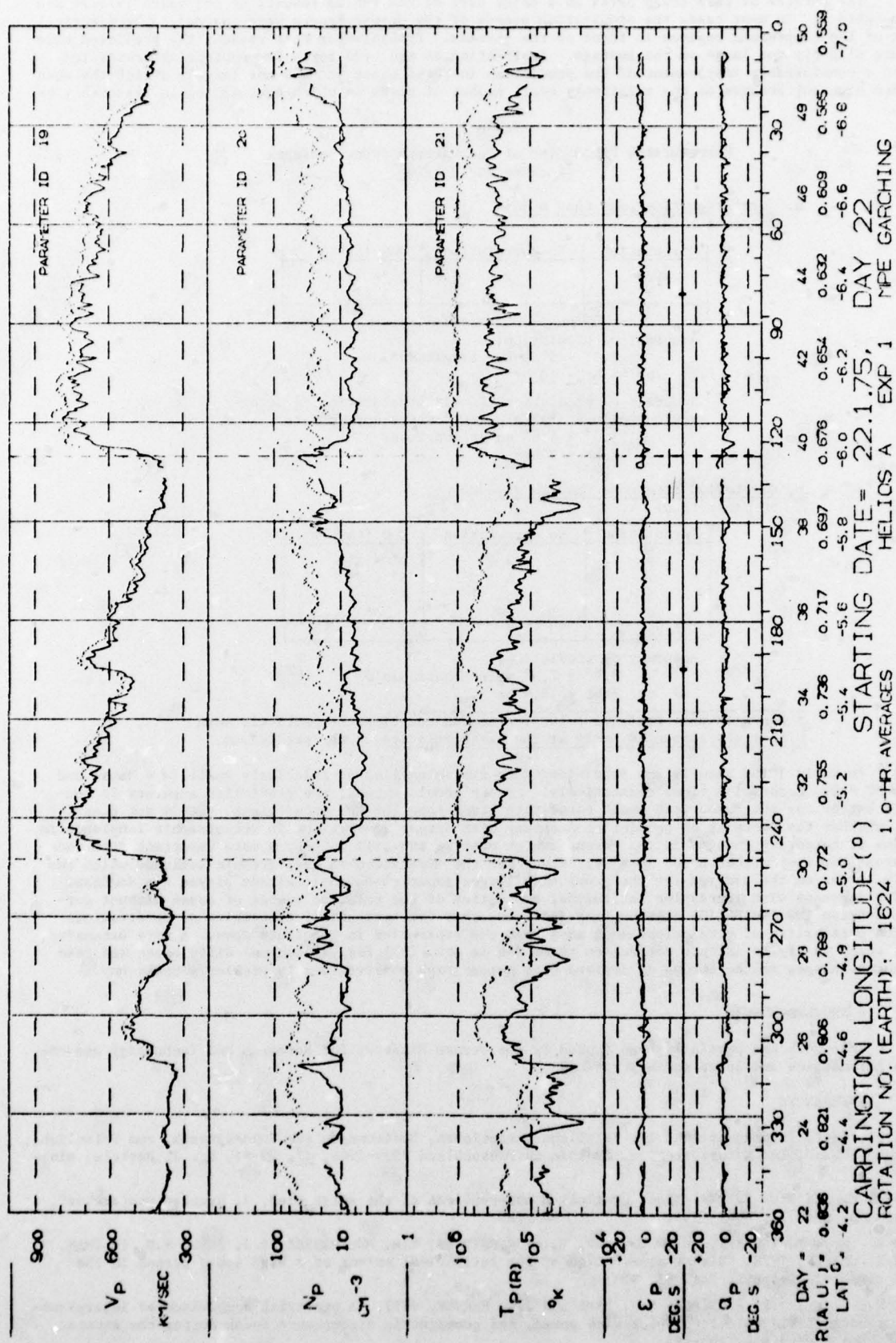
Figure 1

DISCUSSION

E.C.Roelof, US

Some of our recent work confirms Dr Rosenbauer's deductions concerning three-dimensional solar wind structure. Nolte, et al. (Solar Physics -, -, 1977) demonstrated the necessity for 3D structure in coronal source of high high-speed streams. D.G.Mitchell, E.C.Roelof and J.H.Wolfe (J. Geophys, Res., Submitted, 1978) have compared Pioneer 10 and 11 solar wind structure with that at 1AU and found many cases of latitude structure which correlate well with the shape and orientation of open magnetic field region in the low corona.

Author's Reply

None

B104

4

AGARD
NATO ⊕ OTAN
7 RUE ANCELLE · 92200 NEUILLY-SUR-SEINE
FRANCE
Telephone 745.08.10 · Telex 610176

DISTRIBUTION OF UNCLASSIFIED
AGARD PUBLICATIONS

AGARD does NOT hold stocks of AGARD publications at the above address for general distribution. Initial distribution of AGARD publications is made to AGARD Member Nations through the following National Distribution Centres. Further copies are sometimes available from these Centres, but if not may be purchased in Microfiche or Photocopy form from the Purchase Agencies listed below.

NATIONAL DISTRIBUTION CENTRES

BELGIUM
Coordonnateur AGARD – VSL
Etat-Major de la Force Aérienne
Quartier Reine Elisabeth
Rue d'Evere, 1140 Bruxelles

CANADA
Defence Scientific Information Service
Department of National Defence
Ottawa, Ontario K1A OZ2

DENMARK
Danish Defence Research Board
Østerbrogades Kaserne
Copenhagen Ø

FRANCE
O.N.E.R.A. (Direction)
29 Avenue de la Division Leclerc
92 Châtillon sous Bagneux

GERMANY
Zentralstelle für Luft- und Raumfahrt-
dokumentation und -information
c/o Fachinformationszentrum Energie,
Physik, Mathematik GmbH
Kernforschungszentrum
7514 Eggenstein-Leopoldshafen 2

GREECE
Hellenic Air Force General Staff
Research and Development Directorate
Holargos, Athens, Greece

ICELAND
Director of Aviation
c/o Flugrad
Reykjavik

ITALY
Aeronautica Militare
Ufficio del Delegato Nazionale all'AGARD
3, Piazzale Adenauer
Roma/EUR

LUXEMBOURG
See Belgium

NETHERLANDS
Netherlands Delegation to AGARD
National Aerospace Laboratory, NLR
P.O. Box 126
Delft

NORWAY
Norwegian Defence Research Establishment
Main Library
P.O. Box 25
N-2007 Kjeller

PORTUGAL
Direcção do Serviço de Material
da Forca Aerea
Rua da Escola Politecnica 42
Lisboa
Attn: AGARD National Delegate

TURKEY
Department of Research and Development (ARGE)
Ministry of National Defence, Ankara

UNITED KINGDOM
Defence Research Information Centre
Station Square House
St. Mary Cray
Orpington, Kent BR5 3RE

UNITED STATES
National Aeronautics and Space Administration (NASA)
Langley Field, Virginia 23365
Attn: Report Distribution and Storage Unit

THE UNITED STATES NATIONAL DISTRIBUTION CENTRE (NASA) DOES NOT HOLD
STOCKS OF AGARD PUBLICATIONS, AND APPLICATIONS FOR COPIES SHOULD BE MADE
DIRECT TO THE NATIONAL TECHNICAL INFORMATION SERVICE (NTIS) AT THE ADDRESS BELOW.

PURCHASE AGENCIES

Microfiche or Photocopy
National Technical
Information Service (NTIS)
5285 Port Royal Road
Springfield
Virginia 22161, USA

Microfiche
Space Documentation Service
European Space Agency
10, rue Mario Nikis
75015 Paris, France

Microfiche
Technology Reports
Centre (DTI)
Station Square House
St. Mary Cray
Orpington, Kent BR5 3RF
England

Requests for microfiche or photocopies of AGARD documents should include the AGARD serial number, title, author or editor, and publication date. Requests to NTIS should include the NASA accession report number. Full bibliographical references and abstracts of AGARD publications are given in the following journals:

Scientific and Technical Aerospace Reports (STAR)
published by NASA Scientific and Technical
Information Facility
Post Office Box 8757
Baltimore/Washington International Airport
Maryland 21240, USA

Government Reports Announcements (GRA)
published by the National Technical
Information Services, Springfield
Virginia 22161, USA